UNIVERSITY OF SOUTHAMPTON
FACULTY OF PHYSICAL AND APPLIED SCIENCES
OPTOELECTRONICS RESEARCH CENTRE

Light-assisted Domain Engineering, Waveguide Fabrication, and Microstructuring of Lithium Niobate

by

Charlie YongJun Ying

Thesis for the degree of Doctor of Philosophy
October 2010

UNIVERSITY OF SOUTHAMPTON

ABSTRACT

FACULTY OF PHYSICAL AND APPLIED SCIENCES
OPTOELECTRONICS RESEARCH CENTRE

Doctor of Philosophy

LIGHT-ASSISTED DOMAIN ENGINEERING, WAVEGUIDE FABRICATION, AND MICROSTRUCTURING OF LITHIUM NIOBATE

by Charlie YongJun Ying

The thesis is focussing on the interaction of lithium niobate with UV and ultrafast laser radiation to achieve 1) ferroelectric domain inversion, 2) waveguide fabrication, and 3) surface microstructuring.

Preferential ferroelectric domain inversion has been demonstrated by ‘latent light-assisted poling’ and ‘inhibition of poling’ using ultrafast laser irradiation at 400 nm and CW highly absorbed UV radiation ($305-244$ nm) respectively. The characteristics of the resultant domains have been experimentally investigated as a function of the fabrication conditions and a theoretical model have been proposed to explain the experimental observations. UV radiation in the 305 nm to 244 nm range have been used for the fabrication of optical waveguides in lithium niobate. The waveguiding characteristics and electro-optic response of the UV written optical channel waveguides have been investigated experimentally. Inhibition of poling and post processing has been used for the fabrication of ridge waveguide structures with enhanced refractive index change. Finally, a method for the fabrication of ultra-smooth lithium niobate single crystal photonic microstructures has been proposed. The method is based on surface tension reshaping of surface microstructures which are produced by preferential poling and subsequent etching. Whispering gallery mode resonators have been fabricated and characterised here.

Contents

List of Figures

List of Tables

Declaration of Authorship

I, Charlie Ying, declare that this thesis titled, ‘Light-assisted Domain Engineering, Waveguide Fabrication, and Microstructuring of Lithium Niobate’ and the work presented in the thesis are both my own, and have been generated by me as the result of my own original research. I confirm that:

- this work was done wholly or mainly while in candidature for a research degree at this University;
- where any part of this thesis has previously been submitted for a degree or any other qualification at this University or any other institution, this has been clearly stated;
- where I have consulted the published work of others, this is always clearly attributed;
- where I have quoted from the work of others, the source is always given. With the exception of such quotations, this thesis is entirely my own work;
- I have acknowledged all main sources of help;
- where the thesis is based on work done by myself jointly with others, I have made clear exactly what was done by others and what I have contributed myself;
- parts of this work have been published as listed in Appx. A.

Signed: ______________________________

Date: ______________________________

The few among the 7 billions who cares and concerns me most
are the only evidence of my existence in the world.

C. Y. J. Ying 2010

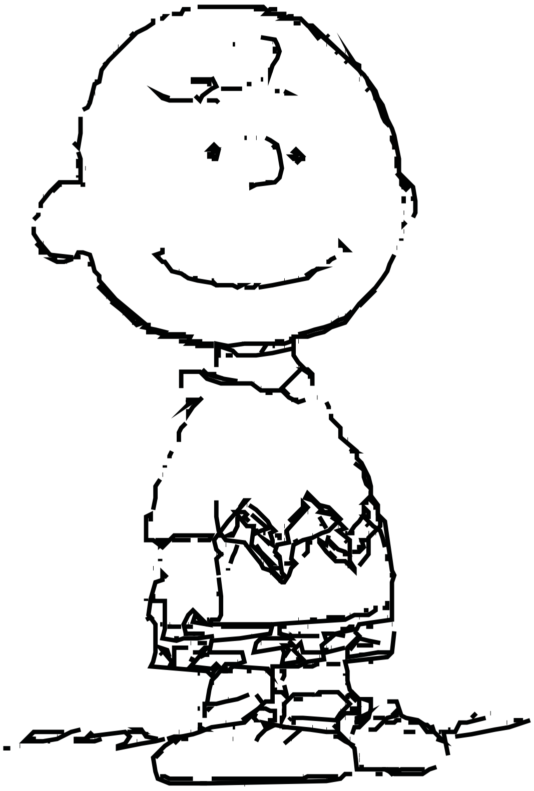

Acknowledgements

My PhD work won't be there without the help of many individuals. I would like to thank both my supervisor Dr. Sakellaris Mailis, and my co-supervisor Prof. Rob W. Eason, for all their efforts in supervising, supporting and encouraging me. I especially appreciate the concern in the first week of my arrival in UK when I was dying of pneumonia and the intense out-of-hour working in the last week when I was submitting the thesis.

Thanks the ORC colleagues: Dr. Collin Sones especially for his initial guidance of my PhD work, Dr. Pranabendu Gangopadhyay for work of the UV-written waveguides, Dr. Christopher E. Valdivia for the discussion of LLAP, code-expert Dr. Alistair Muir for the crystal heating model, Dr. Senthil Ganapathy and Prof. Mikhail Zervas for the resonator characterisation and discussion, Dr. Anna Peacock for the µm-Raman work and the comments on my PhD-plus presentation, Dr. Pier Sazio and Dr. Vasilis Apostolopoulos for the comments and feedbacks in my 9- and 15-month viva respectively, Prof. David Shepherd for the mock PhD-plus interview, Kamalpreet Kaur for lending the translation stage, ORC technician Simon Butler especially for the Christmas helps with his pneumonia, and physics clean room technician Zondy Webber for all the support of my experiments.

Thanks also the lovely Bonn collaborators: (pre-Dr.) Hendrik Steigerwald for the intensive lab work, discussion and the well preparation of my visits, Dr. Elisabeth Soergel for all the prompt PFM work and warm-hearted welcome of my visit, Prof. Boris Sturman for the discussion of the Li ion transport, Ákos Hoffmann for the support of equipments, Tobias Jungk and Florian Johann for the PFM work, and Prof. Karsten Buse for providing the UV laser, invitation of the visit, and the discussion on poling-inhibition.

Finally, thanks for the ORC Scholarship and special thanks to my family for the consistent support throughout my PhD.

Abbreviations

AC	**A**lternating **C**urrent
AFM	**A**tomic **F**orce **M**icroscope
BPVE	**B**ulk **P**hoto**V**oltaic **E**ffect
CB	**C**onduction **B**and
CCD	**C**harge **C**oupled **D**evice
CLN	**C**ongruent **L**ithium **N**iobate
CW	**C**ontinuous **W**ave
DC	**D**irect **C**urrent
DFG	**D**ifference **F**requency **G**eneration
DI	**D**e**I**onised
EFP	**E**lectric **F**ield **P**oling
EO	**E**lectro-**O**ptic
FE	**F**erro**E**lectric
FWHM	**F**ull **W**idth at **H**alf-**M**aximum
HF	**H**dro**F**luoric
IR	**I**nfra**R**ed
LAP	**L**ight-**A**ssisted **P**oling
LLAP	**L**atent **L**ight-**A**ssisted **P**oling
LN	**L**ithium **N**iobate
LT	**L**ithium **T**antalate
MEMS	**M**icro-**E**lectro-**M**echanical **S**ystems
MOES	**M**icro-**O**pto-**E**lectromechanical **S**ystems
NA	**N**umerical **A**perture
NMR	**N**uclear **M**agnetic **R**esonance
NPM	**N**on-**P**hase **M**atching

ODT	**O**ptical **D**amage **T**hreshold
OIC	**O**ptical **I**ntegrated **C**ircuit
OPG	**O**ptical **P**arametric **G**eneration
PE	**P**roton **E**xchange
PFM	**P**iezoresponse **F**orce **M**icroscopy
PI	**P**oling-**I**nhibition
PPLN	**P**eriodically **P**oled **L**ithium **N**iobate
PR	**P**hoto**R**efractive
PVE	**P**hoto**V**oltaic **E**ffect
QED	**Q**uantum **E**lectro**D**ynamics
QPM	**Q**uasi **P**hase **M**atching
SAW	**S**urface **A**coustic **W**ave
SEM	**S**canning **E**lectron **M**icroscope
SFG	**S**um **F**requency **G**eneration
SFM	**S**canning **F**orce **M**icroscopy
SHG	**S**econd **H**armonic **G**eneration
SLN	**S**toichiometric **L**ithium **N**iobate
TIR	**T**otal **I**nternal **R**eflection
UV	**U**ltra**V**iolet
VB	**V**alence **B**and
WDM	**W**avelength-**D**ivision-**M**ultiplexed
WGM	**W**hispering **G**allery **M**ode
WGR	**W**hispering **G**allery **R**esonators

Physical Constants

speed of light $c = 2.997\,924\,58 \times 10^{8}\ \mathrm{m\,s^{-1}}$

elementary charge $e = 1.602\,176\,462 \times 10^{-19}\ \mathrm{C}$

permittivity of vacuum $\epsilon_0 = 8.854\,187\,817 \times 10^{-12}\ \mathrm{F\,m^{-1}}$

permeability of vacuum $\mu_0 = 1.256\,637\,061 \times 10^{-6}\ \mathrm{N\,A^{-2}}$

Planck constant $h = 6.626\,068\,765 \times 10^{-34}\ \mathrm{J\,s}$

reduced Planck constant, $h/2\pi$ $\hbar = 1.054\,571\,596 \times 10^{-34}\ \mathrm{J\,s}$

Boltzmann constant $k_{\mathrm{B}} = 1.380\,650\,324 \times 10^{23}\ \mathrm{J\,K^{-1}}$

Symbols

Symbol	**Description**	**Unit**
α	optical intensity absorption coefficient	$\mathrm{m^{-1}}$
α_{00}	attenuation coefficient for the fundamental mode	$-$
α_{01}	modal attenuation coefficient	$-$
β	propagation constant	$\mathrm{rad\,m^{-1}}$
β	stretch factor	$-$
β_{ijk}	photovoltaic coefficients	$\mathrm{A\,W^{-1}}$
$\chi_{ij}^{(1)}, \boldsymbol{\chi}^{(1)}$	linear susceptibility coefficient	$-$
ϵ_{ij}	permittivity	$\mathrm{F\,m^{-1}}$
$\epsilon_{\mathrm{r}}, \epsilon_{\mathrm{r},ij}, \boldsymbol{\epsilon}_{\mathrm{r}}$	dielectric constant, relative permittivity	$-$
η	normalised diffraction efficiency	$-$
$\eta_{ij}, \delta\eta_{ij}$	dielectric impermeability tensor and its change	$-$
λ	wavelength of light	m
λ_0	free-space light wavelength	m
$\lambda_{\mathrm{p}}, \lambda_{\mathrm{r}}$	probe, record beam wavelength	m
Λ	photorefractive or intensity grating period	m
Λ_{g}	grating period of PPLN	m
μ_{c}	mobility of carriers	$\mathrm{m^2\,V^{-1}\,s^{-1}}$
ν	frequency of light	$\mathrm{s^{-1}}$
ω	angular frequency of AC voltage	$\mathrm{rad\,s^{-1}}$
$\omega_0, \omega_1, \omega_2$	angular frequency of light	$\mathrm{rad\,s^{-1}}$
ρ	charge density	$\mathrm{C\,m^{-3}}$
ρ	fraction of the circulating power remained	$-$
σ, σ_{ij}	stress, stress tensor	Pa

$\sigma, \sigma_{\mathrm{ph}}, \sigma_{\mathrm{d}}, \sigma_x, \sigma_z$	electrical conductivity, photo-, dark conductivity, along x, along z	$\Omega^{-1}\,\mathrm{m}^{-1}$
τ	averaged relaxation time of the stored hologram, time constant	s
τ_{e}	recombination lifetime of electrons	s
$\tau_{I\sim 0}$	$\sim$ dark decay time constant	s
τ_L	time constant	s
θ	half-angle between the two beams	$^{\circ}$
ε	stored energy in the cavity	J
$\varepsilon, \varepsilon_{kl}$	strain tensor	–
$\varepsilon_1, \varepsilon_2$	electron energy	J
$\varepsilon_{\mathrm{act}}$	activation energy	J
a_1, a_2, a_3, c	3 equivalent a-axes and 1 polar axis of hexagonal unit cell	–
A	LLAP inverted domain area	m^2
c	positive ion concentration	m^{-3}
c_{Li}	mol% of $\mathrm{Li_2O}$ in LN	–
d	thickness	m
d_{ij}	piezoelectric coefficients	$\mathrm{C\,N^{-1}}$
d_{ijk}, d_{il}	second order susceptibility coefficient	$\mathrm{m\,V^{-1}}$
D	diffusion coefficient	$\mathrm{m^2\,s^{-1}}$
D_0	pre-exponential diffusion constant	$\mathrm{m^2\,s^{-1}}$
$\hat{\mathbf{e}}$	unit vector along light polarisation	–
e_i, e_j, e_k^*	unit vector components ('*' for conjugate) of the light polarisation	–
$E, \mathbf{E}$	electric field	$\mathrm{V\,m^{-1}}$
$\mathbf{E}_{1\mathrm{i}}, \mathbf{E}_{2\mathrm{i}}, \mathbf{E}_{1\mathrm{d}}, \mathbf{E}_{2\mathrm{d}}, \mathbf{E}_{1\mathrm{t}}, \mathbf{E}_{2\mathrm{t}}$	electric field of i: incident, d: diffracted, t: transmitted light	$\mathrm{V\,m^{-1}}$
$E_{\mathrm{c}}, E_{\mathrm{cf}}, E_{\mathrm{cr}}$	coercive field, forward E_{c}, reverse E_{c}	$\mathrm{V\,m^{-1}}$
$E_{\mathrm{diff}}, \mathbf{E}_{\mathrm{diff}}$	diffusion field	$\mathrm{V\,m^{-1}}$
$E_{\mathrm{D}}, E_{\mathrm{D1}}, E_{\mathrm{D2}}$	effective defect field	$\mathrm{V\,m^{-1}}$
$\mathbf{E}_{\mathrm{ext}}$	externally applied field	$\mathrm{V\,m^{-1}}$
E_{int}	internal field	$\mathrm{V\,m^{-1}}$

E_{itrs}	intrinsic threshold coercive field	$\mathrm{V\,m^{-1}}$
E_{n}	nucleation field	$\mathrm{V\,m^{-1}}$
$E_{\mathrm{pv}}, \mathbf{E}_{\mathrm{pv}}$	photovoltaic field	$\mathrm{V\,m^{-1}}$
E_{pyro}	pyroelectric field	$\mathrm{V\,m^{-1}}$
$E_{\mathrm{sc}}, \mathbf{E}_{\mathrm{sc}}$	space-charge electric field	$\mathrm{V\,m^{-1}}$
E^{*}_{sc}	amplitude of the space-charge electric field modulation	$\mathrm{V\,m^{-1}}$
f_0	resonance frequency	$\mathrm{s^{-1}}$
δf_{FWHM}	full width at half-maximum bandwidth	$\mathrm{s^{-1}}$
F	finesse	–
F	free energy density	$\mathrm{J\,m^{-3}}$
FSR	free spectral range	m
g	rate of electron excitation	$\mathrm{m^{-3}\,s^{-1}}$,
g_0, g_2, g_4, g_6	temperature dependent constant	various
i, j	pixel numbers	–
i, j, k, l	integer variables	–
I	light intensity	$\mathrm{W\,m^{-2}}$
I_0	averaged light intensity	$\mathrm{W\,m^{-2}}$
I_{p}	probe beam intensity	$\mathrm{W\,m^{-2}}$
$I_{\mathrm{wg}}, I_{\mathrm{ref}}$	spectral output intensity of the waveguide, and a reference	$\mathrm{V\,m^{-1}}$
$\mathbf{j}$	electric current density	$\mathrm{A\,m^{-2}}$
$\mathbf{j}_{\mathrm{dft}}$	drift current density	$\mathrm{A\,m^{-2}}$
$j_{\mathrm{diff}}, \mathbf{j}_{\mathrm{diff}}$	diffusion current density	$\mathrm{A\,m^{-2}}$
$j_{\mathrm{pv}}, j_{\mathrm{pv},i}, \mathbf{j}_{\mathrm{pv}}$	photovoltaic current density	$\mathrm{A\,m^{-2}}$
δk	wavevector mismatch	$\mathrm{rad\,m^{-1}}$
$k_1, k_2, k_3, \mathbf{k}_1, \mathbf{k}_2$	wavevector of light	$\mathrm{rad\,m^{-1}}$
k_{G}	Glass constant	$\mathrm{m\,A\,W^{-1}}$
$K, \mathbf{K}$	intensity grating vector	$\mathrm{rad\,m^{-1}}$
K_{00}, K_{01}	coupling coefficients	–
K_{g}	grating vector of PPLN	$\mathrm{rad\,m^{-1}}$
l_{c}	coherent length	m
L_0	length constant	m

L_0	waveguide length	m
m	modulation index of light contrast	–
mp_1, mp_2, mp_3	mirror planes of hexagonal unit cell	–
n	refractive index	–
δn	refractive index change	–
δn_0	saturation value of the refractive-index change	–
δn_B	birefringence at domain wall	–
n_eff	effective refractive index, mode index	–
n_i, n_j	refractive index components along the $i^\mathrm{th}, j^\mathrm{th}$ axis	–
δn_max	index contrast of the waveguide	–
$n_\mathrm{o}, n_\mathrm{e}$	ordinary, extraordinary refractive index	–
$n_{\mathrm{o},\perp}, n_{\mathrm{o},\parallel}$	ordinary index n_o perpendicular and parallel to a domain wall	–
n_s	substrate refractive index	–
N	defect dipole concentration	$\mathrm{m^{-3}}$
N_c	concentration of charge carriers	$\mathrm{m^{-3}}$
$N_{\mathrm{Fe}^{3+}}, N_{\mathrm{Nb_{Li}}}$	ion concentration	$\mathrm{m^{-3}}$
N_pol	polaron concentration	$\mathrm{m^{-3}}$
p_i	pyroelectric vector coefficients	$\mathrm{C\,m^{-2}\,K^{-1}}$
p_{ijkl}	photoelastic (strain-optic) coefficient	–
P	electric polarisation	$\mathrm{C\,m^{-2}}$
δP	spontaneous polarisation change	$\mathrm{C\,m^{-2}}$
$P_\mathrm{D}, P_\mathrm{D1}, P_\mathrm{D2}$	defect electric polarisation, from $\mathrm{Nb_{Li}}$, from $\mathrm{V_{Li}}$	$\mathrm{C\,m^{-2}}$
P_s	spontaneous electric polarisation	$\mathrm{C\,m^{-2}}$
$P_{\omega_0,i}$	electron polarisation at ω_0	$\mathrm{C\,m^{-2}}$
$P^{(1)}_{\omega_0,i}, P^{(2)}_{\omega_0,i}$	linear, second order electron polarisation	$\mathrm{C\,m^{-2}}$
q	charge of the charge carrier	C
Q	Q factor	–
r	radius	m
$\mathbf{r}$	spatial coordinate	m
r_eff	effective linear electro-optic coefficient	$\mathrm{m\,V^{-1}}$
r_{ijk}, r_{il}	linear electro-optic coefficient	$\mathrm{m\,V^{-1}}$
$\overline{R}_{\mathrm{Fe}^{3+}}, \overline{R}_{\mathrm{Nb_{Li}}}$	mean distance between two ions	m

S	entropy	$\mathrm{J\,K^{-1}}$
t	time	s
t_0	characteristic time	s
t_M	Maxwell relaxation time	s
$T, \delta T$	temperature, temperature change	K
T_c	Curie temperature	K
V_ac	amplitude of the AC voltage in PFM	V
V_dc	offset voltage in PFM	V
V_m	mode volume	$\mathrm{m\,V^2}$
V_tip	voltage applied on the PFM tip	V
$\delta w^+, \delta w^-$	stabilisation energy from each defect dipole	J
x, y, z	Cartesian axes	m
$\delta x, \delta z$	grid spacing resolution	m
x, z	lateral, depth dimension	m
x_1, x_2, x_3	Cartesian axes	m
$\delta z(\mathrm{Nb}), \delta z(\mathrm{Li})$	displacement of ions from centre position of oxygen octahedra	m

Synopsis

While optical telecommunication has experienced rapid development in recent years enabling extremely high transmission capacity (> 10 Tbit/s), the processing capability however remains limited by the relatively low-capacity current electronic systems. Faster, all optical processing is therefore required in order to improve the performance of optical telecommunication networks of the future. Additionally, as the merits of photonic devices are now well recognised by the industry there is an increasing demand for multi-functionality and dense integration of photonic devices.

Lithium niobate is an optical ferroelectric crystal which is already an industrial standard having found numerous applications in modern day photonics. This material could provide innovative solutions for the demands of modern day information handling due to its wide range of useful physical and optical properties. This thesis represents a step towards the identification of flexible processing methods for the domain engineering, waveguide fabrication, and microstructuring of lithium niobate to enable the fabrication of advanced densely integrated photonic devices.

Chap. 1 contains an introduction to ferroelectric lithium niobate crystals. The basic properties of ferroelectric materials are outlined here: ferroelectric phase transitions and Landau theory for the free energy density. The physical and optical properties of lithium niobate single crystals which are relevant to this thesis are also reviewed. The introductory chapter finally contains 1) a description of ferroelectric domain inversion in lithium niobate, 2) an outline of the available domain engineering methods, some of which are the subject of this thesis, and 3) the relevant domain visualisation methods.

Chap. 2 discusses the technique of 'latent light-assisted poling' of undoped congruent lithium niobate (CLN). Experimental data on the relaxation of the nucleation field following irradiation with ultrafast laser at 400 nm are presented here. The sizes of the resultant domains were investigated as a function of 1) intensity of laser illumination, 2) the magnitude of the applied electric field, and 3) the delay time between illumination and EFP. Finally, the latent light-assisted poling dynamics were compared with the decay dynamics of photorefractive gratings to identify the role of the photo-induced space charge distribution in the light-assisted poling process.

Chap. 3 presents the UV laser-induced inhibition of poling in LN crystals. UV laser irradiation of the $+z$ polar surface of the crystal results in local suppression of poling during a subsequent electric field poling step. The range of UV laser wavelengths used was: 244 nm to 305 nm. The resulting poling-inhibited domains have been investigated as a function of the fabrication conditions. A theoretical model based on the migration of lithium ions under the influence of the steep temperature gradients (due to UV absorption) and the resultant pyroelectric field has been developed to explain the experimental observations.

Chap. 4 contains an investigation of UV laser-induced refractive index changes in CLN crystals and its application for the fabrication of optical channel waveguides. The waveguiding characteristics and the electro-optic response of the UV written waveguides was investigated as a function of the fabrication conditions for waveguides written with UV wavelengths ranging from 244 nm to 305 nm. The mode index and the maximum refractive index change were deduced by analysing the mode intensity profiles. Finally, inhibition of poling was used to overlay an inverted domain with the waveguide structure in order to fabricate ridge waveguide structures after further processing with chemical etching. The poling inhibition step resulted in a further increase of the refractive index change in the waveguides improving their performance.

Chap. 5 presents a method for the fabrication of ultra-smooth single crystal microstructures out of CLN crystals. The method is based on surface tension reshaping as a result of preferential surface melting of the crystal at temperatures close to but lower than the melting temperature of the crystal. Successful fabrication of whispering gallery mode (WGM) micro-resonators has been achieved by the surface tension reshaping of deeply etched domain-engineered microstructures. The fabrication procedures and some initial results of optical coupling experiments are presented here.

Finally, Chap. 6 contains a summary of suggestions for future work which is based on this thesis. The Appx. A lists the related published papers emanating from this work.

1

Introduction

1.1 Lithium niobate ($LiNbO_3$)

Crystalline lithium niobate (LN, $LiNbO_3$) is an artificial dielectric crystal, first synthesised and described in 1928 [Zachariasen 28], then reported to be ferroelectric in 1949 [Matthias 49]. The interest in LN increased since 1965 when application of the Czochralski technique for growth of large single crystals with good homogeneity was reported [Ballman 65, Fedulov 65], followed by a series of papers from Bell Laboratories that first thoroughly established the basic properties of LN [Nassau 66a, Nassau 66b, Abrahams 66b, Abrahams 66c, Abrahams 66a]. With its numerous properties [Weis 85] (electrooptic, piezoelectric, acoustooptic, photorefractive, pyroelectric, photovoltaic, ferroelectric, and optical nonlinearity), LN has been exploited for applications in many areas. The development has been rapid resulting in almost a thousand publications and tons of crystal grown each year. A number of books have been comprehensively compiled LN's properties and processing [Wong 89, Volk 08a, Prokhorov 90, Kuz‘minov 97]. This chapter mainly summarises the physical and optical properties of LN, particularly with respect to fabrication and characterisation details, and also the domain engineering of LN which is one of the main focuses of this PhD work.

1.2 Ferroelectrics

Ferroelectrics, as defined by Lines and Glass [Lines 77], are substances which, in a certain range of temperatures and isotropic pressures in the absence of an external electric field, have a built-in spontaneous electric polarisation P_s with unit $\mathrm{C\,m^{-2}}$, that has two or more orientational states and can be switched from one state to the other by an external electric field.

Any two of the orientational states of ferroelectrics are identical in their crystal structure and differ only in the direction of the electric polarisation vector. Regions with uniform polarisation in a ferroelectric are called *ferroelectric domains*. A ferroelectric may comprise many such regions, in which case it is said to have a multi-domain structure, or alternatively it can exist in a single domain state. The plane that separates two domain regions is called *domain wall*.

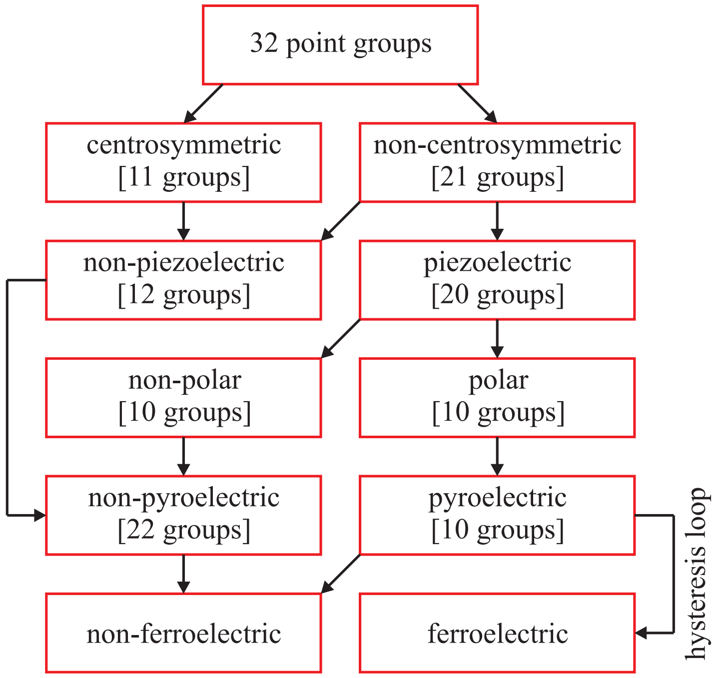

FIGURE 1.1: Classification of piezoelectric, pyroelectric and ferroelectric properties in 32 point groups. Replotted from [Gupta 07].

In general, as indicated in Fig. 1.1 of the schematic tree of the 32 classes in crystal systems [Gupta 07], all ferroelectric materials in their ferroelectric phase are pyroelectric, piezoelectric, and non-centrosymmetric (e.g., lack a center of inversion symmetry). The lack of inversion symmetry endows ferroelectrics with possible nonlinear optical responses that are odd-rank polar tensor properties (e.g., 3^{rd} rank: linear electro-optic effect r_{ijk} and sum/difference frequency generation d_{ijk}).

Ferroelectricy can be experimentally determined usually through the measurements of the hysteresis loop. A *ferroelectric hysteresis loop* $P(E)$ is a measurement of the average spontaneous polarisation in a material as a function of the applied E-field. It originates from the energy required to move the domain walls between domains of different polarisations and then change the net polarisation of the ferroelectric material by altering the size of various domains [Elliott 98]. A typical hysteresis loop of congruent LN is shown in Fig. 1.2 [Gopalan 97]. It shows that the spontaneous polarisation $-P_{\mathrm{s}}$ or $+P_{\mathrm{s}}$ is only eliminated by applying a forward E_{cf} or reverse E_{cr} respectively, both referred to as the *coercive field* E_{c}, at which the ferroelectric has precisely half the switchable ferroelectric dipoles pointing in the direction of the applied field, corresponding

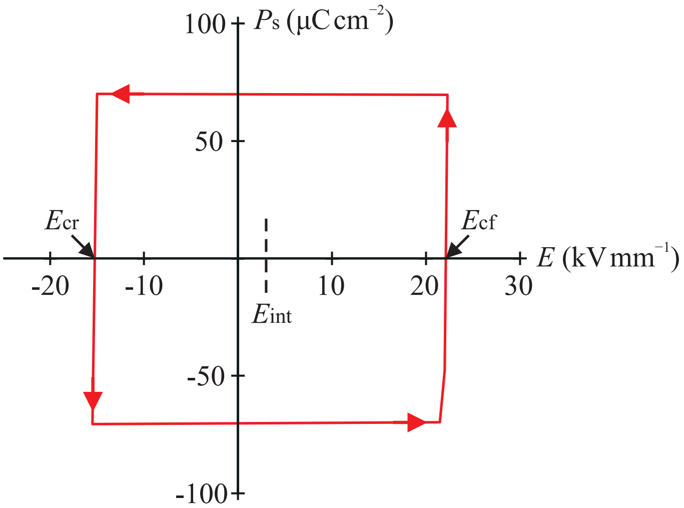

FIGURE 1.2: Hysteresis loops (spontaneous polarisation P_s versus applied E-field) of congruent LN replotted from [Gopalan 97]. (E_{cf}, E_{cr}: forward, reverse coercive field; E_{int} = internal field.)

to the point where the net polarisation is zero. A further increase of the field magnitude reverses the polarisation to $+P_s$ or $-P_s$ respectively.

Among all the ferroelectrics, LN has received intense attention due to its high value of P_s and Curie temperature T_c as shown in Table 1.1 of a comparison with other ferroelectrics. The high value of P_s endows LN with large nonlinear optical coefficients while the high T_c ensures the high thermal stability of the crystal.

TABLE 1.1: Comparison of the spontaneous polarisation P_s, Curie temperature T_c, and largest nonlinear coefficient d_{max} for some common ferroelectrics [Lines 77].

Crystal	P_s (µC cm^{-2})	T_c (°C)	d_{max} (pm V^{-1})
Lithium Niobate	71	1210	$d_{33} = -33$
Lithium Tantalate	50	665	$d_{33} = -21$
Barium Titanate	26	135	$d_{31} = 19$
Potassium Titanyl Phosphate (KTP)	20	936	$d_{33} = 13.7$
Potassium Dihydrogen Phosphate (KDP)	4.8	-150	$d_{36} = 0.43$
Rochelle Salt	0.5	24	–

1.2.1 Ferroelectric phase transitions and Landau theory

As the temperature is increased above the Curie temperature T_c [Lines 77], a ferroelectric undergoes a phase transition from the ferroelectric state to a non-polarised paraelectric state, characterised by a symmetric ionic configuration which effectively eliminates the internal dipole moment, and therefore the spontaneous polarisation. It arises microscopically because as temperature is raised the thermal vibrations of the atoms in the solid cause fluctuations which overcome the potential barrier between the two (or more) wells. When the crystal is cooled through T_c, elastic restoring forces return the crystal structure to the ferroelectric phase, so that the centers of positive and negative charge within the unit cell no longer coincide. Hence, the higher symmetry of the paraelectric phase is lost and the P_s recovered. As the crystal continues to cool down from T_c, further distortion of the unit cell increases the charge separation, and hence the values for P_s. Phase transitions can be classified as first or second order transitions: if the phase transition is continuous in terms of order parameter (spontaneous polarisation P_s), it is a second order phase transition, otherwise, if discontinuous, it is then a first order phase transition.

Macroscopic theory, *Landau theory*, provides a useful description of ferroelectric phase transitions. Any crystal in a thermodynamic equilibrium state can be completely specified by the values of a number of variables, e.g., temperature T, entropy S, E-field E, polarisation P, stress σ, and strain ε. Usually external E-fields E and/or elastic stresses σ is applied, the polarisation and strain are regarded as 'internal' or dependent variables. The Landau free energy density, F, of a ferroelectric can be expressed as a power series of the spontaneous polarisation value P as [Kittel 04]

$$F(P;T,E) = -EP + g_0 + \frac{1}{2}g_2P^2 + \frac{1}{4}g_4P^4 + \frac{1}{6}g_6P^6 + \cdots \tag{1.1}$$

where g_0 is a temperature-dependent constant; $g_4, g_6 > 0$ for ferroelectrics with second-order (continuous) phase transition such as for LN; and $g_2(T)$ varies linearly with temperature as $g_2(T) = \gamma(T - T_\mathrm{c})$ with $\gamma > 0$. It can be seen in Fig. 1.3(a) that if $T > T_\mathrm{c}$, then $g_2(T) > 0$, and the free energy density F has a minimum at the origin − non-polar paraelectric phase, while on the other hand, if $T < T_\mathrm{c}$, then $g_2(T) < 0$, the free energy density F has a minimum at a finite polarisation P. Here, the ground state has a spontaneous polarisation and thus is a ferroelectric. Also as can be seen in Fig. 1.3(a) the polarisation goes to zero with increasing temperature

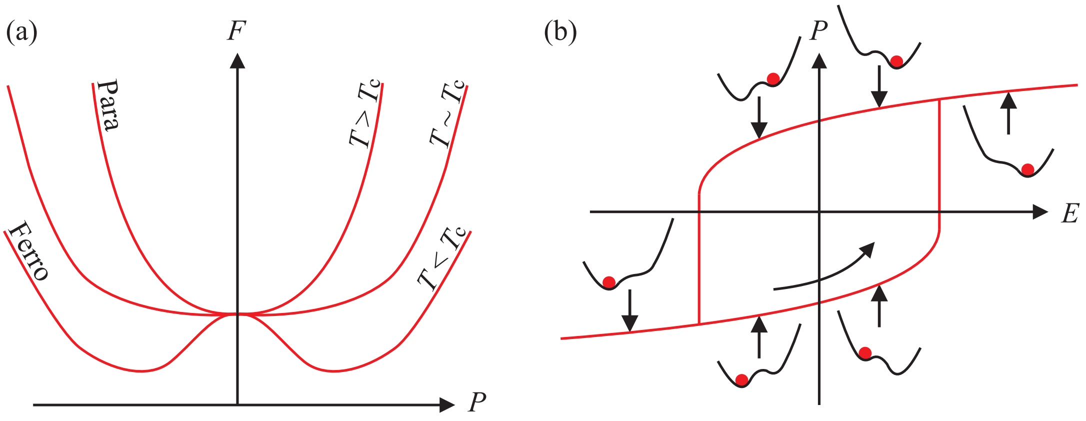

FIGURE 1.3: (a): the Landau free energy density F as a function of polarisation and temperature for a second order phase transition. (b): the hysteresis loop and the schematic pictures of the tilted F vs. P upon applying an external E-field E in an idealised ferroelectric; the red spots indicate the position of polarisation.

in a continuous fashion (second-order phase transition). Upon applying an E-field E, the two stable states no longer have the same energy due to the electric polarisation energy $-EP$. The potential wells are tilted by the E-field as shown in Fig. 1.3(b). It is also clear that a small field will not necessarily immediately switch the polarisation from one direction to the other because there is a barrier to be overcome, therefore leading to the hysteresis loop.

1.3 Crystal structure

As many optical or physical properties of LN are closely related to its lattice symmetry. The crystal structure of LN will be discussed first. The majority of material which is commercially available today is grown using the Czochralski method and is lithium deficient. The nonstoichiometry of the congruent material, as it is called, leads to a specific defect structure which will be discussed here as well.

1.3.1 LN crystal structure

In the ferroelectric (FE) phase, the crystal family or crystal system of LN is trigonal, meaning that it has one threefold axis of rotation, defined as the polar axis, or c-axis. With the addition of 3 mirror planes that are 60° apart and intersect at the polar axis, it is categorised as belonging to the crystal class (point group) C3v in the Schönflies notation or 3m in the Hermann-Mauguin notation [Lines 77]. Within the C3v point group, it belongs to the R3c space group [Abrahams 66c]. Fig. 1.4 illustrates three mirror planes, mp_1, mp_2 and mp_3 and the c-axis by depicting a hexagonal unit cell of LN (without oxygen planes for clarity). For a hexagonal unit cell, the $+c$ axis is defined as being directed out of the c face that becomes negatively charged upon compression [Committe 49], while the three equivalent a-axes (a_1, a_2, a_3) are 120° apart and lie in a plane normal to the c-axis. According to the adopted convention, these axes are chosen to be perpendicular to the mirror planes of symmetry [Committe 49]. The coordinate system used to describe the physical tensor properties of trigonal LN is however a Cartesian crystallographic x, y, z system. Fig. 1.4 also illustrates the standard convention for choosing the principal axes within the hexagonal unit cell in LN [Nye 87a, Weis 85]: 1) the z-axis is chosen to be parallel to the c-axis, also known as the *optic axis*, 2) the x-axis is chosen to coincide with any of the equivalent a-axes, a_1, a_2, or a_3, and then 3) the y-axis is chosen such that the system of x-, y-, z-axes is right handed (therefore lie in a plane of mirror symmetry). When working with tensors the x, y, z principal axes are often referred to as the x_1, x_2, and x_3 axes, respectively.

LN is also called an oxygen octahedra ferroelectric [Gopalan 07] as the crystal structure consists of a sequence of close-packed, face sharing, oxygen octahedra stacked along the polar axis as shown in Fig. 1.5(b) of a LN unit cell. The oxygen octahedra are filled along the positive polar

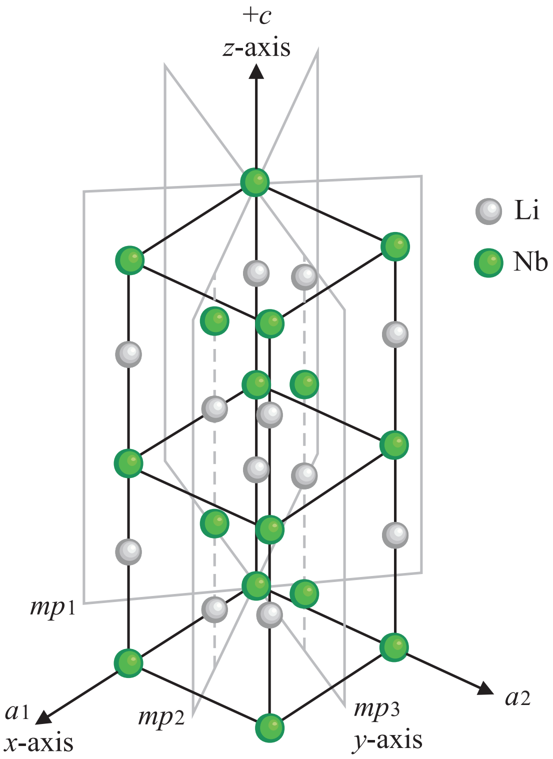

FIGURE 1.4: Hexagonal unit cell of LN indicating the 1) polar c-axis, 2) mirror planes mp_1, mp_2, mp_3, 3) a-axes a_1, a_2, a_3, and 4) the corresponding Cartesian x-, y-, z-axis.

direction, $+c$ direction (for perfect crystal structuring) in the following order [Abrahams 66c]: lithium, niobium, vacancy, $\cdots$ All the oxygen octahedra in LN are distorted and their stacking of the oxygen octahedra is in a screw-like manner [Prokhorov 90]. Fig. 1.5(a) shows the detailed oxygen arrangement around the central metal ions for each of the six layers. It shows that the oxygen atoms do not form columns parallel to the trigonal axis but instead are staggered [Abrahams 66c]. Two formulae units of LN form one unit cell because of staggered oxygens that repeat after two consecutive operations of the c-glide symmetry [Gopalan 07] as indicated in Fig. 1.5(b).

Fig. 1.5(c) is drawn perpendicular to the close-packed oxygen planes with these planes indicated by several horizontal straight lines. The near-neighbour Li and Nb atoms are each displaced slightly away from the octahedra centres (dashed lines) along the c-axis which is known from X-ray and neutron structure determination and also indicated in Fig. 1.5(c): $\delta z(\mathrm{Nb}) = 0.258$ Å and $\delta z(\mathrm{Li}) = 0.690$ Å [Abrahams 66a], with each oxygen layer separation of 2.310 Å [Prokhorov 90]. It is the ordered displacement of the cations from the symmetry positions which gives rise to a permanent dipole moment in the crystals, and the energy barriers for ionic movement that gives rise to the room temperature stability of this spontaneous polarisation. Each neighbouring Li-Nb pair, acts as individual dipoles which can all be aligned either ‘up’ or ‘down’ giving rise to two possible domain orientations.

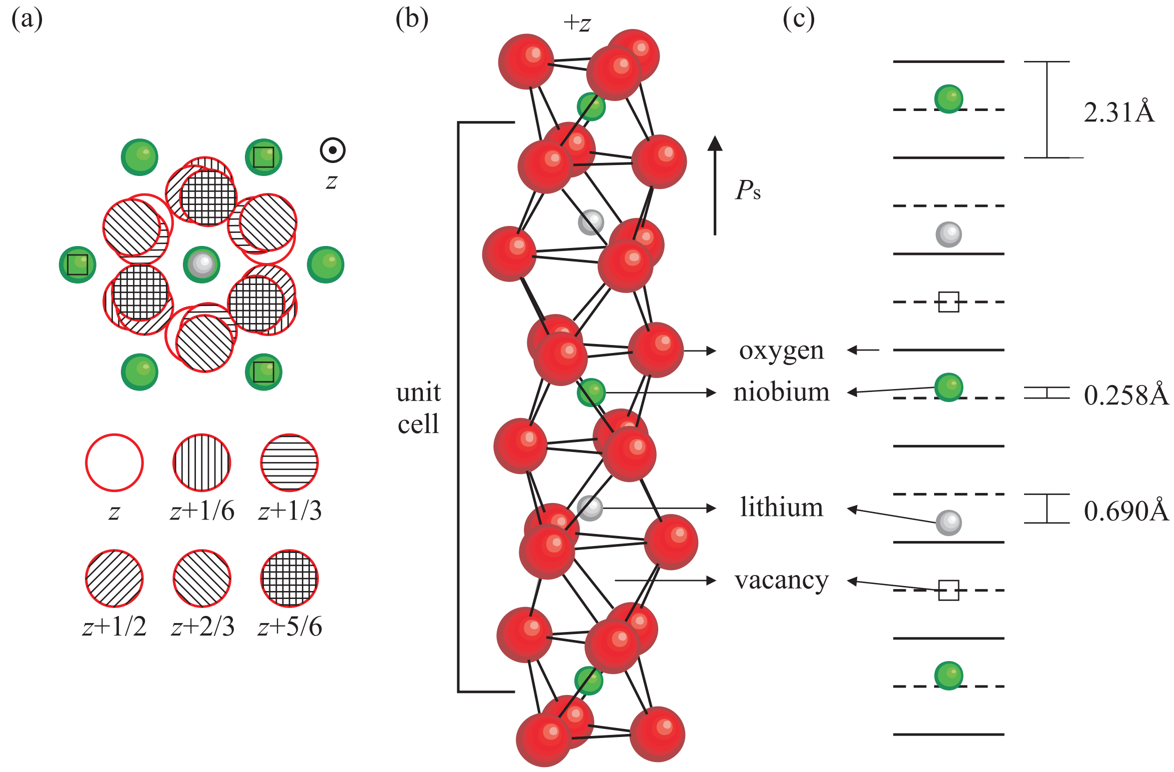

FIGURE 1.5: (b): the crystal structure of LN unit cell replotted from [Gopalan 07]. (a): the relative arrangement of O atoms about the Li and Nb atoms in LN corresponding to the sequence of the unit cell replotted from [Prokhorov 90]. (c): the relative positions of the Li and Nb atoms in relation to the O planes represented by the black lines. The dashed lines represent the center plane between two O planes.

1.3.2 Defect model for congruent LN

The nominal congruent composition of 48.45 mol% Li_2O and 51.55 mol% Nb_2O_5 [O'Bryan 85], at which LN single crystals grow from the melt with uniform composition, necessarily corresponds to the presence of excess Nb atoms and empty Li sites in the crystal lattice that leads to the formation of defects in the structure. Several different intrinsic defect models of congruent LN (CLN) have been proposed in the literature with some disagreement as to the precise nature of this defect structure. They have been reviewed in detail in [Rauber 78, Schirmer 91]. The three intrinsic (structure) charge-balanced defect models in congruent LN include (1: [Prokhorov 90]; 2: [Schirmer 91, Abrahams 86]; 3: [Lerner 68, Iyi 92, Zotov 94]):

1. $[Li_{0.944}\square_{0.056}]Nb[O_{2.972}\square_{0.028}]$: lithium vacancies $(V_{Li})^{-}$ and oxygen vacancies $(V_O)^{2+}$
2. $[Li_{0.951}Nb_{0.049}][Nb_{0.961}\square_{0.039}]O_3$: niobium antisites $(Nb_{Li})^{4+}$ and niobium vacancies $(V_{Nb})^{5-}$
3. $[Li_{0.95}\square_{0.04}Nb_{0.01}]NbO_3$: niobium antisites $(Nb_{Li})^{4+}$ and lithium vacancies $(V_{Li})^{-}$

The relative merits of each model have been discussed in [Kim 01]. Despite these differing models, defect model 3, Li site vacancy model, is commonly accepted as valid and considerations of all defect reconstructions in LN are discussed in its framework. According to precise data from X-ray and neutron diffraction [Iyi 92] only 1% of the Li sites are occupied by Nb, whereas about 4% of the Li sites are empty (Li vacancies). This existence of a high concentration of Li vacancies in CLN was confirmed by other structure reports [Wilkinson 93, Zotov 94, Zotov 95] and nuclear magnetic resonance (NMR) studies [Blumel 94]. It was proposed in [Ivanova 98, Yatsenko 97] that the bulk non-stoichiometric dipolar defect complex in LN is composed of a $\mathrm{Nb_{Li}}$ surrounded by three $\mathrm{V_{Li}}$ in the nearest neighborhood, plus one independent $\mathrm{V_{Li}}$ along the polar z direction. Thus, the nonstoichiometry is not randomly distributed but organised as defect clusters. These defect clusters can themselves possess a defect polarisation P_{D} that is different from the lattice polarisation P_{s}. This defect model is also supported by X-ray and neutron diffuse scattering of CLN [Zhdanov 78, Zotov 95, Ivanov 78]. Then the basic concept of bulk dipolar defect clusters was used to explain domain stabilisation and internal fields in ferroelectrics [Arlt 88, Lambeck 77, Warren 96, Kim 01]. Some of the conclusions will be summarised here.

The relative stabilities of various defect cluster arrangements of $\mathrm{V_{Li}}$ around a $\mathrm{Nb_{Li}}$ have been determined using density functional theory combined with thermodynamic calculations [Xu 10]. Fig. 1.6(b) depicts the stable defect state of one such defect cluster for an up domain in CLN proposed in [Kim 01]. A stoichiometric lithium niobate (SLN) unit cell in Fig. 1.6(a) is shown in comparison to the proposed stable defect states at room temperature. The defect state in (b) is achieved by slowly cooling the crystal in a single-domain state from high temperature such that the point defects (especially Li vacancies) have enough ionic mobility to form and then freeze into such stable defect clusters at room temperature. The defect complex shown in Fig. 1.6(b) certainly possesses an electrical dipole moment arising primarily along the z-axis. It has two contributions: 1) P_{D1} from the $\mathrm{Nb_{Li}}$ antisite defect, and 2) P_{D2} from the relative arrangement of the $\mathrm{V_{Li}}$ around a $\mathrm{Nb_{Li}}$. In a stable defect state, the two defect polarisation components are assumed to be parallel to the lattice polarisation P_{s} as indicated in Fig. 1.6(b).

Upon applying an E-field for domain reversal, $\mathrm{Nb_{Nb}}$ moves to the opposite point of the asymmetric position in its octahedron, $\mathrm{Li_{Li}}$ and $\mathrm{Nb_{Li}}$ pass through the oxygen plane to the adjacent vacant octahedron, while $\mathrm{V_{Li}}$ remains at the same position due to the low ionic mobility of Li at room temperature. Therefore, while the polarisation component of P_{D1} from the $\mathrm{Nb_{Li}}$ antisite defect has been reversed with spontaneous polarisation P_{s}, that of P_{D2} from the $\mathrm{V_{Li}}$ remains uninverted: the stable defect clusters in Fig. 1.6(b) (with $+P_{\mathrm{s}}$, $+P_{\mathrm{D1}}$, $+P_{\mathrm{D2}}$) are domain reversed and result in a domain state with *frustrated defects* as shown in Fig. 1.6(c) (with $-P_{\mathrm{s}}$, $-P_{\mathrm{D1}}$, $+P_{\mathrm{D2}}$).

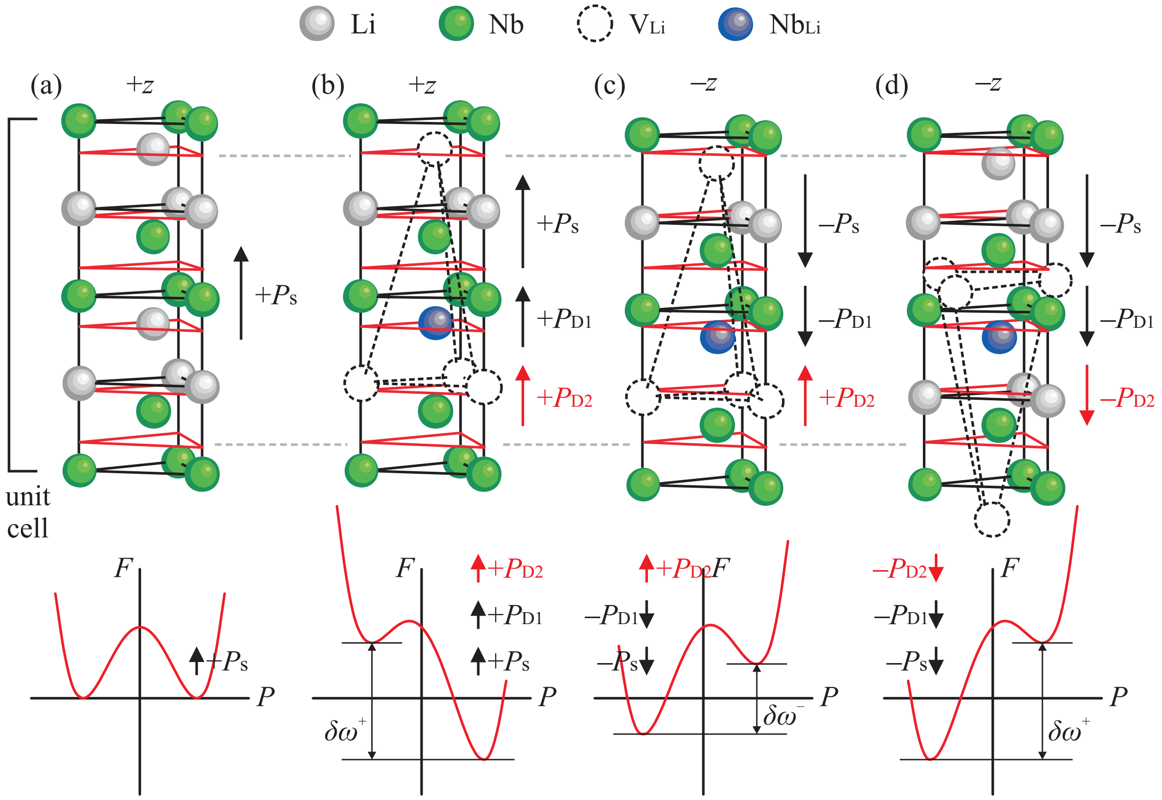

Figure 1.6: Schematics of a possible defect complex involving $\mathrm{Nb_{Li}}$ and $\mathrm{V_{Li}}$ with its corresponding free energy density vs. polarisation at the bottom, replotted from [Gopalan 07]. (a): a stoichiometric crystal with no defects. (b): a defect dipole complex in its low-energy configuration. Upon polarisation reversal, state b become state c in which the dipole is in a frustrated state. State c will relax to state d after annealing at $> 150°\mathrm{C}$, which allows diffusion of $\mathrm{V_{Li}}$. The defect polarisation P_{D1} and P_{D2} shown in (b-d) are from the $\mathrm{Nb_{Li}}$ antisite defect and from the relative arrangement of the $\mathrm{V_{Li}}$ around a $\mathrm{Nb_{Li}}$ respectively. The oxygen planes are represented by red triangles.

The frustrated state is not stable. However, by heating above 150°C, Li ions are activated [Gopalan 00, Bergmann 68] and therefore Li vacancies can be rearranged according to the inverted lattice and lead to the energy-favourable stable state of a down domain in Fig. 1.6(d).

The energy diagram at the bottom of Fig. 1.6(b-d) represents the free energy density of the lattice polarisation, including the interaction energy resulting from the interaction between defect polarisation (P_{D1}, P_{D2}) and bulk lattice polarisation (P_{s}) to the total lattice energy. For a first order ferroelectric phase transition, the free energy density F in a ferroelectric state can be modified from Eq. 1.2 as shown in [Cross 87]

$$F(P;T,E) = -EP + g_0 - \frac{1}{2}|g_2|P^2 + \frac{1}{4}|g_4|P^4 - E_{\mathrm{D}}P \tag{1.2}$$

where E_{D} is the effective defect field. Note that the above equation is applicable near the spontaneous lattice polarisation $+/-P_{\mathrm{s}}$ states at the minimum energy only. Comparing the free energy density of a stable defect in Fig. 1.6(b) to that in (a) of a perfect lattice, the $+P_{\mathrm{s}}$ lattice polarisation state (indicated by $\uparrow$) is stabilised by the defect polarisation by an amount of δw^+ per defect dipole with respect to the $-P_{\mathrm{s}}$ state. If all the defect dipoles are aligned parallel to the $+P_{\mathrm{s}}$ direction in Fig. 1.6(b), then the magnitude of the defect field E_{D} for the stable state in (b), which also has two components E_{D1} and E_{D2} corresponding to the two of defect polarisations, is given by [Arlt 88]

$$E_{\mathrm{D1}} + E_{\mathrm{D2}} = E_{\mathrm{D}}(\mathrm{stable}) = \frac{N\delta w^+}{2P_{\mathrm{s}}} \tag{1.3}$$

where N is total number of defect dipoles per unit volume. Similar approach can be applied for the frustrated state in Fig. 1.6(c) so that

$$E_{\mathrm{D1}} - E_{\mathrm{D2}} = E_{\mathrm{D}}(\mathrm{frustrated}) = \frac{N\delta w^-}{2P_{\mathrm{s}}} \tag{1.4}$$

'$-$' is applied in Eq. 1.4 as the two components of defect polarisation, $-P_{\mathrm{D1}}$ and $+P_{\mathrm{D2}}$, are in opposite direction as shown in Fig. 1.6(c). Note that the effective defect fields E_{D} of stable and frustrated states in Eq. 1.3 and 1.4 are not equal, a direct consequence of the uninverted frustrated defect dipole component $+P_{\mathrm{D2}}$ related to $\mathrm{V_{Li}}$ in Fig. 1.6(b,c). The threshold coercive field E_{c} can be written as $E_{\mathrm{c}} = E_{\mathrm{D}} + E_{\mathrm{itrs}}$, where $E_{\mathrm{itrs}} \sim [F(0) - F(P_{\mathrm{s}})]/P_{\mathrm{s}}$ deduced from Eq. 1.2 is the intrinsic threshold coercive field of exactly stoichiometric LN with no defects present. Thus, it can be expected and experimentally observed that reversal back from state in Fig. 1.6(c) to that in (b), called reverse poling, requires a different coercive field of E_{cr} due to the different value of E_{D} in Eq. 1.4 compared to that in Eq. 1.3 for forward poling. Thus, this difference between the two coercive fields reflects an internal field $E_{\mathrm{int}} \sim (E_{\mathrm{cf}} - E_{\mathrm{cr}})/2$ as the offset in the hysteresis loop in Fig. 1.2. Assuming that the magnitude of the intrinsic threshold coercive field, E_{itrs}, does not change between domain state in Fig. 1.6(b) and (c), the internal field E_{int}, can be deduced from Eq. 1.3 and 1.4 as [Gopalan 07, Kim 01]

$$E_{\mathrm{int}} = E_{\mathrm{D2}} \approx \frac{N(\delta w^+ - \delta w^-)}{4P_{\mathrm{s}}} \tag{1.5}$$

It reveals that the internal field E_{int} is actually the effective defect field E_{D2}, originating from the $\mathrm{V_{Li}}$-related uninverted frustrated defect dipole component $+P_{\mathrm{D2}}$, and the magnitude of E_{int} clearly depends linearly on the density of defect dipoles which is experimentally observed [Gopalan 00]. Some experimental studies suggested that the effect of the nonstoichiometric defect clusters, especially surface $\mathrm{Nb_{Li}}$ [Yan 06], leads to the coercive field by enhancing the pinning of domain wall motion [Kim 01]. Macroscale domain nucleation and growth have been studied in real time via electro-optic imaging microscopy [Gopalan 00, Gopalan 99a]. In CLN, it was observed that local but pinned domain wall motion can occur on a micrometer scale under E-fields that are well below the coercive field of 21 kV mm^{-1} [Yang 99, Agronin 06]. The coercive fields can then be considered as the fields at which a pinning-depinning transition occurs.

The size of defect clusters is restricted to ∼ 11.4 Å (about four cation sites), while the average spacing between defect clusters along the chains is estimated to be ∼ 76 Å [Zotov 95]. The temperature dependence of diffuse X-ray streaks suggests that at low temperatures, the lateral correlations between defect clusters become quite substantial. With increasing temperature, these correlations decrease, resulting in more random 1D disorder [Zotov 95]. The changes in the threshold coercive and internal fields with temperature [Battle 00] also point to the breaking up of the 3D clusters with heating followed by reformation of the defect dipole in an energetically favourable orientation upon cooling down to room temperature.

It's necessary to mention again that the defect and internal electric fields are not to be thought of as actual electric fields, but as energy equivalents to the differences in the energy levels between different states. These energy differences can include not only electro-static energy differences but elastic energy differences as well due to lattice distortions. The electrical dipoles associated with defect complexes can therefore also have elastic dipole components [Arlt 88].

1.4 Linear optical properties

1.4.1 Transmission and absorption

LN has a wide transparency window over the visible part of the spectrum which makes it a very useful optical material. The transparency region starts in the ultraviolet at ∼ 350 nm and reaches the infrared (IR) ∼ 5 µm [Rauber 78]. The transmission curve is extremely flat over this

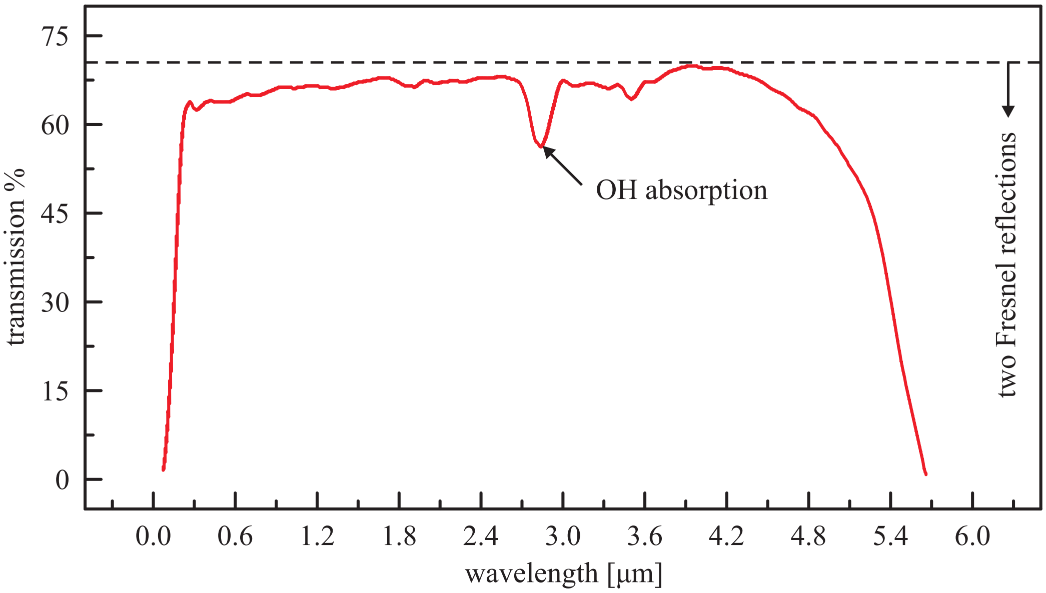

Figure 1.7: Optical transmission spectrum of LN, replotted after [Prokhorov 90]. The maximum transmission that is ∼ 70% is limited by the two Fresnel reflections. OH-absorption band at 2870 nm is also indicated by the arrow.

range with the only appreciable dip occurring at 2870 nm due to the presence of OH-groups within the crystal. A typical transmission curve of undoped congruent LN is shown in Fig. 1.7 [Prokhorov 90]. Beyond the transparency region of IR, there is a region of absorption peaks due to lattice vibrations up to about 60 µm, corresponding to the extensive phonon absorption band. The electronic band structure of LN around the Fermi level is determined mainly by the NbO_6 octahedra since the upper level of the valence band is formed by the oxygen 2p states (O electron configuration = $1s^2 2s^2 2p^4$) and the lower level of the conduction band is formed by the niobium 4d states (Nb electron configuration = $5s^1 4d^4$). The band gap of LN is around 3.7 − 3.9 eV [Prokhorov 90]. The optical properties of LN in the UV region have been studied by Mamedov et al. [Mamedov 85] for photon energies between 0 and 35 eV. The absorption coefficients (at room temperature) of LN at wavelengths which are used in the work presented here are listed in Table 1.2.

TABLE 1.2: The absorption coefficients α, and absorption depths α^{-1}, of undoped CLN for the UV wavelengths ($\lambda = 244, 300, 302, 305$ nm) at room temperature.

λ (nm)	α (m^{-1})	α^{-1} (µm)	Reference
244	3×10^7	0.033	[Mamedov 84]
300.3	9.55×10^4	10.47	[Redfield 74]
302.4	6.61×10^4	15.14	[Redfield 74]
305.5	3.71×10^4	26.98	[Redfield 74]

1.4.2 Refractive index

Since almost all waveguide formation methods rely in some way on the variation of the refractive index with the composition and also certain applications depend on the refractive indices, a precise description of the refractive indices of LN is required. LN is a negatively birefringent uniaxial crystal. A polarisation parallel to the optic axis sees an extraordinary refractive index (n_e) and a polarisation perpendicular to the optic axis sees an ordinary refractive index (n_o). As the ordinary refractive index is larger than the extraordinary refractive index, $n_e < n_o$, the crystal is said to be negative uniaxial. The birefringence of lithium niobate is relatively large ($n_o - n_e =\sim 0.1$ typically).

The refractive indices of LN were thoroughly studied by Schlarb and Betzler [Schlarb 93], who carefully measured both the ordinary (n_o) and extra ordinary (n_e) refractive index of LN in the composition range from 47 to 50 mol% Li_2O over a wavelength range from 400 to 1200 nm, and a temperature range of 50 − 600 K. The authors then proposed a Sellmeier equation for refractive index as [Schlarb 93]

$$n_i^2 = \frac{50 + c_{Li}}{100} \frac{A_{0,i}}{(\lambda_{0,i} + \mu_{0,i} F)^{-2} - \lambda^{-2}} + \frac{50 - c_{Li}}{100} \frac{A_{1,i}}{(\lambda_{1,i} + \mu_{1,i} F)^{-2} - \lambda^{-2}} - A_{IR,i}\lambda^2 + A_{UV} \quad (1.6)$$

$$F = f(T) - f(T_0)$$

$$f(T) = (T+273)^2 + 4.0238 \times 10^5 \left[\coth\left(\frac{261.6}{T+273}\right) - 1\right]$$

where c_{Li} is the mol% of Li_2O; λ is the wavelength in nm in vacuum; 'i' = 'e' or 'o'; T is the temperature in °C; and reference temperature $T_0 = 24.5$°C. The above general Sellmeier equation is only valid from the far infrared up to the UV region. The values of all parameters are given in Table 1.3. Fig. 1.8, as the refractive index calculated from the Sellmeier equation, shows the dispersion of n_e and n_o of CLN (e.g., at 633 nm and 1550 nm), and also reveals (e.g., at 1050 nm) that unlike the ordinary index n_o, the extraordinary index n_e strongly depends on the stoichiometry of the crystal. Specifically, n_e increases as Li_2O is removed from the crystal but n_o is practically unaffected [Carruthers 71]: for $(Li_2O)_v(Nb_2O_5)_{1-v}$, $dn_e/dv = -1.6$ in the $0.48 < v < 0.50$ range.

TABLE 1.3: Parameters of the generalised Sellmeier equation Eq. 1.6 [Schlarb 93].

n_o	n_e
$A_{0,o} = 4.5312 \times 10^{-5}$	$A_{0,e} = 3.9466 \times 10^{-5}$
$\lambda_{0,o} = 223.219$	$\lambda_{0,e} = 218.203$
$A_{1,o} = 2.7322 \times 10^{-5}$	$A_{1,e} = 8.3140 \times 10^{-5}$
$\lambda_{1,o} = 260.26$	$\lambda_{1,e} = 250.847$
$A_{IR,o} = 3.6340 \times 10^{-8}$	$A_{IR,e} = 3.0998 \times 10^{-8}$
$A_{UV} = 2.6613$	$A_{UV} = 2.6613$
$\mu_{0,o} = 2.1203 \times 10^{-6}$	$\mu_{0,e} = 7.5187 \times 10^{-6}$
$\mu_{1,o} = -1.8275 \times 10^{-4}$	$\mu_{1,e} = -3.8043 \times 10^{-5}$

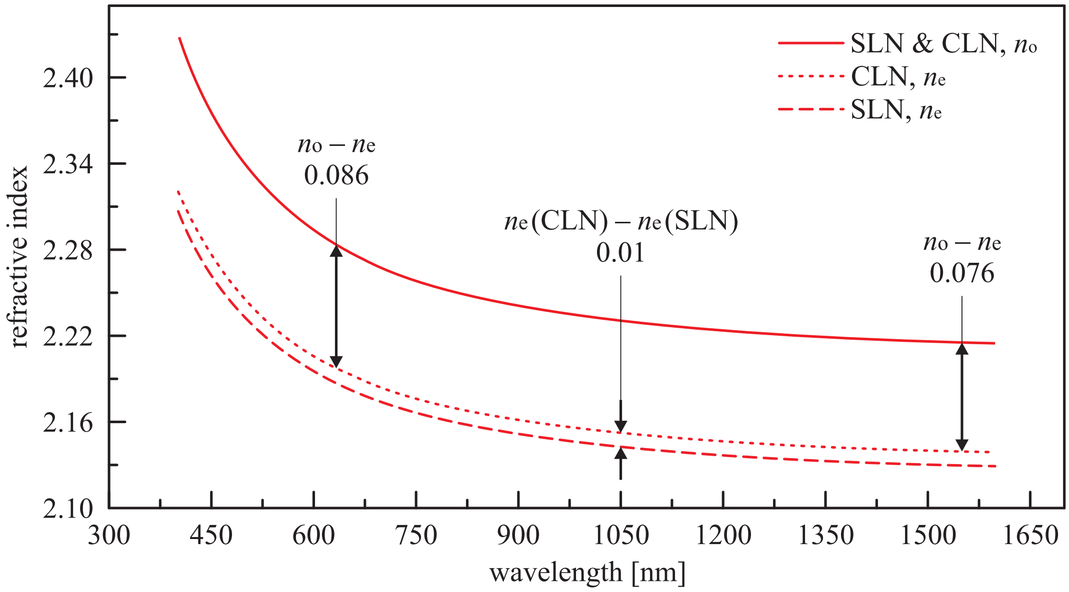

FIGURE 1.8: Extra-ordinary and ordinary refractive indices for congruent and stoichiometric LN, replotted from [Wellington 07a, Schlarb 93]. Birefringence values at 633 nm and 1550 nm of CLN, and n_e difference of CLN and SLN crystal at 1050 nm are indicated.

1.5 Nonlinear optical properties

1.5.1 Second order nonlinear susceptibility

If the electrons are in an effective anharmonic potential as in a dipolar bond, polarisation of the electrons for a specific frequency ω_0 will be nonlinear as

$$\begin{gathered} P_{\omega_0,i} = P^{(1)}_{\omega_0,i} + P^{(2)}_{\omega_0,i} \qquad i = 1,2,3 \\ P^{(1)}_{\omega_0,i} = \epsilon_0 \chi^{(1)}_{ij} \left(-\omega_0;\omega_0\right) E_{\omega_0,j} \qquad i,j = 1,2,3 \\ P^{(2)}_{\omega_0,i} = 2\epsilon_0 K \left(-\omega_0;\omega_1,\omega_2\right) d_{ijk} \left(-\omega_0;\omega_1,\omega_2\right) E_{\omega_1,j} E_{\omega_2,k} \qquad i,j,k = 1,2,3 \\ \omega_1 + \omega_2 = \omega_0 \\ K\left(-\omega_0;\omega_1,\omega_2\right) = 2^{l+m-2} p \end{gathered} \tag{1.7}$$

where $P^{(1)}_{\omega_0,i}$ is the linear polarisation component with linear susceptibility of χ_{ij}; $P^{(2)}_{\omega_0,i}$ is the second order or quadratic nonlinearity with second order nonlinear susceptibility tensor of d_{ijk}; ω_1, ω_2 are the frequencies components; p is the number of distinct permutations of ω_1, ω_2; m is the number of zero frequencies for ω_1, ω_2 (i.e., DC field); $l = 1$ if $\omega_0 \neq 0$, otherwise $l = 0$; and ϵ_0 is the permittivity of free space. The Kleinman symmetry rule is applied: as long as there is no strong dispersion between the wavelengths of the mixing fields, all terms d_{ijk} which result from rearrangement of the subscripts j, k are equal based upon intrinsic permutation symmetry arguments [Boyd 92]. Thus the d_{ijk} tensor can be described by a contracted notation expressed using two indices d_{il}, with l defined as in Table 1.4, permitting the convenient rearrangement of the third-order tensor into a 3×6 two-dimensional matrix.

TABLE 1.4: Definition of the contracted notation.

jk:	11	22	33	23, 32	31, 13	12, 21
l:	1	2	3	4	5	6

Therefore, taking into account the symmetry of point group 3m of LN, the second order nonlinear polarisation response can be expressed in matrix form as

$$\begin{bmatrix} P^{(2)}_{\omega_0,1} \\ P^{(2)}_{\omega_0,2} \\ P^{(2)}_{\omega_0,3} \end{bmatrix} = 2\epsilon_0 K \begin{bmatrix} & & & & d_{15} & -d_{22} \\ -d_{22} & d_{22} & & d_{15} & & \\ d_{31} & d_{31} & d_{33} & & & \end{bmatrix} \begin{bmatrix} E_{\omega_1,1} E_{\omega_2,1} \\ E_{\omega_1,2} E_{\omega_2,2} \\ E_{\omega_1,3} E_{\omega_2,3} \\ E_{\omega_1,2} E_{\omega_2,3} + E_{\omega_2,2} E_{\omega_1,3} \\ E_{\omega_1,1} E_{\omega_2,3} + E_{\omega_2,1} E_{\omega_1,3} \\ E_{\omega_1,1} E_{\omega_2,2} + E_{\omega_2,1} E_{\omega_1,2} \end{bmatrix} \tag{1.8}$$

The nonvanishing d_{il} tensor elements of LN are presented in Table 1.5 and their values depend on the frequencies involved. From Maxwell equation, it can be derived that the induced polarisation $P^{(2)}_{\omega_0,i}$ oscillating at ω_0 can radiate a free wave also at frequency ω_0 via

$$\nabla \times \nabla \times \mathbf{E}_{\omega_0} = \frac{\omega_0^2}{c^2}\boldsymbol{\epsilon}_{\mathrm{r},\omega_0}\mathbf{E}_{\omega_0} + \omega_0^2\mu_0\mathbf{P}^{(2)}_{\omega_0} \tag{1.9}$$

$$\boldsymbol{\epsilon}_{\mathrm{r},\omega_0} = \mathbf{1} + \boldsymbol{\chi}^{(1)}(-\omega_0;\omega_0)$$

where μ_0 is the permeability of vacuum; $\boldsymbol{\epsilon}_{r,\omega_0}$ is the relative permittivity tensor at ω_0; and $\mathbf{1}$ is the unit dyadic. As the new frequency ω_0 can be generated from ω_1 and ω_2, a number of nonlinear optical effects are observed as a result of this second order interaction, i.e., sum frequency generation (SFG), second harmonic generation (SHG), parametric amplification, and optical parametric generation (OPG).

TABLE 1.5: The nonvanishing d_{il} tensor elements ($\mathrm{pm\,V^{-1}}$) of lithium niobate measured at 1.064 µm [Yariv 85].

d_{31}	d_{33}	d_{22}	Reference
−5.95	−34.4	4.08	[Yariv 85]
−5.8	−33	2.8	[Prokhorov 90]
−5.95	−34.4	2.5	[Choy 76, Pruneri 96]
−4.3	−27	2.1	[Roberts 92]

1.5.2 Quasi-phase matching

From Eq. 1.8, it obviously shows that with $E_{\omega_1,i}$ and $E_{\omega_2,i}$ having wavevectors of k_1 and k_2 respectively, the fronts of constant phase of induced polarisation $P^{(2)}_{\omega_0,i}$ will move through the medium with wavevector of $k_1 + k_2$ and phase velocity of $\omega_0/k_1 + k_2$, giving rise to the idea of a polarisation 'wave'. The radiated electric wave with frequency ω_0, on the other hand, travels with a phase velocity of ω_0/k_0. If $k_0 \neq k_1 + k_2$, then the polarisation wave and electric wave do not remain in phase synchronism which is general due to dispersion. If the wavevector mismatch $\delta k = k_0 - k_2 - k_1 \neq 0$ is left uncorrected, as the beams propagate through the crystal their phase will become increasingly mismatched, resulting in less efficient frequency conversion, until eventually the beams will start to destructively interfere. Fortunately, quasi-phase matching (QPM) first proposed by Armstrong et al. [Armstrong 62] has been developed to achieve efficient frequency conversion in 1962. An overview of quasi-phase-matching (QPM) is provided in [Byer 97].

The coherence length is defined as the distance over which a relative π phase shift is experienced between the induced polarisation wave and the radiated electric wave [Fejer 92]

$$l_{\mathrm{c}} = \frac{\pi}{\delta k} \tag{1.10}$$

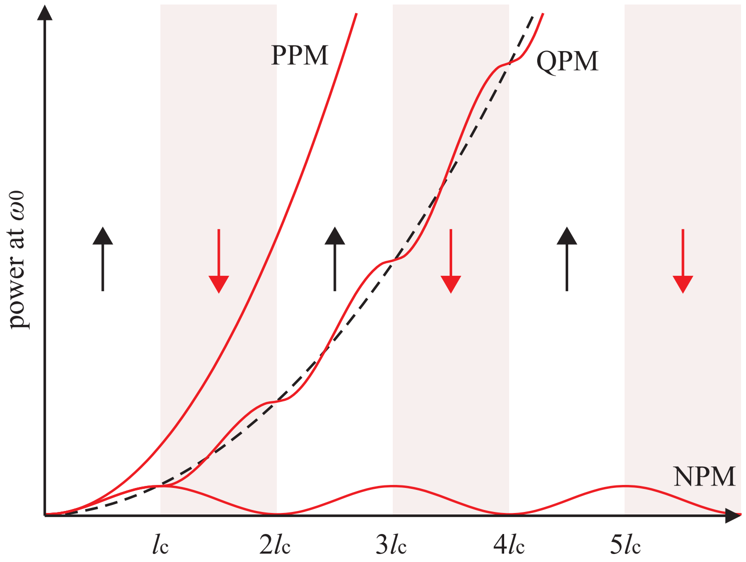

Figure 1.9: Comparison of relative phase-matching efficiencies for non-phase matching (NPM), perfect phase matching (PPM) and quasi-phase matching (QPM). The arrows indicate the direction of the spontaneous polarisation.

As shown in the non-phase matching (NPM) trace in Fig. 1.9 the power of ω_0 oscillates sinusoidally with the distance traveled through the nonlinear crystal: it oscillates at a period of $2l_c$ with the first l_c showing increasing power and the second l_c, decreasing power. *Quasi-phase matching* (QPM) referred to the alternating sign of d_{il} in Eq. 1.8 at every l_c which can introduce a π phase in the next l_c length for the induced polarisation, therefore also the newly radiated light at frequency ω_0. Thus, it enables monotonically building up of the power at ω_0 as shown in Fig. 1.9 of the QPM trace. In terms of momentum conversion, QPM introduces into the material a grating vector $K_g = 2\pi/\Lambda_g$, where $\Lambda_g = 2l_c$ is the grating period, and the phase-matching condition becomes $\delta k = k_0 - k_2 - k_1 - K_g = 0$

1.6 Electrical conductivity

Conductivity from room temperature to 1000°C

The origin of the dark conductivity in as-grown, undoped or low iron doped LN at temperature < 1000°C has been the subject of extensive investigation. The determination was made by [Bollmann 77], where a proportional relationship between the hydrogen concentration and the conductivity was demonstrated in LN at temperatures from 400°C to 1000°C which was later supported in [Klauer 92, Schmidt 89]. Hence, the dominant protonic conductivity in LN has been verified for both at elevated and room temperature. The thermally activated charge transport obeys an Arrhenius-type dependence on the temperature with the conductivity σ given by [Klauer 92]

$$\sigma = \sigma_0 \exp\left(-\frac{\varepsilon_{\mathrm{act}}}{k_{\mathrm{B}}T}\right) = \frac{N_{\mathrm{c}}q^2D_0}{k_{\mathrm{B}}T}\exp\left(-\frac{\varepsilon_{\mathrm{act}}}{k_{\mathrm{B}}T}\right) \tag{1.11}$$

where $\varepsilon_{\mathrm{act}}$ is the activation energy; k_{B} is the Boltzmann constant; T is the temperature; N_{c} is the concentration of charge carriers; and D_0 is the pre-exponential diffusion constant. The activation energy of protons has been measured to be 1.23 eV and 1.17 eV for undoped and Fe-doped congruent LN respectively, and diffusion of protons was suggested to be accomplished by jumping to the nearest O^{2-} ion from its previous bound position [Klauer 92]. In spite of the solid conclusion of protons as contributing to the conductivity of the crystal, recent publications reveal diverse opinions about the origin of the ionic conductivity. While some still support the proton transport as being responsible for the ionic conductivity via observing the dependence of conductivity on the proton concentration [de Miguel-Sanz 02, Yang 01], others believe that Li ions are responsible for the ionic conductivity. The data shown in [Brands 08] points to Li^+ as the moving ions: on the one hand a 20% smaller activation energy was measured in stoichiometric LN compared with CLN, which has a different Li concentration, and on the other hand no strong dependence of the conductivity on the hydrogen concentration was observed, which varied by a factor of 50 in the crystals used. This point was further supported by [Basun 08] where it was shown that the dark conductivity remains fairly constant for samples with considerably different H^+ concentration. The activation energy and the relevant positive ion together with the investigated temperature range and crystal type are listed in Table 1.6. Electrical conductivity has been measured along different axes of the x and z crystallographic axes in the temperature range of 460 – 620°C, using the AC impedance spectroscopy technique [Niitsu 04]. It was revealed that although no difference in the activation energy of conduction was found, a slight but

TABLE 1.6: Activation energy $\varepsilon_{\mathrm{act}}$ and identified conductive ions (C. I.) for various iron doping of CLN crystals within the investigated temperature T.

T (°C)	Fe-doping	Treatment	C. I.	$\varepsilon_{\mathrm{act}}$ (eV)	Reference
80 – 600	undoped	as-grown	H	1.23	[Klauer 92]
80 – 600	660 ppm	as-grown	H	1.17	[Klauer 92]
80 – 115	0.1 mol%	as-grown	H	0.95	[de Miguel-Sanz 02]
50 – 91	0.1 mol%	oxidised	H	0.95	[de Miguel-Sanz 02]
72 – 182	0.05 wt% Fe_2O_3	H-reduced	H	1	[Yang 01]
30 – 144	0.05 wt% Fe_2O_3	H-enhanced	H	0.97	[Yang 01]
97 – 227	0.05 mol%	as-grown	Li	1.11	[Basun 08]
97 – 227	0.05 mol%	oxidised	Li	1.11	[Basun 08]
170 – 700	undoped	as-grown	Li	1.2	[Brands 08]
460 – 620	undoped	dried	–	x, z: 1.24	[Niitsu 04]
300 – 700	undoped	as-grown	–	z: 0.9, x: 0.87	[Chen 07]

– = unidentified
x/z: = along x/z

unequivocal difference in electrical conductivity (about 0.16 on a log scale with $\sigma_z > \sigma_x$) was observed between the two axes.

Conductivity above 1000°C

The conductivity above 1000°C has been studied in [Mehta 91]. The high temperature equilibrium conductivity (950 – 1050°C) of CLN can be resolved into two components: an electronic part that is dependent on the oxygen partial pressure and an ionic part that is pressure independent. It revealed that at low O_2 pressure, electronic conductivity dominates the electrical conductivity, while at high O_2 pressure, the electrical conductivity originates mostly from ionic conductivity. It accords with the early study that the electrical conductivity is completely ionic at 1 atm of oxygen pressure and 1000 K, while for low partial pressure the electrical conductivity (at 1000 K) becomes completely electronic [Jorgensen 69]. It was concluded from the comparison of Li ion diffusion and electrical conductivity measurements that the ionic conductivity is determined solely by Li ions [Ptashnik 85]. From the temperature dependence of the ionic conductivity, the activation energy for the Li ionic transport is obtained as 1.43 eV (later corrected in [Birnie 93] as 1.55 eV). Possible diffusion paths of Li ions in LN have been discussed in [Birnie 93]. It suggests that the Li ion motion requires a free Li vacancy close to the substitution site (regardless of temperature).

1.7 Photovoltaic effect

The bulk photovoltaic effect (BPVE) is manifested as a short-circuit current through a solid that is uniformly illuminated by sub-bandgap light [Glass 74, Glass 75, Belinicher 80, Sturman 80, von Baltz 83] first described by Glass et al. in 1974 [Glass 74]. From the microscopic point of view, it can be understood as an asymmetric charge transfer process that takes place upon photoexcitation of an electron or hole from an impurity in the material [Schlarb 95, Abdi 99, Furukawa 00]. These charges move in a particular direction inside the crystal without the presence of an external E-field, and thus, the displacement of these charges corresponds to a current. This is illustrated in Fig. 1.10, which depicts bound and free eigensolutions for electron motion in an asymmetric square well. The electron is bound at energy ε_1, however, when it is excited to energy ε_2 it is free to move in only one direction as indicated in Fig. 1.10. Even though tunneling may occur the probability of motion to the left is lower than motion to the right. Thus if the asymmetry has the same sense in all equivalent defects, photoexcitation of charge carriers will result in a photocurrent. A more thorough treatment is given in [Lines 77].

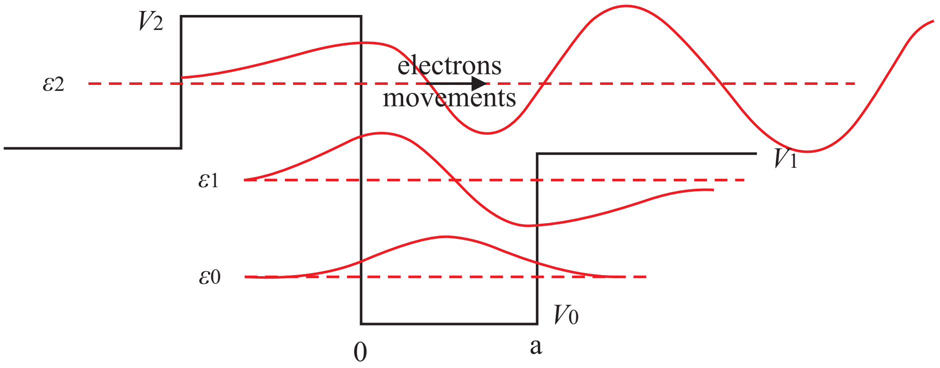

Figure 1.10: Asymmetric quantum well with bound and free eigensolutions to Schrödinger's equation replotted from [Glass 74].

The tensor relationship between the short-circuit photovoltaic current density and the illumination can be described by the following linear expression [Sturman 92]:

$$j_{\mathrm{pv},i} = \beta_{ijk} e_j e_k^* I \qquad i,j,k = 1,2,3 \tag{1.12}$$

where $j_{\mathrm{pv},i}$ is the vector of photovoltaic current density; $\beta_{ijk} = \beta_{ikj}^*$ is the third rank complex photovoltaic tensor (27 elements) which is proportional to the number of dopants and their photoexcitation cross-section; e_j, e_k^* are unit vector components ('*' for conjugate) of the light polarisation; and I is the light intensity.

For linearly polarised light (referred to as linear PVE with $\beta_{ijk} = \beta_{ikj}$), photovoltaic current can be derived for LN applying Neumann's principle as [Sturman 92, Arizmendi 04]

$$\begin{bmatrix} j_{\mathrm{pv},1} \\ j_{\mathrm{pv},2} \\ j_{\mathrm{pv},3} \end{bmatrix} = I \begin{bmatrix} & & & & \beta_{15} & -\beta_{22} \\ -\beta_{22} & \beta_{22} & & \beta_{15} & & \\ \beta_{31} & \beta_{31} & \beta_{33} & & & \end{bmatrix} \begin{bmatrix} e_1 e_1^* \\ e_2 e_2^* \\ e_3 e_3^* \\ e_2 e_3^* + e_3 e_2^* \\ e_1 e_3^* + e_3 e_1^* \\ e_1 e_2^* + e_2 e_1^* \end{bmatrix} \tag{1.13}$$

Thus, the bulk PVE in LN can be described by four independent coefficients β_{15}, β_{22}, β_{31}, and β_{33}. These coefficients for iron-doped LN at a free-space wavelength of 500 nm are: $\beta_{22} = 1.5 \times 10^{-10}$ A W^{-1}, $\beta_{31} = 6 \times 10^{-9}$ A W^{-1}, and $\beta_{33} = 6.8 \times 10^{-9}$ A W^{-1} [Fridkin 79]. Festl et al. re-confirmed the tensor nature of the bulk photovoltaic effect and measured tensor coefficients in both iron-doped and copper-doped LN [Festl 82]. It was revealed that the bulk photovoltaic currents are completely determined by the number of filled impurity traps, e.g., Fe^{2+} or Cu^{+} ions. In all cases a linear dependence of the current density on the concentration of Fe^{2+} or Cu^{+}

ions is observed

$$\frac{j_{\mathrm{pv}}}{I} \propto \mathrm{Fe}^{2+}, \mathrm{Cu}^{+} \tag{1.14}$$

As for LN, $\beta_{33} \sim \beta_{31} \gg \beta_{22}, \beta_{15}$, therefore the photovoltaic current is in all cases mostly along the z or photovoltaic axis. For this reason, most often the photovoltaic current is presented in a scalar form as

$$j_{\mathrm{pv}} = \alpha k_{\mathrm{G}} I \tag{1.15}$$

where α is the optical absorption coefficient at the corresponding wavelength assumed to be isotropic; and k_{G} is the so-called Glass constant characterising the photovoltaic activity of the given impurity in the particular lattice. The stationary photovoltaic field $\mathbf{E}_{\mathrm{pv}}$ is expressed as [Volk 08b]

$$\mathbf{E}_{\mathrm{pv}} = \frac{\mathbf{j}_{\mathrm{pv}}}{\sigma_{\mathrm{ph}} + \sigma_{\mathrm{d}}} \tag{1.16}$$

where σ_{ph} and σ_{d} are photo- and dark conductivities, respectively. From Eq. 1.15 and 1.16, it is revealed that for relatively low light intensities corresponding to $\sigma_{\mathrm{ph}} > \sigma_{\mathrm{d}}$ and assuming the usual dependence $\sigma_{\mathrm{ph}} \propto I$, the photovoltaic field $\mathbf{E}_{\mathrm{pv}}$ saturates independently of I. The photovoltaic current produces a charge accumulation on the end faces of the crystal or in the shadow region outside the illuminated zone, which leads to a space-charge field in the illuminated regions. In steady state the photovoltaic current will be compensated by the drift current and the potential drop caused by this space-charge field $\mathbf{E}_{\mathrm{sc}} = -\mathbf{E}_{\mathrm{pv}}$, the value of which in single-domain LN and LT is up to 10^{7} V m^{-1} in an open circuit [Krätzig 77]. Although no devices based directly in this effect have been proposed, it plays an important role in the photorefractive effect.

1.8 Linear electro-optic effect

The linear electro-optic (EO) effect is a change in the refractive indices of a material caused by the application of an E-field. This effect is widely used in the fabrication of LN optical modulators for applications in optical telecommunications. A detailed theoretical treatment of the effect is available in [Wemple 72], but a brief outline will be presented here.

A description of the electro-optic effect can be given using the ‘index ellipsoid’. In optics, an *index ellipsoid* is a diagram of an ellipsoid that depicts the orientation and relative magnitude of refractive indices in a crystal. The general index ellipsoid is defined by the relation [Nye 87a]:

$$\eta_{ij} n_i n_j = 1 \qquad i, j = 1, 2, 3 \tag{1.17}$$

$$n^2 = n_i^2 \qquad i = 1, 2, 3$$

where η_{ij} is the dielectric impermeability tensor being inverse to the relative static permittivity tensor: $\eta_{ij} = 1/\epsilon_{\mathrm{r},ij} = \epsilon_0/\epsilon_{ij}$; n is the refractive index; and n_i, n_j are the components (projections) of refractive index n along the $i^{\mathrm{th}}, j^{\mathrm{th}}$ axis.

When an E-field $\mathbf{E}$ is applied to a crystal, a corresponding change in the refractive index occurs. Mathematically, the linear electro-optic effect is represented as a deformation of the index ellipsoid, expressed as changes in the constants of the index ellipsoid η_{ij}:

$$\eta_{ij}(\mathbf{E}) - \eta_{ij}(0) = \delta\eta_{ij}(\mathbf{E}) = r_{ijk}E_k \qquad i, j, k = 1, 2, 3 \tag{1.18}$$

where r_{ijk} is the linear (Pockels effect) electro-optic coefficients of a third rank tensor with units of $\mathrm{m\,V^{-1}}$. Eq. 1.18 is applicable under the influence of an applied constant or low-frequency ($<$ optical frequencies) E-field. It should be mentioned that in applications of EO materials, where the applied E-field is small compared to the intra-atomic E-field, the quadratic EO effect (Kerr effect) is very small and can be neglected as compared with the linear term, i.e., no quadratic EO effect is observed for E-fields of up to 65 kV mm^{-1} in LN [Luennemann 03].

Using the properties of the index ellipsoid, it can be shown that $\eta_{ij} = \eta_{ji}$, thus $\delta\eta_{ij} = \delta\eta_{ji}$. As a result, the linear EO effect can be expressed in matrix form. Setting the crystal axis of LN to the index ellipsoid and applying Neumann's principle to the 3m point group, the linear EO effect of LN in matrix from is deduced to be

$$\begin{bmatrix} \delta\eta_{11} \\ \delta\eta_{22} \\ \delta\eta_{33} \\ \delta\eta_{32}, \delta\eta_{23} \\ \delta\eta_{31}, \delta\eta_{13} \\ \delta\eta_{21}, \delta\eta_{12} \end{bmatrix} = \begin{bmatrix} & -r_{22} & r_{13} \\ & r_{22} & r_{13} \\ & & r_{33} \\ & r_{51} & \\ r_{51} & & \\ -r_{22} & & \end{bmatrix} \begin{bmatrix} E_1 \\ E_2 \\ E_3 \end{bmatrix} = \begin{bmatrix} -r_{22}E_2 + r_{13}E_3 \\ r_{22}E_2 + r_{13}E_3 \\ r_{33}E_3 \\ r_{51}E_2 \\ r_{51}E_1 \\ -r_{22}E_1 \end{bmatrix} \tag{1.19}$$

Thus, the linear EO effect in LN can be described by four independent coefficients, $r_{13}(= r_{23})$, $r_{22}(= -r_{12} = -r_{61})$, r_{33} and $r_{51}(= r_{42})$. The measured values of these coefficients are listed in Table 1.7 and depend on the mechanical constraints imposed on the crystal: clamped or unclamped case corresponds to the high and low frequency E-field respectively. For a specific linear polarisation of light along unit vector of $\hat{\mathbf{e}} = (e_1, e_2, e_3)$ which also defines the direction

TABLE 1.7: High- and low-frequency values for the electrooptic coefficients of LN: r_{il}, with unit of 10^{-12} $\mathrm{m\,V^{-1}}$ at $\lambda = 0.63$ µm [Yariv 85].

	r_{22}	r_{33}	r_{13}	r_{51}
high frequency $= 50 - 86$ Mc s^{-1}	3.4	30.8	8.6	28
low frequency	6.8	30.9	9.6	32.6

of refraction index in the index ellipsoid ($n_1, n_2, n_3 = ne_1, ne_2, ne_3$), its corresponding refractive index can be derived from Eq. 1.17 as $\eta_{ij}e_ie_j = n^{-2}(0)$ with no E-field, and $[\eta_{ij} + \delta\eta_{ij}(\mathbf{E})]e_ie_j = n^{-2}(\mathbf{E})$ with an E-field applied, thus,

$$n^{-2}(\mathbf{E}) - n^{-2}(0) = -2n^{-3}\delta n(\mathbf{E}) = \delta\eta_{ij}(\mathbf{E})e_ie_j \qquad i,j = 1,2,3 \tag{1.20}$$

derives the refractive index change $\delta n(\mathbf{E})$ due to the E-field.

The largest and most useful linear electro-optic coefficient in LN is the r_{33} component (Table 1.7). An external E-field in the z-direction gives rise to a change in the extraordinary index n_e, as well as a change in the ordinary refractive index n_o. The applied E-field E_3 modify the ellipsoid Eq. 1.20 to read,

$$-2n^{-3}\delta n(E_3) = (r_{13}e_1^2 + r_{13}e_2^2 + r_{33}e_3^2)E_3 \tag{1.21}$$

As no cross-terms are involved, the principle axes are not changed. For the refractive index along the three principle axes: n_1 (n_o), n_2 (n_o), and n_3 (n_e), they correspond to unit light polarisation of $\hat{\mathbf{e}} = (e_1, e_2, e_3) = (1,0,0), (0,1,0), (0,0,1)$ respectively, thus, substitution into Eq. 1.21 obtains

$$\delta n_\mathrm{o}(E_3) = -\frac{1}{2}n_\mathrm{o}^3 r_{13}E_3 \tag{1.22}$$

$$\delta n_\mathrm{e}(E_3) = -\frac{1}{2}n_\mathrm{e}^3 r_{33}E_3$$

The modified ellipse is shown in Fig. 1.11 with E-field of opposite directions.

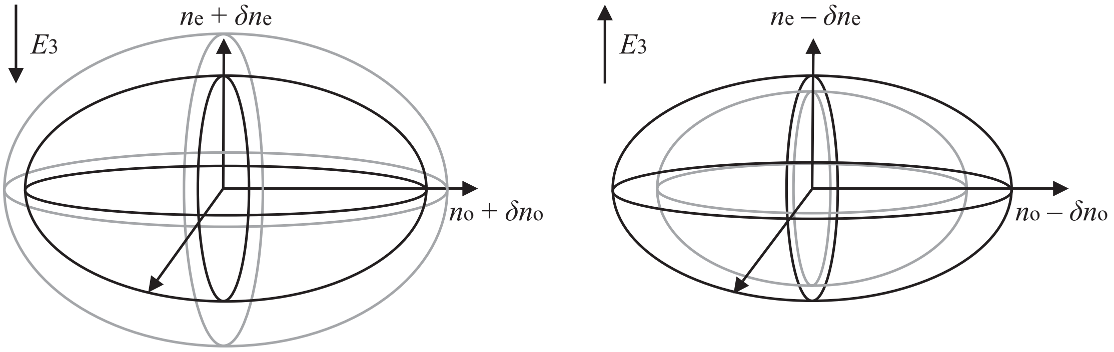

Figure 1.11: LN crystal ellipsoid (black) and its modified (grey) size by the action of an applied field along z-axis in opposite directions replotted from [Frejlich 07].

1.9 Photorefractive effect

The photorefractive (PR) effect is a non-instantaneous, non-local, light induced change to the refractive index δn that persists for some time after the illumination has been removed [Günter 88]. It was first discovered in 1966 by Ashkin et al. [Ashkin 66] as a light-induced refractive-index change in LN, known as *optical damage*. Later, Chen et al. [Chen 68, Chen 69] successfully utilised the refractive-index changes for the storage of volume phase holograms leading to the term *photorefractive effect*. The magnitude of δn which can vary from 10^{-6} to 10^{-3} depends on the laser radiation intensity ($10^{-1} - 10^{3}$ W cm^{-2}) and its fluence ($1 - 10^{3}$ J cm^{-2}). This refractive index change is reversible and has a dark relaxation time ranging from 10^{-4} s to several years, depending on the temperature of the crystal and the impurity concentration [Wong 89]. However, homogeneous illumination can assist relaxation by allowing photoexcited charges to erase the index modulation.

The origin of the photorefractive effect has been discussed in detail in [Buse 97, Günter 06, Günter 07a, Günter 07b]. An outline of the photorefractive recording is presented here.

1. $I(\mathbf{r}) \rightarrow N_{\mathrm{c}}(\mathbf{r})$: inhomogeneous illumination with intensity pattern $I(\mathbf{r})$, where $\mathbf{r}$ is the spatial coordinate, excites electrons into the conduction band and/or holes into the valence band either by photo-ionisation of inter-band defects in the case of visible light, or band to band photo-excitation in the case of UV light. The distribution of photo-excited charge carriers is denoted by $N_{\mathrm{c}}(\mathbf{r})$.

2. $N_{\mathrm{c}}(\mathbf{r}) \rightarrow \mathbf{j}(\mathbf{r})$: the free-charge carriers migrate, e.g., because of drift, bulk photovoltaic effects, and diffusion, inducing a spatially modulated electric current with density $\mathbf{j}(\mathbf{r})$.

3. $\mathbf{j}(\mathbf{r}) \rightarrow \rho(\mathbf{r})$: an appreciable charge density modulation $\rho(\mathbf{r})$ is built up after charges become trapped in regions of low light intensity.

4. $\rho(\mathbf{r}) \rightarrow \mathbf{E}_{\mathrm{sc}}(\mathbf{r})$: the resulting space-charge electric field $\mathbf{E}_{\mathrm{sc}}(\mathbf{r})$ acts against further charge transport, and finally a steady-state space charge field is established.

5. $\mathbf{E}_{\mathrm{sc}}(\mathbf{r}) \rightarrow \delta n(\mathbf{r})$: the space-charge field modulates the refractive index because of the linear electrooptic effect.

1.9.1 Charge transport

The charge migration, current density $\mathbf{j}(\mathbf{r})$, consists of three important contributions: 1) diffusion current, 2) bulk photovoltaic currents, and 3) drift current. This section generally introduces each of the contribution [Günter 06].

Carrier diffusion

When a photorefractive crystal is illuminated with spatially patterned light, this produces a spatially patterned mobile carrier distribution. Initially the excited carrier concentration in the regions of high intensity is higher than in regions of low intensity. Because of the spatial gradient of the carrier density, the mobile charge carriers migrate to the regions of lower intensity. The current density due to this diffusion transport $\mathbf{j}_{\mathrm{diff}}$ is given by

$$\mathbf{j}_{\mathrm{diff}} = -qD\nabla N_{\mathrm{c}} \tag{1.23}$$

$$D = \mu_{\mathrm{c}} k_{\mathrm{B}} T/|q|$$

where $q = +/-e$ is the charge of the carrier ($+/-$ for hole or electrons); D is the diffusion coefficient of the material which in general is a tensor quantity; N_{c} is the carrier density; and μ_{c} is the carrier mobility.

Drift

The displacement of charge carriers from their parent ions results in a spatially dependent carrier concentration that causes a space charge field $\mathbf{E}_{\mathrm{sc}}$. This intrinsic electric field and a possibly externally applied field $\mathbf{E}_{\mathrm{ext}}$ will add up, and create a drift current density

$$\mathbf{j}_{\mathrm{dft}} = \sigma(\mathbf{E}_{\mathrm{sc}} + \mathbf{E}_{\mathrm{ext}}) \tag{1.24}$$

$$\sigma = \sigma_{\mathrm{d}} + \sigma_{\mathrm{ph}} = \sigma_{\mathrm{d}} + |q| N_{\mathrm{c}} \mu_{\mathrm{c}}$$

where $\sigma, \sigma_{\mathrm{d}}, \sigma_{\mathrm{ph}}$ are the conductivity, dark conductivity and photoconductivity respectively.

Photovoltaic effect

As discussed in Sec. 1.7, the photovoltaic current density is given by Eq. 1.15 as

$$\mathbf{j}_{\mathrm{pv}} = \alpha k_{\mathrm{G}} I \hat{\mathbf{z}} \tag{1.25}$$

where α is the absorption coefficient; k_{G} is the Glass constant; I is the incident intensity; and $\hat{\mathbf{z}}$ is the unit vector along $+z$ axis.

Space charge field in steady state

The total current density can then be written as the sum of contributions from drift, diffusion and the photovoltaic effect:

$$\mathbf{j} = \mathbf{j}_{\mathrm{diff}} + \mathbf{j}_{\mathrm{dft}} + \mathbf{j}_{\mathrm{pv}} = -qD\nabla N_{\mathrm{c}} + \sigma(\mathbf{E}_{\mathrm{sc}} + \mathbf{E}_{\mathrm{ext}}) + \alpha k_{\mathrm{G}} I \hat{\mathbf{z}} \tag{1.26}$$

When reaching the steady-state, there is no further charge transport, thus $\mathbf{j} = 0$ and the space-charge field $\mathbf{E}_{\mathrm{sc}}$ in the absence of external field is derived from Eq. 1.26 as

$$\mathbf{E}_{\mathrm{sc}} = -\left[\frac{\alpha k_{\mathrm{G}} I \hat{\mathbf{z}}}{\sigma} + \frac{-qD\nabla N_{\mathrm{c}}}{\sigma}\right] = -[\mathbf{E}_{\mathrm{pv}} + \mathbf{E}_{\mathrm{diff}}] \tag{1.27}$$

where $\mathbf{E}_{\mathrm{pv}}$ and $\mathbf{E}_{\mathrm{diff}}$ are the photovoltaic field and diffusion field respectively.

In LN the dominant charge migration mechanism is the bulk photovoltaic effect [Glass 74]. However the charge migration may sometimes also be a result of diffusion (as in a PR grating with small grating period). The charge distribution, thus, $\mathbf{E}_{\mathrm{sc}}$ and δn, remains in the crystal for some time even when it is not illuminated. In this case, only the crystal dark conductivity contributes to redistribute the charge. By contrast, upon uniform illumination that provides the photoconductivity, the charge is redistributed homogeneously after some time depending on light intensity and incident spectrum. Consequently the refractive index change is erased.

1.9.2 Photorefractive impurities

The origin of photoexcitable charges is related to the presence of certain impurities or color centers which can be ionised optically. In LN the most active photorefractive impurities are Fe, Cu and Mn in two valence states: $\mathrm{Fe}^{2+}/\mathrm{Fe}^{3+}$, $\mathrm{Cu}^{+}/\mathrm{Cu}^{2+}$, and $\mathrm{Mn}^{2+}/\mathrm{Mn}^{3+}$ [Phillips 72] that forms localised states in the bandgap. The origin of the photorefractive effect in CLN is generally accepted to be due to the presence of iron impurities during the growth process [Buse 97] which are present in small concentrations even in undoped crystals, although doping is common to increase photorefractive response.

The two different oxidation states of iron Fe^{2+} and Fe^{3+} act as electron donor and acceptor respectively (and/or as hole acceptor and donor respectively) that provide a means to store charge distributions in the crystal. The Fe^{2+} and Fe^{3+} ions can be excited by absorption of photons to produce electrons and holes respectively via:

$$\mathrm{Fe}^{2+} + h\nu \rightarrow \mathrm{Fe}^{3+} + e^{-}(\mathrm{CB})$$

$$\mathrm{Fe}^{3+} + h\nu \rightarrow \mathrm{Fe}^{2+} + h^{+}(\mathrm{VB})$$

where h is Planck's constant; ν is the frequency of the incident beam; and CB, VB refer to conduction and valence band. Whether the electrons or holes dominate the charge transport depends on the oxidation state ratio of $\mathrm{Fe}^{2+}/\mathrm{Fe}^{3+}$. With ultraviolet light, for larger Fe^{3+} concentration, the excitation of holes dominates, while for larger Fe^{2+} concentration, the electrons dominate [Orlowski 78]. However, for visible light electrons dominate the charge transport in Fe:LN over the entire oxidisation/reduction range [Günter 07b]. For as-grown undoped LN, the concentration ratio $\mathrm{Fe}^{2+}/\mathrm{Fe}^{3+}$ in the congruent as-grown LN crystals is usually in the range of $0.1-0.2$ [Volk 08c]. And it is generally agreed that the photoexcited carriers are electrons that come from Fe^{2+} impurities in LN crystals [Glass 74, Phillips 72] (~ 5 ppm [Korkishko 97]) and the photorefractive sensitivity is proportional to its Fe^{2+} concentration [Peterson 71].

1.10 Pyroelectric effect

The *Pyroelectric effect* refers to the relationship between the temperature change δT, and spontaneous polarisation change δP that is written as [Weis 85]

$$\delta P_i = p_i \delta T \qquad i = 1, 2, 3 \tag{1.28}$$

where p_i are the pyroelectric vector coefficients. In LN this affect is due to the movement of the Li and Nb ions relative to the oxygen layers. Since the movement is only in a direction parallel to the z-axis, the pyroelectric tensor is of the form $p_i = (0, 0, p_3)$. The pyroelectric coefficient $p_3 = -4 \times 10^{-5}\ \mathrm{C\,K^{-1}\,m^{-2}}$ for LN [Savage 66].

The relaxation time of the depolarising field due to bulk conductivity is about 2 h at 80°C [Prokhorov 90]. It implies an accumulation of charges on the $+z$ and $-z$ face of the crystal if the temperature change is faster than that. The negative value of p_3 indicates that upon cooling the $+z$ face will become more positively charged. Thus an E-field will be set up by uncompensated surface charges, known as the *pyroelectric* effect. If the positive and negative crystal faces of a z-cut sample are short-circuited, the direction of the pyroelectrically induced current can be used to determine the polarity of the crystal.

1.11 Piezoelectric and converse piezoelectric effect

Piezoelectric effect

LN exhibits an induced polarisation change under applied stress referred to as *piezoelectric effect* and is expressed as

$$\begin{bmatrix} \delta P_1 \\ \delta P_2 \\ \delta P_3 \end{bmatrix} = \begin{bmatrix} & & & & d_{15} & -2d_{22} \\ -d_{22} & d_{22} & & d_{15} & & \\ d_{31} & d_{31} & d_{33} & & & \end{bmatrix} \begin{bmatrix} \sigma_{11} \\ \sigma_{22} \\ \sigma_{33} \\ \sigma_{32}, \sigma_{23} \\ \sigma_{31}, \sigma_{13} \\ \sigma_{21}, \sigma_{12} \end{bmatrix} \tag{1.29}$$

where δP_1, δP_2, δP_3 is the induced polarisation change; d_{ij} is the piezoelectric coefficients (not to be confused with the second order susceptibility coefficients in Eq. 1.8); σ_{11}, σ_{22}, σ_{33} are the tensile stress components (positive by convention) or compressive stress components (negative by convention); and σ_{32}, σ_{23}, σ_{31}, σ_{13}, σ_{21}, σ_{12} are shear stress components. Note that $d_{15} = d_{24}$, $d_{22} = -d_{21} = -d_{16}/2$, and $d_{31} = d_{32}$. Thus the piezoelectric effect in LN can be described by four independent coefficients d_{15}, d_{22}, d_{31}, and d_{33}. Measured values for these quantities are presented in Table 1.8 .

TABLE 1.8: Piezoelectric strain coefficients ($\times 10^{-11}$ C N^{-1}).

d_{15}	d_{22}	d_{31}	d_{33}	Reference
6.92	2.08	−0.085	0.60	[Smith 71]
6.8	2.1	−0.1	0.6	[Warner 67]
7.4	2.1	−0.087	1.6	[Yamada 67]

Converse piezoelectric effect

LN also exhibits a slight change in shape (strain) with an applied oriented E-field E_i, called the *converse piezoelectric effect*. It can be shown through a thermodynamic argument that the coefficients connecting the induced strain and the applied E-field are identical to those connecting the induced polarisation and the applied stress in the direct piezoelectric effect [Nye 87b]. The converse piezoelectric effect can be expressed in matrix form as

$$\begin{bmatrix} \varepsilon_{11} \\ \varepsilon_{22} \\ \varepsilon_{33} \\ (\varepsilon_{32}+\varepsilon_{23})/2 \\ (\varepsilon_{31}+\varepsilon_{13})/2 \\ (\varepsilon_{21}+\varepsilon_{12})/2 \end{bmatrix} = \begin{bmatrix} & -d_{22} & d_{31} \\ & d_{22} & d_{31} \\ & & d_{33} \\ & d_{15} & \\ d_{15} & & \\ -2d_{22} & & \end{bmatrix} \begin{bmatrix} E_1 \\ E_2 \\ E_3 \end{bmatrix} \tag{1.30}$$

where ε_{11}, ε_{22}, ε_{33} are the elastic tensile strain components (positive) or compressive strain components (negative); and ε_{32}, ε_{23}, ε_{31}, ε_{13}, ε_{21}, ε_{12} are the elastic shear strain components.

These two effects allow the transduction from mechanical energy into electrical energy and vice versa which gives rise to many useful applications. In LN the main application of the piezoelectric and converse-piezoelectric effect has been the creation of either bulk or surface acoustic waves (SAW) with the use of interdigital electrodes. The converse-piezoelectric effect has also been used in the detection and characterisation of ferroelectric domain structure [Jungk 06].

1.12 Domain engineering of $LiNbO_3$

1.12.1 Introduction

Many applications of LN crystals utilise its high second-order nonlinear response, which requires the inversion of the sign of the d_{il} nonlinear coefficient in Eq. 1.8, or equivalently the spontaneous polarisation P_s, in order to achieve QPM condition. Micron/nano-scale bulk or surface domain patterns could have applications in micro-electro-mechanical systems (MEMS) and micro-opto-electromechanical systems (MOEMS) devices, electro-optic switches, nonlinear optical and piezoelectric devices etc. The process to control the sign of d_{il} is called *domain engineering*. The section will discuss 1) the crystal structure upon domain inversion, 2) approaches of domain engineering, and 3) domain visualisation techniques.

1.12.2 Crystal structure upon domain inversion

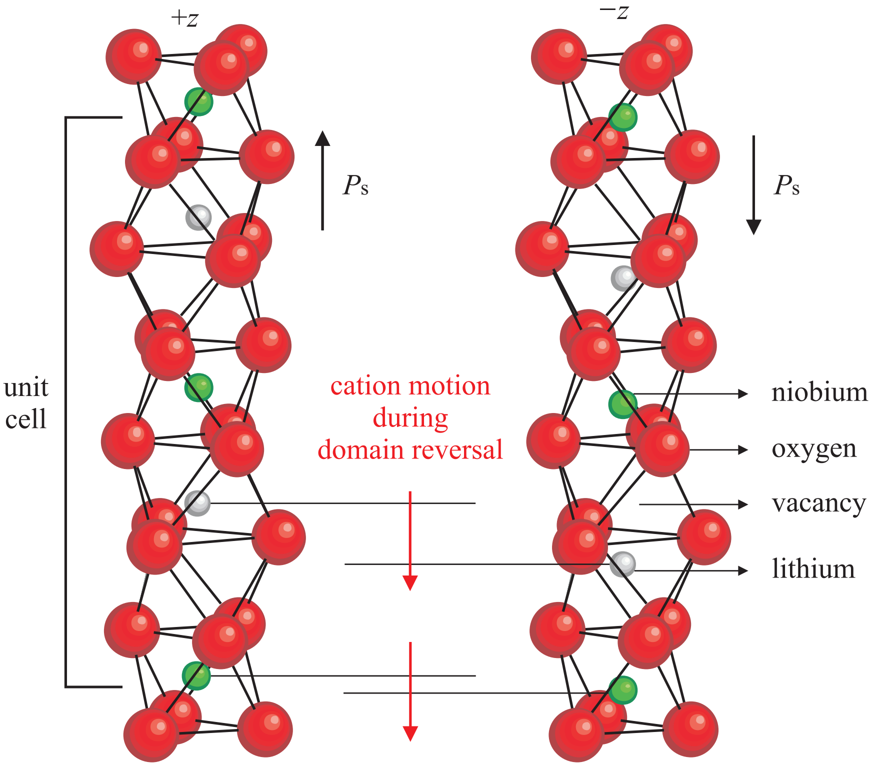

FIGURE 1.12: Cation motion during domain reversal replotted from [Gopalan 07]: 1) a small displacement of the Nb from one asymmetric position to the other equivalent position respect to the center of its octahedron along the z-axis within the same octahedron, and 2) a corresponding motion of the Li from one octahedron, through the intermediate close-packed oxygen plane, to an equivalent displacement in the adjacent vacant octahedron.

It is the position of the metallic ions in the ferroelectric phase (for LN, Li^+ and Nb^{5+} ions) that are responsible for the existence of the electric dipole moment. As illustrated in Fig. 1.12, in order to invert this moment and hence change the direction of polarisation, the ions of lithium and niobium must undergo a transition within the oxygen lattice which is 1) a small displacement of the Nb from one asymmetric position to the other equivalent position respect to the center of its octahedron along the z-axis within the same octahedron, and 2) a corresponding motion of the Li from one octahedron, through the intermediate close-packed oxygen plane, to an equivalent displacement in the adjacent vacant octahedron. The direction of motion of these cations defines the positive end of the spontaneous polarisation, P_s. Given that there are only two permitted directions along z ($\pm z$), only two possible domain orientations can exist, $\pm P_\mathrm{s}$. The required force for the transition is very large and can only been created using high electric fields across the optical axis.

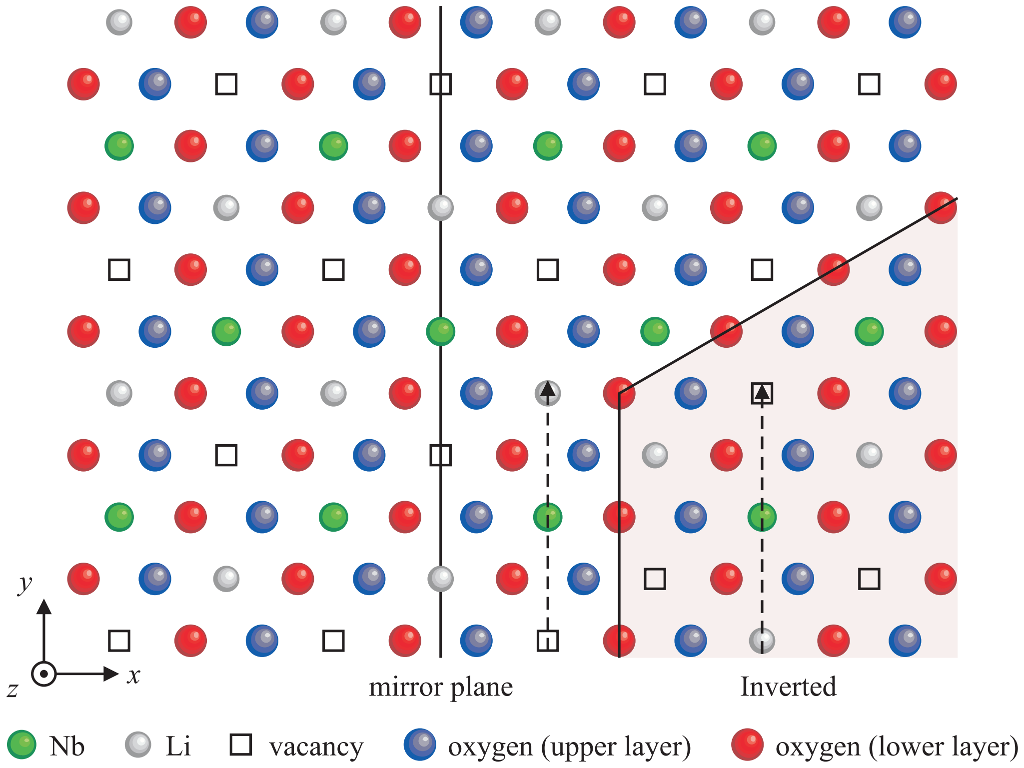

FIGURE 1.13: A layer of LN crystal lattice (the lattice distortions have been ignored for simplicity) replotted from [Valdivia 07]. The mirror plane, perpendicular to the x-axis, is indicated. Ion heights are in the order (bottom to top): O^{2-} (blue), Nb^{5+}, V, Li^{+}, O^{2-} (purple). The shaded region at the right bottom corner indicates an inverted domain with the order of cation ions and vacancies reversed along the original y direction as indicated by the dashed arrows, but remaining the same along the x direction.

To investigate the crystal structure upon domain inversion, two slices of crystal structure are shown in Fig. 1.13 and 1.14. Fig. 1.13 is a layer of LN crystal lattice in the z-face. Right-bottom shows a lattice layer of an inverted domain. It is revealed that looking along the original $+y$ direction of the virgin crystal, the order of cations and vacancies filling the oxygen octahedral interstices changing from virgin state of $\{$V, Nb, Li, $\cdots\}$ to domain inverted state of $\{$Li, Nb, V, $\cdots\}$ as indicated with the dashed arrows. The reversal of the cation order in the original

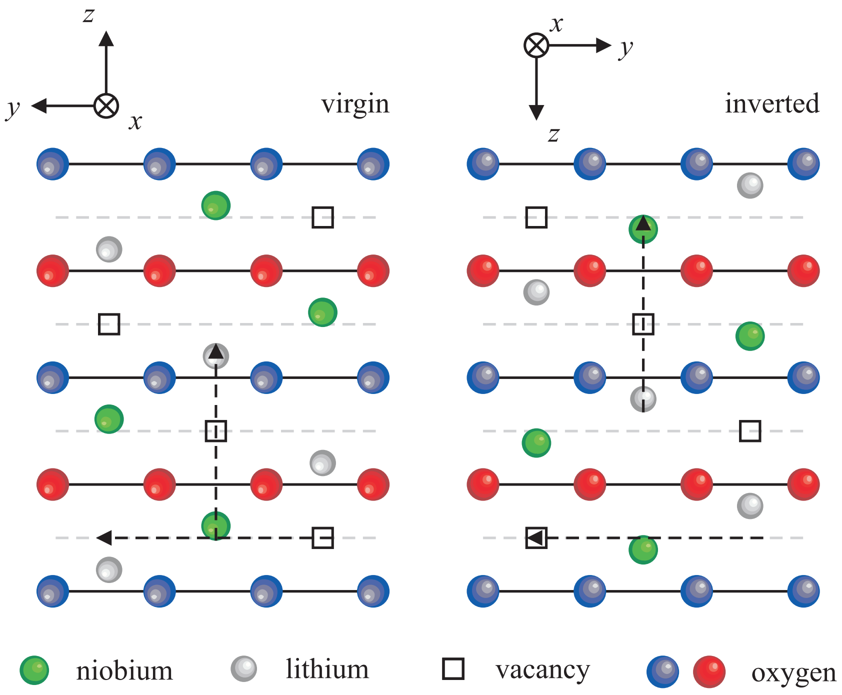

FIGURE 1.14: A layer of crystal lattice of (a) virgin and (b) domain-inverted LN replotted from [Valdivia 07]. The order of cation ions and vacancies is reversed along both y and z direction as indicated by the dashed arrows.

$+y$ direction is also shown as dashed arrows in a x-face slice of the crystal lattice in Fig. 1.14. Moreover, the dashed arrows along the z-axis illustrate a reversal along the original $+z$ direction as well: from the virgin state of $\{\text{Nb, V, Li}, \cdots\}$ to the domain inverted state of $\{\text{Li, V, Nb}, \cdots\}$. As both these states are equivalent, the crystal exhibits two stable states. Thus, domain reversal from $+P_\text{s}$ to $-P_\text{s}$ can be considered as a twofold rotation operation of the unit cell about one of the x-axes (rotation of 180° about x-axes), and as a result, inversion occurs not only for the z-axis but for the y-axis as well.

1.12.3 Approaches of domain engineering

Several techniques are available to realise domain inversion. The most technologically important of ferroelectric crystals is electric-field poling (EFP). Some of the others require the use of high temperature, sometimes approaching the Curie point [Miyazawa 79, Qin 97, Nakamura 87, Huang 94, Webjörn 89a, Webjörn 89b]. Some use electron beam bombardment [Haycock 86, Keys 90], scanning electron [Yamada 91], or ion beams [Li 06]. Recent methods involve the use of scanning force microscopy (SFM) with voltages applied on the tip and similar apparatus [Xue 03, Rosenman 03, Tanaka 06, Mohageg 05, Lilienblum 10]. However, the thesis work here focuses on the light-assisted poling and EFP. Both are described in this section.

Electric field poling

EFP is the most widely used and reliable method of domain engineering, particularly in the LN and LT family of crystals for fabrication of periodically poled LN (PPLN). It enables the spatially preferential domain inversion via patterned electrodes commonly defined by photolithography. The patterned electrodes can be realised in two ways. In the first approach, shown in Fig. 1.15(a), the pattern is photolithographically transferred on to a metal layer which acts as a patterned electrode usually insulated by a overlayer of photoresist or silica [Yamada 93], while on the opposite face a uniform electrode is used. In the second approach, shown in Fig. 1.15(b), photoresist is used as a patterned insulating layer with uniform liquid electrodes on both faces [Webjörn 94]. In both instances of EFP, a positive voltage is applied to the $+z$ face and the $-z$ face is typically grounded. Domain nucleation occurs at the edges of the electrodes where the E-field is highest [Nakamura 02]. The domain then spreads both longitudinally and laterally away from the electrode, where the outward growth of the domain is self-terminating [Nakamura 02] due to the exponential dependence of wall-velocity on the E-field [Gopalan 98], which reduces away from the electrode. However, self-assembled polystyrene spheres in the openings of the patterned photoresist can effectively add edges to the electrode throughout the region to be poled and therefore counteract the preferential nucleation at the electrode edges [Peng 06].

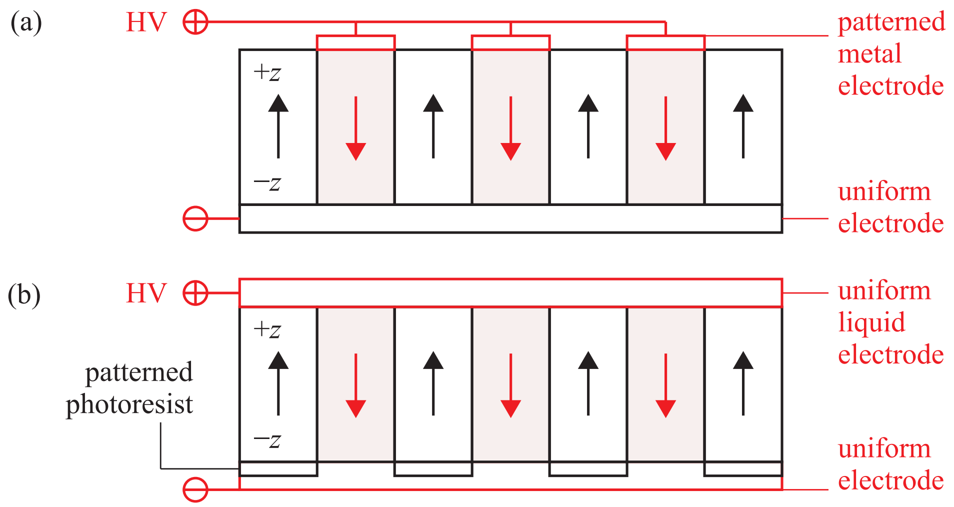

FIGURE 1.15: Electric-field periodic poling setup using (a) metal and (b) photoresist patterning of the electrodes on the $+z$ and $-z$ face, respectively, forming bulk PPLN replotted from [Valdivia 07]. Red regions are the inverted domains.

EFP has been used to form high-quality PPLN, applying a single long voltage pulse (hundreds of milliseconds) until the desired area has inverted [Yamada 93, Webjörn 94, Chen 94]. An adaptation of the above technique is referred to as *pulsed EFP*, where multiple short-duration voltage pulses (typically of order 1 ms) are applied to the crystal to improve the uniformity of the poled structures. Initial voltage pulses nucleate domains on the z-faces, whereas subsequent pulses were observed to provide faster growth along the z-axis as compared to the lateral dimensions, thus enabling the fabrication of domains with high aspect ratio [Yamada 98, Mizuuchi 04].

The longer edges of the patterned electrodes are usually designed to be parallel to the y-axis of the crystal. This is due to anisotropic domain propagation of domain walls, where domains grow faster along the y direction than in the x direction [Sheng 06]. Therefore to achieve domain patterns as loyal to the electrode pattern as possible, domains oriented with their walls along the y-axes are preferred. This is understandable due to the tendency for inverted domains to form hexagonal structures in LN as shown in Fig. 1.16, following the underlying threefold crystalline symmetry. Domain patterning is not limited to periodically poled structures but also other feature shapes including cylindrical lenses [Yamada 96].

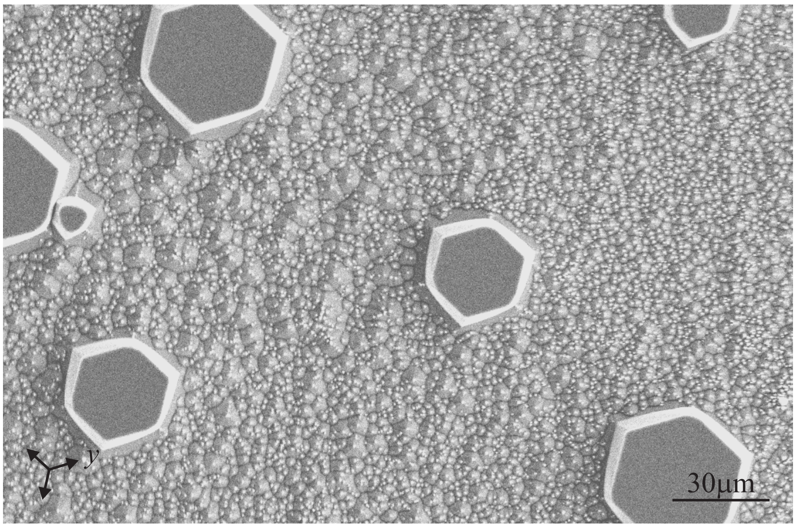

Figure 1.16: SEM image of hexagonal domains with domain wall along y-axis formed during EFP. Domain structures were revealed by HF etching.

Optimal poling and initial nucleation were observed when the metal layers was patterned on the $+z$ face (or photoresist on the $-z$ face) [Miller 98]. Metal electrodes have been observed to reduce the measured bulk polarisation of the crystal after several poling cycles, called *ferroelectric fatigue* or *ageing*. Using tap water, an ionic conductor, has shown no change in the polarisation over many poling cycles [Tian 05]. The cause of the fatigue may result from the formation of a dielectric surface layer, suppression of domain inversion by surface or volume defects, and/or domain wall pinning. Furthermore, SFM-poling shown that nucleation on the $-z$ face was easier and more stable than on the $+z$ face [Xue 03]. Therefore photoresist patterning, which also requires fewer fabrication steps, appears to have an advantage over metal electrode patterns.

Among the advantages of the EFP method are 1) the ability for domain inversion to occur at room temperature, 2) the use of lithographically-defined patterns for fast parallel processing intrinsically compatible with microelectronics fabrication, and 3) the ability to reliably define regular rectangular domains with high aspect-ratios aligned along a y-axis. This technique has led to the birth and wide-spread adoption of PPLN as the domain-engineered material ideally suited for QPM nonlinear interactions in the infrared to visible wavelength regimes, for second harmonic generation [Houe 95] and optical parametric processes [Myers 95].

Poling with light illumination

Illumination by a optical radiation, either near UV or in the blue-green spectral region, was found to affect the E_c value and hence domain switching. The related publications have been summarised in the appendix of [Muir 08a]. However a brief summary of the optically assisted/induced processes will be given here.

Light-assisted poling

In the majority of experiments involving light illumination, the incident light produced a temporary local reduction in the coercive field or nucleation field, thereby requiring a smaller E-field to initiate domain nucleation and sustain domain wall movement. The techniques are referred to as *light-assisted poling* (LAP).

In most experiments of LAP, illumination of LN directly displays a coercive field reduction. Simultaneous illumination with patterned light and application of a uniform E-field in LN produced 15 µm domain periods using a mercury lamp [Fujimura 03]. The coercive and nucleation field reductions are 10% and 50% respectively. Using UV lines of an Ar^+ laser, 8 µm period of segmented inversion points were formed [Müller 03]. A direct-write approach using a confocal microscope with $\lambda = 488$ nm light from an Ar^+ laser has produced 2 µm domain features in undoped and Er-doped LN [Dierolf 04]. LAP is very attractive for applications, because in principle it permits recording of very fine domain features (in the range of microns or even submicron) controlled by the diameter of a focused laser beam [Dierolf 04, Sones 05b].

Direct optical poling

Light illumination has also been used to form inverted domains directly without the application of an externally applied E-field. Surface microdomains were fabricated in CLN crystals under intense pulsed UV irradiation with wavelengths from 248 nm to 329 nm [Wellington 07b, Brown 02, Mailis 03, Valdivia 05, Sones 05a, Mailis 05]. Using phase masks and a recording wavelength $\lambda = 248$ nm, regular domain patterns with a grating period of 726 nm were obtained [Sones 05a]. Even under a nonpatterned light-beam the emerging microdomains tend to self-organise and form regular patterns corresponding to the crystal point symmetry observed on irradiated z-faces independently of their polarity [Valdivia 05] which is interestingly similar to the patterns observed on the z cuts of Fe:LN crystals when irradiation by photoactive light (CW 488 nm, $0.1 - 1\ \mathrm{W\,cm^{-2}}$) and in situ chemical etching [Boyland 00]. Direct optical domain inversion was also realised by scanning a focused CW UV laser beam at $\lambda = 244$ nm on the $-z$ face of undoped, iron doped and titanium in-diffused CLN crystals [Muir 08b].

1.12.4 Domain visualisation

Some of the methods used for the visualisation of ferroelectric domain distributions have been reviewed in [Bermúdez 00, Soergel 05]. Domain visualisation using each technique cannot guarantee that the observed image faithfully reflects the domain structure as there might be other explanations for the observed image. Therefore, several visualisation methods must be used to corroborate the domain-nature of the structure. The visualisation methods that were used in the thesis work are 1) optical methods, 2) preferential HF etching, and 3) piezoresponse force microscopy.

Optical techniques

In perfect optically uniaxial crystals, domains of opposite orientation alter the sign of the second order nonlinear susceptibility coefficient d_{il} in Eq. 1.7, while leaving $\chi_{ij}^{(1)}$ unaffected. Therefore, no refractive index difference exists between ideal domains of opposite orientation and simple microscopy should be incapable of distinguishing them. Yet, several optical methods of domain visualisation have been demonstrated and are in common use to probe the switching process and the domain distribution over the crystal bulk.

In real domain engineered materials, the inversion of the domain symmetry between adjacent regions of the crystal forces a strong mechanical strain-induced birefringence in the vicinity the nonideal (thick) domain walls due to the photoelastic effect [Weis 85]

$$\delta\eta_{ij} = p_{ijkl}\varepsilon_{kl} \qquad i, j, k, l = 1, 2, 3 \tag{1.31}$$

where $\delta\eta_{ij}$ is the second-rank tensor describing the change in dielectric impermeability of the material; ε_{kl} is the second-rank strain tensor; and p_{ijkl} is the fourth-rank photoelastic (strain-optic) tensor. In congruent crystals the strain induced birefringence is as high as $\delta n_{\mathrm{B}} = |n_{\mathrm{o},\perp} - n_{\mathrm{o},\|}| = 10^{-5} - 10^{-4}$ [Yang 98, Yang 99] where subscripts $\perp$ and $\|$ correspond to ordinary index, n_{o}, perpendicular and parallel to a domain wall. However, birefringence is significantly lower in stoichiometric crystals, for example, approximately 10^{-6} in near stoichiometric $\mathrm{LiTaO_3}$ (LT). Viewing these structures along the polar z-axis under crossed polarisers in an optical microscope allows the visualisation of these domain walls [Gopalan 96], although this contrast can be eliminated by subsequent annealing [Kim 05].

The inverted axis of the crystal between adjacent domains leads to the opposite sign of linear EO coefficient r_{ijk} in Eq. 1.18. Thus, if applying a uniform E-field $< E_{\mathrm{c}}$, additional optical contrast can be provided [Gopalan 99b]. The refractive indices in the adjacent domains are changed according to Eq. 1.20. However, the applicable voltage range is limited by domain re-inversion and spreading. Using CLN or CLT, this is not a barrier to optical visualisation. However, SLN and SLT materials are more sensitive to low voltages, placing a much lower limit on the maximum applicable voltage and thus reducing the observable EO refractive index contrast. A combination of the electro-optic refractive index change between the antiparallel domains under external fields and additional contrast caused by mechanical strains at the domain walls permitted the use of the electro-optic imaging microscope for the observation of slow domain dynamics in LN [Gopalan 99a].

Furthermore, upon EFP poling of CLN with defect clusters from the stable state in Fig. 1.6(b) to a frustrated state in Fig. 1.6(c), it results in an increase in the ordinary index: $\delta n_\mathrm{o} = n_\mathrm{o}(\text{frustrated}) - n_\mathrm{o}(\text{stable}) \sim 1 \times 10^{-3}$, with a step transition range of ~ 20 µm across the wall [Kim 05]. In addition, a sharp index profile kink of $\delta n_\mathrm{o} \sim \pm 3 \times 10^{-3}$ is also assumed to localise at the center of the domain wall over a width ≤ 2 µm [Kim 05]. '+' or '−' refers to the side of the stable state or the domain-inverted frustrated state respectively. Therefore, even with randomly polarised white light optical microscopy, the domain walls with δn_o can show a weak scattering and thus appear darker than the matrix in transmission [Gopalan 99b]. It was confirmed that the contrast is nonstoichiometry related by annealing the crystal above 150°C, followed by cooling back which results in a near-complete loss of the optical contrast across the wall. The loss of optical contrast was also found in SLN.

Chemical etching

In LN differential etching of the ferroelectric domain orientations was first used to observe the domain and defect structure of crystals as reported in 1966 [Nassau 66a]. A set of different etchants have been used including a 2:1 mixture of 30% H_2O_2 and NaOH at 50°C, hydrofluoric (HF) acid with $KMnO_4$, and hydrofluoric acid with caustic potash (potassium hydroxide). More recently, Sones et al. [Sones 02b] carried out a comprehensive study into the differential etching rates in z-cut LN. Using the standard mixture of nitric and hydrofluoric acid, it was found that the etching rate of the $-z$ face at room temperature was ~ 0.8 µm h^{-1}, rising to ~ 30 µm h^{-1} at 95°C. However, there was no evidence of etching of the $+z$ face at either of these temperatures. The etch characteristics along the z direction of LN are shown schematically in Fig. 1.17, viewed in cross-sectional profile. The y-faces also exhibit a similar etch characteristic, with the $-y$ face etching much faster than the $+y$ face in HF acid [Niizeki 67]. The cross-sectional profile of periodic domain structures such as PPLN is often visualised by y-face etching of an appropriately cut and polished crystal. The x-face, on the other hand, shows no preferential etching. Experiments were also carried out using only HF, which was found to yield better results than the HF/HNO_3 mixture, in terms of faster etch rates (a factor of two higher) and smoothness of the etched surface [Sones 02b]. No etching was observed using nitric acid alone. A comparison of room-temperature etch rates in pure HF for the y and z-faces is shown in Table 1.9. Sones et

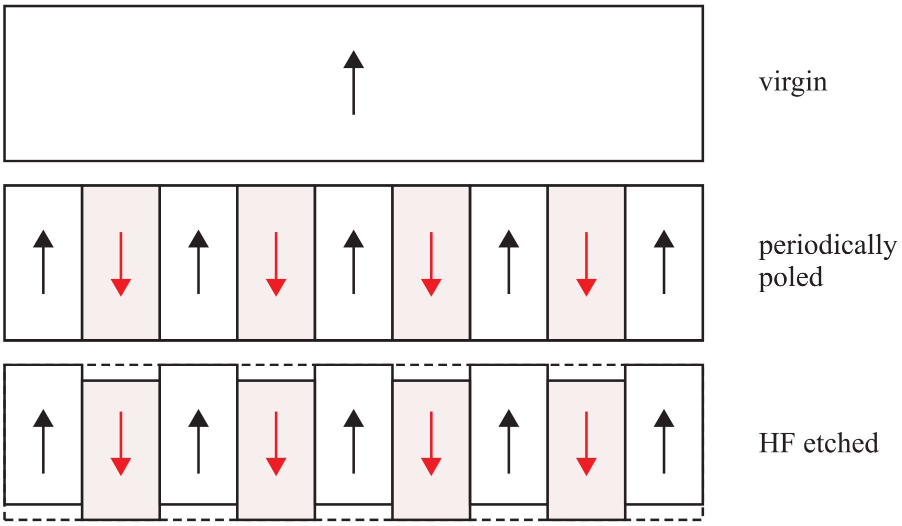

FIGURE 1.17: Schematic of HF etching of LN along the z direction, viewed in cross-section. The arrows indicate the spontaneous polarisations. The dashed lines represent the crystal surface prior to chemical etching. Replotted from [Valdivia 07].

TABLE 1.9: Etching rates of LN in 48% HF acid at room temperature (μm h^{-1}).

Axis	$-$face	$+$face	Reference
z	0.8	nil	[Sones 02b]
y	0.08 – 0.11	0.04 – 0.05	[Valdivia 07]

al. [Sones 02b] also suggested that the etching mechanism is initiated by surface protonation. It explains some of the qualitative observations that 1) differential etching – the negative face is etched faster due to easier absorption of the positively charged proton, and 2) faster etching – the etch rate increases with increasing concentration of acidic protons. The surface protonation mechanism is supported by the observation that the fluorine ions diffuse preferentially into the positive z-face of LN crystals [Bermudez 98].

The advantages of preferential HF etching are 1) it replaces the problem of imaging domain structures with the more conventional problem of imaging topographical features using scanning electron microscopy (SEM), atomic force microscopy (AFM), or other surface-profiling methods, and 2) it does not require complex or expensive equipment. Despite these, HF etching is a destructive process which may limit the usefulness of the domain engineered sample for further application.

As well as being a domain visualisation method, wet etching can be used as a method for making microstructured devices in combination with specific domain pattern. Such devices include alignment grooves for efficient fibre-pigtailing to LN modulators [Barry 98] and piezoelectrically controlled micro-cantilevers [Sones 02a].

In the thesis work, all wet etching was performed using 48% HF acid solution at room temperature with stirring, unless otherwise stated. Depending on the purpose, the etch duration could range from just a few minutes up to days. Usually a brief HF etching for revealing domain structures refers to a $\sim$ 15 min etching period if not explicitly stated, while a deep HF etching can be hours and even days to fabricate ridge structures and initial structures for high temperature surface tension reshaping.

Piezoresponse Force Microscopy

Piezoresponse force microscopy (PFM) is an alternative method for domain visualisation that using a modified atomic force microscope (AFM) via applying an oscillating voltage to a metallised AFM tip in contact mode. The voltage applied to a piezoelectric material causes a deformation of the surface via the converse piezoelectric effect which is detected by the AFM tip. In the last decade, PFM has been used extensively to study ferroelectric domains. This section will focus on 180° domain walls in LN single crystals. The bibliography on domain observations in LN by PFM methods can be found in [Soergel 05, Scrymgeour 05, Gruverman 06].

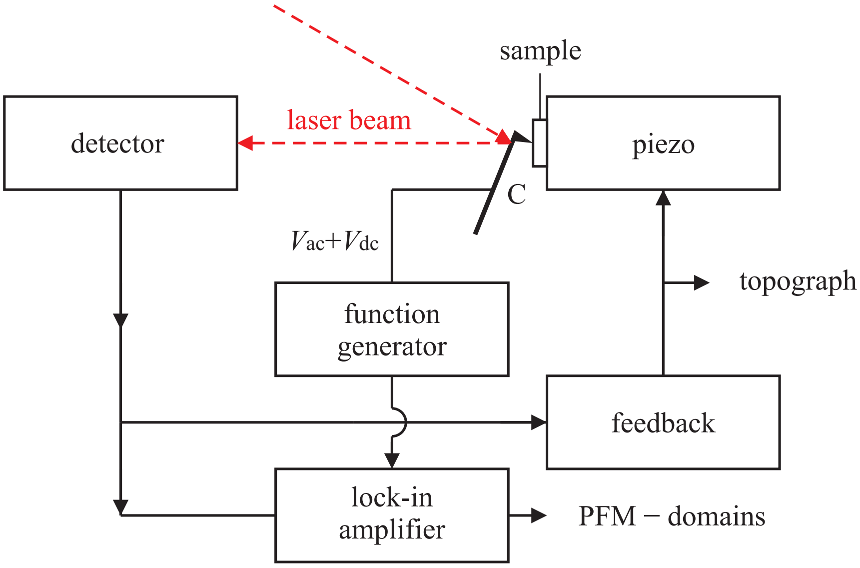

FIGURE 1.18: Schematic setup for the PFM replotted from [Soergel 05]. An alternating voltage $V_{\text{ac}}\cos(\omega t)$ with an optional offset V_{dc} is applied to the conducting tip. The back side of the sample is grounded. A contact-mode feedback is used. The domain signal is read out with a lock-in amplifier operating at the frequency of the alternating voltage that is applied to the tip. (C = Cantilever.)

The setup of PFM is depicted schematically in Fig. 1.18. The conducting tip is electrically contacted, and a modulated alternating voltage $V_{\text{ac}}\cos(\omega t)$ with an optional offset voltage V_{dc} is applied

$$V_{\text{tip}} = V_{\text{dc}} + V_{\text{ac}}\cos(\omega t) \tag{1.32}$$

where V_{tip} is the voltage applied on the tip; V_{ac} is the amplitude of the AC voltage applied on the tip typically of $2.5 - 7.5$ V; ω is the angular frequency of the modulation voltage with value $2\pi \times 5 - 50$ kHz that is much less than the cantilever resonance frequency (> 100 kHz); and t is the time. The feedback loop is to compensate for the topographic variations in order to maintain the constant force in contact mode, the time constant of which is large compared to the period of modulation of the applied voltage and hence not affected by the periodically modulated movement of the cantilever. Read out of the PFM domain signal is performed with a lock-in amplifier, measuring the amplitude of the cantilever vibration and its phase with respect to the applied modulated voltage $V_{\text{ac}}\cos(\omega t)$. A PFM can generate many types of measured data. The primary PFM signals are the amplitude A (magnitude of cantilever deflection), and phase θ (phase of cantilever deflection).

When an external E-field E_3 applied along z-axis of LN crystal, the induced strain due to converse piezoelectric effect can be deduced from Eq. 1.30 as,

$$\begin{bmatrix} \varepsilon_{11} \\ \varepsilon_{22} \\ \varepsilon_{33} \end{bmatrix} = \begin{bmatrix} d_{31}E_3 \\ d_{31}E_3 \\ d_{33}E_3 \end{bmatrix} \tag{1.33}$$

Thus, the induced surface thickness change δd can be derived as

$$\begin{aligned} \delta d &= \int \varepsilon_{33}\,\mathrm{d}x_3 = \int d_{33}E_3\,\mathrm{d}x_3 = d_{33}\int E_3\,\mathrm{d}x_3 \\ &= d_{33}[-V_{\text{tip}}] = d_{33}[-V_{\text{dc}} - V_{\text{ac}}\cos(\omega t)] \qquad \text{(tip on the } +z \text{ face)} \end{aligned} \tag{1.34}$$

where x_3 is the z-axis. It should be noted that the change in the thickness of the sample is dependent upon the voltage and not the E-field at the tip. This is true even for an inhomogeneous E-field. Fig. 1.19 illustrates the piezoresponse across the single 180° domain wall when the PFM probe scans across the LN domain wall region from $+z$ to $-z$ face. $-d_{33}V_{\text{dc}}$ is the static displacement due to a DC applied voltage V_{dc} across the sample. To first order, the deformation of the surface has the same frequency as the driving voltage $V_{\text{ac}}\cos(\omega t)$. The sign of d_{33} is altered for opposite domains. Fig. 1.19 schematically illustrates (a) an opposite domain structure and applied E-field, and (b) its corresponding surface displacement due to the E-field. For the $+z$ face, the application of a positive bias V_{tip} on the tip (E-field pointing into the crystal and antiparallel to the ferroelectric polarisation P_{s}), results in a negative value of $-d_{33}V_{\text{tip}}$, therefore contraction of the sample surface through the d_{33} coefficient and π out-of-phase with the driving voltage $V_{\text{ac}}\cos(\omega t)$. However, for the $-z$ face of a domain, the sign of d_{33} is altered that leads to a positive value of $-d_{33}V_{\text{tip}}$, therefore an expansion of the surface and in-phase with the driving voltage $V_{\text{ac}}\cos(\omega t)$. The amplitude of piezoelectric response on both $+z$ and $-z$ should be equal and the phase changes 180° for a purely electromechanical response from two 180° domains as shown in Fig. 1.19(c) and (d) respectively. Differences, if any, may arise from defects,

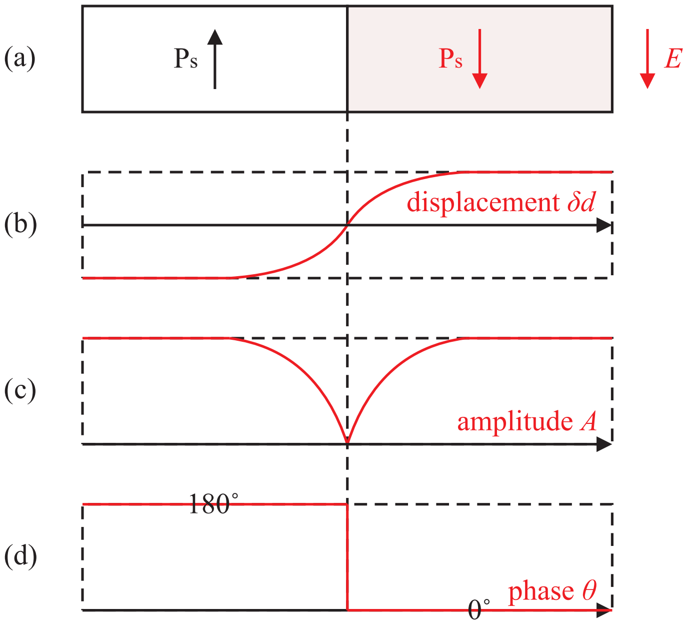

Figure 1.19: Schematic piezoresponse across the single 180° domain wall in LN. (a): schematic opposite domain structure and applied E-field. (b): the surface displacement due to the E-field across the domain wall displaced in (a). (c), (d): the piezoresponse signal [both (c) amplitude A and (d) phase θ] across the domain wall. Replotted from [Tian 06].

nonstoichiometry, and other extrinsic effects that may not follow the domain symmetry. At the domain boundary the amplitude is reduced because of mechanical constraints.

The advantages of PFM are 1) high resolution of nanometres, and 2) in most case nondestructive. It has however a limited depth resolution ~ 1.7 µm and therefore cannot differentiate between surface and bulk domain structures.

References

[Abdi 99] F. Abdi, M. Aillerie, M. Fontana, P. Bourson, T. Volk, B. Maximov, S. Sulyanov, N. Rubinina & M. Wöhlecke, *Influence of Zn doping on electrooptical properties and structure parameters of lithium niobate crystals*, Appl. Phys. B, vol. 68, pages 795–799, 1999.

[Abrahams 66a] S. C. Abrahams, W. C. Hamilton & J. M. Reddy, *Ferroelectric lithium niobate. 4. single crystal neutron diffraction study at 24° C*, J. Phys. Chem. Solids, vol. 27, no. 6-7, pages 1013–1018, June 1966.

[Abrahams 66b] S. C. Abrahams, H. J. Levinstein & J. M. Reddy, *Ferroelectric lithium niobate. 5. polycrystal X-ray diffraction study between 24° and 1200° C*, J. Phys. Chem. Solids, vol. 27, no. 6-7, pages 1019–1026, June 1966.

[Abrahams 66c] S. C. Abrahams, J. M. Reddy & J. L. Bernstein, *Ferroelectric lithium niobate. 3. single crystal X-ray diffraction study at 24° C*, J. Phys. Chem. Solids, vol. 27, no. 6-7, pages 997–1012, June 1966.

[Abrahams 86] S. C. Abrahams & P. Marsh, *Defect structure dependence on composition in lithium niobate*, Acta Crystallogr. B, vol. 42, pages 61–68, 1986.

[Agronin 06] A. Agronin, Y. Rosenwaks & G. Rosenman, *Direct observation of pinning centers in ferroelectrics*, Appl. Phys. Lett., vol. 88, page 072911/1Ű3, 2006.

[Arizmendi 04] L. Arizmendi, *Photonic applications of lithium niobate crystals*, Phys. Status Solidi A, vol. 201, no. 2, pages 253–283, 2004.

[Arlt 88] G. Arlt & H. Neumann, *Internal bias in ferroelectric ceramics: origin and time dependence*, Ferroelectrics, vol. 87, pages 109–120, 1988.

[Armstrong 62] J. A. Armstrong, N. Bloemergen, J. Ducuing & P. S. Pershan, *Interactions between light waves in a nonlinear dielectric*, Phys. Rev., vol. 127, pages 1918–1939, 1962.

[Ashkin 66] A. Ashkin, G. D. Boyd, J. M. Dziedzic, R. G. Smith, A. A. Ballman, J. J. Levinstein & K. Nassau, *Optically induced refractive index inhomogeneities in* $LiNbO_3$ *and* $LiTaO_3$, Appl. Phys. Lett., vol. 9, pages 72–74, 1966.

[Ballman 65] A. A. Ballman, *The growth of piezoelectric and ferroelectric materials by the Czochralski technique*, J. Am. Ceram. Soc., vol. 48, pages 112–113, 1965.

[Barry 98] I. E. Barry, G. W. Ross, P. G. R. Smith, R. W. Eason & G. Cook, *Microstructuring of lithium niobate using differential etch-rate between inverted and non-inverted ferroelectric domains*, Mater. Lett., vol. 37, no. 4-5, pages 246–254, 1998.

[Basun 08] S. A. Basun, G. Cook & D. R. Evans, *Direct temperature dependence measurements of dark conductivity and two-beam coupling in* $LiNbO_3$*:Fe*, Opt. Express, vol. 16, pages 3993–4000, 2008.

[Battle 00] C. C. Battle, S. Kim, V. Gopalan, K. Borkacy & M. C. Gupta, *Ferroelectric domain reversal in congruent* $LiTaO_3$ *at elevated temperatures*, Appl. Phys. Lett., vol. 76, page 2436, 2000.

[Belinicher 80] V. I. Belinicher & B. I. Sturman, *The photogalvanic effect in media lacking a center of symmetry*, Sov. Phys. Usp., vol. 23, pages 199–223, 1980.

[Bergmann 68] G. Bergmann, *The electrical conductivity of* $LiNbO_3$, Solid State Commun., vol. 6, pages 77–79, 1968.

[Bermudez 98] V. Bermudez, F. Caccavale, C. Sada, F. Segato & E. Dieguez, *Etching effect on periodic domain structures of lithium niobate crystals*, J. Cryst. Growth, vol. 191, page 589, 1998.

[Bermúdez 00] V. Bermúdez, A. Gil, L. Arizmendi, J. Cochero, A. M. Baro & E. Dieguez, *Techniques of observation and characterization of the domain structure in periodically poled lithium niobate*, J. Mater. Res., vol. 15, pages 2814–21, 2000.

[Birnie 93] D. P. Birnie, *Analysis of diffusion in lithium niobate*, J. Mater. Sci., vol. 28, no. 2, pages 302–315, 1993.

[Blumel 94] J. Blumel, E. Born & T. Metzger, *Solid-state NMR-study supporting the vacancy defect model in congruent Lithium-Niobate*, J. Phys. Chem. Solids, vol. 55, page 589, 1994.

[Bollmann 77] W. Bollmann & H. J. Stöhr, *Incorporation and mobility of* OH^- *ions in* $LiNbO_3$ *crystals*, Phys. Status Solidi A, vol. 39, pages 477–484, 1977.

[Boyd 92] R. W. Boyd, Nonlinear optics, Academic Press, 1992.

[Boyland 00] A. J. Boyland, S. Mailis, I. E. Barry, R. W. Eason & M. Kaczmarek, *Latency effects and periodic structures in light induced frustrated etching of Fe:doped* $LiNbO_3$, Appl. Phys. Lett., vol. 77, pages 2792–2794, 2000.

[Brands 08] K. Brands, M. Falk, D. Haertle, T. Woike & K. Buse, *Impedance spectroscopy of iron-doped lithium niobate crystals*, Appl. Phys. B, vol. 91, no. 2, pages 279–281, 2008.

[Brown 02] P. T. Brown, S. Mailis, I. Zergioti & R. W. Eason, *Microstructuring of lithium niobate single crystals using pulsed UV laser modification of etching characteristics*, Opt. Mater., vol. 20, pages 125–134, 2002.

[Buse 97] K. Buse, *Light-induced charge transport processes in photorefractive crystals I: models and experimental methods*, Appl. Phys. B, vol. 64, no. 3, pages 273–291, February 1997.

[Byer 97] R. L. Byer, *Quasi-phase matched nonlinear interactions and devices*, J. Nonlinear Opt. Phys. Mater., vol. 6, pages 549–592, 1997.

[Carruthers 71] J. R. Carruthers, G. E. Peterson, M. Grasso & P. M. Bridenbaugh, *Nonstoichiometric and crystal growth of lithium niobate*, J. Appl. Phys., vol. 42, page 1846, 1971.

[Chen 68] F. S. Chen, J. T. LaMacchia & D. B. Fraser, *Holographic storage in* $LiNbO_3$, Appl. Phys. Lett., vol. 13, page 223, 1968.

[Chen 69] F. S. Chen, *Optically induced change of refractive indices in* $LiNbO_3$ *and* $LiTaO_3$, J. Appl. Phys., vol. 40, page 3389, 1969.

[Chen 94] Q. Chen & W. P. Risk, *Periodic poling of* $KTiOPO_4$ *using an applied electric field*, Electron. Lett., vol. 30, pages 1516–1517, 1994.

[Chen 07] R. H. Chen, L. F. Chen & C. T. Chia, *Impedance spectroscopic studies on congruent* $LiNbO_3$ *single crystal*, J. Phys.: Condens. Matter, vol. 19, page 086225, 2007.

[Choy 76] M. M. Choy & R. L. Byer, *Accurate second order susceptibility of visible and infrared nonlinear crystal*, Phys. Rev. B, vol. 14, pages 1693–1706, 1976.

[Committe 49] IRE Standards Committe, *IRE standards on piezoelectric crystals*, Proc. IRE, vol. 37, page 1378, 1949.

[Cross 87] L. E. Cross, *Relaxor ferroelectrics*, Ferroelectrics, vol. 76, pages 241–267, 1987.

[de Miguel-Sanz 02] E. M. de Miguel-Sanz, M. Carrascosa & L. Arizmendi, *Effect of the oxidation state and hydrogen concentration on the lifetime of thermally fixed holograms in* $LiNbO_3$*:Fe*, Phys. Rev. B, vol. 65, page 165101, 2002.

[Dierolf 04] V. Dierolf & C. Sandmann, *Direct-write method for domain inversion patterns in LiNbO*$_3$, Appl. Phys. Lett., vol. 84, no. 20, pages 3987–3989, 2004.

[Elliott 98] S. R. Elliott, The physics and chemistry of solids, Wiley, 1998.

[Fedulov 65] S. A. Fedulov, Z. I. Shapiro & P. B. Ladyzhinskii, *The growth of crystals of LiNbO*$_3$*, LiTaO*$_3$ *and NaNbO*$_3$ *by the Czochralski method*, Sov. Phys. Crystallogr., vol. 10, pages 218–220, 1965.

[Fejer 92] M. M. Fejer, G. A. Magel, D. H. Jundt & R. L. Byer, *Quasi-phase-matched second harmonic generation: tuning and tolerances*, IEEE J. Quantum Electron., vol. 28, pages 2631–2654, 1992.

[Festl 82] H. G. Festl, P. Hertel E. Krätzig & R. von Baltz, *Investigations of the photovoltaic tensor in doped LiNbO*$_3$, Phys. Status Solidi B, vol. 113, pages 157–162, 1982.

[Frejlich 07] J. Frejlich, Photorefractive materials, Chapter 1: electro-optic effect, page 17, Wiley-Interscience, 2007.

[Fridkin 79] V. M. Fridkin & R. M. Magomadov, *Anomalous photovoltaic effect in LiNbO*$_3$*:Fe in polarized light*, Sov. Phys. JETP Lett., vol. 30, pages 686–688, 1979.

[Fujimura 03] M. Fujimura, T. Sohmura & T. Suhara, *Fabrication of domain-inverted gratings in MgO:LiNbO*$_3$ *by applying voltage under ultraviolet irradiation through photomask at room temperature*, Electron. Lett., vol. 39, no. 9, pages 719–721, 2003.

[Furukawa 00] Y. Furukawa, K. Kitamura, S. Takekawa, A. Miyamoto, M. Terao & N. Suda, *Photorefraction in LiNbO*$_3$ *as a function of [Li]/[Nb] and MgO concentrations*, Appl. Phys. Lett., vol. 77, pages 2494–2496, 2000.

[Glass 74] A. M. Glass, D. von der Linde & T. J. Negran, *High-voltage bulk photovoltaic effect and the photorefractive process in LiNbO*$_3$, Appl. Phys. Lett., vol. 25, no. 4, pages 233–235, 1974.

[Glass 75] A. M. Glass, D. von der Linde, D. H. Auston & T. J. Negran, *Excited state polarization, bulk photovoltaic effect and the photorefractive effect in electrically polarized media*, J. Electron. Mater., vol. 4, pages 915–943, 1975.

[Gopalan 96] V. Gopalan & M. C. Gupta, *Origin of internal field and visualization of 180° domains in congruent LiTaO*$_3$ *crystals*, J. Appl. Phys., vol. 80, pages 6099–6106, 1996.

[Gopalan 97] V. Gopalan & M. C. Gupta, *Origin and characteristics of internal fields in* $LiNbO_3$ *crystals*, Ferroelectrics, vol. 198, page 49, 1997.

[Gopalan 98] V. Gopalan & T. E. Mitchell, *Wall velocities, switching times, and the stabilization mechanism of 180° domains in congruent* $LiTaO_3$ *crystals*, J. Appl. Phys., vol. 83, pages 941–954, 1998.

[Gopalan 99a] V. Gopalan, S. S. A. Gerstl, A. Itagi, T. E. Mitchell, Q. X. Jia, T. E. Schlesinger & D. D. Stancil, *Mobility of 180° domain walls in congruent* $LiTaO_3$ *measured using real-time electro-optic imaging microscopy*, J. Appl. Phys., vol. 86, pages 1638–46, 1999.

[Gopalan 99b] V. Gopalan & T. E. Mitchell, *In situ video observation of 180° domain switching in* $LiTaO_3$ *by electro-optic imaging microscopy*, J. Appl. Phys., vol. 85, no. 4, pages 2304–2311, 1999.

[Gopalan 00] V. Gopalan, N. A. Sanford, J. A. Aust, K. Kitamura & Y. Furukawa, Handbook of advanced electronic and photonic materials and devices, vol. 4 ferroelectric and dielectrics, Chapter 2: crystal growth, characterization, and domain studies in lithium niobate and lithium tantalate ferroelectrics, pages 57–114, Academic, 2000.

[Gopalan 07] V. Gopalan, V. Dierolf & D. A. Scrymgeour, *Defect-domain wall interactions in trigonal ferroelectrics*, Ann. Rev. Mater. Res., vol. 37, pages 449–489, 2007.

[Gruverman 06] A. Gruverman & S. V. Kalinin, *Piezoresponseforce microscopy and recent advances in nanoscale studies of ferroelectrics*, J. Mater. Sci., vol. 41, pages 107–116, 2006.

[Günter 88] P. Günter & J. P. Huignard, Photorefractive materials and their applications I: fundamental phenomena, volume 61 of *Topics in Applied Physics*, Springer, Berlin, 1988.

[Günter 06] P. Günter & J. P. Huignard, Photorefractive materials and their applications 1: basic effects, volume 113 of *Springer Series in Optical Sciences*, Springer, Berlin, 2006.

[Günter 07a] P. Günter & J. P. Huignard, Photorefractive materials and their applications 2: materials, volume 114 of *Springer Series in Optical Sciences*, Springer, Berlin, 2007.

[Günter 07b] P. Günter & J. P. Huignard, Photorefractive materials and their applications 3: applications, volume 115 of *Springer Series in Optical Sciences*, Springer, Berlin, 2007.

[Gupta 07] M. C. Gupta & J. Ballato, editeurs, The handbook of photonics, second edition, Chapter 6: ferroelectric materials, pages 6–2, CRC Press, 2007.

[Haycock 86] P. W. Haycock & P. D. Townsend, *A method of poling $LiNbO_3$ and $LiTaO_3$ below T_c*, Appl. Phys. Lett., vol. 48, pages 698–700, 1986.

[Houe 95] M. Houe & P. Townsend, *An introduction to methods of periodic poling for second-harmonic generation*, J. Phys. D: Appl. Phys., vol. 28, pages 1747–1763, 1995.

[Huang 94] L. Huang & N. A. F. Jaeger, *Discussion of domain inversion in $LiNbO_3$*, Appl. Phys. Lett., vol. 65, no. 14, pages 1763–1765, 1994.

[Ivanov 78] S. A. Ivanov, A. E. Korneev, E. V. Kolontsova & Y. N. Venevtsev, *Temperature dependence of intensity of diffuse X-ray scattering in single crystals of $LiTaO_3$*, Kristallografiya, vol. 23, pages 1071–1073, 1978.

[Ivanova 98] E. M. Ivanova, N. A. Sergeev & A. V. Yatsenko, *Analysis of intrinsic defects in the lithium niobate structure by the NMR ^7Li method*, Kristallografiya, vol. 43, pages 337–40, 1998.

[Iyi 92] N. Iyi, K. Kitamura, F. Izumi, J. K. Yamamoto, T. Hayashi, H. Asano & S. Kimura, *Comparative study of defect structures in lithium niobate with different compositions*, J. Solid State Chem., vol. 101, no. 2, pages 340–352, 1992.

[Jorgensen 69] P. J. Jorgensen & R. W. Bartlett, *High temperature transport processes in lithium niobate*, J. Phys. Chem. Solids, vol. 30, no. 12, pages 2639–2648, 1969.

[Jungk 06] T. Jungk, A. Hoffmann & E. Soergel, *Quantitative analysis of ferroelectric domain imaging with piezoresponse force microscopy*, Appl. Phys. Lett., vol. 89, page 163507, 2006.

[Keys 90] R. Keys, A. Loni, R. de la Rue, C. Ironside, J. Marsh, B. Luff & P. Townsend, *Fabrication of domain reversed gratings for SHG in $LiNbO_3$ by electron beam bombardment*, Electron. Lett., vol. 26, pages 188–190, 1990.

[Kim 01] S. Kim, V. Gopalan, K. Kitamura & Y. Furukawa, *Domain reversal and nonstoichiometry in lithium tantalate*, J. Appl. Phys., vol. 90, no. 6, pages 2949–2963, 2001.

[Kim 05] S. Kim & V. Gopalan, *Optical index profile at an antiparallel ferroelectric domain wall in lithium niobate*, Mater. Sci. Eng. B, vol. 120, no. 1-3, pages 91–94, 2005.

[Kittel 04] C. Kittel, Introduction to solid state physics, Wiley, 2004.

[Klauer 92] S. Klauer, M. Wöhlecke & S. Kapphan, *Influence of H-D isotopic substitution on the protonic conductivity of* $LiNbO_3$, Phys. Rev. B, vol. 45, no. 6, page 2786, 1992.

[Korkishko 97] Y. N. Korkishko & V. A. Fedorov, Ion exchange in single crystals for integrated optics and optoelectronics, Cambridge International Science Publishing, 1997.

[Krätzig 77] E. Krätzig & H. Kurz, *Spectroscopic investigation of photovoltaic effects in doped* $LiNbO_3$, J. of Electrochem. Soc., vol. 124, pages 131–134, 1977.

[Kuz'minov 97] Y. S. Kuz'minov, Lithium niobate crystals, Cambridge International Science Publishing, 1997.

[Lambeck 77] P. V. Lambeck & G. H. Jonker, *Ferroelectric domain stabilization in* $BaTiO_3$ *by bulk ordering of defects*, Ferroelectrics, vol. 22, pages 729–731, 1977.

[Lerner 68] P. Lerner, C. Legras & J. P. Dumas, *Stoechiometrie des monocristaux de metaniobate de lithium*, J. Crysr. Growth, vol. 3, pages 231–235, 1968.

[Li 06] X. Li, K. Terabe, H. Hatano, H. Zeng & K. Kitamura, *Domain patterning thin crystalline ferroelectric film with focused ion beam for nonlinear photonic integrated circuits*, J. Appl. Phys., vol. 100, page 106103, 2006.

[Lilienblum 10] M. Lilienblum, A. Ofan, A. Hoffmann, O. Gaathon, L. Vanamurthy, S. Bakhru, H. Bakhru, R. M. Osgood & E. Soergel, *Low-voltage nanodomain writing in He-implanted lithium niobate crystals*, Appl. Phys. Lett., vol. 96, no. 8, page 082902, February 2010.

[Lines 77] M. E. Lines & A. M. Glass, Principles and applications of ferroelectrics and related materials, Clarenon Press, 1977.

[Luennemann 03] M. Luennemann, U. Hartwig, G. Panotopoulos & K. Buse, *Electrooptic properties of lithium niobate crystals for extremely high external electric fields*, Appl. Phys. B, vol. 76, pages 403–406, 2003.

[Mailis 03] S. Mailis, C. Riziotis, I. T. Wellington, P. G. R. Smith, C. B. E. Gawith & R. W. Eason, *Direct ultraviolet writing of channel waveguides in congruent* *lithium niobate single crystals*, Opt. Lett., vol. 28, no. 16, pages 1433–1435, 2003.

[Mailis 05] S. Mailis, C. L. Sones, J. G. Scott & R. W. Eason, *UV laser-induced ordered surface nanostructures in congruent lithium niobate single crystals*, Appl. Surf. Sci., vol. 247, pages 497–503, 2005.

[Mamedov 84] A. M. Mamedov, M. A. Osman & L. C. Hajieva, *VUV reflectivity of* $LiNbO_3$ *and* $LiTaO_3$ *single crystals*, Appl. Phys. A, vol. 34, no. 3, pages 189–192, 1984.

[Mamedov 85] A. M. Mamedov, L. S. Hajiyeva, I. S. Ibragimova & B. S. Aliyeva, *Vacuum ultraviolet (VUV) reflectivity and electron states in* $LiNbO_3$, Physica B+C, vol. 128, pages 61–68, 1985.

[Matthias 49] B. T. Matthias & J. P. Remeika, *Ferroelectricity in the ilmenite structure*, Phys. Rev., vol. 76, no. 12, page 1886, December 1949.

[Mehta 91] A. Mehta, E. K. Chang & D. M. Smyth, *Ionic transport in* $LiNbO_3$, J. Mater. Res., vol. 6, no. 4, pages 851–854, 1991.

[Miller 98] G. D. Miller, *Periodically poled lithium niobate: modeling, fabrication, and nonlinear-optical performance*, PhD thesis, Department of electrical engineering, Stanford University, 1998.

[Miyazawa 79] S. Miyazawa, *Ferroelectric domain inversion in Ti-diffused* $LiNbO_3$ *optical waveguides*, J. Appl. Phys., vol. 50, pages 4599–4603, 1979.

[Mizuuchi 04] K. Mizuuchi, A. Morikawa, T. Sugita & K. Yamamoto, *Electric-field poling in Mg-doped* $LiNbO_3$, J. Appl. Phys., vol. 96, pages 6585–6590, 2004.

[Mohageg 05] M. Mohageg, D. V. Strekalov, A. A. Savchenkov, A. B. Matsko, V. S. Ilchenko & L. Maleki, *Calligraphic poling of lithium niobate*, Opt. Express, vol. 13, pages 3408–3419, 2005.

[Muir 08a] A. C. Muir, *Interactions of single-crystal lithium niobate surfaces with ultraviolet laser radiation*, PhD thesis, Optoelectronics Research Centre, University of Southampton, Southampton, 2008.

[Muir 08b] A. C. Muir, C. L. Sones, S. Mailis, R. W. Eason, T. Jungk, A. Hoffman & E. Soergel, *Direct-writing of inverted domains in lithium niobate using a continuous wave ultra violet laser*, Opt. Express, vol. 16, no. 4, pages 2336–2350, February 2008.

[Müller 03] M. Müller, E. Soergel & K. Buse, *Influence of ultraviolet illumination on the poling characteristics of lithium niobate crystals*, Appl. Phys. Lett., vol. 83, no. 9, pages 1824–1826, 2003.

[Myers 95] L. E. Myers, R. C. Eckardt, M. M. Fejer, R. L. Byer, W. R. Bosenberg & J. W. Pierce, *Quasi-phase-matched optical parametric oscillators in bulk periodically poled* $LiNbO_3$, J. Opt. Soc. Am. B, vol. 12, pages 2102–2116, 1995.

[Nakamura 87] K. Nakamura, H. Ando & H. Shimizu, *Ferroelectric domain inversion caused in* $LiNbO_3$ *plates by heat treatment*, Appl. Phys. Lett., vol. 50, no. 20, pages 1413–1414, 1987.

[Nakamura 02] K. Nakamura, J. Kurz, K. Parameswaran & M. M. Fejer, *Periodic poling of magnesium-oxide-doped lithium niobate*, J. Appl. Phys., vol. 91, no. 7, pages 4528–4534, 2002.

[Nassau 66a] K. Nassau, H. J. Levinstein & G. M. Loiacono, *Ferroelectric lithium niobate. 1. growth, domain structure, dislocations and etching*, J. Phys. Chem. Solids, vol. 27, no. 6-7, pages 983–988, June 1966.

[Nassau 66b] K. Nassau, H. J. Levinstein & G. M. Loiacono, *Ferroelectric lithium niobate. 2. preparation of single domain crystals*, J. Phys. Chem. Solids, vol. 27, no. 6-7, pages 989–996, June 1966.

[Niitsu 04] G. T. Niitsu, H. Nagata & A. C. M. Rodrigues, *Electrical properties along the X and Z axes of* $LiNbO_3$ *wafers*, J. Appl. Phys., vol. 95, pages 3116–3119, 2004.

[Niizeki 67] N. Niizeki, T. Yamada & H. Toyoda, *Growth ridges, etched hillocks, and crystal structure of lithium niobate*, Jpn. J. Appl. Phys., vol. 6, pages 318–326, 1967.

[Nye 87a] J. F. Nye, Physical properties of crystals, Oxford: Clarendon Press, 1987.

[Nye 87b] J. F. Nye, Physical properties of crystals, Chapter 7: piezoelectricity, third-rank tensors, page 115, Oxford: Clarendon Press, 1987.

[O'Bryan 85] H. M. O'Bryan, P. K. Gallagher & C. D. Brandle, *Congruent composition and Li-rich phase boundary of* $LiNbO_3$, J. Am. Ceram. Soc., vol. 68, pages 493–496, 1985.

[Orlowski 78] R. Orlowski & E. Krätzig, *Holographic method for the determination of photoinduced electron and hole transport in electro-optic crystals*, Solid State Commun., vol. 27, page 1351, 1978.

[Peng 06] L. H. Peng, Y. H. Chen, C. D. Lin, L. F. Lin & A. H. Kung, *Sub-micrometer domain engineering on periodically poled lithium niobate*, J. Cryst. Growth, vol. 292, pages 328–331, 2006.

[Peterson 71] G. E. Peterson, A. M. Glass & T. J. Negran, *Control of the susceptibility of lithium niobate to laser-induced refractive index change*, Appl. Phys. Lett., vol. 19, page 130, 1971.

[Phillips 72] W. Phillips, J. J. Amodei & D. S. Staebler, *Optical and holographic storage properties of transition metal doped lithium niobate*, RCA Rev., vol. 33, pages 94–109, 1972.

[Prokhorov 90] A. M. Prokhorov & Y. S. Kuz‘minov, Physics and chemistry of crystalline lithium niobate, Hilger, IOP Publishing Ltd, Bristol, BS1 6NX, England, 1990.

[Pruneri 96] V. Pruneri, *Electric field periodically inverted LiNbO*$_3$ *for optical frequency conversion*, PhD thesis, Optoelectronics Research Centre, University of Southampton, 1996.

[Ptashnik 85] V. B. Ptashnik, T. Y. Dunaeva & I. V. Myasnikov, *Self-diffusion of lithium niobate single crystal*, Izv. Akad. Nauk Neorg. Muter., vol. 21, page 2076, 1985.

[Qin 97] Y. Q. Qin, Y. Y. Zhu, S. N. Zhu, H. Shu & N. B. Ming, *Electron probe microanalysis of periodic domain inversion in LiNbO*$_3$ *by Ti diffusion*, Mater. Lett., vol. 30, pages 231–234, 1997.

[Rauber 78] A. Rauber, Current topics in material science, vol. 1, Chapter 7: chemistry and physics of lithium niobate, page 481, North-Holland, 1978.

[Redfield 74] D. Redfield & W. J. Burke, *Optical-absorption edge of LiNbO*$_3$, J. Appl. Phys., vol. 45, no. 10, pages 4566–4571, 1974.

[Roberts 92] D. A. Roberts, *Simplified characterization of uniaxial and biaxial nonlinear optical crystals: a plea for standardization of nomenclature and conventions*, IEEE J. Quantum Electron., vol. 28, pages 2057–2074, 1992.

[Rosenman 03] G. Rosenman, P. Urenski, A. Agronin, Y. Rosenwaks & M. Molotskii, *Submicron ferroelectric domain structures tailored by high-voltage scanning probe microscopy*, Appl. Phys. Lett., vol. 82, pages 103–105, 2003.

[Savage 66] A. Savage, *Visual system-response functions and estimating reflectance*, J. Appl. Phys., vol. 37, page 3071, 1966.

[Schirmer 91] O. F. Schirmer, O. Thiemann & M. Wöhlecke, *Defects in LiNbO*$_3$ *I. experimental aspects*, J. Phys. Chem. Solids, vol. 52, pages 185–200, 1991.

[Schlarb 93] U. Schlarb & K. Betzier, *Refractive indices of lithium niobate as a function of wavelength and composition*, J. Appl. Phys., vol. 73, pages 3472–3476, 1993.

[Schlarb 95] U. Schlarb, M. Wöhlecke, B. Gather, A. Reichert, K. Betzler, T. Volk & N. Rubinina, *Refractive indices of Zn-doped lithium niobate*, Opt. Mater., vol. 4, page 791, 1995.

[Schmidt 89] N. Schmidt, K. Betzler, M. Grabs, S. Kapphan & F. Klose, *Spatially resolved second-harmonic generation investigations of proton-induced refractive-index changes in LiNbO*$_3$, J. Appl. Phys., vol. 65, pages 1253–1256, 1989.

[Scrymgeour 05] D. A. Scrymgeour & V. Gopalan, *Nanoscale piezoelectric response across a single antiparallel ferroelectric domain wall*, Phys. Rev. B, vol. 72, page 024103, 2005.

[Sheng 06] Y. Sheng, T. Wang, B. Ma, E. Qu, B. Cheng & D. Zhang, *Anisotropy of domain broadening in periodically poled lithium niobate crystals*, Appl. Phys. Lett., vol. 88, page 041121, 2006.

[Smith 71] R. T. Smith & F. S. Welsh, *Temperature dependence of the elastic, piezoelectric, and dielectric constants of lithium tantalate and lithium niobate*, J. Appl. Phys., vol. 42, no. 6, pages 2219–2230, 1971.

[Soergel 05] E. Soergel, *Visualization of ferroelectric domains in bulk single crystals*, Appl. Phys. B, vol. 81, pages 729–751, 2005.

[Sones 02a] C. Sones, S. Mailis, V. Apostolopoulos, I. E. Barry, C. Gawith, P. G. R. Smith & R. W. Eason, *Fabrication of piezoelectric micro-cantilevers in domain-engineered LiNbO*$_3$ *single crystals*, J. Micromech. Microeng., vol. 12, no. 1, pages 53–57, 2002.

[Sones 02b] C. L. Sones, S. Mailis, W. S. Brocklesby, R. W. Eason & J. R. Owen, *Differential etch rates in z-cut LiNbO*$_3$ *for variable HF/HNO*$_3$ *concentrations*, J. Mater. Chem., vol. 12, no. 2, pages 295–298, 2002.

[Sones 05a] C. L. Sones, C. E. Valdivia, J. G. Scott, S. Mailis, R. W. Eason, D. A. Scrymgeour, V. Gopalan, T. Jungk & E. Soergel, *Ultraviolet laser-induced sub-micron periodic domain formation in congruent undoped lithium niobate crystals*, Appl. Phys. B, vol. 80, page 341, 2005.

[Sones 05b] C. L. Sones, M. C. Wengler, C. E. Valdivia, S. Mailis, R. W. Eason & K. Buse, *Light-induced order-of-magnitude decrease in the electric field for domain nucleation in MgO-doped lithium niobate crystals*, Appl. Phys. Lett., vol. 86, no. 21, page 212901, 2005.

[Sturman 80] B. Sturman, *The photogalvanic effect – a new mechanism of nonlinear wave interaction in electrooptic crystals*, Sov. J. Quantum Electron., vol. 10, pages 276–278, 1980.

[Sturman 92] B. I. Sturman & V. M. Fridkin, The photovoltaic and photorefractive effects in noncentrosymmetric materials, Gordon and Breach Science Publishers, 1992.

[Tanaka 06] K. Tanaka, Y. Hiranaga & Y. Cho, *Real information storage using ferroelectrics with a density of 1 Tbit/inch*^{2}, Ferroelectrics, vol. 340, pages 99–105, 2006.

[Tian 05] L. Tian & V. Gopalan, *Comparison of domain reversal and electro-optic properties of congruent and stoichiometric lithium tantalate*, Proc. SPIE, vol. 5728, pages 278–282, 2005.

[Tian 06] L. L. Tian, *Nanoscale probing and photonic applications of ferroelectric domain walls*, PhD thesis, Department of Materials Science and Engineering, The Pennsylvania State University, Southampton, 2006.

[Valdivia 05] C. E. Valdivia, C. L. Sones, J. G. Scott, S. Mailis, R. W. Eason, D. A. Scrymgeour, V. Gopalan, T. Jungk, E. Soergel & I. Clark, *Nanoscale surface domain formation on the +z face of lithium niobate by pulsed UV laser illumination*, Appl. Phys. Lett., vol. 86, page 022906, 2005.

[Valdivia 07] C. E. Valdivia, *Light-induced ferroelectric domain engineering in lithium niobate & lithium tantalate*, PhD thesis, Optoelectronics Research Centre, University of Southampton, Southampton, 2007.

[Volk 08a] T. Volk & M. Wöhlecke, Lithium niobate: defects, photorefraction and ferroelectric switching, Springer, 2008.

[Volk 08b] T. Volk & M. Wöhlecke, Lithium niobate: defects, photorefraction and ferroelectric switching, Chapter 3: general introduction to photorefraction in $LiNbO_3$, page 53, Springer, 2008.

[Volk 08c] T. Volk & M. Wöhlecke, Lithium niobate: defects, photorefraction and ferroelectric switching, Chapter 2: point defects in $LiNbO_3$, page 28, Springer, 2008.

[von Baltz 83] R. von Baltz, C. Lingerfelder & R. Rupp, *Nonlocal photovoltaic response function for the interpretation of hologram writing in ferroelectric crystals*, Appl. Phys. A, vol. 32, pages 13–18, 1983.

[Warner 67] A. W. Warner, M. Onoe & G. A. Coquin, *Determination of elastic and piezoelectric constants for crystals in class (3m)*, J. Acoust. Soc. Amer., vol. 42, pages 1223–1231, 1967.

[Warren 96] L. Warren, G. E. Pike, K. Vanheusden, D. Dimos, B. A. Tuttle & J. Robertson, *Defect-dipole alignment and tetragonal strain in ferroelectrics*, J. Appl. Phys., vol. 79, pages 9250–7, 1996.

[Webjörn 89a] J. Webjörn, F. Laurell & G. Arvidsson, *Blue light generated by frequency doubling of laser diode light in a lithium niobate channel waveguide*, Photon. Technol. Lett., vol. 1, pages 316–318, 1989.

[Webjörn 89b] J. Webjörn, F. Laurell & G. Arvidsson, *Fabrication of periodically domain-inverted channel waveguides in lithium niobate for second harmonic generation*, J. Lightwave Technol., vol. 7, pages 1597–1600, 1989.

[Webjörn 94] J. Webjörn, V. Pruneri, P. S. Russell, J. R. M. Barr & D. C. Hanna, *Quasi-phase-matched blue-light generation in bulk lithium niobate, electrically poled via periodic liquid electrodes*, Electron. Lett., vol. 30, pages 894–895, 1994.

[Weis 85] R. S. Weis & T. K. Gaylord, *Lithium niobate: summary of physical properties and crystal structure*, Appl. Phys. A, vol. 37, no. 4, pages 191–203, August 1985.

[Wellington 07a] I. T. Wellington, *Direct UV writing of structures in lithium niobate and lithium tantalate*, PhD thesis, Optoelectronics Research Centre, University of Southampton, Southampton, 2007.

[Wellington 07b] I. T. Wellington, C. E. Valdivia, T. J. Sono, C. L. Sones, S. Mailis & R. W. Eason, *Ordered nano-scale domains in lithium niobate single crystals via phase-mask assisted all-optical poling*, Appl. Surf. Sci., vol. 253, pages 4215–4219, 2007.

[Wemple 72] S. H. Wemple & M. DiDomenico, *Electrooptical and nonlinear optical properties of crystals*, Appl. Solid State Sci., vol. 3, pages 263–383, 1972.

[Wilkinson 93] A. P. Wilkinson, A. K. Cheetham & R. H. Jarman, *The defect structure of congruently melting lithium niobate*, J. Appl. Phys., vol. 74, page 3080, 1993.

[Wong 89] K. K. Wong, Properties of lithium niobate, EMIS Datareview, IEEE, 1989.

[Xu 10] H. Xu, D. Lee, S. B. Sinnott, V. Dierolf, V. Gopalan & S. R. Phillpot, *Structure and diffusion of intrinsic defect complexes in $LiNbO_3$ from density functional theory calculations*, J. Phys.: Condens. Matter, vol. 22, page 135002, 2010.

[Xue 03] D. Xue, S. Wu, Y. Zhu, K. Terabe, K. Kitamura & J. Wang, *Nanoscale domain switching at crystal surfaces of lithium niobate*, Chem. Phys. Lett., vol. 377, page 475, 2003.

[Yamada 67] T. Yamada, N. Niizeki & H. Toyoda, *Piezoelectric and elastic properties of lithium niobate single crystals*, Jpn. J. Appl. Phys., vol. 6, page 151, 1967.

[Yamada 91] M. Yamada & K. Kishima, *Fabrication of periodically reversed domain structure for SHG in $LiNbO_3$ by direct electron beam lithography at room temperature*, Electron. Lett., vol. 27, pages 828–829, 1991.

[Yamada 93] M. Yamada, N. Nada, M. Saitoh & K. Watanabe, *First-order quasi-phase matched $LiNbO_3$ waveguide periodically poled by applying an external field for efficient blue second-harmonic generation*, Appl. Phys. Lett., vol. 62, no. 5, pages 435–436, 1993.

[Yamada 96] M. Yamada, M. Saitoh & H. Ooki, *Electric-field induced cylindrical lens, switching and deflection devices composed of the inverted domains in $LiNbO_3$ crystals*, Appl. Phys. Lett., vol. 69, pages 3659–3661, 1996.

[Yamada 98] M. Yamada & M. Saitoh, *Fabrication of a periodically poled laminar domain structure with a pitch of a few micrometers by applying an external electric field*, J. Appl. Phys., vol. 84, no. 4, pages 2199–2206, 1998.

[Yan 06] W. Yan, L. Shi, Y. Kong, Y. Wang, H. Liu, J. Xu, S. Chen, L. Zhang, Z. Huang, S. Liu & G. Zhang, *The electrostatic depinning mechanism of domain wall for near-stoichiometric lithium niobate crystals*, J. Phys. D: Appl. Phys., vol. 39, no. 19, pages 4245–4249, 2006.

[Yang 98] T. J. Yang & U. Mohideen, *Nanoscale measurement of ferroelectric domain wall strain and energy by near-field scanning optical microscopy*, Phys. Lett. A, vol. 250, page 205, 1998.

[Yang 99] T. J. Yang, V. Gopalan, P. J. Swart & U. Mohideen, *Direct observation of pinning and bowing of a single ferroelectric domain wall*, Phys. Rev. Lett., vol. 82, no. 20, page 4106, May 1999.

[Yang 01] Y. Yang, I. Nee, K. Buse & D. Psaltis, *Ionic and electronic dark decay of holograms in* $LiNbO_3$*:Fe crystals*, Appl. Phys. Lett., vol. 78, no. 26, pages 4076–4078, 2001.

[Yariv 85] A. Yariv, Optical electronics, Holt McDougal, 1985.

[Yatsenko 97] A. V. Yatsenko, E. N. Ivanova & N. A. Sergeev, *NMR study of intrinsic defects in congruent* $LiNbO_3$ *. 1. "unoverlapping" defects*, Physica B, vol. 240, pages 254–262, 1997.

[Zachariasen 28] W. H. Zachariasen, *Untersuchungen äuber die kristallstruktur von sesquioxydenund verbindungen* ABO_3, Skr. Norske Vid.-Akad., vol. 4, page 312, 1928.

[Zhdanov 78] G. S. Zhdanov, E. V. Kolontsova, A. E. Korneev & S. A. Ivanov, *X-ray diffuse scattering from single crystal* $LiNbO_3$ *and* $LiTaO_3$ *as a function of temperature between* $20-750° C$, Ferroelectrics, vol. 21, pages 463–465, 1978.

[Zotov 94] N. Zotov, H. Boysen, F. Frey, T. Metzger & E. Born, *Cation substitution models of congruent* $LiNbO_3$ *investigated by X-ray and neutron powder diffraction*, J. Phys. Chem. Solids, vol. 55, page 145, 1994.

[Zotov 95] N. Zotov, F. Frey, H. Boysen, H. Lehnert, A. Hornsteiner & B. Strauss, *X-ray and neutron diffuse scattering in* $LiNbO_3$ *from 38 to 1200 K*, Acta Crystallogr. B, vol. B51, pages 961–972, 1995.

2

Latent light-assisted poling of $LiNbO_3$

2.1 Introduction

The most common domain engineering technique for LN is electric field poling (EFP), where a photolithographically-patterned electrode on one of the z-faces provides a spatially modulated E-field along the z-axis [Yamada 93, Yamada 98]. Recent research investigating the influence of light on EFP revealed that the regions being illuminated require a lower *nucleation field*, E_n (the E-field required for microscopic ferroelectric domain nucleation) in both undoped congruent LN (CLN) and MgO-doped CLN (MgO:CLN) using CW [Wang 09, Steigerwald 09, Fujimura 03, Sones 05, Dierolf 04, Wengler 04] and pulsed laser light [Valdivia 06] in a process referred to as *light-assisted poling* (LAP). Utilising ultrafast lasers at wavelengths ranging between 305 nm and 800 nm, LAP has been observed to produce significant E_n reductions, of up to two orders of magnitude for MgO:CLN [Valdivia 06].

In all cases of LAP reported thus far, the light illumination was concurrent with the application of the external E-field. In this chapter, it will be shown that in undoped CLN, the E_n reduction can be observed even several hours after irradiation with ultrafast ($\sim$ 150 fs) laser light at a wavelength of 400 nm. Using this technique, called *latent light-assisted poling* (LLAP), the two processes of light illumination and application of an external E-field can be de-coupled. Interestingly, for undoped congruent lithium niobate crystals, the E_n reduction in LLAP (62%) is significantly larger compared to that measured in simultaneous LAP (42%) under identical irradiation conditions [Valdivia 06]. The latent effect has not been observed in MgO:CLN for the time scales employed in the experiments here, despite the strong effect observed using regular LAP [Valdivia 06]. The dependence of LAP and LLAP on the MgO-doping suggests a space-charge-related mechanism, meaning that the effects are attributed to the formation of a photo-induced space-charge distribution which assists local ferroelectric domain nucleation. The low dark conductivity in the undoped CLN allows the photo-induced space-charge distribution to persist for a significant period of time after its formation, while in the MgO:CLN any photo-induced space-charge distribution decays much faster due to the much higher dark conductivity which also makes this crystal less susceptible to photorefractive damage. The presence of a photo-induced space-charge distribution and the corresponding space-charge field induce a refractive index change in LN via the linear electro-optic effect. Probing of this photorefractive index change provides an excellent tool for the investigation of the LLAP dynamics.

Therefore, in Sec. 2.2 the domain nucleation for varying time delays between light illumination and application of the external E-field in undoped CLN is presented, while in Sec. 2.3, after giving a basic theory of photorefractive gratings and the two-center charge transport model, the LLAP dynamics are compared to the decay of a photorefractive grating formed by the space-charge field, which confirms the space charge hypothesis. Then in Sec. 2.4, possible mechanisms are proposed to explain LLAP and corresponding LAP.

2.2 Latent light-assisted poling

2.2.1 Experimental setup

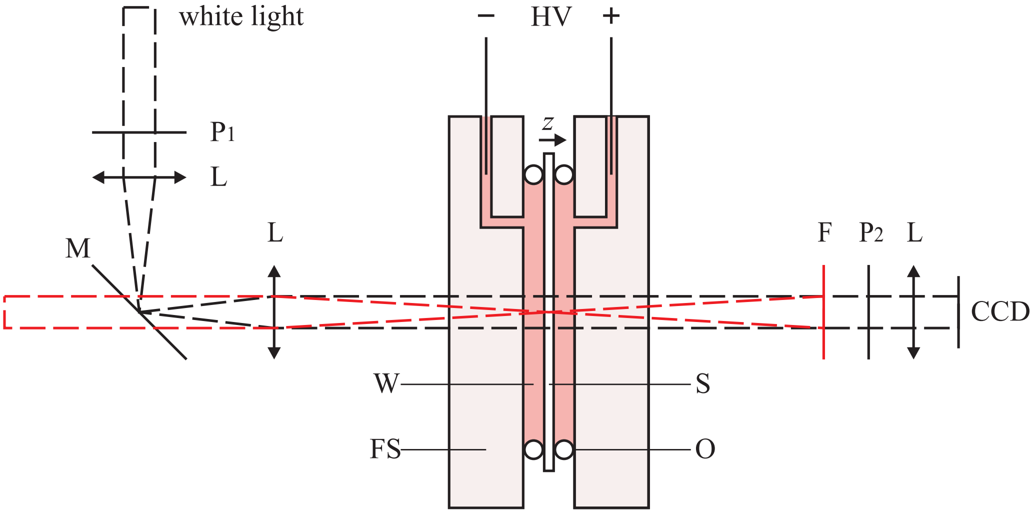

FIGURE 2.1: LLAP setup, showing the focusing of the illuminating fs-pulsed beam incident on the $-z$ face of a lithium niobate sample held between water electrodes using transparent fused silica plates. The white light is of low intensity and used only for visualisation of the poling process via the crossed polariser and CCD camera. (P_1, P_2 = crossed polarisers; L = lens; F = filter to block the fs-pulsed laser light; M = dielectric mirror; HV = high voltage; W = water; S = LN sample; FS = fused silica; O = O-ring.)

To investigate the process of LLAP, 0.5-mm thick, z-cut, optical grade, undoped CLN crystals from Crystal Technology, Inc. (US) were held within a transparent cell which enabled the simultaneous light illumination of the crystal and the application of an external E-field. The experimental setup used for the LLAP experiments is shown in Fig. 2.1. The transparent cell was constructed out of UV-grade fused silica. The LN sample was held tightly by insulating silicone O-rings. Holes drilled through the fused silica holder permitted the liquid electrodes (DI water) to come in contact with the faces of the crystal. The laser used for the LLAP experiments was a Coherent ultrafast laser system in the Femtosecond Applications of Science and Technology (FAST) shared facility at the Optoelectronics Research Centre, providing $\sim$ 150 fs pulses at 400 nm operated at a repetition rate of 250 kHz. The laser beam was focused by a lens onto the crystal. After the laser illumination, high voltage was applied across the crystal via the liquid electrodes. In-situ visualisation of the poling process was possible via a white light lamp collimated through the crystal. The filter blocked the fs-pulsed laser light from the visualisation end of the setup. The strain-induced birefringence at the domain walls of inverted domains [Gopalan 00] was revealed by crossed polarisers (P_1 and P_2), allowing the visualisation as the walls formed and grew, while apart from the induced ordinary index increase for the inverted domains [Kim 05], the applied voltage can provide additional electro-optic refractive index contrast. The application of an E-field E_3 along the z-axis gives rise to an ordinary index difference across a 180° domain wall by Eq. 1.22: $\delta n_o(E_3) = -\frac{1}{2}n_o^3 r_{13} E_3$, where r_{13} is the electro-optic coefficient and n_o the ordinary index. The index difference leads to scattering of light at the wall which is optically imaged [Gopalan 99].

The crystal was subjected to a sequence of processing steps as follows. First, the crystal was sequentially domain-inverted three times sequentially, leaving it with a domain orientation antiparallel to its virgin state. This was done to condition the crystal in order to avoid the first poling cycle which is known to have a higher coercive field [Ro 00] and exhibits erratic domain propagation due to pinning on defect sites [Kim 01]. Second, the fs-pulsed laser beam (which has a Gaussian intensity profile) was focused onto the front $-z$ face to a spot radius of $\sim$ 15 µm and illuminated the crystal for a duration of 30 s. The crystal was then repositioned and a new spot was illuminated with identical conditions after a subsequent delay of 30 s. The process was repeated to systematically illuminate a number of spots at precisely controlled times. Third, following the last spot and a final 30 s delay, the voltage was ramped up to the desired value over a period of 30 s, whereupon the maximum voltage was maintained for 300 s, and then ramped back down to 0 V over a final period of 30 s. The *voltage delay time* for each spot is defined as the elapsed time from the end of its illumination to the end of the first voltage ramp. Thus, each spot corresponds to different values of voltage delay time. The illumination times, time delays and E-field application duration which were chosen to demonstrate the effect are not necessarily the optimal experimental conditions. After the above procedure, the samples were briefly etched in hydrofluoric (HF) acid to reveal the preferentially inverted ferroelectric LLAP domains. The area of these inverted domains, as measured from scanning electron microscopy (SEM) images, was investigated as a function of the voltage delay time for different laser intensities and E-fields.

2.2.2 Results

The inverted LLAP domains formed on the $-z$ face and were, in all cases, of limited depth. However, LLAP domains have been pushed through to the opposite face of the crystal by using higher magnitude of the E-field or longer E-field application times or a combination of the two. It is important to note that under the process of LLAP, domain inversion occurred only at the locations where the crystal had been previously illuminated. As with regular (simultaneous) LAP, LLAP also formed domains which followed the shape of the illuminating spot and were reproducible between different spots and samples. Etching of LN crystals in HF acid reveals the inverted ferroelectric LLAP domains as shown in Fig. 2.2. The LLAP conditions for these particular inverted domains were: laser intensity of 9 GW cm^{-2}, applied E-fields of (a) 14 kV mm^{-1} and (b) 8 kV mm^{-1}, and the same voltage time delay of 570 s. In Fig. 2.2, the LLAP domain walls of (a) follow the crystal symmetry due to the high E-field applied which allowed expansion of this domain beyond the confines of the illuminating laser spot area. However, the domain did not form a regular hexagon as is typical for EFP domains, forming instead an irregular octagon with domain walls parallel to both the y- and x-axes. The walls labeled 1, 2, 4, 5, 7, 8 are parallel to y-axes, while walls labeled 3, 6 are parallel to x-axes, contrary to the regular domain wall growth in CLN [Lobov 06]. The LLAP domain walls of Fig. 2.2(b) also run parallel to both y- and x-axes, in addition to many more rounded segments, generally following the shape of illumination much more closely due to the lower applied E-field. Domain walls following the x-axis imply a condition of incomplete screening of the depolarisation field [Shur 05], likely a result of the redistribution of the photo-excited space charges prior to application of the external E-field.

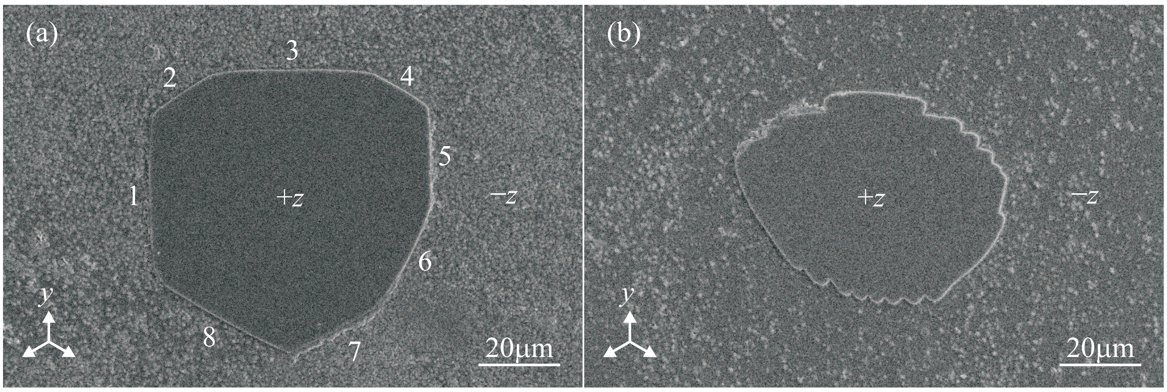

FIGURE 2.2: Preferentially inverted ferroelectric LLAP domains, revealed as unetched $+z$ face after HF etching, are induced by $I = 9$ GW cm^{-2} of 400 nm fs-laser irradiation, followed by applied E-fields of (a) 14 kV mm^{-1} and (b) 8 kV mm^{-1} after a same voltage delay time of 570 s in undoped CLN. LLAP domain walls run parallel to both y- and x-axes, particularly for the higher E-field in (a).

The nucleation and growth of LLAP domains was investigated by varying the illumination intensity and the applied E-field for a series of spots. Fig. 2.3 shows plots of the square root of the inverted LLAP domain areas as a function of voltage delay time for (a) different applied E-fields and (b) laser intensities. The square root of the inverted domain area is presented here rather than the area itself because it represents the evolution of one linear dimension (1D) of the inverted domain and can be compared in a straightforward manner with the temporal evolution of a 1D space-charge distribution, discussed in Sec. 2.3.5. Fig. 2.3 reveals that, for all exposure

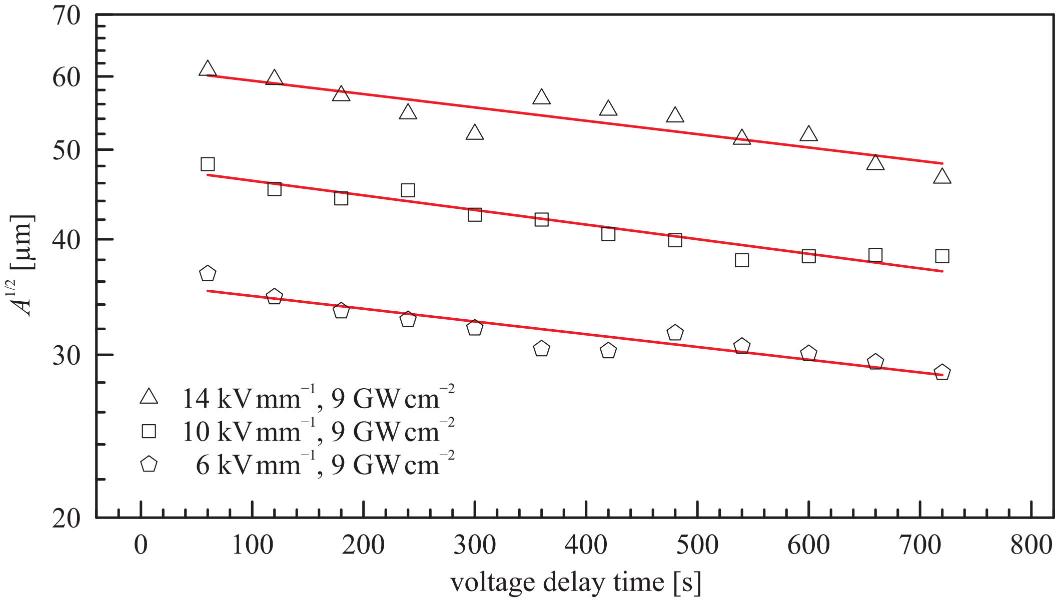

(a) $I = 9$ GW cm^{-2} and variable E-field amplitude

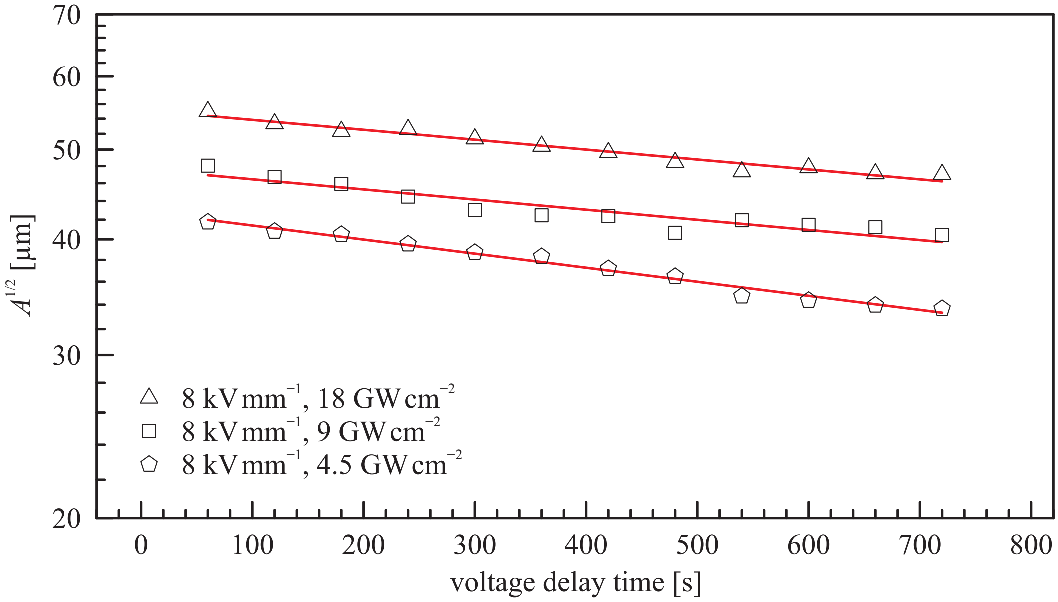

(b) $E = 8$ kV mm^{-1} and variable laser intensity

FIGURE 2.3: Log-linear plots of the square root of the inverted LLAP domain areas, $A^{1/2}$, as a function of voltage delay time, measured from SEM images of HF-etched samples with conditions: (a) $I = 9$ GW cm^{-2} and variable E-field amplitude, and (b) $E = 8$ kV mm^{-1} and variable laser intensity. The solid red lines represent single exponential decay function fits.

conditions, the poled area increases with decreasing voltage delay time. It is expected that at even shorter voltage delay times than those applied in the experiments, the poled areas would be correspondingly even larger. The experimental protocol here however limits the shortest applicable voltage delay time to 60 s.

Additionally, Fig. 2.3(a) and Fig. 2.3(b) show that the poled area increases with E-field amplitude and laser intensity respectively. Of particular interest is that domain inversion was observed even for an E-field as low as 6 $\mathrm{kV\,mm^{-1}}$ in Fig. 2.3(a), a reduction of 62% from the dark E_n (15.8 $\mathrm{kV\,mm^{-1}}$ in the reverse poling direction). This is a surprising result as the minimum intensity-dependent E_n observed with simultaneous illumination shown a reduction of only 42% in LAP experiments using the same experimental setup, as reported in [Valdivia 06]. Nevertheless, LLAP formed a sizeable domain even when 6 $\mathrm{kV\,mm^{-1}}$ was applied nearly 700 s after illumination. An E-field of 6 $\mathrm{kV\,mm^{-1}}$ is not necessarily the minimum amplitude to achieve LLAP, but rather represents the minimum value tested under these exposure conditions.

The straight lines which appear in Fig. 2.3 correspond to single exponential decay functions, fitted to the square root of the inverted domain area data points as,

$$A^{1/2} = L_0 \exp(-t/\tau_L) \tag{2.1}$$

where A is the LLAP inverted domain area; L_0 is a constant; and τ_L is the time constant of the 1-D length reduction. The results of the fittings are listed in Table 2.1. The close values

TABLE 2.1: Summary of constants L_0, time constants τ_L, decay rates τ_L^{-1} and the relative reductions $\delta A^{1/2}$ from 60 s to 720 s of the linear dimension of the LLAP inverted domains in undoped CLN for different experimental conditions.

E ($\mathrm{kV\,mm^{-1}}$)	I ($\mathrm{GW\,cm^{-2}}$)	L_0 (µm)	τ_L (s)	τ_L^{-1} ($\times10^{-4}$ $\mathrm{s^{-1}}$)	$\delta A^{1/2}$
8	4.5	42.4	2860 ± 120	3.50 ± 0.29	0.206
8	9	47.3	3970 ± 470	2.52 ± 0.61	0.153
8	18	54.8	4050 ± 250	2.47 ± 0.31	0.150
14	9	60.8	3010 ± 450	3.33 ± 1.02	0.197
10	9	47.5	2750 ± 250	3.64 ± 0.67	0.213
6	9	35.5	3150 ± 390	3.17 ± 0.80	0.189

of decay rate (τ_L^{-1}) show that the length-reduction of the inverted domains with voltage delay time is very similar despite the very diverse experimental conditions in both laser exposure and value of applied E-field. Any differences should be attributed to 1) the fitting uncertainty ($\sim$ 10% in Table 2.1) due to the limited range of delay time ($60 - 720$ s) compared to the final extracted time constants about 3000 s fitted by limited number of data points, 2) the stochastic nature of ferroelectric domain nucleation and expansion, and 3) the presence of local defects in the crystal which also govern domain nucleation and growth during regular EFP [Yan 06]. For more accurate measurements, it is necessary to average over many exposure locations as the local crystal quality appears to have a noticeable impact on the growth of LLAP domains. It should be noted here that actually a more reasonable fitting is by a stretched exponential decay instead of a single-exponential decay considering the tunneling-involved charge migration at shallow energy levels [Sturman 08], the reason for which will be discussed in Sec. 2.3.2. However, the short measurement range and the limited number of data points can induce a significant uncertainty in the fitting of the stretched exponential decay function. Fitting a single exponential function is acceptable however for this short range of time delays (60 – 720 s). A parameter $\delta A^{1/2}$, defined as the relative reduction of $A^{1/2}$ from 60 s to 720 s, expressed as

$$\delta A^{1/2} = 1 - A^{1/2}_{720\mathrm{s}}/A^{1/2}_{60\mathrm{s}} \tag{2.2}$$

is to be used for comparison with the photorefractive grating decay in Sec. 2.3.5. The $\delta A^{1/2}$ values for each set of data in Fig. 2.3 are derived from the single exponential fitting and are listed in Table 2.1.

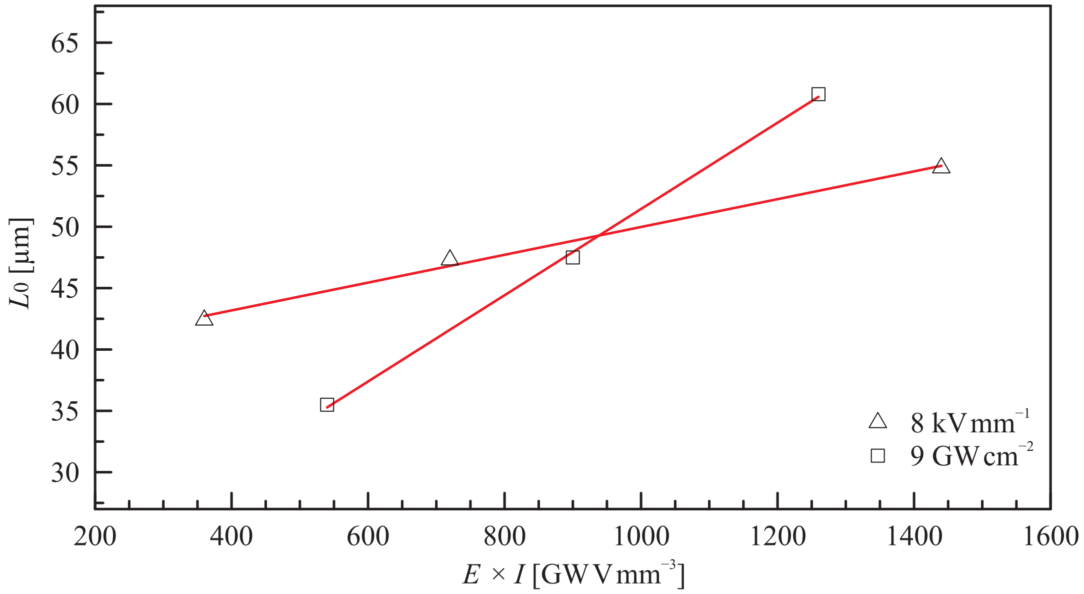

FIGURE 2.4: Plot of the fitting parameter L_0 versus the product of the applied external E-field and the intensity I, $E \times I$, for a specific E-field (8 kV mm^{-1}) and a specific intensity (9 GW cm^{-2}). The solid red lines represent linear fits.

Also, Fig. 2.4 shows that for an E-field (8 kV mm^{-1}) or intensity (9 GW cm^{-2}), the fitting parameter L_0 linearly increases with the intensity I or the E-field within that range. Considering condition-independent time constants τ_L, the larger slope of L_0 for constant intensity suggests that, for the same voltage delay time, the inverted domain area is more sensitive to the applied E-field rather than the intensity.

Further investigations of the LLAP domain area for voltage delays up to 10 hours are shown in Fig. 2.5. However, for delay times beyond 700 s, the samples were kept in the dark before the application of the E-field instead of being illuminated constantly by a broadband light source

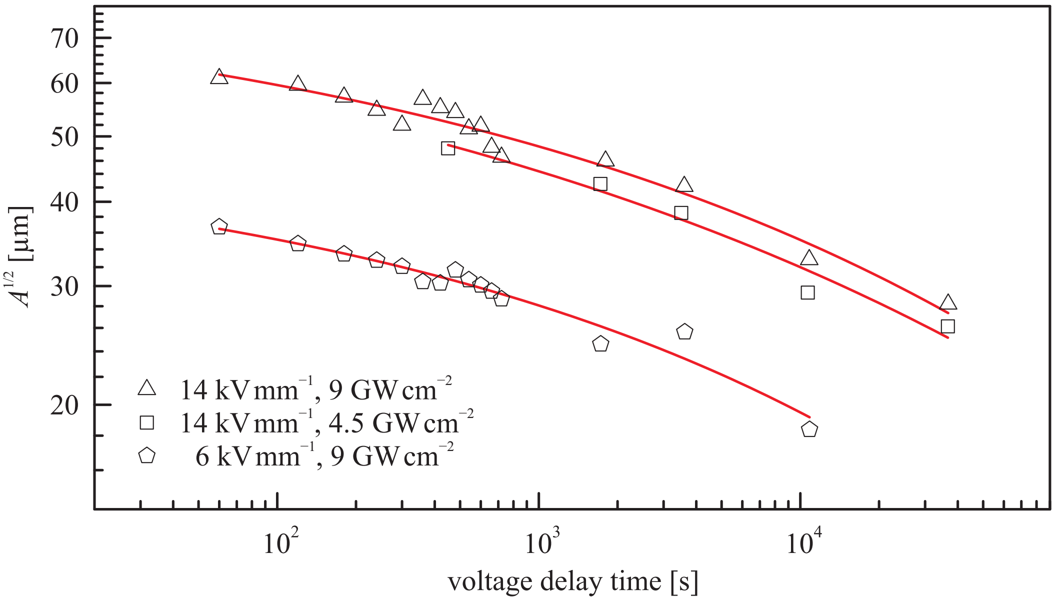

FIGURE 2.5: Log plot of the square root of the inverted LLAP domain area, $A^{1/2}$, as a function of the voltage delay time for different laser intensities and E-fields. The solid red lines serve as a guide to the eye.

as in the short voltage delays experiments (< 700 s) which is likely to influence the relaxation rate of the space-charge distributions as will be discussed in Sec. 2.3.4. Additionally for longer time delays the inverted domains become fragmented, hence the domain area measurements are increasingly inaccurate. Preferential nucleation was observed even for time delays as long as 24 hours after laser irradiation, however the resulting domains were severely fragmented for the experimental conditions used, and thus are not included in Fig. 2.5. It is possible that higher laser intensities, higher E-fields, and/or longer exposures could produce solid domains as shown in Fig. 2.2 even for such long voltage delay times.

2.3 Photorefractive grating dynamics

Considering 1) the inverted domain area reduces with voltage delay time and more importantly 2) the relatively small dependence of the decay rate (or time constant) on the experimental conditions (laser intensity, E-field value), they suggest that the effect may be related to the relaxation of a space-charge distribution formed by the intense laser irradiation of the crystal. Photo-excited charge carriers in undoped CLN can be electrons (or holes) excited from impurity or defect energy levels to the conduction band (or valence band), and/or electron-hole pairs excited directly across the band-gap via two-photon absorption especially at high intensities [Beyer 05]. Charge carriers can migrate to and become trapped at the dark region with low conductivity. Then, after illumination, the migrated photo-excited charges redistribute in the dark or under the influence of ambient light. The decay (redistribution) of the photo-excited space charges is thus reflected in the reduction of the inverted domain area as a function of the voltage time delay. As the presence of a photo-induced space-charge distribution and the corresponding space-charge field induces a refractive index change in LN via the linear electro-optic effect, probing of this photorefractive index change provides an excellent tool for the investigation of the LLAP dynamics. It was done in this section by investigating the decay dynamics of a photorefractive grating written in the sample with the same fs-pulsed laser.

A brief background of the photorefractive effect is outlined in Sec. 2.3.1 followed by the introduction of a two-centre charge transport model in Sec. 2.3.2 as responsible for the charge transport in undoped CLN. Finally, the photorefractive grating recording experiment results will be presented in Sec. 2.3.4 and will be compared with LLAP experiments in Sec. 2.3.5.

2.3.1 Theory of photorefractive grating recording

The basics of photorefractive grating recording can be found in numerous monographs and reviews (e.g., [Lines 77, Sturman 92, Günter 88, Günter 89, Günter 06, Günter 07a, Günter 07b, Solymar 96, Buse 07]). A change of the refractive index of electro-optic photoconductors is caused, via the electro-optic effect, by the formation of a photo-induced space-charge field E_{sc}.

Fig. 2.6 shows the superposition of two mutually coherent plane waves with identical incident intensities, thus E-field $|\mathbf{E}_{1\mathrm{i}}| = |\mathbf{E}_{2\mathrm{i}}|$, and with wave vectors of $\mathbf{k}_1$ and $\mathbf{k}_2$. In the LN grating recording arrangement, the usual geometry is where the grating vector is parallel to the polar axis $\mathbf{K} \parallel z$, and the incident beam polarisations are either both s polarisations ($\mathbf{E}_{1\mathrm{i}} \parallel \mathbf{E}_{2\mathrm{i}} \perp \mathbf{k}_1 \& \mathbf{k}_2$) or both p polarisations ($\mathbf{E}_{1\mathrm{i}} \& \mathbf{E}_{2\mathrm{i}} \perp \mathbf{k}_1 \times \mathbf{k}_2$) as shown in Fig. 2.6(a) and Fig. 2.6(b) respectively. The two plane waves produce an interference intensity pattern which can be described by:

$$I(z) = I_0(1 + m\cos Kz) \tag{2.3}$$

where $K = 4\pi \sin\theta/\lambda$ is the spatial frequency of the interference pattern; θ is the half-angle between the k-vectors of the incident plane waves as indicated in Fig. 2.6; λ is the wavelength of the recording light in vacuum; z is the spatial coordinate; I_0 is the averaged light intensity; and m is the modulation index, the value of which for various arrangements of incident beam polarisations have been discussed in [Eichler 06]. With equal intensities, for the s polarisation arrangement, $m = 1$, while for p polarisation arrangement, $m = \cos^2\theta - \sin^2\theta$.

The stationary photovoltaic field E_{pv} is expressed from Eq. 1.15 and 1.16 as: $E_{\mathrm{pv}} = \alpha k_{\mathrm{G}} I/[\sigma_{\mathrm{ph}} + \sigma_{\mathrm{d}}]$. For the case of single type of charge carrier, the photoconductivity equals to $\sigma_{\mathrm{ph}} = N_{\mathrm{c}}\mu_{\mathrm{c}}|q|$ where N_{c}, μ_{c}, and q are the carrier density, mobility, and charge respectively. In the case of $\sigma_{\mathrm{d}} \ll \sigma_{\mathrm{ph}}$, a scalar presentation of the diffusion field E_{diff} corresponding to the intensity distribution

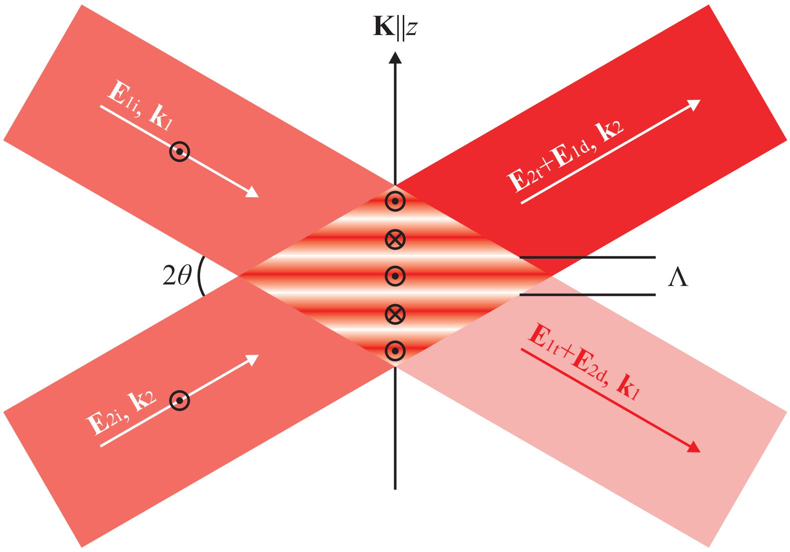

(a) s-polarisation arrangements

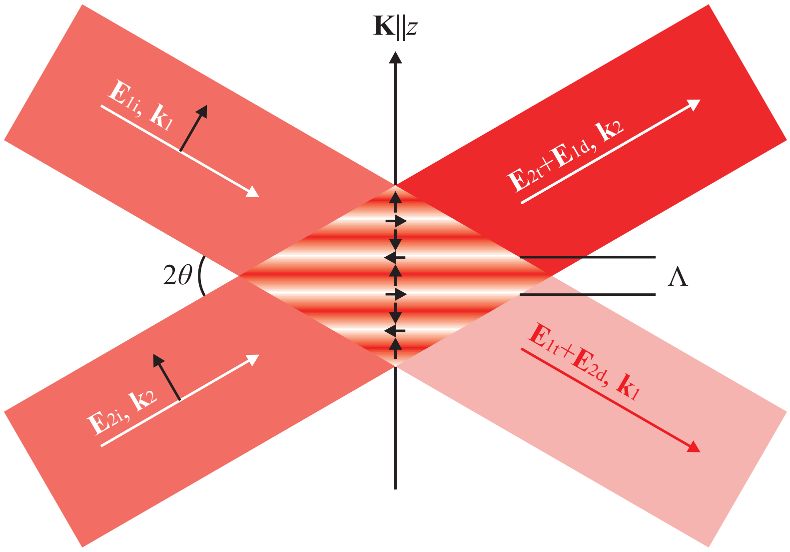

(b) p-polarisation arrangements

FIGURE 2.6: Periodic intensity pattern produced by interference of two incident light waves with identical intensities, thus E-field $|\mathbf{E}_{1\mathrm{i}}| = |\mathbf{E}_{2\mathrm{i}}|$, and with wave vectors of $\mathbf{k}_1$ and $\mathbf{k}_2$. For simplicity, grating vector $\mathbf{K} \parallel z$. (a) and (b) show respectively s and p polarisation arrangements of incident beams. (Λ = grating period; θ = half-angle between the k-vectors; $\rightarrow$, $\odot$ (out of paper), $\otimes$ (into paper) = phases; subscripts 'i', 't', 'd' = incident, transmitted, diffracted.)

of Eq. 2.3 can be derived from diffusion current j_{diff} of Eq. 1.23 as

$$E_{\text{diff}}(z) = j_{\text{diff}}(z)/\sigma_{\text{ph}} \tag{2.4}$$

$$E_{\text{diff}}(z) = -\frac{k_B T \nabla N_c}{q N_c}$$

Assuming $N_c \propto I$, thus from Eq. 2.3,

$$E_{\text{diff}}(z) = \frac{k_B T}{q} \frac{Km \sin Kz}{1 + m \cos Kz} \tag{2.5}$$

where $q = +/-e$ for holes/electrons.

Principal distinctions of the diffusion field, Eq. 2.5, from the photovoltaic field Eq. 1.16 are independent of E_{diff} on the light intensity and a shift of the field grating by $\pi/2$ with respect to the interferogram Eq. 2.3. The photoexcited carriers transferred by either of the listed mechanisms or their combination are captured by traps (if any) to form a spatially modulated space-charge field E_{sc}. In steady state, the E_{sc} is derived from Eq. 1.27. If the photovoltaic mechanism is dominant, then $E_{\text{sc}}(z) = -E_{\text{pv}}(z)$ and is in phase with the interferogram, which is most often realised in iron-doped $LiNbO_3$. If the diffusion mechanism prevails and the photoconductivity is of single type of charge carrier, then $E_{\text{sc}}(z) = -E_{\text{diff}}(z)$.

For the crystals investigated here, undoped CLN and MgO doped CLN, in the literature photorefractive grating experiments have been conducted at UV wavelengths, the results of which are listed in Table 2.2. In Ref. [Jungen 92], it was reported that for undoped CLN at wavelength of 351 nm and 454 nm, diffusion dominated charge transport with grating period of $0.36 - 1.8$ µm and photovoltaic field measured to be 0.55 kV cm^{-1}, which accords with the much larger amplitude values of the diffusion fields for real grating periods $\Lambda \approx 1$ µm, approximately 1.5 kV cm^{-1} calculated from Eq. 2.5. The diffusion domination was also reported in highly MgO doped LN crystals [> optical damage threshold (ODT)] at UV wavelength of 325 nm [Xin 10] and 351 nm [Xu 00] with grating period of 0.45 µm and 0.3 µm respectively. Thus, here in the case of UV wavelength at 400 nm and grating period at 1 µm, it is reasonable to conclude that

TABLE 2.2: Dominant charge transport and charge carriers for undoped and MgO doped CLN at various wavelength λ and photorefractive grating period Λ.

Doping	λ (nm)	Λ (µm)	Transport	Carriers	Ref.
undoped CLN	351	$0.36 - 1.8$	diffusion	holes	[Jungen 92]
	454	$0.36 - 1.8$	diffusion	electrons	[Jungen 92]
	514	$0.36 - 1.8$	BPVE	electrons	[Jungen 92]
MgO doped CLN ($0 - 9$ mol%)	325	0.45	diffusion	electrons	[Xin 10]
	351	0.3	diffusion	holes	[Xu 00]

BPVE = bulk photovoltaic effect

the diffusion dominates the charge transport. Therefore, the following analysis will be based on diffusion-dominated charge transport for the photorefractive grating.

The space-charge field $E_{\mathrm{sc}}(z)$, via linear EO effect, leads to a refractive index change given by

$$2\delta n = -n^3 r_{\mathrm{eff}} E_{\mathrm{sc}}(z) \tag{2.6}$$

where r_{eff} is the effective electro-optic coefficient for the given crystal configuration. In $LiNbO_3$ with grating vector parallel to the polar axis ($\mathbf{K} \parallel z$), the expression of the effective electro-optic coefficient r_{eff} can be deduced from Eq. 1.21 for the extraordinary polarisation of the recording beams

$$r_{\mathrm{eff}} = r_{13} \sin^2\theta + r_{33}\cos^2\theta \tag{2.7}$$

and for ordinary beams

$$r_{\mathrm{eff}} = r_{13}$$

In the case of diffusion as the dominant transport mechanism, $E_{\mathrm{sc}}(z) = -E_{\mathrm{diff}}(z)$, and thus, from Eq. 2.6 and Eq. 2.5, $\delta n \propto q^{-1} \sin Kz$. The refractive index modulation, δn, forms a grating shifted

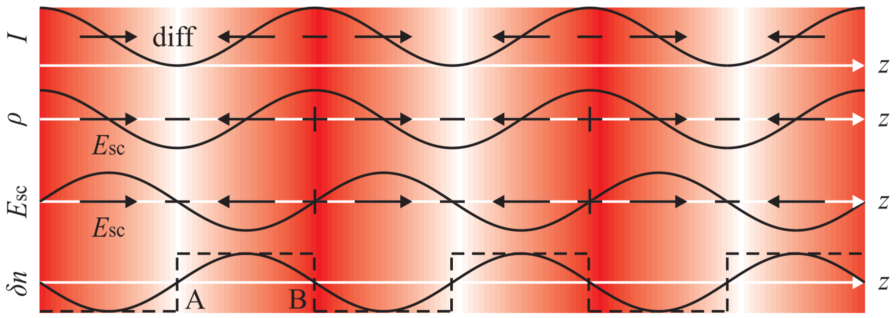

(a) electrons as charge carriers

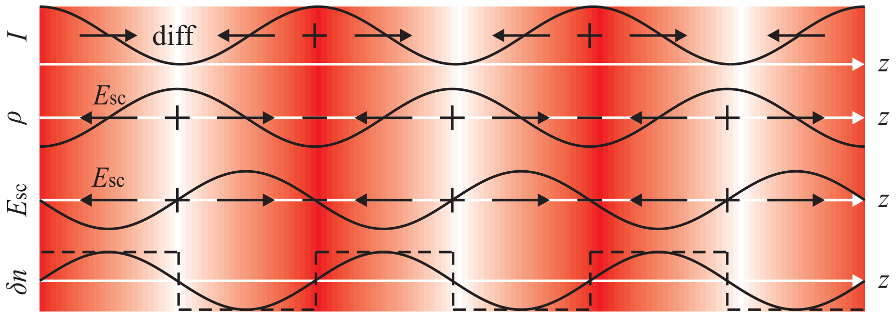

(b) holes as charge carriers

FIGURE 2.7: Response of a photorefractive material to a non-uniform intensity pattern of $I(z)$. Photo-ionisation produces charge carriers: (a) electrons or (b) holes diffuse until reaching a steady state with spatial charge density of $\rho(z)$. The space charge distribution $\rho(z)$ builds a space charge field $E_{\mathrm{sc}}(z)$ that via the linear EO effect induces a refractive index grating δn with a $\pi/2$ phase shift with respect to the intensity I. The dashed lines in $\delta n(z)$ is a step approximation for the analysis of energy transfer at points A and B in Fig. 2.8.

by $\pi/2$ as compared to the intensity (Eq. 2.3), the so-called nonlocal response [Kukhtarev 76, Kukhtarev 79b, Kukhtarev 79a]. It should be mentioned that if E_{pv} and E_{diff} are comparable, then the shift of the grating is less than $\pi/2$. Fig. 2.7 shows the diffusion process with (a) electrons or (b) holes as charge carriers: non-uniform intensity I excites charge carriers, (a) electrons or (b) holes, which diffuse to form a space charge distribution ρ. The space charge distribution ρ builds a space charge field E_{sc} that via the linear EO effect induces a refractive index grating δn with a $\pi/2$ phase shift with respect to the intensity I.

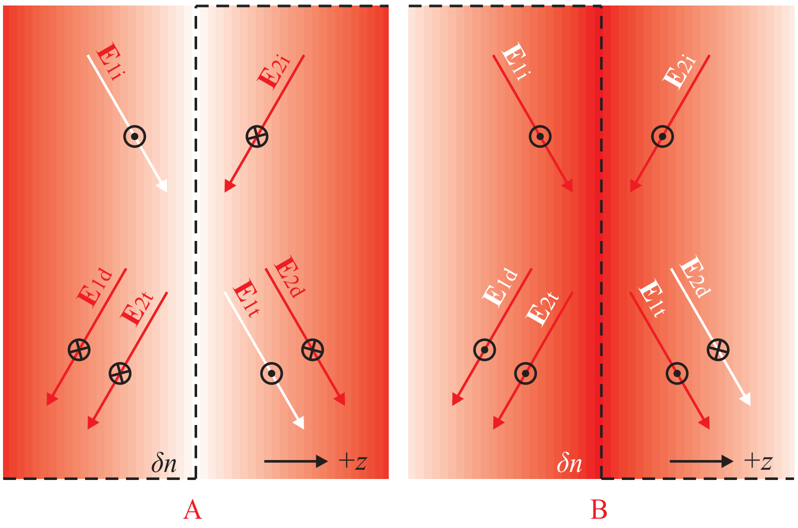

(a) s polarisation arrangements

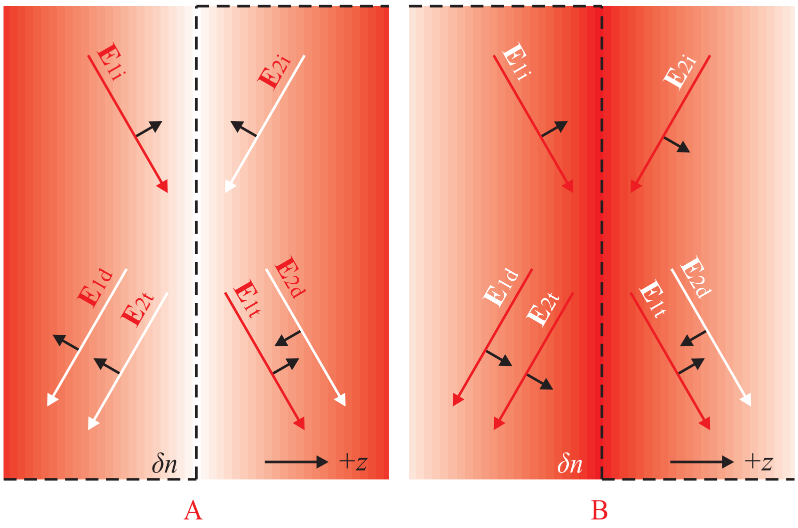

(b) p polarisation arrangements

FIGURE 2.8: Energy transfer in the case of electrons as charge carriers after diffusion under a non-uniform intensity distribution. Refraction and reflection at point A and B in Fig. 2.7(a) are exemplified for both (a) s and (b) p polarisation arrangements. Subscripts and phases have the same meaning as in Fig. 2.6 except that in this case of step refractive index change, 'd' refers to *reflected*. Red and white arrows are mutually destructive beams, while same color beams are constructive.

Due to the diffusion-induced nonlocal response of δn to the intensity, energy transfer occurs between two incident beams. In order to simply demonstrate it, graded refractive gratings in Fig. 2.7 are approximately represented by step refractive gratings in dashed lines. Thus, reflection and refraction occur at each step change of refractive index which are exemplified at points A and B in the case of electrons as charge carriers in Fig. 2.7(a). Fig. 2.8 shows that E-fields of two transmitted beams at point A and B are derived from a combination of $\mathbf{E}_{1\mathrm{t}} + \mathbf{E}_{2\mathrm{d}}$ (towards $+z$) and $\mathbf{E}_{2\mathrm{t}} + \mathbf{E}_{1\mathrm{d}}$ (towards $-z$), where subscripts '1', '2', 't', 'd' mean beam 1, beam 2, transmitted, and diffracted respectively (in this case of step refractive index change, 'd' refers to *reflected*). s and p polarisation arrangements are shown in Fig. 2.8(a) and Fig. 2.8(b) respectively. With points A and B located at an intensity minimum and maximum respectively, this determines the local incident beam phases at the points to be as indicated in Fig. 2.8. Assuming that the incident angle on the step index interface $(90° - \theta)$ is smaller than both the Brewster's angle and the critical angle which is close to 45° and 90° respectively for small value of δn, from Fresnel's equations for reflection and refraction [Bennett 09] the phases for the reflected and refracted beams at the step index interface can be derived as in Fig. 2.8: 1) zero phase shift for transmission, 2) zero phase shift for reflection from smaller refractive index medium, and 3) π phase shift for reflection from larger refractive index medium. For a clear illustration, in Fig. 2.8 red and white arrows are mutually destructive beams, while same color beams are constructive. Therefore, it can be seen that in all cases, at A or B, s or p polarisations, $\mathbf{E}_{1\mathrm{t}} + \mathbf{E}_{2\mathrm{d}}$ always have the different color, thus, add destructively, while $\mathbf{E}_{2\mathrm{t}} + \mathbf{E}_{1\mathrm{d}}$ have the same color, therefore add constructively. It indicates an energy transfer towards $\mathbf{E}_{2\mathrm{t}} + \mathbf{E}_{1\mathrm{d}}$, or in other words, $-z$ direction. Similar analysis for hole charge carriers can lead to the conclusion that energy transfer occurs towards $+z$. The energy transferring direction is often taken as an indication of the type of the dominant charge carriers [Günter 88]. The results of determined dominant charge carriers for undoped and MgO doped CLN are also listed in Table 2.2.

A characteristic parameter of the grating recording is the diffraction efficiency, η, defined as the ratio of the diffracted power to the incident power. For equal intensities of the two recording beams, the diffraction efficiency η for a hologram (taking into account the optical absorption of the crystal) is predicted by the coupled-wave theory as [Kogelnik 69]

$$\eta = \exp\left(\frac{-\alpha L}{\cos\theta}\right)\sin^2\left(\frac{\pi \delta n L}{\lambda \cos\theta}\right) \tag{2.8}$$

$$\delta n = -\frac{1}{2} n^3 r_{\mathrm{eff}} E^*_{\mathrm{sc}}$$

where α is the absorption coefficient; L is the hologram thickness; r_{eff} is the effective electro-optic coefficient for the given crystal configuration; n is the average refractive index; and E^*_{sc} is the amplitude of the space-charge electric field modulation. In the case of diffusion charge transport, it derives from Eq. 2.5 to be: $E^*_{\mathrm{sc}} = k_{\mathrm{B}} T K m / |q|$.

2.3.2 Two-center charge transport model

Analysis of photorefractive grating recording involves consideration of the charge transport scheme: charges, energy levels, excitations and relaxations. It has been well reviewed in [Buse 97b, Buse 97a] and [Sturman 08], and a short summary is presented here.

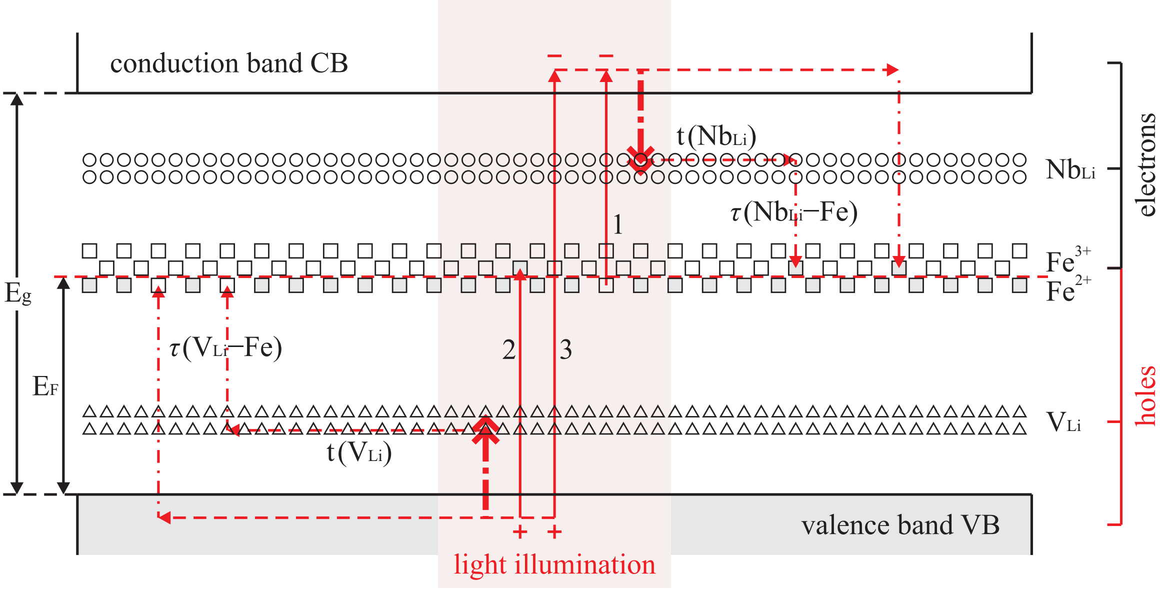

FIGURE 2.9: Energy band structure of undoped CLN showing the valence, conduction band, and intermediate energy levels of Nb_{Li}^{5+}, Fe^{2+}/Fe^{3+}, V_{Li}. When light is present, electrons can be excited via 1) $Fe^{2+} \rightarrow$ CB, 2) VB $\rightarrow Fe^{3+}$, and 3) VB $\rightarrow$ CB. Electrons can transport via two channels, through CB, and Nb_{Li} denoted as $t(Nb_{Li})$ in the figure [Sturman 08], while holes transport via VB, and V_{Li} denoted as $t(V_{Li})$ in the figure. Thick red arrows indicate the strongest recombination channel (for the CB, it is CB $\rightarrow Nb_{Li}$; and for the VB, it is VB $\rightarrow V_{Li}$). (E_g = energy gap; E_F = Fermi energy; $\tau(Nb_{Li} - Fe)$, $\tau(V_{Li} - Fe)$ = recombination time.)

Fig. 2.9 outlines the band structure of CLN, showing the conduction band (CB), valence band (VB) and the various intermediate energy levels: Nb_{Li}^{5+}, Fe^{2+}/Fe^{3+}, V_{Li}. In equilibrium at room temperature with no light illumination, ionised Fe ions are presented as Fe^{2+} which act as electron donor or hole acceptor, while others presented as Fe^{3+} are electron acceptor or hole donors. Nb_{Li}^{5+} and V_{Li} are empty as electron [Sturman 08] and hole acceptors (traps) [Donnerberg 89] respectively.

As indicated in Fig. 2.9, three possible excitation paths of electrons (shown as three thin solid red arrows) between CB, VB and the intermediate energy levels during pulsed UV light illumination are:

1. Electrons from Fe^{2+} to conduction band (electron conductivity)
2. Electrons from valence band to Fe^{3+} (hole conductivity)

3. Electrons via two-photon absorption from valence band to conduction band (both electron and hole conductivity)

Excitation 1 (or 2) corresponds to electron (or hole) dominated conductivity, while the involvement of excitation 3 can contribute to both electron and hole conductivity. For the photorefractive grating recording experiment described in the next section, the dominant charge carriers have not been experimentally determined via two-beam coupling due to the very low gain, moreover, no conclusion can be made from literature. For undoped CLN, it has been reported that holes and electrons are the dominant charge carrier at 351 nm and at 454 nm respectively as shown in Table 2.2. In the case here of fs-pulse laser illumination, the applied wavelength 400 nm is in-between these two wavelengths, thus, the dominant charge carrier cannot be determined from the literature. Neither can the main charge carrier be determined for MgO doped lithium niobate. Strong UV photorefraction is achieved in MgO:CLN. It was reported that at 351 nm [Xu 00] and 325 nm [Xin 10], holes and electrons are the dominant charge carriers respectively.

Since it's not determined which charge carrier dominates in the LLAP and photorefractive experiments, both cases of electron and hole transport schemes are discussed. It will be shown that in both cases, a two-centre charge transport model should be applied, considering the additional charge transport channel of Nb_{Li} for electrons and V_{Li} for holes, the transport of which is distance-dependent and via tunneling/hopping.

Firstly, consider the excitation scheme 1 with electrons as dominant charge carriers, Fe^{2+} and Fe^{3+} as electron donors and acceptors (deep traps) respectively. As discussed in Sec. 1.3.2, CLN possesses a considerable lithium deficiency of about 4%, and about 1% of the Nb ions are located on Li sites as intrinsic antisite defects Nb_{Li} to maintain overall charge neutrality. The intrinsic defect $Nb^{4+}_{Li}/Nb^{5+}_{Li}$ is more shallow than Fe^{2+}/Fe^{3+} with respect to the conduction band edge. The photon energy of infrared radiation is sufficient to excite electrons from Nb^{4+}_{Li} to the conduction band [Berben 00, Herth 05]. Therefore, apart from the CB, the shallow energy level Nb_{Li} with its considerable concentration can also contribute to the conductivity via electron tunneling/hopping as an additional channel.

In undoped or low concentration iron-doped CLN, the concentration of the antisite defects ($\sim 10^{20}$ cm^{-3}) is much larger than the concentration of deep traps, $N_{Nb_{Li}} \gg N_{Fe^{3+}}$. Fig. 2.9 also shows the energy scheme of the two-centre charge transport model (Nb_{Li} and Fe). According to [Sturman 08], the main channel of the photo-excitation is $Fe^{2+} \rightarrow$ CB. The strongest recombination channel for the CB is CB $\rightarrow Nb_{Li}$ as the thick red arrow in Fig. 2.9, while channel CB $\rightarrow Fe^{3+}$ is expected to be negligible. Channel $Nb_{Li} \rightarrow Fe^{3+}$ possesses the longest recombination time $\tau(Nb_{Li} - Fe)$ as indicated in Fig. 2.9.

When charge carriers, electrons, are photoexcited from a deep trap of Fe^{2+} into shallow traps of the intrinsic defect Nb^{5+}_{Li} (Nb on Li site in the valence state 5+), the coulomb interaction and phonon coupling between the excited charge and the surrounding ions can lead to a local deformation of the crystal lattice, creating $\mathrm{Nb}_{\mathrm{Li}}^{4+}$ centers, so-called *small bound polarons*. The resulting lattice polarisation acts as a potential well that hinders the movements of the charge, thus decreasing its mobility. Moving through the crystal, the electron carries the lattice distortion with it as a cloud of phonons accompanying the electron.

A model proposed by Berben [Berben 00] suggests that the dark-decay dynamics or the recombination of the small bound polarons involves a hopping/tunnelling process which takes into account the distance-dependent electron transition probabilities. Since $N_{\mathrm{Nb_{Li}}} \gg N_{\mathrm{Fe}^{3+}}$, the mean distance between two neighboring shallow centres, $\overline{R}_{\mathrm{Nb_{Li}}} \approx N_{\mathrm{Nb_{Li}}}^{-1/3}$, is noticeably shorter than the mean distance between the deep centres, $\overline{R}_{\mathrm{Fe}^{3+}} \approx N_{\mathrm{Fe}^{3+}}^{-1/3}$, and also than the mean distance between centres $\mathrm{Nb_{Li}}$ and Fe^{3+} ($\sim \overline{R}_{\mathrm{Nb_{Li}}}$). Recombination of $\mathrm{Nb_{Li}} \rightarrow \mathrm{Fe}^{3+}$ therefore involves a hopping process where the average hopping probability of a single hop (tunneling event) for centres $\mathrm{Nb_{Li}}$ is exponentially small [proportional to the factor $\exp(-\overline{R}_{\mathrm{Nb_{Li}}})$] due to a very small overlap of the wave functions for the neighboring centres. The factor is sharply decreasing with increasing hopping distance $\overline{R}_{\mathrm{Nb_{Li}}}$.

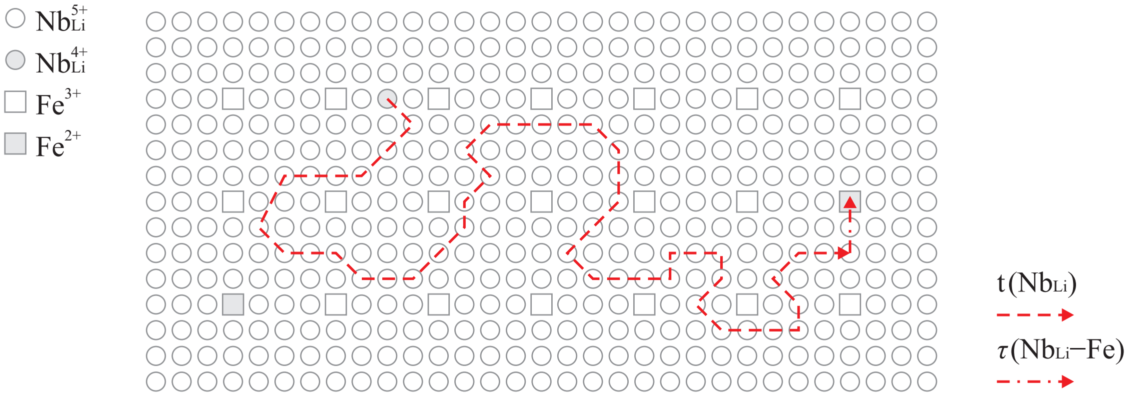

FIGURE 2.10: Migration of an electron over $\mathrm{Nb_{Li}}$ (circles) and recombination to the ground state Fe^{3+} (empty squares). Replotted from [Sturman 08].

The physical picture of recombination $\mathrm{Nb_{Li}} \rightarrow \mathrm{Fe}^{3+}$, proposed in [Sturman 08], can be presented as in Fig. 2.10. An electron migrates/diffuses by hopping from one $\mathrm{Nb_{Li}}$ center to another [t($\mathrm{Nb_{Li}}$) tunneling process in Fig. 2.9] until it approaches eventually a deep recombination center Fe^{3+}. Only after that can a recombination occur. The important point is that electrons trapped at Fe or $\mathrm{Nb_{Li}}$ are localised. Thus, the probabilities of excitation and recombination depend on the physical distance between different centres. Considering this distance-dependent excitation and recombination rates, the lifetime of an individual polaron thus also depends on the distance to the next available deep electron trap and the distance between two neighboring shallow centres. Since the electrons trapped in this shallower centre increase the light absorption in the red and near infrared, the dark decay of the polaron concentration N_{pol} was observed by monitoring the relaxation of the absorption changes: $\alpha(t) \propto N_{\mathrm{pol}}(t)$. The distance-dependent electron transition from small polarons Nb_{Li}^{4+} to deep traps Fe^{3+} (recombination) is experimentally observed to follow the stretched-exponential decay,

$$N_{pol}(t) = N_{pol}(t = 0) \exp[-(t/\tau)^{\beta}] \tag{2.9}$$

with $0 < \beta < 1$, which is also supported by computer simulations [Berben 00].

This additional channel of electron migration via tunneling/hopping on Nb_{Li}, along with its stretched-exponential behavior of relaxation, leads to the stretched-exponential behavior of an elementary holographic grating decay, with the refractive-index amplitude, δn, described by [Peithmann 02]

$$\delta n(t) = \delta n_0 \exp[-(t/\tau)^{\beta}] \tag{2.10}$$

where δn_0 is the saturation value of the refractive-index change; t is the time; τ is the averaged relaxation time of the stored hologram; and β is the stretch factor.

Considering the hole conductivity of excitation scheme 2, similar to the electron conductivity, the energy level V_{Li} in between Fe^{2+} and valence band is expected to have a similar function as Nb_{Li} to the electron conductivity, as an additional transport channel (two-centre charge transport scheme). Holes trapped at V_{Li} form bound V_{Li}^{+} hole polarons. The lifetime of V_{Li}^{+} hole polarons again depends on the distances between neighboring V_{Li}, and distances between V_{Li} and Fe^{2+}. Until holes occasionally approach a deep recombination centre Fe^{2+}, recombination occurs. Therefore, the same stretched exponential decay of refractive index change can be expected for hole conductivity.

For scheme 3, as both electrons and holes are excited, charge excitation of scheme 3 includes the charge transport in both scheme 1 and 2. Additionally, direct electron-hole recombination needs to be taken into account too. However, for the intensity range applied here, it is still considered as too low to induce considerable two-photon absorption.

2.3.3 Experimental setup

Single crystal LN is an electro-optic (EO) photoconductor and is known to exhibit photorefractive behavior [Arizmendi 94] which can be enhanced in the visible spectral range by doping the crystal with iron for data storage applications [Mok 93]. Although the photorefractive effect is less pronounced in undoped crystals due to the lack of photo-excitable impurities, it is still present [Bai 97, Jermann 95] and well known as ‘optical damage’. Therefore it can be used as a tool to study the dynamics of photo-induced space-charge distributions which is proposed to be the main mechanism for the LLAP and LAP.

Here photorefractive gratings have been recorded in undoped CLN crystals by two-beam interference using the same laser source applied for LLAP in order to study the dynamics of any space-charge fields that have been formed as a result of the ultrafast laser exposure and compare it with the domain inversion dynamics in LLAP. The results of the photorefractive grating recording experiments provided a new insight to the effect of LLAP: a direct evaluation of the role of the space-charge distribution to the LLAP effect and also explaining a number of experimental observations such as the absence of latent effects in MgO-doped LN crystals and the significant reduction of the E_n in MgO:CLN in LAP.

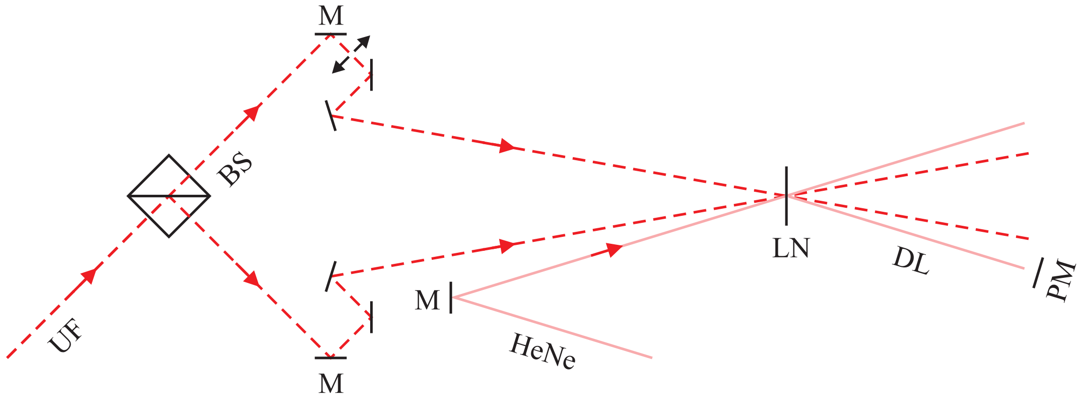

FIGURE 2.11: Interferometric setup for recording and monitoring photorefractive gratings in LN using 150 fs ultrafast (UF) laser pulses at $\lambda_r = 400$ nm. The diffracted light (DL) of a CW HeNe laser at $\lambda_p = 633$ nm incident at the Bragg angle was used to monitor the grating recording/decay. (M = mirror; BS = beam splitter; PM = optical power-meter.) The external crossing angle of recording beams in air is $2\theta = 21.6°$, corresponding to a photorefractive grating period $\Lambda =\sim 1$ µm. Spot radius of the ultrafast and HeNe lasers are 0.5 and 0.4 mm respectively. The polarisations of both lasers were in the plane of the page (horizontal, p-polarisation). The arrowed dashed line indicates the variable arm of the interferometer.

The experimental setup which was used for the recording of volume gratings in LN crystals is outlined in the schematic of Fig. 2.11. The original train of ultrafast laser pulses (400 nm, 150 fs) was divided into two parts with equal intensity by a cube beam splitter and the resulting beams were made to interfere in the LN crystal after propagating via the two separate arms of a Michelson interferometer. For ultrashort pulse interference it is important to achieve both spatial and temporal overlap of the two pulses, hence the length of one arm of the interferometer was adjustable in order to achieve zero time delay. Monitoring of the grating recording and decay was achieved by measuring the diffracted power from a CW HeNe laser ($\lambda_p = 633$ nm) incident at the Bragg angle, as shown in Fig. 2.11. The diffracted signal exhibited strong sensitivity to the polarisation of the probe beam, a fact that ensures that the grating is due to refractive index change as a result of the photorefractive (PR) effect and is not an absorption grating.

2.3.4 Results

The dynamic behavior (recording and decay) of PR gratings in both undoped CLN from Crystal Technology, Inc. (US) and 5 mol% MgO:CLN from Yamaju Ceramics Co., Ltd. (Japan) was investigated. The decay of the space-charge distribution in both crystals was monitored by measuring the power of the diffracted probe beam ($\lambda_{\mathrm{p}} = 633$ nm) in the absence of the two recording beams ($\lambda_{\mathrm{r}} = 400$ nm). The normalised temporal evolution of the square root of the

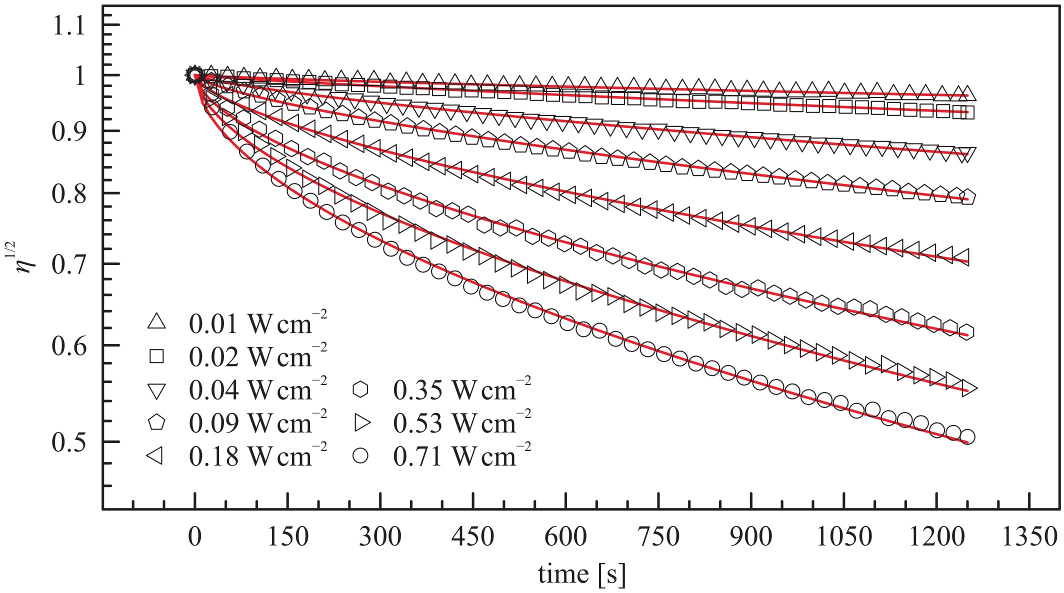

(a) undoped CLN

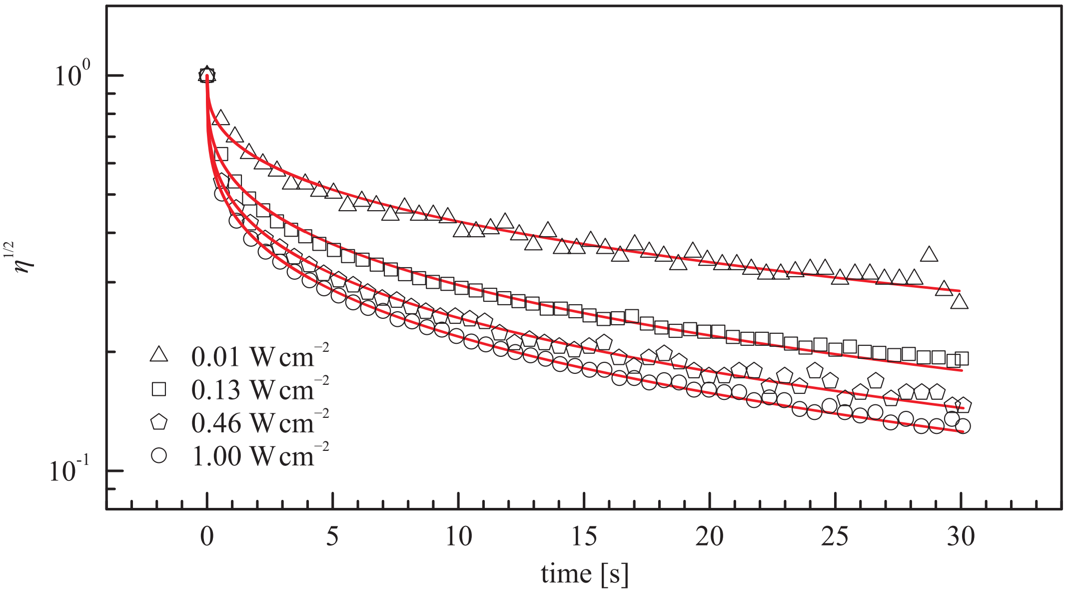

(b) MgO:CLN

FIGURE 2.12: Decays of the square root of the normalised PR grating diffraction efficiency, $\eta^{1/2}$, in (a) undoped CLN and (b) MgO:CLN for different probe laser intensities, I_{p}. The solid red curves correspond to stretched exponential decay fits.

diffraction efficiency, $\eta^{1/2}$, which is proportional to the amplitude of the space charge field (Eq. 2.8), is plotted as a function of time in Fig. 2.12(a) and Fig. 2.12(b) for undoped CLN and MgO:CLN, respectively. As the decay rate of the PR grating in both crystals was influenced by the intensity of the probe HeNe laser, several decay curves corresponding to different values of the probe beam intensity were obtained as indicated in the graphs of Fig. 2.12. It was found that a stretched exponential decay curve described by the equation,

$$\eta^{1/2} = \exp[-(t/\tau)^{\beta}] \tag{2.11}$$

exhibits an improved fit as compared to a single exponential decay curve, where η is the normalised diffraction efficiency; t is the time; τ is the averaged relaxation time of the recorded hologram; and β is the stretch factor [Peithmann 02]. From the stretched exponential fit, the averaged relaxation time, τ, was derived for different HeNe laser intensities and the corresponding values are summarised in Table 2.3. The use of a stretched exponential function, also known as Kohlrausch-Williams-Watts function, is appropriate here as it describes a process that consists of a distribution of different relaxation processes [Berben 00]. The physical interpretation of a stretched exponential decay of space charge distributions in undoped CLN has been described in Sec. 2.3.2. For electron-dominant charge transport, it is attributed to the large amount ($\sim 10^{20}$ cm^{-3}) of the intrinsic Nb_{Li} anti-site defects which exist in undoped CLN, while for hole-dominant charge transport, it might be due to the V_{Li} that traps holes to form hole polarons. Thus, in both cases, an additional channel is provided for the charge transport via hopping or tunneling processes apart from the conventional contribution of the CB or VB for electrons or for holes respectively [Sturman 08]. The stretch factor β reflects the level of involvement of the additional charge transport channel. It has been plotted versus the incident power in Fig. 2.13,

TABLE 2.3: Summary of the averaged relaxation time τ, stretch factors β, decay rates τ^{-1}, and the relative reduction of the normalised PR grating diffraction efficiency $\delta\eta^{1/2}$ from 60 s to 720 s, recorded in undoped CLN and MgO:CLN for different HeNe laser intensities I_p.

Crystal	I_p (W cm^{-2})	τ (s)	β	τ^{-1} (s^{-1})	$\delta\eta^{1/2}$
undoped CLN	0.71	2400	0.560	4.17×10^{-4}	0.318
	0.53	3040	0.581	3.29×10^{-4}	0.282
	0.35	4060	0.602	2.46×10^{-4}	0.239
	0.18	6370	0.640	1.57×10^{-4}	0.179
	0.088	10100	0.694	9.90×10^{-5}	0.123
	0.044	16600	0.734	6.01×10^{-5}	0.0802
	0.018	29600	0.841	3.38×10^{-5}	0.0378
	0.0088	81500	0.779	1.23×10^{-5}	0.0213
MgO:CLN	1.0	2.27	0.282	4.41×10^{-1}	
	0.46	3.01	0.287	3.32×10^{-1}	
	0.13	5.29	0.312	1.89×10^{-1}	
	0.013	15.8	0.355	6.34×10^{-2}	

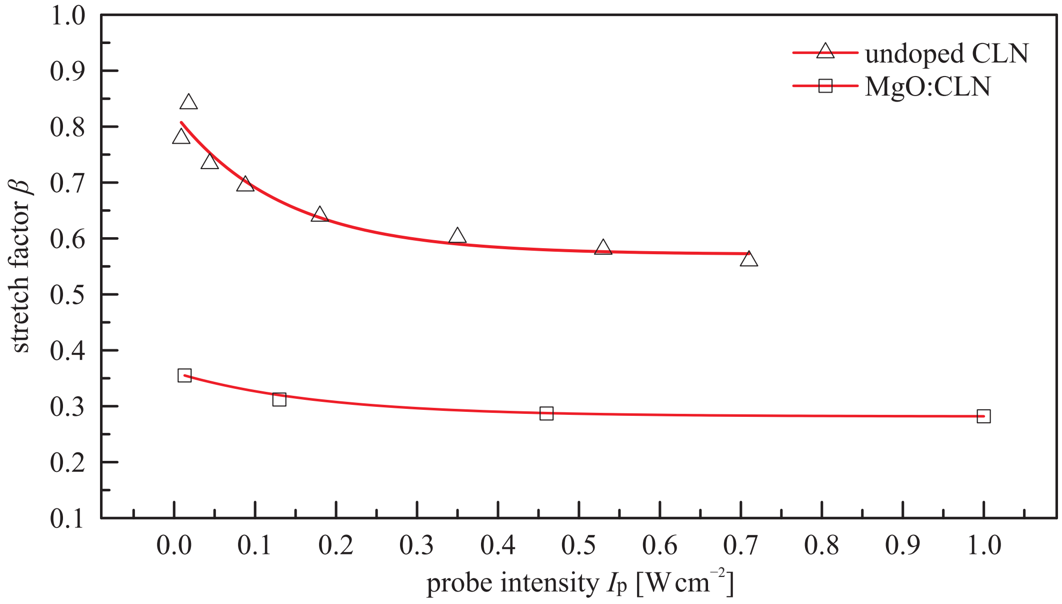

FIGURE 2.13: The stretch factor β vs. incident power I_p for undoped (triangles) and MgO-doped (squares) CLN. The solid red curves are guides to the eye.

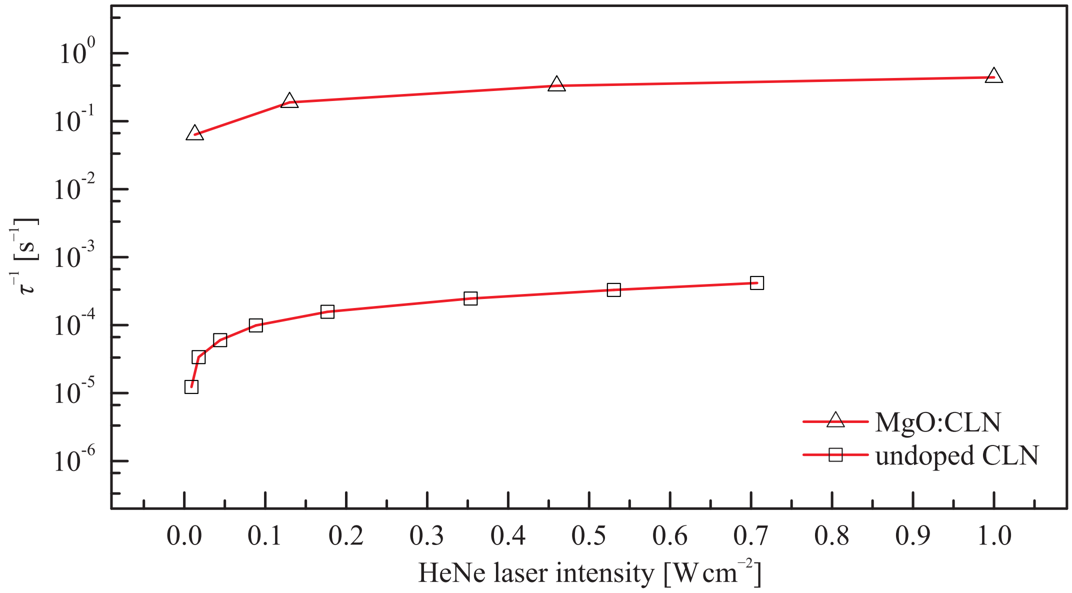

FIGURE 2.14: Decay rate (τ^{-1}) as a function of the probe HeNe laser intensity for undoped CLN (squares) and MgO:CLN (triangles). The solid red curves are guides to the eye.

and as expected for both undoped and MgO-doped CLN the value of stretch factor decreases with increasing incident red power. This means that charge transport on this channel via hopping/tunneling becomes more significant with increasing HeNe laser intensity due to an increase of excited polarons concentration.

Fig. 2.14 shows a plot of the decay rate (τ^{-1}) as a function of the probe HeNe laser intensity. The main observation which can be made from the plot in Fig. 2.14 and Table 2.3 is that the photorefractive gratings in undoped CLN show a sufficiently slow decay, with time constants > 2400 s, thus a significant amount of the space-charge distribution should still be present at the timescales where LLAP is observed. On the other hand, PR gratings in MgO:CLN decay three to four orders of magnitude faster than gratings recorded in undoped CLN, with time constants < 15.8 s, shorter than the smallest voltage time delay which is 60 s, and this likely explains why LLAP was not observed for MgO:CLN crystals for the timescales applied here. The fast decay of PR gratings in MgO:CLN is a consequence of the high dark conductivity of this material which is $4 - 5$ orders of magnitude higher than undoped CLN according to e.g [Mizuuchi 04]. The dark conductivity of the crystal can be determined via [Nee 00]

$$\sigma_{\mathrm{d}} = \epsilon_{\mathrm{r}}\epsilon_0\tau_{I\sim 0}^{-1} \tag{2.12}$$

where $\epsilon_{\mathrm{r}} = 28$ is the dielectric constant of LN [Smith 71, Mansingh 85]; ϵ_0 is the permittivity of free space; and $\tau_{I\sim 0}$ is the decay time constant corresponding to a sufficiently low probe HeNe laser intensity, thus approaching the dark decay. The inverse of $\tau_{I\sim 0}$ can be estimated by substituting the lowest I_{p} values for undoped CLN and MgO:CLN in Table 2.3 which is ~ 0.01 W cm^{-2}. Fig. 2.14 shows that at low HeNe laser intensity in the case of MgO:CLN, the τ^{-1} values are slow-decreasing hence the dark conductivity can be approximated by the conductivity at ~ 0.01 W cm^{-2}. However, for undoped CLN, τ^{-1} decreases quickly at low HeNe intensities, hence inducing a considerable uncertainty in estimating the value of dark conductivity. For this reason, another grating decay experiment was conducted using a probe laser at a longer wavelength (800 nm), which did not affect the decay rate [Bai 97]. This measurement provided a value for the dark conductivity of undoped CLN which was very close to the value that corresponded to the HeNe intensity of $I_{\mathrm{p}} \sim 0.01$ W cm^{-2}. According to Eq. 2.12, the corresponding dark conductivities were derived to be 1.57×10^{-11} Ω^{-1} m^{-1} and 3.05×10^{-15} Ω^{-1} m^{-1} for MgO:CLN and undoped CLN respectively, reconfirming the $4 - 5$ orders of magnitude difference which has been reported in the literature [Mizuuchi 04].

2.3.5 Comparison with LLAP

To relate the PR grating decay to the delay time dependence of the inverted LLAP domain area, the relative reduction of the square root of the normalised PR grating diffraction efficiency, $\delta\eta^{1/2}$, for the same time period in Fig. 2.3, from 60 s to 720 s, was derived from the stretched-exponential fitting for each HeNe laser intensity. The values of relative reduction are listed in Table 2.3 and plotted in Fig. 2.15. In that time period in undoped CLN, comparing the relative reduction of the square root of the normalised PR grating diffraction efficiency, $\delta\eta^{1/2}$, with that of the square root of the inverted domain areas in LLAP, $\delta A^{1/2}$, it is seen that the corresponding relative reduction for the domain length is larger than the corresponding $\sim$dark PR grating decay. The range of the relative reduction for the square root of the inverted domain areas in Fig. 2.3

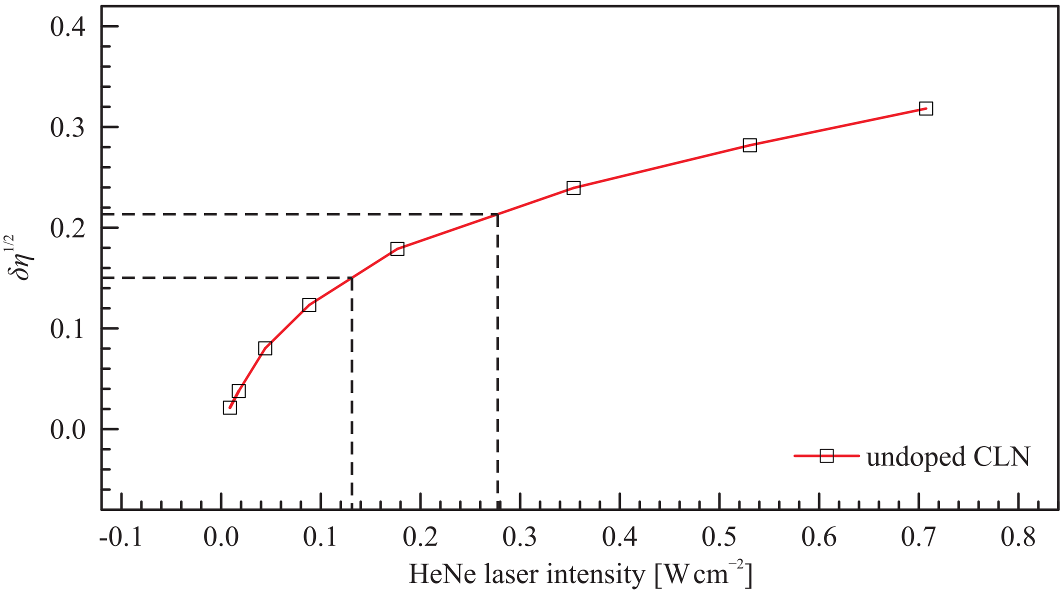

FIGURE 2.15: Relative reduction of the square root of the normalised diffraction efficiency of the PR grating from 60 s to 720 s, $\delta\eta^{1/2}$, as a function of HeNe laser intensity for undoped CLN. The solid red curve is a guide to the eye. The range of the relative reduction of the square root of the inverted LLAP domain areas in Table 2.1, $\delta A^{1/2}$, is indicated by the horizontal lines while the vertical lines indicate the corresponding range of HeNe laser intensities.

is indicated by the dashed horizontal lines in Fig. 2.15 while the vertical dashed lines indicate the corresponding range of probe HeNe laser intensities ($0.13 - 0.28$ W cm^{-2}). It is believed that this is due to the fact that in the LLAP experiments the crystals were not kept in the dark but were continuously illuminated by a broadband light source (halogen bulb) for the in-situ visualisation of the poling process. The decay of the photo-induced space-charge distribution (hence the reduction of the inverted LLAP domain area with voltage delay time) should have been accelerated as a result of uniform illumination with radiation that contains a significant portion of short wavelength spectral components to which the crystal is more sensitive.

The saturated diffraction efficiency of the PR gratings recorded in MgO:CLN was measured to be 1.5×10^{-4} which is one order of magnitude higher as compared to the corresponding saturated diffraction efficiency for undoped CLN crystals (1.3×10^{-5}) of the same thickness under identical recording and probing conditions. The diffraction efficiency of the grating was measured in real time during the recording of the grating with all three beams present simultaneously in the crystal. This difference in the diffraction efficiency corresponds to a 3.4 times larger amplitude of the space-charge field, and thus a 3.4 times larger number of photo-induced charges being formed in MgO:CLN as compared to undoped CLN. This observation is of particular importance as it is in accordance with the much higher nucleation field reduction in MgO:CLN which is observed in LAP experiments [Valdivia 06].

Finally, the larger reduction of the E_n which was observed in LLAP for undoped CLN as compared with simultaneous LAP [Valdivia 07] cannot be explained with the data obtained here. The association of this nucleation reduction difference with transient photo-excited charges [Beyer 05], which can screen the slowly evolving space-charge field in the presence of the ultrafast laser illumination and which decays much faster than the LLAP observation times, might be excluded, because no sudden change of diffraction efficiency has been observed upon blocking the writing fs-laser beams. A possible explanation might be that a portion of the photo-excited charges drift under the influence of the external poling field to the surface, thus, partially screening the poling field to a lower value which the crystal actually experiences. As a result, poling of the crystal in LAP requires a larger E-field as compared to the LLAP to compensate the screening. Another explanation might be related to the photoconductivity gradient that is proposed by Wengler [Wengler 05].

2.4 Proposed mechanism

UV photo-excited charge carriers in undoped CLN can be electrons excited from Fe^{2+} level to the conduction band, holes excited from Fe^{3+} level to the valence band, and electron-hole pairs excited directly across the band-gap via two-photon absorption [Beyer 05] especially at high intensities. The driving force responsible for the migration of these photo-induced charges can be diffusion and/or the photovoltaic effect, resulting in a non-uniform space-charge distribution after illumination. Possible mechanisms for LLAP based on these photo-excited charges have been proposed, including 1) photovoltaic effect, 2) diffusion, and 3) screening of defect clusters to reduce the pinning strength.

The space-charge field produced by this space-charge distribution, if along the poling field, can contribute in a straightforward manner to the E_n reduction. Both the photovoltaic effect and diffusion can produce such space-charge distributions, with a component of space-charge field aligning along the poling field at the $-z$ face where domain nucleation occurs. The photovoltaic case can be explained as in Fig. 2.16(a): with the photovoltaic current flowing parallel to the spontaneous polarisation, surface compensation charges are countered by photo-excited charges, leaving the dipoles at least partially uncompensated at the surface. The uncompensated depolarisation field is oriented along the poling direction [Shur 05] and thus adds to the externally applied E-field, locally reducing the E_n. The process of producing such a space-charge field by diffusion of electrons as charge carriers has been discussed in detail in [Wang 09] and described as in Fig. 2.16(b). Photo-excited charge carriers, electrons, drift to the un-irradiated region and the remaining holes or ionised Fe^{3+}, creating an opposite electric field at $+z$ and $-z$ faces, with that at the $-z$ face parallel to the poling field, thus, assisting the local nucleation.

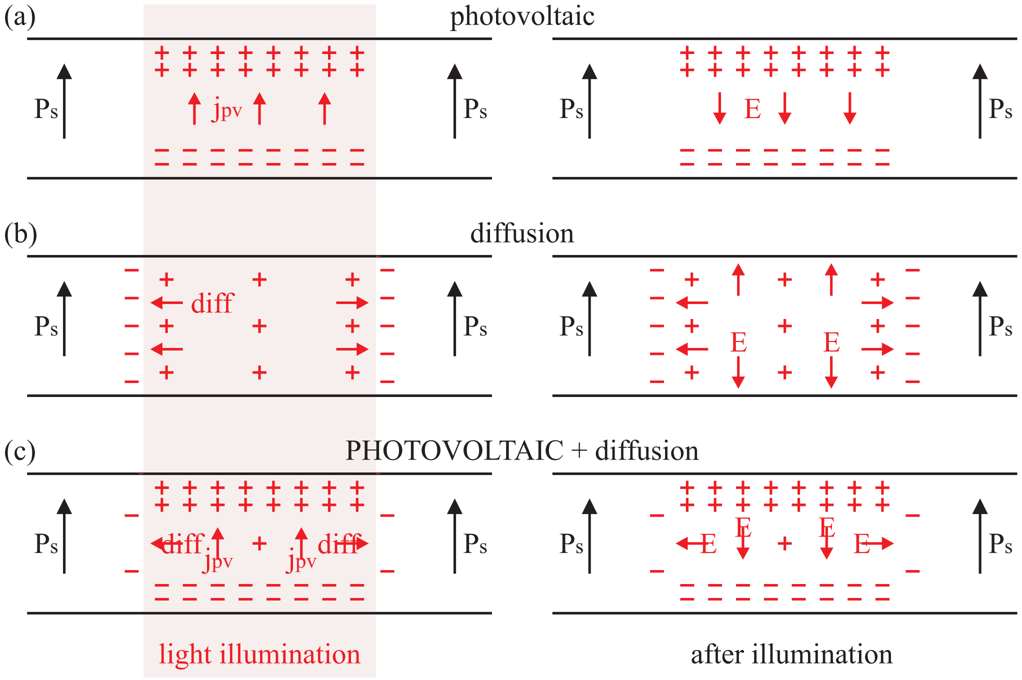

FIGURE 2.16: Charge transport with light illumination under (a) photovoltaic effect and (b) diffusion. A space charge distribution is formed as a result of illumination and therefore a space charge field. In both cases, space charge fields at the $-z$ face are parallel to the poling field, thus assisting the local nucleation. In (c), both photovoltaic effect and diffusion are included with photovoltaic effect as dominant.

Additionally, photo-excited charges on the surface can screen the surface defects responsible for the domain nucleation [Yan 06], which might also contribute to the E_n reduction. The explanation of light-induced reduction of the nucleation field, involving the reduction of pinning strength in defect centers, was first proposed in [Sones 05]. Domain growth under low E-fields is dominated by domain pinning [Kim 01]. The amount of domain pinning is strongly dependent upon stoichiometry, and hence pinning is directly proportional to the defect density. As discussed in Sec. 1.3.2, the defects involved are likely to be the Nb_{Li} anti-site and V_{Li} defect clusters which present an energy barrier for the crossing of a domain wall, hence acting as pinning sites [Kim 01]. However, domain wall movement and bowing between pinning defects has been observed in undoped CLN under E-fields an order of magnitude lower than the coercive field [Yang 99]. Therefore it is proposed that light may cause a reduction in the pinning strength of these defects, allowing domain wall movement at a lower E-field. Under this model, microscopic domains nucleate at surface defect sites as observed in regular EFP. Illumination, however, reduces the ability of the pinning centers to inhibit domain growth in the subsequent EFP, while the preferential poled area depends on the time delay between the two steps for the photo-excited charges to redistribute in the dark or under the influence of ambient light.

The way photo-excited charges screen the defect cluster might be straightforwardly attributed to the presence of Nb_{Li}^{4+} polarons and/or V_{Li}^{+} polarons. As mentioned in Sec. 1.3.2, for undoped

CLN, the spontaneous polarisation is actually stabilised by the defect cluster composed of one $\mathrm{Nb_{Li}^{5+}}$ and four $\mathrm{V_{Li}}$. Thus, electrons on $\mathrm{Nb_{Li}^{5+}}$ ($\mathrm{Nb_{Li}^{4+}}$ polarons) and holes on $\mathrm{V_{Li}}$ ($\mathrm{V_{Li}^{+}}$ polarons) can be functionalised as a screening to the defect cluster, that can greatly reduce the contribution of defect clusters to the stabilisation of the spontaneous polarisations (thus requiring a lower coercive field for poling), and moreover, weaken their pinning strength during EFP. It is worth mentioning that the lowest $E_\mathrm{n} \sim 6$ kV mm^{-1} achieved here is very close to the coercive field of some SLN of about $6 - 6.5$ kV mm^{-1} [Volk 08] which might suggest that if all the defect clusters are perfectly screened by electrons on $\mathrm{Nb_{Li}}$ and holes on $\mathrm{V_{Li}}$, the poling behavior just shifts to that of SLN.

Note here that a mechanism based on screening of defect clusters by electrons and holes requires the lifetime of responsible polarons to be comparable to the voltage delay time of minutes and hours. It might at first glance contradict the literature that the lifetime of $\mathrm{Nb_{Li}^{4+}}$ polarons in iron-doped LN is reported to be from µs to ms [Berben 00], much shorter than the time delays applied here, so the electrons on the $\mathrm{Nb_{Li}}$ level cannot be remain until the EFP step. However, recalling that the lifetime of an individual polaron depends on the distance to the next deep trap, it might be the case that in undoped CLN the lifetime is much longer, even hours and days due to the much smaller deep trap concentration of $\mathrm{Fe^{3+}}$ for electrons, or it might be that the main contribution of LLAP comes from the holes on $\mathrm{V_{Li}}$ that is expected to have a much lower mobility as compared to electrons. One additional experiment has been performed to support the idea that the photo-excited charges can still be present as polarons on $\mathrm{Nb_{Li}}$ and/or $\mathrm{V_{Li}}$ minutes after light illumination. The fs-pulsed laser at 400 nm was used to uniformly illuminate an area of ~ 3 mm diameter, and subsequently, some minutes after illumination, the HeNe laser at 633 nm was used to record a grating at the illuminated area in the crystal by two beam interference. Considerable diffraction efficiency was observed which means that even after minutes a considerable number of charges were still present at $\mathrm{Nb_{Li}}$ and/or $\mathrm{V_{Li}}$ levels that can be excited to the CB or VB with the red laser, while electrons/holes on deep traps of $\mathrm{Fe^{3+}/Fe^{2+}}$ cannot be excited at the HeNe wavelengths. Therefore, it seems that the assumption of long lifetime of polarons in undoped CLN has some merit.

Although three possible mechanisms have been proposed based on photo-excited space charges, they are not independent and the actual mechanism can be a combination of them. As mentioned, in the UV the photovoltaic field was measured to be 0.55 kV cm^{-1} [Jungen 92], while with a focused laser beam radius of 15 µm, Eq. 2.5 yields a value of the diffusion field as 0.05 kV cm^{-1}, much smaller than the photovoltaic field. Therefore, it is reasonable to expect that during LLAP, the photovoltaic field dominates over the diffusion field, and the resultant space-charge distribution can be as illustrated in Fig. 2.16(c). The space charges (electrons and holes) trapped and accumulated on the surface ($-z$ and $+z$ face respectively) can be presented as polarons; thus, apart from forming an electric field parallel to the poling field at the $-z$ face, they can contribute to the screening of defect clusters on the surface, the effect of which is much stronger compared to the case if screening occurs only locally and decays via local recombination. As electrons accumulated on the $-z$ face via photovoltaic field can screen surface Nb_{Li}^{5+} that is primarily responsible for domain wall pinning [Yan 06, Kim 01], it likely explains the preferential domain nucleation always on the $-z$ face. The decay (redistribution) of the space charges is thus reflected in the reduction of the inverted domain area as a function of the voltage time delay. All LLAP results which have been presented thus far correspond to experiments with undoped CLN crystals. No LLAP was observed for 5 mol% MgO-doped CLN (MgO:CLN) under these experimental conditions.

2.5 Applications

LLAP enables the de-coupling of the light illumination and application of the externally E-field, and has been demonstrated in undoped CLN. De-coupling these two steps can potentially improve the ferroelectric domain engineering process as it allows for independent design of each step. This includes the choice of illuminating wavelength and intensity to maximise the light-matter interaction, and choice of electrode materials for the optimisation of the ferroelectric capacitor circuit for poling. Additionally, separation of the two processing steps can simplify the apparatus required, permitting the poling of thicker crystals or utilising a larger area of the crystal by limiting surface leakage currents near the edges via the use of insulating oils (e.g., silicone oil). Furthermore, long life-time of polarons excited by fs-pulsed lasers can also find applications in hologram storage.

2.6 Summary

The chapter has shown that the LLAP in undoped CLN, and the associated E_n reduction can be observed even after several hours following irradiation with ultrafast (~ 150 fs) laser light at a wavelength of 400 nm. The domain nucleation for varying time-delays between light illumination and application of the external E-field in undoped CLN has been investigated. It was found that the size of the resulting inverted ferroelectric LLAP domains depends on the intensity, applied voltage, and the time delay between the light illumination and the application of the E-field. The dynamics of LLAP were attributed to the presence of a photo-induced space-charge distribution. The photorefractive effect in undoped CLN and MgO:CLN crystals was used as a tool for the monitoring of the dynamics of photo-induced space-charge distributions in these crystals. Good agreement between the relaxation dynamics of LLAP domain inversion and the PR grating was observed for undoped CLN, while the fast decay of the PR gratings observed in MgO:CLN explains the absence of the latent effect in this crystal. Finally the 10× higher diffraction efficiency of PR gratings in MgO:CLN suggests a much larger amount of the photo-excited space charges in this crystal thus explaining the significant reduction of the nucleation field in this crystal during simultaneous light assisted poling (LAP). Three possible mechanisms have been proposed based on space charges: 1) photovoltaic effect 2) diffusion and 3) defect cluster screening. And a combination of three mechanisms most possibly approaches the truth.

References

[Arizmendi 94] L. Arizmendi & F. Agulló-López, *$LiNbO_3$: a paradigm for photorefractive materials*, MRS Bull., vol. 19, no. 3, pages 32–38, 1994.

[Bai 97] Y. S. Bai & R. Kachru, *Nonvolatile holographic storage with two-step recording in lithium niobate using cw lasers*, Phys. Rev. Lett., vol. 78, no. 15, pages 2944–2947, 1997.

[Bennett 09] J. M. Bennett, Handbook of optics, third edition volume I: geometrical and physical optics, polarized light, components and instruments, Chapter 12, page 12.8, McGraw-Hill Professional, 2009.

[Berben 00] D. Berben, K. Buse, S. Wevering, P. Herth, M. Imlau & Th. Woike, *Lifetime of small polarons in iron-doped lithium-niobate crystals*, J. Appl. Phys., vol. 87, no. 3, pages 1034–1041, 2000.

[Beyer 05] O. Beyer, D. Maxein, K. Buse, B. Sturman, H. T. Hsieh & D. Psaltis, *Femtosecond time-resolved absorption processes in lithium niobate crystals*, Opt. Lett., vol. 30, no. 11, pages 1366–1368, 2005.

[Buse 97a] K. Buse, *Light-induced charge transport processes in photorefractive crystals I: models and experimental methods*, Appl. Phys. B, vol. 64, no. 3, pages 273–291, February 1997.

[Buse 97b] K. Buse, *Light-induced charge transport processes in photorefractive crystals II: materials*, Appl. Phys. B, vol. 64, no. 4, pages 391–407, March 1997.

[Buse 07] Karsten Buse, Jörg Imbrock, Eckhard Krätzig & Konrad Peithmann, Photorefractive materials and their applications 2: materials, Chapter 4, pages 83–126, Springer, 2007.

[Dierolf 04] V. Dierolf & C. Sandmann, *Direct-write method for domain inversion patterns in $LiNbO_3$*, Appl. Phys. Lett., vol. 84, no. 20, pages 3987–3989, 2004.

[Donnerberg 89] H. Donnerberg, S. M. Tomlinson, C. R. A. Catlow & O. F. Schirmer, *Computer-simulation studies of intrinsic defects in $LiNbO_3$ crystals*, Phys. Rev. B, vol. 40, no. 17, page 11909, December 1989.

[Eichler 06] H. J. Eichler & A. Hermerschmidt, Photorefractive materials and their applications 1: basic effects, volume 113 of *Springer Series in Optical Sciences*, Chapter 2, page 14, Springer, Berlin, 2006.

[Fujimura 03] M. Fujimura, T. Sohmura & T. Suhara, *Fabrication of domain-inverted gratings in MgO:LiNbO*$_3$ *by applying voltage under ultraviolet irradiation through photomask at room temperature*, Electron. Lett., vol. 39, no. 9, pages 719–721, 2003.

[Gopalan 99] V. Gopalan & T. E. Mitchell, *In situ video observation of 180° domain switching in LiTaO*$_3$ *by electro-optic imaging microscopy*, J. Appl. Phys., vol. 85, no. 4, pages 2304–2311, 1999.

[Gopalan 00] V. Gopalan, N. A. Sanford, J. A. Aust, K. Kitamura & Y. Furukawa, Handbook of advanced electronic and photonic materials and devices, vol. 4 ferroelectric and dielectrics, Chapter 2: crystal growth, characterization, and domain studies in lithium niobate and lithium tantalate ferroelectrics, pages 57–114, Academic, 2000.

[Günter 88] P. Günter & J. P. Huignard, Photorefractive materials and their applications I: fundamental phenomena, volume 61 of *Topics in Applied Physics*, Springer, Berlin, 1988.

[Günter 89] P. Günter & J. P. Huignard, Photorefractive materials and their applications II: survey of applications, volume 62 of *Topics in Applied Physics*, Springer, Berlin, 1989.

[Günter 06] P. Günter & J. P. Huignard, Photorefractive materials and their applications 1: basic effects, volume 113 of *Springer Series in Optical Sciences*, Springer, Berlin, 2006.

[Günter 07a] P. Günter & J. P. Huignard, Photorefractive materials and their applications 2: materials, volume 114 of *Springer Series in Optical Sciences*, Springer, Berlin, 2007.

[Günter 07b] P. Günter & J. P. Huignard, Photorefractive materials and their applications 3: applications, volume 115 of *Springer Series in Optical Sciences*, Springer, Berlin, 2007.

[Herth 05] P. Herth, D. Schaniel, Th. Woike, T. Granzow, M. Imlau & E. Krätzig, *Polarons generated by laser pulses in doped LiNbO*$_3$, Phys. Rev. B, vol. 71, no. 12, page 125128, March 2005.

[Jermann 95] F. Jermann, M. Simon & E. Krätzig, *Photorefractive properties of congruent and stoichiometric lithium niobate at high light intensities*, J. Opt. Soc. Am. B, vol. 12, no. 11, pages 2066–2070, 1995.

[Jungen 92] R. Jungen, G. Angelow, F. Laeri & C. Grabmaier, *Efficient ultraviolet photorefraction in LiNbO*$_3$, Appl. Phys. A, vol. 55, no. 1, pages 101–103, July 1992.

[Kim 01] S. Kim, V. Gopalan, K. Kitamura & Y. Furukawa, *Domain reversal and nonstoichiometry in lithium tantalate*, J. Appl. Phys., vol. 90, no. 6, pages 2949–2963, 2001.

[Kim 05] S. Kim & V. Gopalan, *Optical index profile at an antiparallel ferroelectric domain wall in lithium niobate*, Mater. Sci. Eng. B, vol. 120, no. 1-3, pages 91–94, 2005.

[Kogelnik 69] H. Kogelnik, *Coupled wave theory for thick hologram gratings*, Bell Syst. Tech. J., vol. 48, page 2909, 1969.

[Kukhtarev 76] N. V. Kukhtarev, *Kinetics of hologram recording and erasure in electrooptic crystals*, Sov. Tech. Phys. Lett., vol. 2, pages 438–440, 1976.

[Kukhtarev 79a] N. V. Kukhtarev, V. B. Markov, S. G. Odulov, M. S. Soskin & V. L. Vinetskii, *Holographic storage in electrooptic crystals. I. steady state*, Ferroelectrics, vol. 22, pages 949–960, 1979.

[Kukhtarev 79b] N. V. Kukhtarev, V. B. Markov, S. G. Odulov, M. S. Soskin & V. L. Vinetskii, *Holographic storage in electrooptic crystals. II. beam coupling and light amplification*, Ferroelectrics, vol. 22, pages 961–964, 1979.

[Lines 77] M. E. Lines & A. M. Glass, Principles and applications of ferroelectrics and related materials, Clarenon Press, 1977.

[Lobov 06] A. I. Lobov, V. Y. Shur, I. S. Baturin, E. I. Shishkin, D. K. Kuznetsov, A. G. Shur, M. A. Dolbilov & K. Gallo, *Field induced evolution of regular and random 2D domain structures and shape of isolated domains in* $LiNbO_3$ *and* $LiTaO_3$, Ferroelectrics, vol. 341, no. 1, pages 109–116, 2006.

[Mansingh 85] A. Mansingh & A. Dhar, *The AC conductivity and dielectric constant of lithium niobate single crystals*, J. Phys. D: Appl. Phys., vol. 18, no. 10, pages 2059–2071, 1985.

[Mizuuchi 04] K. Mizuuchi, A. Morikawa, T. Sugita & K. Yamamoto, *Polarisation-switching-induced resistance change in ferroelectric Mg-doped* $LiNbO_3$ *single crystals*, Electron. Lett., vol. 40, no. 13, pages 819–820, 2004.

[Mok 93] F. H. Mok, *Angle-multiplexed storage of 5000 holograms in lithium niobate*, Opt. Lett., vol. 18, no. 11, pages 915–917, 1993.

[Nee 00] I. Nee, M. Müller, K. Buse & E. Krätzig, *Role of iron in lithium-niobate crystals for the dark-storage time of holograms*, J. Appl. Phys., vol. 88, no. 7, pages 4282–4286, 2000.

[Peithmann 02] K. Peithmann, K. Buse & E. Krätzig, *Dark conductivity in copper-doped lithium niobate crystals*, Appl. Phys. B, vol. 74, no. 6, pages 549–552, 2002.

[Ro 00] J. H. Ro & M. Cha, *Subsecond relaxation of internal field after polarization reversal in congruent* $LiNbO_3$ *and* $LiTaO_3$ *crystals*, Appl. Phys. Lett., vol. 77, no. 15, pages 2391–2393, 2000.

[Shur 05] V. Y. Shur, Nucleation theory and applications, Chapter 6, pages 178–214, Wiley VCH, Weinheim, 2005.

[Smith 71] R. T. Smith & F. S. Welsh, *Temperature dependence of the elastic, piezoelectric, and dielectric constants of lithium tantalate and lithium niobate*, J. Appl. Phys., vol. 42, no. 6, pages 2219–2230, 1971.

[Solymar 96] L. Solymar, D. J. Webb & A. Grunnet-Jepsen, The physics and applications of photorefractive materials, volume 11 of *Oxford Series in Optical and Imaging Sciences*, Oxford University Press, 1996.

[Sones 05] C. L. Sones, M. C. Wengler, C. E. Valdivia, S. Mailis, R. W. Eason & K. Buse, *Light-induced order-of-magnitude decrease in the electric field for domain nucleation in MgO-doped lithium niobate crystals*, Appl. Phys. Lett., vol. 86, no. 21, page 212901, 2005.

[Steigerwald 09] H. Steigerwald, F. Luedtke & K. Buse, *Ultraviolet light assisted periodic poling of near-stoichiometric, magnesium-doped lithium niobate crystals*, Appl. Phys. Lett., vol. 94, no. 3, page 032906, 2009.

[Sturman 92] B. I. Sturman & V. M. Fridkin, The photovoltaic and photorefractive effects in noncentrosymmetric materials, Gordon and Breach Science Publishers, 1992.

[Sturman 08] B. Sturman, M. Carrascosa & F. Agulló-López, *Light-induced charge transport in* $LiNbO_3$ *crystals*, Phys. Rev. B, vol. 78, no. 24, page 245114, 2008.

[Valdivia 06] C. E. Valdivia, C. L. Sones, S. Mailis, J. D. Mills & R. W. Eason, *Ultrashort-pulse optically-assisted domain engineering in lithium niobate*, Ferroelectrics, vol. 340, no. 1, pages 75–82, 2006.

[Valdivia 07] C. E. Valdivia, *Light-induced ferroelectric domain engineering in lithium niobate & lithium tantalate*, PhD thesis, Optoelectronics Research Centre, University of Southampton, Southampton, 2007.

[Volk 08] T. Volk & M. Wöhlecke, Lithium niobate: defects, photorefraction and ferroelectric switching, Chapter 7: polarization reversal and ferroelectric domains in $LiNbO_3$ crystals, page 185, Springer, 2008.

[Wang 09] W. Wang, Y. Kong, H. Liu, Q. Hu, S. Liu, S. Chen & J. Xu, *Light-induced domain reversal in doped lithium niobate crystals*, J. Appl. Phys., vol. 105, no. 4, page 043105, 2009.

[Wengler 04] M. C. Wengler, B. Fassbender, E. Soergel & K. Buse, *Impact of ultraviolet light on coercive field, poling dynamics and poling quality of various lithium niobate crystals from different sources*, J. Appl. Phys., vol. 96, no. 5, pages 2816–2820, 2004.

[Wengler 05] M. C. Wengler, U. Heinemeyer, E. Soergel & K. Buse, *Ultraviolet light-assisted domain inversion in magnesium-doped lithium niobate crystals*, J. Appl. Phys., vol. 98, no. 6, page 064104, 2005.

[Xin 10] F. Xin, G. Zhang, F. Bo, H. Sun, Y. Kong, J. Xu, T. Volk & N. M. Rubinina, *Ultraviolet photorefraction at 325 nm in doped lithium niobate crystals*, J. Appl. Phys., vol. 107, no. 3, page 033113, 2010.

[Xu 00] J. Xu, G. Zhang, F. Li, X. Zhang, Q. Sun, S. Liu, F. Song, Y. Kong, X. Chen, H. Qiao, J. Yao & L. Zhao, *Enhancement of ultraviolet photorefraction in highly magnesium-doped lithium niobate crystals*, Opt. Lett., vol. 25, no. 2, pages 129–131, 2000.

[Yamada 93] M. Yamada, N. Nada, M. Saitoh & K. Watanabe, *First-order quasi-phase matched* $LiNbO_3$ *waveguide periodically poled by applying an external field for efficient blue second-harmonic generation*, Appl. Phys. Lett., vol. 62, no. 5, pages 435–436, 1993.

[Yamada 98] M. Yamada & M. Saitoh, *Fabrication of a periodically poled laminar domain structure with a pitch of a few micrometers by applying an external electric field*, J. Appl. Phys., vol. 84, no. 4, pages 2199–2206, 1998.

[Yan 06] W. Yan, L. Shi, Y. Kong, Y. Wang, H. Liu, J. Xu, S. Chen, L. Zhang, Z. Huang, S. Liu & G. Zhang, *The electrostatic depinning mechanism of domain wall for near-stoichiometric lithium niobate crystals*, J. Phys. D: Appl. Phys., vol. 39, no. 19, pages 4245–4249, 2006.

[Yang 99] T. J. Yang, V. Gopalan, P. J. Swart & U. Mohideen, *Direct observation of pinning and bowing of a single ferroelectric domain wall*, Phys. Rev. Lett., vol. 82, no. 20, page 4106, May 1999.

3

UV laser-induced poling-inhibition in $LiNbO_3$

3.1 Introduction

It has been reported that continuous wave ultraviolet laser irradiation at $\lambda = 244$ nm on the $+z$ face of undoped and MgO doped congruent lithium niobate single crystals has been observed to inhibit ferroelectric domain inversion directly beneath the illuminated regions during a subsequent EFP step [Sones 08]. The effect, which is referred to as *poling-inhibition* (PI), has been confirmed by both differential HF etching and piezoresponse force microscopy (PFM). The effect allows the fabrication of arbitrarily shaped domains in lithium niobate and forms the basis of a high spatial resolution microstructuring approach when followed by chemical etching. However, the exact depth of the poling-inhibited ferroelectric domains and the dependence of their depth on the fabrication conditions was largely unknown although a minimum depth of ~ 100 nm was assumed based on the calculated PFM depth sensitivity: subsequent experimental investigation however suggested a depth sensitivity of ~ 1.7 µm.

In this chapter, UV-laser induced inhibition of poling in undoped and MgO doped CLN crystals using a range of writing wavelengths (244, 275.4, 300.3, 302.4 and 305.5 nm) has been fully investigated. The depth, the width and the quality of the PI domains were measured as a function of the UV-writing conditions (wavelength, writing speed and intensity), revealing achievable domain depths and widths ranging from $1.5 - 4.3$ µm and $2.9 - 12.3$ µm respectively which are suitable for waveguide applications. The depth of the PI domains was measured by wedge-polishing the edge of a PI domain-carrying sample at a shallow angle ($\sim 5°$) followed by 48% HF acid etching. The depth and width of the PI domains could then be measured directly and was seen to increase with increasing laser intensity and exposure time. It was found that both depth and width values were largely insensitive to the illuminating UV laser wavelength. The wedge polishing process and subsequent etching has allowed the detailed investigation of the poling-inhibition behavior under extreme poling conditions (large poling field hence fast domain wall propagation). A possible mechanism for poling-inhibition has been proposed based on Li ion migration under the combination of a temperature gradient plus pyroelectric field.

3.2 Fabrication and characterisation of PI domains

The experimental work which is presented in this section investigates the size (depth and width) of PI domains, a parameter which is of importance for photonic applications, as a function of the fabrication conditions. The size was measured via wedge-poling of the PI domains followed by preferential HF etching. PI domain depth and width were found to range from $1.5 - 4.3$ µm and $2.9 - 12.3$ µm respectively, thus enabling the PI domains to overlap with waveguides. Furthermore, the PI domain size seems to be wavelength-independent from $275 - 305$ nm while similar to that of 244 nm.

3.2.1 Experimental procedures

The crystals investigated were 0.5 mm thick, z-cut, optical-grade, undoped CLN (Crystal Technology, Inc., US) and 5 mol% MgO:CLN (Yamaju Ceramics Co., Japan). The CW UV laser sources used were 1) a tunable Coherent Innova Sabre DBW 25/7 argon ion laser system which could be tuned to emit radiation at wavelengths of 275.4, 300.3, 302.4 and 305.5 nm, and 2) a Coherent Innova 300C FreD argon ion laser which operates at 244 nm via frequency doubling. The laser beam with Gaussian intensity distribution was focused either by a fused silica lens ($f = 37.5$ mm) or by a microscope objective onto the $+z$ face of the crystal to a spot with radius of approximately 3 µm or 0.5 µm respectively. Linear UV-illuminated tracks along the crystallographic direction and individual spot exposures were performed by scanning the sample in front of the static focused laser beam using a combination of a computer-controlled 2D translation stage and an optical shutter. The range of the laser intensity and writing speed were $1.2 - 2.1\ \mathrm{GW\,m^{-2}}$ and $0.1 - 1.0\ \mathrm{mm\,s^{-1}}$ respectively. The UV energy fluence used varied from $7 - 120\ \mathrm{MJ\,m^{-2}}$. After UV illumination, the crystals subsequently underwent 20 full poling cycles (uniform poling forward and backward) by EFP using the same experimental setup as in Fig. 2.1 shown in Chap. 2. This conditioning step was applied due to the observation that the domain wall propagation and expansion is smoother after multiple poling cycles, with no jerky domain wall motion which is common during EFP of virgin congruent lithium niobate [Gopalan 98]. This is attributed to the lower poling voltage required after multiple poling cycles than that of the virgin crystal value [Ro 00, Brown 99], thus, ensuring a slower domain wall velocity [Nakamura 02].

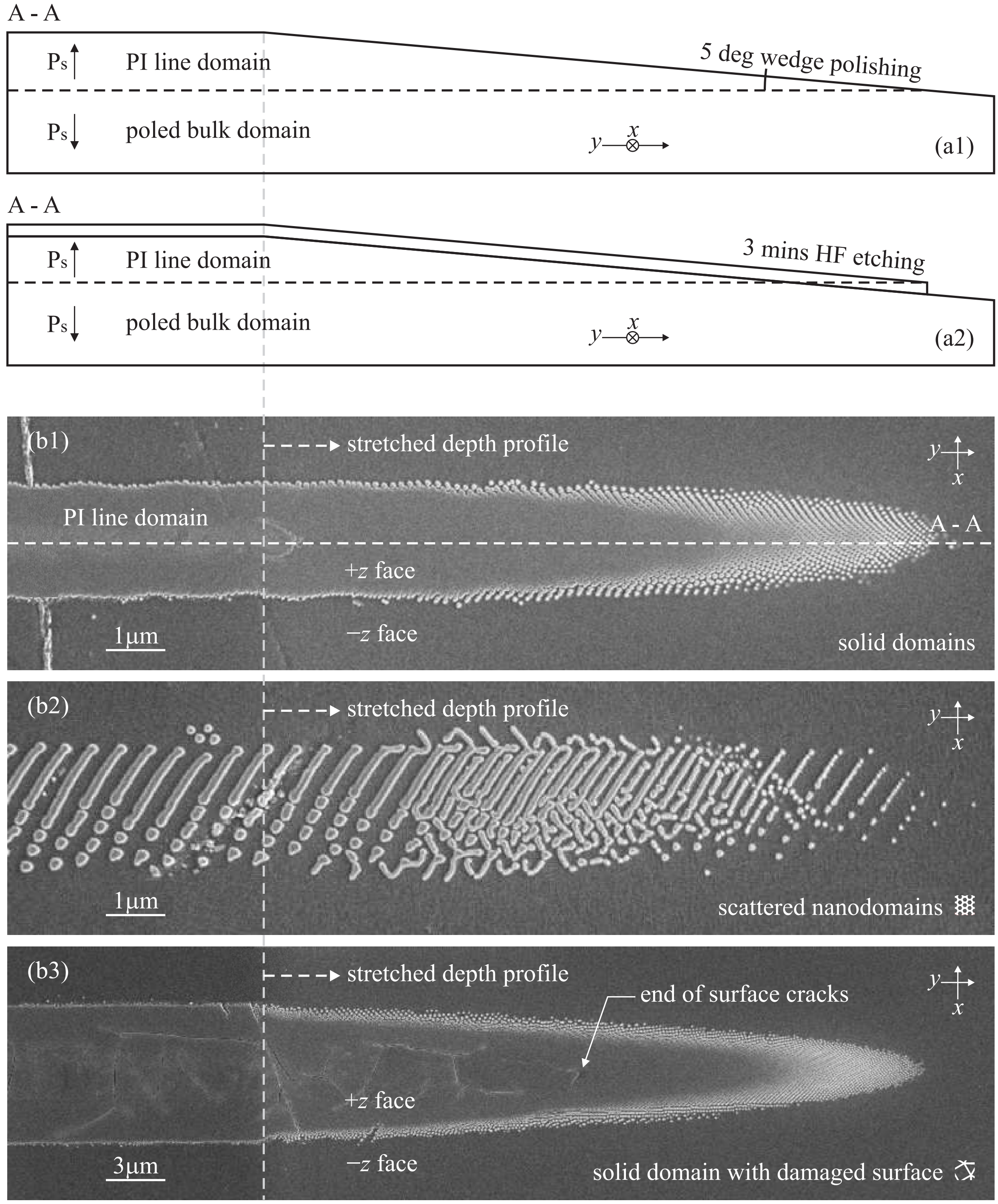

FIGURE 3.1: Schematic of the sample cross section along the A-A line, as shown in the SEM image (b1), indicating the wedge polishing at 5° (a1) before and (a2) after HF etching. b1, b2, b3: SEM images of the etched wedge-polished PI domains to show their stretched depth profile. The PI domains are fabricated under different conditions showing three different quality states: (b1) solid domains with no surface damage, (b2) scattered nanodomains, and (b3) solid domains with a laser damaged surface. The dashed line indicates the slope change. The symbols on the bottom right of the (b2) and (b3) images indicate the domain quality and will be used in the rest of the text.

The importance of a smooth and slow domain wall motion to the realisation of poling-inhibition will be discussed in detail in Sec. 3.5.2.

After the multiple poling cycles, a slow forward poling is conducted at the lowest possible poling voltage: the poling voltage was ramped at 0.1 $\mathrm{kV\,s^{-1}}$ up to 9.7 kV, while above 9.7 kV, it was ramped up at a much slower rate of 0.01 $\mathrm{kV\,min^{-1}}$ until domain nucleation is observed. Then the voltage was always kept at a constant level throughout the poling process (the value varies from sample to sample, but was always below 10.1 kV). The process takes typically $30 - 60$ mins for a 10×10 $\mathrm{mm^2}$ sample and finally the voltage is ramped down at a rate of 1 $\mathrm{kV\,s^{-1}}$. The result of this process is a uniformly poled crystal apart from the UV pre-illuminated regions where poling has been inhibited [Sones 08].

To investigate the depth of PI domains, the crystal surface which carries the linear PI domain was wedge-polished at approximately 5°. Fig. 3.1(a1) shows a schematic of the profile (A-A) along the center of a PI line domain track along the y-axis in Fig. 3.1(b1). Then the sample was immersed in HF acid (48%) for 3 minutes at room temperature, yielding an etched depth of ~ 30 nm of the $-z$ face as shown in Fig. 3.1(a2). The brief etching can provide sufficient Scanning Electron Microscope (SEM) contrast to reveal the domain structure [Sones 02] as illustrated in Fig. 3.1(b1-3). Wedge polishing is applied here instead of common y-face polishing due to its following advantages. Firstly, wedge polishing magnifies the shallow domain depth of the PI domains by a factor of $1/\tan 5° = 11.43$, which improves the resolution of the measurement and is less sensitive to the edge quality as compared with direct etching of the y-face. In Fig. 3.1, the grey dashed line indicates the change of slope. The wedge polished z-face thus reveals the stretched depth profile. The width and depth were then measured from SEM images, an example of which is shown in Fig. 3.1(b1-3).

3.2.2 PI domains characteristics: depth, width and surface quality

Measurements of the wedge polished samples yield a plot of the depth and width of PI line domains as a function of the writing speed using a focussed UV laser beam radius of ~ 3 µm, as is shown in Fig. 3.2. The various data points in the plots correspond to different writing conditions (wavelength, UV laser intensity). It is seen that PI domains written with 300, 302 and 305 nm (triangles, squares and pentagons respectively) have similar values of depth and width for the same writing conditions (laser intensity, writing speed). For all the conditions used, the values of PI domain depth and width range from $1.5 - 4.3$ µm and $2.9 - 12.3$ µm respectively. This result shows that it is possible to fabricate PI domains with depths that match typical waveguide dimensions. From the SEM images the PI line domains can be grouped into 3 different types as a function of their surface quality as shown in Fig. 3.1(b1-3): (b1) – solid domains with no surface damage, (b2) – scattered nanodomains, and (b3) – solid domains with a laser-damaged surface.

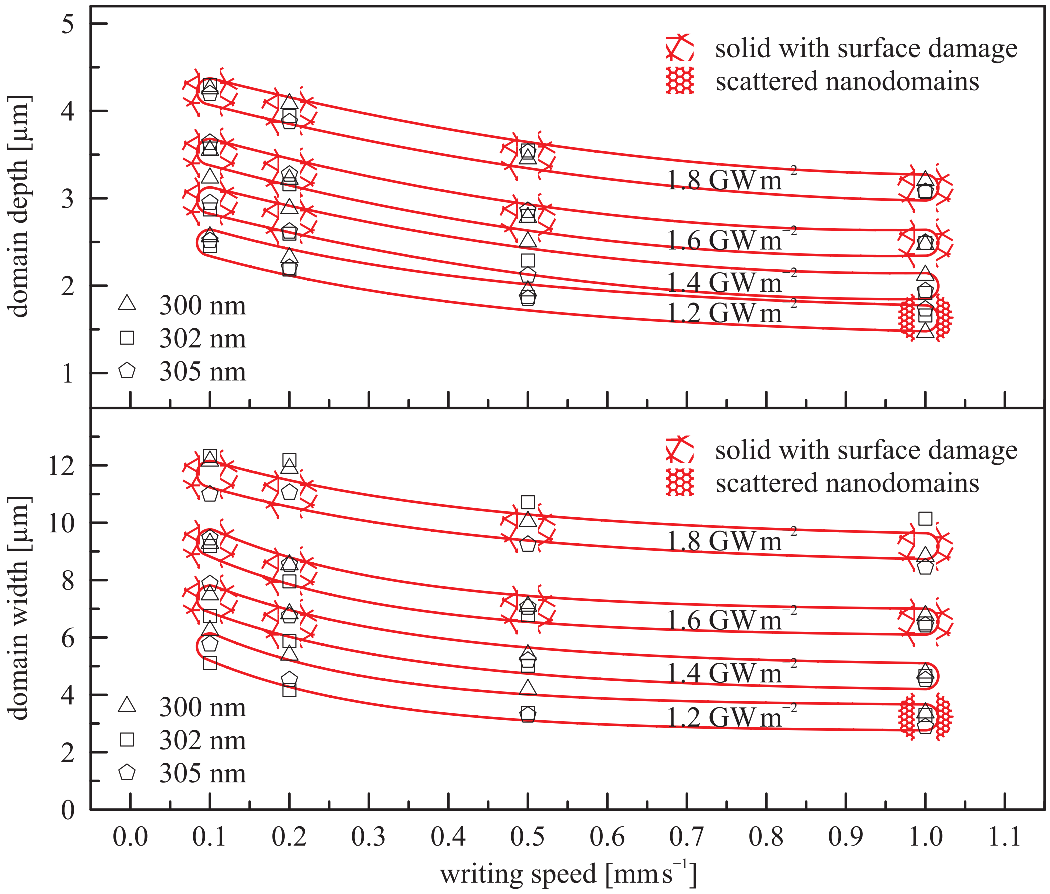

FIGURE 3.2: The depth and width of PI line domains in undoped CLN for different UV wavelengths (as measured from the SEM images of wedge polished samples) plotted as a function of the writing speed. The data for the same intensity, together with the value of intensity, are enclosed within the individual red curves. The red symbols correspond to various surface qualities as in Fig. 3.1(b1-3).

For all the PI domains with surface damage, the PI domain depth is always deeper than the damage as shown in Fig. 3.1(b3). The results of surface quality are indicated in Fig. 3.2 using the symbols which were defined in Fig. 3.1. In general, all three wavelengths result in similar surface quality for the same exposure conditions. There is however a window of exposure conditions that can provide solid domains with no surface damage, which is considered as optimum for applications. At the lower limit of laser power or at the higher limit of writing speed the result is scattered nanodomains, while too high laser power or too slow writing speed can result in solid domains with surface damage. A measurement of PI line domain depth and width written by 244 nm has also been done. The depth is measured to be around 2.5 µm for PI solid domain with no surface damage, similar to the value obtained by the longer wavelength (300 – 305 nm) here. From this result it can be concluded that the optical absorption length is not a crucial parameter for the formation of the PI domains.

Another measurement with a wider range of writing intensity, also including the data for 275 nm

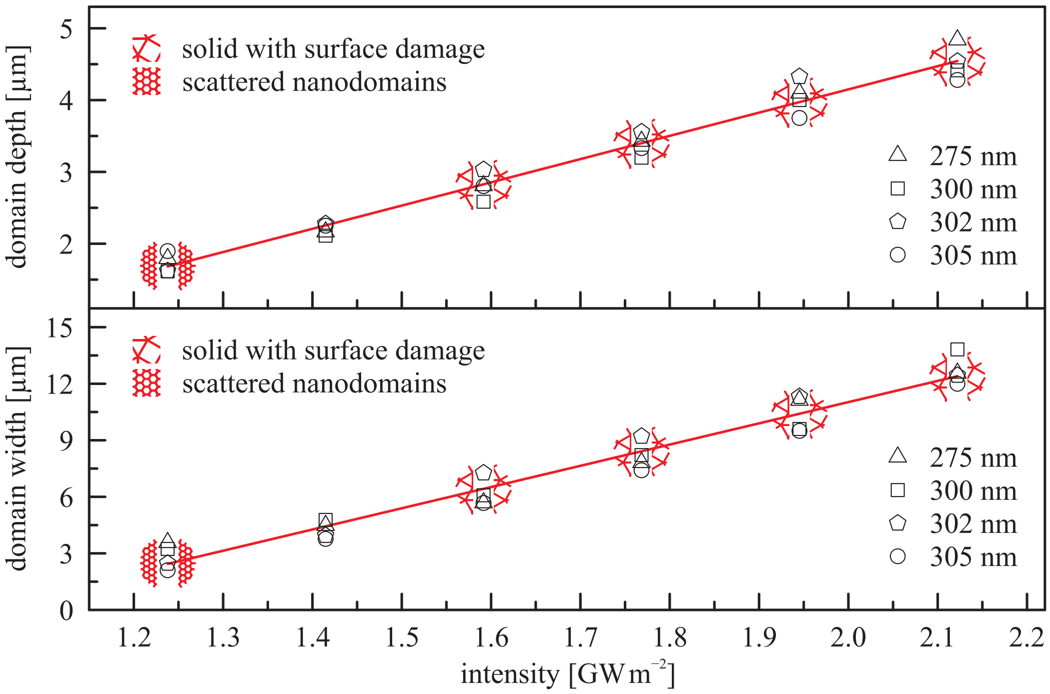

FIGURE 3.3: The depth and width versus writing intensity of PI line domains in undoped CLN, written with wavelength of 275.4, 300.3, 302.4, and 305.5 nm, and writing speed of 1.0 mm s^{-1} with focused beam radius of ∼ 3 µm. The red line represents a linear fitting of the experimental data and the red symbols correspond to various surface qualities as defined in Fig. 3.1(b1-3).

written PI line domains, is shown in Fig. 3.3. The additional data confirmed the similarity of the results written with the other four wavelengths. Additionally, they reveal that, in the investigated range, the PI domain width and depth increase linearly with the writing intensity as suggested by the red linear fitting line, while below the lowest intensity applied as indicated in Fig. 3.3 (I < 1.24 GW m^{-2}), no poling-inhibition was observed, thus implying a threshold intensity for poling-inhibition to occur.

The dependence of PI domain depth and width on the energy fluence was also investigated. Since all UV writing wavelengths show very similar results regarding surface quality, depth and width, for a specific writing condition, only results of 302 nm written PI domains are shown here. The energy fluence here can be varied by changing the writing speed while keeping the laser intensity constant or by changing the intensity while keeping the writing speed constant. The PI domain depth and width versus fluence for a specific writing speed (1.0 mm s^{-1}) and a specific writing intensity (1.2 GW m^{-2}) have been plotted in Fig. 3.4 with data obtained from Fig. 3.2. The plot reveals that the depth and width of the PI domains are much more sensitive to the intensity of the UV laser rather than the dwell time (controlled by the writing speed).

Data of PI domain depth and width from Fig. 3.2 were also replotted as depth versus width in Fig. 3.5. It shows that, regardless of the writing speed, writing intensity and wavelength, all the data generally follows a linear relationship as revealed by the linear fitting (red line),

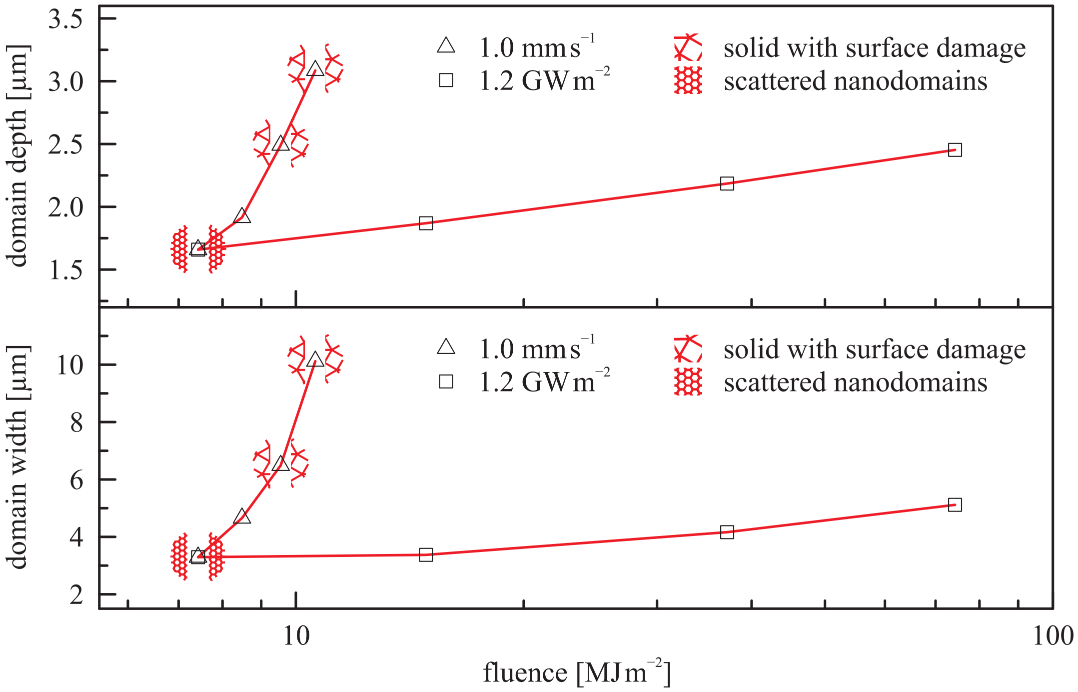

FIGURE 3.4: The depth and width versus UV laser fluence for 302 nm written PI line domains in undoped CLN for a specific writing speed (triangles, 1.0 mm s^{-1}) and a specific writing intensity (squares, 1.2 GW m^{-2}). The data are obtained from Fig. 3.2.

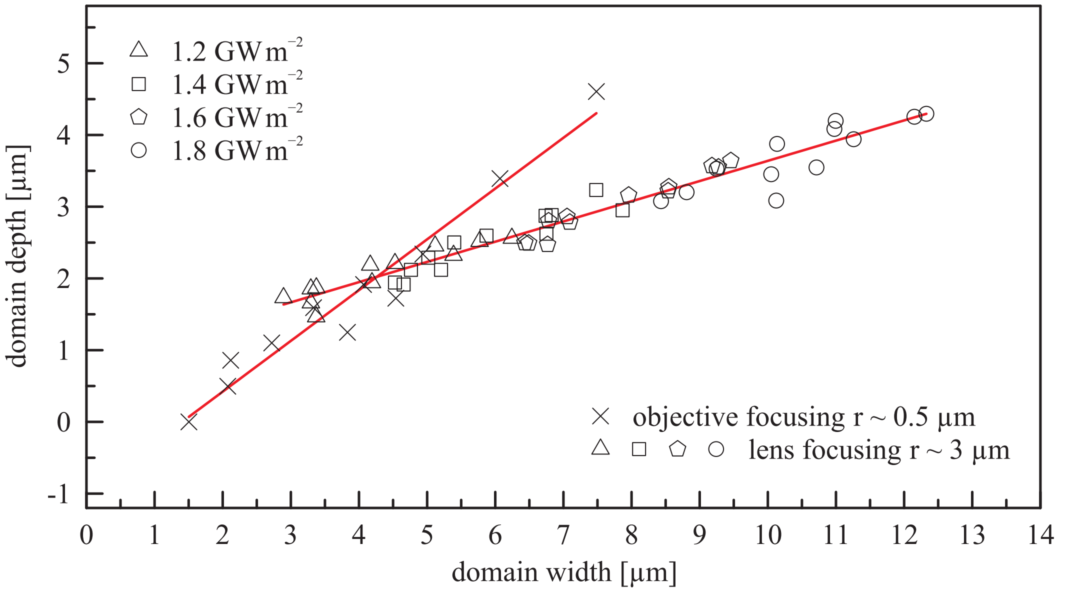

FIGURE 3.5: PI domain depth versus width for different writing conditions. All the data from Fig. 3.2, obtained with a 3 µm radius Gaussian beam, are plotted together with another set of PI domain data produced by tighter focusing to a beam radius of ~ 0.5 µm. The red lines correspond to linear fitting.

while domain depth and width is larger with higher writing intensity. Another set of data for PI domains was produced by tighter focusing, using a microscope objective, to a spot radius of ~ 0.5 µm with UV wavelengths of 275 and 305 nm, writing speed of 0.01 mm s^{-1}, and various incident powers of $5 - 35$ mW. It however reveals that the depth/width ratio of the PI domains is a function of the laser spot radius: the depth vs. width data obtained by tighter focussing also follows but with a different linear dependence as shown in Fig. 3.5. The higher slope for the tighter focusing means that with increasing of the PI domain width, PI domain depth also penetrates deeper into the bulk.

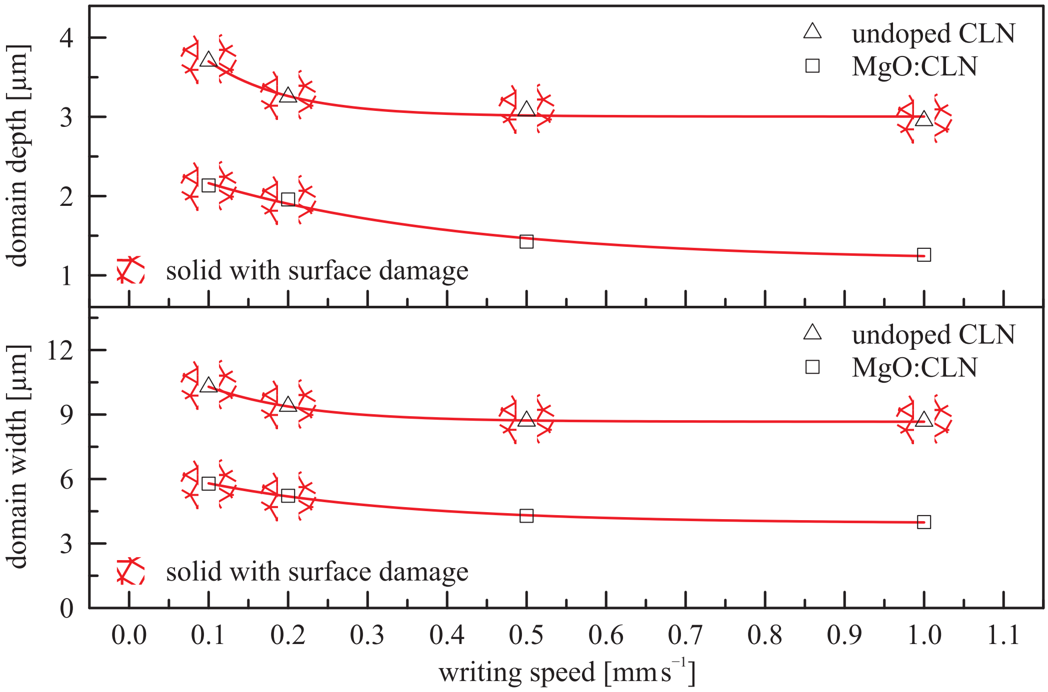

FIGURE 3.6: Comparison of PI domain depth and width in undoped and MgO doped CLN with the same writing condition: 275 nm, 38 mW, $0.1 - 1$ mm s^{-1}.

Poling-inhibition in MgO:CLN has also been investigated. It was found that for the same writing conditions the sizes of the PI domains are approximately half that of undoped CLN as shown in Fig. 3.6. The surface quality symbols at 0.5 and 1.0 mm s^{-1} of both crystals suggests that MgO:CLN has a higher threshold for surface damage.

3.2.3 Thermal stability of PI domains

Many applications of domain engineered LN require operating at temperatures higher than room temperature. Additionally, waveguide fabrication requires high temperature treatment. Consequently the thermal stability of the PI domains needs to be evaluated for future applications. The thermal stability of PI domains with and without surface damage in Fig. 3.7(a1) and Fig. 3.7(b1) respectively was investigated by post-annealing at 300°C for 7 hours, followed by another

7 mins HF etching to reveal whether the PI domains can maintain their polarisation state. The results are shown in Fig. 3.7(a2) and 3.7(b2) which indicate that the PI domains survive the thermal annealing.

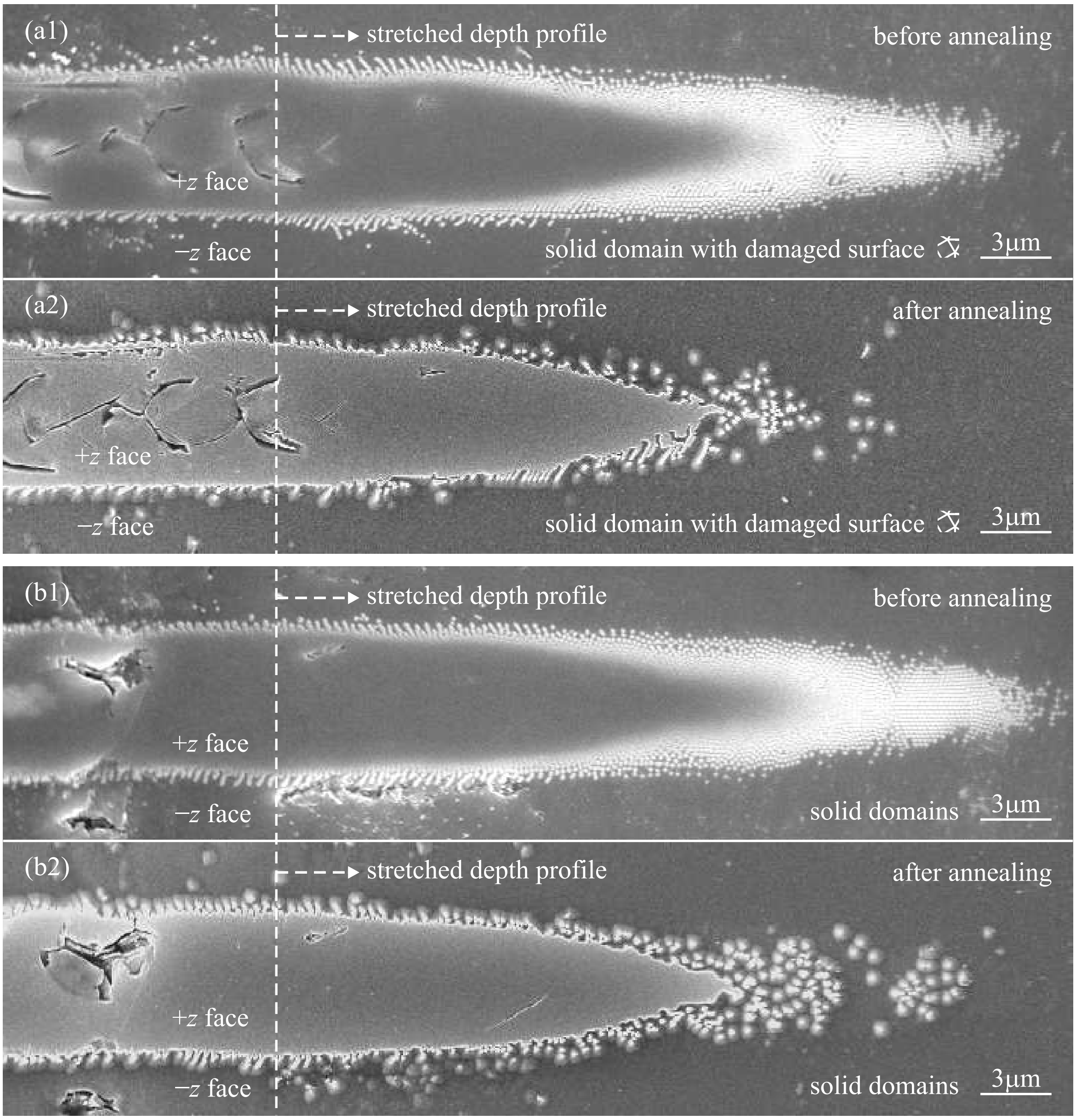

FIGURE 3.7: (a1) and (b1) SEM images of wedge-polished and HF-etched solid PI domain tracks fabricated at two different UV laser intensity levels. (a2) and (b2) show the same domains after annealing at 300°C for 7 hours followed by 7 mins HF etching. The dashed lines indicate the point of slope change as a result of wedge polishing.

3.3 Poling-inhibition under fast poling

Although all the results of poling-inhibition up to this point correspond to low-field poling below 20.2 kV mm^{-1}, poling-inhibition has also been observed when higher E-fields (up to 22 kV mm^{-1}) were used. The characteristics of the PI domains which can be obtained by high-field poling provide hints for the understanding of the PI mechanism. To illustrate the difference between the PI domains obtained from low- and high-field poling, a 0.5-mm thick sample carrying UV laser irradiated tracks (referred to here as the *latent image*) has been poled sequentially at 10.1 and 11 kV. The poling process has been recorded in Fig. 3.8 using the setup shown in Fig. 2.1 as a series of optical microscopy images. The recording time (min:sec) and poling voltage are indicated at the top left and bottom right corners respectively. The latent images of lines are visible as faint horizontal lines in the figure due to slight surface damage and/or refractive index increase [Mailis 03] after UV writing. The poling process which is shown in the image sequence of Fig. 3.8 is as follows: (00:00) – domain nucleation on both $+z$ and $-z$ face occurs preferentially at the latent image positions under the low poling voltage of 10.1 kV [Steigerwald 10]; (03:00–15:07) – preferential poling occurs along one of the latent image sites plus domain expansion from other nucleation sites, i.e., from the edge of the insulating O-ring (seen on the left and right sides of the images); (15:07) – the poling voltage is switched to 11 kV causing fast domain wall movement [Nakamura 02] with abrupt jerky domain wall motion [Shur 05] that accomplished poling of the whole sample in less than 1 second; (15:08) – shows faint contrasts in the former position of the

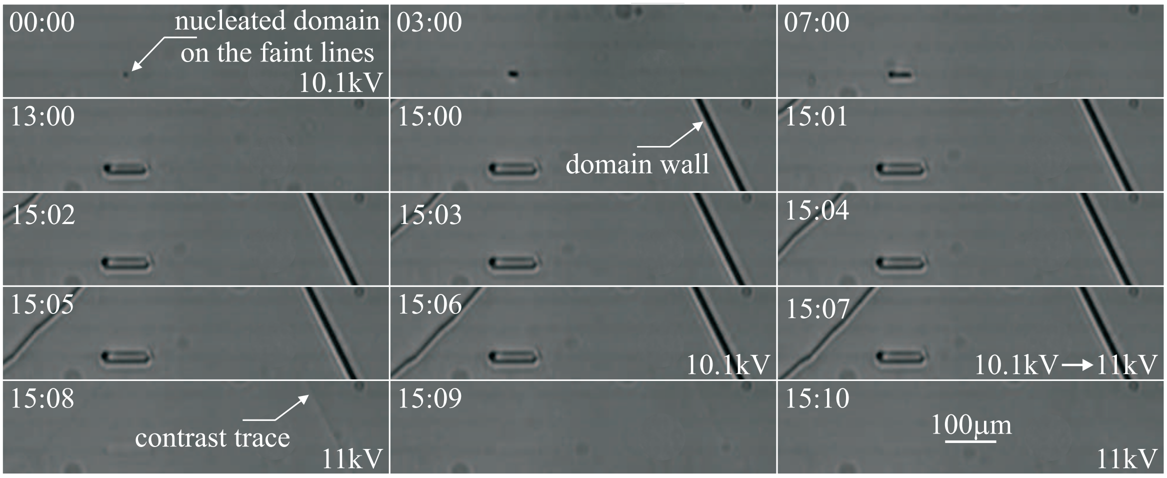

FIGURE 3.8: In-situ visualisation of the domain expansion and propagation. Top left corner lists the recording time in 'min:sec'. Bottom right corner indicates the poling voltage (if not indicated, then it remains the same as in the previous image). The latent images can be seen as faint horizontal lines. (00:00): preferential nucleation close to the latent image, providing sufficient strain-induced contrast for observation of domain wall. (03:00–15:07): slow domain wall expansion and propagation at low poling voltage of 10.1 kV, and from (15:07) poling voltage is switched to 11 kV. (15:08): completion of fast poling process, yet some residual strain at the former domain wall position remains as faint contrast. In (15:09–15:10), the residual strain disappears. The scale bar shown in (15:10) applies to all images.

domain wall due to the residual strain [Gopalan 00]; (15:09−15:10) – within the next 2 seconds, this contrast disappears.

The resultant domain structures of the sample that was poled with both low- and high- poling voltage in Fig. 3.8 was revealed by preferential HF etching and is shown in Fig. 3.9(a). The region which is shown in the images of Fig. 3.9 is exactly the same as the one shown in the images of Fig. 3.8. The regions enclosed in the white dashed lines correspond to poling at 10.1 kV,

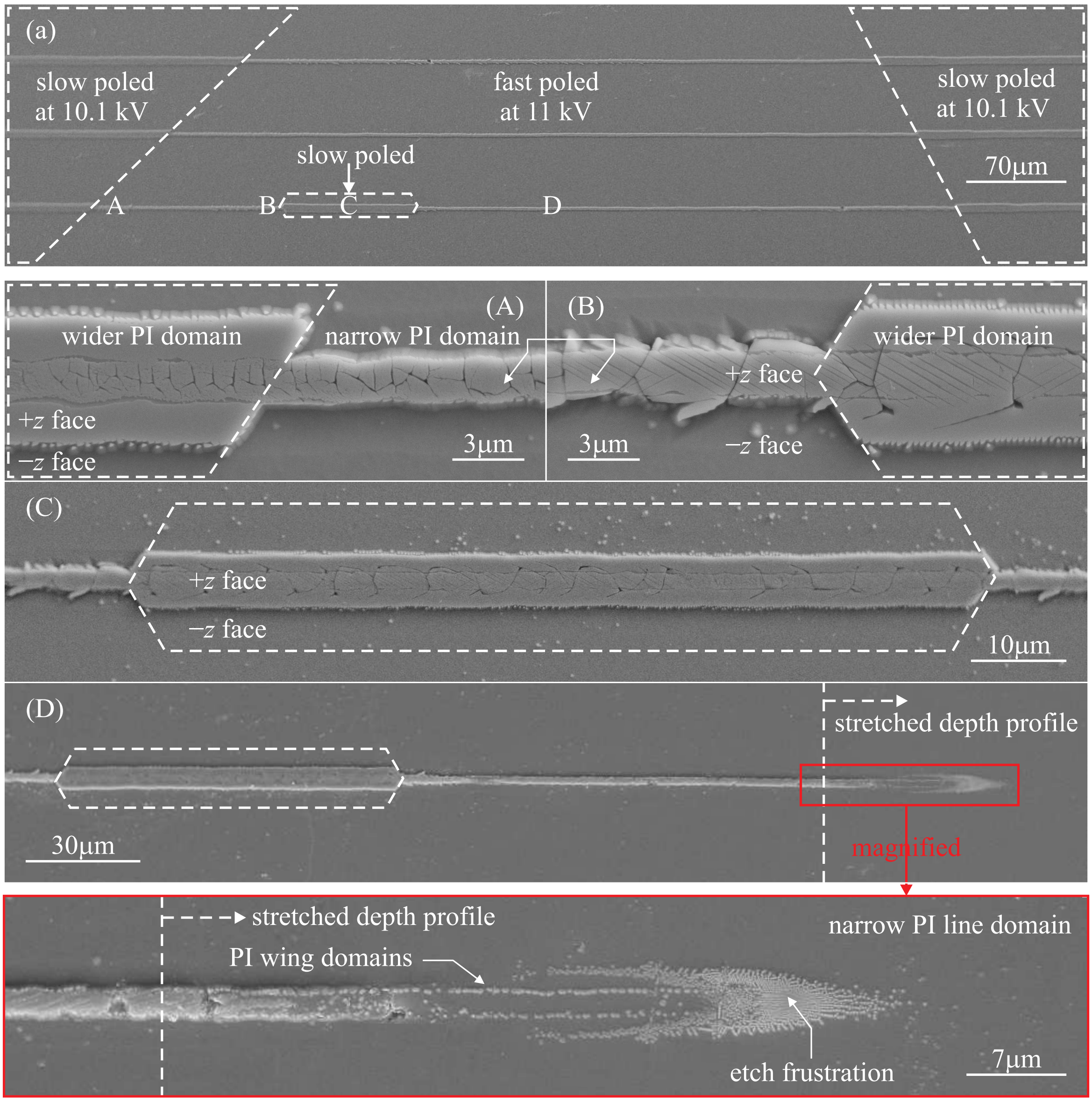

FIGURE 3.9: (a): the sample with PI domains poled at 10.1 kV and 11 kV in Fig. 3.8 was briefly HF etched to reveal the resultant domain structure. Enclosed in the white dashed lines are the regions poled at 10.1 kV that can correlate to the domain state in Fig. 3.8(15:07). A, B, C in (a) are the regions where poling voltage switched to the higher value. These areas are magnified in (A), (B), (C). To investigate the narrow PI domain profile in depth, PI line domain at position D in (a) was wedge-polished and briefly HF-etched as shown in (D) with magnified detail. The white dashed lines correspond to the change of slope due to wedge polishing.

while the rest was poled at 11 kV. Positions A, B, C in Fig. 3.9(a), where the poling voltage was switched to 11 kV, are magnified in Fig. 3.9(A-C). These images indicate that the width of the PI domains varies from 6 µm in the case of slow poling to 2 µm in the case of fast poling. The existence of PI domains with different widths resulting from high and low poling voltages suggests the existence of two regimes of poling-inhibition. Wedge polishing of the narrower PI domains followed by HF etching at D position in Fig. 3.9(a) revealed its depth profile in Fig. 3.9(D) and in the magnified detail. The depth profile shows that the narrower PI domain has a depth of about 300 nm. Furthermore, apart from this superficial PI domain, a buried etch-frustrated region (dense nanodomains) was also found at a depth of 4.4 µm as shown in Fig. 3.9(D). The position of this buried dense nanodomain region is similar to the end of the wider PI domains. A comparison between fast and slow poling applied in samples which had been inscribed with the same latent images is shown in Fig. 3.10. The SEM images shown in Fig. 3.10 correspond to the wedge polished and etched samples which are slow poled (a1.0, a0.5 and a0.1) and fast poled (b1.0, b0.5 and b0.1). The numbers '1.0', '0.5', and '0.1' after the letter correspond to the writing speed in $\mathrm{mm\,s^{-1}}$. Comparing the set with the same writing speed (a1.0−b1.0, a0.5−b0.5, a0.1−b0.1), it reveals that the buried etch-frustrated nanodomains as a result of the fast poling are located at a similar depth to the PI domains resulting from the slow poling, and follow the same trend that slower writing speed results in deeper buried domains. The magnified region of the buried nanodomains in Fig. 3.10(c) show that their density varied with depth but there is always a region where the density is high enough to make them useful in waveguide applications, which is later revealed to be composed of dense nano lines along the z-axis in Fig. 3.11.

Furthermore, Fig. 3.11(a1-3) shows that, for some writing conditions, only the etch-frustrated regions were formed but not the superficial PI domains after the fast poling process. Thus, it suggests that the etch-frustrated region seems to have an even higher energy barrier than that of the superficial surface PI domains. The detail of the etch-frustrated region in Fig. 3.11(a1-3) was magnified in Fig. 3.11(b1-3) which show that the very dense domain is actually made of dense regular nano line domains along the z-axis (any features in the wedge polished regions revealed the profile in depth). Fig. 3.12 shows the dependence on the writing speed of the nano line average separation measured at the densest part (along the red line in Fig. 3.11), which reveals that slow writing speed leads to denser nano lines.

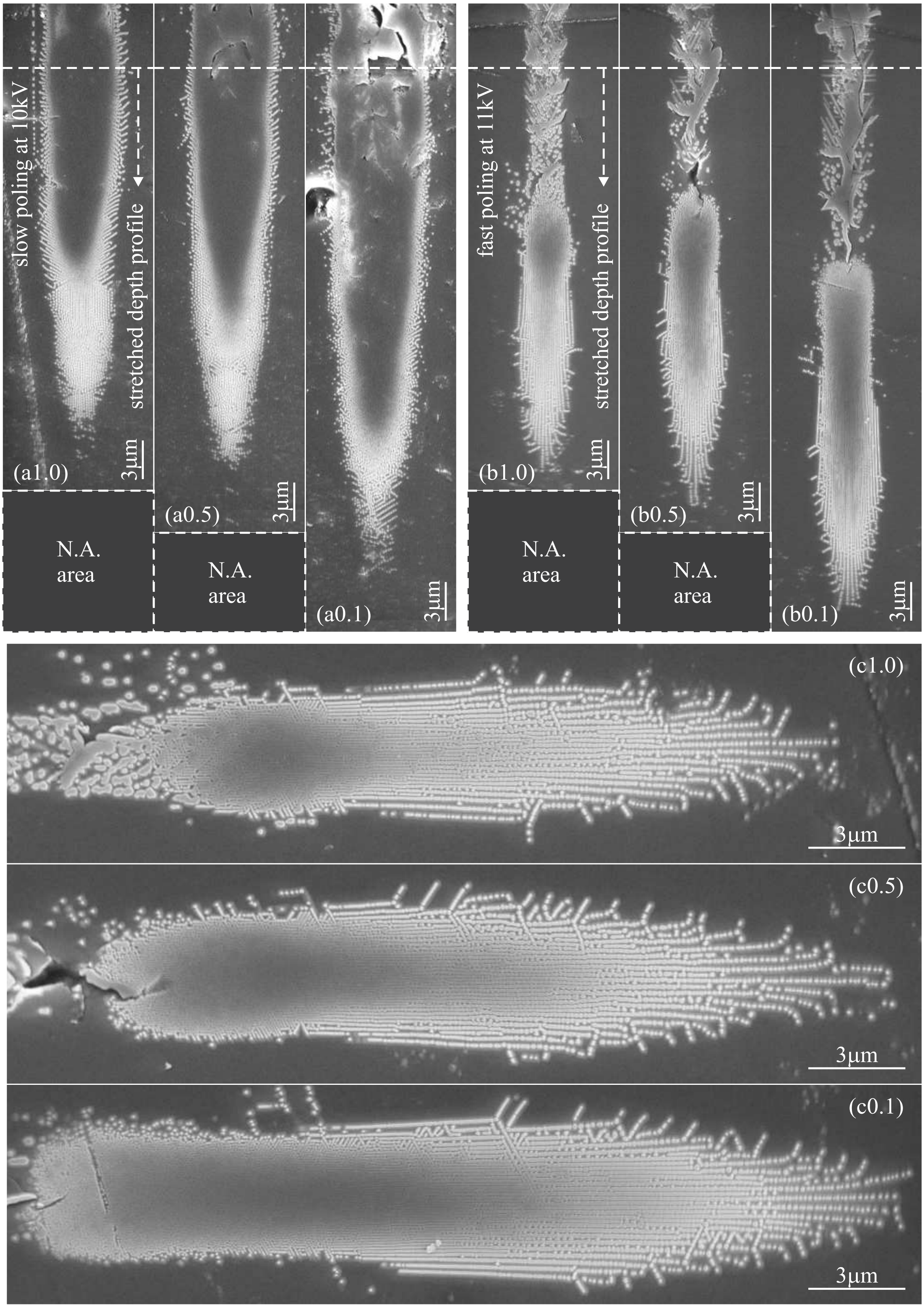

FIGURE 3.10: PI domains for the same writing conditions but poled at a low poling voltage of 10 kV in (a1.0-0.1) and high poling voltage of 11 kV in (b1.0-0.1). Wedged-polishing (with dashed line indicating the slope change) and briefly HF etching revealed the PI domain depth profile. The number after ‘a’ and ‘b’ indicates the writing speed in mm s^{-1}. (c1.0-0.1) illustrate the magnified images of the buried PI domains in (b1.0-0.1), suggesting that the etch-frustrated region as shown in Fig. 3.9(D) can be very dense.

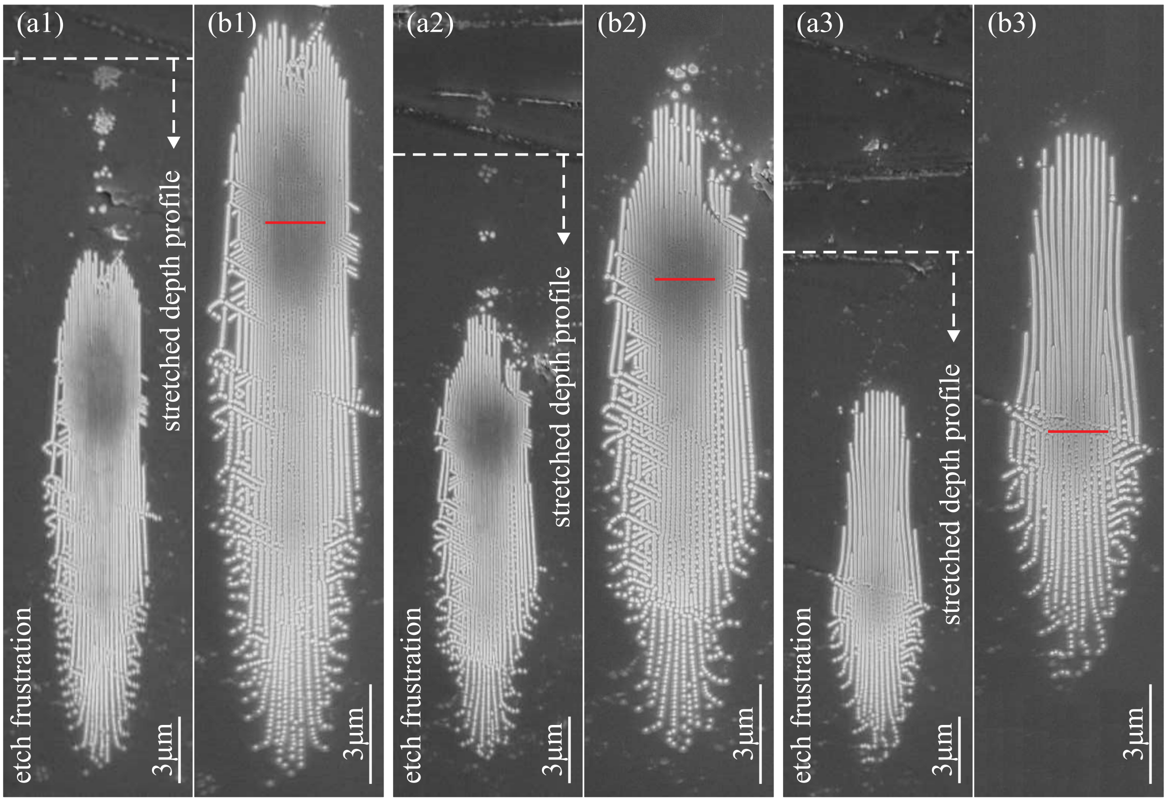

FIGURE 3.11: (a1-3): fast-poled PI domains, written with 300 nm, 35 mW and various writing speeds of 0.1, 0.2, 0.5 mm s^{-1} respectively with 3 µm beam radius, were wedge-polished (below the dashed line) and briefly HF etched. Only the buried etch-frustrated part of PI domains was formed with no superficial PI domain as shown in Fig. 3.10(b). (b1-3) shows the magnified etch-frustrated region of (a1-3) revealing the dense nano lines along the z-axis which actually compose the 'solid' buried PI domain. The red line indicates where the average separations of the nano lines are measured.

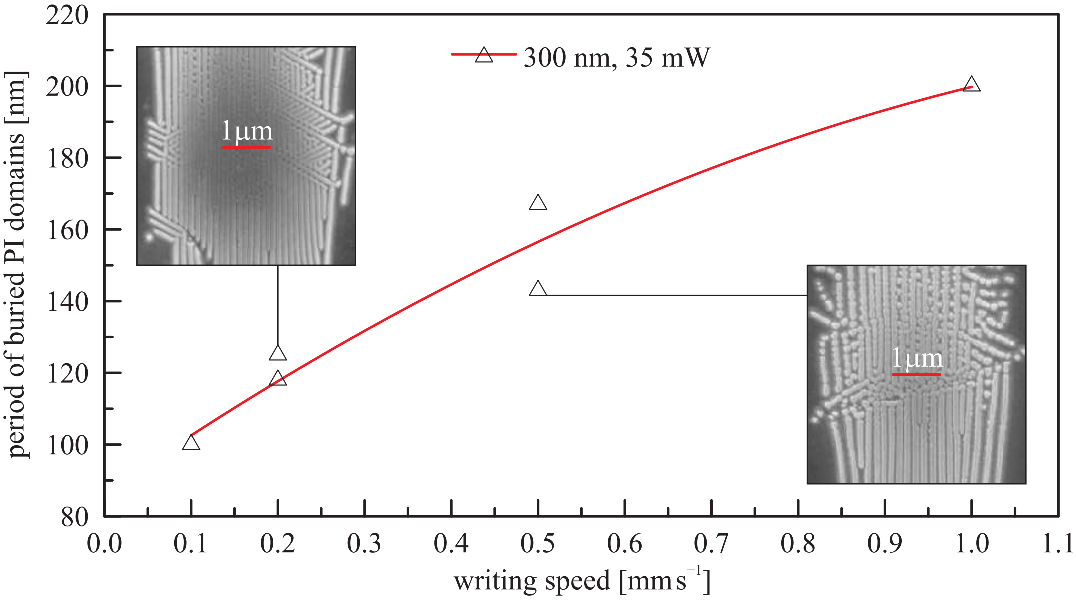

FIGURE 3.12: Dependence of the nano line average separation on the writing speed of the buried PI domains measured at the densest part (red line) in Fig. 3.11. Insets illustrate the SEM images from which the data points were obtained.

3.4 Proposed mechanism

Explanation for poling-inhibition involves the understanding of electron and hole excitations, and ion (lithium ions and protons) activation, along with their transport in the crystal during UV heating and subsequent cooling. Here the following mechanism is proposed. The UV radiation is strongly absorbed within a small volume close to the surface of the crystal causing the temperature to increase. The temperature on the illuminated surface can be as high as the melting point $\sim 1250°\mathrm{C}$, reducing rapidly with depth, thus producing a large temperature gradient. Under this temperature distribution, Li ions migrate by diffusion but also under the influence of the pyroelectric field which is formed in the heated volume. Li diffusion produces a primary Li deficient region with a depth of a few hundreds of nanometers. However, the strength of the pyroelectric field which varies with the depth (due to the presence of the temperature gradient) further redistributes the migrated Li ions to produce a secondary minimum of Li concentration, this time below the surface of the crystal. Due to the higher coercive field corresponding to the lower Li ion concentration, the Li deficient region inhibits the domain wall propagation during poling. The combined effect of the two Li deficient regions is responsible for the diversion of the propagating domain wall during the slow poling. However, the complex Li ion redistribution is resolved during fast poling, producing the buried PI domains which were presented in Sec. 3.3.

3.4.1 Temperature distribution

The temperature distribution which is formed as a consequence of the UV irradiation of the crystal will be considered first. The model which was presented in [Muir 06] shows that the temperature distribution is of a much larger scale as compared to the absorption length of the laser radiation in the material. That model suggested that for sufficiently low writing speed $\ll 0.2\,\mathrm{m\,s^{-1}}$, the temperature distribution is independent of the writing speed. Fig. 3.13 presents the simulated temperature distribution along x (lateral) and z (depth) axes from illuminated point $(0, 0)$ for various absorption coefficients from 10^5 $\mathrm{m^{-1}}$ to 10^9 $\mathrm{m^{-1}}$ at a writing power of 31.7 mW, and laser beam radius of 3 µm. The graphs reveal that for absorption coefficients from 1.8×10^7 $\mathrm{m^{-1}}$ to 10^9 $\mathrm{m^{-1}}$, the temperature profile along x and z is almost the same. The choice for the power of 31.7 mW is due to the fact that for this power the peak temperature is exactly at the melting point of LN (1520 K) for the absorption coefficient at 244 nm of 3×10^8 $\mathrm{m^{-1}}$. Above this melting point, the crystal becomes liquid and the model is no longer valid.

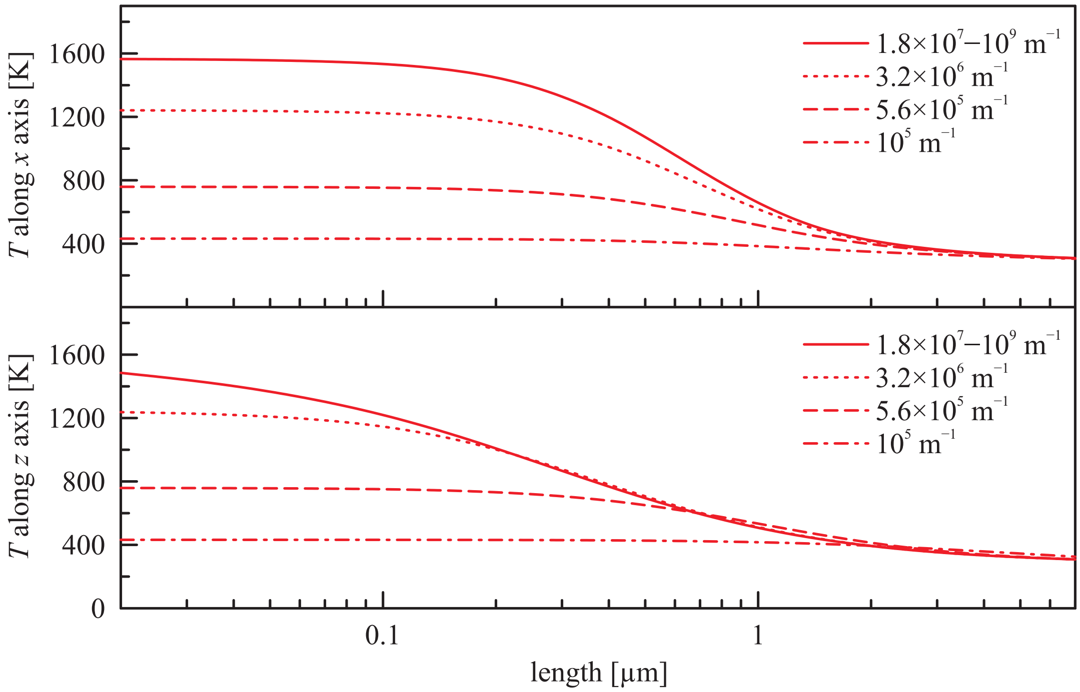

FIGURE 3.13: Simulated temperature distribution along x and z-axes induced by a static spot of UV illumination at $(0, 0)$ position with a writing power of 31.7 mW, writing beam radius of 3 µm and various absorption coefficients.

3.4.2 Migrating charges

The next step is to consider all the charges and ions that can be excited and activated during UV writing, and how they can attribute to the PI effect. It is proposed in this section that the coercive field increase due to the Li deficiency is the main mechanism responsible for PI, while photoexcited electrons provide the charge compensation for the Li migration.

Electrons and holes

Electrons and holes can be excited both optically and thermally during UV writing. Optically, UV light with photon energy ranging from 4.066 eV (305 nm) to 5.082 eV (244 nm) can excite electron-hole pairs directly across the band-gap of 3.78 eV [Dhar 90] and can also excite electrons from the defect levels (Fe^{2+}). The volume where the UV absorption occurs can thus act as a source of photo-excited charges. Thermally, electrons can be excited from the trapped levels (Fe^{2+}) [Carrascosa 93]. Additionally with decreased Li^+ concentration due to Li^+ diffusion, the electron density can also increase locally in the Li deficient volume via the reduction process [Huang 94] – lithium niobate is basically an n-type conductor at high temperature [Smyth 83, Jorgensen 69]. The excited electrons and holes can migrate by diffusion, or drift.

Lithium ions and protons

Due to the high temperature and the steep temperature gradient that is formed during UV writing, H^+ and Li^+ ions with activation energy of 1.23 eV [Klauer 92] and 1.55 eV [Mehta 91, Birnie 93] respectively can become mobile within the heated volume and move under the influence of the temperature gradient. Any migration of positive charges can be readily compensated by photo- or thermally-excited electrons.

In undoped CLN crystals grown by the Czochralski method, hydrogen is often present, with a concentration of about 5.65×10^{18} cm^{-3} [Klauer 92]. Recent H^1 nuclear magnetic resonance (NMR) measurement determined that protons can substitute Li^+ ions and locate on the longest O−O bond (336 pm) within the oxygen triangle nearest to the substituted Li site [Kong 00]. Within the temperature range of $80-600°$C, proton migration has been confirmed and diffusion of protons was suggested to be accomplished by jumping to the nearest O^{2-} ion from its previous bound position close to an oxygen [Klauer 92]. The activation energy and the pre-exponential diffusion constant of protons in undoped CLN have been derived from the measurement of the electrical dark conductivity in [Klauer 92]. The side-diffusion of protons under the high temperature and large temperature gradient produce a local proton deficient volume at the surface with an accumulated proton-rich region in depth. It has been reported that proton exchange (PE) can increase the poling voltage for undoped CLN, the proposed mechanism being that the exchanged PE:LN layer is less conductive than the virgin crystal and hence acts as an isolating film in the surface layer when the crystal is exposed to EFP. Thus, polarisation reversal is selectively inhibited by means of PE, at least for a field below 22.6 kV mm^{-1} [Grilli 06]. Similar to the case of proton exchange, with accumulated diffused protons in depth, the required local poling voltage might increase as well which can also contribute to the poling-inhibition. However, considering the 4 orders of magnitude lower concentration of protons in undoped CLN compared to that of proton exchange in [Grilli 06] in which most Li^+ ions were exchanged and even the ferroelectric property was lost, the contribution of the diffused protons in undoped CLN to the poling-inhibition can be safely ignored.

It was suggested that Li ions diffuse via hopping through Li vacancies [Birnie 93]. In undoped CLN crystals, about 4% of the Li sites are empty [Iyi 92]. Due to the steep temperature gradient, it is expected that most Li^+ ions, at the illuminated regions, diffuse sidewards and inwards within the bulk as suggested in [Muir 06] instead of out of the crystal as Li_2O. The Li_2O out-diffusion commonly observed after Ti-indiffusion for waveguide fabrication [Ranganath 77], has a much higher activation energy of around $\varepsilon_{act} \sim 3$ eV [Carruthers 74, Wood 81] compared to that of side-diffusion ~ 1.55 eV [Mehta 91, Birnie 93]. Thus, Li outdiffusion might occur only at the very top layer within nanometers of the surface at the highest temperature. Hence, Li side-diffusion leads to a Li deficient volume at the surface as is schematically illustrated in Fig. 3.14(a). Fig. 3.14(b) shows the lithium concentration profile at $x = 0$ along the z-axis, and the corresponding coercive field profile which is related to the concentration of Li ions [Bermúdez 00]. This suggests that the Li-deficient volume formed locally at the illuminated surface, having higher coercive field, can contribute directly to the poling-inhibition.

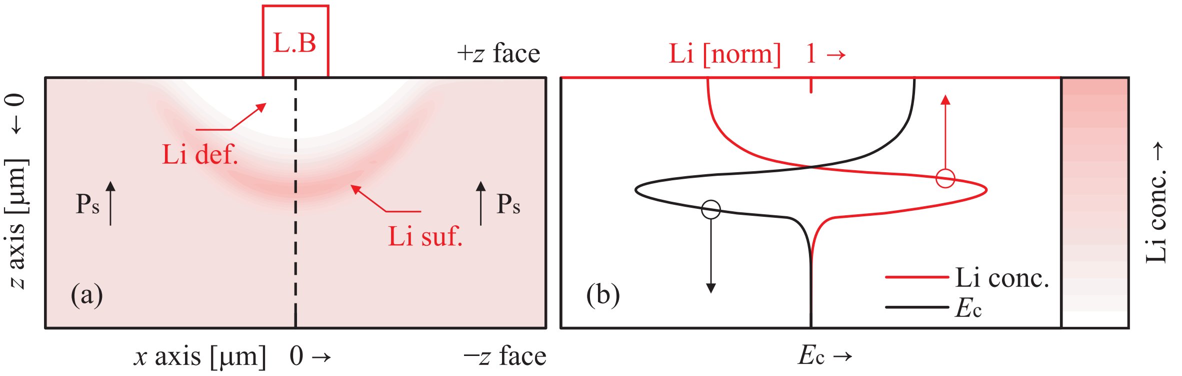

FIGURE 3.14: (a): Schematic of the Li ion concentration distribution under the temperature gradient induced by a static spot UV illumination of the $+z$ face at $(0, 0)$ position. The UV illumination results in a Li deficient volume close to the surface. The arrows indicate the polarisations of the sample and L.B. stands for laser beam. (b): the lithium concentration at $x = 0$ along z-axis is represented by the red curve and the corresponding coercive field E_c variation by the black curve.

3.4.3 Transport mechanism

Diffusion

Based on the proposed mechanism of Li ion migration, a diffusion model has been developed, assuming the photo- and thermally-excited electron concentration is sufficient to provide charge compensation. The model simulates the positive ion diffusion under a peak temperature distribution, induced by a static spot illumination of a Gaussian beam onto the crystal surface, for a reasonable period of time depending on the writing speed. A static illumination model is applied here instead of a moving illumination source model which was actually conducted in the experiment. This is because for sufficient low writing speed $\ll 0.2\ \mathrm{m\,s^{-1}}$, the temperature distribution is writing speed independent [Muir 06], thus, a moving light source is equivalent to a static light source lasting for a specific period of time. The peak temperature distribution was derived with the method developed in [Muir 06], while the diffusion kinetics follow the diffusion equation of [Muir 06]

$$c_t = \nabla^2(Dc) \tag{3.1}$$

$$D = D_0 \exp(-\varepsilon_{\mathrm{act}}/k_{\mathrm{B}}T)$$

where c is the positive ion concentration; t is the time; D is the diffusion coefficient; D_0 is the pre-exponential diffusion constant; $\varepsilon_{\mathrm{act}}$ is the activation energy; k_{B} is the Boltzmann constant; and T is the temperature.

Consider two-dimension x-z Cartesian coordinates, with origin at the static UV illuminated position and the z is the length in crystal depth. Thus,

$$\nabla^2 = \partial_x^2 + \partial_z^2$$

Let $u(x, z, t) = D(x, z)c(x, z, t)$, therefore, $c_t = (\partial_x^2 + \partial_z^2)u$. Since $D(x, z)$ is not time dependent, times (×) a $D(x, z)$ on the both sides derives

$$u_t = D(\partial_x^2 + \partial_z^2)u \tag{3.2}$$

Then, the Crank-Nicolson method together with the Alternating Direction Implicit (ADI) method was used to numerically solve the differential equation. The diffusion of Li ions are simulated and the parameters for modelling are: pre-exponential diffusion constant $D_0 = 5.1 \times 10^{-1}$ cm^2 s^{-1} [Mehta 91, Birnie 93], and activation energy $\varepsilon_{\text{act}} = 1.55$ eV [Mehta 91, Birnie 93]. Fig. 3.15 il-

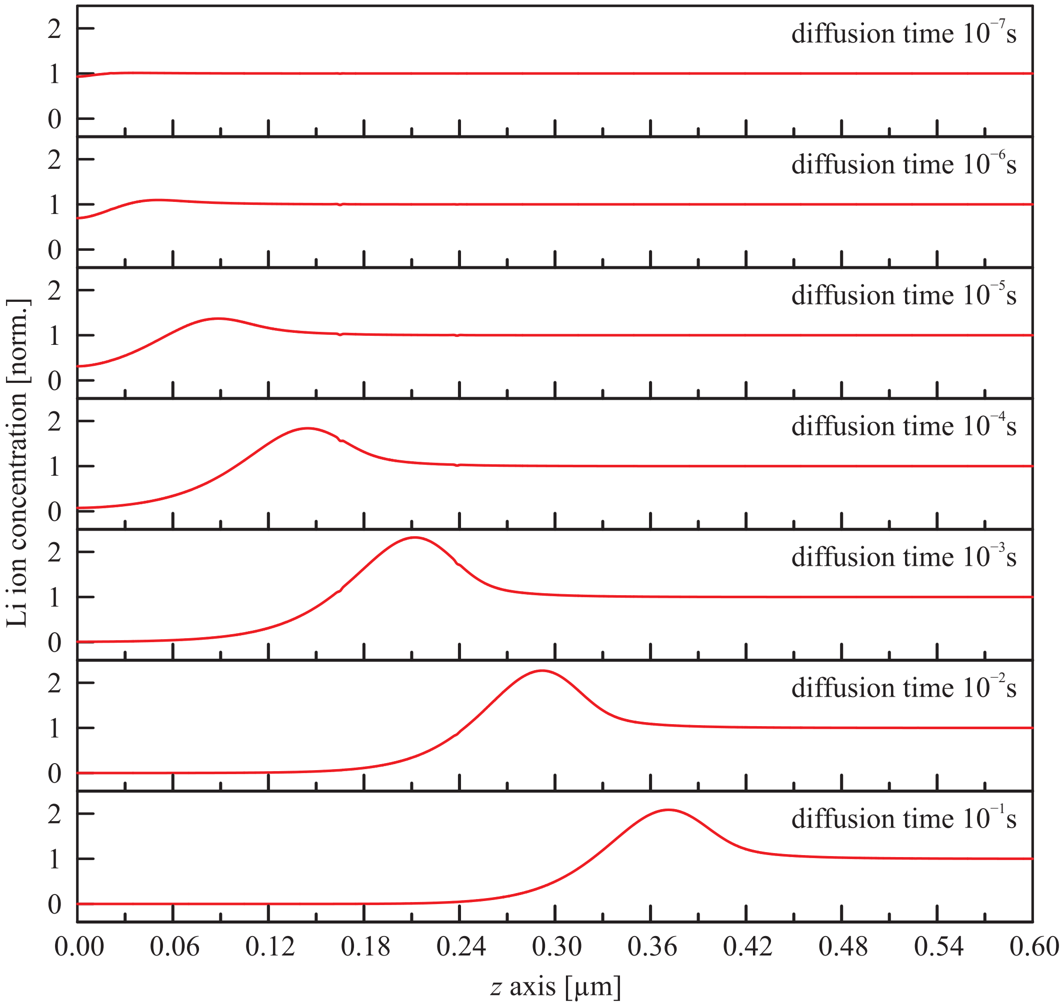

FIGURE 3.15: The simulated time-dependent diffusion process of Li^+ ions at $x = 0$ along the z-axis under the temperature distribution simulated with writing power of 31.7 mW and 3 µm Gaussian beam radius.

lustrates the simulation result of a time series for Li^+ ion diffusion profiles in depth at different diffusion times, driven by the temperature distribution obtained from simulation with UV writing power of 31.7 mW and beam radius of 3 µm [Muir 06]. It shows that even after 0.1 s of diffusion time, which is much longer than the actual diffusion time of milliseconds during UV writing, Li^+ ions diffuse into the depth only about a few hundred nanometers only. Thus, comparing such shallow diffusion of Li ions with the PI domain depth of microns, it suggests that Li diffusion alone cannot be the only mechanism for PI. Another mechanism for Li transport further into the depth should be responsible, and it is suggested here that it can be the photovoltaic effect or the pyroelectric effect. The photovoltaic effect is negligible at high temperatures close to the Curie temperature. Therefore, the other possible driving force for Li transport further into the depth, which can produce the second Li deficient region, is proposed to be the pyroelectric field.

Pyroelectric fields and pyroelectric drift

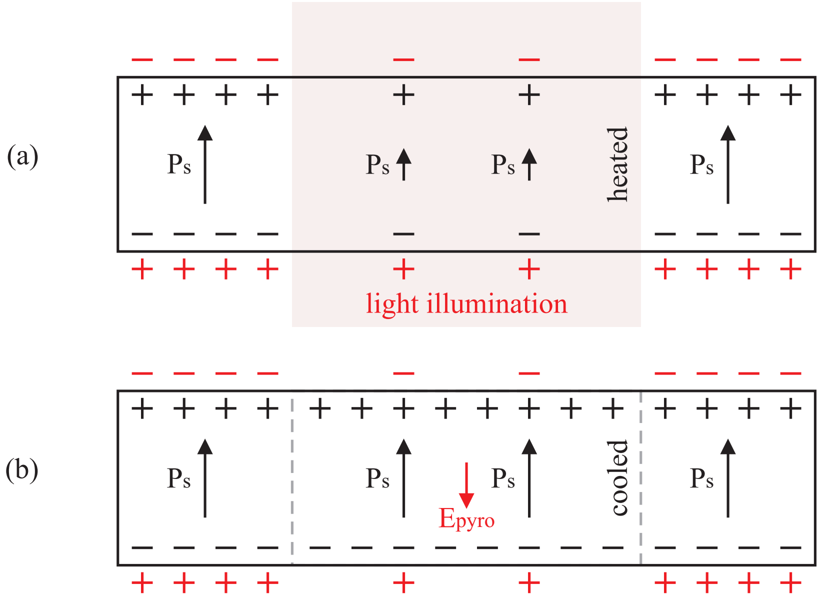

FIGURE 3.16: (a): absence of pyroelectric field during UV illumination in the heated volume due to the photoconductivity. (b): due to the absence of light and recovery of polarisation, the pyroelectric field increases in the cooled volume. The pyroelectric field is along the $-z$ direction. The black and red '+, −' correspond to surface charges of the electric dipole and the compensating charges respectively.

In the absence of charge compensation, the pyroelectric field would be of the order of $P_s/\epsilon_0\epsilon_r$, where ϵ_r is the relative dielectric constant. For the spontaneous polarisation of LN crystals, $P_s \approx 7 \times 10^{-5}\ \mathrm{C\,cm^{-2}}$, and $\epsilon_r \approx 30$, this net pyroelectric field would be above $10^7\ \mathrm{V\,cm^{-1}}$ leading to electrical breakdown. During UV light illumination, the charge compensation by electrons however strongly diminishes the pyroelectric field. Importantly, the charge compensation parameter is t_0/t_M, where $t_M = \epsilon_0\epsilon_r/\sigma_{ph}$ is the Maxwell relaxation time; $t_0 =$ *beam radius/writing speed* is the characteristic time of the temperature changes; and σ_{ph} is the photo-conductivity. σ_{ph} can be estimated as $\sigma_{ph} = eg\mu_e\tau_e$, where $g = \alpha I_0/\hbar\omega$ is the rate of electron excitation to be measured in $cm^{-3}\,s^{-1}$; μ_e is the mobility of electrons; and τ_e is the recombination lifetime of electrons. Correspondingly, the characteristic pyroelectric field can be estimated as

$$E_{\mathrm{pyro}} = 2P_s t_M / \epsilon_0 \epsilon_r t_0 \tag{3.3}$$

It is expected that due to the electrons compensating of polarisation charges during UV light illumination, the effective pyroelectric field is much smaller than the net pyroelectric field because $t_M \ll t_0$. Thus, Li ion transport under the pyroelectric field during UV writing can be ignored. However, upon blocking the UV illumination, the local heated crystal volume cools down and regains the former spontaneous polarisation, while with conductivity switching from photoconductivity to the much lower dark conductivity, the pyroelectric field due to the recovery of polarisation is not compensated and can then become considerable. The pyroelectric field during and after UV illumination is illustrated in Fig. 3.16(a) and (b) respectively. The pyroelectric field E_{pyro} after UV illumination is along the $-z$ axis as indicated in Fig. 3.16(b), thus, can cause the Li ions to drift further into the depth.

It should be noted that both diffusion and the pyroelectric effect are cylindrically symmetric along the z-axis and the incident beam. This symmetry is reflected upon the shape of the resultant PI domains. Fig. 3.17 shows an (a) SEM and a (b) PFM image of a dot PI domain that illustrates this symmetry feature. The PI domain was fabricated by static irradiation of the surface with a Gaussian beam. The regular circular feature (red dashed circle) in Fig. 3.17 correlates perfectly to the cylindrical-symmetric laser beam, and is most suitable for direct-writing lithography applications.

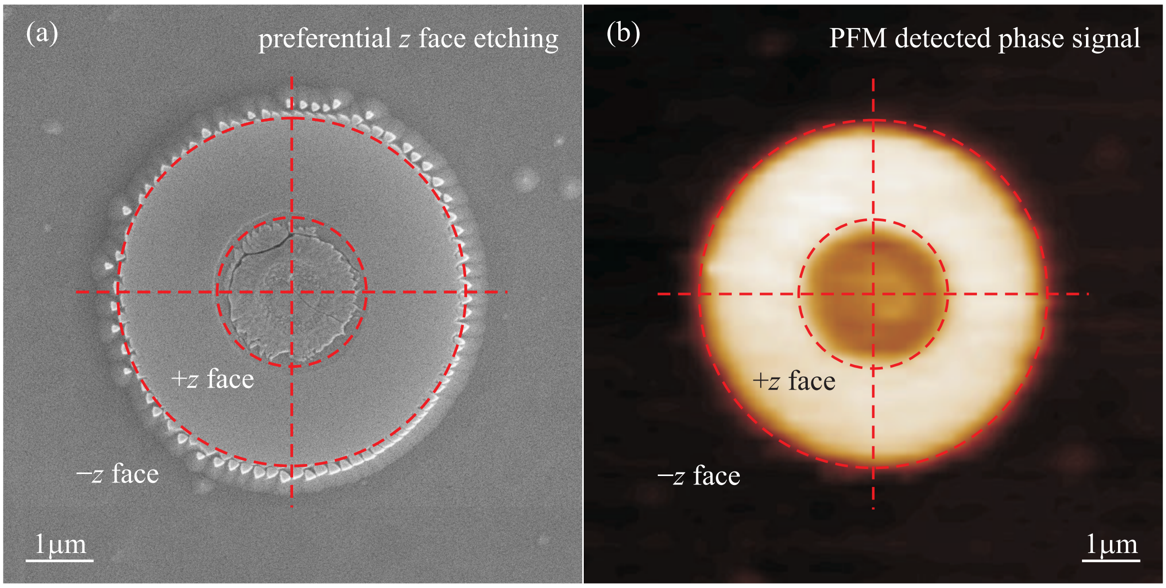

Figure 3.17: PI dot domains were fabricated by the PI process of a static illuminated region with a Gaussian beam. The PI domain features were revealed by (a) HF etching and (b) PFM. The red dashed circles well fit the circular outline and the central melted layer.

Exclusion of space charge field

Finally, it should be noted that a possible contribution of a space charge field to the poling-inhibition should be excluded. Poling-inhibition can be realised in 5 mol% MgO:CLN crystals with high dark electronic conductivity, thus any possible space charge distribution would decay in seconds [Ying 09], and not remain until the subsequent EFP. Additionally, the irrelevance of a space charge field to the poling-inhibition was also confirmed by annealing of the latent image before the EFP process. It is expected that annealing the crystal at 250°C for 1 hour can activate both protons and electrons in the crystal and compensate any space charge field (both proton and deep trapped electrons are mobile at temperatures higher than 230°C [Carrascosa 93]). Thus, after fabricating the latent image by UV writing, one sample has been placed in a furnace for 1 hour at 250°C. After a slow EFP process, both preferential HF etching and PFM verified that PI domains still exist which confirms the irrelevance of a space charge field (and actually also protons) to the poling-inhibition [Steigerwald 10]. The most convincible clue might come from the PI domains developed from the post-light-illuminated latent image. A sample with a latent image was placed in DI water and uniformly illuminated with a CW 457.9 nm argon ion laser light at an intensity of 10 mW cm^{-2} for hours to eliminate any space charge field. Then with a standard poling-inhibition process, the PI domains structures were revealed by HF etching as shown in Fig. 3.18. It shows that latent images with or without a post-illumination led to the same PI domain size that safely excludes the relevance of any space charge field to the poling-inhibition.

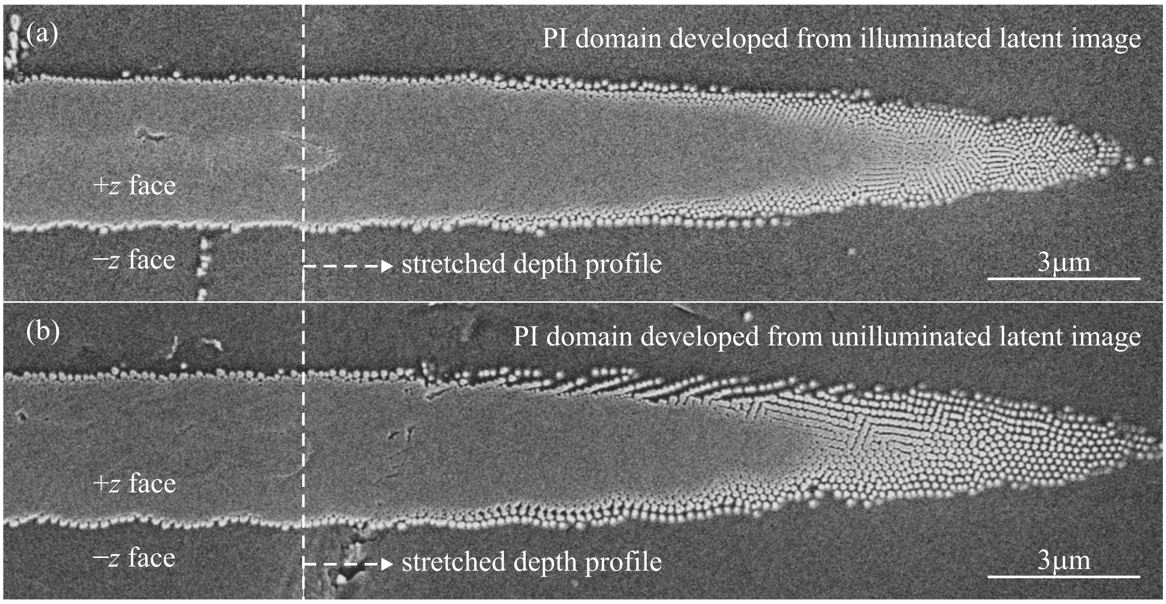

FIGURE 3.18: PI domains were developed from latent images (a) with and (b) without a post-illumination process before the subsequent EFP. The PI domains were wedge-polished and HF-etched to reveal the domain structure. The light illumination of latent image was via a CW 457.9 nm argon ion laser light at an intensity of 10 mW cm^{-2} for hours. It reveals that in both cases, the PI domain size is basically the same.

In summary, it was proposed that UV writing of the $+z$ face of LN crystal induces a local heating of the crystal and leads to a redistribution of Li^+ under both diffusion and pyroelectric field. Two Li deficient regions on the surface and in depth respectively are then formed with higher coercive field so that if the domain wall kinetic energy is not high enough, they can inhibit the local poling process and therefore resulting in PI domains.

3.5 Discussion

3.5.1 Similarity of results for $244 - 305$ nm

Based on the proposed mechanism, several experimental observations of PI domain size can be explained by the simulation of Li diffusion and the estimation of Li drift under the influence of the pyroelectric field for the high temperature distribution calculated in [Muir 06].

The Li deficiency, as the proposed mechanism for PI, is induced by diffusion and the pyroelectric field, both of which are initialised by the temperature distribution. Therefore, the similarity of PI domain sizes resulting from the use of short and long UV wavelengths suggests a similar temperature distribution for the entire range of applied wavelength as a premise for the further discussion of the mechanism, i.e., the absorption coefficients are all larger than 3.2×10^6 m^{-1} as shown in Fig. 3.13. It seems at first glance to contradict the literature as listed in Table 1.2 which shows that the absorption depth at the longest wavelengths can be of order a few microns. However, the effective absorption depth of UV light is also a function of temperature. As indicated in [Redfield 74], the higher the temperature, the higher the absorption at a specific wavelength; for example, at a wavelength of 305 nm with photon energy of 4.065 eV, the absorption coefficient of CLN at 469 K is almost 1 order of magnitude higher than that at 300 K. Thus, the effective absorption coefficients in the heated LN crystal during UV writing might be much larger than the values quoted in the literature and the UV absorption coefficients throughout the range of UV wavelengths used is expected to be $> 3.2 \times 10^6$ m^{-1}. This is also supported by the fact that for the entire wavelength range from 244 nm to 305 nm, the writing intensity required for poling-inhibition is the same within 10% which means that the same power level was used to heat a similar volume to a point at which PI can occur.

The next task is to estimate the depth of the PI domains which are created as a result of the temperature distributions. It can be reasonably expected that the resultant diffused Li ion distribution is pretty much dependent on the region of relatively low temperature (~ 500°C). The very surface temperature difference indicated in Fig. 3.13 for absorption coefficients of 3.2×10^6 m^{-1} and $> 1.8 \times 10^7$ m^{-1}, where the temperature is yet high (> 700°C along z), is not expected to shift the diffused Li ion distribution too much. Fig. 3.19 shows the simulated result of diffused Li ions under the absorption-dependent temperature distribution with writing

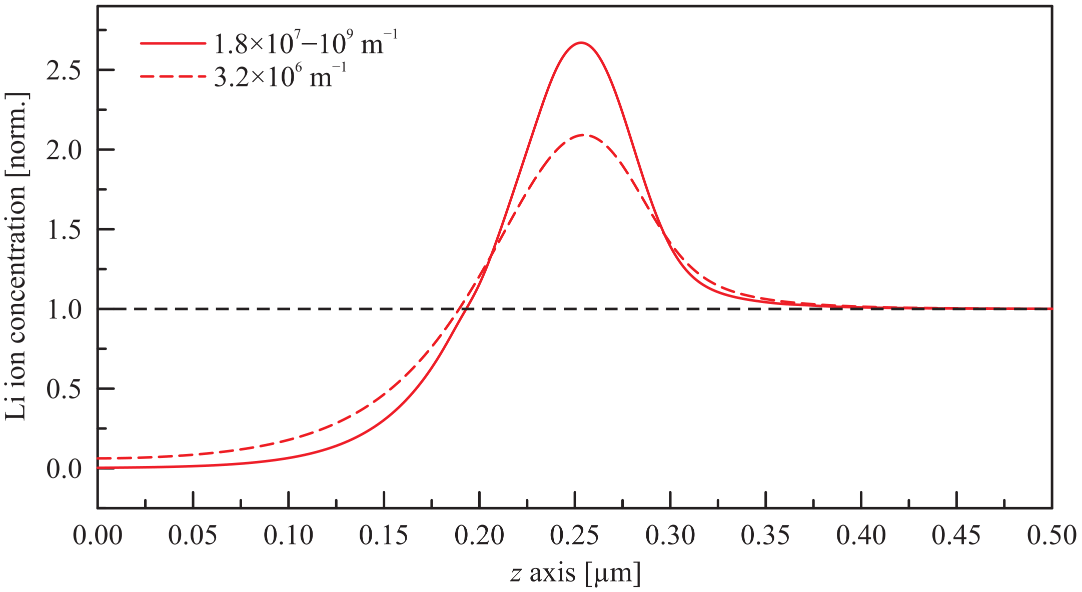

FIGURE 3.19: Simulated lithium ion concentration (normalised) along z-axis with writing condition of 31.7 mW writing power, 0.1 mm s^{-1} writing speed and 3 µm Gaussian beam radius for absorption coefficients of 3.2×10^6 m^{-1} and $> 1.8 \times 10^7$ m^{-1}.

speed of 0.1 mm s^{-1}. It exhibits that although absorption coefficients of 3.2×10^6 m^{-1} and $> 1.8 \times 10^7$ m^{-1} result in different temperature values at the high temperature region as shown in Fig. 3.13, it does not affect too much the final Li ion distribution along the z-axis. More importantly, the corresponding Li deficient regions (Li < 1), which have a higher coercive field, are almost the same. Finally, notice that the diffusion results are derived under the assumption that the photo- or thermally-excited electrons are sufficient to provide the charge compensation or in other words, the electron conductivity is larger than the ionic conductivity σ_{Li} anywhere in the diffused region.

As the diffusion depth of Li ions is less than 300 nm, it is necessary to consider any other mechanism that can push the lithium distribution further below the surface. The pyroelectric drift is being proposed here. As discussed in Sec. 3.4.3, during cooling, the Li ions can be further driven into the depth by the pyroelectric field. Fig. 3.16 shows a simple illustration assuming an instantaneous blocking of the UV light just to illustrate the origin of the pyroelectric field and how it can drive Li ions into the depth. In reality, instead of a sudden block of light illumination, the crystal actually suffers a gradual decrease of light illumination during the removing of the laser beam and cooling. Therefore, the characteristic pyroelectric field is still photoconductivity dependent as

$$E_{\text{pyro}}(z) = \frac{2[P_{\text{s}} - P_{\text{s}}(z)]}{[\sigma_{\text{ph}}(z) + \sigma_{\text{d}}(z)]t_0} \tag{3.4}$$

where $\sigma_{\text{d}}(z)$ is the dark conductivity from thermally-excited electrons. Considering the position dependence of $P_{\text{s}}(z)$ and $\sigma_{\text{ph}}(z)$ along the depth, a local maximum of the pyroelectric field in depth is expected to form which can drive Li ions further into the depth and produce another

Li deficient region separate from that on the surface which is formed due to the diffusion. From the previous discussion, all the parameters in Eq. 3.4 of the pyroelectric field are independent of the wavelength apart from the photoconductivity $\sigma_{\mathrm{ph}}(z)$ which is determined by the absorption coefficient. Thus, in order for the deep Li ions to drift the same distance under the pyroelectric field for all the wavelengths used in the experiments, the wavelength dependence of $\sigma_{\mathrm{ph}}(z)$ should also be eliminated after approximately a PI depth of 2 µm. This is actually supported by the premise that the absorption coefficient for all wavelengths used in the experiments is high enough to result in a similar temperature distribution. Thus, in this case, beyond the depth of ~ 2 µm the conductivity in Eq. 3.4 is dominated by the dark conductivity and can lead to the same value of pyroelectric field for the entire wavelength range. The charge compensation of the Li is provided by the thermally (instead of photo-excited) electrons. Thus, it can result in the same pyroelectric drift of Li ions beyond a depth of 2 µm and produces a second Li deficient region in depth apart from that on the surface due to diffusion. The existence of a second Li deficient region is supported by the fast poling experimental results shown in Sec. 3.3 and discussed in Sec. 3.5.2.

In summary, the explanation for the uniformity of the PI domain sizes for all the range of UV wavelengths used is based on the assumption that the absorption coefficients for wavelength from 244 to 305 nm is high enough to 1) lead to a similar temperature distribution and 2) provide negligible photoconductivity in depth. The PI depth is determined by the deeper Li deficient region induced by the pyroelectric effect.

3.5.2 Fast-poled PI domain structure

The above detailed discussion of Li transport under diffusion and the pyroelectric field can also be used to explain the results of fast poling which were presented in Sec. 3.3. Due to a local maximum of $E_{\mathrm{pyro}}(z)$ in depth, another Li deficient volume can be formed below the surface of the crystal as discussed previously.

Hence there are two separate Li deficient volumes, one located very close to the surface due to direct diffusion of Li under the influence of the temperature gradients and the second due to drift of the redistributed Li under the influence of the pyroelectric field. This complex Li concentration profile can explain the PI domains which were observed in fast poling experiments and were shown in Fig. 3.10.

The two Li deficient regions due to the diffusion and pyroelectric field are schematically illustrated in Fig. 3.20 with the dashed half circle and a full circle respectively. In the case of slow poling, the surface and deeper Li deficient volume defines the PI domain width and depth respectively as indicated in Fig. 3.20(a). In the case of fast poling however, after the local propagation-inhibiting of the domain wall in Fig. 3.20(a), the domain wall, due to the higher

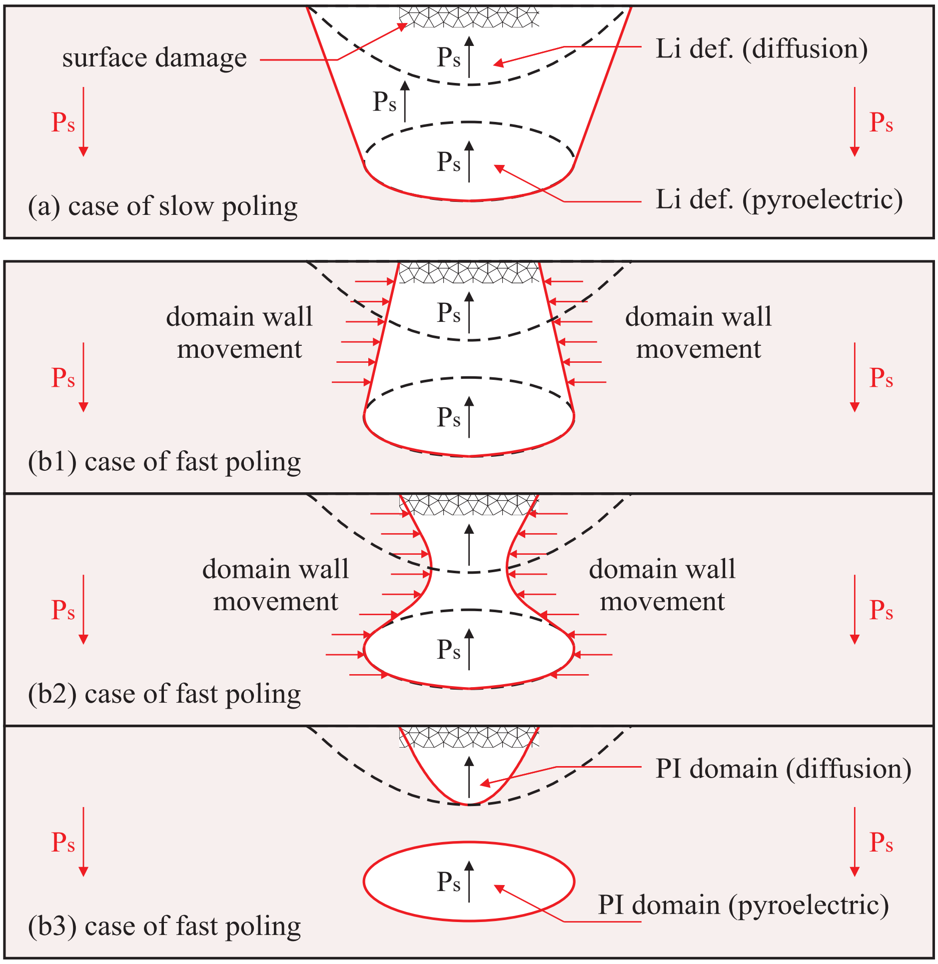

FIGURE 3.20: Illustration of possible domain wall propagation during slow and fast poling. (a): In the case of slow poling the surface and deeper Li deficient volume defines the PI domain width and depth respectively. In the case of fast poling (b1, b2, b3) the applied E-field encourages further expansion of the domain wall which can now resolve the two separate Li deficient volumes. The width of surface PI domain in this case is observed to be defined by the surface damaged region.

domain wall kinetic energy, bends inwards as shown in Fig. 3.20(b1) and (b2), merges again and approaches the diffusion-induced Li deficiency at the surface as shown in Fig. 3.20(b3), thus resolving the complex Li distribution profile. Fig. 3.20(b) also illustrates the experimental observation in Fig. 3.9(D) and 3.10(b) that the width of the surface PI domain is defined by the surface damaged region. Therefore, it suggests that the proposed mechanism based on the two regions of Li deficiency induced by diffusion (shallower) and pyroelectric field (deeper) can explain the domain structures observed in the case of fast poling: the narrower surface PI domain is due to the diffusion-induced Li deficiency, while the etch-frustrated region in depth (dense nanodomains) is due to the pyroelectric-induced Li deficiency, which also explains its similar depth to the slow-poled PI domains because of their same origin of the deep pyroelectric-induced Li deficiency.

3.6 Future work

One of the future tasks is to further investigate the proposed mechanism. The best proof of the mechanism that was presented in the previous section would be to directly measure the Li profile of a latent image. Direct detection of lithium using standard analytical techniques is very challenging due to the fact that Li is a light element. The Li concentration profile however might be measured using Raman spectroscopy by monitoring the width of the Li related Raman line [Chen 01, Zheng 04, Kostritskii 05]. Post-annealing of the latent image can provide some further clues. By annealing a latent image at various temperatures (100°C, 200°C, 300°C etc.) for different time periods, uniformisation of the Li distribution can occur. Via measuring the sizes of the resultant PI domains which is actually a direct reflection of the Li distribution after post-annealing, it can reveal 1) at what temperature, the Li re-distribution occurs and 2) how the re-distribution develops with the annealing time. Additionally, to support the proposed mechanism even further, the following experiments are proposed. A far infrared laser (CO_2) can be used instead of a UV laser to induce inhibition of poling because the temperature-induced Li ion transport is proposed as the main mechanism. The CO_2 laser, which emit at a wavelength of 10.6 µm, can also lead to local surface heating close to the melting point of the CLN crystal. Although the absorption coefficient at 10.6 µm at room temperature is rather small ($5 \times 10^3 - 1 \times 10^4$ m^{-1} [Li 00]) the temperature dependence of the absorption coefficient [Redfield 74] might provide substantial absorption to obtain temperatures similar to the ones obtained in the UV case. The depth of the PI domains makes them useful in waveguide applications, however further control of their depth might prove useful for other applications

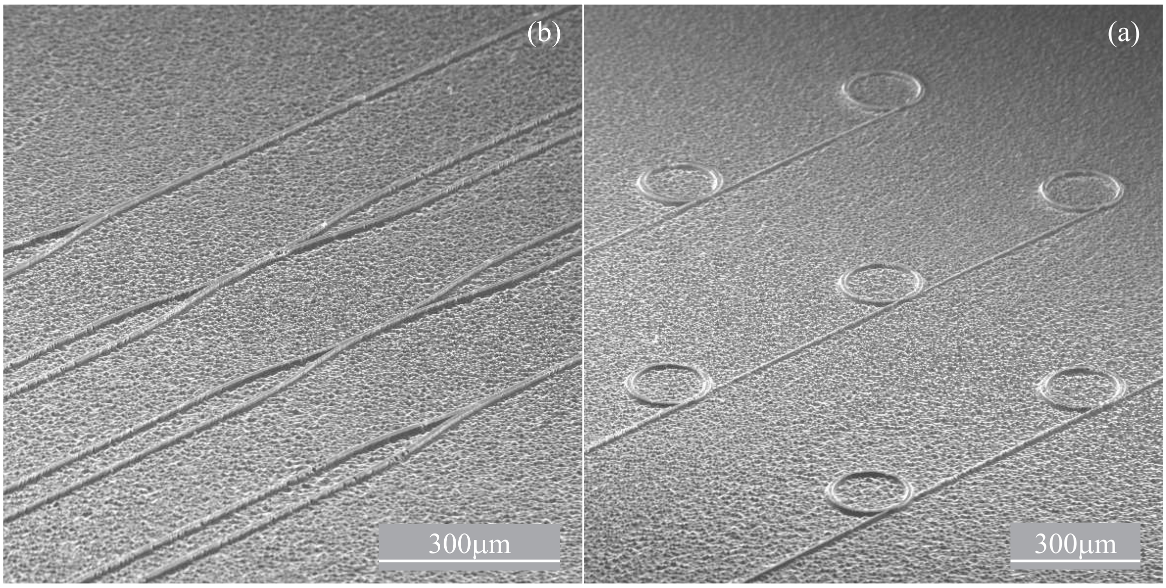

FIGURE 3.21: Micro-structures of (a) coupler and (b) ring developed from HF-etching of PI curve domains.

including buried waveguides and bulk devices. Therefore further work into finding methods for extending the depth of these domains should be done. Furthermore, the PI domain structures can be used as etch stops for the fabrication of surface relief structures such as ridges. These ridge structures can act as waveguides (due to the UV irradiation step [Mailis 03, Ganguly 09]) and can be shaped to form single channels, couplers, interferometers or even resonant structures such as ring or disc resonators. Some examples of such structures that have already been produced using PI methods are shown in Fig. 3.21.

3.7 Summary

In summary, UV-laser induced poling-inhibition provides a new approach for domain engineering in lithium niobate. The process is straightforward and simple, not involving any clean room environment. Any domain structures can be directly defined by direct UV laser writing followed by EFP. Longer wavelengths (275, 300, 302, 305 nm), different from the earlier work of 244 nm, has been applied to realise poling-inhibition under a range of different writing conditions of wavelength, writing intensity and writing speed in undoped and MgO doped CLN. The PI domain depth and width have been then measured by wedge-polishing followed by HF acid etching. The results indicate a similarity between the wavelengths of $275 - 305$ nm regarding PI domain depth, width and surface quality. Writing intensity turns out to be the most sensitive parameter while writing speed is effectively unimportant. Also, the relationship between domain depth and width are investigated under two different focusing conditions. Compared with 244 nm written PI domains, the depth given by longer wavelength are not deeper but similar. Fast poling of latent images reveals some buried PI domains. A possible mechanism of poling-inhibition, based on Li deficiency induced coercive field increase, has been proposed. The Li deficiency is due to both the diffusion and the pyroelectric field. Due to the short diffusion range of hundred of nanometers, the PI size or more specifically, the PI depth, is determined mainly by the pyroelectric drift. The proposed mechanism along with a heating model of the crystal suggested a high absorption coefficient for all the applied wavelengths which successfully explained some experimental results obtained.

References

[Bermúdez 00] V. Bermúdez, L. Huang, D. Hui, S. Field & E. Diéguez, *Role of stoichiometric point defect in electric-field-poling lithium niobate*, Appl. Phys. A, vol. 70, no. 5, pages 591–594, 2000.

[Birnie 93] D. P. Birnie, *Analysis of diffusion in lithium niobate*, J. Mater. Sci., vol. 28, no. 2, pages 302–315, 1993.

[Brown 99] P. T. Brown, G. W. Ross, R. W. Eason & A. R. Pogosyan, *Control of domain structures in lithium tantalate using interferometric optical patterning*, Opt. Commun., vol. 163, pages 310–316, 1999.

[Carrascosa 93] M. Carrascosa & L. Arizmendi, *High-temperature photorefractive effects in* $LiNbO_3$*:Fe*, J. Appl. Phys., vol. 73, no. 6, pages 2709–2713, 1993.

[Carruthers 74] J. R. Carruthers, I. P. Kaminow & L. W. Stulz, *Diffusion kinetics and optical waveguiding properties of outdiffused layers in lithium niobate and lithium tantalate*, Appl. Opt., vol. 13, no. 10, pages 2333–2342, 1974.

[Chen 01] Y. L. Chen, J. J. Xu, X. J. Chen, Y. F. Kong & G. Y. Zhang, *Domain reversion process in near-stoichiometric* $LiNbO_3$ *crystals*, Opt. Commun., vol. 188, no. 5-6, pages 359–364, 2001.

[Dhar 90] A. Dhar & A. Mansingh, *Optical properties of reduced lithium niobate single crystals*, J. Appl. Phys., vol. 68, no. 11, pages 5804–5809, 1990.

[Ganguly 09] P. Ganguly, C. L. Sones, Y. J. Ying, H. Steigerwald, K. Buse, E. Soergel, R. W. Eason & S. Mailis, *Determination of refractive indices from the mode profiles of UV-written channel waveguides in* $LiNbO_3$*-crystals for optimization of writing conditions*, J. Lightwave Technol., vol. 27, no. 16, pages 3490–3497, August 2009.

[Gopalan 98] V. Gopalan, T. E. Mitchell & K. E. Sicakfus, *Switching kinetics of 180° domains in congruent* $LiNbO_3$ *and* $LiTaO_3$ *crystals*, Solid State Commun., vol. 109, no. 2, pages 111–117, 1998.

[Gopalan 00] V. Gopalan, N. A. Sanford, J. A. Aust, K. Kitamura & Y. Furukawa, Handbook of advanced electronic and photonic materials and devices, vol. 4 ferroelectric and dielectrics, Chapter 2: crystal growth, characterization, and domain studies in lithium niobate and lithium tantalate ferroelectrics, pages 57–114, Academic, 2000.

[Grilli 06] S. Grilli, C. Canalias, F. Laurell, P. Ferraro & P. De Natale, *Control of lateral domain spreading in congruent lithium niobate by selective proton exchange*, Appl. Phys. Lett., vol. 89, no. 3, page 032902, 2006.

[Huang 94] L. Huang & N. A. F. Jaeger, *Discussion of domain inversion in $LiNbO_3$*, Appl. Phys. Lett., vol. 65, no. 14, pages 1763–1765, 1994.

[Iyi 92] N. Iyi, K. Kitamura, F. Izumi, J. K. Yamamoto, T. Hayashi, H. Asano & S. Kimura, *Comparative study of defect structures in lithium niobate with different compositions*, J. Solid State Chem., vol. 101, no. 2, pages 340–352, 1992.

[Jorgensen 69] P. J. Jorgensen & R. W. Bartlett, *High temperature transport processes in lithium niobate*, J. Phys. Chem. Solids, vol. 30, no. 12, pages 2639–2648, 1969.

[Klauer 92] S. Klauer, M. Wöhlecke & S. Kapphan, *Influence of H-D isotopic substitution on the protonic conductivity of $LiNbO_3$*, Phys. Rev. B, vol. 45, no. 6, page 2786, 1992.

[Kong 00] Y. Kong, J. Xu, W. Zhang & G. Zhang, *The site occupation of protons in lithiumniobate crystals*, J. Phys. Chem. Solids, vol. 61, no. 8, pages 1331–1335, 2000.

[Kostritskii 05] S. Kostritskii, K. Gallo, C. B. E. Gawith, P. G. R. Smith, S. Mailis & R. W. Eason. *Micro-Raman study of UV-written channel $LiNbO_3$ waveguides.* In ISDS, pages –, Ekaterinburg, Russia, 2005.

[Li 00] J. Li, L. Liu, Y. Liu & C. Zhou, *Temperature dependence of a local thermal fixed photorefractive hologram in $LiNbO_3$ by CO_2 laser heating*, Microw. Opt. Technol. Lett., vol. 26, no. 2, pages 89–93, 2000.

[Mailis 03] S. Mailis, C. Riziotis, I. T. Wellington, P. G. R. Smith, C. B. E. Gawith & R. W. Eason, *Direct ultraviolet writing of channel waveguides in congruent lithium niobate single crystals*, Opt. Lett., vol. 28, no. 16, pages 1433–1435, 2003.

[Mehta 91] A. Mehta, E. K. Chang & D. M. Smyth, *Ionic transport in $LiNbO_3$*, J. Mater. Res., vol. 6, no. 4, pages 851–854, 1991.

[Muir 06] A. C. Muir, G. J. Daniell, C. P. Please, I. T. Wellington, S. Mailis & R. W. Eason, *Modelling the formation of optical waveguides produced in $LiNbO_3$ by laser induced thermal diffusion of lithium ions*, Appl. Phys. A, vol. 83, no. 3, pages 389–396, 2006.

[Nakamura 02] K. Nakamura, J. Kurz, K. Parameswaran & M. M. Fejer, *Periodic poling of magnesium-oxide-doped lithium niobate*, J. Appl. Phys., vol. 91, no. 7, pages 4528–4534, 2002.

[Ranganath 77] T. R. Ranganath & S. Wang, *Suppression of Li_2O out-diffusion from Ti-diffused $LiNbO_3$ optical waveguides*, Appl. Phys. Lett., vol. 30, no. 8, pages 376–379, 1977.

[Redfield 74] D. Redfield & W. J. Burke, *Optical-absorption edge of $LiNbO_3$*, J. Appl. Phys., vol. 45, no. 10, pages 4566–4571, 1974.

[Ro 00] J. H. Ro & M. Cha, *Subsecond relaxation of internal field after polarization reversal in congruent $LiNbO_3$ and $LiTaO_3$ crystals*, Appl. Phys. Lett., vol. 77, no. 15, pages 2391–2393, 2000.

[Shur 05] V. Y. Shur, Nucleation theory and applications, Chapter 6, pages 178–214, Wiley VCH, Weinheim, 2005.

[Smyth 83] D. M. Smyth, *Defects and transport in $LiNbO_3$*, Ferroelectrics, vol. 50, no. 1-4, pages 419–428, 1983.

[Sones 02] C. L. Sones, S. Mailis, W. S. Brocklesby, R. W. Eason & J. R. Owen, *Differential etch rates in z-cut $LiNbO_3$ for variable HF/HNO_3 concentrations*, J. Mater. Chem., vol. 12, no. 2, pages 295–298, 2002.

[Sones 08] C. L. Sones, A. C. Muir, Y. J. Ying, S. Mailis, R. W. Eason, T. Jungk, Á. Hoffmann & E. Soergel, *Precision nanoscale domain engineering of lithium niobate via UV laser induced inhibition of poling*, Appl. Phys. Lett., vol. 92, no. 7, page 072905, 2008.

[Steigerwald 10] H. Steigerwald, M. Lilienblum, F. von Cube, Y. J. Ying, R. W. Eason, S. Mailis, B. Sturman, E. Soergel & K. Buse, Origin of UV-induced poling inhibition in lithium niobate crystals, volume -, Phys. Rev. B (submitted), 2010.

[Wood 81] Van E. Wood, N. F. Hartman, A. E. Austin & C. M. Verber, *Stoichiometry dependence of lithium outdiffusion in $LiNbO_3$*, J. Appl. Phys., vol. 52, no. 2, pages 1118–1120, 1981.

[Ying 09] Y. J. Ying, C. E. Valdivia, C. L. Sones, R. W. Eason & S. Mailis, *Latent light-assisted poling of $LiNbO_3$*, Opt. Express, vol. 17, no. 21, pages 18681–18692, 2009.

[Zheng 04] Y. Zheng, E. Shi, S. Wang, Z. Lu, S. Cui, L. Wang & W. Zhong, *Domain structures and etching morphologies of lithium niobate crystals with different Li contents grown by TSSG and double crucible Czochralski method*, Cryst. Res. Technol., vol. 39, no. 5, pages 387–395, 2004.

4

Characterisation of UV-written channel waveguides in $LiNbO_3$

4.1 Introduction

Lithium niobate ($LiNbO_3$) is a versatile optical material commonly used in photonics as an appropriate platform for implementation of integrated optical circuits [Sohler 08] because of its high electro-optic, acousto-optic and nonlinear-optic coefficients [Weis 85]. Metal ion indiffusion, proton exchange, and ion-implantation are the techniques most widely used to fabricate waveguides in (LN), which are a basic building block in optical integrated circuits (OICs). UV-writing of optical waveguides [Mailis 03, Gallo 07] is a recent addition to this list of fabrication processes for this substrate, and offers a direct writing facility that obviates many fabrication steps of the former techniques. Direct writing of single- and multi-mode graded-index channel waveguides in congruent $LiNbO_3$ has been demonstrated using CW laser light at a writing wavelength of 244 nm [Mailis 03]. Since its inception, the UV directly written waveguide procedure has held considerable promise because of its single-step process which is well suited for complex micro-optical devices such as micro-opto-electromechanical systems (MOEMS), where photolithography for waveguide fabrication becomes challenging [Sones 02a]. It was proposed that the formation of UV-written waveguides is due to the high optical absorption of LN at ultraviolet wavelengths and hence the high temperatures induced near the surface [Muir 06]; side-diffusion of lithium then takes place which in turn induces an increase of the extra-ordinary index of refraction [Schlarb 93], and this process has been modeled in [Muir 06]. Thus, after the first demonstration of direct UV-written waveguides in LN, a full characterisation is required for future application in photonics.

An outline of the processes that will be discussed in this chapter is presented schematically in Fig. 4.1. Direct writing of graded-index channel waveguides in undoped congruent LN using

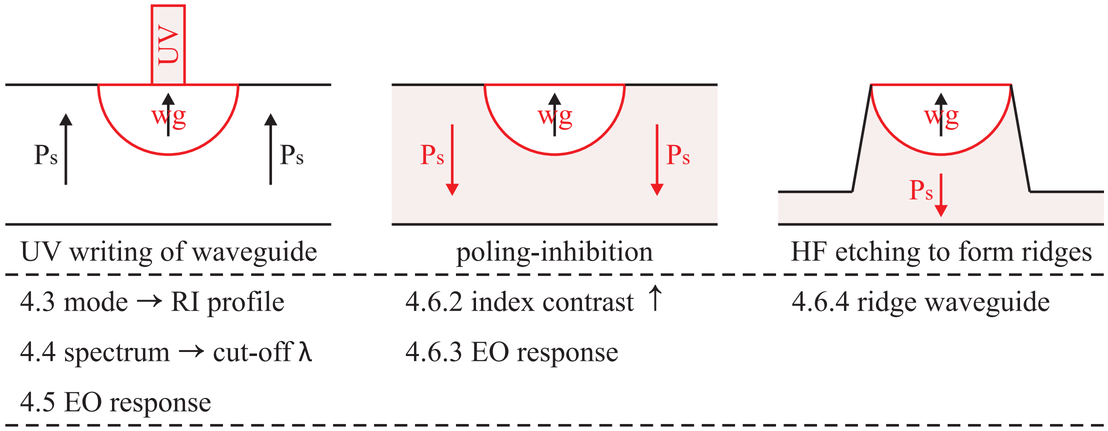

Figure 4.1: Schematic outline of the work which is presented in this chapter and its distribution in subsections. (RI = refractive index; EO = electro-optic; ↑ = value increased; → = 'derives'.)

CW UV laser light within a writing wavelength range of $275 - 305$ nm has been investigated. The channel waveguides were fabricated by focused laser direct writing on the $+z$ face of the crystal. For all UV writing conditions reported here single-mode waveguides for 632.8 nm were produced. The mode indices and refractive index profiles were then determined simultaneously from the measured near-field intensity profiles, and then the maximum refractive index change was calculated. The results reveal that for optimum writing conditions a maximum refractive index change of ~ 0.0026 can be achieved at 632.8 nm. A white light laser-supercontinuum source has been used for the investigation of the spectral response of the waveguides. The spectral data was used to determine the various regimes of waveguide operation from multimode to cut-off. It has been observed that an optimum writing condition for these waveguides exists where the refractive index change is maximised and hence the cut-off wavelength of the waveguide shifts to longer wavelengths. The experimental study was also extended to the electro-optic properties of these waveguides. Measurements of mode-width, mode-depth, and refractive-index change of waveguides with various applied voltages, and finally direct interferometric measurements of the electro-optic coefficient of waveguides written at different UV wavelengths revealed that electro-optic response of the waveguide reduces with increasing recording wavelength, with 275 nm written waveguides having the highest electro-optic response (31 pm V^{-1}) compared to waveguides written with 300, 302, and 305 nm light. As the writing conditions of waveguides are close to that for poling-inhibition as discussed in Chap. 3. LN substrates with UV-written waveguides on $+z$ face have been poled to form local poling-inhibited domains [Sones 08] that overlapped with the waveguide. It was observed that poling-inhibition results in a significant enhancement of the refractive index contrast between the bulk crystal and the UV irradiated tracks. Finally, the fabrication of ridge waveguides has been demonstrated as a result of HF etching of poling-inhibited waveguide channels.

4.2 UV-writing of waveguides

The LN crystals investigated here are 0.5 mm thick, optical graded, z-cut, undoped congruent LN from Crystal Technology Inc. (US). Direct laser writing on LN was achieved using a Coherent Innova Sabre 25/7 argon ion laser that delivered continuous wave (CW) output at 275, 300, 302, and 305 nm wavelengths with a maximum power of 200 mW. The laser beam was focused by a fused silica lens (focal length: 37.5 mm) onto the crystal surface to a spot with a radius of approximately 3 µm at the focal point. Channel waveguides were written on $+z$ face of the crystal by scanning the sample via a computer-controlled 2D translation stage, along the crystallographic y-axis at different laser beam powers ($35 - 60$ mW) and different writing speeds ($0.1 - 1.0$ mm s^{-1}). The UV energy fluence varied from $0.7 - 12.7$ kJ cm^{-2}. The crystals were preconditioned by performing five poling cycles (one cycle being a forward and subsequent reverse domain inversion process) before the writing. Following the direct writing, all the waveguides were edge-polished and used for characterisation. It is most important that the waveguide end-face is polished to enable optical coupling.

4.3 Mode and refractive index profiles

4.3.1 Theory for the determination of the refractive index profile

The mode index and the refractive index profiles of the waveguide cross-section are important characterisation tasks. The mode index is defined as the effective refractive index of the waveguide mode which is an important parameter of single-mode channel waveguides and is an essential input for design consideration for several basic components of OICs, such as directional couplers and Y-junctions. Accurate determination of refractive index profiles and mode indices, as a function of fabrication parameters, is therefore fundamental for characterising waveguide optical properties.

A non-destructive method was used to estimate the refractive index distribution in a waveguide from its mode field intensity profile. It requires no previous knowledge of the shape of the refractive index distribution, and does not require the waveguide to have any kind of cross-sectional symmetry. The outline of the computation steps is as follows: 1) the measured near-field profile is fitted with a Gaussian (or Hermite-Gaussian) distribution for lateral (or depth) near-field intensity profile; 2) the results of the fit are used to compute the refractive index profile using Eq. 4.3 by taking the mode index equal to the substrate index; and then 3) the mode index value is increased to get the minimum refractive index change to be equal to zero outside the waveguide region.

To evaluate the index profile from the mode field distribution, it is assumed that 1) only the fundamental mode of propagation is excited, 2) the refractive index change δn is very small compared to the refractive index of the substrate n_{s} ($\delta n \ll n_{\mathrm{s}}$), and 3) no phase variation exists across the measured wavefield: this is quite valid since the mode field intensity is measured at the waveguide endface where the phase variation is negligible, then the scalar wave equation for the fundamental mode can be expressed as [McCaughan 83]

$$\nabla^2 A(x,z) + [k_0^2 n^2(x,z) - \beta^2] A(x,z) = 0 \tag{4.1}$$

$$A(x,z) = I^{1/2}(x,z)$$

$$k_0 = 2\pi/\lambda_0$$

where $I(x,z)$ is the intensity distribution of the fundamental mode; λ_0 is the free-space wavelength of the light propagating in the waveguide; $n(x,z)$ is the refractive index distribution of the waveguide; β is the propagation constant of the fundamental mode; x and z correspond to lateral and depth dimensions of the waveguide; and the light propagates along the y-direction. Therefore, applying an inversion of the scalar waveguide Eq. 4.1 leads to the following expression for deriving the refractive index distribution,

$$n^2(x,z) = \frac{\beta^2}{k_0^2} - \frac{\nabla^2 A(x,z)}{k_0^2 A(x,z)} \tag{4.2}$$

Hence, the UV-induced refractive index change, $\delta n(x,z)$, of a single-mode waveguide may be expressed as

$$\delta n(x,z) = [n_{\mathrm{eff}}^2 - \nabla^2 A/(k_0^2 A)]^{1/2} - n_{\mathrm{s}} \tag{4.3}$$

$$n_{\mathrm{eff}} = \beta/k_0$$

where n_{s} is the substrate refractive index at the appropriate wavelength; and n_{eff} is the effective refractive index of the mode or mode index. Thus $\delta n(x,z)$ can be evaluated numerically from Eq. 4.3 using the lateral and depth near-field intensity profiles of the single-mode UV-written waveguides. In principle, the mode index can be derived using Eq. 4.3 from the measurement of the intensity away from the channel waveguide, where $\delta n(x,z)$ tends to zero [McCaughan 83]. In practice, however, due to high-spatial-frequency noise (which is amplified by the Laplacian operator) on the tails of the mode where the mode field is very small, it is impossible to evaluate the mode index accurately from Eq. 4.3. Since the electric field is very small outside the waveguide, the second term inside the square root in Eq. 4.3 tends to diverge and introduce errors in the measurement. As the difference between the mode index and substrate refractive index is a small quantity, the mode index may be approximated by the substrate index in Eq. 4.3. This incorporates an error in the absolute values of the induced refractive index change [Mansour 96]. Here the mode index value has been adjusted by using an algorithm, so that the minimum value of refractive index change is zero outside the waveguide boundary. By this process one can determine the accurate refractive index change and mode index of the single-mode waveguide simultaneously. A similar approach has been adopted previously by Chakraborty et al. [Chakraborty 01] to compute accurate mode profiles from one-dimensional effective refractive index distributions of Ti:$LiNbO_3$ waveguides and directional couplers by a matrix method. To reduce noise effects in Eq. 4.3, the measured near-field intensity profiles of the UV-written waveguides were fitted by Gaussian (lateral profiles) and Hermite-Gaussian (depth profiles) distributions before processing. Application of a local least-squares method to minimise noise in measured intensity profiles is a common practice [Helms 90, Fatadin 06] and these curve fits are fairly accurate for the intensity profiles of the UV-written waveguides in LN. The requirement of the validity of the scalar-wave equation, namely that the index changes slowly, holds for all $n(x, z)$ in these waveguides except at the air-substrate interface where the refractive index changes abruptly ($\delta n/n_\mathrm{s} \sim 0.55$). To avoid this problem the depth refractive index profile was computed starting from slightly below the surface where the maximum mode intensity has been measured. To determine the refractive index profiles of the waveguide, Eq. 4.3 is solved numerically using [McCaughan 83, Mansour 96]

$$\frac{\nabla^2 A}{A} = \frac{A_{i-1,j} + A_{i+1,j} - 2A_{i,j}}{(\delta x)^2 A_{i,j}} + \frac{A_{i,j-1} + A_{i,j+1} - 2A_{i,j}}{(\delta z)^2 A_{i,j}} \tag{4.4}$$

where δx and δz are the horizontal and vertical spacing between the data points, i.e., the grid spacing resolution. Here i and j are the pixel numbers.

A typical plot of the measured intensity profile at 632.8 nm wavelength along the lateral (x-axis) direction is shown in Fig. 4.2(a) as the black curve. The raw data has been processed to generate the refractive index profile of the waveguide by assuming that the mode index is equal to the substrate index which is equal to 2.2027 at 632.8 nm wavelength [Born 99]. Obviously problems arise, because any calculation of a second derivative (Eq. 4.4) is very sensitive to rapid intensity variations. Hence a smooth profile is required for the calculations. Without any curve fitting, a determination of the refractive index seems to be impossible, as demonstrated by the black curve shown in the graph of Fig. 4.2(b), which shows the index profile calculated from the raw intensity profile using Eq. 4.3 [black curve in Fig. 4.2(a)]. Obviously, the data for the change of the refractive index of the waveguide is submerged in the noise because of the random fluctuations of the modal intensity in the spatial domain especially at the waveguide edges where the signal to noise ratio decreases significantly. Therefore the measured intensity profile was fitted with a Gaussian distribution [red curve in Fig. 4.2(a)] and the computation process was repeated thereby getting an index profile shown in Fig. 4.2(b) as the red solid curve. It may be noticed from the figure that the refractive index changes become negative (−0.00123) at the two ends of the profile outside the waveguide boundary, where it should be nearly zero. This is the result of the assumption that the mode index is equal to the substrate index, which incorporates a large

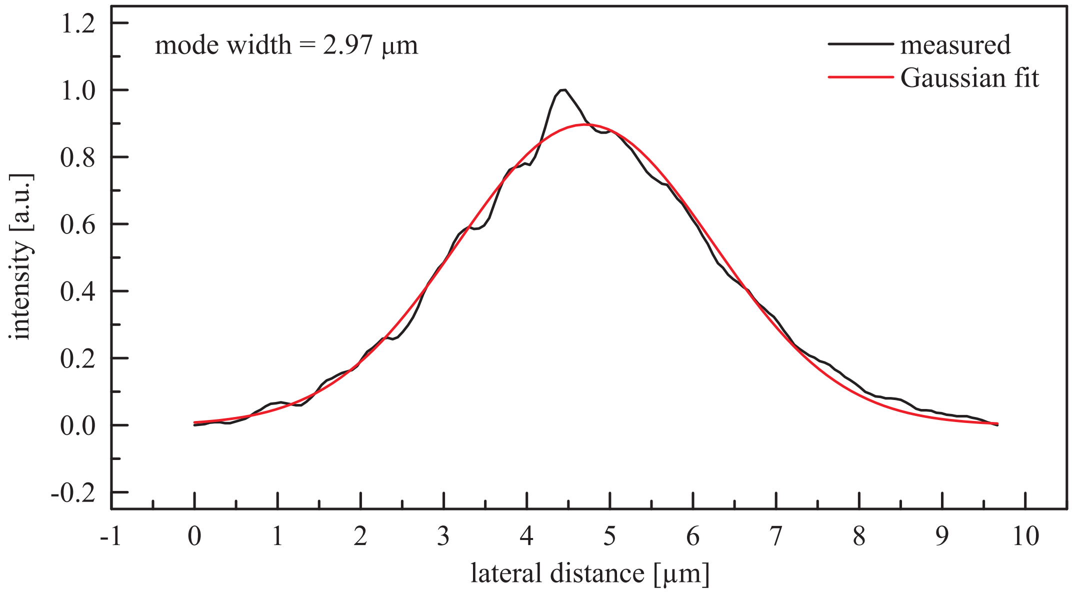

(a) lateral intensity profile

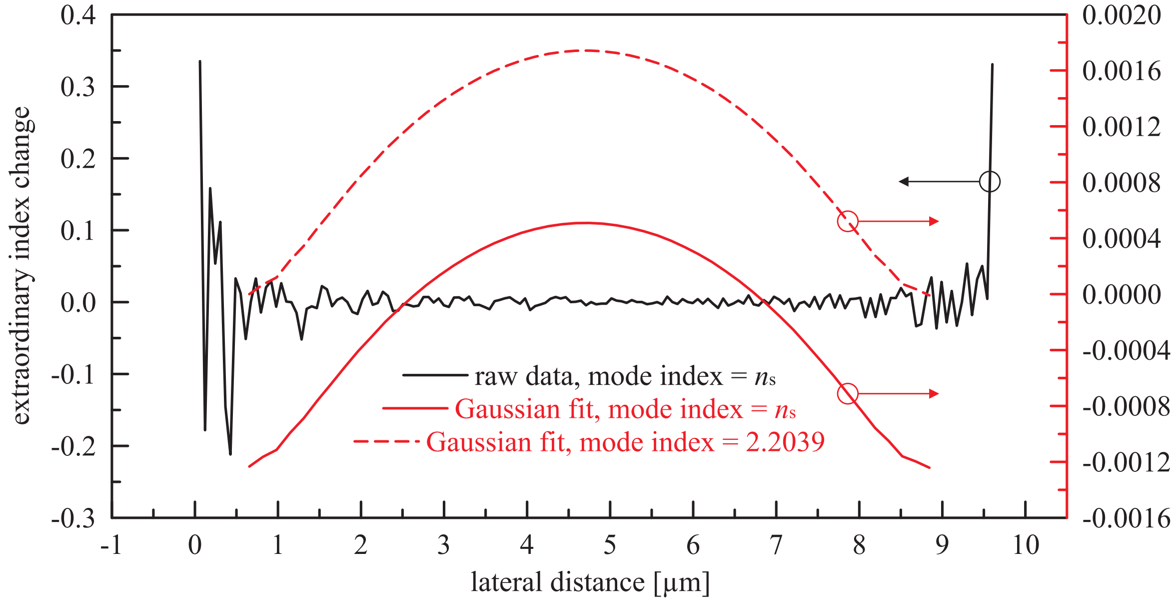

(b) computed refractive index change

FIGURE 4.2: Lateral intensity profile and corresponding calculated profile of refractive index change. In (a), black curve is the measured lateral intensity profile of a waveguide written with 305 nm at a writing power of 35 mW and a speed 0.1 mm s^{-1}. Mode width calculated at FWHM is 2.97 µm. The red line represents the Gaussian distribution fitting of the lateral mode profile. In (b), the black curve is the calculated refractive index change from the raw data in (a) (assuming mode index = substrate index); the red solid curve is the reconstructed profile of refractive index change using the fitted Gaussian distribution in (a) (assuming mode index = substrate index). The mode index value was then increased (to 2.2039) so that the minimum refractive index change outside the waveguide region equals zero. The adjusted refractive index change is represented as the red dashed curve in (b).

error in the absolute refractive index values of a weakly guiding waveguide where the refractive index change is a small quantity. Therefore the mode index value was increased in Eq. 4.3 to get the minimum refractive index change to be equal to zero ($\leq 10^{-6}$) outside the waveguide region. The reconstructed profile is shown in Fig. 4.2(b) as the red dashed curve with the mode index value 2.2039. Therefore, this process can simultaneously extract the values of refractive indices and mode index of the waveguide.

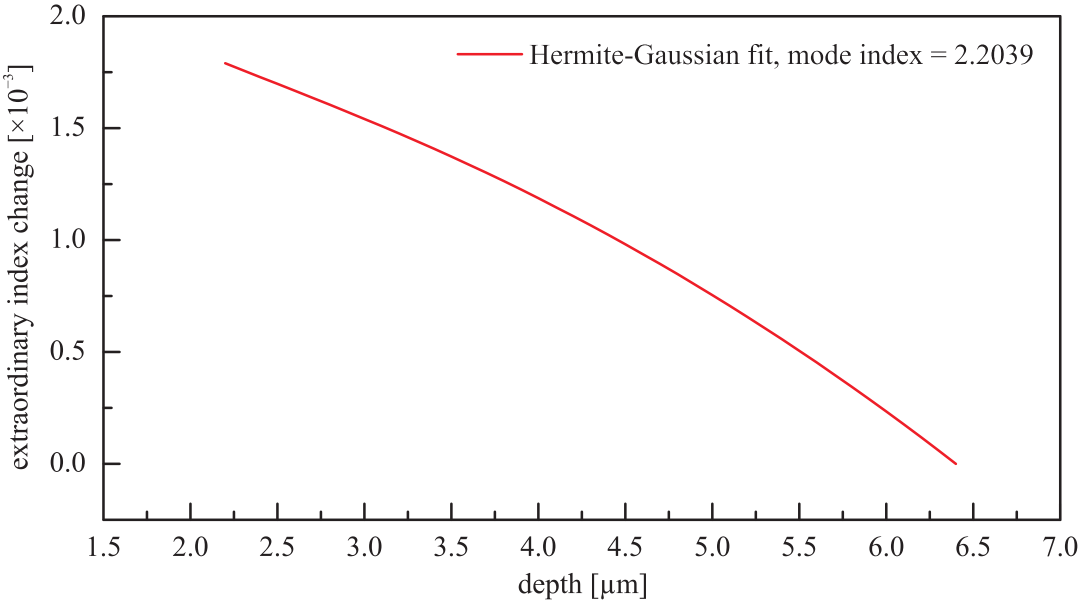

FIGURE 4.3: Depth refractive index profile of the waveguide with writing conditions same as in Fig. 4.2.

The same procedure is also followed for the reconstruction of depth (along the z-axis) refractive index profile (Fig. 4.3). In this case the intensity profile is fitted with a Hermite-Gaussian function because of the asymmetry in the structure. Since at the air-$LiNbO_3$ interface the process incorporates an error because of the abrupt index change, the refractive index profile is computed starting from the peak intensity position of the measured mode intensity profile, which is 2.24 μm below the surface for the waveguide in Fig. 4.3. The computed maximum refractive index changes (and mode indices) for the same waveguide, obtained from lateral and depth intensity profiles, match within 2.3% (and 0.0012%), which makes us confident about the computation process.

4.3.2 Mode profile measurement

The mode profile of the waveguides was measured using the standard near-field measurement setup shown in Fig. 4.4. The source used was a He-Ne laser (632.8 nm) at 1 mW power coupled via a 10× objective to a single-mode optical fibre, which was subsequently butt-coupled to one end of the UV-written waveguide. The substrate containing the waveguides was mounted on a

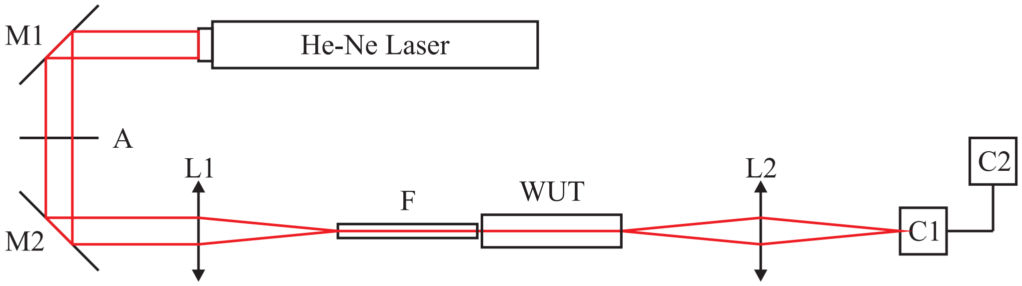

FIGURE 4.4: Near-field intensity profile measurement setup. (M1, M2 = mirrors; A = attenuator; L1 = 10× objective; L2 = 40× objective; F = single mode fibre; WUT = waveguide under test; C1 = CCD Camera; C2 = computer.)

high precision 4-axis translation stage in order to achieve the best possible coupling between the fibre and the waveguide. TM waveguide modes only could be excited in the UV written LiNbO$_3$ waveguides suggesting an increment in the extraordinary refractive index only. The output of the waveguide was imaged onto a CCD camera by means of a 40× microscope objective (with a numerical aperture of 0.65). Image analysis was performed using a beam profiling software (Newport LBP, USB2). The resolution limit of the 40× objective is 0.6 µm, using Abbe's criterion for coherent light from an object [Born 99]. Special care has been taken to image exactly the end-face and for perpendicular incidence of the optical beam on the camera, which otherwise would give rise to significant errors in measured mode profiles. Once the mode image of the waveguide was recorded, the normalised intensity profiles along horizontal (x-axis) and vertical directions (z-axis) were generated by the software.

4.3.3 Mode index as a function of writing power

Fig. 4.5 shows the (a) maximum refractive index changes and (b) mode indices calculated from the measured near-field intensity profiles of the UV-written single-mode waveguides for different writing powers at each of the writing wavelengths (275, 302, and 305 nm) and at a writing speed of 1.0 $\mathrm{mm\,s^{-1}}$. The plot suggests that an optimum writing power exists for each wavelength where the refractive index change and mode index are maximum ($\sim$ 35, 41 and 45 mW for 305, 302 and 275 nm respectively). It also provides a writing power range, where an appreciable maximum refractive index change occurs. In the lower power limit of this range the crystal is under-exposed to the UV radiation hence a smaller refractive index is observed. However the fact that the refractive index change decreases in the higher power limit is counter-intuitive as the maximum refractive index change should continue to increase with increasing laser power and eventually saturate to a certain value. The reduction is expected to be due to the surface damage. A look at the surface topography of the UV irradiated area provides a clue about the nature of the mechanism that causes a decrease of the measured refractive index change at the high power limit. Fig. 4.6 shows typical scanning electron microscopy (SEM) images of the UV

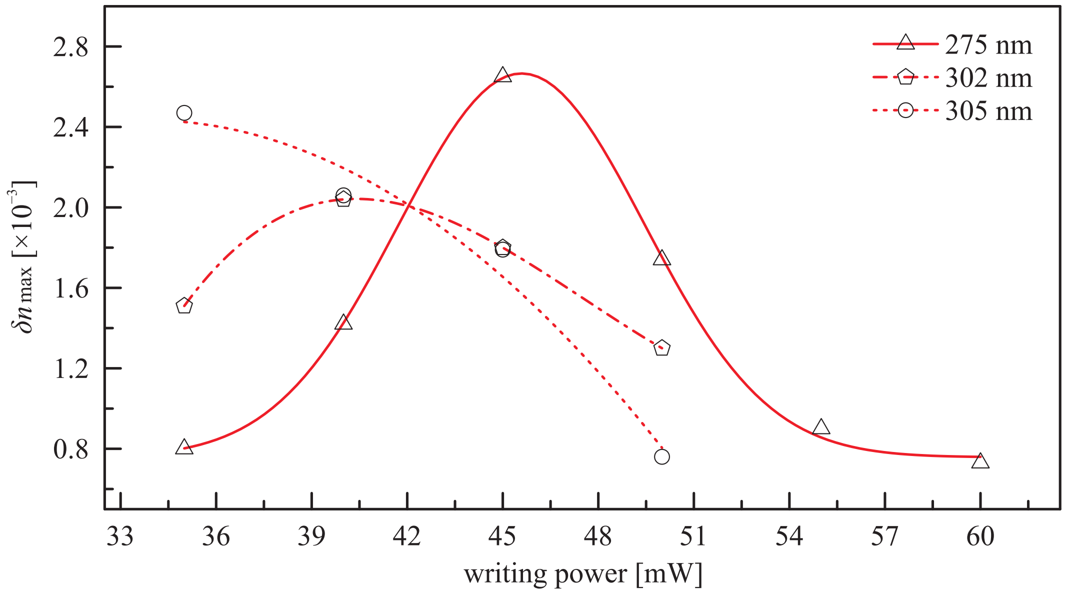

(a) maximum refractive index changes

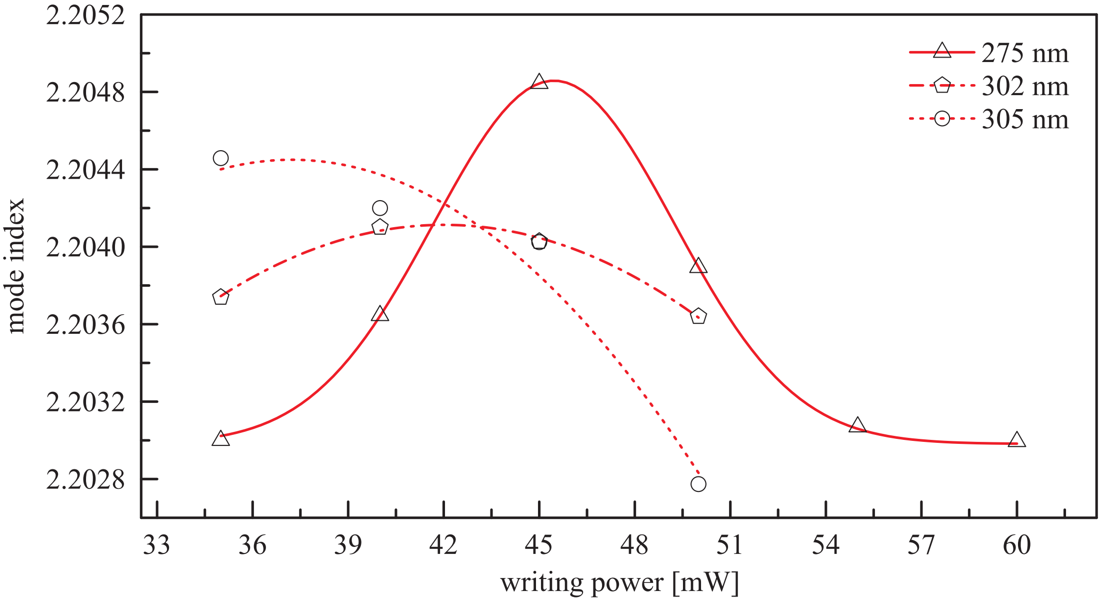

(b) mode indices

FIGURE 4.5: Computed results of (a) maximum refractive index changes and (b) mode indices extracted from the measured near-field intensity profiles of the UV-written single-mode waveguides for different writing powers at each of the writing wavelengths, 275, 302, and 305 nm. The writing speed was 1.0 mm s^{-1}.

irradiated crystal surface at the high power limit for two different wavelengths. These SEM images show extensive surface damage which is expected to induce a reduction of the measured maximum refractive index because this damage is more evident in the layers which are close to the surface where the refractive index should be maximum. As a result of the surface layer damage the optical mode shifts further into the bulk (towards the undamaged volume) where, however, the refractive index change is smaller. The power dependence of the refractive index

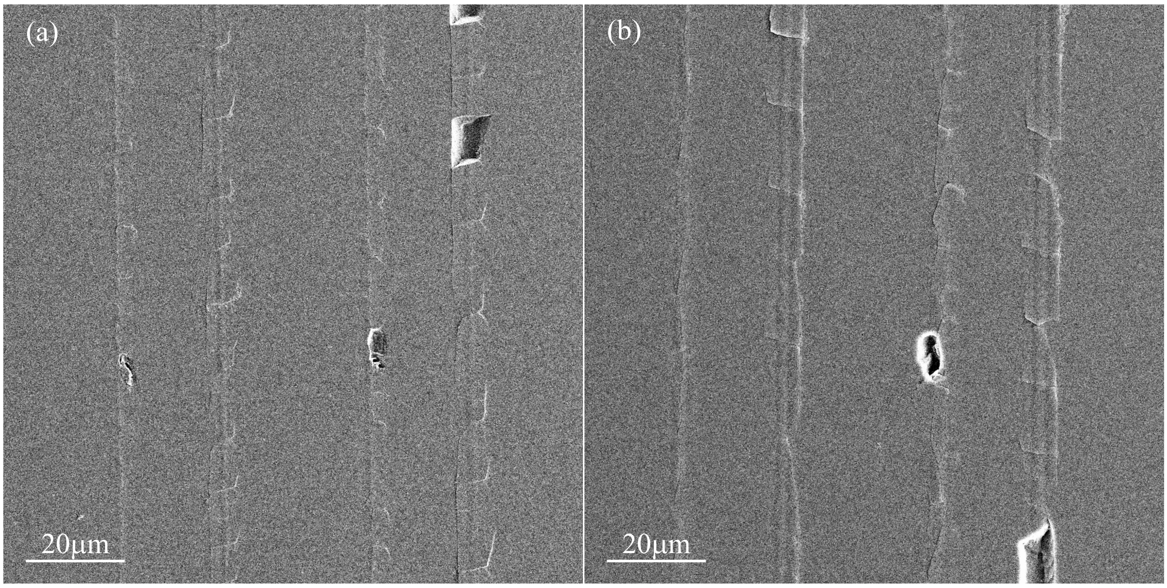

FIGURE 4.6: SEM image of surface damage of UV-written channel waveguides: (a) written at writing wavelength 275 nm and power 55 mW, and (b) written at writing wavelength 305 nm and power 50 mW.

change which is shown in Fig. 4.5 is therefore the result of a trade-off between under-exposure (low power) and surface damage (high power).

UV laser-induced surface damage has been investigated elsewhere [Ródenas 07], which shows that it induces a permanent local stress on the micron-scale dimension, which may consequently decrease the local refractive index of LN to some extent [Deshpande 05]. Raman analysis of the exposed region also shows some loss of crystalline property of the material [Burghoff 07], indicating that while LN may suffer some change in chemical composition near the surface, however, it remains unchanged in the bulk.

4.3.4 Mode index as a function of writing speeds

Fig. 4.7 shows the variation of maximum refractive index changes and mode indices for different writing speeds at the writing wavelengths 300, 302, and 305 nm. The data points are fitted with Gaussian curves. In all cases the writing power was 35 mW. Once again an optimal writing speed exists for inducing a maximum refractive index change, which is approximately 0.75 and 0.3 $\mathrm{mm\,s^{-1}}$ for 305 and 302 nm wavelengths, respectively. At 300 nm only a part of the distributions has been determined. Both the variations of maximum refractive index change and of mode index with writing speed follow the same trend. From all the refractive index data it seems that the maximum refractive index change for any writing condition is limited by the surface damage along the waveguide, and its maximum possible value is about 0.0026 at 632.8 nm. This corresponds to a mode index value of ~ 2.2048. It is not possible to increase the UV-induced

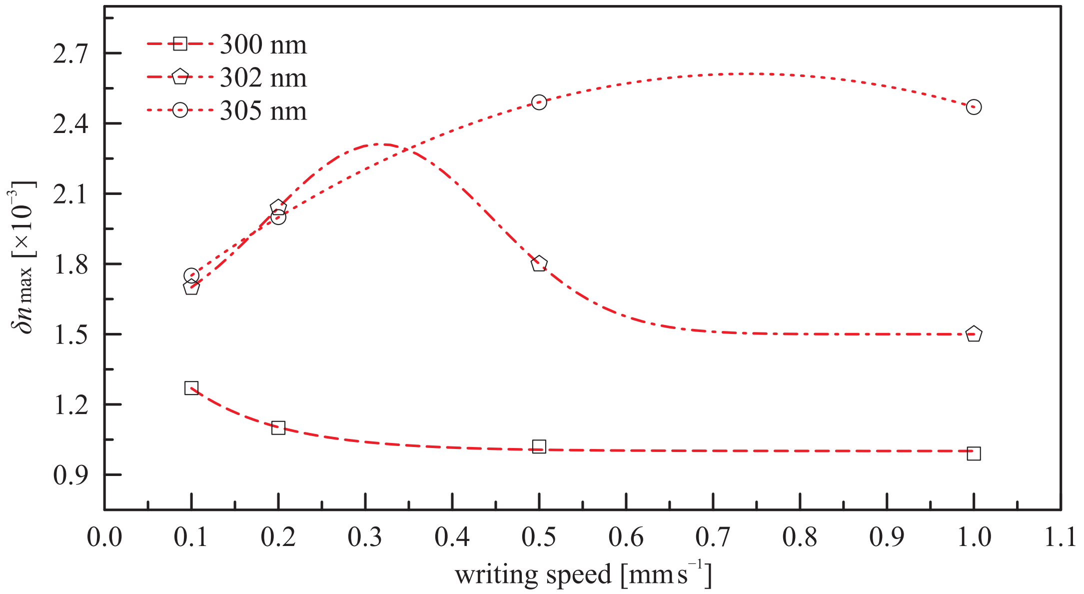

(a) maximum refractive index changes

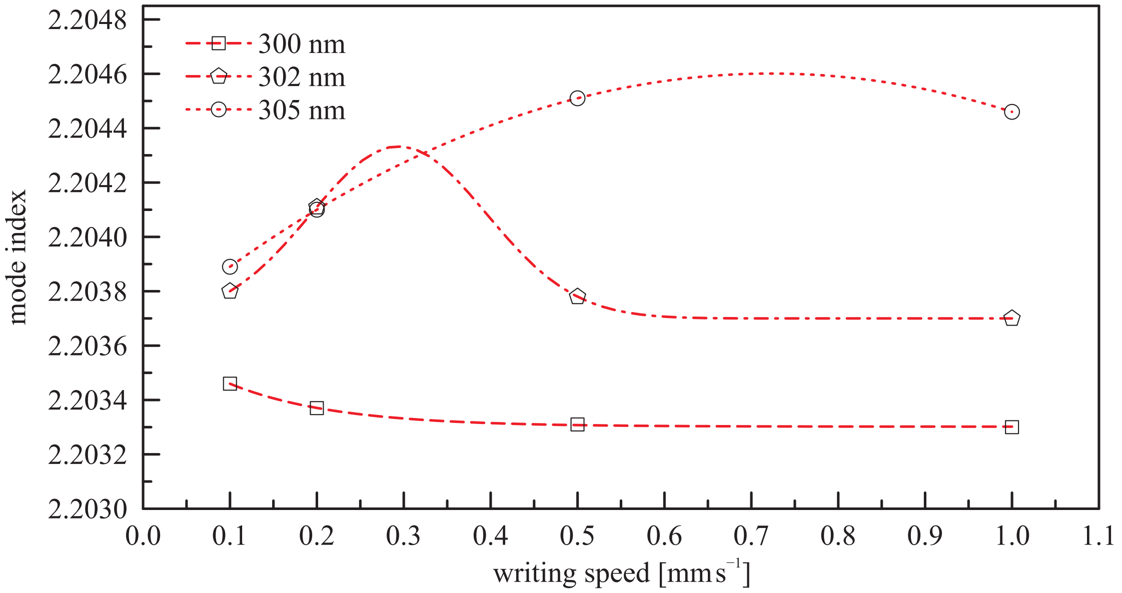

(b) mode indices

FIGURE 4.7: Computed (a) maximum refractive index changes and (b) mode indices for waveguides with different writing speed and wavelength.

refractive index change indefinitely by increasing the laser fluence and/or decreasing the writing wavelength (due to the extremely rapid onset of absorption increase [Redfield 74]). The refractive index of a waveguide written at 244 nm at 45 mW and writing speed 0.83 mm s^{-1} was also determined. The waveguide was written almost two years ago. The computed maximum refractive index change and mode index for this waveguide are about 0.0013 and 2.2036, respectively.

4.3.5 Effect of crystal orientation

Waveguides have also be produced by UV-writing on the $-z$ face of LN. Fig. 4.8 shows a comparison of the maximum refractive index change induced at different writing speeds for the writing of undoped CLN channel waveguides into the $+z$- and $-z$ faces. The writing power was 35 mW with same focused beam radius of 3 µm, and the writing wavelength was 305 nm. It is clear in Fig. 4.8 that the optical properties of the UV-written waveguides in LN also depend on the crystal orientation. The maximum index changes for $-z$ face written waveguides are, in general, lower than those for waveguides written on the $+z$ face.

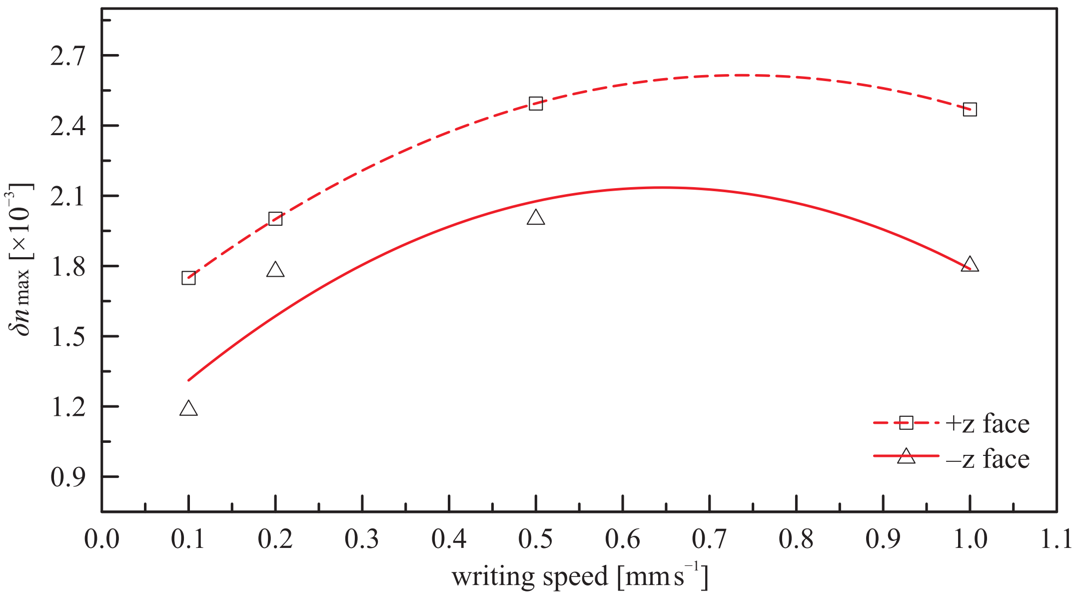

FIGURE 4.8: Maximum refractive index change versus writing speed for $+z$ and $-z$ faces of LiNbO$_3$ (writing power = 35 mW, and writing wavelength = 305 nm).

4.4 Spectral analysis and cut-off wavelength determination

4.4.1 Introduction

For most applications, single-mode waveguides are essential in order to achieve optimised device performance, and hence the determination of single-mode operating range and cut-off wavelength of the waveguide are fundamental for characterising waveguide optical properties. Spectral analysis is a characterisation method which has been originally developed for determining the effective cut-off wavelength of optical fibre [van Leeuwen 84] and later for Ti-indiffused [Lang 94] and proton exchanged [McConaghy 95] waveguides. Here this method is applied for the characterisation of UV-written waveguides. In this section, the spectral response of the direct UV-written channel waveguides in congruent LiNbO$_3$ was investigated using a white light laser-supercontinuum source. The spectral data was used to determine the various regimes of waveguide operation from multimode to cut-off. It has been observed that an optimum writing condition for these waveguides exists where the refractive index change is maximised and hence the cut-off wavelength of the waveguide shifts to longer wavelengths.

4.4.2 Theoretical considerations

To eliminate the spectral response of the launch and detection components of the experimental setup (such as the broadband source and the detector), the spectral output intensity of the waveguide (I_{wg}) was normalised by a reference intensity spectrum (I_{ref}) acquired by the optical system without the presence of the waveguide. This normalisation also minimises the effect of chromatic aberrations of the microscope lenses. Typical normalised transmission spectra of two different UV-written waveguides are shown in Fig. 4.9. The spectrum shown in Fig. 4.9(a) corresponds to a waveguide that exhibits multimode transmission at shorter wavelengths and can be divided into four regions [McConaghy 95]. In region-1 the waveguide supports the two lowest order modes and the normalised transmission spectrum ($I_{\mathrm{wg}}/I_{\mathrm{ref}}$) can be described as

$$I_{\mathrm{wg}}/I_{\mathrm{ref}} = K_{00} + K_{01} \tag{4.5}$$

where K_{00} and K_{01} are the coupling coefficients for the lowest and next higher order modes, respectively. Region-2 describes the wavelength regime where the second mode cut-off is approached. In this case normalised transmission spectrum is given by

$$I_{\mathrm{wg}}/I_{\mathrm{ref}} = K_{00} + K_{01} \exp(-\alpha_{01} L_0) \tag{4.6}$$

where α_{01} and L_0 are the modal attenuation coefficient of the higher order mode and length of the guide, respectively. As the wavelength becomes longer the cut-off of the second mode is passed and region-3 covers the wavelength range where the fundamental mode is still far from cut-off. The intensity ratio in this region may be given as

$$I_{\mathrm{wg}}/I_{\mathrm{ref}} = K_{00} \tag{4.7}$$

Finally as the fundamental mode cut-off is approached in region-4, the normalised transmission spectrum is

$$I_{\mathrm{wg}}/I_{\mathrm{ref}} = K_{00} \exp(-\alpha_{00} L_0) \tag{4.8}$$

where α_{00} is the attenuation coefficient for the fundamental mode. In Eq. 4.5, 4.6, 4.7, 4.8, the modal coupling and attenuation coefficients are wavelength dependent.

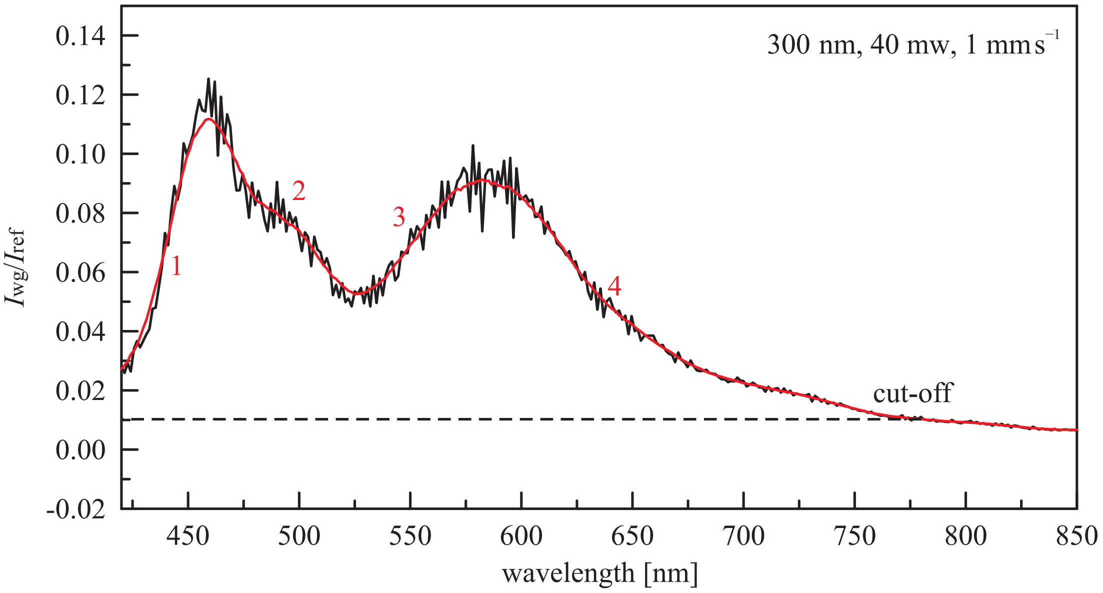

(a) 300 nm, 40 mW, 1 mm s^{-1}

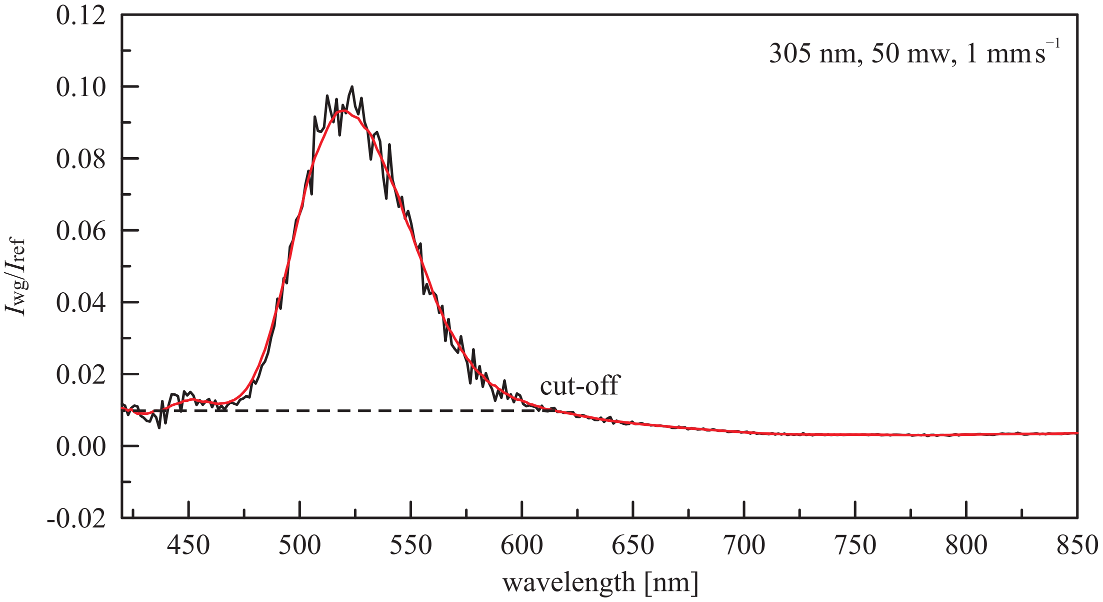

(b) 305 nm, 50 mW, 1 mm s^{-1}

FIGURE 4.9: Typical spectral responses of the fabricated UV-written waveguides: (a) with writing wavelength: 300 nm, power: 40 mW, speed: 1 mm s^{-1}; and (b) with writing wavelength: 305 nm, power: 50 mW, speed: 1 mm s^{-1}.

Here, the mode cut-off point was defined as 10% of the peak normalised intensity. Hence for the waveguide shown in Fig. 4.9(a), which was written at the 300 nm wavelength, with a laser power of 40 mW and a writing speed 1.0 mm s^{-1}, the multimode region is $<$ 514 nm, whereas the guide is single-moded within the wavelength range from 514 nm to 780 nm, where 780 nm is practically the waveguide cut-off wavelength. For the waveguide shown in Fig. 4.9(b), written with 305 nm wavelength, 50 mW power and 1 mm s^{-1} laser writing speed, the single-mode range is from 408 nm to 615 nm.

4.4.3 Waveguide spectra acquisition and analysis

For the spectrum measurement inside the waveguide, a supercontinuum fibre laser (Fianium, Femtopower 1060, with a wavelength range: 408−1800 nm) was coupled into the waveguides using a 10× microscope objective. The output of each waveguide was imaged by a second microscope objective onto a circular aperture (iris diaphragm) spatial filtering the optical noise from the light originating from the waveguides, and it was subsequently coupled to an optical spectrum analyser. A schematic of the experimental setup is shown in Fig. 4.10. The numerical aperture of the launching objective lens (NA = 0.25) was chosen to be high enough to excite all possible guided modes of the waveguides. The $LiNbO_3$ substrate containing the waveguides was mounted onto a high precision 4-axis translation stage. All these spectral measurements were performed below the photorefractive damage threshold of the waveguides, which was confirmed by the non-dependency of the normalised transmission spectra on the input power. The measured spectral response has been analysed to determine the wavelength range for multi-mode and single-mode operation respectively and the cut-off wavelength of the UV-written waveguides.

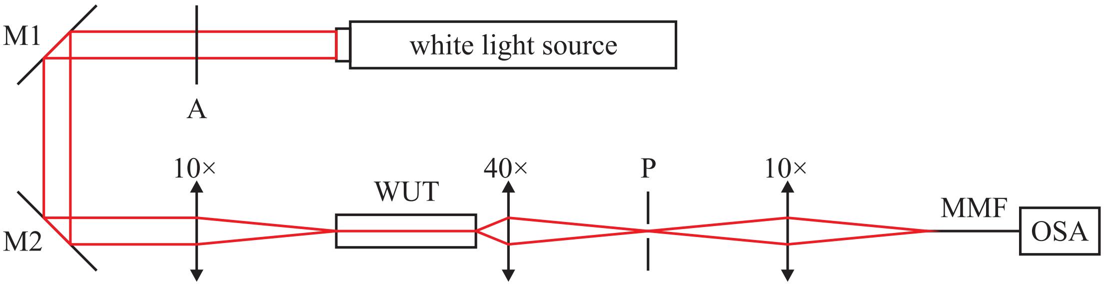

FIGURE 4.10: Experimental setup for spectral characterisation. (M1, M2 = mirrors; P = adjustable pinhole; MMF = multimode fibre; OSA = optical spectrum analyser; WUT = waveguide under test.)

The cut-off wavelengths were measured for all the waveguides written with various writing wavelengths, laser powers, and writing speeds. The variations of the cut-off wavelength of the waveguides written with different wavelengths, as a function of laser power and writing speed are shown in Fig. 4.11(a) and (b) respectively. These results confirm the previous observation in Sec. 4.3 [Ganguly 09] that for each writing wavelength an optimum writing condition (writing power and speed) exists where the induced refractive index change is maximised, because as the refractive index change or the contrast of the waveguide ($\delta n_{\max}$) increases, the cut-off shifts to longer wavelengths.

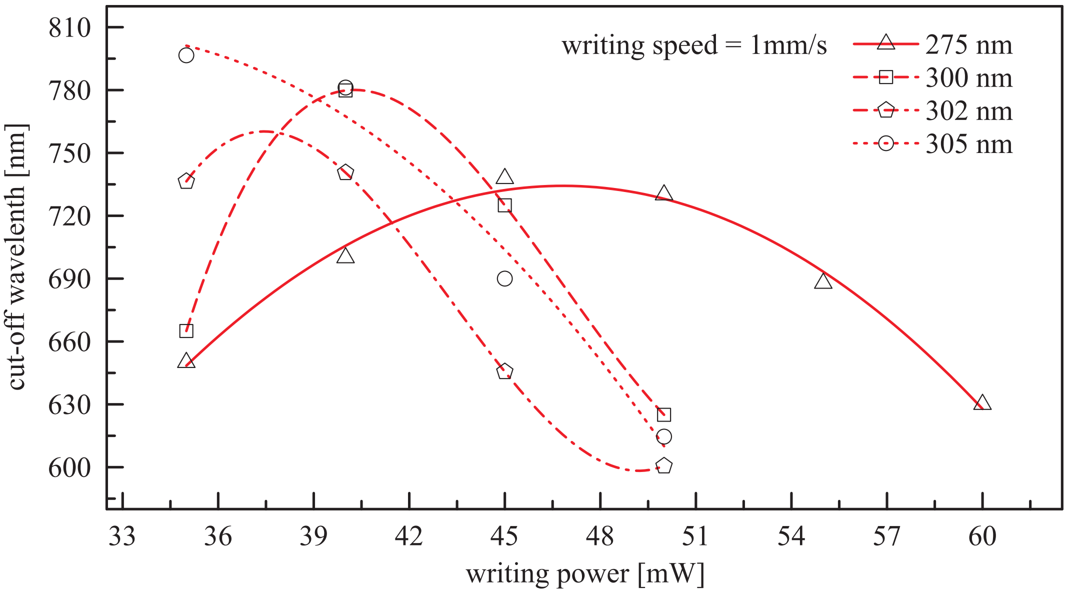

(a) various laser writing power

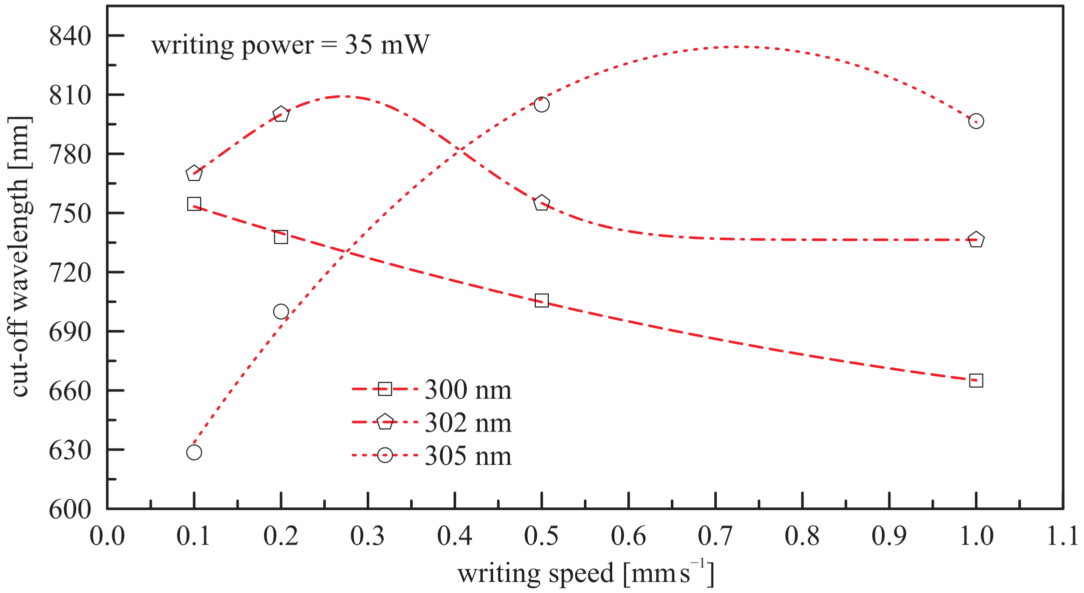

(b) various writing speed

FIGURE 4.11: Variations of cut-off wavelengths of the waveguides with: (a) laser writing power, and (b) writing speed.

4.4.4 Electro-optic shift of the waveguide cut-off

The change of the spectral response of the UV-written waveguides under the influence of an external electric field was used to investigate the electro-optic behavior of the waveguides. A pair of thin gold film electrodes of thicknesses $\sim$ 10 nm was sputtered onto the two opposite faces of the 500 µm thick substrate containing the waveguides. The electrodes were used to apply a variable voltage across the substrate and the corresponding normalised transmission spectra

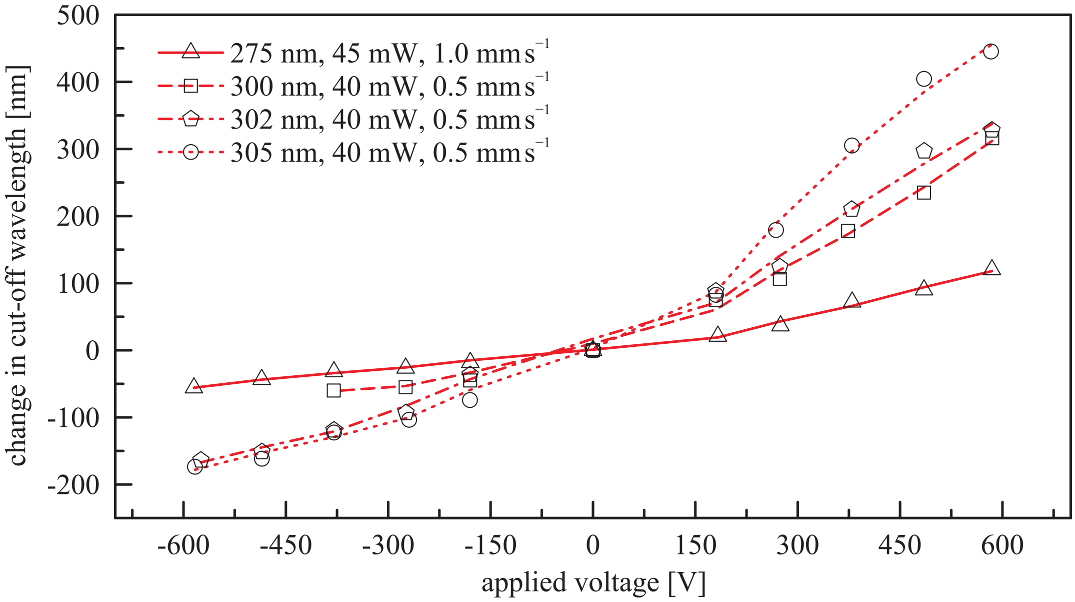

FIGURE 4.12: Changes in cut-off wavelengths of the waveguides with applied voltages for 275, 300, 300, and 305 nm writing wavelengths.

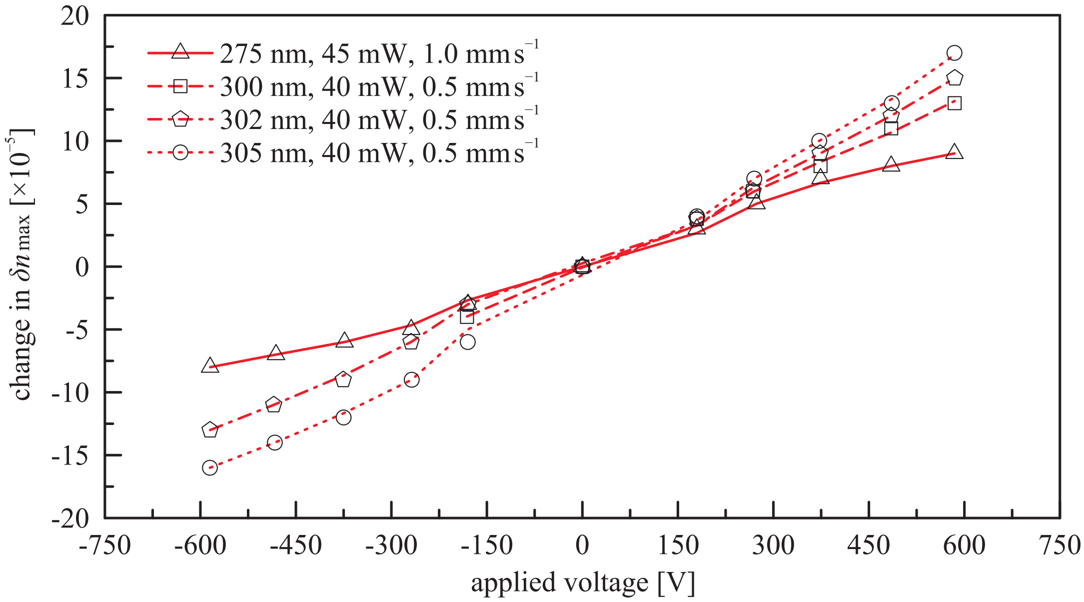

FIGURE 4.13: Changes in contrast of the waveguides written with 275, 300, 302, and 305 nm wavelengths with applied voltages.

of the waveguides were measured. The applied DC voltage used in the experiment ranged from −600 to +600 V, corresponding to a uniformly applied DC electric field ranging from −1.2 to +1.2 V μm^{-1} along the z-axis of the $LiNbO_3$ crystal. The changes in cut-off wavelengths of the waveguides, written with different wavelengths, for various applied voltages were measured. These experimental data directly correspond to the relative refractive index changes or changes in the contrast of the waveguides with respect to the substrate, via the linear electro-optic (Pockels) effect. Results of the measurements for cut-off wavelength change with applied DC

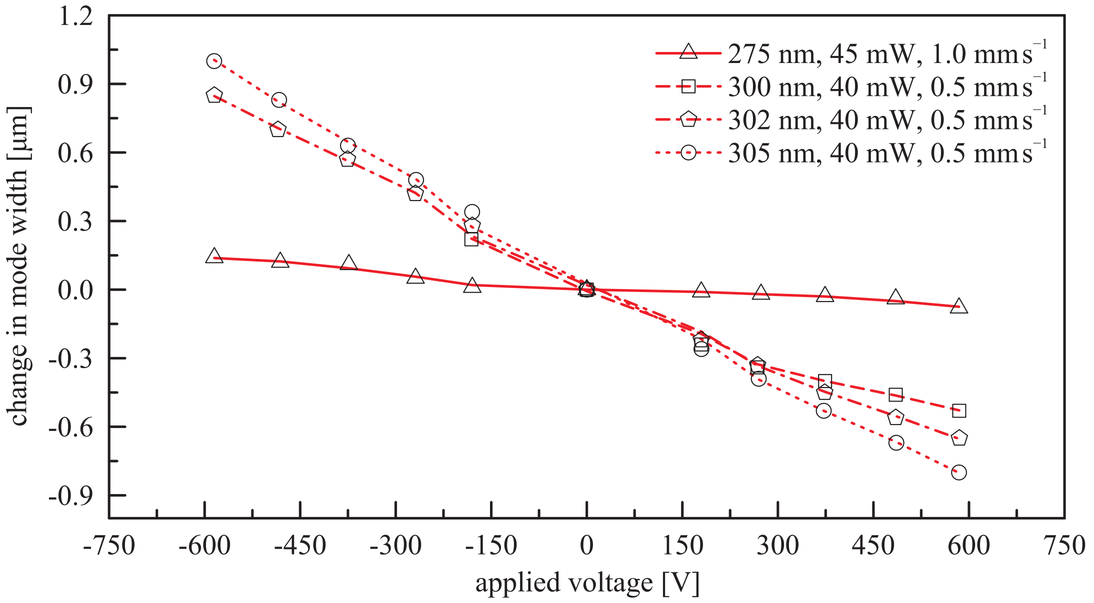

(a) mode width

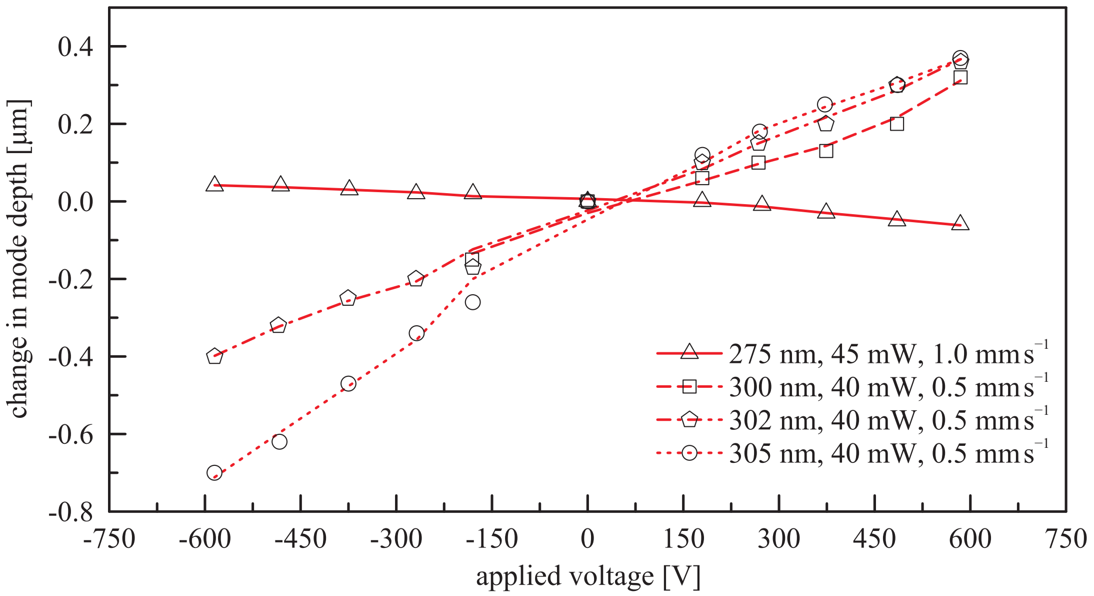

(b) mode depth

FIGURE 4.14: Changes in mode width (a) and mode depth (b) with applied voltages for the waveguides written with 275, 300, 302, and 305 nm wavelengths.

voltages of waveguides written with four different UV wavelengths are shown in the graph of Fig. 4.12. It may be observed in the graph that the waveguides written with 275 nm exhibit the lowest change in cut-off wavelength with applied voltages in the range from −600 to +600 V. The changes in cut-off wavelengths of the waveguides gradually increase with the writing wavelength. In the present electrode configuration, where a uniform electric field is applied across the whole crystal containing the waveguides, the change in cut-off wavelength will depend on the change in refractive index contrast of the waveguides with respect to the substrate. Hence for waveguides with the same electro-optic coefficients as that of $LiNbO_3$ substrate, there shouldn't be any appreciable change in the cut-off wavelength. However, waveguides which have a reduced electro-optic coefficient with respect to the substrate will exhibit a more significant change in cut-off wavelength with the applied voltage. Thus the results in Fig. 4.12 indicate that a waveguide written with 275 nm has an electro-optic coefficient, r_{33}, closest to the substrate value in comparison to waveguides written with longer wavelengths. In fact, the electro-optic coefficient decreases monotonically with the increase in writing wavelength. The measured change in contrast of these waveguides with respect to the substrate refractive index at 632.8 nm transmitting wavelength (Fig. 4.13), for different applied voltages, supports these experimental observations. The changes in mode width and mode depth of these UV-written waveguides with the applied voltages are shown in Fig. 4.14. All these waveguides are single-moded in nature at this wavelength within the applied voltage range. As expected the changes in mode widths and mode depths with the applied voltages are relatively small for the waveguide written with 275 nm wavelength, whereas, for other waveguides significant changes in mode widths and mode depths are observed.

The markedly different responses of the waveguides with applied voltage suggest a difference in the relative values of electro-optic coefficient (r_{33}) of the UV-written waveguides compared to those for the bulk substrate under different writing wavelengths. Hence it was necessary to proceed to a direct measurement of the effective electro-optic coefficient.

4.5 Electro-optic response

4.5.1 Introduction

The electro-optic properties of these waveguides need to be assessed for subsequent applications in waveguide optical switches and modulators, which are key integrated-optical components that can be implemented in $LiNbO_3$. Therefore, electro-optic characterisation of UV-written waveguides in $LiNbO_3$ is of absolute necessity from the device point of view. In the previous section, the spectral response of the waveguides written with different UV wavelengths markedly differs with applied voltage which suggests a difference in the value of the electro-optic coefficient (r_{33}) of the UV-written waveguides compared to those for the bulk substrate. Hence it was necessary to proceed to a direct measurement of the effective electro-optic coefficient. The electro-optic response measurements confirm that the electro-optic coefficient in waveguides written at longer wavelengths is lower ($r_{33} = 14\ \mathrm{pm\,V^{-1}}$ at 305 nm) as compared to waveguides written at shorter wavelengths ($r_{33} = 31\ \mathrm{pm\,V^{-1}}$ at 275 nm).

4.5.2 Experiment setup

For a quantitative characterisation of the electro-optic response of the waveguides written at different wavelengths, the r_{33} electro-optic coefficient was measured using a Mach-Zehnder interferometric setup, a schematic of which is shown in Fig. 4.15. A He-Ne laser beam (632.8 nm) was divided by a 50/50 cube beam-splitter (BS1) into the two arms of the interferometer. The waveguide under test was placed in one arm of the interferometer, and light was in- and out-coupled using microscope objectives. In the reference arm a variable attenuator (A2) was placed to balance the optical power between the two arms of the interferometer. Finally the beams from the two arms were recombined using a second cube beam-splitter (BS2) as shown in the schematic. The polarisation of the input light was made parallel to the z-axis of the crystal. A pinhole with diameter ~ 25 µm was used to sample the interference fringes and to enable the detection of phase shifts as a variation of the transmitted optical power measured by a Si photo-detector. An optical chopper (frequency: 170 Hz) in conjunction with a lock-in-amplifier was used to improve the signal-to-noise ratio (typically ~ 50) of the detection system. A 6.3× microscope objective was also placed to magnify the output interference pattern and hence improve the resolution of the pinhole-detector assembly. The entire experimental setup was on a vibration-isolated table and the interferometric section was covered to minimise the effect of random phase changes caused by air-flow in the two arms of the interferometer. The applied voltage introduces a refractive index change in the waveguide via the electro-optic effect thereby introducing a phase difference between the two arms of the interferometer. This phase difference produces a spatial shift in the interference fringes, and hence a change in detector output. The half-wave voltage V_π (the voltage required to produce a π-phase shift) was measured in this way. This is related

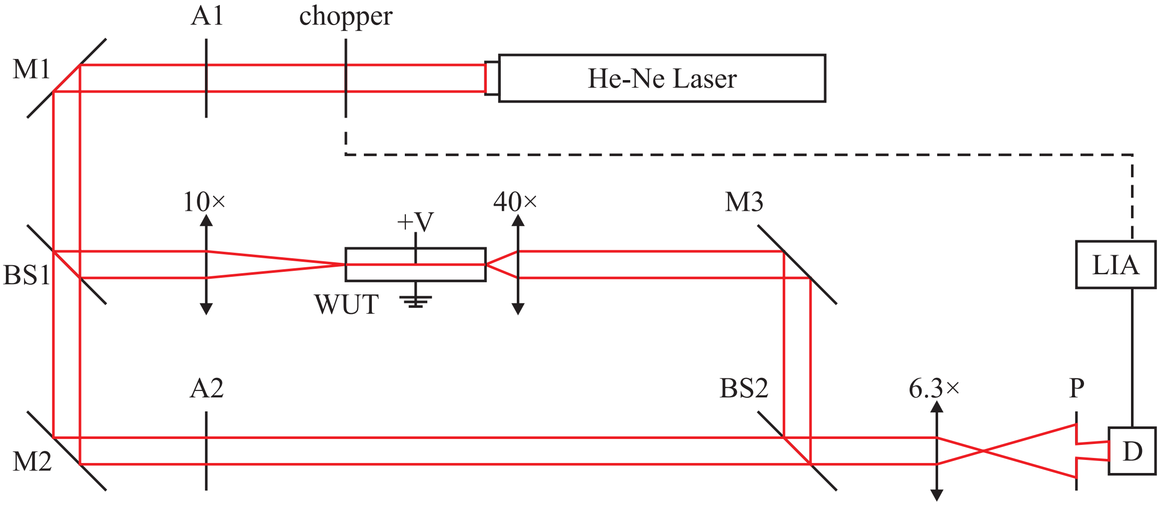

FIGURE 4.15: Experimental setup for the measurement of electro-optic coefficient of the waveguide. (A1, A2 = optical attenuator; M1, M2, M3 = mirrors; BS1, BS2 = beam splitter; WUT = waveguide under test; V = applied voltage; P1, P2 = adjustable pinhole; D = detector; LIA = lock-in amplifier.)

to the r_{33} coefficient of the waveguide by the following equation [Méndez 01, Ducharme 87]

$$r_{33} = \frac{\lambda d}{n_{\text{eff}}^3 L V_\pi} \tag{4.9}$$

where λ is the operating wavelength (632.8 nm); d is the substrate thickness (500 µm); n_{eff} is the effective refractive index of the waveguide; and L is the length of the electrode-covered waveguide section (9 mm). In Eq. 4.9 it was assumed 100% overlapping of the applied electric field with the waveguide propagation mode which is a valid approximation in the present configuration [Wooten 93]. The experiment was repeated for a number of waveguides written with different writing wavelengths and powers, and the r_{33} coefficient for each waveguide was determined by using Eq. 4.9. No phase drift due to optical 'photorefractive' damage was observed over the duration of the measurements.

4.5.3 Results and discussion

The interferometrically measured electro-optic coefficient (r_{33}) of the waveguides written with these four different wavelengths and writing powers (45, 50, 55, 60 mW) are summarised in the graph shown in Fig. 4.16. All the waveguides were written with a writing speed of 1.0 mm s^{-1}. The measurements were performed with a DC applied field at room temperature (20°C), for a probe wavelength of 632.8 nm. Typical variations of normalised detector output with applied voltage are presented in Fig. 4.17 for the waveguides with different writing wavelengths. It may be concluded from these results that the electro-optic coefficient is as low as 14 pm V^{-1} for waveguides written with 305 nm wavelength, but increases with decreasing writing wavelength, to a value (31 pm V^{-1}) that is close to the bulk r_{33} value of the crystal, for 275 nm writing wavelength. It may also be noticed that the electro-optic coefficients of the waveguides are effectively independent of the writing laser powers within the studied experimental range here. For comparison, the r_{33} coefficient of a Ti-indiffused channel waveguide was also measured, using the same experimental apparatus. The measured value of 35 pm V^{-1} is $\sim$ 13% higher than the values for waveguides written with 275 nm wavelength. The AC (upto 10 kHz) electro-optic response of the waveguides was also studied using the same interferometric setup. A DC bias ($0 - 100$ V) was also applied along with the sinusoidal AC signal ($V_{\text{pp}} = 35 - 155$ V) to set the phase difference between the interferometer arms to $\pi/2$, effectively increasing the detection sensitivity. It was observed that within the studied frequency range the frequency response of the UV-written waveguides is similar to that of the Ti-indiffused waveguide.

The reason for the reduction of the electro-optic coefficient at 300, 300, and 305 nm writing wavelengths, is not clearly understood at the moment. Since lithium out-diffused waveguides are known to produce highly efficient electro-optic modulators [Nishihara 89, Kaminow 74], some other mechanisms dominant during waveguide fabrication at these longer writing wavelengths,

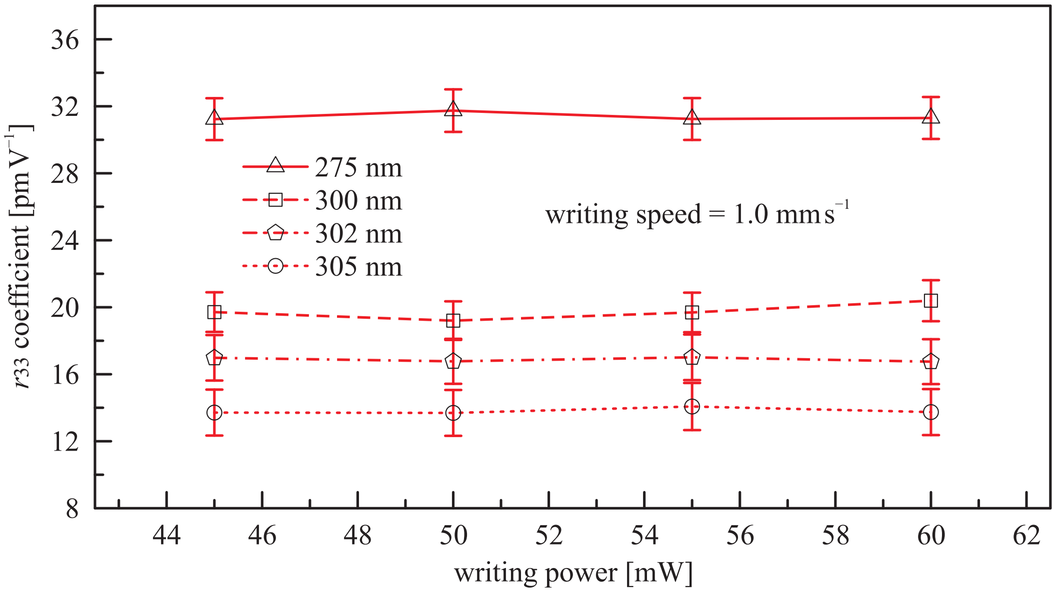

FIGURE 4.16: Measured electro-optic coefficients (r_{33}) of the waveguides for different writing wavelengths and powers.

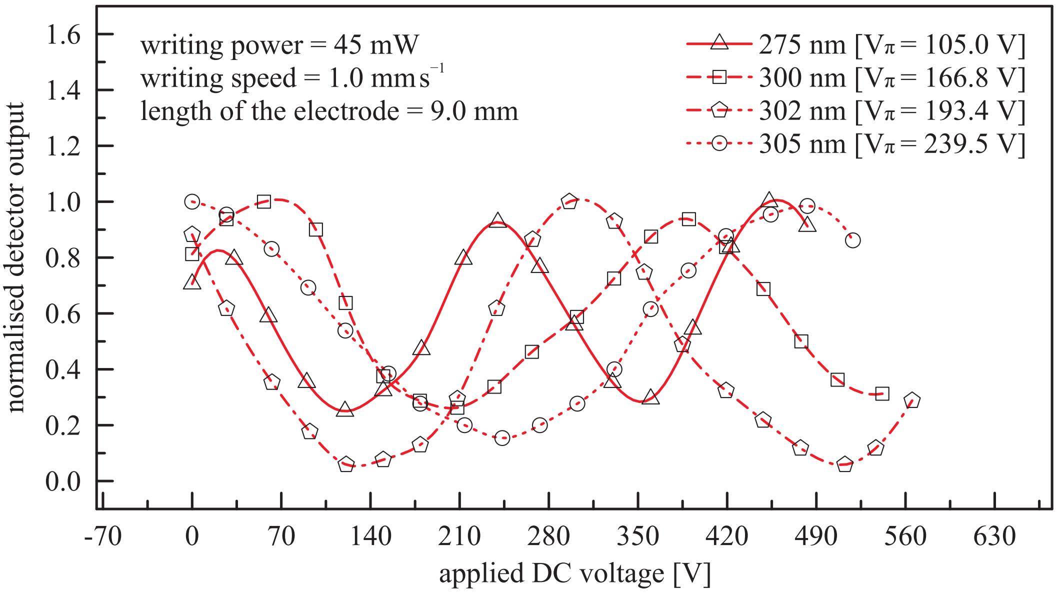

FIGURE 4.17: Variation of normalised detector output with the applied voltages for 275, 300, 302, and 305 nm writing wavelengths of the waveguides.

could possibly be the cause. One such plausible explanation could be due to the formation of all-optically inverted ferroelectric domains within the illuminated region [Muir 08]. The depth of these inverted domain on the $+z$ face at a shorter UV wavelength (244 nm) has been estimated to be of order $30 - 50$ nm. However, the dependence of the depths of such all-optically inverted domain on the writing wavelength has not been studied. The presence of such inverted domains within the waveguide volume will reduce the average phase shift for a given value of the applied voltage which will consequently appear as a reduced EO coefficient. Another possible mechanism which would result in a reduced EO response is damage induced in the crystal by the UV-laser writing step. As the absorption depth for the longer wavelengths is greater, the corresponding damaged volume extends further into the waveguide region, and hence a reduced value for the measured EO coefficient would be obtained for these wavelengths. The UV illuminated tracks were investigated by piezoresponce force microscopy (PFM) in order to identify the cause for the reduction in the EO response. The PFM investigation shown indeed a limited contrast associated with the UV illumination which could be attributed either to a shallow inverted domain or a damaged volume. The PFM results were inconclusive mainly due to the limitation in the depth resolution of the device which is comparable to the dimensions of the waveguiding volume [Johann 09].

4.6 Poling of the UV-written waveguides

4.6.1 Introduction

It should be noted that the writing conditions for UV-written waveguides are very close to those for poling-inhibition as discussed in Chap. 3. Thus, upon domain inversion of the sample that carries UV-written waveguides on the $+z$ face, poling-inhibited domains will form along the UV irradiated tracks overlapping with the waveguides. The effect of this local poling-inhibited domain to the waveguide has been investigated. It was found that after poling, the refractive index contrast of waveguides has been enhanced. The EO response was simulated and measured for the head-to-head domain configuration. And finally, waveguides with local poling-inhibited domains have been etched in HF to develop into ridge waveguides.

4.6.2 Enhanced refractive index contrast after poling

It has been reported in the literature that a refractive index increase is observed in the newly poled region as a consequence of EFP. This refractive index increase has been measured using digital holography [de Angelis 04] and Scanning Near Field Microscopy [Gopalan 07] and is attributed to the internal field which originates from the presence of frustrated defect clusters in the newly inverted domain region. An enhancement of the refractive index of the newly poled area encapsulating the waveguide channel (as in the case of the poling inhibition) is expected to affect negatively the performance of the waveguide by reducing the refractive index contrast between the channel and this newly poled substrate region. Surprisingly, a significant increase was observed in the refractive index contrast of the waveguide channels following the poling-inhibition step rather than a decrease as suggested in the literature. A comparison of the maximum refractive index contrasts for waveguides written with different UV laser intensities

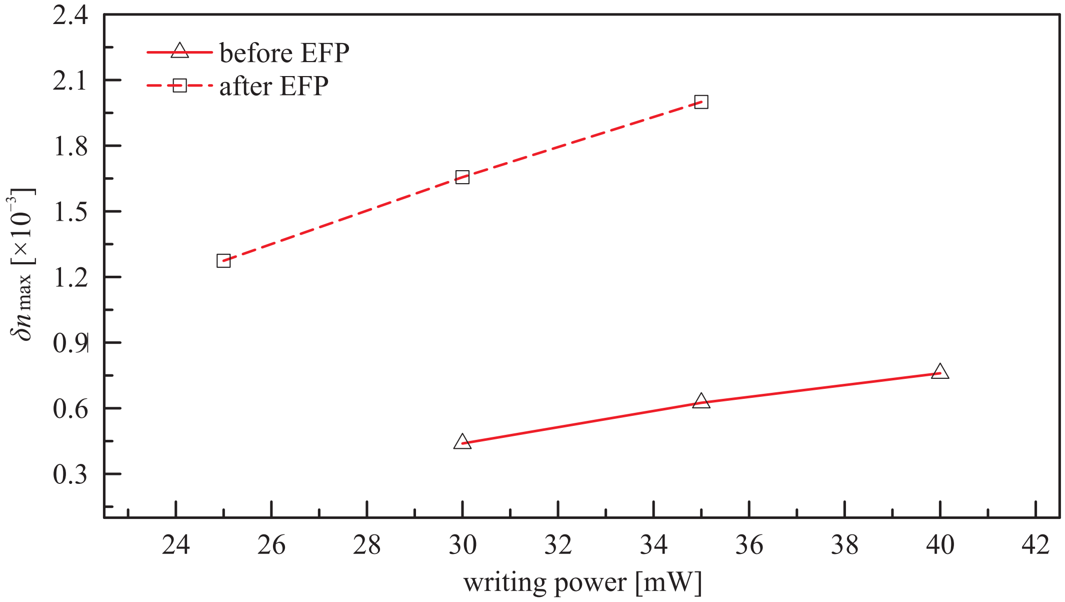

FIGURE 4.18: Plot showing variation of maximum refractive index change before and after EFP.

before and after the EFP step is shown in Fig. 4.18. All of these waveguides were written using the same writing speed ($0.1\ \mathrm{mm\,s^{-1}}$) and spot radius (~ 3 µm). As seen in the plot of Fig. 4.18 at writing power of 30 and 35 mW, a greater than threefold increase in the maximum refractive index contrast of the waveguide channels can be observed after the EFP step. The effect of refractive index contrast enhancement is additionally demonstrated by the observation of waveguide propagation after the EFP step in UV tracks written at low writing power of 25 mW in Fig. 4.18, where the refractive index contrast provided by just UV irradiation alone (prior to the EFP step) was insufficient to support waveguide modes.

An explanation for the experimentally observed enhancement of the refractive index contrast can be provided by a refractive index discontinuity which occurs on the domain boundary as reported in [Gopalan 07]. According to this report the refractive index changes abruptly in the vicinity of the domain boundary. It decreases in the newly poled domain and increases suddenly in the unpoled part of the crystal on the opposite side of the domain boundary. This abrupt refractive index transition takes place within a width ranging from 2 µm to 4 µm and provides the appropriate refractive index profile to explain the observed enhancement of the refractive index contrast within the waveguide.

4.6.3 Electro-optic response of waveguides with local anti-parallel domains

With such an inverted domain configuration in the waveguide region, the effective EO coefficient can suffer a change. Therefore, due to its importance for any application, the EO response of UV-written waveguides that overlapped with poling-inhibited domain regions after poling has

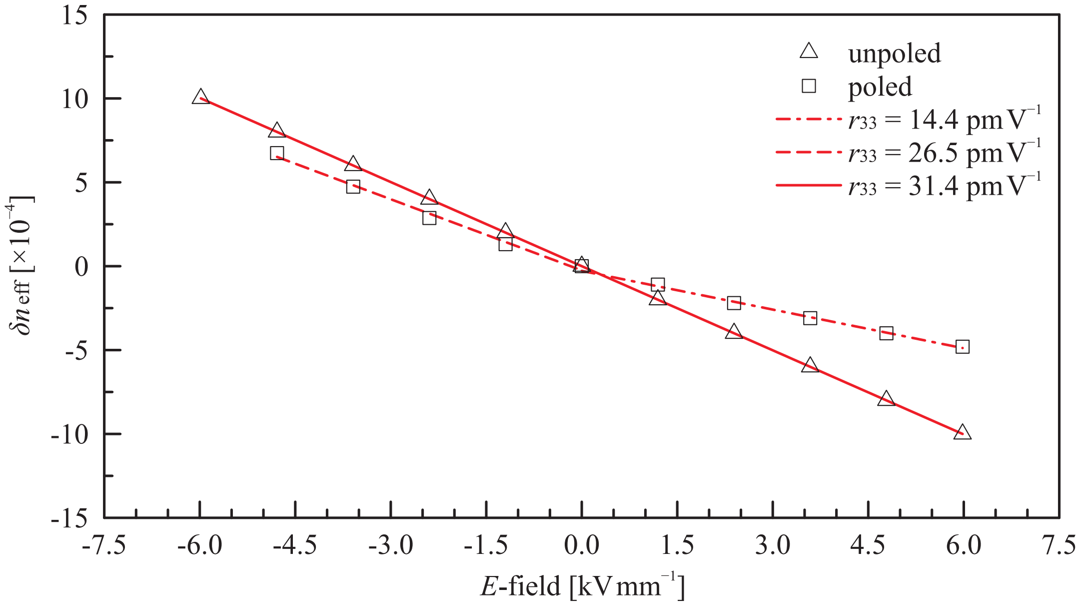

FIGURE 4.19: The change of mode index versus the applied E-field for both unpoled and poled UV-written waveguides.

been simulated by using the software package RSoft. Fig. 4.19 shows the change of mode index versus the applied E-field for both unpoled and poled UV-written waveguides. The effective EO coefficient were derived from: $r_{\mathrm{eff}} = -2\delta n/n^3 E$. It reveals that, for unpoled UV-written waveguides the effective EO coefficient, as expected, equals the bulk EO coefficient, while for poled waveguides, the values are smaller than the bulk, more specifically, 46% and 85% of the bulk value for positive and negative values of applied E-fields respectively. However, preliminary experimental results measured and confirmed a significant enhancement of 50% for the effective EO coefficient for both positive and negative applied E-fields.

4.6.4 Ridge waveguides

Due to the preferential etching of LN crystals, waveguides with a $+z$ face can be further processed via HF etching into ridge waveguides. Ridge waveguide superstructures can provide better lateral confinement of the optical mode due to the much higher index contrast as compared to their conventional counterparts. Additionally, the stronger optical confinement and smaller modal dimensions in such structures should enhance the efficiency of any nonlinear processes. In literature, several different methods have been investigated for the production of ridge waveguides in LN. Most of them utilise an etching step that defines the ridge geometry and a separate waveguide fabrication step [Kaminow 74, Cheng 95, Hu 07] such as the commonly used ion-indiffusion or proton-exchange processes. Delineation of the ridge is achieved either via wet etching in an acid mixture containing HF acid or through dry etching processes such as ion beam milling [Guarino 07] or plasma etching [Noguchi 95]. Acid-based wet etching, based on the differential

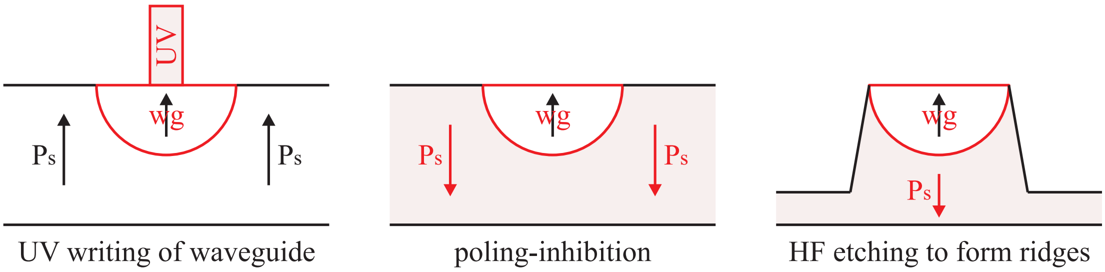

FIGURE 4.20: Schematic of the fabrication process showing the three sequential fabrication steps of UV patterning, EFP, and wet-etching.

etching behavior of the two opposite polar z-faces has also been reported as an alternative approach for defining ridges in domain engineered LN [Barry 99]. The mandatory step required to induce the vertical refractive index contrast either precedes or follows the wet or dry etching process. The compatibility of the two steps is essential and hence a recipe with the appropriate sequential steps has to be adhered to for producing ridge waveguides in this crystal. In all of these approaches, a clean-room based photolithographic step is incorporated to define the ridge on an already produced planar waveguide or to define the waveguide on a pre-structured ridge. In this section, subsequent differential wet etching of the local poling-inhibited domain structures after UV irradiation results in the creation of ridges, which further support already existing optical guided-wave propagation.

As shown in Fig. 4.20, after the second step of poling in the sample that carries the UV-written waveguides, a set of parallel stripes of $+z$ polar surface (poling-inhibited domains) was formed and embedded in a uniform $-z$ polar surface background. The ridge structures are finally produced in the last fabrication step which is wet etching in HF acid. The formation of the ridge structures results from the differential etching between the two opposite polar surfaces of LN in HF acid [Sones 02b]. When the poled samples are etched in HF acid the sets of parallel domains

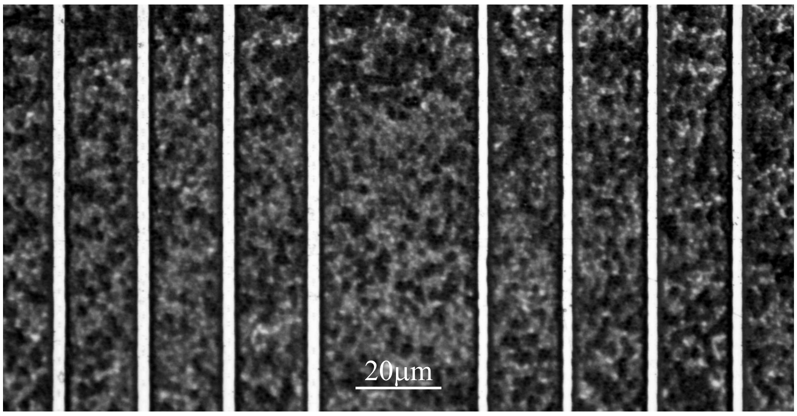

FIGURE 4.21: Optical microscope image of two sets of ridges produced using different UV laser intensities.

with $+z$ orientation act as etch-stop layers whereas the surrounding $-z$ face gradually etches down to reveal sets of parallel ridges.

Fig. 4.21 shows an optical microscope image of two sets of parallel ridges (each set consisting of four ridges corresponding to identical UV writing conditions) formed using this fabrication route. All of the ridges have been produced by UV writing at a speed of 0.1 mm s^{-1}. However, each set of four ridges correspond to a different UV laser intensity. The set on the left of the image has been written with an incident intensity of $\sim$ 0.17 MW cm^{-2} whereas, the set on the right has been written using a slightly lower intensity of $\sim$ 0.14 MW cm^{-2}. A small difference in the writing intensity was observed to influence the width of the poling-inhibited region and hence the width of the corresponding ridges.

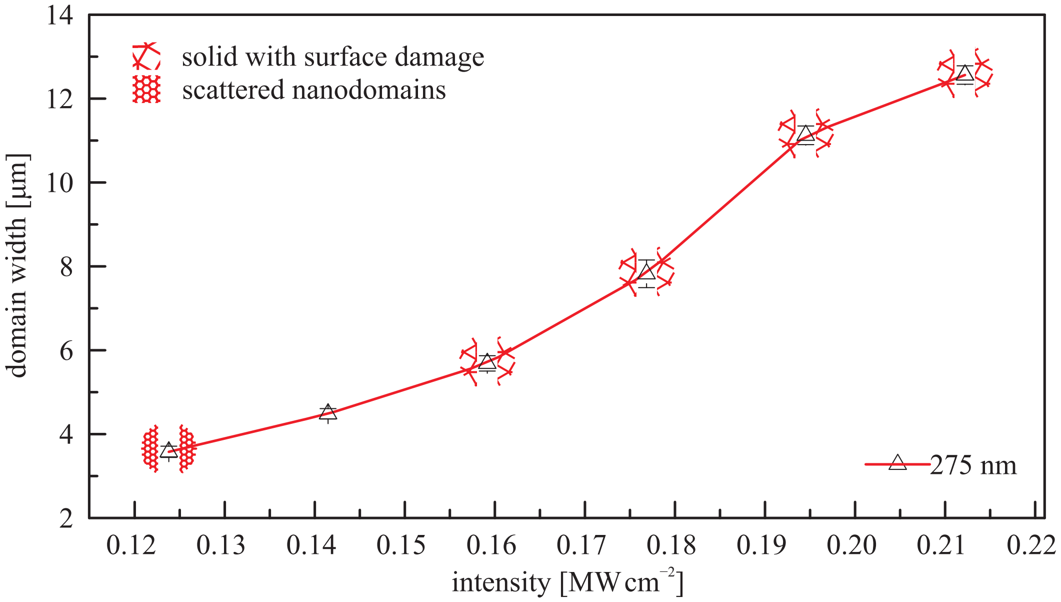

Figure 4.22: Plot of the poling-inhibited domain width as a function of the UV laser intensity with writing λ of 275 nm.

The impact of the laser intensity on the width of the resulting ridges was studied systematically and the results are summarised in Fig. 4.22. The figure shows a plot of the domain width, and hence that of the ridge structure as a function of the UV laser intensity which was used in the relevant fabrication step. As seen in Fig. 4.22 the widths of the poling-inhibited domains are proportional to the UV laser intensity between 0.15 MW cm^{-2} to 0.2 MW cm^{-2}.

Scanning electron microscopy (SEM) images of the cross-sections of ridges were obtained after mechanical polishing of the samples, and typical examples are presented in Fig. 4.23. The ridges in Fig. 4.23(a) and (b) correspond to writing intensities of 0.17 MW cm^{-2} and 0.14 MW cm^{-2} respectively and the difference in their width resulting from this slight variation of the intensity is evident. The symmetric cross-sectional profile of the ridges is a manifestation of them being aligned to the crystallographic y direction. The noticeable roughness of the planar surfaces ($-z$

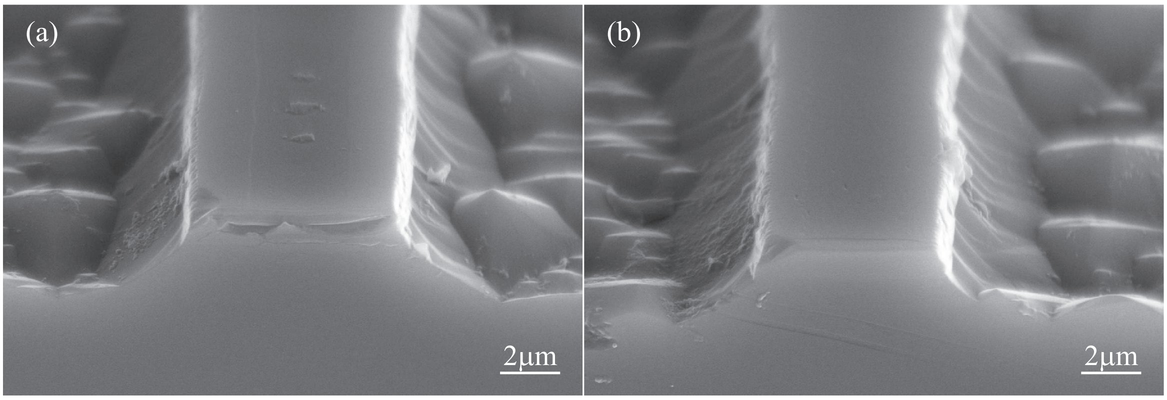

Figure 4.23: SEM images of the polished end faces of two ridges fabricated with different UV laser intensities (SEM image acquired at 60° tilt).

faces) on either sides of the ridge is typical of the etching of $-z$ faces in HF [Sones 02b]. However, the sidewalls of the ridges are sufficiently free of this background surface roughness and hence are not expected to unduly affect the guided optical mode. The UV laser intensity employed during the direct laser writing step also has a significant impact on the quality of the ridge structures. Specifically, UV intensities higher than ~ 0.19 MW cm^{-2} lead to severe damage of the top-surface, whereas intensities lower than ~ 0.13 MW cm^{-2} result in poorly defined ridge side-walls. However, there exists a definite range of intensity that corresponds to the optimum fabrication parameters. After mechanical polishing of the waveguide ends, laser light (633 nm HeNe laser) was end-fire coupled into the ridge waveguides using a microscope objective lens in order to investigate the optical characteristics of the structures. Fig. 4.24 shows the near-field intensity profile collected using a second objective lens that imaged the output face of the ridge on to a CCD camera. This mode profile corresponds to a ridge structure formed using a UV laser intensity of ~ 0.14 MW cm^{-2}.

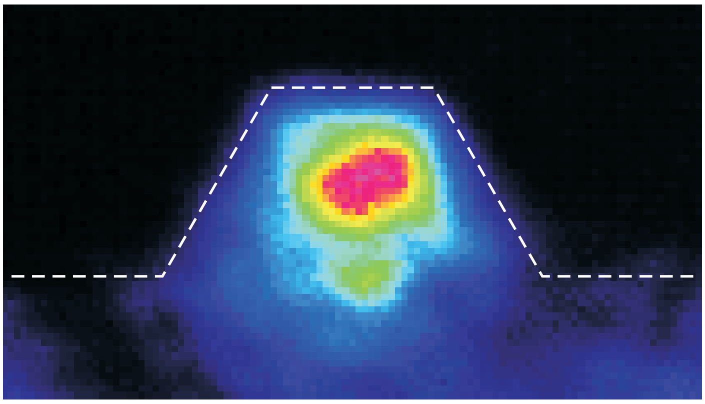

Figure 4.24: Near-field intensity profile obtained at 633 nm. The dashed line outlines the physical shape of the ridge structure.

4.7 Summary

UV-written waveguides using 275 – 305 nm CW laser irradiation were fully investigated. The maximum refractive index change and mode index were determined from the measured near-field intensity distribution, suggesting that for optimum writing conditions a maximum possible refractive index change of ~ 0.0026 can be achieved at a 632.8 nm probe wavelength. The spectral response in the waveguide was measured, from which the cut-off wavelength was derived. Measurements of cut-off wavelengths of the waveguides for different writing powers and writing speeds confirm the existence of optimum writing conditions for maximum refractive index changes of these waveguides. Changes in cut-off wavelengths of the waveguides with applied uniform electric field across the substrate indicate that electro-optic response decreases with increasing writing wavelengths. This experimental observation was verified by measuring the mode-widths, mode-depths, and refractive-index contrasts of the waveguides at various applied voltages. Direct measurements of the unclamped electro-optic coefficients (r_{33}) of the waveguides written with different wavelengths were also performed by an interferometric method. It was observed that the r_{33} coefficient is maximum (31 $\mathrm{pm\,V^{-1}}$) for 275 nm writing wavelength, whereas it is reduced to 14 $\mathrm{pm\,V^{-1}}$ for waveguides written with 305 nm writing wavelength. Upon poling, local poling-inhibited domains were formed at the waveguide region. A threefold enhancement of index contrast was observed and the simulation derived EO response to have r_{33} values of 14.4 and 26.5 $\mathrm{pm\,V^{-1}}$ for positive and negative E-field respectively: promisingly the experimental results however measured an EO coefficient enhancement of 50%. Finally a method for the fabrication of ridge waveguides was demonstrated based on HF etching of the poling-inhibited domains produced following EFP of the UV-written waveguides. The method utilises a continuous wave (CW) UV laser direct writing procedure that provides both the definition of the ridge pattern and the production of the necessary refractive index contrast for vertical confinement in a single step. It can reduce the complexity of fabrication and would be extremely well-suited for the implementation of the dense compact photonic circuits envisaged for future optoelectronic integration technologies. Additionally, the method allows for a straightforward fabrication of arbitrary patterns as allowed by the direct laser writing, which makes it particularly attractive for custom fabrication of photonic micro-structures. Here the fabrication of simple waveguide ridges was demonstrated only as a proof of principle. However it is possible, using this methodology, to create more complex guided-wave superstructures such as ring-resonators and couplers.

References

[Barry 99] I. E. Barry, G. W. Ross, P. G. R. Smith & R. W. Eason, *Ridge waveguides in lithium niobate fabricated by differential etching following spatially selective domain inversion*, Appl. Phys. Lett., vol. 74, no. 10, pages 1487–1488, 1999.

[Born 99] M. Born & E. Wolf, Principles of optics, Cambridge University Press, 1999.

[Burghoff 07] J. Burghoff, C. Grebing, S. Nolte & A. Tunnermann, *Waveguides in lithium niobate fabricated by focused ultrashort laser pulses*, Appl. Surf. Sci., vol. 253, no. 19, pages 7899–7902, 2007.

[Chakraborty 01] R. Chakraborty, P. Ganguly, J. C. Biswas & S. K. Lahiri, *Modal profiles in Ti:*$LiNbO_3$ *two-waveguide and three-waveguide couplers by effective-index-based matrix method*, Opt. Commun., vol. 187, no. 1-3, pages 155–163, 2001.

[Cheng 95] R. S. Cheng, W. L. Chen & W. S. Wang, *Mach-Zehnder modulators with lithium niobate ridge waveguides fabricated by proton-exchange wet etch and nickel indiffusion*, IEEE Photonics Technol. Lett., vol. 7, page 1282, 1995.

[de Angelis 04] M. de Angelis, S. De Nicola, A. Finizio, G. Pierattini, P. Ferraro, S. Grilli & M. Paturzo, *Evaluation of the internal field in lithium niobate ferroelectric domains by an interferometric method*, Appl. Phys. Lett., vol. 85, no. 14, pages 2785–2787, 2004.

[Deshpande 05] D. C. Deshpande, A. P. Malshe, E. A. Stach, V. Radmilovic, D. Alexander, D. Doerr & D. Hirt, *Investigation of femtosecond laser assisted nano and microscale modifications in lithium niobate*, J. Appl. Phys., vol. 97, no. 7, pages 074316–074316–9, 2005.

[Ducharme 87] S. Ducharme, J. Feinberg & R. Neurgaonkar, *Electrooptic and piezoelectric measurements in photorefractive barium titanate and strontium barium niobate*, IEEE J. Quantum Electron., vol. 23, no. 12, pages 2116–2121, 1987.

[Fatadin 06] I. Fatadin, D. Ives & M. Wicks, *Accurate magnified near-field measurement of optical waveguides using a calibrated CCD camera*, J. Lightwave Technol., vol. 24, no. 12, pages 5067–5074, 2006.

[Gallo 07] K. Gallo, C. B. E. Gawith, I. T. Wellington, S. Mailis, R. W. Eason, P. G. R. Smith, D. J. Richardson & S. M. Kostritskii, *Ultraviolet writing of channel waveguides in proton-exchanged* $LiNbO_3$, J. Appl. Phys., vol. 101, no. 1, page 014110, 2007.

[Ganguly 09] P. Ganguly, C. L. Sones, Y. J. Ying, H. Steigerwald, K. Buse, E. Soergel, R. W. Eason & S. Mailis, *Determination of refractive indices from the mode profiles of UV-written channel waveguides in LiNbO*$_3$*-crystals for optimization of writing conditions*, J. Lightwave Technol., vol. 27, no. 16, pages 3490–3497, August 2009.

[Gopalan 07] V. Gopalan, V. Dierolf & D. A. Scrymgeour, *Defect-domain wall interactions in trigonal ferroelectrics*, Ann. Rev. Mater. Res., vol. 37, pages 449–489, 2007.

[Guarino 07] A. Guarino, G. Poberaj, D. Rezzonico, R. Degl'Innocenti & P. Günter, *Electro-optically tunable microring resonators in lithium niobate*, Nat. Photon., vol. 1, no. 7, pages 407–410, July 2007.

[Helms 90] J. Helms, J. Schmidtchen, B. Schüppert & K. Petermann, *Error analysis for refractive-index profile determination from near-field measurements*, J. Lightwave Technol., vol. 8, no. 5, pages 625–633, 1990.

[Hu 07] H. Hu, R. Ricken, W. Sohler & R. B. Wehrspohn, *Lithium niobate ridge waveguides fabricated by wet etching*, IEEE Photonics Technol. Lett., vol. 19, no. 6, pages 417–419, 2007.

[Johann 09] F. Johann, Y. J. Ying, T. Jungk, A. Hoffmann, C. L. Sones, R. W. Eason, S. Mailis & E. Soergel, *Depth resolution of piezoresponse force microscopy*, Appl. Phys. Lett., vol. 94, no. 17, pages 172904–3, April 2009.

[Kaminow 74] I. P. Kaminow, V. Ramaswamy, R. V. Schmidt & E. H. Turner, *Lithium niobate ridge waveguide modulator*, Appl. Phys. Lett., vol. 24, no. 12, pages 622–624, June 1974.

[Lang 94] T. Lang, L. Thévenaz, Z. B. Ren & P. Robert, *Cut-off wavelength measurements of Ti:LiNbO*$_3$ *channel waveguides*, Meas. Sci. Technol., vol. 5, no. 9, pages 1124–1130, 1994. Swiss Federal Inst of Technology, Lausanne, Switz Compilation and indexing terms, Copyright 2008 Elsevier Inc. 94112442169 0957-0233 Cut off wavelengths Polarizers Channel waveguides Electromagnetic attenuation.

[Mailis 03] S. Mailis, C. Riziotis, I. T. Wellington, P. G. R. Smith, C. B. E. Gawith & R. W. Eason, *Direct ultraviolet writing of channel waveguides in congruent lithium niobate single crystals*, Opt. Lett., vol. 28, no. 16, pages 1433–1435, 2003.

[Mansour 96] I. Mansour & F. Caccavale, *An improved procedure to calculate the refractive index profile from the measured near-field intensity*, J. Lightwave Technol., vol. 14, no. 3, pages 423–428, 1996.

[McCaughan 83] L. McCaughan & E. E. Bergmann, *Index distribution of optical waveguides from their mode profile*, J. Lightwave Technol., vol. 1, pages 241–244, 1983.

[McConaghy 95] C. F. McConaghy, K. F. Hunenberg, D. Sweider, M. Lowry & R. A. Becker, *White light spectral analysis of lithium niobate waveguides*, J. Lightwave Technol., vol. 13, no. 1, pages 83–87, 1995.

[Méndez 01] A. Méndez, G. de la Paliza, A. García-Cabañes & J. M. Cabrera, *Comparison of the electro-optic coefficient* r_{33} *in well-defined phases of proton exchanged* $LiNbO_3$ *waveguides*, Appl. Phys. B, vol. 73, no. 5, pages 485–488, October 2001.

[Muir 06] A. C. Muir, G. J. Daniell, C. P. Please, I. T. Wellington, S. Mailis & R. W. Eason, *Modelling the formation of optical waveguides produced in* $LiNbO_3$ *by laser induced thermal diffusion of lithium ions*, Appl. Phys. A, vol. 83, no. 3, pages 389–396, 2006.

[Muir 08] A. C. Muir, C. L. Sones, S. Mailis, R. W. Eason, T. Jungk, A. Hoffman & E. Soergel, *Direct-writing of inverted domains in lithium niobate using a continuous wave ultra violet laser*, Opt. Express, vol. 16, no. 4, pages 2336–2350, February 2008.

[Nishihara 89] H. Nishihara, M. Haruna & T. Suhara, Optical integrated circuits, McGraw-Hill, 1989.

[Noguchi 95] K. Noguchi, O. Mitomi, H. Miyazawa & S. Seki, *A broadband Ti:*$LiNbO_3$ *optical modulator with a ridge structure*, J. Lightwave Technol., vol. 13, no. 6, pages 1164–1168, 1995.

[Redfield 74] D. Redfield & W. J. Burke, *Optical-absorption edge of* $LiNbO_3$, J. Appl. Phys., vol. 45, no. 10, pages 4566–4571, 1974.

[Ródenas 07] A. Ródenas, D. Jaque, C. Molpeceres, S. Lauzurica, J. L. Ocaña, G. A. Torchia & F. Agulló-Rueda, *Ultraviolet nanosecond laser-assisted micro-modifications in lithium niobate monitored by* Nd^{3+} *luminescence*, Appl. Phys. A, vol. 87, no. 1, pages 87–90, April 2007.

[Schlarb 93] U. Schlarb & K. Betzier, *Refractive indices of lithium niobate as a function of wavelength and composition*, J. Appl. Phys., vol. 73, pages 3472–3476, 1993.

[Sohler 08] W. Sohler, H. Hu, R. Ricken, V. Quiring, C. Vannahme, H. Herrmann, D. Büchter, S. Reza, W. Grundkötter, S. Orlov, H. Suche, R. Nouroozi & Y. Min, *Integrated optical devices in lithium niobate*, Opt. Photonics News, vol. 19, pages 24–31, 2008.

[Sones 02a] C. Sones, S. Mailis, V. Apostolopoulos, I. E. Barry, C. Gawith, P. G. R. Smith & R. W. Eason, *Fabrication of piezoelectric micro-cantilevers in domain-engineered $LiNbO_3$ single crystals*, J. Micromech. Microeng., vol. 12, no. 1, pages 53–57, 2002.

[Sones 02b] C. L. Sones, S. Mailis, W. S. Brocklesby, R. W. Eason & J. R. Owen, *Differential etch rates in z-cut $LiNbO_3$ for variable HF/HNO_3 concentrations*, J. Mater. Chem., vol. 12, no. 2, pages 295–298, 2002.

[Sones 08] C. L. Sones, A. C. Muir, Y. J. Ying, S. Mailis, R. W. Eason, T. Jungk, Á. Hoffmann & E. Soergel, *Precision nanoscale domain engineering of lithium niobate via UV laser induced inhibition of poling*, Appl. Phys. Lett., vol. 92, no. 7, page 072905, 2008.

[van Leeuwen 84] K. A. H. van Leeuwen & H. T. Nijnuis, *Measurement of higher-order mode attenuation in single-mode fibers: effective cutoff wavelength*, Opt. Lett., vol. 9, no. 6, pages 252–254, June 1984.

[Weis 85] R. S. Weis & T. K. Gaylord, *Lithium niobate: summary of physical properties and crystal structure*, Appl. Phys. A, vol. 37, no. 4, pages 191–203, August 1985.

[Wooten 93] E. L. Wooten & W. S. C. Chang, *Test structures for characterization of electrooptic waveguide modulators in lithium niobate*, IEEE J. Quantum Electron., vol. 29, no. 1, pages 161–170, 1993.

5

$LiNbO_3$ whispering gallery mode resonators

5.1 Introduction

Optical microresonators have numerous applications in photonics. The thermal-reflow process (or hot embossing) has been used to reduce significantly sidewall surface roughness in polymer (polystyrene) microring resonators [Chao 04a, Chao 04b], and this is clearly a very useful technique because it enables post-fabrication fine-tuning of microresonator performance. However, for the fabrication of complex, multilayer devices this procedure is less useful as the high temperatures needed to reflow the polymer film could also disturb lower cladding layers and possibly alter optically active dopant molecules. Recently, a process for producing silica toroidal-shaped microresonators-on-a-chip with Q factors in excess of 10^8 by using a combination of lithography, dry etching and a selective reflow process has been demonstrated [Armani 03]. By selectively heating and reflowing a patterned and undercut microdisk with the use of a CO_2 laser, a toroidal resonator with an atomically smooth surface was obtained. However, bulk melting is obviously not suitable for materials with an underlying crystalline structure because it destroys the initial crystal properties and possibly stoichiometry. Moreover, during solidification, the original spherical droplet of the melt may turn into an irregularly shaped structure with multiple facets and crystal growth steps.

This chapter presents a fabrication method of LN microresonators based on the surface melting at the temperature close to, but below, the melting point to surface-reshape the micro-structured crystalline LN by surface tension, which can produce ultra-smooth surfaces while maintaining the useful crystalline properties. There are many existing works on the theory and reviews of whispering gallery resonators including [Stratton 07, Snyder 83, Barber 88, Chang 96, Fields 00, Datsyuk 01, Oraevsky 02, Vahala 03, Benson 06]. In the first several sections of the chapter, the whispering gallery mode (WGM) theory, characterisation, structures, coupling, pumping, materials and fabrication, are briefly introduced. Following this, the fabrication process that includes three steps of domain engineering, deep HF etching and thermal treatment is described. Crystal quality after thermal treatment was investigated by piezoresponse force microscopy (PFM), micro-Raman and preferential HF etching that confirmed the as-virgin-bulk single crystalline property. Preliminary optical characterisation then was performed on such a resonator structure after thermal treatment.

5.2 Whispering gallery modes

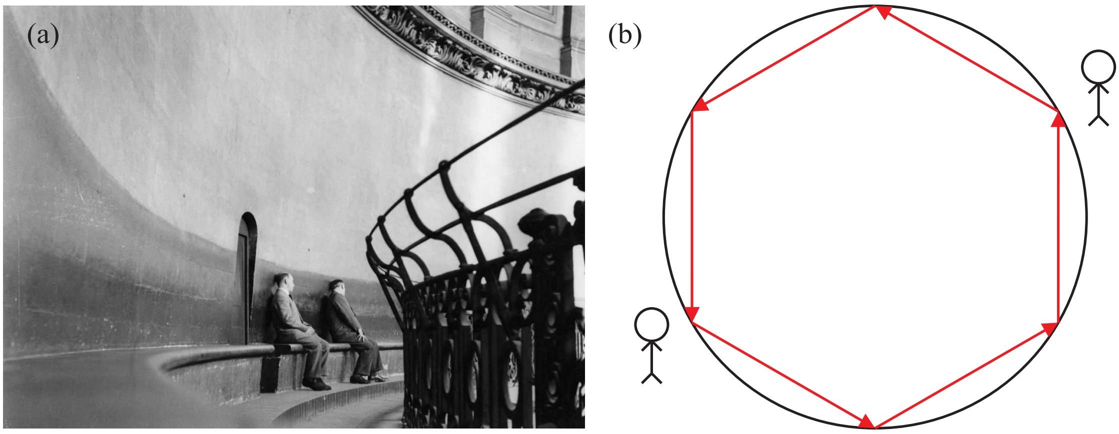

FIGURE 5.1: (a): the circular wall in St. Paul's Cathedral where the whispering-gallery mode was first discovered. (b): illustration of propagation path of acoustic waves along the circular wall with diameter of 42 m.

Whispering-gallery modes (WGM) are found in circular path resonant cavities. The WGM was discovered in 1910 when Lord Rayleigh was conducting experiments on acoustic waves in the dome of St. Paul's Cathedral as shown in Fig. 5.1 [Rayleigh 12]. The experiment is to investigate the sound propagation of the speaker in the oval shaped dome in the cathedral. The distant listeners at specific locations were able to hear the whispering voice of the speaker from the dome in the cathedral. This whispering sound was described as an acoustic wave traveling along the wall path. Generalised properties of electromagnetic resonances in dielectric spheres were widely discussed afterwards, with emphasis on the microwave, not yet optical, modes of the spheres [Gastine 67, Affolter 73]. The first observations of WGMs in optics, optical whispering gallery resonators (WGR), can be attributed to solid-state WGM lasers. Laser action has been studied in $Sm:CaF_2$ crystalline resonators [Garrett 61], whose size was in the millimeter range. Pulsed laser operation due to complete internal reflection in a ruby ring at room temperature has been observed [Walsh 63]. Short-lived transient oscillations rather than spikes in the laser output were explained by assuming a WGM Q of 10^8 to 10^9.

Optical whispering-gallery resonators trap light in compact volumes by the mechanisms of total internal reflection (TIR) of the light beam between the guiding medium and the surrounding medium with the resonance condition achieved via mode wavefront matching per round trip. Therefore, optical whispering gallery resonators enable light amplification, and select out specific (resonant) frequencies of light that can be emitted or coupled into optical guides, and can thereby lower the thresholds for lasing. Recent resonators have radii from 1 to 100 µm (microresonators) and can be fabricated in a wide range of materials. Optoelectronic devices based on optical microresonators that strongly confine photons form a basis for next-generation compact-size, low-power and high-speed photonic circuits. By tailoring the resonator shape, size or material composition, the microresonator can be tuned to support a spectrum of optical modes with the required polarisation, frequency and emission patterns. This offers the potential for developing new types of photonic devices such as light emitting diodes, low-threshold microlasers [Sandoghdar 96, McCall 92, Spillane 02], ultra-small optical filters [Jiao 87] and switches [Blom 97] for wavelength-division-multiplexed (WDM) networks, color displays, etc. Furthermore, novel designs of microresonators open up very challenging fundamental science applications beyond optoelectronic device technologies. The interaction of active or reactive material with the modal fields of optical microresonators provides key physical models for basic research [Yokoyama 92, Yamamoto 93, Chang 96, Vahala 03] such as cavity quantum electrodynamics (QED) experiments [Klitzing 01], spontaneous emission control [Yokoyama 95], nonlinear optics, bio chemical sensing [Chao 03] and quantum information processing. Microresonator characterisation, structures, coupling and lasing are briefly introduced in the next sections.

5.3 Characterisation of whispering gallery resonators

For various applications it is often critical to realise a microresonator with compact size (small modal volume), low loss (high mode quality factor), and large free spectral range (FSR).

5.3.1 Mode volume

Basic properties of a WGR include its geometrical characteristics of the field localisation (mode volume). Mode volume (V_m) is defined as the integral of $E^2\delta v$ in the resonator [Kriezis 92]

$$V_\mathrm{m} = \int E^2 \,\mathrm{d}v \tag{5.1}$$

The volume of WGMs is an especially important parameter for nonlinear applications of the resonators [Braginsky 89]. Also while using resonators as lasers which provide gain through interaction of active atoms with trapped waveforms, the number of active atoms, being a measure of the gain, depends on the mode volume. The comparative characteristics of volumes of WGMs in various kinds of WGRs can be found in [Spillane 05, Kippenberg 04, Vahala 03]. WGMs with the smallest mode volumes, close to one cubic wavelength, were realised in photonic crystal resonators [Painter 99, Srinivasan 04], disordered media resonators [Srinivasan 04], microdisks [Gayral 99, Gayral 00], and microrings [Little 98]. It should be noted that although ultra-compact microresonators enable large-scale integration and single-mode operation for a broad range of wavelengths, such miniature resonators have much smaller Q-factors than bigger WGM resonators.

5.3.2 Quality factor

Q-factor of an optical resonator is a measure of the resonator capacity to circulate and store light. There are actually two different common definitions of the Q factor of a resonator. The first definition is the ratio of the energy stored to the energy dissipated in the microresonator: the Q factor is 2π times the ratio of the stored energy to the energy dissipated per oscillation cycle, or equivalently the ratio of the stored energy to the energy dissipated per radian of the oscillation. For a microwave or optical resonator, one oscillation cycle is understood as corresponding to the field oscillation period, not the round-trip period. Therefore, Q factor can be expressed as

$$Q = -\frac{2\pi f_0 \varepsilon}{\mathrm{d}\varepsilon/\mathrm{d}t} \tag{5.2}$$

where f_0 is the resonance frequency; ε is the stored energy in the cavity.

In practical device applications, the high Q of the microresonator mode translates into a narrow resonance linewidth, long decay time, and high optical intensity. Thus, Q factor can also be defined via resonance bandwidth: as indicated in Fig. 5.2 the Q factor is the ratio of the resonance frequency f_0 and the full width at half-maximum (FWHM) bandwidth δf_{FWHM} of the resonance

$$Q = \frac{f_0}{\delta f_{\mathrm{FWHM}}} = \frac{\lambda_0}{\delta \lambda_{\mathrm{FWHM}}} \tag{5.3}$$

Both definitions are equivalent only in the limit of weakly damped oscillations, i.e. for high Q values. Some other important relations relating Q factor to other quantities involve:

1. The average lifetime of a resonant photon in the cavity is proportional to the cavity Q. The Q factor equals 2π times the exponential decay time of the stored energy times the optical frequency.

2. The Q factor equals 2π times the number of oscillation periods required for the stored energy to decay to e^{-1} ($\sim 37\%$) of its initial value.

3. The Q factor of an optical resonator equals the finesse times the optical frequency divided by the free spectral range.

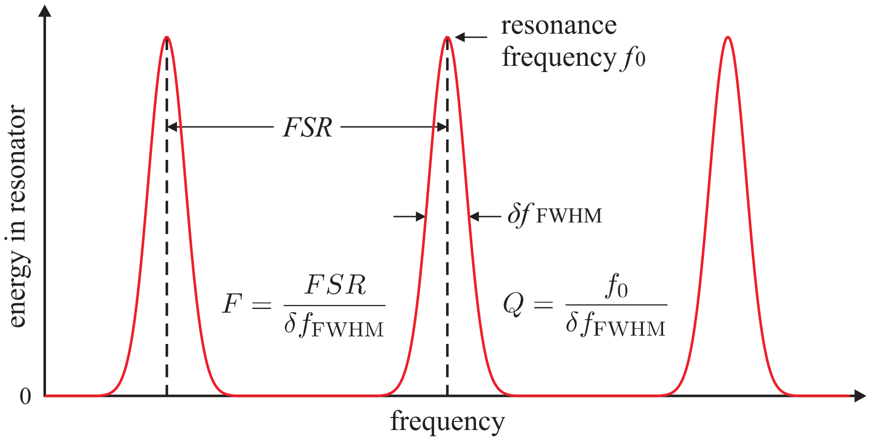

FIGURE 5.2: The energy in the resonator versus frequency in the resonator. The resonance frequency f_0, its full width at half-maximum (FWHM) bandwidth δf_{FWHM}, Q factor Q, finesse F, and free spectral range FSR are indicated.

High-Q optical resonators have various applications in fundamental research (e.g., in quantum optics) and also in telecommunications (i.e. as optical filters for separating WDM channels). Also, high-Q reference cavities are used in frequency metrology, i.e. for optical frequency standards. The Q factor then influences the precision with which the optical frequency of a laser can be stabilised to a cavity resonance. When the Q factor of a laser resonator is abruptly increased, an intense laser pulse (giant pulse) can be generated. This method is called *Q switching* . The ratio Q/V_{m} determines the strength of various light-matter interactions in the microresonator, i.e., enhancement of the spontaneous emission rate, and should be maximised for microlaser applications and QED experiments. However, high-Q microresonators of optical-wavelength size (small V_{m}) are difficult to fabricate, as the WG-mode Q-factor decreases exponentially with the cavity size, and thus in general the demands for a high Q-factor and compactness (large FSR, small V_{m}) are contradictory. Possibilities for achieving very high Q values lie with toroidal silica microcavities with dimensions of the order of 100 µm and Q factors well above 10^8 [Armani 03], and silica microspheres with whispering gallery resonator modes exhibiting Q factors around 10^{10} [Lefevre-Seguin 99].

5.3.3 Free spectral range and finesse

The free spectral range (FSR) of an optical resonator (cavity) is the spacing between neighboring high-Q resonances as shown in Fig. 5.2. Wide FSR is often required to accommodate many WDM channels within the erbium amplifier communications window. The finesse of an optical resonator (cavity) is defined as its free spectral range divided by the (full width at half-maximum) bandwidth of one resonance as:

$$F = \frac{FSR}{\delta f_{\text{FWHM}}} \tag{5.4}$$

It is fully determined by the resonator losses and is independent of the resonator length. If a fraction ρ of the circulating power is remaining after one round-trip (i.e., a fraction $1-\rho$ of the power is lost) when there is no incident field from outside the resonator, the finesse is

$$F = \frac{2\pi}{1-\rho} \tag{5.5}$$

where the approximation holds for low losses (i.e. for high finesse).

A high finesse can be useful for optical spectrum analysis, because it allows the combination of a large free spectral range with a small resonator bandwidth. Therefore, a high spectral resolution in a wide spectral range is possible. A very high finesse (above 10^6) can be achieved in certain microcavities based on whispering gallery modes.

5.4 Optical resonator structures

The spectra of optical modes supported by microresonators are shape and size dependent. A very wide range of microresonator shapes has been explored over the years for various applications. Fig. 5.3 lists some of the most popular optical microresonator types using TIR as light confinement, as well as their modal field intensity distribution and basic features. The most widely used are rotationally symmetric structures such as spheres, cylinders, toroids, and disks, which have been shown to support very high-Q whispering-gallery modes whose modal field intensity distribution is concentrated near the dielectric-air interface [Benson 06].

Silica microspheres [Fig. 5.3(a)] exhibit the highest ($\sim 9\times10^9$) Q-factors [Vernooy 98, Laine 01, Braginsky 89, Gorodetsky 96, Lefevre-Seguin 97], yet have a very dense spectrum of multiple-degenerate WGM, which complicates their application for spectral analysis or laser stabilisation.

Recently proposed micro-toroidal resonators [Fig. 5.3(b)] [Ilchenko 01, Armani 03, Vahala 03, Polman 04] not only demonstrate very high WGM Q-factors approaching those of microspheres but also enable reduction of WGM volume, increase of resonator FSR, and on-chip integration with other components.

Circular high-index-contrast microring and microdisk resonators [Fig. 5.3(c)] based on planar waveguide technology with diameters as small as $1-10$ µm are able to support strongly-confined WGM with typical Q-factors of 10^4-10^5 and are widely used as microlaser cavities [Levi 93, Baba 97b, Cao 00, Zhang 96] and add/drop filters for WDM networks [Hagness 97, Little 97, Little 99, Chin 99, Kippenberg 03, Savchenkov 04]. Recently, record Q-factors have been demonstrated in wedge-edge microdisk resonators (Q in excess of 10^6 [Kippenberg 03]) and in polished crystalline microcavities ($Q > 10^{10}$ [Savchenkov 04]).

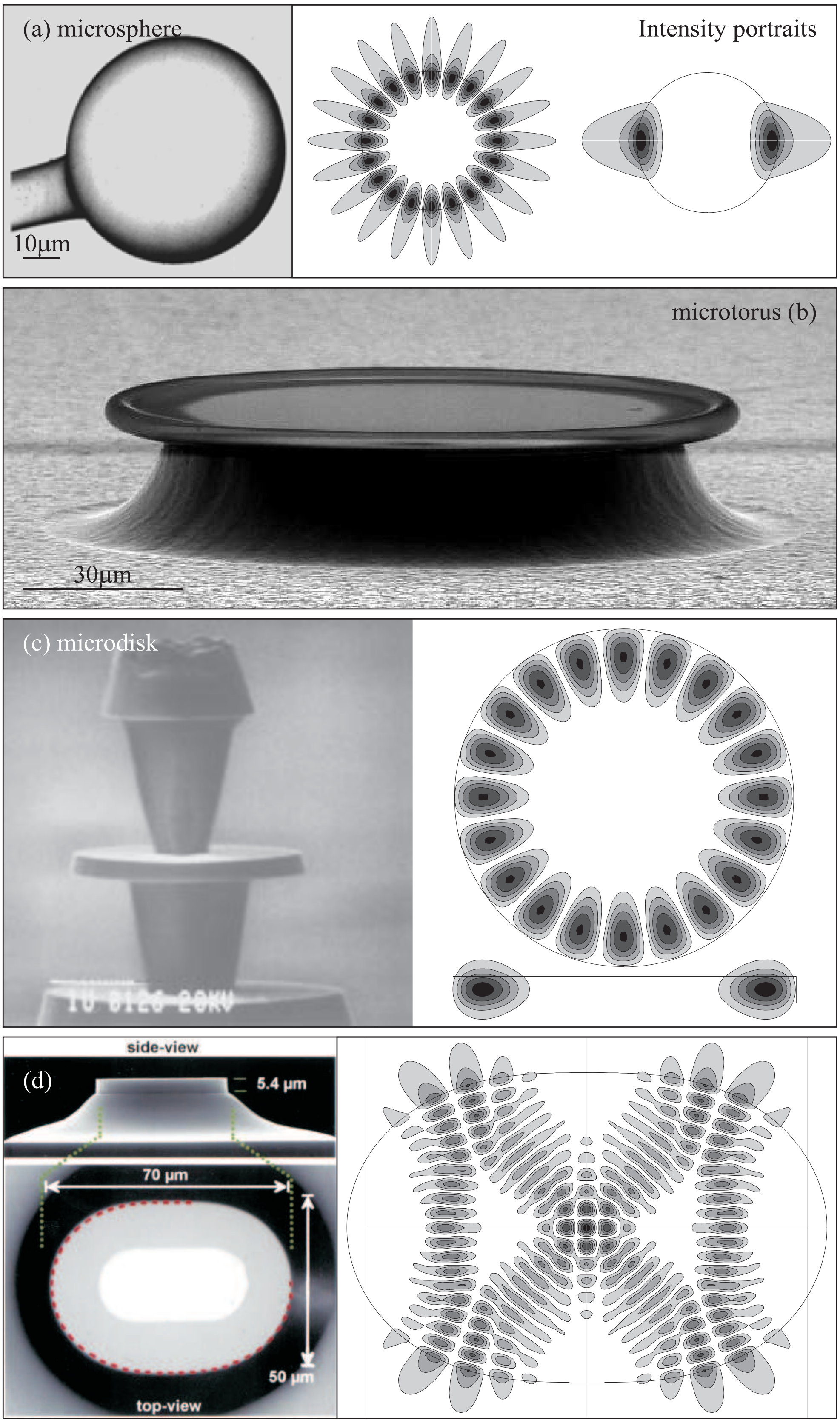

FIGURE 5.3: Types of optical microresonators summarised in [Benson 06]. (a): microspheres and I of $\mathrm{WG}_{10,1}$ mode: $Q = 10^7 - 9 \times 10^9$, large V_m, dense model spectrum, challenging on-chip integration. (b): microtorus: $Q = 5 \times 10^8$, $V_\mathrm{m} <$ spheres, reduced azimuthal-mode spectrum, suitable for on-chip integration. (c): microdisk (microring) and I of $\mathrm{WG}_{10,1}$ mode: $Q = 10^4 - 10^5$, small V_m, higher-radial-order WGM eliminated, suitable for planner integration. (d): quadrupolar and bow-tie mode: $Q = 850 - 1500$, highly directional emission, high FSR of the bow-tie modes, efficient coupling to planner waveguides.

Along with circular microdisk resonators, cavities of elliptical [Noeckel 94, Backes 99, Boriskina 03, Kim 04], quadrupolar [Noeckel 94, Gmachl 98, Fukushima 04, Gianordoli 00, Chin 99] and square [Poon 01, Ling 03, Manolatou 99, Hammer 02, Fong 03, Guo 03, Boriskina 04, Boriskina 05] shapes have attracted much interest. Depending on their size and degree of deformation, these microresonators can support several types of optical modes with significantly different Q-factors, near-field intensity distributions, and emission patterns: bow-tie modes in quadrupoles in Fig. 5.3(d), distorted WG modes, volume and two-bounce oscillations, etc. Such resonators offer advantage for various filter and laser applications as they provide splitting of the doubly-degenerate WG modes, directional light emission and more efficient microresonator-to-straight-waveguide coupling.

5.5 Microresonator coupling techniques

One of the most difficult challenges in the design and fabrication of integrated microresonator-based photonic devices and systems is the efficient coupling of light into and out of a microresonator without compromising its narrow resonance linewidth. Furthermore, the cost and robustness of fabrication, simplicity of the microresonator-to-coupler alignment, as well as ability to provide on-chip integration are very important factors in the development of advanced microresonator couplers. Actually, the WGR-based devices became commercially available [Little 04] only recently, because of a well-developed waveguide coupling technique.

Free-beam optics does not allow efficient coupling with ultra-high-Q WGMs in large enough resonators. Such coupling relies upon radiative exchange of a WGM with external space. This radiative exchange is extremely small and simply negligible in the vast majority of experiments. The efficiency of optical power transfer in/out of a microresonator is actually controlled by 1) manipulating the overlap between the resonator and coupler mode fields, 2) matching of the mode propagation constants (phase synchronisation), or 3) changing the length of the evanescent-field coupling region. The efficient coupling to the microresonators can be achieved by various evanescent techniques, such as the following:

1. prism coupling [Fig. 5.4(a)]: the light was directed to the surface of the prism to achieve the total internal reflection. The evanescent field was presented at the surface and was coupled into the spherical resonator [Braginsky 89, Gorodetsky 94, Collot 93].
2. tapered fibre coupling [Fig. 5.4(b)]: the fibre was heated and stretched to achieve a very thin coupling region. Light traveled along the silica waist and coupled the evanescent field to the resonator that was in close proximity [Knight 97].
3. angle-polished fibre coupling [Fig. 5.4(c)]: it combines the use of an optical fibre and the advantage of the prism coupling method. The core-guided wave undergoes total internal

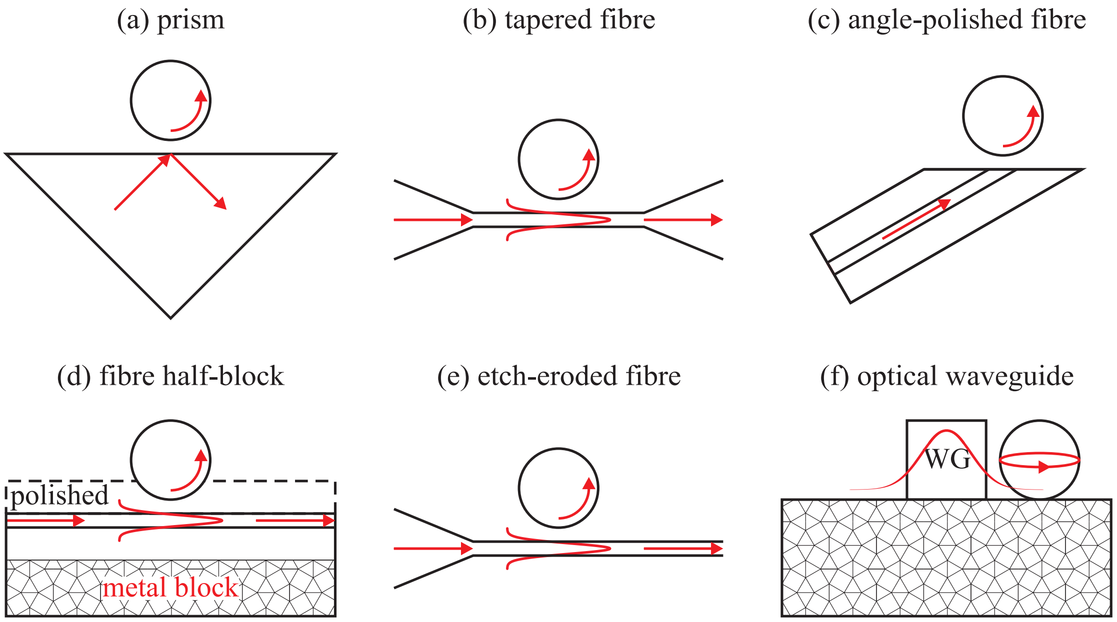

FIGURE 5.4: Various types of microresonator coupling devices. (a): prism coupling. (b): tapered fibre coupling. (c): angle-polished fibre coupling. (d): fibre half-block coupling. (e): etch-eroded fibre coupling. (f): optical waveguide coupling.

reflection, however, it is more convenient since the evanescent field at the angle-polished tip of the fibre is generated from the light that propagates through the fibre [Ilchenko 99].

4. fibre half-block coupling [Fig. 5.4(d)]: a polished-to-core optical fibre is buried in a metal block which allows the resonator to interact directly with the evanescent field from the fibre core [Knight 95, Serpengüzel 95, Griffel 96, Dubreuil 95].

5. etch-eroded fibre coupling [Fig. 5.4(e)]: the fibre cladding was chemically eroded, by using hydrofluoric acid as an etching solution, so that the core of the fibre could be exposed fully. The interaction of the evanescent fields will take place only at the core of the coupling region [Laine 99].

6. waveguide coupling [Fig. 5.4(f)]: it provides a better coupling structure for complex circuit integration with microdisk and microring resonators [Little 00, Laine 00, Yariv 99].

Each of the methods requires careful alignment, because the gap between the microsphere and the prism has to be at an optimum to achieve high coupling efficiency.

5.6 WGM lasers

Lasers belong to one of the most obvious applications of WGRs. The high quality factor of the resonators allows for significant reduction of the lasing threshold. Additionally, narrow linewidths of

WGMs warrant narrow spectral characteristics of the lasers. The first WGM lasers were realised in solid materials [Garrett 61, Walsh 63, Roess 64]. The essential elements of the laser system consist of the laser medium, pumping process, and feedback element. The population inversion occurs when the atoms are pumped from the ground level of the system to the upper level. Laser action is obtained when the atoms decay from the metastable level to the lower level by stimulated emission. Microresonators, microsphere particles and microdroplets, doped with rare-earth (or lanthanide) ions or dyes, exhibit laser action when these active impurities in the host material are excited. Rare-earth ions in the form of trivalent ions such as neodymium (Nd^{3+}), thulium (Tm^{3+}), praesodymium (Pr^{3+}), erbium (Er^{3+}) and ytterbium (Yb^{3+}) are widely used as dopants, while the well known host materials in use are glasses and crystals.

5.7 $LiNbO_3$ WGM resonators

Progress in the design and fabrication of high-quality optical microresonators is closely related to the development of novel optical materials and technologies. The key material systems used for microresonator fabrication include silica, silica on silicon, silicon, silicon on insulator, silicon nitride and oxynitride, polymers, semiconductors such as GaAs, InP, GaInAsP, GaN, etc, and crystalline materials such as lithium niobate and calcium fluoride. Of course, GaAs, InP, and GaN- based semiconductors have attracted much attention as the materials for microresonator device fabrication [Baba 97a, Gianordoli 00, Grover 01], as they enable very compact resonator structures that can perform passive (coupling, splitting and multiplexing) and active (light generation, amplification, detection, modulation) functions in the same material system. Other attractive materials for high-Q microresonator fabrication, which combine a wide optical transparency window, a good electro-optic coefficient and nonlinearity, are crystalline materials such as lithium niobate [Savchenkov 05] which is the main investigated material of this thesis.

5.7.1 Q factor considerations

Crystalline materials could theoretically exhibit higher Q factors as they have a perfect lattice without the imperfections, inclusions, and inhomogeneities that are always present in amorphous materials and which can be sources of optical power loss. The window of transparency for many crystalline materials is also much wider than amorphous materials. Therefore, with sufficiently high purity material, much smaller attenuation in the middle of the transparency window can be expected as both the Rayleigh scattering edge and the multi-phonon absorption edge are pushed further apart towards the ultraviolet and infrared regions, respectively. Moreover, crystals may suffer fewer, or no, extrinsic absorption caused by chemisorption of OH^- ions and water [Benabid 99]. For LN crystals, high $Q \sim 2 \times 10^8$ at $\lambda = 2.014$ µm ($\alpha \leq 5 \times 10^{-4}$ cm^{-1}) has been reported for a multiple total-internal-reflection resonator [Serkland 94]. The same value of Q at $\lambda = 1.3$ µm was obtained in a polished disk resonator [Savchenkov 04].

5.7.2 Nonlinear applications

Apart from the high Q provided by the optical crystals, the motivation behind LN WGM resonators is also to utilise the signal stored at resonance within the cavity to enhance the efficiency of nonlinear optical processes such as nonlinear frequency generation. For a second order nonlinear optical process in the small signal regime, the conversion efficiency is proportional to the fundamental intensity and the square of the propagation length within the optical device. Obviously, higher efficiency for this kind of process in traditional linear devices requires a longer length that imposes a limitation for integration with any other micro-optical systems. However, high Q within a microcavity implies a longer effective integration length within a small volume. Hence multiple round trips within the microcavity can equate to the longer length of larger non-resonant devices. Therefore, they can serve as platforms for efficient nonlinear optical processes while at the same time maintaining small devices size, both compact and integratable with other devices.

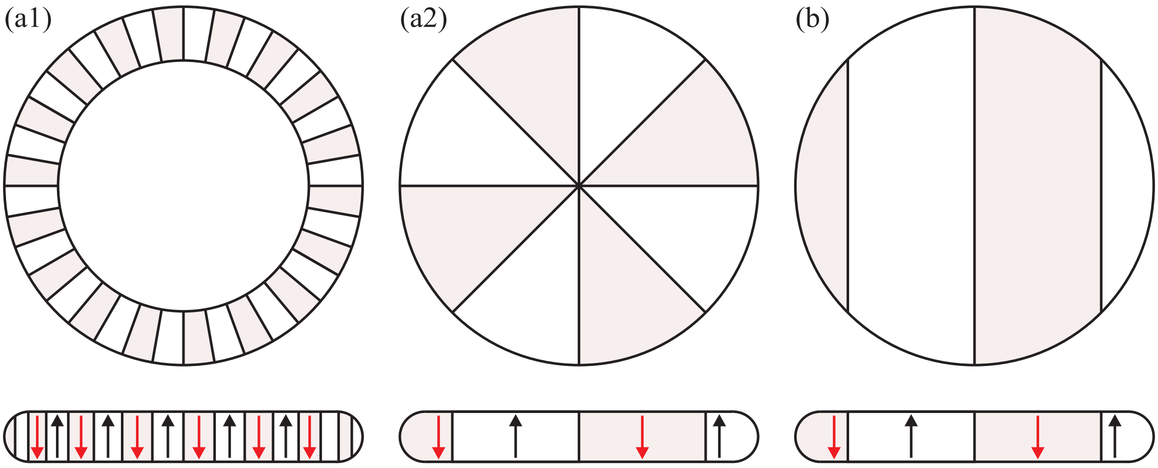

FIGURE 5.5: Examples of periodic poling to achieve quasi phase matching for WGMs. Red regions are the poled parts with inverted polarisations. (a1) [Sasagawa 09] and (a2) [Ilchenko 03]: poling symmetric with respect to the cavity center. (b2) [Ilchenko 03]: stripelike poling.

For a build-up of nonlinear frequency generation, a phase matching condition between fundamental wave and nonlinear frequency generation needs to be satisfied. This can be achieved either by quasi-phase matching (periodic poling of a resonator structure) [Sasagawa 09, Ilchenko 03] as shown in Fig. 5.5 or by Fresnel phase matching [Raybaut 07]. Fresnel phase matching is achieved by utilising the relative Fresnel phase shift between the fundamental wave and nonlinear frequency generation, induced upon total internal reflection (TIR) at the medium-air interface, to compensate for the dispersion phase mismatch.

5.7.3 Fabrication of $\mathrm{LiNbO_3}$ WGM resonators

Recent advances in polishing techniques have allowed the fabrication of large ($\sim$ 5 mm-diameter and 100 µm thick) disk and toroidal microresonators of crystalline materials, including LN that find use as highly efficient electro-optical modulators [Savchenkov 05, Savchenkov 04] and harmonic generator [Sasagawa 09]. Q factors as high as $Q > 10^{10}$ has been achieved [Savchenkov 04]. With the approach of polishing, the original crystal structure and composition is preserved, and the unique nonlinear crystal properties are enhanced with the small volume of the high-Q cavity. Total internal reflection at the walls of the WGRs provides the effect of an ultra-broadband mirror, allowing very high Q-factors across the whole material transparency range. This property makes crystalline WGRs a unique tool for optical materials studies.

Due to the strong etching resistance of LN crystals, the waveguide structures and then fabrication techniques that are used in other materials to produce a microring resonator cannot be applied for $\mathrm{LiNbO_3}$. Titanium-diffused and proton exchanged waveguides on $\mathrm{LiNbO_3}$ provide insufficient lateral optical confinement, which results in a serious leakage of optical power in the small-radius microring resonator. Under such a restriction, only millimeter-radius ring resonators can be produced in $\mathrm{LiNbO_3}$ [Mahapatra 85, Chen 04]. Their extremely small free-spectral range (FSR) has seriously limited the range of applications. This problem of insufficient lateral optical confinement however has been well solved recently by microstructuring of LN so that ridges at the waveguides provide the strong lateral confinement. The techniques of microstrucuring involve wet-etching [Wang 07b, Wang 07a], ion slicing [Guarino 07], or $\mathrm{Ar^+}$ sputtering [Majkic 08]. The high lateral optical confinement thus enables small dimensions of micro-rings (radius $<$ 100 µm) with $1.5 - 2.0$ nm FSR. The results have been listed in Table 5.1 summarised in [Majkic 08].

TABLE 5.1: Properties of microring LN resonators summarised in [Majkic 08]: fabrication techniques, propagating wavelength λ, refractive index change δn, radius of rings r, loss, and FSR.

Fabrication	λ (µm)	δn	r (µm)	Loss ($\mathrm{dB\,cm^{-1}}$)	FSR (nm)	Ref.
PE	0.79	~ 0.01	1500	$1.4 - 4.2$	0.027	[Mahapatra 85]
Ti-indiffusion	1.5	≤ 0.04	100	–	1.42	[Wang 07b, Wang 07a]
F-implantation	1.5	0.65	80	7.8	2.0	[Majkic 08]
Ion slicing	1.5	0.65	100	17	1.66	[Guarino 07]

PE = proton exchange
F = Fluorine

Here, a surface melting thermal treatment was applied to both form the resonator structure and simultaneously reduce the surface roughness.

5.8 Fabrication of LiNbO$_3$ WGM structures via surface tension reshaping

In this section, LN WGM resonators fabricated via surface tension reshaping of micro-structured crystalline substrates is demonstrated which can produce ultra-smooth surfaces with low scattering loss, while maintaining the useful crystalline properties of the original material. The method is based on the observation that annealing of a crystal at temperatures close to, but lower than, the melting point induces preferential melting of a surface layer [Lipowsky 90] (surface melting). Upon cooling the melted surface layer re-crystallises, seeded by the bulk that remains solid during the process, and is reshaped by the surface tension to form ultra-smooth single crystal superstructures. The fabrication process involves three steps of: 1) domain engineering to produce domain structures of limited depth, 2) HF etching to produce the initial surface microstructures, and 3) annealing to temperatures close to the melting point to achieve surface melting and surface tension reshaping of the initial structure. The schematic is illustrated in Fig. 5.6.

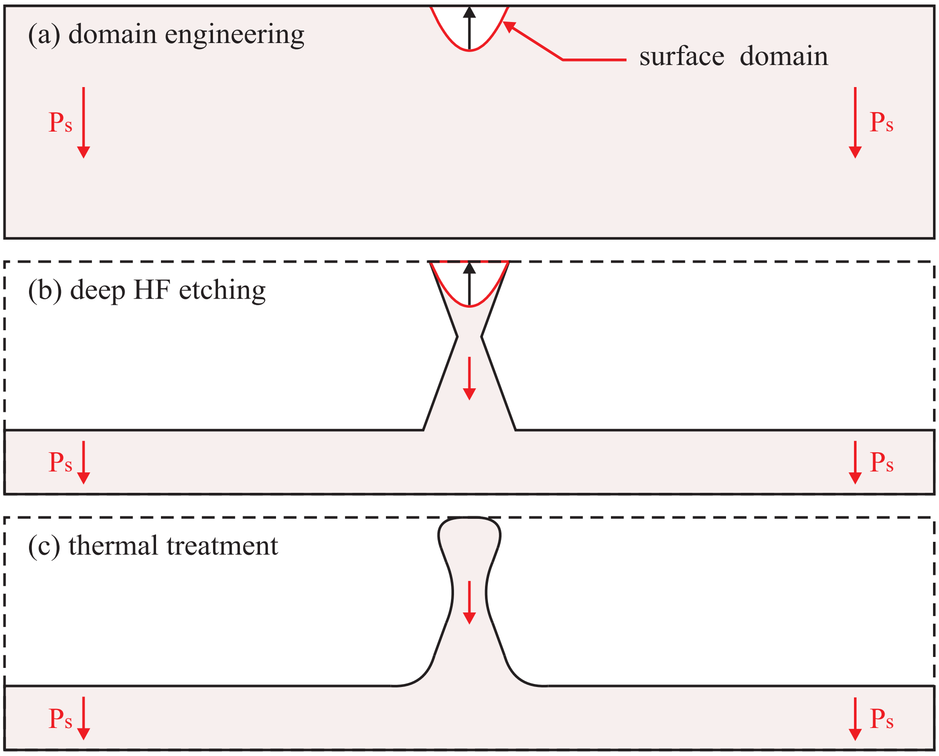

FIGURE 5.6: Schematic of the process to fabricate LN resonators via surface melting. (a): domain engineering to produce a surface domain. (b): preferential HF etching to fabricate the initial surface microstructures. (c): thermal treatment.

5.8.1 Initial structures for thermal treatment

The crystals used were 0.5 mm thick, optical grade, z-cut, undoped congruent LN wafers from Crystal Tech, Inc. (US). Domain engineering was achieved either by poling-inhibition or light-assisted poling. The domain engineering methods were applied to define disc shaped $+z$ surface domains with $5 - 30$ µm diameter, e.g., a 5 µm PI disc domain in Fig. 5.7. Upon HF etching, the disk domain pattern develops into a micro-structured pillar as illustrated in Fig. 5.8(a1-3). The undercut top section which is schematically illustrated in Fig. 5.8(a1-3) is a consequence of the limited depth of the domain structures which is crucial for forming a structure that can provide vertical confinement.

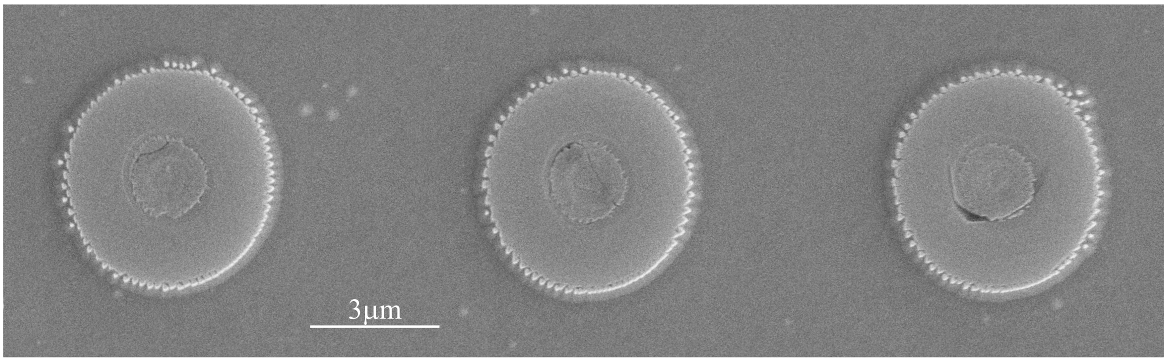

FIGURE 5.7: 5 µm $+z$ face disk domains fabricated via poling-inhibition. Brief HF etching was used to reveal the domain structures.

5.8.2 Thermal treatment

The melting temperature for congruently melting lithium niobate crystals is 1257°C (data provided by Crystal technology, Inc. US) and the Curie temperature which marks the ferroelectric to paraelectric phase transition is 1142°C (however this value does depend on the exact composition of the crystal and changes substantially with the lithium content). After fabrication of the initial etched structure, the samples were then heated to a temperature which is close to the melting temperature of the crystal. The appropriate temperature to achieve good quality resonators was found to be a function of the initial structure dimensions. Although the thermal treatment temperature is below the melting point of the bulk, preferential melting of the surface is possible with the thickness of the melted zone being a function of the temperature [Lipowsky 90].

The thermal treatment was conducted in a furnace with oxygen flow at 0.5 $\mathrm{L\,min^{-1}}$ to suppress the Li$_2$O outdiffusion. The temperature ramping rate in all cases of thermal treatment, unless specifically stated, is $3°\mathrm{C\,min^{-1}}$ for heating. The cooling rate was also set to be $3°\mathrm{C\,min^{-1}}$, however in the low temperature range below 400°C it is not determined by the furnace temperature controller and is much slower than this value. The position of the sample in the furnace

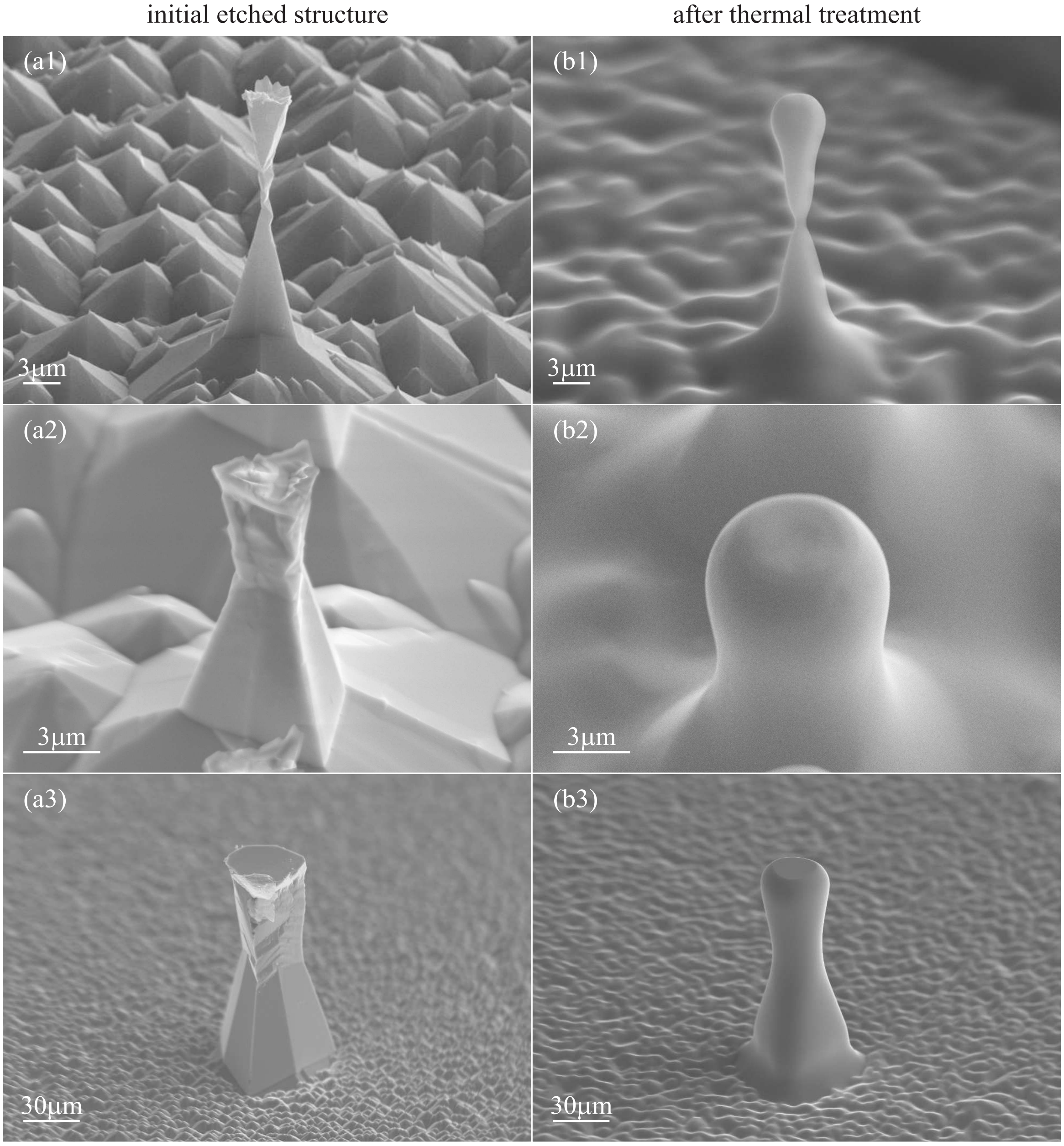

FIGURE 5.8: SEM images tilted at 60°. (a1-3): initial structures developed from HF etching of $+z$ face disk domains with various dimensions. (b1-3): ultrasmooth resonator structures after thermal treating the corresponding initial structure in (a1-3).

was found to have an impact to the homogeneity of the thermal treatment: i.e. if the sample is placed upside-down on the edges of an alumina boat (with platinum wire in between) as shown in Fig. 5.9(a), the region closer to the alumina boat edge seems to experience higher temperature than the area away from the edge. The heating inhomogeneity can be eliminated by hanging the sample in the center of the furnace using platinum wires. The temperature during the thermal treatment is monitored by a thermocouple placed next to the sample.

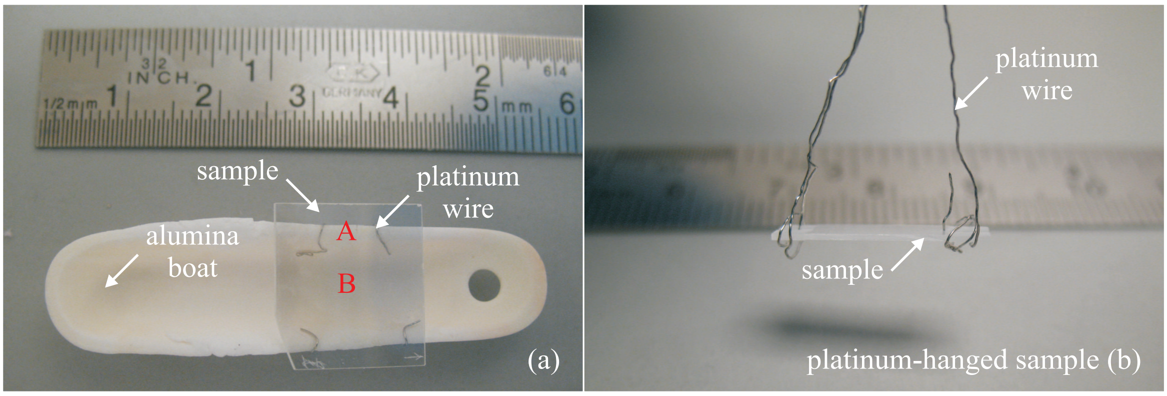

FIGURE 5.9: (a): sample is placed upside-down on a alumina boat with platinum wires in-between. The region at the boat edges, at point A, tends to melt more severely than in the centre, at point B. (b): sample supported by platinum wires.

5.8.3 Surface tension reshaped structures

In Fig. 5.8 which was shown in the previous Sec. 5.8.1, the transition between the initial etched microstructure to the final, reshaped by surface tension, was illustrated. Such structures are suitable for supporting WGMs while the smooth side surface guarantees low scattering loss. Its small dimensions (< 50 µm) can reduce dramatically the number of supported WGMs and increase the device FSR. Both features are beneficial in a number of advanced optical applications such as optical filters and lasers. Fig. 5.10 shows a variety of obtained surface tension reshaped structures with a wide range of sizes and shapes that are expected to be suitable for WGM resonator applications, i.e. (a): 5 µm sphere, (b): 3 µm capsule, (c-d): 3 µm double spheres, (e-g) and (h-i): 7 and 30 µm pillars. It was found that a correspondence exists between the initial structure, thermal-treatment conditions and the final structure. The dynamics of how the initial structure develops into the resultant structure for a specific thermal treatment condition need to be further investigated and modeled. However, the present experimental results suggest that for substantial reshaping to occur the thickness of the surface melted layer must be comparable to the dimensions of the initial microstructure. Hence, larger structures require higher temperatures for reshaping. Fig. 5.11 lists a series of successive 1-hour thermal treatments of a pillar structure with increasing temperature from 1212°C to 1253°C. The succession of SEM images shows that although some smoothing of sharp feature can be observed at lower temperatures, substantial reshaping of this particular pillar requires a temperature of 1253°C which is much higher than in the case of smaller structures.

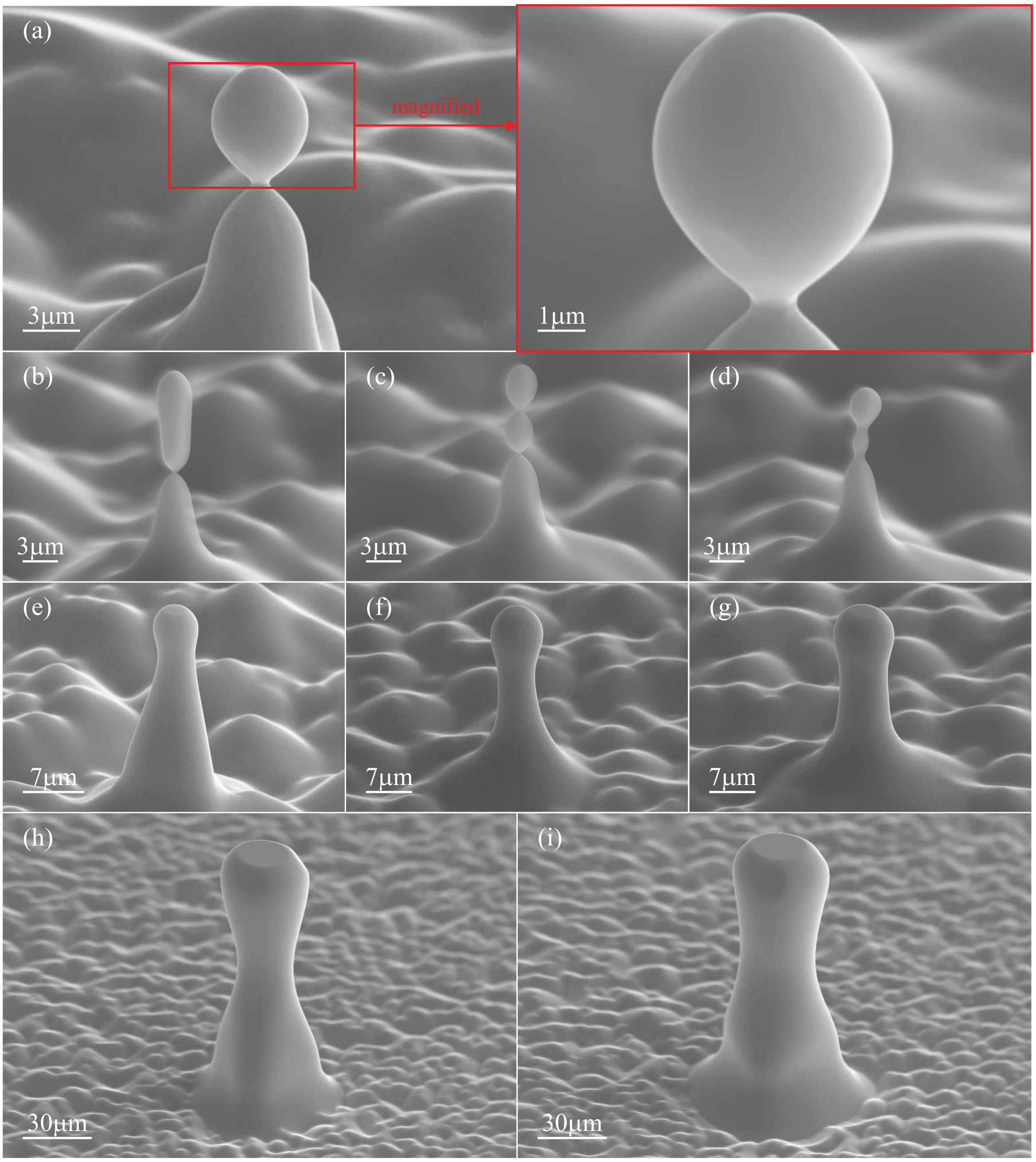

FIGURE 5.10: SEM images tilted at 60° of various structures fabricated from thermal treating the initial structure under different conditions.

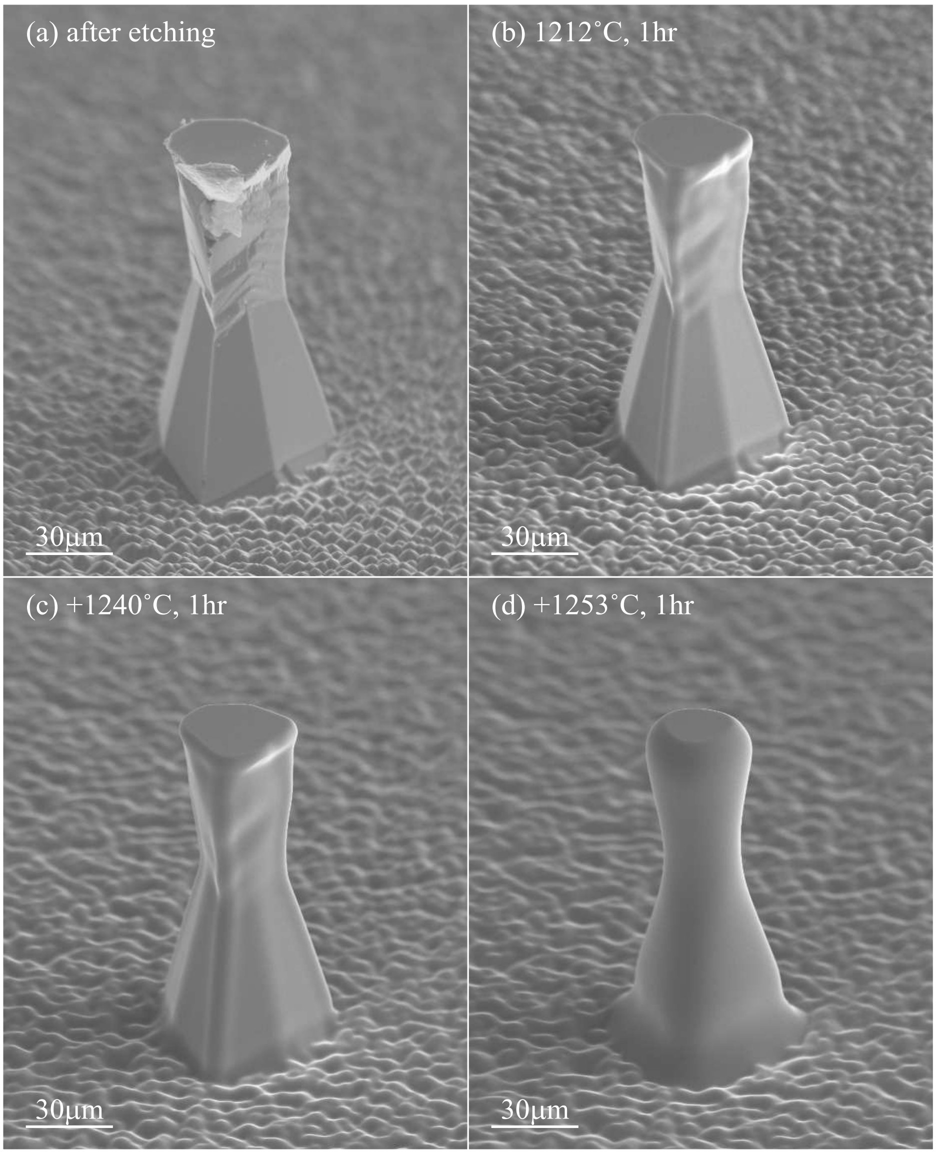

FIGURE 5.11: SEM images tilted at 60° of an initial structure that had undergone a series of 1-hour thermal treatments at progressively increasing temperatures at: 1212, 1214, 1217, 1223, 1240, and 1253°C. (a): initial structure before thermal treatment. (b), (c), and (d): structure after first 1-hour 1212°C, the 1-hour 1240°C, and the 1-hour 1253°C thermal treatment respectively.

5.9 Crystal quality after thermal treatment

In order to assess the quality of the crystal after the thermal process the annealed crystal surface was investigated using piezoresponse force microscopy (PFM) [Jungk 06], Raman spectroscopy and finally chemical etching.

5.9.1 Piezoresponse force microscopy

A series of small area PFM scans was performed on various locations of the thermal-treated microstructured substrate. All PFM images obtained in these scans shown the very same uniform grey-level, and thus the same piezoresponse, indicating that the melted and re-solidified surface is single domain and piezoelectric. In order to quantify the piezoresponse obtained on the annealed substrate, a comparative measurement was performed on an untreated multi-domain single crystal (PPLN). It thereby showed that the amplitude of the PFM signal measured on the microstructured substrate is identical to the one on the $-z$ face of the untreated sample. In addition, strong surface charging on the re-solidified material was observed [Johann 09]. Based on this evidence it was concluded that the annealed microstructured substrate is both single crystal and ferroelectric. Micro-Raman spectroscopy and chemical etching further corroborated the PFM results.

5.9.2 Micro-Raman

A sample was prepared for Raman spectroscopic investigation of a thermally treated crystal. Fig. 5.12(a) shows a 2D array of micro-pyramids which exhibit a rough side surface and a sharp tip developed from prolonged etching of poling-inhibited disc shaped domains. The sample was then subjected to thermal treatment to a temperature of 1130°C for 50 hrs in a continuous flow of oxygen gas. The temperature was ramped up at a rate of $5°\mathrm{C\,min^{-1}}$ and after the required dwell time it was ramped down also at a rate of $5°\mathrm{C\,min^{-1}}$. The surface topography after annealing is shown in the SEM image of Fig. 5.12(b) and also in 5.12(c, d) at different views. It is obvious that all the sharp features have been smoothed out as the micro-structures have been reshaped by the surface tension. Then, a set of spatially-selective Raman spectra was acquired from different positions on the thermal-treated micro-structured substrate as indicated in Fig. 5.12(b, c and d). The micro-Raman spectrometer which was used to acquire the spectra employed a ×50 microscope objective to both focus the probe laser beam and collect the Raman signal. The depth resolution of the system is limited by the depth of focus of the objective which is less than 1 µm. Fig. 5.13 shows a set of Raman spectra which were acquired from a single reshaped tip. These Raman spectra were taken under different focusing conditions and can be compared to a reference spectrum (solid line) taken from an unstructured and untreated

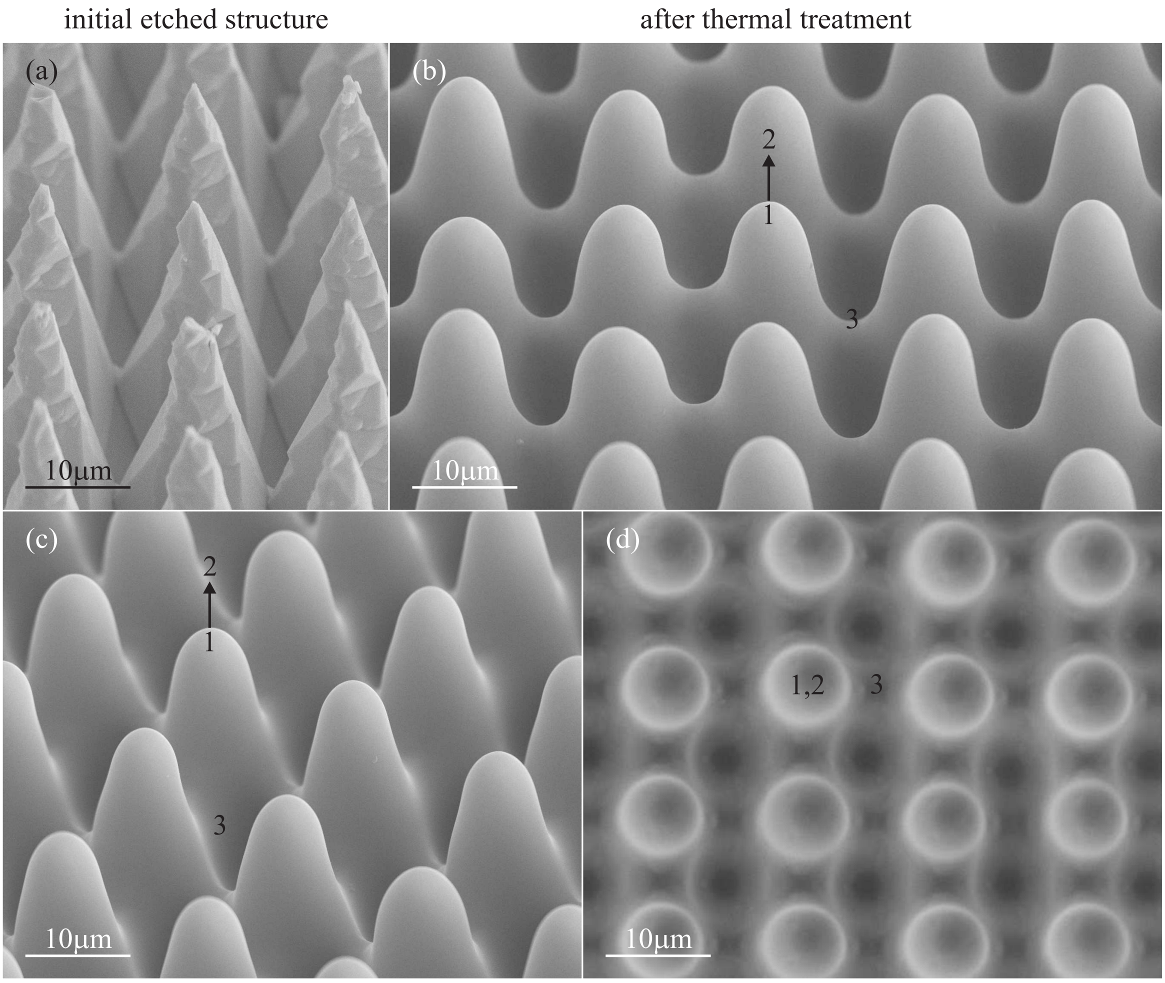

Figure 5.12: SEM images (image a, b, c tilted at 60°). (a): 2D array of micro-pyramids produced by etching of poling-inhibited disc domains. (b),(c), and (d): two different tilted views, and one top view of the surface tension reshaped array after thermal treatment. The numbers correspond to points where micro Raman spectra (Fig. 5.13) was acquired from.

z-cut substrate in the $z(yy)z$ configuration [Ridah 97]. The dashed line (spectrum 1) corresponds to a well-focused acquisition from a spot on the top of a single tip, while the dash-dotted line (spectrum 2) corresponds to a slightly defocused acquisition on the same spot. Finally the dotted line (spectrum 3) corresponds to a spot between two adjacent tips (focused acquisition). The acquisition of spectra under different focusing conditions was performed in order to collect signals from the surface layers of the structure, which had experienced melting, in order to detect any possible structural changes after the process. However, there was no obvious difference between these spectra (dashed and dash-dotted line in Fig. 5.13).

Further observation of the spectra reveals that some Raman lines corresponding to the reshaped tips appear to be shifted with respect to the corresponding peaks in the reference spectrum (the 582 cm^{-1} peak in particular) while others (like the 432 cm^{-1} and 873 cm^{-1} peaks) exhibit a relative intensity change as compared to the reference spectrum. Raman spectra of crystalline

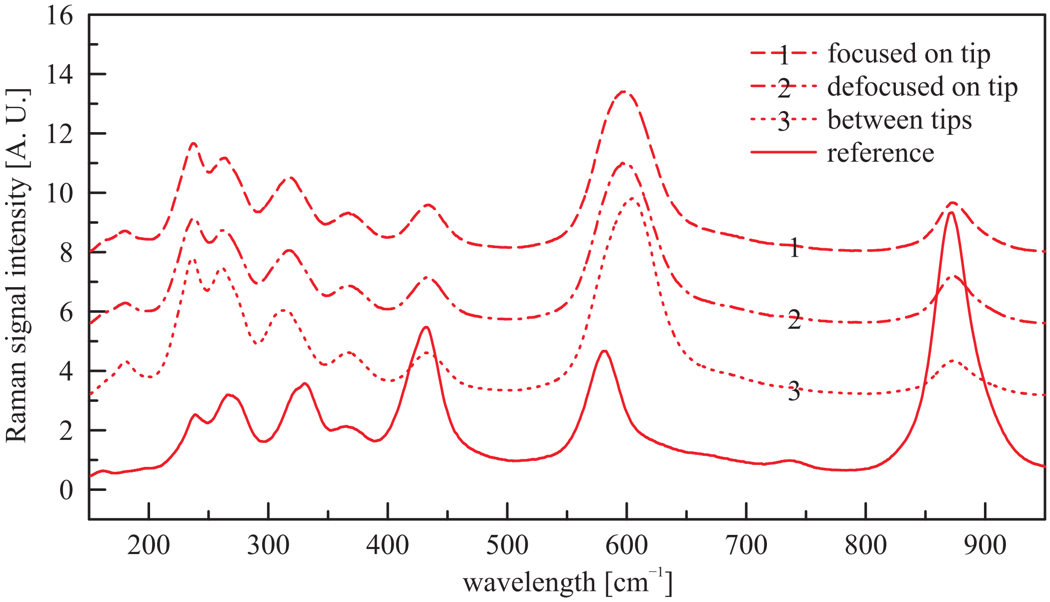

FIGURE 5.13: Raman spectra acquired from different points on the annealed microstructured sample shown in Fig. 5.12(b, c and d) and with different focusing conditions as indicated in the legend. The solid line corresponds to a spectrum that was taken from a virgin z-cut sample in the $z(yy)z$ configuration. An offset was introduced between spectra for clarity.

materials however are subject to selection rules which depend on the specifics of the crystal face and polarisation mode of the exciting beam and the detection channel. Since the annealed structure is curved it does not present a pure z-face to the incidence direction of the interrogating laser beam: the entrance/exit faces are in general different compared to the reference z-cut substrate. Additionally, the curved interfaces can alter the polarisation state of both the exciting beam and of the collected signal. These factors which influence both the position and intensity of the Raman peaks are likely to be responsible for the differences which are observed between the various Raman spectra taken from the reshaped surface and the reference spectrum taken from the pure z-cut crystal.

5.9.3 Preferential HF etching

The lateral differential etching between opposite y-faces has been used earlier for the visualisation of the ferroelectric domain structure of the crystal. However, as a consequence of the threefold symmetry of the lithium niobate crystal structure, there are three indistinguishable pairs of y-faces corresponding to three y-axes which are rotated by 120° with respect to each other. This threefold symmetry can be readily identified in the x-y cross-section of etched isolated inverted domains. Here HF acid etching was used to look for this characteristic threefold symmetry on the re-solidified crystal features in order to assess the quality of the thermally treated crystal. Fig. 5.14(a) shows an SEM image of a smoothed feature as a result of the surface tension reshaping that took place during the thermal treatment. After brief etching (15 mins) in HF

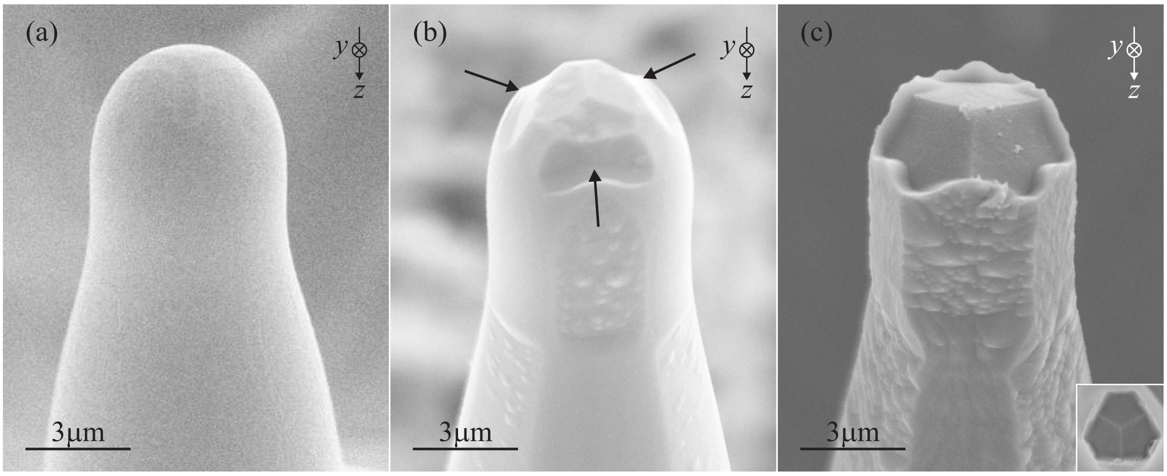

FIGURE 5.14: SEM images tilted at 60°. (a): a surface tension reshaped feature. (b): a feature briefly etched in HF for 15 mins showing characteristic y-face differential etching as indicated by the arrows. (c): a further 3-hour etching reveals the threefold symmetric in the inner part of the reshaped structure.

acid, characteristic facets (due to differential etching between opposite y-faces) start to emerge revealing the characteristic threefold-symmetry of lithium niobate as shown in the SEM image of Fig. 5.14(b). A further 3-hour etching reveals the threefold-symmetry in the inner part of the reshaped structure. Thus, it verifies that both the surface layer and the inner part of reshaped structure after thermal treatment is still crystalline with threefold symmetry.

5.9.4 Thermal treatment temperature > Curie temperature

It is important to note that the temperatures which are used for the thermal treatment are not necessarily lower than the Curie temperature. In the cases where the temperature was kept just below the Curie point, it is expected that the bulk of the processed material is still single crystal and ferroelectric throughout the thermal processing, while the surface undergoes melting. However even when the crystal was treated at temperatures higher than the Curie temperature it was found that there is always a substantially deep layer of the crystal that maintains a single polarisation state. Although similar observations have been made in thermally-treated LiTaO$_3$ crystals at temperatures exceeding the Curie temperature [Åhlfeldt 94], such results on LiNbO$_3$ have not been reported. The prolonged thermal treatment can lead to lithium out-diffusion which may be substantial and which consequently leads to domain inversion on the $+z$ face of the crystal. As a result a uniform domain-inverted layer is formed with a depth which depends on the duration of the thermal treatment. It was observed that in extreme cases where a crystal slab is annealed at temperatures exceeding the Curie point, the depth of the domain-inverted layer can reach half the slab thickness. Interestingly though both of the two sections of the slab remain single domain. Etching in HF acid is routinely used to reveal the presence of

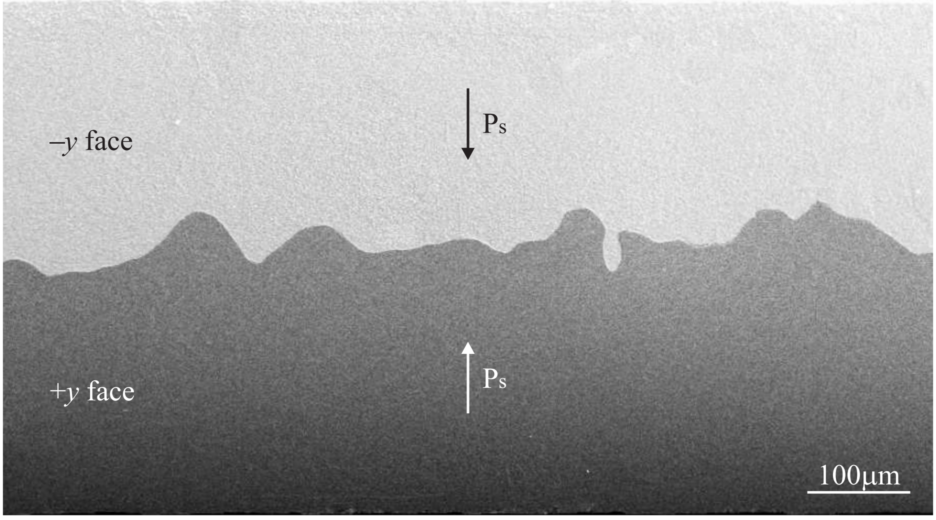

FIGURE 5.15: Etching of the y-face of a z-cut crystal slab annealed at $T = 1200°\mathrm{C}$ (above the Curie temperature) for 10 hrs reveals the resultant ferroelectric domain structure.

inverted ferroelectric domains in lithium niobate as the two opposite z-faces of the crystal etch at different rates (actually the $+z$ face remains totally unaffected by the acid) [Sones 02]. However, differential etching can also be observed between opposite y-faces of the crystal. The topography of the etched y-face can reveal the domain structure of a multi-domain lithium niobate crystal because, as has been shown in [Sono 06], domain inversion corresponds to a 180° rotation of the z-axis around the x-axis of the crystal. Consequently the y-axis is also rotated by 180° and hence opposite ferroelectric domains present opposite y-faces on the same y surface. The etched y-face of the crystal slab which was thermally treated at a temperature (1200°C) exceeding the Curie temperature (1142°C) is shown in the SEM image of Fig. 5.15 where the two single domain regions are clearly visible due to the differential etching of the opposite y-faces which are presented on the same y surface as indicated in the figure. The top edge of the image corresponds to the original $-z$ face of the sample while the bottom edge corresponds to the original $+z$ face which has now been domain-inverted, as a consequence of thermal annealing, to form a $-z$ face. Consequently, after annealing the crystal presents a $-z$ face on both z surfaces.

5.10 Optical characterisation of resonators

Some preliminary results on the optical characterisation of surface tension reshaped WGM LN microresonators will be presented here. The WGM microresonator structure that has been investigated is shown in the SEM image of Fig. 5.16. The microresonator diameter at its widest point was estimated to be 80 µm from the SEM image. Fig. 5.17 illustrates the experimental configuration used to simultaneously excite and probe the optical resonances. A U-shaped (diameter $\sim$ 1 cm) multi-mode silica fibre taper with a waist diameter of about 2 µm was used to couple

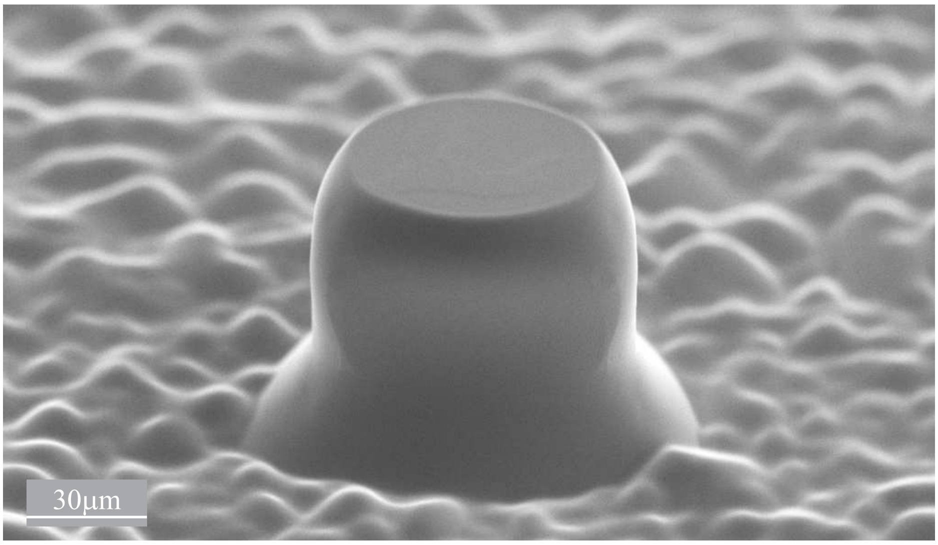

FIGURE 5.16: 60°-tilted SEM image of the resonator structure used for optical characterisation.

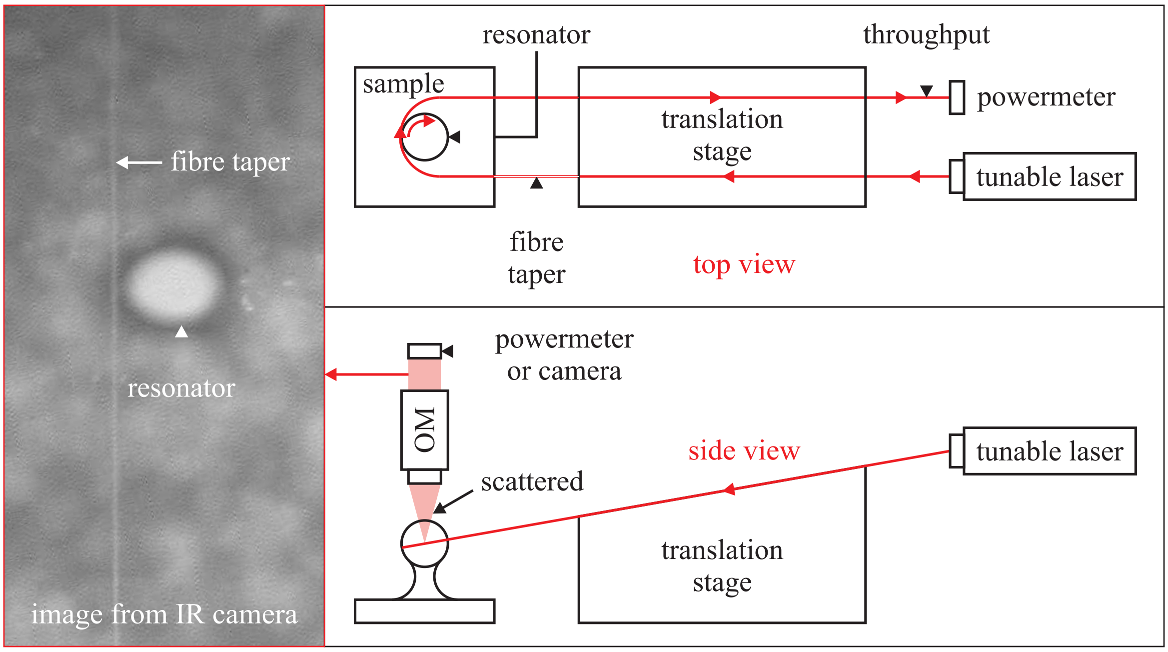

FIGURE 5.17: Schematic of the experimental configuration used to simultaneously excite and probe the optical modes in the microresonator. An optical micrograph shows a tapered optical fibre coupled to the microresonator.

light into and out of the microresonator. Micro-positioning stages were used to place the tapered fibre in close proximity to the resonator. It was observed that the fibre taper, when approaching the resonator, is attracted by the resonator and sticks to it. Therefore, keeping a small accurate distance between fibre and resonator is impossible and in all experiments the fibre taper was in physical contact with the microresonator. The resonator has been excited at various points by moving the point of contact between the structure and the taper at different heights.

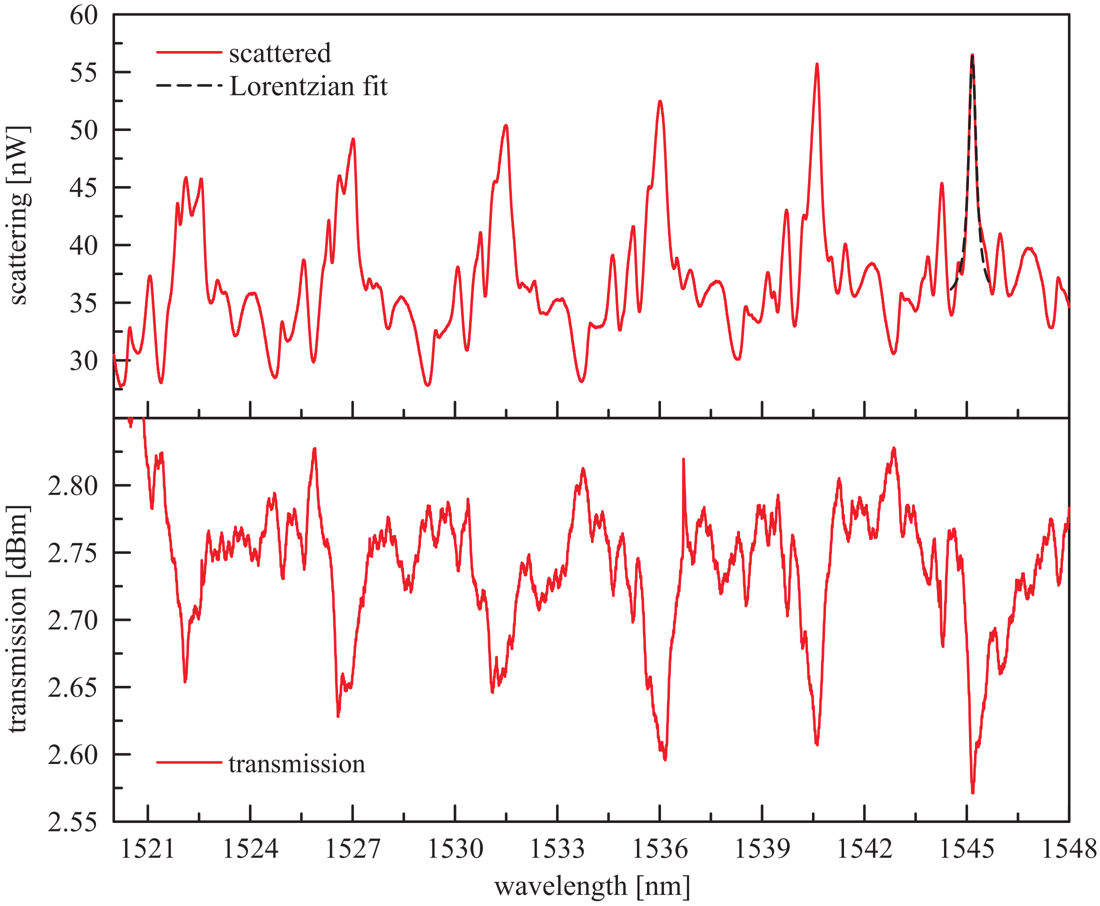

FIGURE 5.18: Scattered and transmitted signal with fitted Lorentzian used for the determination of Q factors of the microresonator.

To couple light into the resonator, one of the pigtails of the fibre taper was connected to a tunable laser. The tunable laser source, which was an Agilent 81600B, with tuning range from 1440 to 1640 nm, was used to scan the wavelength of the incoupled light. The laser linewidth was 100 kHz and the tuning step was 0.1 pm. An infra-red camera was used to image the resonator when excited with the laser. To investigate the resonances, the other end of the fibre taper was connected to a InGaAs detector to monitor the transmitted light power during the scanning of the input wavelength. The light scattered from the resonator was collected by the objective which was used for the observation of the coupling and was monitored using a second InGaAs detector. Fig. 5.18 shows the transmitted and scattered spectra of the microresonator. Lorentzian fits were applied to the measured data in order to calculate the Q of the dominant resonances. The Q factor was deduced to be around 5600 with a FSR of 4.55 nm.

5.11 Future work

The transition from the initial microstructure to the final surface tension reshaped structure needs to be well understood, and most importantly controlled, in order to be used for any practical application. It is therefore important to be able to model the heat treatment process in order to be able to predict the final reshaped structure and to define the processing conditions.

Furthermore due to the differential etching between opposite y-faces, the initial circular shape of the PI disc domains develops into a pillar [Fig. 5.19(a)] with a triangular cross section as shown in Fig. 5.19(b). However, microresonators with a circular cross section are more desirable as they will exhibit higher Q factors. One way to circumvent this problem is by pre-shaping the initial PI domain in order to compensate for the effect of the differential y-face etching, i.e., as the red dashed shape in Fig. 5.19(b).

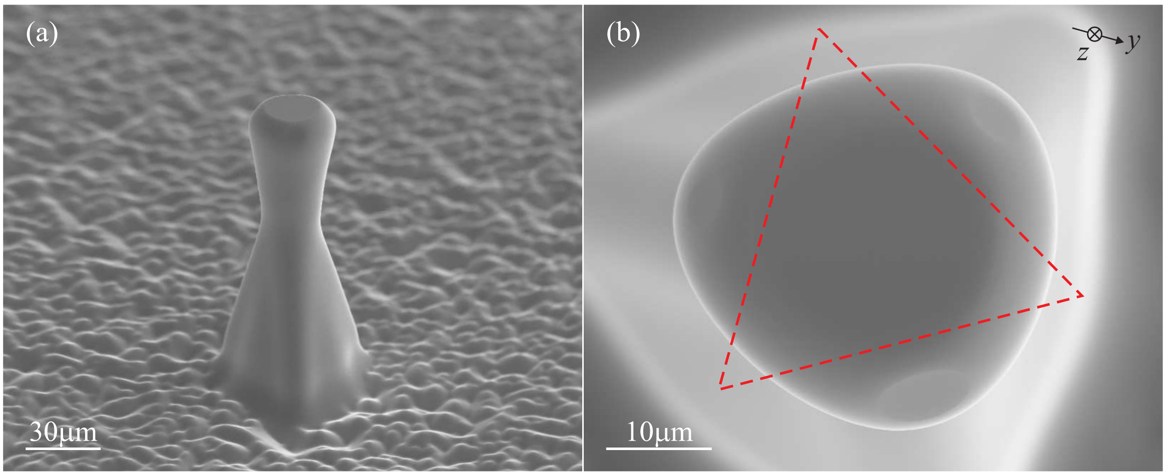

FIGURE 5.19: SEM images tilted at 60°. (a): a thermally-treated toroidal resonator structure. (b): view of the top reveals its non-circular shape with characteristic threefold symmetry. The red dashed lines are the proposed domain structure to compensate the preferential etching in order to obtain a more circular shape after etching and thermal treatment.

Improvements in the optical characterisation involves firstly better coupling into high index LN resonators with also fibre tapers fabricated out of higher index glass. The wavelength selectivity and the strength of evanescent excitation of the resonator depends upon the degree of phase-matching and spatial overlap between the tapered-fibre field and the resonator mode fields at the different positions of the tapered fibre. Thus, refractive index difference of silica fibre ($\sim 1.44 - 1.46$ at 1550 nm) that applied in Sec. 5.10 and LN ($n_\mathrm{e} \sim 2.139$ at 1550 nm) can lead to an inefficient coupling.

Finally, the resonator can be doped with rare earth ions, such as Nd or Er for lasing applications. Doped resonators can be pumped collectively (without having to couple into WGM's while the resonances can be readily detected in the lasing spectrum). This is a scheme that can significantly simplify the optical characterisation process.

5.12 Summary

Thermal treatment of micro-structured lithium niobate substrates at temperatures close to, but below the melting point, allows surface tension to reshape preferentially melted surface zones of the crystal. The fabrication process involves domain engineering, HF deep etching and thermal treatment. Resonator structures of different dimensions have been fabricated. The reshaped surface re-crystallises upon cooling to form a single crystal again as it is seeded by the bulk which remains solid throughout the process. The preserved crystal quality after thermal treatment was investigated and confirmed by PFM, micro-Raman, and preferential HF etching. This procedure yields ultra-smooth single crystal superstructures suitable for the fabrication of photonic micro-components with low scattering loss. Preliminary optical characterisation was conducted in a resonator structure which gives a Q factor of 5600 and FSR of 4.55 nm.

References

[Affolter 73] P. Affolter & B. Eliasson, *Electromagnetic resonances and Q-factors of lossy dielectric spheres*, IEEE Tran. Microwave Theor. Techn., vol. MTT-21, pages 573–578, 1973.

[Armani 03] D. K. Armani, T. J. Kippenberg, S. M. Spillane & K. J. Vahala, *Ultra-high-Q toroid microcavity on a chip*, Nature, vol. 421, pages 905–908, 2003.

[Baba 97a] T. Baba, *Photonic crystals and microdisk cavities based on GaInAsP-InP system*, IEEE J. Select. Topics Quantum Electron., vol. 3, pages 808–828, 1997.

[Baba 97b] T. Baba, M. Fujita, A. Sakai, M. Kihara & R. Watanabe, *Lasing characteristics of GaInAsP/InP strained quantum-well microdisk injection lasers with diameter of 2-10 μm*, IEEE Photonics Technol. Lett., vol. 9, pages 878–880, 1997.

[Backes 99] S. A. Backes, J. R. A. Cleaver, A. P. Heberle, J. J. Baumberg & K. Köhler, *Threshold reduction in pierced microdisk lasers*, Appl. Phys. Lett., vol. 74, pages 176–178, 1999.

[Barber 88] P. W. Barber & R. K. Chang, editeurs, Optical effects associated with small particles, World Scientific, 1988.

[Benabid 99] F. Benabid, M. Notcutt, L. Ju & D. G. Blair, *Rayleigh scattering in sapphire test mass for laser interferometric gravitational-wave detectors I. measurement of scattering attenuation coefficient*, Opt. Commun., vol. 167, pages 7–13, 1999.

[Benson 06] T. M. Benson, S. V. Boriskina, P. Sewell, A. Vukovic, S. C. Greedy & A. I. Nosich, Frontiers in planar lightwave circuit technology: design, simulation, and fabrication, Chapter 2: micro-optical resonators for microlasers and integrated optoelectronics, recent advances and future challenges, pages 39–70, Springer, 2006.

[Blom 97] F. C. Blom, D. R. van Dijk, H. J. W. M. Hoekstra, A. Driessen & T. J. A. Popma, *Experimental study of integrated-optics microcavity resonators: toward an all-optical switching device*, Appl. Phys. Lett., vol. 71, pages 747–749, 1997.

[Boriskina 03] S. V. Boriskina, T. M. Benson, P. Sewell & A. I. Nosich, *Tuning of elliptic whispering-gallery-mode microdisk waveguide filters*, J. Lightwave Technol., vol. 21, pages 1987–1995, 2003.

[Boriskina 04] S. V. Boriskina, T. M. Benson, P. Sewell & A. I. Nosich, *Spectral shift and Q-change of circular and square-shaped optical microcavity modes due to periodical sidewall surface roughness*, J. Opt. Soc. Am. B., vol. 10, pages 1792–1796, 2004.

[Boriskina 05] S. V. Boriskina, T. M. Benson, P. Sewell & A. I. Nosich, *Optical modes in imperfect 2-D square and triangular microcavities*, IEEE J. Quantum Electron., vol. 41, pages 857–862, 2005.

[Braginsky 89] V. B. Braginsky, M. L. Gorodetsky & V. S. Ilchenko, *Quality-factor and nonlinear properties of optical whispering gallery modes*, Phys. Lett. A, vol. 137, pages 393–397, 1989.

[Cao 00] H. Cao, J. Y. Xu, W. H. Xiang, Y. Ma, S. H. Chang, S. T. Ho & G. S. Solomon, *Optically pumped InAs quantum dot microdisk lasers*, Appl. Phys. Lett., vol. 76, pages 3519–3521, 2000.

[Chang 96] R. K. Chang & A. J. Campillo, editeurs, Optical processes in microcavities, World Scientific, 1996.

[Chao 03] C. Y. Chao & L. J. Guo, *Biochemical sensors based on polymer microrings with sharp asymmetrical resonance*, Appl. Phys. Lett., vol. 83, pages 1527–1529, 2003.

[Chao 04a] C. Y. Chao & L. J. Guo, *Reduction of surface scattering loss in polymer microrings using thermal-reflow technique*, IEEE Photonics Technol. Lett., vol. 16, pages 1498–1500, 2004.

[Chao 04b] C. Y. Chao & L. J. Guo, *Thermal-flow technique for reducing surface roughness and controlling gap size in polymer microring resonators*, Appl. Phys. Lett., vol. 84, pages 2479–2481, 2004.

[Chen 04] J. X. Chen, T. Kawanishi, K. Higuma, S. Shinada, J. Hodiak, M. Izutsu, W. S. C. Chang & P. K. L. Yu, *Tunable lithium niobate waveguide loop*, IEEE Photonics Technol. Lett., vol. 16, pages 2090–2092, 2004.

[Chin 99] M. K. Chin, C. Youtsey, W. Zhao, T. Pierson, Z. Ren, S. L. Wu, L. Wang, Y. G. Zhao & S. T. Ho, *GaAs microcavity channel-dropping filter based on a race-track resonator*, IEEE Photonics Technol. Lett., vol. 11, pages 1620–1622, 1999.

[Collot 93] L. Collot, V. Lefevre-Seguin, M. Brune, J. M. Raimond & S. Haroche, *Very high-Q whispering-gallery mode resonances observed on fused silica microspheres*, Europhys. Lett., vol. 23, pages 327–334, 1993.

[Datsyuk 01] V. V. Datsyuk & I. A. Izmailov, *Optics of microdroplets*, Physics-Uspekhi, vol. 44, no. 10, page 1061, 2001.

[Dubreuil 95] N. Dubreuil, J. C. Knight, D. K. Leventhal, V. Sandoghdar, J. Hare & V. Lefevre, *Eroded monomode optical fiber for whispering-gallery mode excitation in fused-silica microspheres*, Opt. Lett., vol. 20, pages 813–815, 1995.

[Fields 00] M. H. Fields, J. Popp & R. K. Chang, *Nonlinear optics in microspheres*, Prog. Opt., vol. 41, pages 1–95, 2000.

[Fong 03] C. Y. Fong & A. W. Poon, *Mode field patterns and preferential mode coupling in planar waveguide-coupled square microcavities*, Opt. Express, vol. 11, pages 2897–2904, 2003.

[Fukushima 04] T. Fukushima & T. Harayama, *Stadium and quasi-stadium laser diodes*, IEEE J. Select. Topics Quantum Electron., vol. 10, pages 1039–1051, 2004.

[Garrett 61] C. G. B. Garrett, W. Kaiser & W. L. Bond, *Stimulated emission into optical whispering gallery modes of spheres*, Phys. Rev., vol. 124, pages 1807–1809, 1961.

[Gastine 67] M. Gastine, L. Courtois & J. L. Dormann, *Electromagnetic resonances of free dielectric spheres*, IEEE Tran. Microwave Theor. Techn., vol. MTT-15, no. 12, pages 694–700, 1967.

[Gayral 99] B. Gayral, J. M. Gerard, A. Lemaitre, C. Dupuis, L. Manin & J. L. Pelouard, *High-Q wet-etched GaAs microdisks containing InAs quantum boxes*, Appl. Phys. Lett., vol. 75, pages 1908–1910, 1999.

[Gayral 00] B. Gayral & J. M. Gerard, *Strong Purcell effect for InAs quantum boxes in high-Q wet-etched microdisks*, Physica E, vol. 7, pages 641–645, 2000.

[Gianordoli 00] S. Gianordoli, L. Hvozdara, G. Strasser, W. Schrenk, J. Faist & E. Gornik, *Long-wavelength ($\lambda = 10\mu m$) quadrupolar-shaped GaAs-AlGaAs microlasers*, IEEE J. Quantum. Electron., vol. 36, pages 458–464, 2000.

[Gmachl 98] C. Gmachl, F. Cappasso, E. E. Narimanov, J. U. Nockel, A. D. Stone, J. Faist, D. L. Sivco & A. Y. Cho, *High-power directional emission from microlasers with chaotic resonances*, Science, vol. 280, pages 1556–1564, 1998.

[Gorodetsky 94] M. L. Gorodetsky & V. S. Ilchenko, *High-Q optical whispering-gallery microresonators: precession approach for spherical mode analysis and emission patterns with prism couplers*, Opt. Commun., vol. 113, pages 133–143, 1994.

[Gorodetsky 96] M. L. Gorodetsky, A. A. Savchenkov & V. S. Ilchenko, *Ultimate Q of optical microsphere resonators*, Opt. Lett., vol. 21, pages 453–455, 1996.

[Griffel 96] G. Griffel, S. Arnold, D. Taskent & A. Serpengüzel, *Morphology-dependent resonances of a microsphere-optical fiber system*, Opt. Lett., vol. 21, pages 695–697, 1996.

[Grover 01] R. Grover, P. P. Absil, V. Van, J. V. Hryniewicz, B. E. Little, O. King, L. C. Calhoun, F. G. Johnson & P. T. Ho, *Vertically coupled GaInAsP-InP microring resonators*, Opt. Lett., vol. 26, pages 506–508, 2001.

[Guarino 07] A. Guarino, G. Poberaj, D. Rezzonico, R. Degl'Innocenti & P. Günter, *Electro-optically tunable microring resonators in lithium niobate*, Nat. Photon., vol. 1, no. 7, pages 407–410, July 2007.

[Guo 03] W. H. Guo, Y. Z. Huang, Q. Y. Lu & L. J. Yu, *Whispering-gallery-like modes in square resonators*, IEEE J. Quantum Electron., vol. 39, pages 1563–1566, 2003.

[Hagness 97] S. C. Hagness, D. Rafizadeh, S. T. Ho & A. Taflove, *FDTD microcavity simulations: design and experimental realization of waveguide-coupled single-mode ring and whispering-gallery-mode disk resonators*, J. Lightwave Technol., vol. 15, pages 2154–2165, 1997.

[Hammer 02] M. Hammer, *Resonant coupling of dielectric optical waveguides via rectangular microcavities: the coupled guided mode perspective*, Opt. Commun., vol. 214, pages 155–170, 2002.

[Ilchenko 99] V. S. Ilchenko, X. S. Yao & L. Maleki, *Pigtailing the high-Q microsphere cavity: a simple fiber coupler for optical whispering-gallery modes*, Opt. Lett., vol. 24, pages 723–725, 1999.

[Ilchenko 01] V. S. Ilchenko, M. L. Gorodetsky, X. S. Yao & L. Maleki, *Microtorus: a high-finesse microcavity with whispering-gallery modes*, Opt. Lett., vol. 26, pages 256–258, 2001.

[Ilchenko 03] V. S. Ilchenko, A. B. Matsko, A. A. Savchenkov & L. Maleki, *Low-threshold parametric nonlinear optics with quasi-phase-matched whispering-gallery modes*, J. Opt. Soc. Am. B, vol. 20, pages 1304–1308, 2003.

[Jiao 87] X. H. Jiao, P. Guillon, L. A. Bermijdez & P. Auxemery, *Whispering-gallery modes of dielectric structures: applications to millimeter-wave bandstop filters*, IEEE Tran. Microwave Theor. Techn., vol. MTT-35, pages 1169–1175, 1987.

[Johann 09] F. Johann & E. Soergel, *Quantitative measurement of the surface charge density*, Appl. Phys. Lett., vol. 95, page 232906, 2009.

[Jungk 06] T. Jungk, A. Hoffmann & E. Soergel, *Quantitative analysis of ferroelectric domain imaging with piezoresponse force microscopy*, Appl. Phys. Lett., vol. 89, page 163507, 2006.

[Kim 04] S. K. Kim, S. H. Kim, G. H. Kim, H. G. Park, D. J. Shin & Y. H. Lee, *Highly directional emission from few-micron-size elliptical microdisks*, Appl. Phys. Lett., vol. 84, pages 861–863, 2004.

[Kippenberg 03] T. J. Kippenberg, S. M. Spillane, D. K. Armani & K. J. Vahala, *Fabrication and coupling to planar high-Q silica disk microcavities*, Appl. Phys. Lett., vol. 83, pages 797–799, 2003.

[Kippenberg 04] T. J. Kippenberg, S. M. Spillane & K. J. Vahala, *Demonstration of ultra-high-Q small mode volume toroid microcavities on a chip*, Appl. Phys. Lett., vol. 85, pages 6113–6115, 2004.

[Klitzing 01] W. Klitzing, R. Long, V. S. Ilchenko, J. Hare & V. Lefevre-Seguin, *Frequency tuning of the whispering-gallery modes of silica microspheres for cavity quantum electrodynamics and spectroscopy*, Opt. Lett., vol. 26, pages 166–168, 2001.

[Knight 95] J. C. Knight, N. Dubreuil, V. Sandoghdar, J. Hare, V. Lefevre-Seguin, J. M. Raimond & S. Haroche, *Mapping whispering-gallery modes in microspheres with a near-field probe*, Opt. Lett., vol. 20, pages 1515–1517, 1995.

[Knight 97] J. C. Knight, G. Cheung, F. Jacques & T. A. Birks, *Phase-matched excitation of whispering-gallery mode resonances by a fiber taper*, Opt. Lett., vol. 22, pages 1129–1131, 1997.

[Kriezis 92] E. E. Kriezis, D. P. Chrissoulidis & A. G. Papagiannakis, Electromagnetics and optics, Chapter 6, page 239, World, 1992.

[Laine 99] J. P. Laine, B. E. Little & H. A. Haus, *Etch-eroded fiber coupler for whispering-gallery-mode excitation in high-Q silica microspheres*, IEEE Photonics Technol. Lett., vol. 11, pages 1429–1430, 1999.

[Laine 00] J. P. Laine, B. E. Little, D. R. Lim, H. C. Tapalian, L. C. Kimerling & H. A. Haus, *Microsphere resonator mode characterization by pedestal anti-resonant reflecting waveguide coupler*, IEEE Photonics Technol. Lett., vol. 12, pages 1004–1006, 2000.

[Laine 01] J. P. Laine, H. C. Tapalian, B. E. Little & H. A. Haus, *Acceleration sensor based on high-Q optical microsphere resonator and pedestal antiresonant reflecting*, Sensors and Actuators A, vol. 93, pages 1–7, 2001.

[Lefevre-Seguin 97] V. Lefevre-Seguin & S. Haroche, *Towards cavity-QED experiments with silica microspheres*, Mater. Sci. Eng. B, vol. 48, pages 53–58, 1997.

[Lefevre-Seguin 99] V. Lefevre-Seguin, *Whispering-gallery mode lasers with doped silica microspheres*, Opt. Mater., vol. 11, pages 153–165, 1999.

[Levi 93] A. F. J. Levi, S. L. McCall, S. J. Pearton & R. A. Logan, *Room temperature operation of submicrometer radius disc laser*, Electron. Lett., vol. 29, pages 1666–1667, 1993.

[Ling 03] T. Ling, L. Liu, Q. Song, L. Xu & W. Wang, *Intense directional lasing from a deformed square-shaped organic-inorganic hybrid glass microring cavity*, Opt. Lett., vol. 28, pages 1784–1786, 2003.

[Lipowsky 90] R. Lipowsky, *Surface-induced disorder and surface melting*, Springer Proc. in Physics, vol. -, pages 158–166, 1990.

[Little 97] B. E. Little, S. T. Chu, H. A. Haus, J. Foresi & J. P. Laine, *Microring resonator channel dropping filters*, J. Lightwave Technol., vol. 15, pages 998–1005, 1997.

[Little 98] B. E. Little, J. S. Foresi, G. Steinmeyer, E. R. Thoen, S. T. Chu, H. A. Haus, E. P. Ippen, L. C. Kimerling & W. Greene, *Ultra-compact Si/SiO*$_2$ *microring resonator optical channel dropping filters*, IEEE Photonics Technol. Lett., vol. 10, pages 549–551, 1998.

[Little 99] B. E. Little, S. T. Chu, W. Pan, D. Ripin, T. Kaneko, Y. Kokubun & E. Ippen, *Vertically coupled glass microring resonator channel dropping filters*, IEEE Photonics Technol. Lett., vol. 11, pages 215–217, 1999.

[Little 00] B. E. Little, J. P. Laine, D. R. Lim & H. A. Haus, *Pedestal antiresonant reflecting waveguides for robust coupling to microsphere resonators and for microphotonics circuits*, Opt. Lett., vol. 25, pages 73–75, 2000.

[Little 04] B. E. Little, S. T. Chu, P. P. Absil, J. V. Hryniewicz, F. G. Johnson, F. Seiferth, D. Gill, V. Van, O. King & M. Trakalo, *Very high-order microring resonator filters for WDM applications*, IEEE Photonics Technol. Lett., vol. 16, pages 2263–2265, 2004.

[Mahapatra 85] A. Mahapatra & W. C. Robinson, *Integrated-optic ring resonators made by proton exchange in lithium niobate*, Appl. Opt., vol. 24, pages 2285–2286, 1985.

[Majkic 08] A. Majkic, M. Koechlin, G. Poberaj & P. Günter, *Optical microring resonators in fluorineimplanted lithium niobate*, Opt. Express, vol. 16, no. 12, pages 8769–8779, June 2008.

[Manolatou 99] C. Manolatou, M. J. Khan, S. Fan, P. R. Villeneuve, H. A. Haus & J. D. Joannopoulos, *Coupling of modes analysis of resonant channel add-drop filters*, IEEE J. Quantum Electron., vol. 35, pages 1322–1331, 1999.

[McCall 92] S. L. McCall, A. F. J. Levi, R. E. Slusher, S. J. Pearton & R. A. Logan, *Whispering-gallery mode microdisk lasers*, Appl. Phys. Lett., vol. 60, pages 289–291, 1992.

[Noeckel 94] J. U. Noeckel, A. D. Stone & R. K. Chang, *Q spoiling and directionality in deformed ring cavities*, Opt. Lett., vol. 19, pages 1693–1695, 1994.

[Oraevsky 02] A. N. Oraevsky, *Whispering-gallery waves*, Quant. Electron., vol. 32, pages 377–400, 2002.

[Painter 99] O. Painter, R. K. Lee, A. Scherer, A. Yariv, J. D. OŠBrien, P. D. Dapkus & I. Kim, *Two-dimensional photonic band-gap defect mode laser*, Science, vol. 284, pages 1819–1821, 1999.

[Polman 04] A. Polman, B. Min, J. Kalkman, T. J. Kippenberg & K. J. Vahala, *Ultralow-threshold erbium-implanted toroidal microlaser on silicon*, Appl. Phys. Lett., vol. 84, pages 1037–1039, 2004.

[Poon 01] W. Poon, F. Courvoisier & R. K. Chang, *Multimode resonances in square-shaped optical microcavities*, Opt. Lett., vol. 26, pages 632–634, 2001.

[Åhlfeldt 94] H. Åhlfeldt, *Single-domain layers formed in heat-treated* $LiTaO_3$, Appl. Phys. Lett., vol. 64, no. 24, pages 3213–3215, 1994.

[Raybaut 07] M. Raybaut, A. Godard, C. Lubin, R. Haidar & E. Rosencher, *Fresnel phase matching: a universal phase matching scheme*, C. R. Physique, vol. 8, pages 1205–1212, 2007.

[Rayleigh 12] L. Rayleigh, *The problem of the whispering gallery*, Scientific Papers, vol. 5, pages 617–620, 1912.

[Ridah 97] A. Ridah, P. Bourson, M. D. Fontana & G. Malovichko, *The composition dependence of the Raman spectrum and new assignment of the phonons in* $LiNbO_3$, J. Phys.: Condens. Matter, vol. 9, pages 9687–9693, 1997.

[Roess 64] D. Roess & G. Gehrer, *Selection of discrete modes in toroidal lasers*, Proc. of IEEE, vol. 52, pages 1359–1360, 1964.

[Sandoghdar 96] V. Sandoghdar, F. Treussart, J. Hare, V. Lefevre-Seguin, J. M. Raimond & S. Haroche, *Very low threshold whispering-gallery-mode microsphere laser*, Phys. Rev. A, vol. 54, pages R1777–R1780, 1996.

[Sasagawa 09] K. Sasagawa & M. Tsuchiya, *Highly efficient third harmonic generation in a periodically poled MgO:LiNbO*$_3$ *disk resonator*, Appl. Phys. Express, vol. 2, no. 12, page 122401, 2009.

[Savchenkov 04] A. A. Savchenkov, V. S. Ilchenko, A. B. Matsko & L. Maleki, *KiloHertz optical resonances in dielectric crystal cavities*, Phys. Rev. A, vol. 70, page 051804, 2004.

[Savchenkov 05] A. A. Savchenkov, V. S. Ilchenko, A. B. Matsko & L. Maleki, *High-order tunable filters based on a chain of coupled crystalline whispering gallery-mode resonators*, IEEE Photonics Technol. Lett., vol. 17, pages 136–138, 2005.

[Serkland 94] D. K. Serkland, R. C. Eckardt & R. L. Byer, *Continuous-wave total-internal-reflection optical parametric oscillator pumped at 1064 nm*, Opt. Lett., vol. 19, page 1046, 1994.

[Serpengüzel 95] A. Serpengüzel, S. Arnold & G. Griffel, *Excitation of resonances of microspheres on an optical fiber*, Opt. Lett., vol. 20, pages 654–656, 1995.

[Snyder 83] A. W. Snyder & J. D. Love, Optical waveguide theory, Chapman and Hall, 1983.

[Sones 02] C. L. Sones, S. Mailis, W. S. Brocklesby, R. W. Eason & J. R. Owen, *Differential etch rates in z-cut LiNbO*$_3$ *for variable HF/HNO*$_3$ *concentrations*, J. Mater. Chem., vol. 12, no. 2, pages 295–298, 2002.

[Sono 06] T. J. Sono, J. G. Scott, C. L. Sones, C. E. Valdivia, S. Mailis, R. W. Eason, J. G. Frey & L. Danos, *Reflection second harmonic generation on a z -cut congruent lithium niobate crystal*, Phys. Rev. B, vol. 74, page 205424, 2006.

[Spillane 02] S. M. Spillane, T. J. Kippenberg & K. J. Vahala, *Ultralow-threshold Raman laser using a spherical dielectric microcavity*, Nature, vol. 415, pages 620–623, 2002.

[Spillane 05] S. M. Spillane, T. J. Kippenberg, K. J. Vahala, K. W. Goh, E. Wilcut & H. J. Kimble, *Ultrahigh-Q toroidal microresonators for cavity quantum electrodynamics*, Phys. Rev. A, vol. 71, page 013817, 2005.

[Srinivasan 04] K. Srinivasan, P. E. Barclay, M. Borselli & O. Painter, *Optical-fiber-based measurement of an ultrasmall volume high-Q photonic crystal microcavity*, Phys. Rev. B, vol. 70, page 081306, 2004.

[Stratton 07] J. A. Stratton, Electromagnetic theory, Wiley-IEEE Press, 2007.

[Vahala 03] K. J. Vahala, *Optical microcavities*, Nature, vol. 424, pages 839–846, 2003.

[Vernooy 98] D. W. Vernooy, V. S. Ilchenko, H. Mabuchi, E. W. Steed & H. J. Kimble, *High-Q measurements of fused-silica microspheres in the near infrared*, Opt. Lett., vol. 23, pages 247–249, 1998.

[Walsh 63] P. Walsh & G. Kemeny, *Laser operation without spikes in a ruby ring*, J. Appl. Phys., vol. 34, pages 956–957, 1963.

[Wang 07a] T. J. Wang & C. H. Chu, *Wavelength-tunable microring resonator on lithium niobate*, IEEE Photonics Technol. Lett., vol. 19, pages 1904–1906, 2007.

[Wang 07b] T. J. Wang, C. H. Chu & C. Y. Lin, *Electro-optically tunable microring resonators on lithium niobate*, Opt. Lett., vol. 32, pages 2777–2779, 2007.

[Yamamoto 93] Y. Yamamoto & R. E. Slusher, *Optical processes in microcavities*, Phys. Today, vol. 46, pages 66–73, 1993.

[Yariv 99] A. Yariv, Y. Xu, R. K. Lee & A. Scherer, *Coupled-resonator optical waveguide: a proposal and analysis*, Opt. Lett., vol. 24, pages 711–713, 1999.

[Yokoyama 92] H. Yokoyama, *Physics and device applications of optical microcavities*, Science, vol. 256, pages 66–70, 1992.

[Yokoyama 95] H. Yokoyama & K. Ujihara, editeurs, Spontaneous emission and laser oscillation in microcavities, CRC Press, 1995.

[Zhang 96] J. P. Zhang, D. Y. Chu, S. L. Wu, W. G. Bi, R. C. Tiberio, C. W. Tu & C. T. Ho, *Directional light output from photonic-wire microcavity semiconductor lasers*, IEEE Photonics Technol. Lett., vol. 8, pages 968–970, 1996.

6

Future work

A set of methods has been presented in this thesis for the processing of lithium niobate crystals in terms of domain engineering, waveguide fabrication and surface micro-structuring which hold potential for the realisation of photonic devices in versatile optical crystal. However, further development will be required to be able to further understand and control several aspects of these methods for practical applications. Some suggestions for further work is given here.

Extension of surface to bulk domain engineering of LN

At present μm size surface domains can be routinely fabricated in LN. However the applicability of these domains is limited to surface waveguides. In order to extend the applicability of the inverted domain structures to buried waveguides or for bulk nonlinear optical processes, it is necessary to be able to increase the depth of the domain structures. Possible approaches for the fabrication of bulk domains structure based on the thesis results should involve pushing the surface domains further into the depth of the crystal. This can be possibly achieved by further laser illumination of a surface domain followed by an EFP poling process. As surface domains exist in a head-to-head configuration compared with the underlying bulk, further irradiation with a laser of the appropriate wavelength could, via a photovoltaic current along the $+z$ axis, accumulate electrons at the domain wall. These electrons can build up a sufficiently high E-field that could assist further expansion of the domain into the crystal using the initial surface domains as nucleation points. Preliminary experiments have indicated that such a scheme is possible, however a more systematic investigation is clearly required.

Sub-micron bulk domains

Some other applications (i.e., gratings or photonic crystals) demand the fabrication of sub-micron domains, which can be achieved by SFM poling, but the depth of these domains however is also very limited. Additionally, optical poling techniques present size restrictions due to the diffraction limit of the incident focused beam. Sub-micron topographical structures on the other hand can be precisely defined by focused ion beaming (FIB) machining. Thus, it might be possible to transfer the topography information into a domain structure. This could be achieved by direct-bonding techniques. In the case of direct-bonded SLN and CLN z-cut crystals that have very good lattice matching, domain wall movement is expected to be continuous. Thus, during EFP via an E-field: $E_{\mathrm{c}}(\mathrm{SLN}) < E < E_{\mathrm{c}}(\mathrm{CLN})$, domain nucleation can be only initialised in the SLN crystal. However, the continuous propagating domain wall movement from SLN crystal to CLN crystal might enable the poling of CLN as well because it avoids the surface pinning by defects in the CLN crystal which is the origin of its high E_{c}. Thus a specific defined topography on SLN (with nm resolution patterning produced by FIB) could be transferred to a domain structure in CLN during the poling of the whole SLN crystal.

Well-defined domain structure with smooth domain walls

The surface domain structures fabricated in the thesis by inhibition of poling do not have sharp edges between the opposite domain regions but show a region which consists of nanodomains revealed after brief HF etching. The presence of these nanodomains can be a source of scattering especially in the fabrication of ridge waveguide structures which will increase the transmission loss in such structures. One approach to overcome this limitation might involve EFP during surface heating by UV direct writing. It's known that at high temperature, nucleation occurs at much lower E-field. Thus, during focused illumination of a crystal surface with deep UV light, the local crystal surface of depth $\sim$ few microns can be heated to a high temperature, close to, or even above the Curie temperature, and a much lower E-field will therefore be required for local domain nucleation. Therefore, if an E-field is present all the time during UV-writing, local domain inversion might occur. This technique takes advantage of 1) domain nucleation at the highest temperature and then expands to roughly the beam diameter, so that the domain wall should be as smooth as that provided by EFP (eliminating any nanodomain roughness, i.e, in poling-inhibition), and 2) the newly inverted domain in the region of the incident laser beam during UV writing is actually connected with neighbouring cooled inverted domains, so these domain walls should be continuous, and therefore result in a continuous domain wall for the whole pattern or path of the inverted domain.

Enhanced effective EO coefficient of UV written waveguides

Preliminary experimental results have demonstrated a 50% increase of the effective EO coefficient in poling-inhibited UV-written waveguides, believed to be due to the overlapping of poling-inhibited domains with the UV-written waveguides and possibly some additional strain. Experiments need to be done to investigate how the domain structure overlaps with the refractive index profile and the intensity mode profile, and how it induces the EO coefficient enhancement. It should be done by actually measurement of the domain profile via wedge polishing and capture of the mode profile, with additional waveguide simulation of the EO effect. Additionally, if it's due to the strain, study of thermal stability might be also necessary.

Low-loss ridge waveguides

Low-loss ridge waveguides can reduce significantly the footprint of integrated optical devices due to the much lower bending loss. Fabrication of low-loss complex ridge waveguide structures such as straight channels, rings, discs etc, can be achieved by chemical etching (or even vapour phase HF etching) of domain structures with smooth domain walls which transfers the domain pattern to a surface topography pattern. The lateral light confinement is provided by the ridges, while the vertical confinement, apart from the UV written induced refractive index contrast, can be redefined by a Ti-indiffusion process.

Optical resonator fabrication, characterisation and its integration

WGM resonator structures have been fabricated via surface tension reshaping of an initial surface micro-structure. The transition from the initial microstructure to the final surface tension reshaped structure needs to be well understood, i.e., by modeling the heat treatment process, in order to be able to predict the final reshaped structure and to define the processing conditions. Further characterisation of the WGM resonator performance is of course required to establish the Q factor limits, the tunability and the nonlinear performance of these structures. Additionally WGM resonators can be doped with rare earth ions, such as Nd or Er for the fabrication of micro lasers. Finally the surface tension reshaping method can be applied to reduce the scattering loss in other ridge structures such as couplers, interferometers, and ring resonators. This will be the subject of my post-doctoral fellowship (PhD+) that I have been awarded.

Appendix A

Publications and presentations

A.1 Journal papers

[Ying 10b, Sones 10a, Steigerwald 10, Ying 09d, Sones 09a, Sones 09d, Ganguly 09, Johann 09, Sones 08a]

A.2 Conference papers

[Ying 10a, Sones 10b, Banks 09, Ying 09c, Mailis 09a, Ying 09b, Sones 09c, Sones 09b, Ying 09a, Mailis 09b, Sones 08b, Mailis 08]

References

[Banks 09] D. P. Banks, K. S. Kaur, C. Grivas, C. L. Sones, P. Gangopadhyay, C. Ying, J. D. Mills, S. Mailis, I. Zergioti, R. Fardel, M. Nagel, T. Lippert, X. Xu, S. P. Banks & R. W. Eason, Femtosecond laser-induced forward transfer for the deposition of nanoscale transparent and solid-phase materials, Proc. LAMPS 2009, Kobe, 29 June, 2009.

[Ganguly 09] P. Ganguly, C. L. Sones, Y. J. Ying, H. Steigerwald, K. Buse, E. Soergel, R. W. Eason & S. Mailis, *Determination of refractive indices from the mode profiles of UV-written channel waveguides in* $LiNbO_3$*-crystals for optimization of writing conditions*, J. Lightwave Technol., vol. 27, no. 16, pages 3490–3497, August 2009.

[Johann 09] F. Johann, Y. J. Ying, T. Jungk, A. Hoffmann, C. L. Sones, R. W. Eason, S. Mailis & E. Soergel, *Depth resolution of piezoresponse force microscopy*, Appl. Phys. Lett., vol. 94, no. 17, pages 172904–3, April 2009.

[Mailis 08] S. Mailis, A. C. Muir, Y. J. Ying, C. L. Sones, R. W. Eason, T. Jungk, A. Hoffmann & E. Soergel, UV laser radiation inhibits domain inversion in lithium niobate, CLEO/QELS 2008, San Jose, 4-9 May, 2008.

[Mailis 09a] S. Mailis, C. L. Sones, P. Ganguly, Y. J. Ying, K. S. Kaur, D. P. Banks & R. W. Eason, Laser-Induced-Forward-Transfer: a rapid prototyping tool for fabrication of photonic devices, COLA 09, Singapore, 22-27 Nov, 2009.

[Mailis 09b] S. Mailis, Y. J. Ying, C. L. Sones, A. C. Peacock, F. Johann, E. Soergel, R. W. Eason & M. N. Zervas, Ultra-smooth lithium niobate single crystal photonic micro-structures, CLEO/IQEC 2009, Baltimore, 31 May, 2009.

[Sones 08a] C. L. Sones, A. C. Muir, Y. J. Ying, S. Mailis, R. W. Eason, T. Jungk, Á. Hoffmann & E. Soergel, *Precision nanoscale domain engineering of lithium niobate via UV laser induced inhibition of poling*, Appl. Phys. Lett., vol. 92, no. 7, page 072905, 2008.

[Sones 08b] C. L. Sones, Y. J. Ying, S. Mailis, R. W. Eason, T. Jungk, H. Steigerwald, A. Hoffman, E. Soergel & K. Buse, UV laser-induced domain inhibition: a route to domain-engineered structuring of lithium niobate, Photonics 2008, New Delhi, 15-17 Dec, 2008.

[Sones 09a] C. L. Sones, P. Ganguly, Y. J. Ying, F. Johann, E. Soergel, R. W. Eason & S. Mailis, *Spectral and electro-optic response of UV-written waveguides in LiNbO$_3$ single crystals*, Opt. Express, vol. 17, no. 26, pages 23755–23764, 2009.

[Sones 09b] C. L. Sones, P. Ganguly, Y. J. Ying, H. Steigerwald, K. Buse, E. Soergel, R. W. Eason & S. Mailis, Spectral analysis of UV-written waveguides in LiNbO$_3$: measurement of cut-off wavelengths, CLEO/Europe-EQEC 2009, Munich, 14-19 Jun, 2009.

[Sones 09c] C. L. Sones, P. Ganguly, Y. J. Ying, H. Steigerwald, K. Buse, E. Soergel, R. W. Eason & S. Mailis, Spectral and electro-optic characterisation of UV-written waveguides in LiNbO$_3$, Photorefractive materials Effects and Devices Control of Light and Matter, PR09, Bad Honnef, 11-14 Jun, 2009.

[Sones 09d] C. L. Sones, K. S. Kaur, P. Ganguly, D. P. Banks, Y. J. Ying, R. W. Eason & S. Mailis, *Laser-Induced-Forward-Transfer: a rapid prototyping tool for fabrication of photonic devices*, Appl. Phys. A, vol. -, pages 393–395, 2009.

[Sones 10a] C. L. Sones, P. Ganguly, Y. J. Ying, E. Soergel, R. W. Eason & S. Mailis, UV laser-assisted fabrication of ridge waveguides in lithium niobate crystals, volume -, Appl. Phys. Lett. (submitted), 2010.

[Sones 10b] C. L. Sones, Y. J. Ying, R. W. Eason, S. Mailis, P. Ganguly & E. Soergel, UV laser-assisted fabrication of ridge waveguides in lithium niobate crystals, ECIO 2010, Cambridge, 7-9 Apr, 2010.

[Steigerwald 10] H. Steigerwald, M. Lilienblum, F. von Cube, Y. J. Ying, R. W. Eason, S. Mailis, B. Sturman, E. Soergel & K. Buse, Origin of UV-induced poling inhibition in lithium niobate crystals, volume -, Phys. Rev. B (submitted), 2010.

[Ying 09a] Y. J. Ying, C. L. Sones, H. Steigerwald, F. Johann, E. Soergel, K. Buse, R. W. Eason & S. Mailis, UV laser-induced poling inhibition in lithium niobate crystals, CLEO/Europe-EQEC 2009, Munich, 14-19 Jun, 2009.

[Ying 09b] Y. J. Ying, C. E. Valdivia, R. W. Eason & S. Mailis, Light assisted poling and the photorefractive effect in lithium niobate, Photorefractive materials Effects and Devices Control of Light and Matter, PR09 (Invited), Bad Honnef, 11-14 Jun, 2009.

[Ying 09c] Y. J. Ying, C. E. Valdivia, R. W. Eason & S. Mailis, The role of the photorefractive effect in ultrafast laser-assisted poling in $LiNbO_3$, The Rank Prize Funds Meeting 2009, Grasmere, 18-21 May, 2009.

[Ying 09d] Y. J. Ying, C. E. Valdivia, C. L. Sones, R. W. Eason & S. Mailis, *Latent light-assisted poling of* $LiNbO_3$, Opt. Express, vol. 17, no. 21, pages 18681–18692, 2009.

[Ying 10a] C. Y. J. Ying, C. L. Sones, A. C. Peacock, F. Johann, E. Soergel, R. W. Eason, M. N. Zervas & S. Mailis, Ultra-smooth lithium niobate micro-resonators by surface tension reshaping, Photon 10, Southampton, 23-26 Aug, 2010.

[Ying 10b] C. Y. J. Ying, C. L. Sones, A. C. Peacock, F. Johann, E. Soergel, R. W. Eason, M. N. Zervas & S. Mailis, *Ultra-smooth lithium niobate photonic micro-structures by surface tension reshaping*, Opt. Express, vol. 18, no. 11, pages 11508–11513, May 2010.

Appendix B

Prints of publications

Latent light-assisted poling of $LiNbO_3$

Y. J. Ying,[1,*] **C. E. Valdivia,**[1,2] **C. L. Sones,**[1] **R. W. Eason**[1] **and S. Mailis**[1]

[1]*Optoelectronics Research Centre, University of Southampton, Southampton, S017 1BJ, UK*
[2]*Centre for Research in Photonics, University of Ottawa, Ottawa, K1N 6N5, Canada*
**yoy@orc.soton.ac.uk*

Abstract: The observation of latent light-assisted poling (LAP) in lithium niobate single crystals is reported. More specifically, the nucleation field is reduced and remains reduced for an extended time period (up to several hours) after irradiation with ultrafast (~150 fs) laser light at a wavelength of 400 nm. The maximum nucleation field reduction measured using latent-LAP (62%) was significantly higher in comparison with regular non-time-delayed LAP (41%) under identical irradiation conditions in undoped congruent lithium niobate crystals. No latent-LAP effect was observed in MgO-doped crystals for the experimental conditions used, despite the strong effect observed using regular LAP. The latent-LAP effect is attributed to the formation of a slowly decaying photo-induced space-charge distribution which assists local ferroelectric domain nucleation. The dynamics of latent-LAP are compared with the dynamics of photorefractive grating decay, recorded in lithium niobate crystals of different doping, confirming the space charge hypothesis.

OCIS codes: (140.3538) Lasers, pulsed; (160.5320) Photorefractive materials; (160.2260) Ferroelectrics; (160.3730) Lithium niobate; (090.5694) Real-time holography.

References and links

1. L. Arizmendi, “Photonic applications of lithium niobate crystals,” Phys. Status Solidi A **201**, 253–283 (2004). *http://dx.doi.org/10.1002/pssa.200303911*
2. I. E. Barry, G. W. Ross, P. G. R. Smith, R. W. Eason, and G. Cook, “Microstructuring of lithium niobate using differential etch-rate between inverted and non-inverted ferroelectric domains,” Mater. Lett. **37**(4-5), 246–254 (1998), http://dx.doi.org/10.1016/S0167-577X(98)00100-1.
3. A. J. Boyland, S. Mailis, J. M. Hendricks, P. G. R. Smith, and R. W. Eason, “Electro-optically controlled beam switching via total internal reflection at a domain-engineered interface in $LiNbO_3$,” Opt. Commun. **197**(1-3), 193–200 (2001), http://dx.doi.org/10.1016/S0030-4018(01)01428-6.
4. R. W. Eason, A. J. Boyland, S. Mailis, and P. G. R. Smith, “Electro-optically controlled beam deflection for grazing incidence geometry on a domain-engineered interface in $LiNbO_3$,” Opt. Commun. **197**(1-3), 201–207 (2001), http://dx.doi.org/10.1016/S0030-4018(01)01429-8.
5. M. Yamada, N. Nada, M. Saitoh, and K. Watanabe, “First-order quasi-phase matched $LiNbO_3$ waveguide periodically poled by applying an external field for efficient blue second-harmonic generation,” Appl. Phys. Lett. **62**(5), 435–436 (1993), http://link.aip.org/link/?APL/62/435/1.
6. M. Yamada, and M. Saitoh, “Fabrication of a periodically poled laminar domain structure with a pitch of a few micrometers by applying an external electric field,” J. Appl. Phys. **84**(4), 2199–2206 (1998), http://link.aip.org/link/?JAP/84/2199/1.
7. W. Wang, Y. Kong, H. Liu, Q. Hu, S. Liu, S. Chen, and J. Xu, “Light-induced domain reversal in doped lithium niobate crystals,” J. Appl. Phys. **105**(4), 043105 (2009), http://dx.doi.org/10.1063/1.3079478.
8. H. Steigerwald, F. Luedtke, and K. Buse, “Ultraviolet light assisted periodic poling of near-stoichiometric, magnesium-doped lithium niobate crystals,” Appl. Phys. Lett. **94**(3), 032906 (2009), http://link.aip.org/link/?APL/94/032906/1.
9. M. Fujimura, T. Sohmura, and T. Suhara, “Fabrication of domain-inverted gratings in MgO:$LiNbO_3$ by applying voltage under ultraviolet irradiation through photomask at room temperature,” Electron. Lett. **39**(9), 719–721 (2003), http://ieeexplore.ieee.org/xpls/abs_all.jsp?isnumber=27015&arnumber=1199952&count=36&index=12.
10. C. L. Sones, M. C. Wengler, C. E. Valdivia, S. Mailis, R. W. Eason, and K. Buse, “Light-induced order-of-magnitude decrease in the electric field for domain nucleation in MgO-doped lithium niobate crystals,” Appl. Phys. Lett. **86**(21), 212901 (2005), http://link.aip.org/link/?APL/86/212901/1.
11. V. Dierolf, and C. Sandmann, “Direct-write method for domain inversion patterns in $LiNbO_3$,” Appl. Phys. Lett. **84**(20), 3987–3989 (2004), http://link.aip.org/link/?APL/84/3987/1.

12. M. C. Wengler, B. Fassbender, E. Soergel, and K. Buse, "Impact of ultraviolet light on coercive field, poling dynamics and poling quality of various lithium niobate crystals from different sources," J. Appl. Phys. **96**(5), 2816–2820 (2004), http://link.aip.org/link/?JAP/96/2816/1.
13. C. E. Valdivia, C. L. Sones, S. Mailis, J. D. Mills, and R. W. Eason, "Ultrashort-pulse optically-assisted domain engineering in lithium niobate," Ferroelectrics **340**(1), 75–82 (2006), http://www.informaworld.com/10.1080/00150190600888983.
14. J. H. Ro, and M. Cha, "Subsecond relaxation of internal field after polarization reversal in congruent $LiNbO_3$ and $LiTaO_3$ crystals," Appl. Phys. Lett. **77**(15), 2391–2393 (2000), http://link.aip.org/link/?APL/77/2391/1.
15. A. I. Lobov, V. Y. Shur, I. S. Baturin, E. I. Shishkin, D. K. Kuznetsov, A. G. Shur, M. A. Dolbilov, and K. Gallo, "Field induced evolution of regular and random 2D domain structures and shape of isolated domains in $LiNbO_3$ and $LiTaO_3$," Ferroelectrics **341**(1), 109–116 (2006), http://www.informaworld.com/smpp/content~db=all~content=a769409747~tab=content.
16. Ya. Vladimir, Shur, "Correlated Nucleation and Self-Organized Kinetics of Ferroelectric Domains," in *Nucleation Theory and Applications*, W. P. S. Dr. Jürn, ed. (2005), pp. 178–214. *http://dx.doi.org/10.1002/3527604790.ch6*
17. W. Yan, L. Shi, Y. Kong, Y. Wang, H. Liu, J. Xu, S. Chen, L. Zhang, Z. Huang, S. Liu, and G. Zhang, "The electrostatic depinning mechanism of domain wall for near-stoichiometric lithium niobate crystals," J. Phys. D Appl. Phys. **39**(19), 4245–4249 (2006), http://www.iop.org/EJ/abstract/0022-3727/39/19/018.
18. B. Sturman, M. Carrascosa, and F. Agulló-López, "Light-induced charge transport in $LiNbO_3$ crystals," Phys. Rev. B **78**(24), 245114 (2008), http://link.aps.org/doi/10.1103/PhysRevB.78.245114.
19. O. Beyer, D. Maxein, K. Buse, B. Sturman, H. T. Hsieh, and D. Psaltis, "Femtosecond time-resolved absorption processes in lithium niobate crystals," Opt. Lett. **30**(11), 1366–1368 (2005), http://ol.osa.org/abstract.cfm?URI=ol-30-11-1366.
20. L. Arizmendi, and F. Agulló-López, "$LiNbO_3$: A paradigm for photorefractive materials," MRS Bull. **19**, 32–38 (1994).
21. F. H. Mok, "Angle-multiplexed storage of 5000 holograms in lithium niobate," Opt. Lett. **18**(11), 915–917 (1993), http://www.opticsinfobase.org/abstract.cfm?URI=ol-18-11-915.
22. Y. S. Bai, and R. Kachru, "Nonvolatile holographic storage with two-step recording in lithium niobate using cw lasers," Phys. Rev. Lett. **78**(15), 2944–2947 (1997), http://prola.aps.org/abstract/PRL/v78/i15/p2944_1.
23. F. Jermann, M. Simon, and E. Krätzig, "Photorefractive properties of congruent and stoichiometric lithium niobate at high light intensities," J. Opt. Soc. Am. B **12**(11), 2066–2070 (1995), http://josab.osa.org/abstract.cfm?URI=josab-12-11-2066.
24. D. Berben, K. Buse, S. Wevering, P. Herth, M. Imlau, and T. Woike, "Lifetime of small polarons in iron-doped lithium–niobate crystals," J. Appl. Phys. **87**(3), 1034–1041 (2000), http://link.aip.org/link/?JAP/87/1034/1.
25. K. Mizuuchi, A. Morikawa, T. Sugita, and K. Yamamoto, "Polarisation-switching-induced resistance change in ferroelectric Mg-doped $LiNbO_3$ single crystals," Electron. Lett. **40**(13), 819–820 (2004), http://ieeexplore.ieee.org/xpls/abs_all.jsp?arnumber=1309740.
26. I. Nee, M. Müller, K. Buse, and E. Krätzig, "Role of iron in lithium-niobate crystals for the dark-storage time of holograms," J. Appl. Phys. **88**(7), 4282–4286 (2000), http://link.aip.org/link/?JAP/88/4282/1.
27. A. Mansingh, and A. Dhar, "The AC conductivity and dielectric constant of lithium niobate single crystals," J. Phys. D Appl. Phys. **18**(10), 2059–2071 (1985), http://www.iop.org/EJ/abstract/0022-3727/18/10/016.
28. R. T. Smith, and F. S. Welsh, "Temperature dependence of the elastic, piezoelectric, and dielectric constants of lithium tantalate and lithium niobate," J. Appl. Phys. **42**(6), 2219–2230 (1971), http://link.aip.org/link/?JAPIAU/42/2219/1.
29. C. E. Valdivia, "Light-induced ferroelectric domain engineering in lithium niobate & lithium tantalate," (PhD thesis, University of Southampton, Southampton, 2007). *http://www.orc.soton.ac.uk/viewpublication.html?pid=3846*

1. Introduction

Single crystal lithium niobate (LN) is a ferroelectric crystal, which exhibits a spontaneous electric polarization along its z-axis, the direction of which can be inverted by the application of an external electric field (*E*-field). Ferroelectric domain engineering of LN has received much interest for applications in nonlinear frequency conversion, electro-optic modulation [1], surface micro-structuring [2], beam switching [3], and deflection [4].

The most common domain engineering technique for LN is electric field poling (EFP), where a photolithographically-patterned electrode provides a spatially modulated *E*-field across the crystal in the z-axis [5,6]. Recent research investigating the influence of light on EFP revealed that illuminated regions require a lower nucleation field, E_n (the *E*-field required for microscopic ferroelectric domain nucleation) in both undoped congruent LN (CLN) and MgO-doped LN using c.w. [7–12] and pulsed laser light [13] in a process referred to as *light-assisted poling* (LAP). Utilizing ultrafast lasers at wavelengths ranging between 305 nm and 800 nm, LAP has been observed to produce significant E_n reductions, of up to two orders of magnitude for MgO:CLN [13].

In all cases of LAP reported thus far, the light illumination was concurrent with the application of the external *E*-field. In this paper we show that in undoped CLN, the E_n reduction can be observed even several hours after light illumination. Using this technique, called *latent light-assisted poling* (LLAP), the two processes of light illumination and application of an external *E*-field can be de-coupled. Interestingly, the E_n reduction in LLAP (62%) is larger compared to that measured in simultaneous LAP (42%) [13]. The latent effect has not been observed in MgO:CLN for the time scales employed in the experiments here. The dependence of LAP and LLAP on the doping suggests a space-charge-related mechanism. The low dark conductivity in the undoped CLN allows a photo-induced space-charge distribution to persist for a significant period of time after its formation, while in the MgO:CLN any photo-induced space-charge distribution decays much faster due to the much higher dark conductivity which makes this crystal less susceptible to the photorefractive damage. The presence of a photo-induced space-charge distribution and the corresponding space-charge field induces a refractive index change in LN via the electro-optic effect. Probing of this photorefractive index change provides an excellent tool for the investigation of the LLAP dynamics. Therefore, the domain nucleation for varying time-delays between light illumination and application of the external *E*-field in undoped CLN is investigated in Section 2, while in Section 3 the LLAP dynamics are compared to the decay of a photorefractive grating formed by the space-charge field.

2. Latent-LAP

To investigate the process of LLAP, 0.5-mm thick, z-cut, optical grade, undoped CLN crystals (Crystal Technology, Inc.) were held within a transparent cell which enabled the simultaneous light illumination of the crystal and the application of an external *E*-field. This arrangement has been used for previous LAP experiments and a detailed description can be found in [10]. The crystal was subjected to a sequence of processing steps as follows. First, the crystal was domain-inverted three times sequentially, leaving it with a domain orientation anti-parallel to its virgin state. This was done to condition the crystal in order to avoid the first poling cycle which is known to have a higher coercive field [14] and exhibit erratic domain expansion as compared to subsequent poling cycles. Second, a pulsed laser beam (~150 fs, 250 kHz, $\lambda = 400$ nm) with a Gaussian intensity profile was focused onto the –z face (front surface) to a spot diameter of ~30 µm for an illumination time of 30 s. The crystal was then repositioned and a new spot was illuminated with identical conditions after a subsequent delay of 30 s. The process was repeated to systematically illuminate a number of spots at precisely controlled times. Third, following the last spot and a final 30 s delay, the voltage was ramped up to the desired value over a period of 30 s, whereupon the maximum voltage was maintained for 300 s, and then ramped back down to 0 V over a final period of 30 s. The *voltage delay time* for each spot is defined as the elapsed time from the end of its illumination to the end of the first voltage ramp. Thus, each spot corresponded to different values of voltage delay time. For the *E*-field step, liquid electrodes were introduced, uniformly covering both crystal faces. The illumination times, time delays and *E*-field application duration were chosen to demonstrate the effect and were not necessarily the optimal experimental conditions. After the above procedure, the samples were briefly etched in hydrofluoric (HF) acid to reveal the preferentially inverted ferroelectric LLAP domains. The area of these inverted domains, measured from scanning electron microscopy (SEM) images, was investigated as a function of the voltage delay time for different laser intensities and *E*-fields.

The inverted LLAP domains formed under all of these exposure conditions were of limited depth, and hence did not extend to the opposite crystal face. However, LLAP domains have been pushed through to the opposite face of the crystal by using higher magnitude of the *E*-field or longer *E*-field application times or a combination of the two. It is important to note that under the process of LLAP, domain inversion occurred only at the locations where the crystal had been previously illuminated. As with regular (simultaneous) LAP, LLAP also formed domains which followed the shape of the illuminating spot and were reproducible between different spots and samples. Etching of the –z face of LN crystal in HF acid reveals the inverted ferroelectric LLAP domains with unetched + z faces as shown in Fig. 1. The LLAP conditions for these particular inverted domains were: laser intensity of 9 GW/cm^2, applied *E*-fields of (a) 14 kV/mm and (b) 8 kV/mm, and voltage time delay of 570 s . As shown in Fig. 1, the LLAP domain walls of (a) follow the crystal symmetry due to the high *E*-field applied which allowed expansion of this domain beyond the confines of the illuminating laser spot area. However, the domain did not form a regular hexagon as is typical for EFP domains, forming instead an irregular octagon with domain walls parallel to both the y- and x-axes. The walls labeled 1, 2, 4, 5, 7, 8 are parallel to y-axes, while walls labeled 3, 6 are parallel to x-axes, contrary to the regular domain wall growth in CLN [15]. The LLAP domain walls of (b) also run parallel to both y- and x-axes, in addition to many more rounded segments, generally following the shape of illumination much more closely due to the lower applied *E*-field. Domain walls following the x-axis imply a condition of incomplete screening of the depolarization field [16], likely a result of the redistribution of the photo-induced space charges prior to application of the external *E*-field.

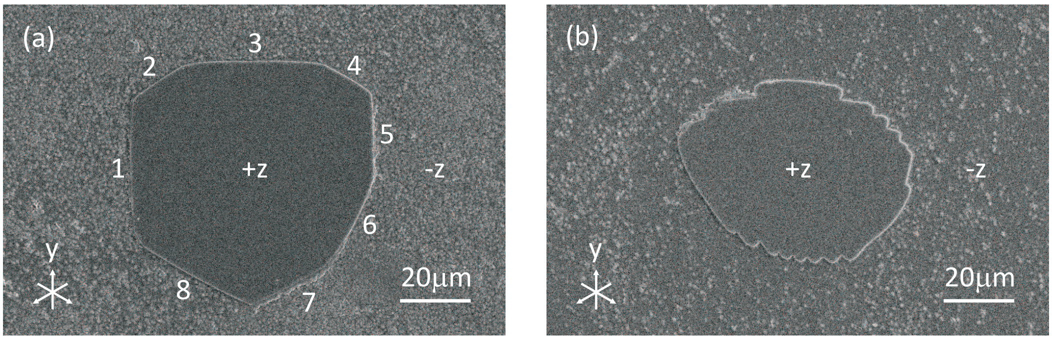

Fig. 1. Preferentially inverted ferroelectric LLAP domains, revealed as unetched + z face after HF etching, are induced by I = 9 GW/cm^2 of 400 nm fs-laser irradiation, followed by applied *E*-fields of (a) 14 kV/mm and (b) 8 kV/mm after a voltage delay time of 570 s in undoped CLN. LLAP domain walls run parallel to both y- and x-axes, particularly for the higher *E*-field in (a).

The nucleation and growth of LLAP domains was investigated by varying the illumination intensity and the applied *E*-field for a series of spots. Figure 2 shows plots of the square root of the inverted LLAP domain areas as a function of voltage delay time for different applied *E*-fields (Fig. 2a) and laser intensities (Fig. 2b). The square root of the inverted domain area is presented here rather than the area itself because it represents the evolution of one linear dimension (1D) of the inverted domain and can be compared in a straightforward manner with the temporal evolution of a 1D space-charge distribution, discussed in Section 3. Figure 2 reveals that, for all exposure conditions, the poled area increases with decreasing voltage delay time. It is expected that at shorter voltage delay times than those applied in the experiments, the poled areas will increase. Our experimental protocol however, limits the shortest applicable voltage delay time to 60 s. Additionally, the poled area increases with increasing laser intensity or *E*-field amplitude. Of particular interest is that domain inversion was observed even for an *E*-field as low as 6 kV/mm (Fig. 2a), a reduction of 62% from the dark E_n (15.8 kV/mm in the reverse poling direction). This is a surprising result as the minimum intensity-dependent E_n observed with simultaneous illumination showed a reduction of only 41% in LAP experiments, as reported in Ref [13], using the same experimental setup. Nevertheless, LLAP formed a sizeable domain even when 6 kV/mm was applied nearly 700 s after illumination. An *E*-field of 6 kV/mm is not necessarily the minimum amplitude to achieve LLAP, but rather represents the minimum value tested under these exposure conditions. The straight lines which appear in Fig. 2a and Fig. 2b corresponds to single exponential decay functions, fitted to the square root of the inverted domain area data points as,

$$A^{1/2} = L_0 \exp\left(-t / \tau_L\right) \quad (1)$$

where A is the LLAP inverted domain area, L_0 is a constant and τ_L is the time constant of the 1-D length reduction. The results of the fittings are listed in Table 1. The close values of decay rate (τ_L^{-1}) show that the length-reduction of the inverted domains with voltage delay time is very similar despite of the very diverse experimental conditions in both laser exposure and value of applied *E*-field. Any differences should be attributed to the uncertainty due to the short range fitting (~10% in Table 1), the stochastic nature of ferroelectric domain nucleation and expansion, and the presence of local defects in the crystal which also govern domain nucleation and growth during regular EFP [17] rather than the exposure and poling conditions. For more accurate measurements, it is necessary to average over many exposure locations as the local crystal quality appears to have a noticeable impact on the growth of LLAP domains. It should be noted here that actually a more reasonable fitting is by a stretched exponential decay instead of a single-exponential decay considering the tunneling-involved charge migration at shallow energy levels [18]. However, the short measurement range and the limited number of data points can induce a significant uncertainty in the fitting of a stretched exponential decay function. Fitting a single exponential function is acceptable however for this short range of time delays (60 s – 720 s). A parameter $\Delta A^{1/2}$, defined as the relative reduction of $A^{1/2}$ from 60 s to 720 s, expressed as

$$\Delta A^{1/2} = 1 - A^{1/2}_{t=720s} / A^{1/2}_{t=60s} \quad (2)$$

can be used for comparison with the photorefractive grating decay in Section 3. The $\Delta A^{1/2}$ values for each point in Fig. 2 are derived from the single exponential fitting and are listed in Table 1.

Table 1. Summary of constants L_0, time constants τ_L, decay rates τ_L^{-1} and the relative reductions $\Delta A^{1/2}$ from 60 s to 720 s of the linear dimension of the LLAP inverted domains in undoped CLN for different experimental conditions.

E (kV/mm)	*I* (GW/cm^2)	L_0 (μm)	τ_L (s)	τ_L^{-1} (× 10^{-4} s^{-1})	$\Delta A^{1/2}$
8	4.5	42.4	2860 ± 120	3.50 ± 0.29	0.206
8	9	47.3	3970 ± 470	2.52 ± 0.61	0.153
8	18	54.8	4050 ± 250	2.47 ± 0.31	0.150
14	9	60.8	3010 ± 450	3.33 ± 1.02	0.197
10	9	47.5	2750 ± 250	3.64 ± 0.67	0.213
6	9	35.5	3150 ± 390	3.17 ± 0.80	0.189

Also, Fig. 3 shows that for an *E*-field (8 kV/mm) or intensity (9 GW/cm^2), the square root of the inverted domain area linearly increases with the intensity or the *E*-field within that range. The larger slope of the data for constant intensity indicates that the domain area is more sensitive to the applied *E*-field rather than the intensity.

Further investigations of the LLAP domain area for voltage delays up to 10 hours are shown in Fig. 4. However, for delay times beyond 700 s, the samples were kept in the dark before the application of the *E*-field, instead of being illuminated constantly by a broadband light source as in the short voltage delays experiments (< 700 s) which is likely to influence the relaxation rate of the space-charge distributions as will be discussed in Section 3. Additionally for longer time delays the inverted domains become fragmented, hence the measurements are increasingly inaccurate. Preferential nucleation was observed for time delays as long as 24 hours after laser irradiation, however the resulting domains were fragmented for the experimental conditions used. It is possible that higher laser intensities, higher *E*-fields, and/or longer exposures could produce solid domains as shown in Fig. 1 even for such long voltage delay times.

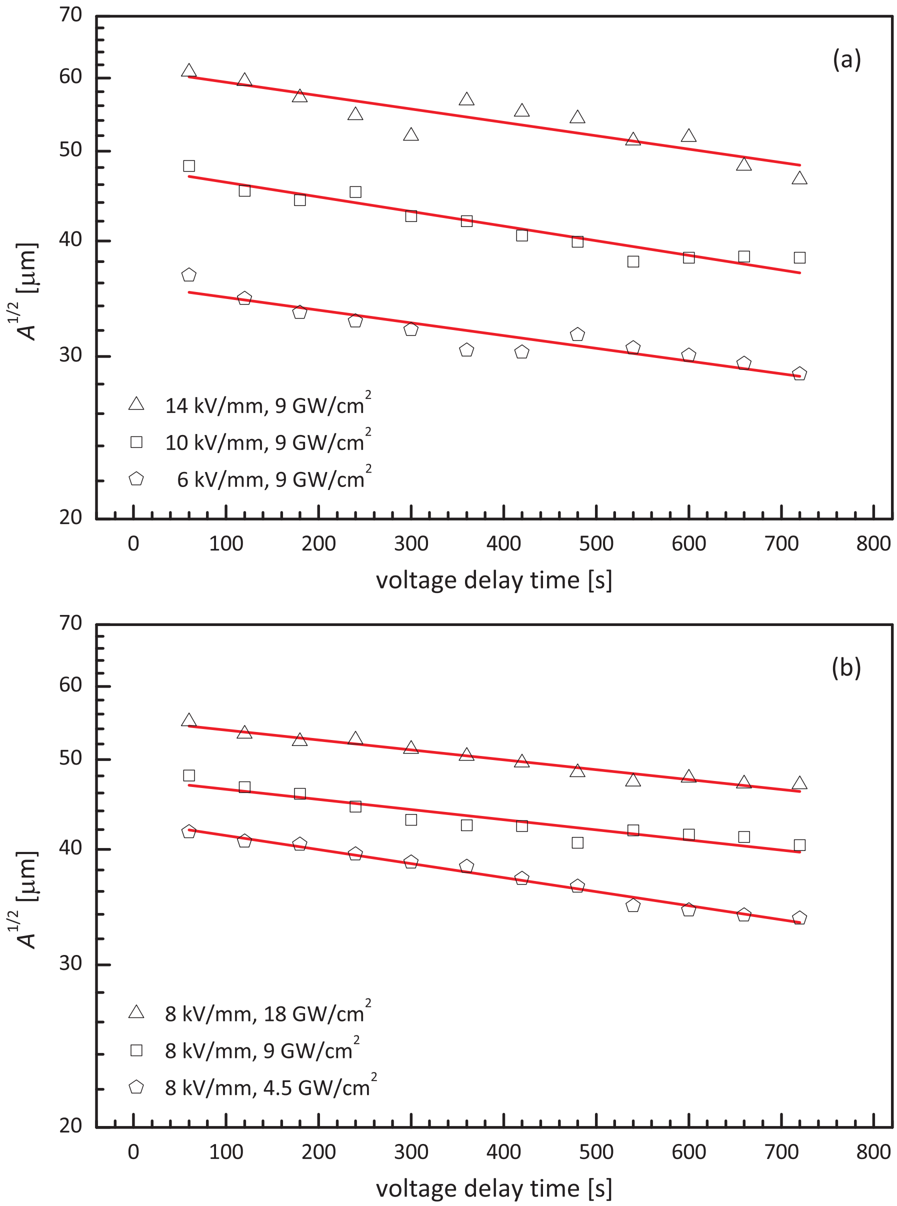

Fig. 2. Log-linear plots of the square root of the inverted LLAP domain areas, $A^{1/2}$, as a function of voltage delay time, measured from SEM images of HF-etched samples with conditions: (a) I = 9 GW/cm^2 and variable *E*-field amplitude; and (b) E = 8 kV/mm and variable laser intensity. The solid red lines represent single exponential decay function fits.

The fact that the inverted domain area reduces as a function of the time between the illumination event and the application of the *E*-field along with the independence of this decay rate (or time constant) on the experimental conditions (laser intensity, *E*-field value) suggests that the effect may be related to the relaxation of a space-charge distribution which has been formed as a result of the intense laser irradiation of the crystal. Photo-excited charge carriers in CLN can be electrons excited from impurity or defect energy levels to the conduction band, and electron-hole pairs excited directly across the band-gap via two-photon absorption [19] especially at high intensities. The driving force responsible for the migration of these photo-induced charges can be diffusion and/or the photovoltaic effect, resulting in a non-uniform space-charge distribution after illumination. The space-charge field produced by this space-charge distribution, if along the poling field, can contribute in a straightforward manner to the E_n reduction. Both the photovoltaic effect and diffusion can produce such space-charge distributions, with a component of space-charge field aligning along the poling field at –z face where domain nucleation occurs. The process of producing such a space-charge field by diffusion has been discussed in detail in Ref [7]. The photovoltaic case can be explained as follows: with the photovoltaic current flowing parallel to the spontaneous polarization, surface compensation charges are countered by photo-induced charges, leaving the dipoles at least partially uncompensated at the surface. The uncompensated depolarization field is oriented along the poling direction [16] and thus adds to the externally applied *E*-field, locally reducing the E_n. Additionally, photo-induced charges on the surface can screen the surface defects responsible for the domain nucleation [17], which might also contribute to the E_n reduction. After illumination, the photo-induced charges redistribute in the dark or under the influence of ambient light. The decay (redistribution) of the photo-induced space charges is thus reflected in the reduction of the inverted domain area as a function of the voltage time delay. All LLAP results which have been presented thus far correspond to experiments with undoped CLN crystals. No LLAP was observed for 5-mol% MgO-doped CLN (MgO:CLN) under these experimental conditions.

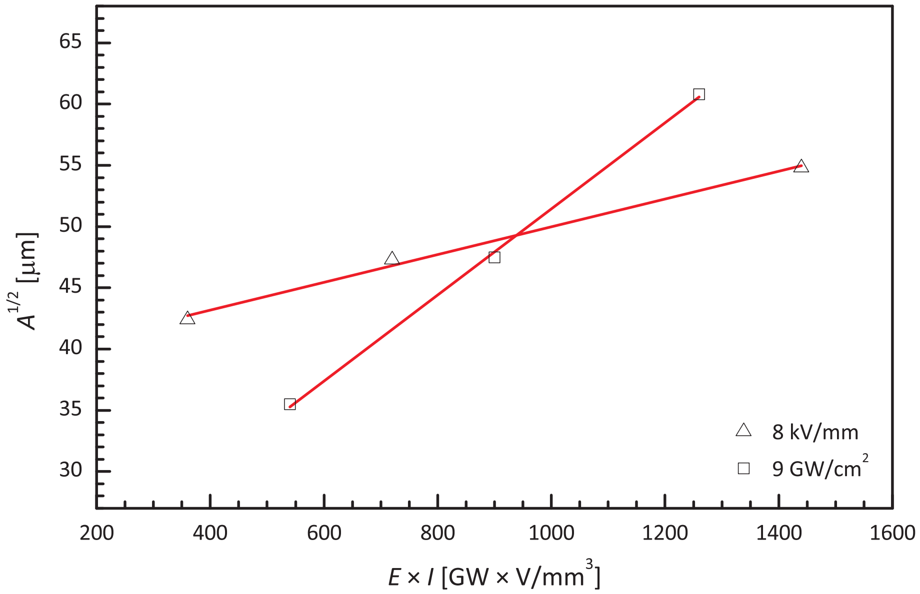

Fig. 3. Plot of the square root of the inverted LLAP domain area, $A^{1/2}$, versus the product of the applied external *E*-field and the intensity, $E \times I$, for a specific *E*-field (8 kV/mm) and a specific intensity (9 GW/cm^2). The solid red lines represent linear fits.

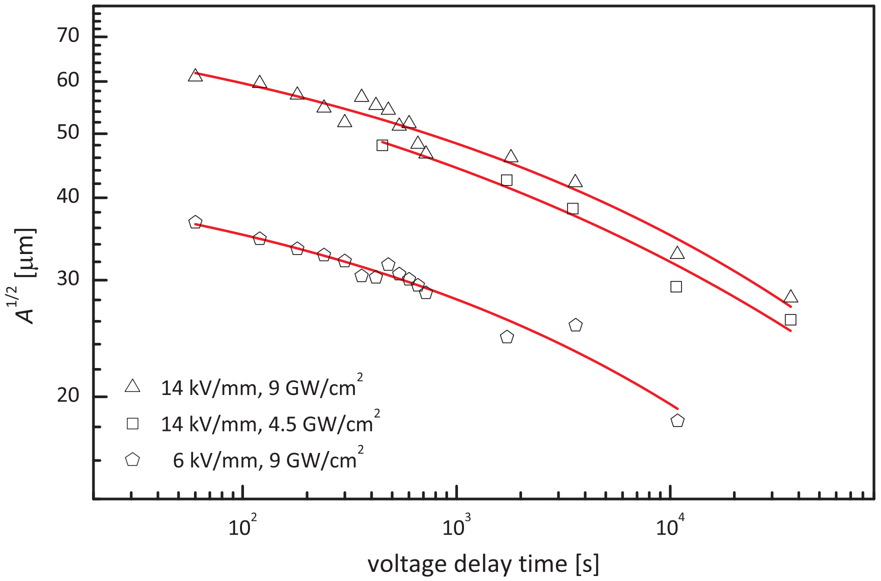

Fig. 4. Log plot of the square root of the inverted LLAP domain area, $A^{1/2}$, as a function of the voltage delay time for different laser intensities and *E*-fields. The solid red lines serve as a guide to the eyes.

3. Photorefractive experiments and discussion

Single crystal LN is an electro-optic (EO) photoconductor and is known to exhibit photorefractive behavior [20] which can be enhanced in the visible spectral range by doping the crystal with iron for data storage applications [21]. Although the photorefractive effect is less pronounced in undoped crystals due to the lack of photo-excitable impurities, it is still present [22,23] and therefore can be used as a tool to study the dynamics of photo-induced space-charge distributions. Here we have recorded photorefractive gratings in undoped CLN crystals by two-beam-interference using the same laser source used for LLAP in order to study the dynamics of any space-charge fields that have been formed as a result of the ultrafast laser exposure and compare with the domain inversion dynamics in LLAP. The results of the photorefractive grating recording experiments provided a new insight to the effect of LLAP: a direct evaluation of the role of the space-charge distribution to the effect and also explaining a number of experimental observations such as the absence of latent effects in MgO-doped LN crystals and the much higher reduction of the E_n in MgO:CLN for LAP.

The experimental setup which was used for the recording of volume gratings in LN crystals is outlined in the schematic of Fig. 5. The original train of ultrafast laser pulses (400 nm, 150 fs) was divided into two parts by a cube beam splitter and the resulting beams were made to interfere in the LN crystal after propagating via the two distinct arms of a Michelson interferometer. For ultrashort pulse interference it is important to achieve both spatial and temporal overlap of the two pulses, hence the length of one arm of the interferometer was adjustable in order to achieve zero time delay. Monitoring of the grating recording and decay was achieved by measuring the diffracted power from a c.w. HeNe laser (λ_p = 633 nm) incident at the Bragg angle, as shown in Fig. 5. The diffracted signal exhibited strong sensitivity to the polarization of the probe beam, a fact that ensures that the grating is due to refractive index change as a result of the photorefractive (PR) effect and is not an absorption grating.

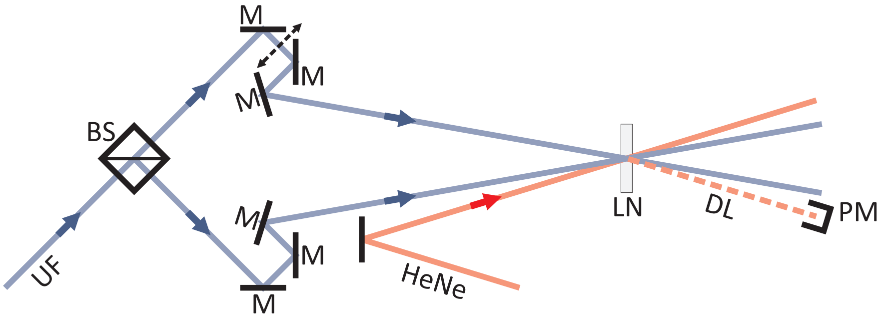

Fig. 5. Interferometric setup for recording and monitoring photorefractive gratings in LN using 150 fs ultrafast (UF) laser pulses at λ_r = 400 nm. The diffracted light (DL) of a c.w. HeNe laser at λ_p = 633 nm incident at the Bragg angle was used to monitor the grating recording/decay. M: mirror, BS: beam splitter, PM: optical power-meter. The period of the grating was ~1 μm. Spot diameters of the ultrafast and HeNe lasers are 1 and 0.8 mm respectively. The polarizations of both lasers were in the plane of the page (horizontal). The arrowed dash line indicates the variable arm of the interferometer.

The dynamic behavior (recording and decay) of PR gratings in both undoped CLN and 5-mol% MgO:CLN (Yamaju Ceramics Co., Ltd.) was investigated. The decay of the space-charge distribution in both crystals was monitored by measuring the power of the diffracted probe beam (λ_p = 633 nm) in the absence of the two recording beams (λ_r = 400 nm). The normalized temporal evolution of the square root of the diffraction efficiency, $\eta^{1/2}$, (which is proportional to the amplitude of the space charge field), is plotted as a function of time in Fig. 6a and Fig. 6b for undoped CLN and MgO:CLN, respectively. As the decay rate of the PR grating in both crystals was influenced by the intensity of the probe HeNe laser, we have obtained several decay curves corresponding to different values of the probe beam intensity as indicated in the graphs of Fig. 6.

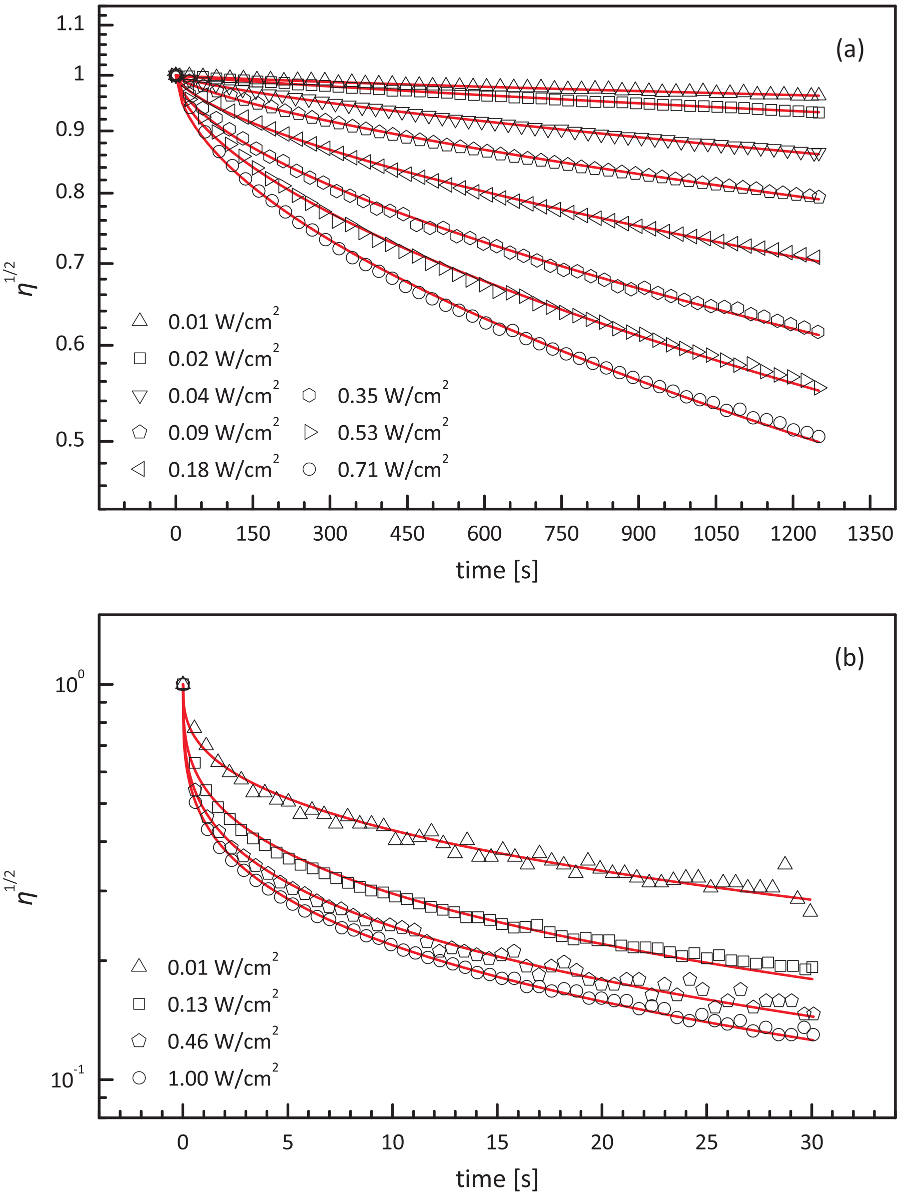

Fig. 6. Decays of the square root of the normalized PR grating diffraction efficiency, $\eta^{1/2}$, in (a) undoped CLN and (b) MgO:CLN for different probe laser intensities, I_p. The solid red curves correspond to stretched exponential decay fits.

We found that a stretched exponential decay curve described by the equation:

$$\eta^{1/2} = \exp\left[-\left(t/\tau\right)^{\beta}\right] \tag{3}$$

exhibits an improved fit as compared to a single exponential decay curve, where η is the normalized diffraction efficiency, t is the time, τ is the averaged relaxation time of the recorded hologram, and β is the stretch factor. The use of a stretched exponential function, also known as Kohlrausch-Williams-Watts function, is appropriate in our case as it describes a process that consists of a distribution of different relaxation processes [24]. The physical content of a stretched exponential decay of space charge distributions in undoped CLN has been described in [18,24] and is attributed to the large amount ($\approx 10^{20}$ cm^{-3}) of the intrinsic Nb_{Li} anti-site defects which exists in undoped CLN and provides an additional channel for the charge transport via hopping or tunnelling processes, apart from the conventional contribution of the conduction band [18]. From the stretched exponential fit, the decay time constant, τ, defined as the time in which the square root of the normalized diffraction efficiency reduces by a factor of e^{-1}, was derived for each probe HeNe laser intensity and the corresponding values are summarized in Table 2.

Table 2. Summary of the decay time constants τ, stretch factors β, decay rates τ^{-1}, and the relative reduction of the normalized PR grating diffraction efficiency $\Delta\eta^{1/2}$ from 60 s to 720 s, recorded in undoped CLN and MgO:CLN for different HeNe laser intensities I_p.

Crystal	I_p (W/cm^2)	τ (s)	β	τ^{-1} (s^{-1})	$\Delta\eta^{1/2}$
undoped CLN	0.71	2400	0.560	4.17×10^{-4}	0.318
	0.53	3040	0.581	3.29×10^{-4}	0.282
	0.35	4060	0.602	2.46×10^{-4}	0.239
	0.18	6370	0.640	1.57×10^{-4}	0.179
	0.088	10100	0.694	9.90×10^{-5}	0.123
	0.044	16600	0.734	6.01×10^{-5}	0.0802
	0.018	29600	0.841	3.38×10^{-5}	0.0378
	0.0088	81500	0.779	1.23×10^{-5}	0.0213
MgO:CLN	1.0	2.27	0.282	4.41×10^{-1}	
	0.46	3.01	0.287	3.32×10^{-1}	
	0.13	5.29	0.312	1.89×10^{-1}	
	0.013	15.8	0.355	6.34×10^{-2}	

Figure 7 shows a plot of the decay rate (τ^{-1}) as a function of the probe HeNe laser intensity. The main observation which can be made from the plot in Fig. 7 and Table 2 is that the photorefractive gratings in undoped CLN show a sufficiently slow decay, with time constants > 2400 s, thus a significant amount of the space-charge distribution should be present at the timescales where LLAP is observed. On the other hand, PR gratings in MgO:CLN decay three to four orders of magnitude faster than gratings recorded in undoped CLN, with time constants < 15.8 s, shorter than the smallest voltage time delay applied here which is 60 s, and this likely explains why LLAP was not observed for MgO:CLN crystals for these timescales. The fast decay of PR gratings in MgO:CLN is a consequence of the high dark conductivity of this material which is 4-5 orders of magnitude higher than undoped CLN according to e.g [25]. The dark conductivity of the crystal can be determined via [26]

$$\sigma_d = \varepsilon\varepsilon_0\tau_{I\approx 0}^{-1} \tag{4}$$

where $\varepsilon = 28$ is the dielectric constant of LN [27,28], ε_0 is the permittivity of free space and $\tau_{I\approx 0}$ is the decay time constant corresponding to a sufficiently low probe HeNe laser intensity, thus approaching the dark decay. The inverse of $\tau_{I\approx 0}$ can be estimated by substituting the lowest I_p values for undoped CLN and MgO:CLN in Table 2 which is ~0.01 W/cm^2. Figure 7 shows that at low HeNe laser intensity in the case of MgO:CLN, the τ^{-1} values are slow-decreasing hence the dark conductivity can be approximated by the conductivity at ~0.01 W/cm^2. However, for undoped CLN, τ^{-1} decreases quickly at low HeNe intensities, hence inducing a considerable uncertainty in estimating the value of dark conductivity. For this reason we conducted a grating decay experiment using a probe laser at a longer wavelength (800 nm), which did not affect the decay rate [22]. This measurement provided a value for the dark conductivity of undoped CLN which was very close to the value that corresponded to the HeNe intensity of I_p ~0.01 W/cm^2. According to Eq. (4), the corresponding dark conductivities were derived to be 1.57×10^{-11} $(\Omega\cdot\mathrm{m})^{-1}$ and 3.05×10^{-15} $(\Omega\cdot\mathrm{m})^{-1}$ for MgO:CLN and undoped CLN respectively, reconfirming the 4-5 orders of magnitude difference which has been reported in the literature [25].

To relate the PR grating decay to the delay time dependence of the inverted LLAP domain area, the relative reduction of the square root of the normalized PR grating diffraction efficiency, $\Delta\eta^{1/2}$, for the same time period in Fig. 2, from 60 s to 720 s, was derived from the stretched-exponential fitting for each HeNe laser intensity. The values of relative reduction are listed in Table 2 and plotted in Fig. 8. Comparing the relative reduction of the square root of the normalized PR grating diffraction efficiency, $\Delta\eta^{1/2}$, in that time period in undoped CLN with that of the square root of the inverted domain areas in LLAP, $\Delta A^{1/2}$, it is seen that the corresponding relative reduction for the domain length is larger than the corresponding ~dark PR grating decay. The range of the relative reduction for the square root of the inverted domain areas in Fig. 2 is indicated by the horizontal lines in Fig. 8 while the vertical lines indicate the corresponding range of probe HeNe laser intensities (0.13 – 0.28 W/cm^2). We believe that this is due to the fact that in the LLAP experiments the crystals were not kept in the dark but were continuously illuminated by a broadband light source (halogen bulb) for the in situ visualization of the poling process. The decay of the photo-induced space-charge distribution (hence the reduction of the inverted LLAP domain area with voltage delay time) should have been accelerated as a result of uniform illumination with radiation that contains a significant portion of short wavelength spectral components to which the crystal is more sensitive.

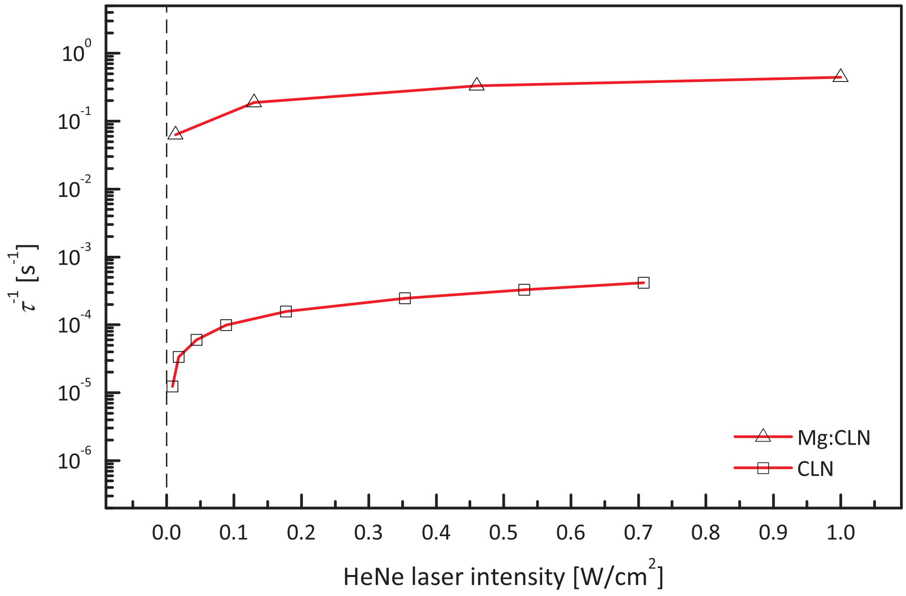

Fig. 7. Decay rate (τ^{-1}) as a function of the probe HeNe laser intensity for undoped CLN (squares) and MgO:CLN (triangles). The solid red curves are guides to the eyes.

The saturated diffraction efficiency of the PR gratings recorded in MgO:CLN was measured to be 1.5 × 10^{-4} which is one order of magnitude higher as compared to the corresponding saturated diffraction efficiency for undoped CLN crystals (1.3 × 10^{-5}) of the same thickness under identical recording and probing conditions. The diffraction efficiency of the grating was measured in real time during the recording of the grating with all three beams present simultaneously in the crystal. This difference in the diffraction efficiency corresponds to a 3.4 times larger amplitude of the space-charge field, and thus a 3.4 times larger amount of photo-induced charges being formed in MgO:CLN as compared to undoped CLN. This observation is of particular importance as it is in accordance with the much higher nucleation field reduction in MgO:CLN which is observed in LAP experiments [13].

Finally, the larger reduction of the E_n which was observed in LLAP for undoped CLN as compared with simultaneous LAP [29] cannot be explained with the data obtained here. However, it is possible that this further reduction in E_n can be associated with transient photo-excited charges [19] which screen the slowly evolving space-charge field in the presence of the ultrafast laser beam and which decay much faster than the LLAP observation times.

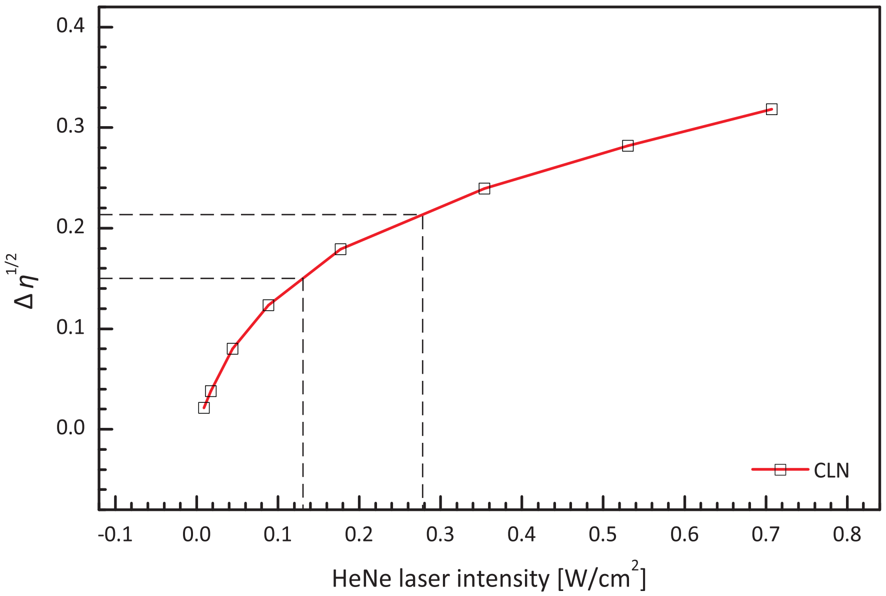

Fig. 8. Relative reduction of the square root of the normalized diffraction efficiency of the PR grating from 60 s to 720 s, $\Delta\eta^{1/2}$, as a function of HeNe laser intensity for undoped CLN. The solid red curve is a guide to the eyes. The range of the relative reduction of the square root of the inverted LLAP domain areas in Table 1, $\Delta A^{1/2}$, is indicated by the horizontal lines while the vertical lines indicate the corresponding range of HeNe laser intensities.

4. Conclusions

LLAP enables the de-coupling of the light illumination and application of the externally *E*-field, and has been demonstrated in undoped CLN. De-coupling these two steps can potentially improve the ferroelectric domain engineering process as it allows for independent design of each step. This includes the choice of illuminating wavelength and intensity to maximize the light-matter interaction, and choice of electrode materials for the optimization of the ferroelectric capacitor circuit for poling. Additionally, separation of the two processing steps can simplify the apparatus required, permitting the poling of thicker crystals or utilizing a larger area of the crystal by limiting surface leakage currents near the edges via the use of insulating oils (e.g. silicone oil). The size of the resulting inverted ferroelectric LLAP domains is a function of the time delay between the light illumination and the application of the *E*-field, which can be as long as ten hours. The dynamics of LLAP were attributed to the presence of a photo-induced space-charge distribution. The photorefractive effect in undoped CLN and MgO:CLN crystals was used as a tool for the monitoring of the dynamics of photo-induced space-charge distributions in these crystals. Good agreement between the relaxation dynamics of LLAP domain inversion and the PR grating was observed for undoped CLN, while the fast decay of the PR gratings observed in MgO:CLN explains the absence of the latent effect in this crystal. Finally the 10 × higher diffraction efficiency of PR gratings in MgO:CLN suggests a much larger amount of the photo-induced space charges in this crystal thus explaining the significant reduction of the nucleation field in this crystal during simultaneous light assisted poling (LAP).

Acknowledgements

The authors would like to acknowledge the financial contribution of the E.U. for funding this research in the framework of the STREP project “3D-DEMO”, the EPSRC Portfolio Partnership in Photonics (EP/C515668/1), and the Natural Sciences and Engineering Research Council of Canada (NSERC).

Spectral and electro-optic response of UV-written waveguides in $LiNbO_3$ single crystals

C.L. Sones[1]*, P. Ganguly[1,3], Y.J. Ying[1], F. Johann[2], E. Soergel[2], R.W. Eason[1], and S. Mailis[1]

[1] *Optoelectronics Research Centre, University of Southampton,*
Southampton, SO17 1BJ, U.K.
[2] *Institute of Physics, University of Bonn, Wegelerstrasse 8, 53115 Bonn, Germany.*
[3] *On leave from Advanced Technology Development Centre, Indian Institute of Technology,*
Kharagpur, 721302, India.
**cls@orc.soton.ac.uk*

Abstract: An experimental study of the spectral and electro-optic response of direct UV-written waveguides in $LiNbO_3$ is reported. The waveguides were written using c.w. laser radiation at 275, 300.3, 302, and 305 nm wavelengths with various writing powers (35-60 mW) and scan speeds (0.1-1.0 mm/sec). Spectral analysis was used to determine the multimode and single mode wavelength regions and, the cut-off point of the fabricated waveguides. Electro-optic characterization of these waveguides reveals that the electro-optic coefficient (r_{33}) decreases for longer writing wavelengths, with a maximum of 31 pm/V for 275 nm and, is reduced to 14 pm/V for waveguides written with 305 nm.

OCIS codes: (130.3730) Lithium niobate; (130.3130) Integrated optics materials; (130.3120) Integrated optics devices; (130.2790) Guided waves.

References and links

1. S. Mailis, C. Riziotis, I. T. Wellington, P. G. R. Smith, C. B. E. Gawith, and R. W. Eason, "Direct ultraviolet writing of channel waveguides in congruent lithium niobate single crystals," Opt. Lett. **28**(16), 1433–1435 (2003).
2. P. Ganguly, C. L. Sones, Y. J. Ying, H. Steigerwald, K. Buse, E. Soergel, R. W. Eason, and S. Mailis, "Determination of Refractive Indices From the Mode Profiles of UV-Written Channel Waveguides in $LiNbO_3$-Crystals for Optimization of Writing Conditions," J. Lightwave Technol. **27**(16), 3490–3497 (2009).
3. A. C. Muir, G. J. Daniell, C. P. Please, I. T. Wellington, S. Mailis, and R. W. Eason, "Modelling the formation of optical waveguides produced in $LiNbO_3$ by laser induced thermal diffusion of lithium ions," Appl. Phys., A Mater. Sci. Process. **83**(3), 389–396 (2006).
4. K. A. H. van Leeuwen, and H. T. Nijnuis, "Measurement of higher-order mode attenuation in single-mode fibers: effective cutoff wavelength," Opt. Lett. **9**(6), 252–254 (1984).
5. T. Lang, L. Thevenaz, Z. B. Ren, and P. Robert, "Cutoff wavelength measurement of $TiLiNbO_3$ channel wave-guides," Meas. Sci. Technol. **5**(9), 1124–1130 (1994).
6. P. Ganguly, B. Umapathi, S. Das, J. C. Biswas, and S. K. Lahiri, "Fabrication and characterisation of $Ti:LiNbO_3$ waveguides," in *International conference on Optics and Optoelectronics* (Dehradun, India, 9–12th December, 1998), pp. 450–455.
7. C. F. McConaghy, K. F. Hunenberg, D. Sweider, M. Lowry, and R. A. Becker, "White-light spectral-analysis of Lithium-Niobate wave-guides," J. Lightwave Technol. **13**(1), 83–87 (1995).
8. A. Mendez, G. De la Paliza, A. Garcia-Cabanes, and J. M. Cabrera, "Comparison of the electro-optic coefficient (r_{33}) in well-defined phases of proton exchanged $LiNbO_3$ waveguides," Appl. Phys. B **73**, 485–488 (2001).
9. S. Ducharme, J. Feinberg, and R. R. Neurgaonkar, "Electrooptic and piezoelectric measurements in photorefractive Barium Titanate and Strontium Barium Niobate," IEEE J. Quantum Electron. **23**(12), 2116–2121 (1987).
10. E. L. Wooten, and W. S. C. Chang, "Test structures for characterization of electrooptic waveguide modulators in lithium niobate," IEEE J. Quantum Electron. **29**(1), 161–170 (1993).
11. A. Ródenas, D. Jaque, C. Molpeceres, S. Lauzurica, J. L. Ocana, G. A. Torchia, and F. Agullo-Rueda, "Ultraviolet nanosecond laser-assisted micro-modifications in lithium niobate monitored by Nd^{3+} luminescence," Appl. Phys., A Mater. Sci. Process. **87**(1), 87–90 (2007).
12. D. C. Deshpande, A. P. Malshe, E. A. Stach, V. Radmilovic, D. Alexander, D. Doerr, and D. Hirt, "Investigation of femtosecond laser assisted nano and microscale modifications in lithium niobate," J. Appl. Phys. **97**(7), 074316 (2005).

13. J. Burghoff, C. Grebing, S. Nolte, and A. Tunnermann, “Waveguides in lithium niobate fabricated by focused ultrashort laser pulses,” Appl. Surf. Sci. **253**(19), 7899–7902 (2007).
14. H. Nishihara, M. Haruna, and T. Suhara, *Optical Integrated Circuits* (McGraw-Hill, New York, 1989).
15. I. P. Kaminow, and V. Ramaswam, “Lithium-Niobate ridge waveguide-modulator,” Appl. Phys. Lett. **24**(12), 622–624 (1974).
16. A. C. Muir, C. L. Sones, S. Mailis, R. W. Eason, T. Jungk, A. Hoffman, and E. Soergel, “Direct-writing of inverted domains in lithium niobate using a continuous wave ultra violet laser,” Opt. Express **16**(4), 2336–2350 (2008).
17. F. Johann, Y. J. J. Ying, T. Jungk, A. Hoffmann, C. L. Sones, R. W. Eason, S. Mailis, and E. Soergel, “Depth resolution of piezoresponse force microscopy,” Appl. Phys. Lett. **94**(17), 172904 (2009).
18. J. A. de Toro, M. D. Serrano, A. G. Cabanes, and J. M. Cabrera, “Accurate interferometric measurement of electro-optic coefficients: application to quasi-stoichiometric $LiNbO_3$,” Opt. Commun. **154**(1-3), 23–27 (1998).

1. Introduction

Since its inception, the UV directly written waveguide [1] procedure in lithium niobate ($LiNbO_3$) single crystals has held considerable promise because it is a single-step process which is well suited for complex micro-optical devices, in addition to conventional optical integrated circuits. Direct writing of graded-index channel waveguides in congruent $LiNbO_3$ has been demonstrated using c.w. laser light within a writing wavelength range of 244 – 305 nm [1,2]. The process has been modeled as a laser-induced thermal diffusion of lithium ions which results in a variation of the local Li concentration which increases the extra-ordinary refractive index of $LiNbO_3$ [2,3] For most applications, single-mode waveguides are essential in order to achieve optimised device performance, and hence the determination of single-mode operating range and cut-off wavelength of the waveguide are fundamental for characterising waveguide optical properties. Spectral analysis is a characterization method which has been originally developed for determining the effective cut-off wavelength of optical fiber [4] and later for Ti-indiffused [5,6] and proton exchanged [7] waveguides, and this may also be applied to these UV-written waveguides. Moreover, the electro-optic properties of these waveguides need to be assessed for subsequent applications in waveguide optical switches and modulators, which are key integrated-optical components that can be implemented in $LiNbO_3$. Therefore, spectral analysis and electro-optic characterisation of UV-written waveguides in $LiNbO_3$ are of absolute necessity from the device point of view.

In this paper a white light laser-continuum source has been used for the investigation of the spectral response of the direct UV-written channel waveguides in congruent $LiNbO_3$. The spectral data was used to determine the various regimes of waveguide operation from multimode to cut-off. It has been observed that an optimum writing condition for these waveguides exists where the refractive index change is maximised and hence the cut-off wavelength of the waveguide shifts to longer wavelengths. The experimental study was extended to the electro-optic properties of these waveguides, which reveals that electro-optic response of the waveguide reduces with increasing recording wavelength, with 275 nm written waveguides having the highest electro-optic response compared to waveguides written with 300.3, 302, and 305 nm light. Measurements of mode-width, mode-depth, and refractive-index change of waveguides with various applied voltages, and finally direct interferometric measurements of the electro-optic coefficient of waveguides written at different UV wavelengths have confirmed this experimental finding.

2. Experimental

2.1. Waveguide fabrication

Direct writing of waveguides in congruent, z-cut $LiNbO_3$ crystal has been achieved using an argon ion laser that yields c.w. output at 275, 300.3, 302, and 305 nm wavelengths. The laser beam was focused onto the crystal surface to a spot of ~4 µm diameter. The waveguides were written on the + z face of the crystal, along the crystallographic y-direction, by scanning the crystal in front of the focussed laser beam using a computer-controlled 2D translation stage. The laser power and scanning speed used in our experiments were within the range of 35-60 mW and 0.1-1.0 mm/sec, respectively, which correspond to UV energy fluences of 0.7-12.0 kJ/cm^2. The strong optical absorption of $LiNbO_3$ at these ultraviolet wavelengths results in an increased local temperature- that induces Li diffusion takes place which forms the waveguides with an increased extra-ordinary index of refraction [1–3]. While the waveguides were in most cases free from surface damage, those written at the higher end of the energy fluence range did exhibit some undesirable surface damage. Following the direct writing, all the waveguides were edge-polished and used for the subsequent spectral and electro-optic characterization.

2.2. Spectral measurements

A supercontinuum fiber laser (Fianium, Femtopower 1060, with a wavelength range: 408 – 1800 nm) was coupled into the waveguides using a 10x microscope objective. The output of each waveguide was imaged by a second microscope objective onto a circular aperture (iris diaphragm) for spatially filtering out the optical noise from the light originating from the waveguides. This was subsequently then coupled to an optical spectrum analyzer. A schematic of the experimental setup is shown in Fig. 1. The numerical aperture of the launching objective lens (NA = 0.25) was chosen to be high enough to excite all possible guided modes of the waveguides. The length of the channel waveguides used in our experiments was 14 mm. The $LiNbO_3$ substrate containing the waveguides was mounted onto a high precision 4-axis translation stage. TM waveguide modes only could be excited in these UV-written waveguides indicative of an increment only in the extra-ordinary refractive index. To eliminate the spectral response of the launch and detection components of the experimental setup (such as the broadband source and the detector), the spectral output intensity of the waveguide (I_{WG}) was normalized by a reference intensity spectrum (I_{REF}) acquired by the optical system without the presence of the waveguide. This normalization also minimizes the effect of chromatic aberrations of the microscope lenses. All these spectral measurements were performed below the photorefractive damage threshold of the waveguides, which was confirmed by the non-dependency of the normalized transmission spectra on the input power. The measured spectral response has been analyzed to determine the wavelength range for multi-mode and single-mode operation respectively and the cut-off wavelength of the UV-written waveguides.

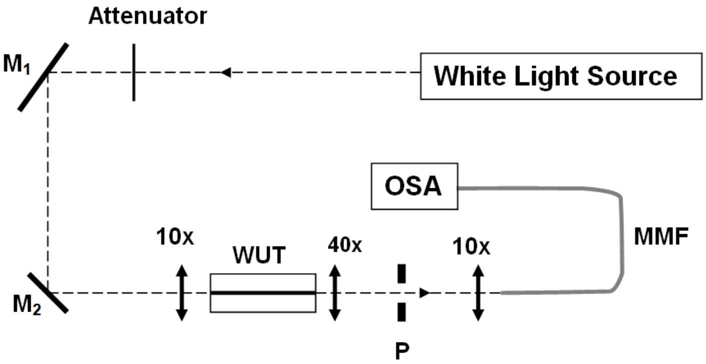

Fig. 1. Experimental setup for spectral characterisation: M_1, M_2 – mirrors, P – adjustable pinhole, MMF – multimode fiber, OSA – optical spectrum analyser, WUT – waveguide under test.

The change of the spectral response of the UV-written waveguides under the influence of an external electric field was used to investigate the electro-optic behavior of the waveguides. A pair of thin gold film electrodes of thicknesses ~10 nm was sputtered onto the two opposite faces of the 500 μm thick substrate containing the waveguides. The electrodes were used to apply a variable voltage across the substrate and the corresponding normalized transmission spectra of the waveguides were measured. The applied dc voltage used in our experiment ranged from −600 to + 600 V, corresponding to a uniformly applied dc electric field ranging from −1.2 to + 1.2 V/μm along the z-axis of the $LiNbO_3$ crystal. The changes in cut-off wavelengths of the waveguides, written with different wavelengths, for various applied voltages were measured. These experimental data directly correspond to the relative refractive index changes or changes in the contrast of the waveguides with respect to the substrate, via the linear electro-optic (Pockels) effect. The markedly different responses of the waveguides with applied voltage suggest a difference in the relative values of electro-optic coefficient (r_{33}) of the UV-written waveguides compared to those for the bulk substrate under different writing wavelengths. Hence it was necessary to proceed to a direct measurement of the effective electro-optic coefficient.

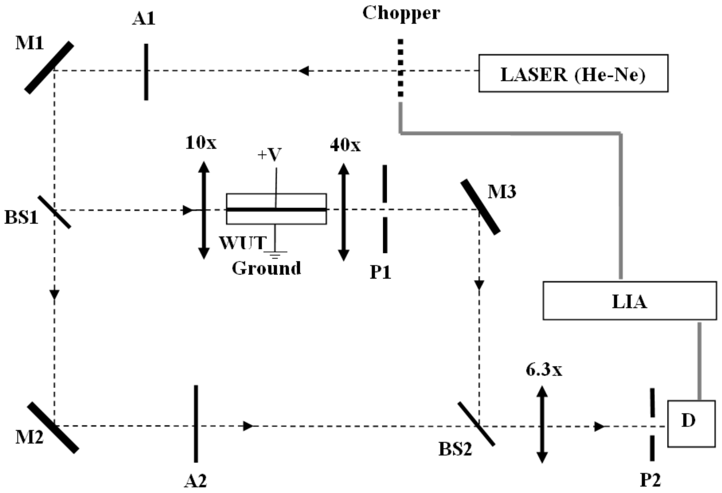

Fig. 2. Experimental setup for the measurement of electro-optic coefficient of the waveguide: A1, A2 – optical attenuator; M1, M2, M3 – mirror; BS1, BS2 – beam splitter; WUT – waveguide under test; V - applied voltage; P1, P2, - adjustable pinhole; D – detector; LIA – lock-in amplifier.

2.3. Electro-optic coefficient measurement

For a quantitative characterization of the electro-optic response of the waveguides written at different wavelengths, we measured the r_{33} electro-optic coefficient using a Mach-Zehnder interferometer setup, a schematic of which is shown in Fig. 2. A He-Ne laser beam (0.6328 µm) was divided by a 50/50 cube beam- splitter into the two arms of the interferometer. The waveguide under test was placed in one arm of the interferometer, and light was in- and out-coupled using microscope objectives. In the reference arm a variable attenuator was placed to balance the optical power between the two arms of the interferometer. Finally the beams from the two arms were recombined using a second cube beam-splitter as shown in the schematic. The polarization of the input light was made parallel to the z-axis of the crystal. Initially a computer-interfaced CCD camera was used to observe the series of elliptical interference fringes at the output. A pinhole with diameter ~25 µm was used to sample the interference fringes and to enable the detection of phase shifts as a variation of the transmitted optical power measured by a Si photo-detector. An optical chopper (frequency: 170 Hz) in conjunction with a lock-in-amplifier was used to improve the signal-to-noise ratio (typically ~50) of our detection system. We also placed a 6.3x microscope objective to magnify the output interference pattern and hence improve the resolution of the pinhole-detector assembly. The entire experimental setup was on a vibration-isolated table and the interferometric section was covered to minimize the effect of random phase changes caused by air-flow in the two arms of the interferometer. The applied voltage introduces a refractive index change in the waveguide via the electro-optic effect thereby introducing a phase difference between the two arms of the interferometer. This small phase difference produces a spatial shift in the interference fringes, and hence a change in detector output. From the plot of the detector output versus the applied voltage, we have measured the half-wave voltage V_π, the voltage required to produce a π-phase shift. This is related to the r_{33} coefficient of the waveguide by the following equation [8,9]

$$r_{33} = \frac{\lambda d}{n_e^3 L V_\Pi} \tag{1}$$

where, λ is the operating wavelength (0.6328 μm), d is the substrate thickness (500 μm), n_e is the effective refractive index of the waveguide, and L is the length of the electrode-covered waveguide section (9 mm). In Eq. (1) we have assumed 100% overlapping of the applied electric field with the waveguide propagation mode which is a valid approximation in the present configuration [10]. The experiment was repeated for a number of waveguides written with different writing wavelengths and powers, and the r_{33} coefficient for each waveguide was determined by using Eq. (1). No phase drift due to optical "photorefractive" damage was observed over the duration of the measurements.

3. Results and discussions

3.1. Analysis of spectral data of the waveguides

Typical normalized transmission spectra of two different UV-written waveguides are shown in Fig. 3. The spectrum shown in Fig. 3(a) corresponds to a waveguide that exhibits multimode transmission at shorter wavelengths and can be divided into four regions [7]. In region-1 the waveguide supports the two lowest order modes and the normalized transmission spectrum (I_{WG}/I_{REF}) can be described as:

$$\frac{I_{WG}}{I_{REF}} = K_{00} + K_{01} \tag{2}$$

where K_{00} and K_{01} are the coupling coefficients for the lowest and next higher order modes, respectively. Region-2 describes the wavelength regime where the second mode cut-off is approached. In this case normalised transmission spectrum is given by:

$$\frac{I_{WG}}{I_{REF}} = K_{00} + K_{01}\, e^{-\alpha_{01} L_0} \tag{3}$$

where α_{01} and L_0 are the modal attenuation coefficient of the higher order mode and length of the guide, respectively. As the wavelength becomes longer the cut-off of the second mode is passed and region-3 covers the wavelength range where the fundamental mode is still far from cut-off. The intensity ratio in this region may be given as:

$$\frac{I_{WG}}{I_{REF}} = K_{00} \tag{4}$$

Finally as the fundamental mode cut-off is approached in region-4, the normalized transmission spectrum is:

$$\frac{I_{WG}}{I_{REF}} = K_{00}\, e^{-\alpha_{00} L_0} \tag{5}$$

where α_{00} is the attenuation coefficient for the fundamental mode. In Eqs. (2-5) the modal coupling and attenuation coefficients are wavelength dependent. We have defined 10% of the peak normalised intensity as the mode cut-off point. Hence for the waveguide shown in Fig. 3(a), which was written at the 300.3 nm wavelength, with a laser power of 40 mW and a scan speed 1.0 mm/sec, the multimode region is <514 nm, whereas the guide is single-moded within the wavelength range from 514 nm to 780 nm, where 780 nm is practically the waveguide cut-off wavelength. For the waveguide shown in Fig. 3(b), written with 305 nm wavelength, 50 mW power and 1 mm/sec laser scan speed, the single-mode range is from 408 nm to 615 nm.

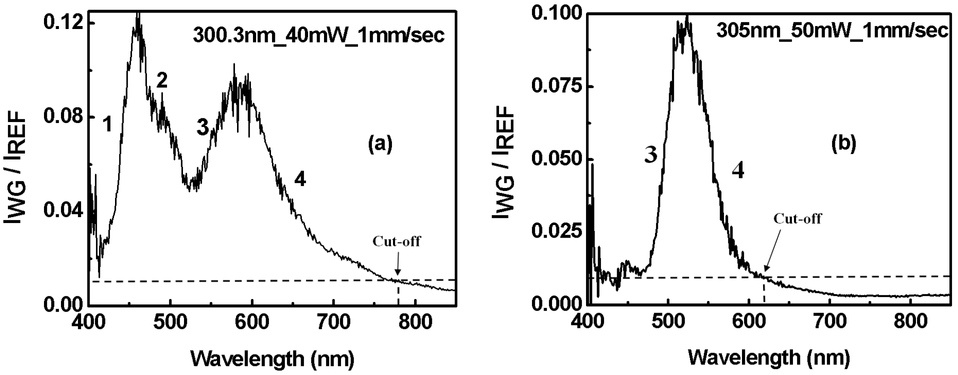

Fig. 3. Typical spectral responses of the fabricated UV-written waveguides: (a) with writing wavelength: 300.3 nm, power: 40 mW, speed: 1 mm/sec; (b) with writing wavelength: 305 nm, power: 50 mW, speed: 1 mm/sec.

We have measured the cut-off wavelengths of all the waveguides written with various writing wavelengths, laser powers, and scan speeds. The variations of the cut-off wavelength of the waveguides written with different wavelengths, as a function of laser power and scan speed are shown in Fig. 4(a) and Fig. 4(b) respectively.

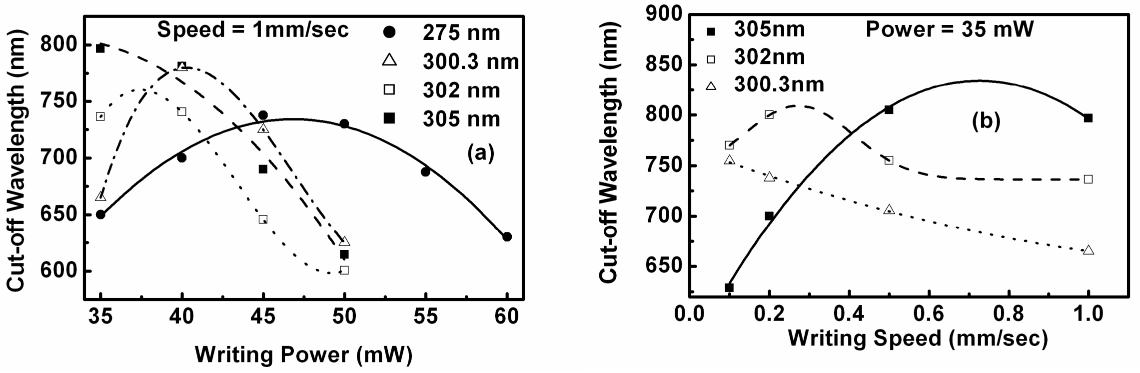

Fig. 4. Variations of cut-off wavelengths of the waveguides with: (a) laser writing power, (b) writing speed.

These results confirm our previous observation [2] that for each writing wavelength an optimum writing condition (writing power and scan speed) exists where the induced refractive index change is maximised. As the refractive index change or the contrast of the waveguide (Δn_{max}) increases, the cut-off shifts to longer wavelengths. This may be because of the trade-off between the laser-induced refractive index change and the strain due to surface damage of the waveguides at higher laser fluences. UV laser-induced surface damage has been investigated by Rodenas et al. in [11], where it was demonstrated that it induces a permanent local stress of micron-scale dimension, causing a decrease in local refractive index of $LiNbO_3$ to some extent [12]. Raman analysis of the exposed region also shows some loss of crystallinity of the material [13], indicating that though $LiNbO_3$ may suffer some change in chemical structure at the superficial surface layer, it remains largely unchanged in the bulk.

3.2. Spectral analysis with applied voltages

Results of the measurements for cut-off wavelength change with applied dc voltages of waveguides written with four different UV wavelengths are shown in the graph of Fig. 5.

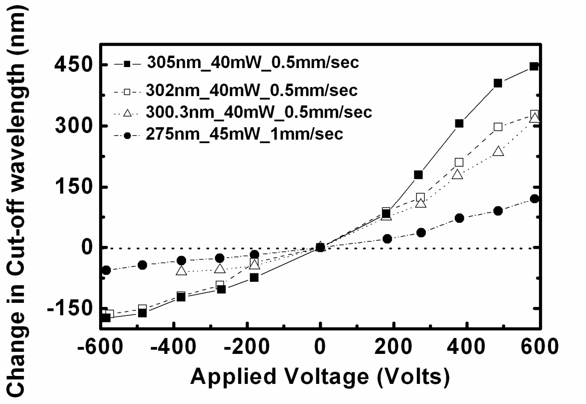

Fig. 5. Changes in cut-off wavelengths of the waveguides with applied voltages for 275, 300.3, 302, and 305 nm writing wavelengths.

It may be observed in the graph that the waveguides written with 275 nm exhibit the lowest change in cut-off wavelength with applied voltages in the range from −600 to + 600 V. The changes in cut-off wavelengths of the waveguides gradually increase with the writing wavelength. In the present electrode configuration, where a uniform electric field is applied across the whole crystal containing the waveguides, the change in cut-off wavelength will depend on the change in refractive index contrast of the waveguides with respect to the substrate. Hence for waveguides with the same electro-optic coefficients as that of $LiNbO_3$ substrate, there shouldn't be any appreciable change in the cut-off wavelength. However, waveguides which have a reduced electro-optic coefficient with respect to the substrate will exhibit a more significant change in cut-off wavelength with the applied voltage. Thus the results in Fig. 5 indicate that a waveguide written with 275 nm has an electro-optic coefficient, r_{33}, closest to the substrate value in comparison to waveguides written with longer wavelengths. In fact, the electro-optic coefficient decreases monotonically with the increase in writing wavelength. The measured change in contrast of these waveguides with respect to the substrate refractive index at 0.6328 μm transmitting wavelength (Fig. 6), for different applied voltages, supports these experimental observations. Maximum refractive index values near the surface for these waveguides without applying any voltages are given in Table 1.

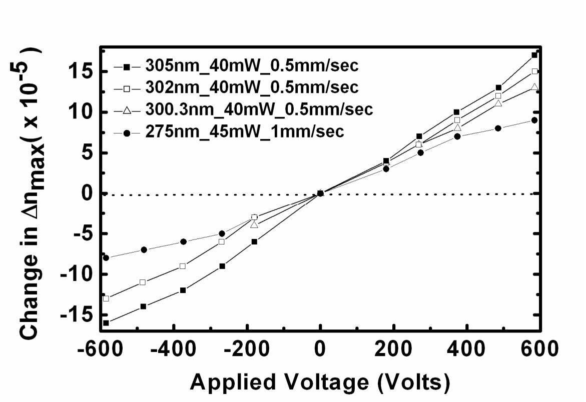

Fig. 6. Changes in contrast of the waveguides written with 275, 300.3, 302, and 305nm wavelengths with applied voltages.

Table 1. Maximum surface refractive index values of different waveguides in Fig. 6.

Laser Writing Wavelength (nm)	Laser Power (mW)	Scan Speed (mm/sec.)	Maximum Refractive Index Near Surface
275	45	1.0	2.204864
300.3	40	0.5	2.203554
302	40	0.5	2.204354
305	40	0.5	2.204154

The changes in mode width and mode depth of these UV-written waveguides with the applied voltages are shown in Fig. 7. The details of the experimental setup for mode profile measurement and determination of refractive index contrast of the waveguides are presented in Ganguly et al. [2]. All these waveguides are single-moded in nature at this wavelength within the applied voltage range. As expected the changes in mode widths and mode depths for the waveguide written with 275 nm wavelength with the applied voltages are relatively small, whereas, for other waveguides significant changes in mode widths and mode depths are observed. It may also be noted that the asymmetry in Fig. 5 for + ve and –ve applied voltages actually reflects the asymmetric behavior of mode depth variation of the waveguides as seen in Fig. 7(b). We have observed a measurable mode shrinkage or expansion along the applied electric field direction for these UV-written waveguides.

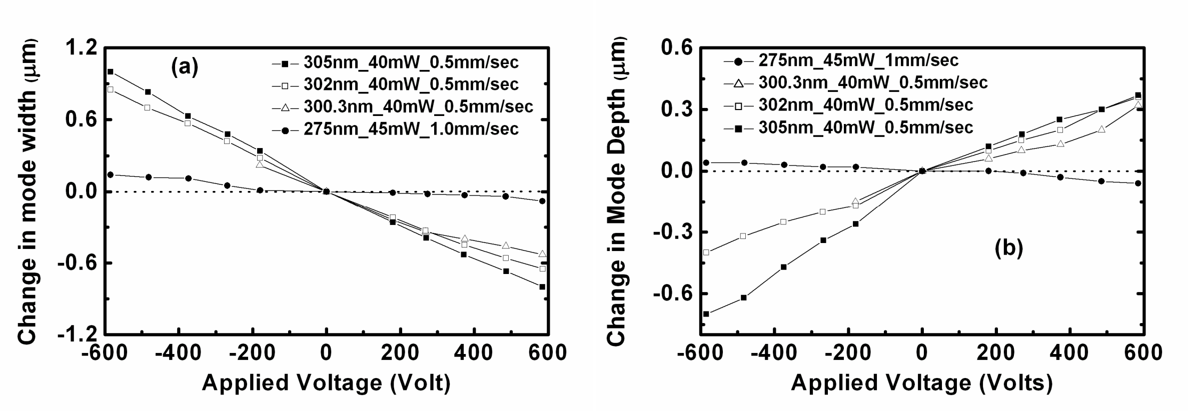

Fig. 7. Changes in mode width (a) and mode depth (b) with applied voltages for the waveguides written with 275, 300.3, 302, and 305nm wavelengths.

3.3. Electro-optic coefficients of the waveguides

The interferometrically measured electro-optic coefficient (r_{33}) of the waveguides written with these four different wavelengths and writing powers (45, 50, 55, 60 mW) are summarized in the graph shown in Fig. 8.

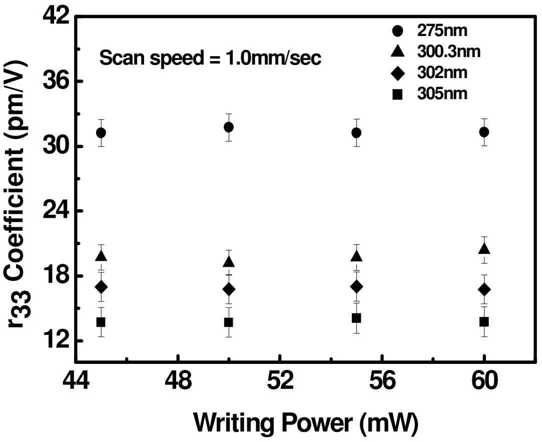

Fig. 8. Measured electro-optic coefficients (r_{33}) of the waveguides for different writing wavelengths and powers.

All the waveguides were written with a scanning speed of 1.0 mm/sec. Our measurements were performed with a dc applied field at room temperature (20 °C), for a probe wavelength of 0.6328 μm. Typical variations of normalised detector output with applied voltage are presented in Fig. 9, for the waveguides with different writing wavelengths. The non-zero minimum detector outputs may be a combined effect of slightly unequal intensity of the two arms of the interferometer under applied voltages and other stray environmental effects. It may be concluded from these results that the electro-optic coefficient is as low as 14 pm/V for waveguides written with 305 nm wavelength, but increases with decreasing writing wavelength, to a value (31 pm/V) that is close to the bulk r_{33} value of the crystal, for 275 nm writing wavelength. It may also be noticed that the electro-optic coefficients of the waveguides are effectively independent of the writing laser powers within our studied experimental range. For comparison we have also measured the r_{33} coefficient of a Ti-indiffused channel waveguide fabricated in our laboratory, using the same experimental apparatus. The measured value of 35 pm/V is ~13% higher than the values for waveguides written with 275 nm wavelength. We also studied the a.c. (upto 10 KHz) electro-optic response of the waveguides using the same interferometric setup. A dc bias (0-100V) was also applied along with the sinusoidal ac signal (V_{pp} = 35-155 V) to set the phase difference between the interferometer arms to π/2, effectively increasing the detection sensitivity. It was observed that within the studied frequency range the frequency response of the UV-written waveguides is similar to that of the Ti-indiffused waveguide.

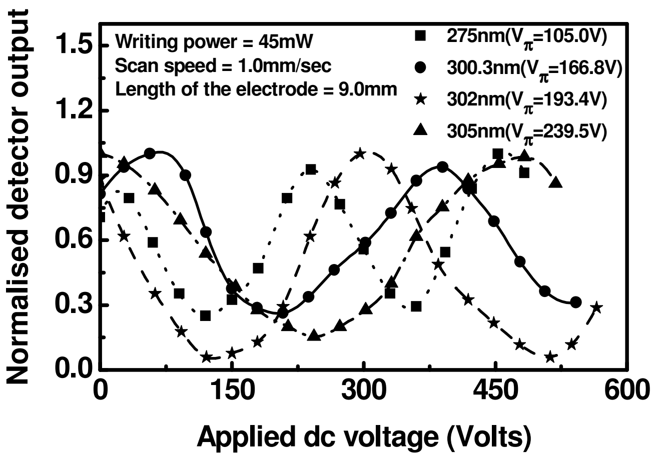

Fig. 9. Variation of normalised detector output with the applied voltages for 275, 300.3, 302, and 305nm writing wavelengths of the waveguides.

The reason for the electro-optic coefficient reduction at 300.3, 302, and 305 nm writing wavelengths, is not clearly understood at the moment. Since lithium out-diffused waveguides are known to produce highly efficient electro-optic modulators [14,15], some other mechanisms dominant during waveguide fabrication at these longer writing wavelengths, could possibly be the cause. One such plausible explanation could be due to the formation of all-optically inverted ferroelectric domains within the illuminated region [16]. The depth of these inverted domains on the + z face at a shorter UV wavelength (244 nm) has been estimated to be of order 30-50 nm. However, the dependence of the depths of such all-optically inverted domain on the writing wavelength has not been studied. The presence of such inverted domains within the waveguide volume will reduce the average phase shift for a given value of the applied voltage which will consequently appear as a reduced EO coefficient. Another possible mechanism which would result in a reduced EO response is damage induced in the crystal by the UV-laser writing step. As the absorption depth for the longer wavelengths is greater, the corresponding damaged volume extends further into the waveguide region, and hence a reduced value for the measured EO coefficient would be obtained for these wavelengths. The UV illuminated tracks were investigated by piezoresponse force microscopy (PFM) in order to identify the cause for the reduction in the EO response. The PFM investigation showed indeed a limited contrast associated with the UV illumination which could be attributed either to a shallow inverted domain or a damaged volume. The PFM results were inconclusive mainly due to the limitation in the depth resolution of the device which is comparable to the dimensions of the waveguiding volume [17].

4. Conclusions

A detailed experimental study on spectral and electro-optic characterization of direct UV-written waveguides in congruent z-cut $LiNbO_3$ crystal has been presented. The waveguides were written with 275, 300.3, 302, and 305 nm wavelengths with various writing powers (35-60 mW) and scan speeds (0.1-1.0 mm/sec). Spectral analysis determined the multimode and single mode wavelength regions, and the cut-off point of the fabricated waveguides. Measurements of cut-off wavelengths of the waveguides for different writing powers and scan speeds confirm the existence of optimum writing conditions for maximum refractive index changes of these waveguides. Changes in cut-off wavelengths of the waveguides with applied uniform electric fields across the substrate indicate that electro-optic response decreases with increasing writing wavelengths. This experimental observation was verified by measuring the mode-widths, mode-depths, and refractive-index contrasts of the waveguides at various applied voltages. Direct measurements of the unclamped electro-optic coefficients (r_{33}) of the waveguides written with different wavelengths were also performed by an interferometric method. It was observed that the r_{33} coefficient is maximum (31 pm/V) for 275 nm writing wavelengths, whereas it is reduced to 14pm/volts for waveguides written with 305 nm writing wavelength. These interferometric measurements have not taken into account the piezoelectric contribution [18] to the phase change of a beam passing through the electro-optic crystal. Nevertheless, this gives a quantitative comparison of the electro-optic coefficients for different waveguides with four different writing wavelengths.

Acknowledgements

We gratefully acknowledge the Royal Society for the International Fellowship of Dr P. Ganguly (No. IIF-2007/R2), the Engineering and Physical Sciences Research Council (EPSRC) for the research funding under grant number EP/C515668, the European Union for funding under the 3-D Demo grant, the Deutsche Forschungsgemeinschaft and the Deutsche Telekom AG. We also acknowledge Prof Karsten Buse and Hendrik Steigerwald for valuable discussions and their support.

Ultra-smooth lithium niobate photonic micro-structures by surface tension reshaping

Charlie Y. J. Ying,[1,*] **Collin L. Sones,**[1] **Anna C. Peacock,**[1] **Florian Johann,**[2]
Elisabeth Soergel,[2] **Robert W. Eason,**[1] **Mikhail N. Zervas**[1] **and Sakellaris Mailis**[1]

[1]*Optoelectronics Research Centre, University of Southampton, Highfield, Southampton, S017 1BJ, UK*
[2]*Institute of Physics, University of Bonn, Wegelerstrasse 8, 53115 Bonn, Germany*
**yoy@orc.soton.ac.uk*

Abstract: Annealing of micro-structured lithium niobate substrates at temperatures close to, but below the melting point, allows surface tension to reshape preferentially melted surface zones of the crystal. The reshaped surface re-crystallizes upon cooling to form a single crystal again as it is seeded by the bulk which remains solid throughout the process. This procedure yields ultra-smooth single crystal superstructures suitable for the fabrication of photonic micro-components with low scattering loss.

OCIS codes: (130.3730) Lithium niobate; (130.2260) Ferroelectrics; (130.3990) Micro-optical devices; (350.3850) Materials processing.

References and links

1. D. K. Armani, T. J. Kippenberg, S. M. Spillane, and K. J. Vahala, “Ultra-high-Q toroid microcavity on a chip,” Nature **421**(6926), 925–928 (2003).
2. M. L. Gorodetsky, A. A. Savchenkov, and V. S. Ilchenko, “Ultimate Q of optical microsphere resonators,” Opt. Lett. **21**(7), 453–455 (1996).
3. V. S. Ilchenko, X. S. Yao, and L. Maleki, “Microsphere integration in active and passive photonics devices,” in Proc. SPIE **3930**, 154–162 (2000).
4. R. Lipowsky, “Surface-induced disorder and surface melting,” in *Springer Proc. in Physics*, (Springer, 1990), 158–166.
5. I. E. Barry, G. W. Ross, P. G. R. Smith, R. W. Eason, and G. Cook, “Microstructuring of lithium niobate using differential etch-rate between inverted and non-inverted ferroelectric domains,” Mater. Lett. **37**(4-5), 246–254 (1998).
6. C. L. Sones, A. C. Muir, Y. J. Ying, S. Mailis, R. W. Eason, T. Jungk, Á. Hoffmann, and E. Soergel, “Precision nanoscale domain engineering of lithium niobate via UV laser induced inhibition of poling,” Appl. Phys. Lett. **92**(7), 072905 (2008).
7. H. Åhlfeldt, “Single-domain layers formed in heat-treated $LiTaO_3$,” Appl. Phys. Lett. **64**(24), 3213–3215 (1994).
8. C. L. Sones, S. Mailis, W. S. Brocklesby, R. W. Eason, and J. R. Owen, “Differential etch rates in z-cut $LiNbO_3$ for variable HF/HNO_3 concentrations,” J. Mater. Chem. **12**(2), 295–298 (2002).
9. T. J. Sono, J. G. Scott, C. L. Sones, C. E. Valdivia, S. Mailis, R. W. Eason, J. G. Frey, and L. Danos, “Reflection second harmonic generation on a z -cut congruent lithium niobate crystal,” Phys. Rev. B **74**(20), 205424 (2006).
10. T. Jungk, A. Hoffmann, and E. Soergel, “Quantitative analysis of ferroelectric domain imaging with piezoresponse force microscopy,” Appl. Phys. Lett. **89**(16), 163507 (2006).
11. F. Johann, and E. Soergel, “Quantitative measurement of the surface charge density,” Appl. Phys. Lett. **95**(23), 232906 (2009).
12. A. Ridah, P. Bourson, M. D. Fontana, and G. Malovichko, “The composition dependence of the Raman spectrum and new assignment of the phonons in $LiNbO_3$,” J. Phys. Condens. Matter **9**(44), 9687–9693 (1997).

1. Introduction

Dense integration of optical waveguide circuits requires large dielectric contrast between the waveguide core and the cladding material which is typically achieved by fabricating devices which consist of super-structures (e.g. ridge waveguides and whispering gallery mode (WGM) resonators) where the optical confinement is high due to the high refractive index contrast between the optical material and the surrounding air. However, one of the sources of optical power loss and performance degradation in such photonic structures is surface imperfections such as residual surface roughness which introduces scattering loss. These fabrication imperfections can be corrected by thermal treatment i.e. using laser annealing methods to locally melt the surface allowing for the surface tension to reshape the relevant structure to

#125099 - $15.00 USD Received 5 Mar 2010; revised 13 Apr 2010; accepted 13 Apr 2010; published 14 May 2010

form an extremely smooth perfect globule. WGM resonators which are fabricated in this way usually exhibit very low scattering loss and hence high Q factors [1,2].

Although such a method can be applied to glass, which is an amorphous material, without undue problems it is rather different if applied to single crystal materials mainly because the single crystal properties are not generally preserved after the melting and cooling cycles [3]. Light propagating in such a poly-crystalline material will experience scattering at the boundaries between adjacent crystallites introducing significant optical loss. Furthermore the macroscopic physical and optical properties of the single crystal will be compromised due to the random orientation of the crystallites hence such a material will not be suitable for electro-optic and non-linear optical applications.

Here we present a method for the surface reshaping of micro-structured crystalline substrates which can produce smooth surfaces while maintaining the useful crystalline properties of the original material. The method is based on the observation that annealing of a crystal at temperatures close to, but lower than, the melting point induces preferential melting of a surface layer [4]. Upon cooling the melted surface layer re-crystallizes, seeded by the bulk that remains solid during the process, and is reshaped by the surface tension to form ultra-smooth single crystal superstructures. In order to demonstrate the potential of this method for the fabrication of photonic structures we have applied it to surface micro-structured lithium niobate, a nonlinear optical ferroelectric crystal which is widely used in the photonics industry.

2. Experiments and results

The melting temperature for congruently melting lithium niobate crystals is 1257°C (provided by Crystal technology, Inc.) and the Curie temperature which marks the ferroelectric to paraelectric phase transition is 1142°C, however this value does depend on the exact composition of the crystal and changes substantially with the lithium content.

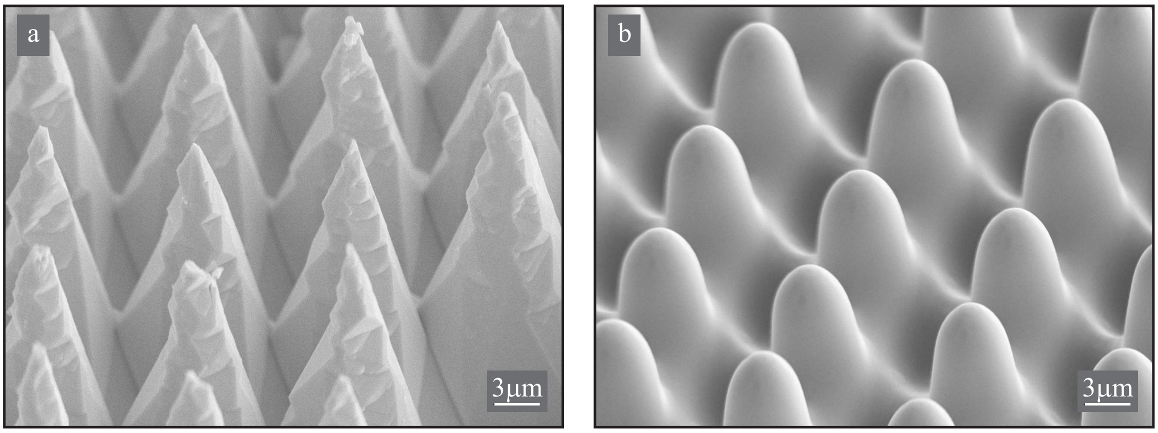

Fig. 1. SEM images of the micro-structured lithium niobate crystal surface (45° tilted) a) after deep etching of a 2D lattice of inverted ferroelectric domains and b) after thermal treatment.

We have prepared a micro-structured z-cut crystal surface by HF etching of a ferroelectric domain-engineered substrate [5]. The micro-structured crystal surface, which is shown in the scanning electron microscopy (SEM) image of Fig. 1a, consists of a 2D array of micro-pyramids which exhibit a rough side surface and a sharp tip. The initial ferroelectric domain inverted lattice in this particular sample consisted of an array of circularly shaped + z polar surfaces and was achieved by UV laser induced poling inhibition [6]. A + z face is not affected by the HF acid, however as the pillar structure develops due to the preferential etching of the crystal surface that surrounds the circular + z domains, the revealed side surface of the pillars is now subject to sideways etching along the three y-directions of the crystal. Hence, after prolonged etching the pole-inhibited domain etches away to produce a single point (as observed in Fig. 1a). The sideways etching is also responsible for the conical shape of the features which are shown in Fig. 1a. The sample was then subjected to thermal

#125099 - $15.00 USD Received 5 Mar 2010; revised 13 Apr 2010; accepted 13 Apr 2010; published 14 May 2010

annealing to a temperature of 1130°C for 50 hrs in a continuous flow of oxygen gas in order to suppress lithium out-diffusion. The temperature was ramped up at a rate of 5 degrees per minute and after the required dwell time it was ramped down also at a rate of 5 degrees per minute. The surface topography after annealing is shown in the SEM image of Fig. 1b. It is obvious that all the sharp features have been smoothed out as the micro-structures have been reshaped by the surface tension.

These surface tension reshaped structures can be defined, to some extent, by the initial shape of the crystal microstructure. Figure 2a shows a lithium niobate microstructured pillar with an undercut top section as a result of HF etching of an isolated surface domain produced by inhibition of poling [6]. After thermal annealing for 50 hrs at 1120°C the pillar is reshaped by the surface tension to form a quasi-oblate spheroid structure as shown in Fig. 2b. Such a structure is suitable for supporting WGMs while the smooth side surface guarantees low scattering loss. Its small dimensions can reduce dramatically the number of supported WGMs and increase the device free spectral range. Both features are beneficial in a number of advanced optical applications such as optical filters and lasers.

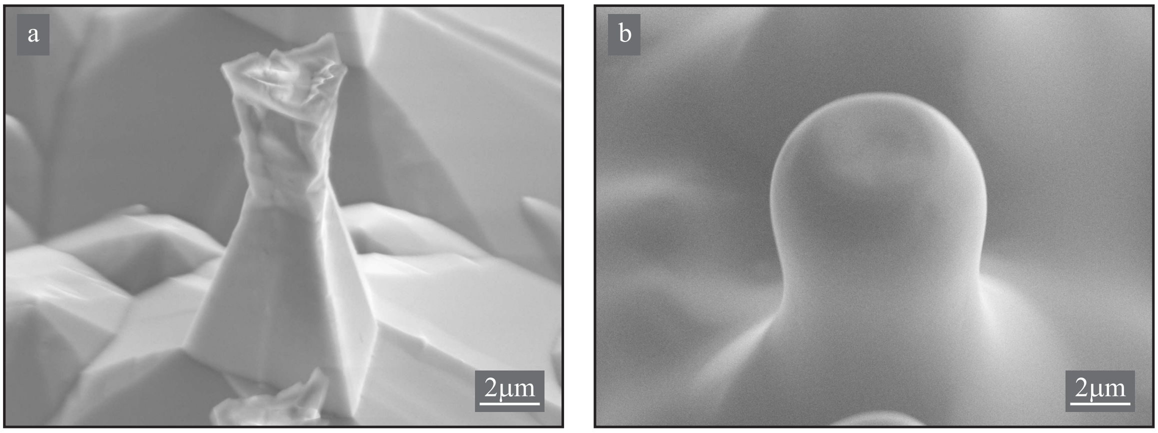

Fig. 2. SEM images of a) the initial structure, comprising an undercut, produced by inhibition of poling followed by deep chemical etching using HF acid, b) corresponding annealed structure showing a quasi-oblate spheroid top. In both images the sample is tilted by 45°.

Although the range of temperatures that the lithium niobate crystals experienced during the thermal treatment were kept below the Curie point and hence well below the melting point, it is evident that, at some point during the process, the surface was in the liquid phase in both examples shown in Figs. 1b and 2b. However, preferential melting of the surface is possible at temperatures lower than the bulk melting temperature, with the thickness of the melted zone being a function of the temperature [4].

In the cases which were presented so far the temperature was kept just below the Curie point. Hence it is expected that the bulk of the processed material is still single crystal and ferroelectric throughout the thermal processing, while the surface undergoes melting to the liquid phase. However even when the crystal was treated at temperatures higher than the Curie temperature we found that there is always a substantially deep layer of the crystal that maintains a single polarization state. Although similar observations have been made in thermally-treated $LiTaO_3$ crystals at temperatures exceeding the Curie temperature [7], we are not aware of any such reports on $LiNbO_3$. Such prolonged thermal treatment can lead to lithium out-diffusion which may be substantial and which consequently leads to domain inversion on the + z face of the crystal. As a result a uniform domain-inverted layer is formed with a depth which depends on the duration of the thermal treatment. We have observed that in extreme cases where a crystal slab is annealed at temperatures exceeding the Curie point the depth of the domain-inverted layer can reach half the slab thickness. Interestingly though both of the two sections of the slab remain single domain.

Etching in HF acid is routinely used to reveal the presence of inverted ferroelectric domains in lithium niobate as the two opposite z faces of the crystal etch at different rates (actually the + z face remains totally unaffected by the acid) [8]. However, differential etching

#125099 - $15.00 USD Received 5 Mar 2010; revised 13 Apr 2010; accepted 13 Apr 2010; published 14 May 2010

can also be observed between opposite y-faces of the crystal. The topography of the etched y-face can reveal the domain structure of a multi-domain lithium niobate crystal because, as has been shown in [9], domain inversion corresponds to a 180° rotation of the z axis around the x axis of the crystal. Consequently the y axis is also rotated by 180° and hence opposite ferroelectric domains present opposite y-faces on the same y surface.

The etched y-face of the crystal slab which was annealed at a temperature exceeding the Curie temperature is shown in the SEM image of Fig. 3 where the two single domain regions are clearly visible due to the differential etching of the opposite y-faces which are presented on the same y-surface as indicated in the figure. The top edge of the image corresponds to the original -z face of the sample while the bottom edge corresponds to the original + z face which has now been domain-inverted, as a consequence of thermal annealing, to form a -z face. Consequently, after annealing the crystal presents a -z face on both z-surfaces.

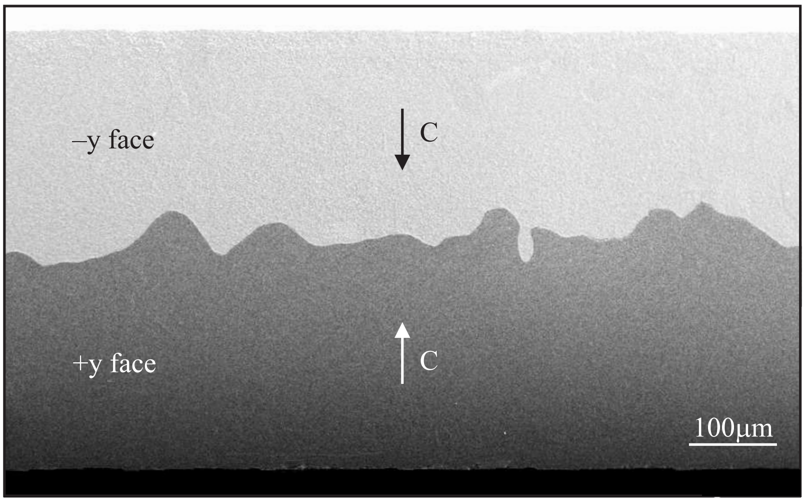

Fig. 3. Etching of the y-face of a z-cut crystal slab annealed at T = 1200°C (above the Curie temperature) for 10 hrs revealing the ferroelectric domain structure.

In order to assess the quality of the crystal after the thermal process the annealed crystal surface was investigated using piezoresponse force microscopy (PFM) [10], Raman spectroscopy and finally chemical etching.

A series of small area PFM scans was performed on various locations of the annealed microstructured substrate. All PFM images obtained in these scans showed the very same uniform grey-level, and thus the same piezoresponse, indicating that the melted and re-solidified surface is single domain and piezoelectric. In order to quantify the piezoresponse obtained on the annealed substrate, we performed a comparative measurement on an untreated multi-domain single crystal (PPLN). We could thereby show, that the amplitude of the PFM signal measured on the microstructured substrate is identical to the one on the -z – face of the untreated sample. In addition, we also observed strong surface charging on the re-solidified material [11]. Based on those evidences we concluded that the annealed microstructured substrate is both single crystal and ferroelectric. Micro-Raman spectroscopy and chemical etching corroborated the PFM results.

A set of spatially-selective Raman spectra has been acquired from different positions on the annealed micro-structured substrate shown in Fig. 1b. The micro-Raman spectrometer which was used to acquire the spectra employed a × 50 microscope objective to both focus the probe laser beam and collect the Raman signal. The depth resolution of the system is limited by the depth of focus of the objective which is less than 1 μm.

Figure 4 shows a set of Raman spectra which were acquired from a single reshaped tip. These Raman spectra were taken at different focusing conditions and can be compared to a reference spectrum (solid line) taken from an unstructured and untreated z-cut substrate in the z(yy)z configuration [12]. The dashed line spectrum corresponds to a well-focused acquisition from a spot on the summit of a single tip, while the dotted line corresponds to a slightly defocused acquisition on the same spot. Finally the dash-dotted line corresponds to a spot between two adjacent tips (focused acquisition).

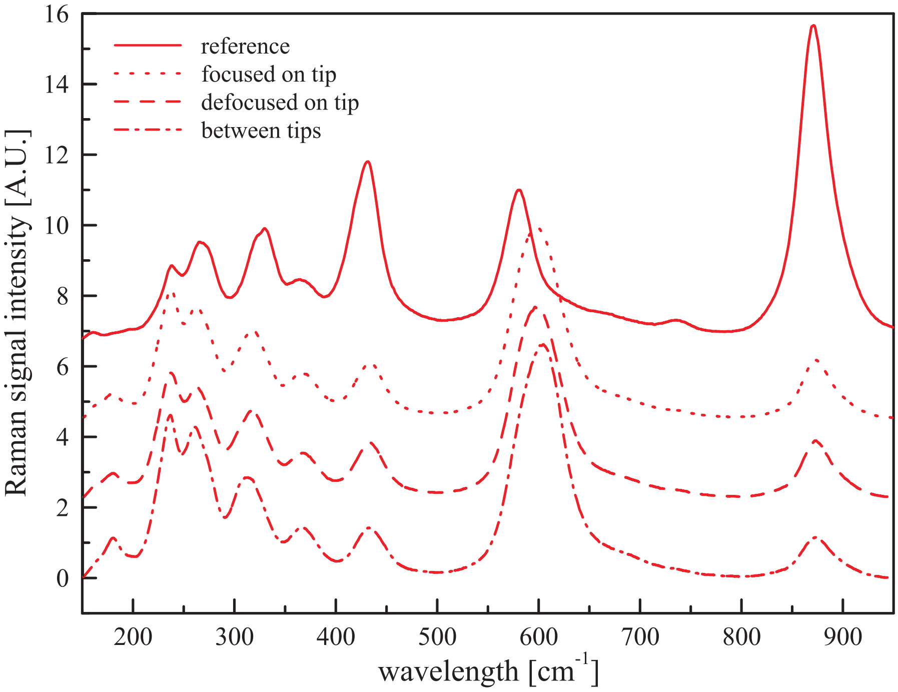

Fig. 4. Raman spectra acquired from different points on the annealed microstructured sample shown in Fig. 1b and with different focusing conditions as indicated in the legend. The solid line corresponds to a spectrum that was taken from a virgin z-cut sample in the z(yy)z configuration. An offset was introduced between spectra for clarity.

The acquisition of spectra under different focusing conditions was performed in order to collect signals from the surface layers of the structure, which had experienced melting, in order to detect any possible structural changes after the process. However, there was no obvious difference between these spectra (dashed line and dotted line in Fig. 4).

Further observation of the spectra reveals that some Raman lines corresponding to the reshaped tips appear to be shifted with respect to the corresponding peaks in the reference spectrum (the 582 cm^{-1} peak in particular) while others (like the 432 cm^{-1} and 873 cm^{-1} peaks) exhibit a relative intensity change as compared to the reference spectrum. Raman spectra of crystalline materials however are subject to selection rules which depend on the specifics of the crystal face and polarization mode of the exciting beam and the detection channel. Since the annealed structure is curved it does not present a pure z-face to the direction of incidence of the interrogating laser beam the entrance/exit faces are in general different compared to the reference z-cut substrate. Additionally, the curved interfaces can alter the polarization state of both the exciting beam and of the collected signal. These factors which influence both the position and intensity of the Raman peaks are likely to be responsible for the differences which are observed between the various Raman spectra taken from the reshaped surface and the reference spectrum taken from the pure z-cut crystal.

The lateral differential etching between opposite y-faces was used earlier for the visualization of the ferroelectric domain structure of the crystal. However, as a consequence of the threefold symmetry of the lithium niobate crystal structure there are three indistinguishable pairs of y-faces corresponding to three y-axes which are rotated by 120° with respect to each other. This threefold symmetry can be readily identified in the x-y cross-section of etched isolated inverted domains. Here we have used HF acid etching to look for this characteristic threefold symmetry on the re-solidified crystal features in order to assess the quality of the thermally treated crystal.

Figure 5a shows an SEM image of a smoothed feature as a result of the surface tension reshaping that took place during the annealing process. After brief etching in HF acid

#125099 - $15.00 USD Received 5 Mar 2010; revised 13 Apr 2010; accepted 13 Apr 2010; published 14 May 2010

characteristic facets (due to differential etching between opposite y-faces) start to emerge revealing the characteristic threefold symmetry of lithium niobate as shown in the SEM image of Fig. 5b.

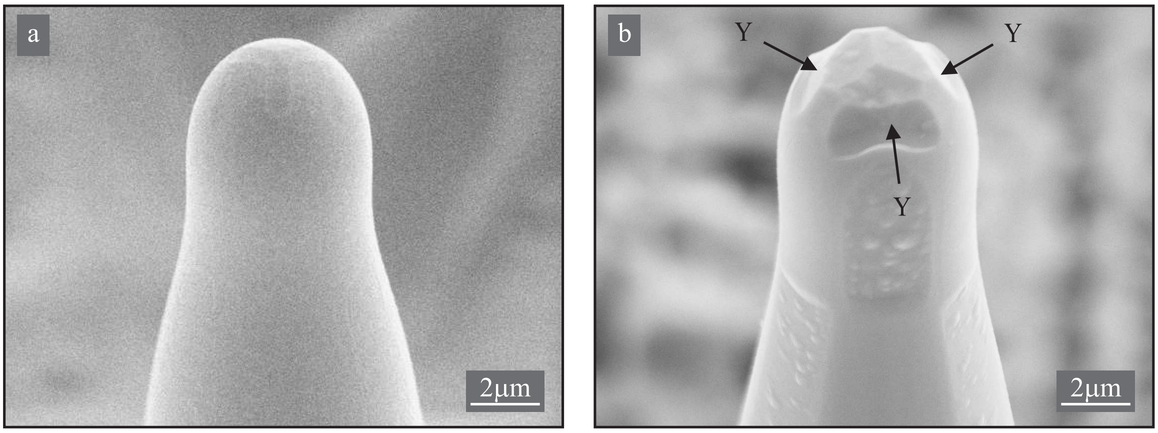

Fig. 5. a) SEM image of a surface tension reshaped feature, b) SEM image of a feature briefly etched in HF showing characteristic y-face differential etching as indicated by the arrows.

3. Conclusions

In summary, we have demonstrated a method for achieving ultra-smooth single crystal lithium niobate structures. The method is based on selective surface melting at temperatures below the Curie point, followed by seeded re-crystallization. The single crystal nature of the re-crystallized surface layer was confirmed experimentally by piezoresponse force microscopy, Raman scattering and chemical etching. Elimination of the residual surface roughness promises a significant reduction of the propagation losses in any micro-structured photonic structure such as ridge waveguides, ring waveguide resonators and lasers enabling the miniaturization of photonic circuits without sacrificing the device performance. Hence, the method is expected to increase dramatically the optical performance of $LiNbO_3$-based crystalline waveguide structures, 1-D and 2-D surface relief gratings and WGM micro-resonators. We further anticipate that this method could also be extended to other crystalline materials.

Acknowledgements

The authors would like to thank the E.U. and the EPSRC (Engineering and Physical Sciences Research Council) for funding via the STREP 3D - DEMO and EP/C515668/1 portfolio grant respectively.

APPLIED PHYSICS LETTERS **92**, 072905 (2008)

Precision nanoscale domain engineering of lithium niobate via UV laser induced inhibition of poling

C. L. Sones,[1] A. C. Muir,[1,a)] Y. J. Ying,[1] S. Mailis,[1] R. W. Eason,[1] T. Jungk,[2] Á. Hoffmann,[2] and E. Soergel[2]
[1]*Optoelectronics Research Centre, University of Southampton, Highfield, Southampton, SO17 1BJ, United Kingdom*
[2]*Institute of Physics, University of Bonn, Wegelerstrasse 8, 53115 Bonn, Germany*

(Received 10 December 2007; accepted 31 January 2008; published online 20 February 2008)

Continuous wave ultraviolet laser irradiation at $\lambda=244$ nm on the $+z$ face of undoped and MgO doped congruent lithium niobate single crystals has been observed to inhibit ferroelectric domain inversion. The inhibition occurs directly beneath the illuminated regions, in a depth greater than 100 nm during subsequent electric field poling of the crystal. Domain inhibition was confirmed by both differential domain etching and piezoresponse force microscopy. This effect allows the formation of arbitrarily shaped domains in lithium niobate and forms the basis of a high spatial resolution microstructuring approach when followed by chemical etching. © *2008 American Institute of Physics*. [DOI: 10.1063/1.2884185]

Domain engineering[1,2] of lithium niobate (LN) is a subject of extensive research and a simple, cheap, and robust method of fabrication of well-defined periodic domain-inverted structures on submicron scales is highly desirable. Spatial domain engineering is used for many optical processes in bulk crystals and waveguides and can also allow for the creation of both freestanding[3] and surface relief structures[4] through the differential etching characteristics of the polar z faces of the crystal. If achievable on the submicron scale, surface structuring through differential etching will allow the implementation of a range of interesting applications such as tunable photonic crystals, ridge waveguide lasers, and multifunctional micromachines.

Previous work has shown that ultraviolet (UV) and visible laser light can either directly invert[5] or assist the domain inversion process in LN.[6–9] In this paper, however, a different effect is presented whereby illumination of the $+z$ face with UV light at $\lambda=244$ nm (with photon energy greater than the LN band gap) *inhibits* domain inversion in illuminated areas during subsequent electric field poling (EFP). Of major importance, the inhibited domains are not restricted in their shape or alignment with the crystal x or y axes, hence, arbitrarily shaped domains can be formed. Some initial results of this effect and its applicability in the creation of micro/nano structures in LN are presented.

A beam from a frequency-doubled Ar-ion laser was focused to a spot size of ~ 2.5 μm on the $+z$ or $-z$ face of either an undoped congruent or 5 mol % MgO-doped LN crystal. Positioning and exposure control of the crystal was achieved by a computer-controlled, three-axis stage system coupled with a mechanical shutter.

For dynamic exposures, sets of parallel lines were drawn on the z faces of the crystals along the crystallographic x or y directions by moving the stages at speeds ranging from 0.05 to 0.3 mm s^{-1}. For static exposures, arrays of illuminated spots with identical exposure times, ranging from a few milliseconds to a few tens of seconds, were formed. The separation between the edges of adjacent illuminated spots in the arrays varied from 0 to 6 μm which permitted us to verify if any proximity effect existed such as that observed in pulsed laser direct poling[5] where the closest approach observed there was of order ~ 2 μm, irrespective of illuminated pattern resolution. For both types of exposures, the power was varied between 20–28 mW.

A two-beam interference scheme that allowed the formation of periodic structures over larger areas of the crystal via single exposures was also investigated. The incident interference fringe pattern had a period of 700 nm and extended over an area of around 2000 μm^2. As with previous experiments, several different exposure times, ranging from tens of milliseconds to tens of seconds, and a range of incident powers were tried.

Each set of illumination conditions was duplicated for both $+z$ and $-z$ face illuminations, to allow a direct comparison of the resultant effects on each of these polar faces. The samples were then poled using the EFP setup described in Ref. 6. The voltage was ramped at 2 kV/min to a value of ~ 10.1 kV, corresponding to an electric field of 20.2 kV/mm across the 0.5 mm thick sample. This value of the applied electric field ensures that domain inversion occurs slowly, which is desirable since the kinetics of the domain wall motion is seen to influence greatly the shape and quality of the resultant structures.

Etching of the poled crystal in aqueous HF acid solution then allows visualization of the formed domain structures through the different etch rates of the two z faces.[10] Piezoresponse force microscopy[11] (PFM) was also used to verify the domain nature of these structures. Lastly, the samples were imaged with a scanning electron microscope (SEM).

Figures 1 and 2 show SEM images of the structures produced by illumination of the single focussed UV beam on the $+z$ face followed by EFP and etching. The images show smooth, continuous unetched sections which correspond to the UV illuminated area of the surface. The etched background is the newly domain inverted area which presents a $-z$ face to the acid and hence etches. Further observation of the SEM images shows that the edges of the structures are

---

[a)] Author to whom correspondence should be addressed. Electronic mail: acm@orc.soton.ac.uk.

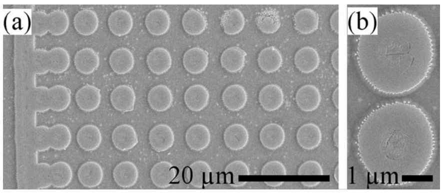

FIG. 1. (a) SEM image of a poling inhibited dot array. Scale bar 20 μm. (b) SEM image of two closely spaced poling inhibited dots.

slightly jagged, possibly due to the Gaussian intensity profile of the illuminating beam.

Interestingly, exposures on the $-z$ face, done for the purpose of comparison, were not seen to inhibit domain inversion. On the contrary, domain inversion was seen to initiate in the illuminated regions and was then followed by domain propagation through the crystal in a random and disorderly fashion. Hence, all the results discussed in this letter correspond to $+z$ face illuminations that result in domain inhibition.

Arrays of dots, such as the ones shown in Fig. 1(a), which are produced by static exposures, can have arbitrary dot separations and no interaction between dots was observed even when the separation between them was less than one micron, Fig 1(b). When illuminated areas overlapped, the regions of inhibited domain inversion merged. This can be seen on the left hand side of Fig. 1(a), where stage backlash distorted the array by reducing the dot spacing. Additional UV exposure of a specific area was not observed to produce any further effect. This can be seen in Fig. 2(a) where a cross-hatched pattern is shown as a result of sequential line scans along the x and y crystallographic axes. A higher magnification SEM image that shows the quality of the overlapped exposure is shown in Fig. 2(b). The sample was tilted by 45° during the SEM scan which allows the observation of the quality of the sidewall of the poling inhibited domain. The SEM images shown in Fig. 2 were obtained after prolonged etching (39 h). As a result, high aspect ratio structures were produced underlining the potential of this method for surface microstructuring.

The potential of this technique to form precisely positioned structures without proximity restrictions demonstrates the practicality of this technique in the implementation of devices such as couplers, y junctions, ring microresonators, and photonic crystals. The width of the area over which inhibition occurs is seen to be dependent upon both the incident power and the dwell time/scanning velocity of the beam with larger domains formed with longer dwell or lower scan speeds. This functionality reiterates the capability of this technique.

The quality of the poling inhibited regions was observed to be dependant upon the domain wall kinetics during the EFP step. It was seen that when the wall movement was smooth and reasonably slow, the inhibition process produced continuous domains. In congruent crystals when the wall movement can be fast, expanding in a "jerky" manner,[1,12] the poling inhibited regions appeared fragmented or did not exist at all in areas corresponding to fast domain wall motion. In the MgO doped crystals where EFP is known to be slower[13,14] and smoother, the inhibited domains appeared to be smooth and continuous everywhere.

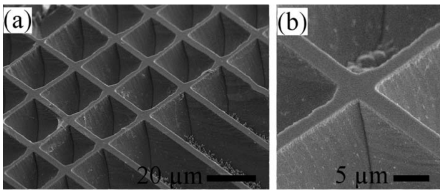

FIG. 2. (a) SEM image of poling inhibited hatched lines after 39 h of HF etching. Sample tilt 45°. (b) High magnification SEM image of a crossing point in (a).

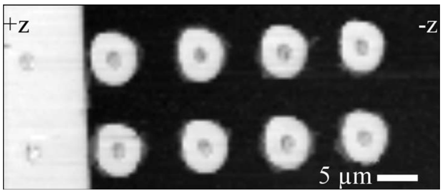

FIG. 3. PFM image of poling inhibited dot array. White=$+z$ face, black=$-z$ face as indicated. White area to left of image is an unpoled bulk domain.

In order to investigate the stability of the inhibited domains the crystal was thermally annealed for 1 h at 215 °C after the EFP step of the process. SEM investigation of the HF etched annealed crystal showed that the poling inhibited domains survived the brief annealing process without any significant change apart perhaps from the fact that after annealing there seems to be a slight improvement on the quality of the edges.

The domain orientation of the inhibited domains was further investigated by PFM which confirmed the observations deduced from chemical etching. Figure 3 shows a PFM image of an area of the crystal that carries a set of static spot illuminations and has also been partially poled (only a fraction of the area was domain inverted). Full contrast is associated with opposite ferroelectric domains where a $+z$ face appears white (left section of the image) while a $-z$ face appears black (right larger section of the image). The dots which appear white in a black background of the PFM image correspond to the UV exposed areas which have maintained their original domain orientation ($+z$) while the surrounding area has been inverted ($-z$) and appears black. The depth sensitivity of the PFM is ~100 nm (Ref. 15) which gives the lower limit to the depth of the inhibited domains. Preliminary investigations of the etched y face indicated that the depth of the domain inhibited area was in the range of 0.5–1 μm, however a systematic investigation will be presented in a future communication.

Interferometric exposures were at much lower laser intensity than single beam exposures due to the larger spot size. Exposure of the $-z$ face, followed by brief etching in HF, resulted in no topographical contrast. Exposure of the $+z$ face followed by bulk EFP and etching produced a periodic relief structure which is shown in the SEM image of Fig. 4.

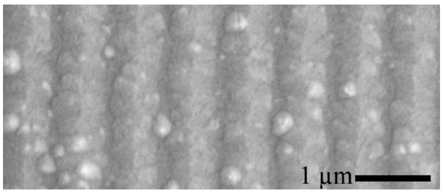

FIG. 4. SEM image of $+z$ face after interferometric exposure, EFP and brief etching.

The SEM image shown in Fig. 4 is qualitatively different to the ones produced at higher intensity. We believe that the surface relief pattern shown in Fig. 4 as revealed by chemical etching is a single domain structure which has originated from a periodic poling inhibited structure. Due to the low intensities used in this experiment the initial poling inhibited areas are expected to be very narrow and shallow hence easily removed by the acid via side etching. However, by using higher UV laser intensities it should be possible to obtain deeper periodic domain structures at the highly desired submicron scale.

We believe that the inhibition of the domain reversal is due to redistributed charges under the crystal surface which increases the coercive field locally. UV illumination leads to photoexcitation of charges and heating of the crystal.[16] A pyroelectric field is formed which drives electrons into the bulk of the crystal and holes toward the surface, producing a short range dipolar electric field distribution, which increases the coercive field locally. When a domain nucleates on the $-z$ face and propagates toward $+z$ face, inversion will not occur in this region where the coercive field is increased and domain propagation will be impeded, leaving a $+z$ surface domain island on a $-z$ background. This mechanism has some similarities to that described by Dierolf and Sandmann[7] for confocal light-assisted poling. However, in our case the driving field for the electrons is created by local heating of the crystal and not an external voltage and is opposite in direction to that of Dierolf and Sandmann,[7] leading to domain inhibition rather than domain inversion. Also, the mechanism we describe is latent and does not require application of the external field during illumination as in their case.

As a method of surface structuring UV poling inhibition followed by etching is simple, inexpensive, and flexible to implement. The shape/size and the quality of the fabricated structures is determined by the incident exposure conditions, in combination with the subsequent EFP parameters and the annealing steps, respectively. Additionally, as the crystallographic symmetry is not observed to impose limitations on the orientations of the created structures, any desired shapes can be achieved. Also the single domain nature of these structures provides the necessary requirement for implementation of efficient nonlinear, piezoelectric, and other domain-orientation-sensitive devices.

In conclusion, exposure of the $+z$ surface of congruent LN single crystals via UV laser radiation at $\lambda = 244$ nm is shown to inhibit domain inversion locally during subsequent EFP and, hence, results in the creation of UV illumination controlled two-dimensional surface structures. Domain inhibition was further verified by PFM and differential wet etching. UV light-induced poling inhibition is attributed to the redistribution of photoexcited charges in the electric field created when the laser heats the crystal, thus, producing a space-charge field which repels the propagating bulk domains during the subsequent EFP step. Finally, this effect, in conjunction with wet etching, was demonstrated to provide an easy alternative method for fabricating useful domain and surface relief structures.

The authors are grateful to the Engineering and Physical Sciences Research Council, UK, and the EU for research funding under Grant No. EP/C515668 and STREP 3D-DEMO respectively.

[1] V. Y. Shur, Ferroelectrics **340**, 3 (2006).
[2] B. J. Rodriguez, R. J. Nemanich, A. Kingon, A. Gruverman, S. V. Kalinin, K. Terabe, X. Y. Lui, and K. Kitamura, Appl. Phys. Lett. **86**, 012906 (2005).
[3] C. Sones, S. Mailis, V. Apostolopoulos, I. E. Barry, C. Gawith, P. G. R. Smith, and R. W. Eason, J. Micromech. Microeng. **12**, 53 (2002).
[4] S. Mailis, G. W. Ross, L. Reekie, J. A. Abernethy, and R. W. Eason, Electron. Lett. **36**, 1801 (2000).
[5] I. T. Wellington, C. E. Valdivia, T. J. Sono, C. L. Sones, S. Mailis, and R. W. Eason, Appl. Surf. Sci. **253**, 4215 (2007).
[6] C. L. Sones, M. C. Wengler, C. E. Valdivia, S. Mailis, R. W. Eason, and K. Buse, Appl. Phys. Lett. **86**, 212901 (2005).
[7] V. Dierolf and C. Sandmann, Appl. Phys. Lett. **84**, 3987 (2004).
[8] M. Müller, E. Soergel, and K. Buse, Appl. Phys. Lett. **83**, 1824 (2003).
[9] M. C. Wengler, U. Heinemeyer, E. Soergel, and K. Buse, J. Appl. Phys. **98**, 064104 (2005).
[10] C. L. Sones, S. Mailis, W. S. Brocklesby, R. W. Eason, and J. R. Owen, J. Mater. Chem. **12**, 295 (2005).
[11] T. Jungk, Á. Hoffmann, and E. Soergel, Appl. Phys. Lett. **89**, 163507 (2006).
[12] V. Gopalan, Q. X. Jia, and T. E. Mitchell, Appl. Phys. Lett. **75**, 2482 (1999).
[13] A. Kuroda, S. Kurimura, and Y. Uesu, Appl. Phys. Lett. **69**, 1565 (1996).
[14] K. Nakamura, J. Kurz, K. Parameswaran, and M. M. Fejer, J. Appl. Phys. **91**, 4528 (2002).
[15] T. Jungk, Á. Hoffmann, and E. Soergel, New J. Phys. **10**, 013019 (2008).
[16] A. C. Muir, G. J. Daniell, C. P. Please, I. T. Wellington, S. Mailis, and R. W. Eason, Appl. Phys. A: Mater. Sci. Process. **83**, 389 (2006).

APPLIED PHYSICS LETTERS **94**, 172904 (2009)

Depth resolution of piezoresponse force microscopy

Florian Johann,[1,a)] Yongjun J. Ying,[2] Tobias Jungk,[1] Ákos Hoffmann,[1] Collin L. Sones,[2]
Robert W. Eason,[2] Sakellaris Mailis,[2] and Elisabeth Soergel[1]
[1]*Institute of Physics, University of Bonn, Wegelerstraße 8, 53115 Bonn, Germany*
[2]*Optoelectronics Research Centre, University of Southampton, Highfield, Southampton, SO17 1BJ, United Kingdom*

(Received 11 March 2009; accepted 8 April 2009; published online 28 April 2009)

Given that a ferroelectric domain is generally a three dimensional entity, the determination of its area as well as its depth is mandatory for full characterization. Piezoresponse force microscopy (PFM) is known for its ability to map the lateral dimensions of ferroelectric domains with high accuracy. However, no depth profile information has been readily available so far. Here, we have used ferroelectric domains of known depth profile to determine the dependence of the PFM response on the depth of the domain, and thus effectively the depth resolution of PFM detection. © *2009 American Institute of Physics*. [DOI: 10.1063/1.3126490]

During the past decade piezoresponse force microscopy (PFM) has become a standard tool for the investigation of ferroelectric domains.[1,2] This is mainly because of its ease of use (no specific sample preparation) combined with its capability for imaging ferroelectric domains with high lateral resolution of <20 nm.[3] Furthermore, PFM is not limited to specific crystallographic orientations of the sample, and hence ferroelectric domains can be visualized with PFM on all faces of the crystal.[4] Being an all-purpose analytical tool, and therefore advantageous with respect to many other relevant techniques used for the investigation of ferroelectric domains,[5] it is often ignored that PFM produces two-dimensional maps only of the domain patterns. The question that arises is: up to what depth below the surface is PFM sensitive? While some earlier attempts at addressing this problem were performed using thin films,[6,7] to date, however, there are no reports on measurements using single crystals. Such samples are needed therefore as they uniquely allow for a defined domain configuration, and thus to quantitatively determine the depth resolution of PFM.

The goal of the investigations which are presented in this paper was to obtain a direct correlation between the depth of a surface domain[8] and the corresponding contrast obtained in PFM measurements. The first challenge was thus to fabricate a sample with ferroelectric surface domains of known depth. A method that can produce such domains in lithium niobate is UV laser-induced inhibition of poling,[9] a brief description of which is given here for clarity. It was found that irradiation of the $+z$ polar surface of lithium niobate crystals with UV laser radiation locally increases the coercive field. Hence, a preirradiated area of the crystal surface will maintain its original polarity after a subsequent uniform electric field poling step. The depth d_0 of those poling inhibited domains is of the order of a few microns, depending on the specific UV-writing conditions, such as the illuminating laser light (wavelength and intensity) and scan speed used.[10] Linear ferroelectric domain tracks several millimeters long were produced by scanning the crystal sample in front of the focused laser beam.

In order to obtain surface domains of different depth d_0 the sample was wedge polished at a shallow angle ($\alpha=5°$). For a domain of $d_0=3\ \mu$m depth we thereby obtained a smooth transition from domain depths of 0–3 μm over a distance of $l=d_0/\sin\alpha\approx 35\ \mu$m. We then briefly etched the sample in hydrofluoric acid (HF) to enable subsequent scanning electron microscopy (SEM) imaging. Figure 1 shows a schematic of the cross sections of the wedge polished sample. In some cases a damaged region is observed in the center of the poling inhibited stripe. This is a consequence of the Gaussian profile of the irradiating UV laser beam where the high intensity portion of the laser beam can lead to localized melting of the surface. The melted region is then rapidly quenched producing a polycrystalline or amorphous layer with no net piezoelectric response.

PFM utilizes a scanning force microscope operated in contact mode with an additional voltage applied to the tip. The imaging of ferroelectric domains with PFM is based on the fact that ferroelectricity implies piezoelectricity, hence mapping the piezoelectric response of the crystal directly reflects its domain structure. To allow sensitive readout of the piezomechanical deformation of the material, an alternating voltage $U\sin\omega t$ is applied to the tip and lock-in detection is used for the measurements. A more detailed description of PFM can be found in Refs. 1, 4, 11, and 12.

For the experiments we used a stand-alone scanning force microscope (SMENA, NT-MDT, Russia). Diamond-coated tips with a nominal radius of 50–70 nm (DCP11, NT-MDT) were utilized. The voltage applied to the tip (5 V_{rms})

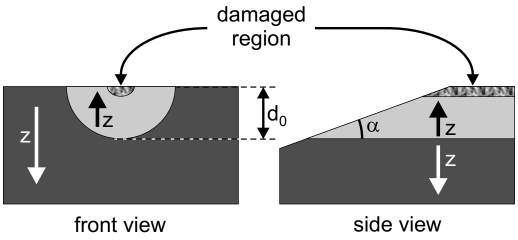

FIG. 1. Illustration of the cross sections of the sample used in the experiments. A lithium niobate crystal with a stripe surface domain (depth d_0) is wedge polished at an angle α. At the center of the domain the crystal is damaged due to high laser irradiation during the fabrication process.

[a)] Electronic mail: johann@physik.uni-bonn.de.

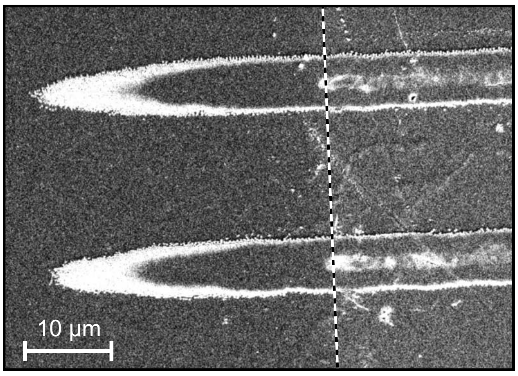

FIG. 2. HF-etched wedge-polished sample imaged with scanning electron microscopy. The dashed line indicates the position of the edge caused by the wedge polishing.

was directly provided by the lock-in amplifier (SRS 830, Stanford Research Systems).

Figure 2 shows an SEM image of a wedge-polished sample with two surface domains. In the right part of the image, the damaged region in the center of the domains is clearly visible. Furthermore, a bright halo around the domains can be observed. This feature is attributed to the imperfect boundary between the pole-inhibited domain and the surrounding bulk domain. Because the sample has been wedge-polished, thus gradually thinning the surface domain, the latter appears as a composite of nanodomains at its thinnest region, as shown in the schematic in Fig. 3(a). To verify this argument we recorded high-resolution PFM images at the tail end of a wedge-polished pole-inhibited domain [Fig. 3(b)]. Obviously the ferroelectric surface domain in this portion is no longer solid but a composite of many nanodomains.

Figure 4 shows the results from the scanning probe microscopy measurements of the whole wedge polished area, where topography (a) and piezoresponse (b) of the sample were recorded simultaneously. To reveal the topography of the HF-etched sample, the slope of the wedge has been subtracted from the image by data processing. The shape of the ferroelectric domain is the same as in Fig. 2. Its maximum depth was determined to be $d_0 = l \sin \alpha = 35.6\ \mu\text{m} \times \sin 5° = 3.1\ \mu\text{m}$. Compared with the topography (a) the PFM image in (b) shows some distinct features of the surface domain. For clarity a schematic of the PFM image is depicted in Fig. 4(c). Four areas showing different amplitudes in the PFM image are identified as follows: (A) the stripe associated with the central damaged region, (B) the area with a solid surface domain, corresponding to a +z-face, (C) the part where isolated nanodomains prevail, and (D) the surrounding area where the full PFM signal for the opposite orientation (−z-face) is detected.

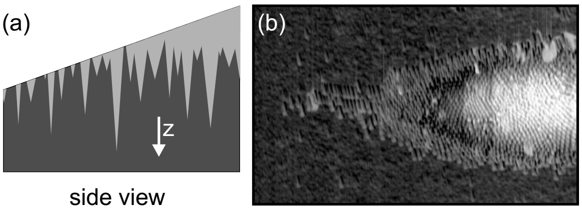

FIG. 3. Schematic (a) of the domain configuration at the limits of the pole-inhibited surface domain. The termination of the domain is not sharp resulting in a grainy domain structure as it can be seen in the PFM image (b). Image size is $15 \times 9\ \mu\text{m}^2$.

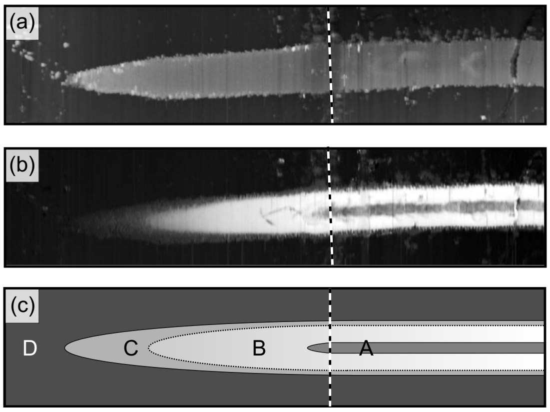

FIG. 4. Topography (a) and simultaneously recorded piezoresponse (b) of the wedge-polished sample shown in Fig. 2. Section (c) shows a schematic of the PFM image with four distinct areas marked. A: damaged region, B: full contrast PFM response corresponding to a +z-face, C: reduced PFM response, and D: surrounding uniform domain (−z-face) area. The dashed lines indicate the position of the edge owing to wedge polishing. For representation purposes, the wedge has been subtracted from the topography image. Image size is $73 \times 16\ \mu\text{m}^2$.

In order to determine the depth resolution of PFM measurements the dependence of the PFM contrast on the depth d of the surface domain must be investigated. We therefore took scan-lines along the ferroelectric domain imaged in Fig. 4(b). Figure 5 shows two scan lines where one passes through the damaged area (black •), while the other does not (gray ×). The letters (A, B, C, and D) correspond to the regions identified in Fig. 4(c). Note that the presumably sharp change in the contrast between area B and C in Fig. 4(b) cannot be observed in the slope of the graphs in Fig. 5. However, these two regions can be distinguished when comparing the noise: in region C where we observed the nanodomains (Fig. 3) the data points fluctuate much more. In addition, at the intersection between B and C the curvature of the graph changes its sign. This again is consistent with our proposition of an uneven transition between the surface domain and the bulk domain, leading to nanodomain regions following sample wedge polishing. A theoretical model should therefore only reflect part B of the measured scan line.

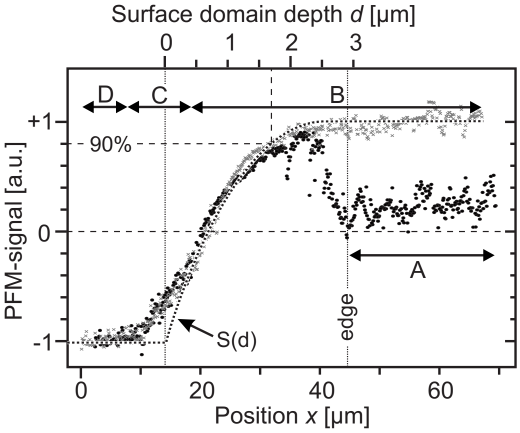

FIG. 5. Scan-lines across the PFM image of Fig. 4(b), one line passes through the damaged area (black •) while the other line does not (gray ×). The letters indicate the areas shown in Fig. 4(c). The curve $S(d)$ is the result of the simulation.

To obtain a reliable value for the depth resolution in PFM we calculated the expected depth dependence of PFM by means of a simplified model. We therefore approximated the spherical apex of the tip (radius r) by a point charge at the distance r from the sample surface. The resulting piezomechanical deformation was then obtained by integrating all contributions of the sample within the volume of the crystal experiencing the electric field from the point charge.[3] The result of our calculation can be seen in Fig. 5 where the curve $S(d)$ reflects favorably the measured slope within part B, as it is expected from the considerations described above. The visible depth d_{vis} of PFM, i.e., the depth below the crystals surface where the contribution to the PFM signal has increased to 90% of that observed with bulk domains in a thick crystal, can be estimated to be $d_{\mathrm{vis}} \approx 1.7\ \mu$m. Obviously PFM cannot provide any information about ferroelectric domains at depths $d > 1.7\ \mu$m. In other words, surface domains with $d > d_{\mathrm{vis}}$ cannot be distinguished from bulk domains by PFM.

It would, however, be useful to establish whether this measurement has a global rather than a material specific value. In order to investigate to what extent this result can be generalized to other ferroelectric materials[13,14] apart from $\mathrm{LiNbO_3}$ we have considered two extreme cases of electrostatic interaction to simulate the interaction between the PFM tip and the surface: (a) parallel-plate capacitor configuration and (b) the point charge model. For case (a), the electric field inside the sample is homogeneous ($E_z = \rho/\varepsilon$, ρ being the surface charge density), thus while the field distribution does not depend on the material parameters, the strength of the field, however, is a function of the material. For the second case (b), where a point charge q is located at a distance r from the sample surface, the electric field E_z inside the crystal, normal to the sample surface, can be written as follows:[3]

$$E_z(x,y,z) = \frac{2q\gamma}{1+\varepsilon_{\mathrm{eff}}} \frac{z+r}{[x^2+y^2+(z+r)^2]^{3/2}}, \qquad (1)$$

whereby $\gamma = \sqrt{\varepsilon_z/\varepsilon_r}$ and $\varepsilon_{\mathrm{eff}} = \sqrt{\varepsilon_z \varepsilon_r}$ and ε_z and ε_r are the dielectric constants of the material (ε_z in z-direction and ε_r perpendicular to z). As can be seen from Eq. (1), again only the amplitude of the electric field depends on the material properties but not its spatial distribution. Although the actual situation of the PFM tip in contact with the surface cannot be accurately described by either case [(a) or (b)] it is expected that, by common sense interpolation of the two extreme cases calculated above, the actual electric field inside the sample is also independent on the material parameters. Consequently, the visible depth for ferroelectric domains in bulk crystals is $d_{\mathrm{vis}} \approx 1.7\ \mu$m, irrespective of the material. Although this depth can be considered to be very small in terms of bulk crystals, this value becomes important when ferroelectric domain patterns in thin films are investigated. Not only is the thickness of the film smaller (typically several 100 nm) than d_{vis} but also the single crystalline grains are of the order of <100 nm. PFM images show therefore averages of several grains lying one above the other, which is why any quantitative conclusions from PFM measurement on such films is challenging. Note that if a lower lateral resolution can be tolerated, the visible depth d_{vis} can be increased by using a tip with larger radius r. Unfortunately the visible depth cannot be increased by applying a higher voltage $U \sin \omega t$ to the tip as a change in the voltage only changes the amplitude of the signal but not the shape of the curve.

In conclusion, we have accomplished a detailed analysis of the depth resolution of PFM. For the case of lithium niobate we have determined the visible depth to be $\approx 1.7\ \mu$m. From basic considerations we concluded that this depth is universal for all bulk crystals, irrespective of the material.

Financial support from the Deutsche Telekom AG, and the European Union, under the STREP 3D-DEMO is gratefully acknowledged.

[1] *Nanoscale Characterisation of Ferroelectric Materials*, 1st ed., edited by M. Alexe and A. Gruverman (Springer, New York, 2004).
[2] T. Jungk, A. Hoffmann, and E. Soergel, Appl. Phys. Lett. **89**, 163507 (2006).
[3] T. Jungk, A. Hoffmann, and E. Soergel, New J. Phys. **10**, 013019 (2008).
[4] T. Jungk, A. Hoffmann, and E. Soergel, New J. Phys. **11**, 033029 (2009).
[5] E. Soergel, Appl. Phys. B: Lasers Opt. **81**, 729 (2005).
[6] X. M. Lu, F. Schlaphof, S. Grafström, C. Loppacher, and L. M. Eng, Appl. Phys. Lett. **81**, 3215 (2002).
[7] L. M. Eng, S. Grafström, C. Loppacher, X. M. Lu, F. Schlaphof, K. Franke, G. Suchaneck, and G. Gerlach, Integr. Ferroelectr. **62**, 13 (2004).
[8] A. C. Busacca, C. L. Sones, V. Apostolopoulos, R. W. Eason, and S. Mailis, Appl. Phys. Lett. **81**, 4946 (2002).
[9] C. L. Sones, A. C. Muir, Y. J. Ying, S. Mailis, R. W. Eason, T. Jungk, A. Hoffmann, and E. Soergel, Appl. Phys. Lett. **92**, 072905 (2008).
[10] Y. J. Ying, C. L. Sones, H. Steigerwald, F. Johann, E. Soergel, K. Buse, R. W. Eason, and S. Mailis, Proceedings of the Conference on Lasers and Electro-Optics, 2009 (unpublished).
[11] *Ferroelectric Crystals for Photonic Applications*, 1st ed., edited by P. Ferraro, S. Grilli, and P. DeNatale (Springer, New York, 2008).
[12] T. Jungk, A. Hoffmann, and E. Soergel, J. Microsc. **227**, 72 (2007).
[13] M. Jazbinsek and M. Zgonik Appl, Appl. Phys. B **74**, 407 (2002).
[14] M. Zgonik, P. Bernasconi, M. Duelli, R. Schlesser, P. Günter, M. H. Garrett, D. Rytz, Y. Zhu, and X. Wu, Phys. Rev. B **50**, 5941 (1994).

UV laser-enabled fabrication of ridge waveguides in lithium niobate crystals

C. L. Sones[1,*], P. Ganguly[2], Y. J. Ying[1], E. Soergel[3], R. W. Eason[1], and S. Mailis[1]
[1]*Optoelectronics Research Centre, University of Southampton, Southampton, SO17 1BJ, United Kingdom*
[2]*Institute of Advanced Technology Development Centre, I.I.T, Kharagpur, India, 721302*
[3]*Institute of Physics, University of Bonn, Wegelerstr. 8, 53115 Bonn, Germany*

UV laser irradiation of lithium niobate polar *z* surface has been used to produce ridge waveguides in congruently melting crystals. UV laser irradiation of the +*z* polar surface is used to define an inverted domain pattern, by inhibition of poling, which transforms into a ridge structure after differential etching in HF. The same laser irradiation step also induces the refractive index change that provides the vertical confinement within the ridge structure. Furthermore, the poling-inhibition step results in a significant enhancement of the refractive index change which was initially induced by the UV laser.

Lithium niobate (LN) because of its distinctive combination of inherent physical properties has found use in a diverse range of applications such as mobile and optical telecommunications. This is also one of the prime reasons LN has always been recognised as an appropriate platform for implementation of integrated optical circuits.

One of the suggested approaches which is quite regularly implemented to further improve the efficiency and compactness of such integrated optical circuits based on components such as modulators and resonators is the use of ridge waveguides instead of conventional diffused [1] or proton exchanged[2] waveguides. Such ridge waveguide superstructures provide better lateral confinement of the optical mode due to the much higher index contrast as compared to their conventional counterparts. Additionally, the stronger optical confinement and smaller modal dimensions resulting in such a structure enhance the efficiency of any nonlinear processes.

Several different methods to produce ridge waveguides in LN have been investigated. Most of these methods utilize an etching step that defines the ridge geometry and a separate waveguide fabrication step[3-5] such as the commonly used ion-indiffusion or proton-exchange processes. Delineation of the ridge is achieved either via wet etching in an acid mixture containing HF acid or through dry etching processes such as ion beam milling [6] or plasma etching [7]. Acid-based wet etching, based on the differential etching behaviour of the two opposite polar z-faces has also been reported as an alternative approach for defining ridges in domain engineered LN [8]. Interestingly, ridge waveguides have also been fabricated by mechanical dicing of planar MgO:LN bonded on to LN [9]. The mandatory step required to induce the vertical refractive index contrast either precedes or succeeds the wet or dry etching process. The compatibility of the two steps is essential and hence a recipe with the appropriate sequential steps has to be adhered to for producing ridge waveguides in LN. In all of the multi-step approaches, a clean-room based photolithographic step is incorporated to define the ridge on an already produced planar waveguide or to define the waveguide on pre-structured ridge.

A fabrication process that essentially reduces or eliminates expensive clean-room based procedures, and thus presents with an uncomplicated low-cost route would be extremely well-suited for the implementation of the dense compact photonic circuits desired of today. The need for realising such a method has been the subject of several research publications, and hence is also the focus for the research presented here-in.

In this contribution we report on an innovative and less demanding method for producing ridge waveguides in *z*-cut LN. This method conforms to the above described goal by using a continuous wave (c.w.) UV laser direct waveguide writing procedure that allows the definition of the ridge pattern and the production of the necessary refractive index change for vertical confinement in a *single* step. UV direct writing (DW) [10,11] is a recently developed method for waveguide fabrication in LN. DW of single- and multi-mode graded-index channel waveguides in congruent LN has been demonstrated using c.w. UV laser light at writing wavelengths within the range of 244 nm,-305 nm [10,11], far and beyond the UV absorption edge of the material. Furthermore, this initial UV exposure of the +*z* face of LN crystals is reported to inhibit domain inversion locally during subsequent electric field poling (EFP) [12]. As a result a ferroelectric domain structure which corresponds to the UV laser irradiated tracks is formed after EFP. Subsequent differential wet etching of these poling-inhibited[12] domain structures results in the creation of surface-relief structures such as ridges, which can support optical propagation because of the already inscribed refractive index change. Any arbitrary light pattern painted on the LN crystal is always faithfully shaped into an identical ferroelectric domain pattern after EFP. Similarly this domain pattern again faithfully constructs a surface relief pattern on subsequent wet etching. Hence using this sequential combination of UV direct waveguide writing, electric field poling and differential wet etching it is possible to create any desirably shaped guided wave superstructures such as ring-resonators and couplers.

A schematic of the fabrication procedure detailing the processing steps that leads to the formation of the ridge waveguides is shown in Fig. 1. The first step in the fabrication sequence involves the inscription of a refractive index change in LN using the UV laser induced DW procedure. A beam from an Ar-ion laser (λ=275 nm), focused to a spot radius of ~3 µm, was used for the spatially selective irradiation of the +*z* face of a congruently melting, undoped LN crystal.

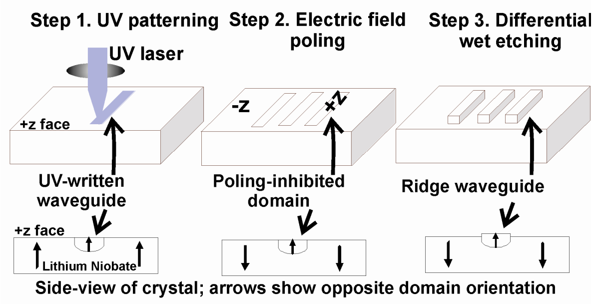

FIG. 1 Schematic of the fabrication process.

Precise control over the positioning and exposure of the illuminating laser beam was achieved by a computer-controlled, three-axis stage system coupled with a mechanical shutter. The laser wavelength used in our experiments was 275 nm. Sets of parallel lines were drawn on the +z faces of the crystals along the "*y*" crystallographic direction by moving the stages at speeds ranging from 0.1 to 1 mm/s. The incident intensity was varied between 0.1 – 0.25 MW/cm^2.

The second step involves EFP to transform the UV written patterns into corresponding domain patterns. Samples with the sets of UV exposed parallel lines using the EFP set-up described in Ref. 12.The sample was first "conditioned" by several forward and reverse poling cycles before the final forward poling step. In this final poling step, the voltage was ramped at 0.1 kV/s to a value of ~ 10 kV which corresponds to an electric field of ~20 kV/mm across the 0.5 mm thick sample. This lower value of the applied electric field as compared to the coercive field of the unconditioned virgin crystal ensures that domain inversion occurs slowly, which is desirable since the kinetics of the domain wall motion is seen to greatly influence the shape, quality and more essentially the continuity of the resultant ridge structures. As described in Ref. 12, the UV exposed areas (i.e. linear tracks) of the +z face, resist domain inversion during subsequent EFP retaining their original (+*z*) polarity whereas the rest of the un-illuminated crystal undergoes domain inversion to a –*z* domain orientation. As shown in Fig. 1, this result in a set of parallel +z domain patterns embedded in a background –z face.

The final fabrication step involves wet etching in HF acid to carve out the surface-relief structures corresponding to the domain patterns created in the previous step. The two opposite polar z surfaces of LN etch differentially in pure HF; the –z face etches at a certain rate whereas the +z face does not etch at all even when exposed to the etchant over several hours. So, when the poled sample are etched in pure HF acid at room temperature, because of this differential etch characteristics, the sets of parallel domains with +z orientation (acting as etch-stops) remain un-etched whereas surrounding –z face gradually etches down to reveal sets of parallel ridges. Fig. 2(a) shows an optical microscope image of two sets of parallel ridges (each set consisting of four ridges) formed using this fabrication route. All of the ridges have been produced by scanning the c.w. UV laser beam at a speed of 0.1 mm/s, however, the set of four lines on the left of the image have been written with an incident intensity of ~ 0.14 MW/cm^2 whereas the ones on the right have been written using a slightly lower intensity ~ 0.12 MW/cm^2. The small difference in the writing intensity influences the width of the poling-inhibited region and hence the slight variation in the widths of these two set of ridges. We have studied systematically the impact of the UV laser intensity on the ridge structures. Fig. 2(b) shows a plot of the etched pole-inhibited width, which corresponds to the width of the ridge structure, as a function of the UV laser intensity.

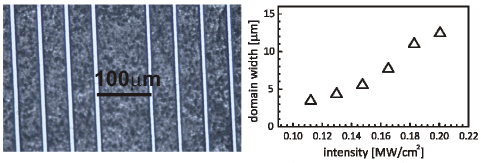

FIG. 2 (a) Optical microscope image of two sets of ridges, (b) Plot showing variation of poling-inhibited domain widths with intensity.

As shown in the plot a range of laser intensities exists where the width increases almost linearly with the laser intensity.

Scanning electron microscopy (SEM) images presented in Fig. 4 show the cross-section view of polished end-faces of two such ridges. The ridges in Fig 3(a) and 3(b) have been written with incident intensities of ~0.14 MW/cm^2 and 0.12 MW/cm^2 respectively. The width of the two ridges near the top is ~ 7 µm and ~6 µm respectively, and their heights are ~ 3.1 µm. As the ridges have been formed by drawing lines parallel to the crystallographic *y* direction they consequently have a symmetric cross-sectional profile. The noticeable roughness of the planar surfaces (-z faces) on either sides of the ridge is a typical manifestation of the wet etching of –z faces in pure HF [13]. The current choice of etching conditions was driven mainly by speed rather than quality. However compared to these rough surfaces, the sidewalls of the ridge waveguides are relatively much smooth and the minimal roughness should not influence the guided optical mode. The UV laser intensity, during the UV writing step, has a significant impact on the quality of the ridge structures. Specifically, UV intensities higher than ~ 0.16 MW/cm^2 lead to damage of the top-surface, whereas intensities lower than ~ 0.11 MW/cm^2 result in poorly defined ridge side-walls.

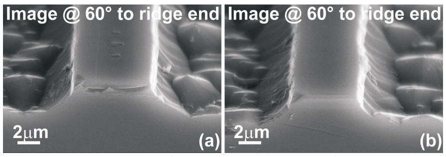

FIG. 3 SEM images of the polished end faces the ridges.

After edge polishing of the samples laser light (633 nm HeNe laser) was end-fire coupled into the ridge waveguides using a microscope objective lens in order to investigate the optical characteristics of the structures.

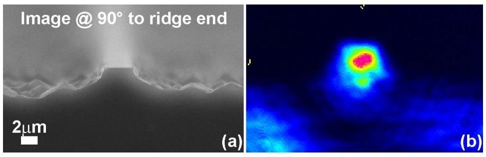

FIG. 4(a) SEM image of polished end-face of a ridge, (b) Near-field intensity profile obtained at 633 nm.

Fig. 5b shows the near-field intensity profile collected using a second objective lens to image the output of the ridge on to a CCD camera. This mode profile corresponds to a ridge structure formed using a UV laser scanning speed of 0.1 mm/s and an incident intensity of ~ 0.12 MW/cm^2.

Since the influence of EFP on the refractive index change pre-established by the UV writing process was unknown, it was prudent/intuitive/practical to study this effect before conclusively ascertaining/quantifying the competence of this fabrication process. In order to study this influence we used a method (described in Ref. 11) that permits for the simultaneous determination of refractive index profiles and mode indices from the measured near-field intensity profiles of optical waveguides. This computational method is useful for extracting the absolute refractive index values of any slowly varying graded index waveguide such as the UV written waveguides described in this paper. The method was used by the authors in Ref 11 for identifying the optimal writing conditions for such UV-written single-mode optical waveguides in LN. After the initial UV writing step (and before EFP), the samples were edge-polished and the near-field intensity profiles of each of the different waveguides that were inscribed on the sample were acquired using the experimental set-up described in Ref. 11. Employing the computational algorithm described in the same, the UV-laser induced maximum refractive index contrast for each of the waveguides was calculated. Following EFP of the samples, which is the next processing step for the fabrication of the ridge structures, the near-field intensity profiles of all the waveguides were recorded again and the maximum refractive index change was re-evaluated to investigate the impact of the EFP on the waveguide properties. Interestingly, we observed a significant refractive index change increase in the UV written optical waveguides following the poling-inhibition step. Fig. 6 shows the calculated maximum refractive index contrasts for a set of waveguides written at the same speed of 0.1 mm/s but different incident intensities, before and after poling.

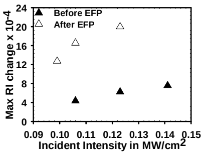

FIG 6. Variation of Max RI change before and after EFP.

For waveguides written with intensities higher than 0.106 MW/cm^2 the change in the maximum refractive index contrast was greater than three-fold. For a waveguides written with an intensity of 0.1 MW/cm^2, there was no measurable RI contrast prior to EFP, and hence were not able to support and optical mode before poling. However, for the same waveguides the maximum RI contrast that was induced due to EFP was of the order of those written with higher intensities. We are currently investigating the cause of this effect which greatly improves the waveguiding abilities of the UV written waveguides. We believe that domain boundaries of the inhibited domains resulting from EFP have the effect of enclosing the waveguiding region…

In conclusion we have presented our preliminary results on a novel method for fabrication of ridge waveguides in LN crystals. The method essentially utilizes a *single* UV-laser DW step to define the vertical confinement of the light in the waveguide and also assist the domain engineering process (poling-inhibition) which, after chemical etching, defines the ridge structures. Moreover, EFP in conjunction with UV DW was observed to improve significantly the propagation capabilities of the UV written waveguides and hence that of the fabricated ridge waveguide. The novel ridge waveguide fabrication method because of its ease of use and versatility should help facilitate the fabrication of compact integrated optical devices with the much desired small footprint.

This work was supported by the European research project 3D-DEMO STREP033297

[1] R. V. Schmidt and I. P. Kaminow, Appl. Phys. Lett. **25**, 458, (1974).

[2] J. L. Jackel, C. E. Rice, and J. J. Veselka, Appl. Phys. Lett. **41**, 607, (1982).

[3] I. P. Kaminow, Ramaswamy.V, R. V. Schmidt, and E. H. Turner, Appl. Phys. Lett. **24**, 622, (1974).

[4] R. S. Cheng, W. L. Chen, and W. S. Wang, IEEE Photonics Technol. Lett. **7**, 1282, (1995).

[5] H. Hu, R. Ricken, W. Sohler, and R. B. Wehrspohn, IEEE Photonics Technol. Lett. **19**, 417, (2007).

[6] A. Guarino, G. Poberaj, D. Rezzonico, R. Degl'Innocenti, and P. Gunter, Nat. Photonics **1**, 407, (2007).

[7] K. Noguchi, O. Mitomi, H. Miyazawa, and S. Seki, Journal of Lightwave Technology **13**, 1164, (1995).

[8] I. E. Barry, G. W. Ross, P. G. R. Smith, and R. W. Eason, Appl. Phys. Lett. **74**, 1487, (1999).

[9] M. Iwai, T. Yoshino, S. Yamaguchi, M. Imaeda, N. Pavel, I. Shoji, and T. Taira, Appl. Phys. Lett. **83**, 3659, (2003).

[10] S. Mailis, C. Riziotis, I. T. Wellington, P. G. R. Smith, C. B. E. Gawith, and R. W. Eason, Optics Letters **28**, 1433, (2003).

[11] P. Ganguly, C. L. Sones, Y. J. Ying, H. Steigerwald, K. Buse, E. Soergel, R. W. Eason, and S. Mailis, Journal of Lightwave Technology **27**, 3490, (2009).

[12] C. L. Sones, A. C. Muir, Y. J. Ying, S. Mailis, R. W. Eason, T. Jungk, A. Hoffmann, and E. Soergel, Appl. Phys. Lett. **92**, 3, (2008).

[13] C. L. Sones, S. Mailis, W. S. Brocklesby, R. W. Eason, and J. R. Owen, J. Mater. Chem. **12**, 295, (2002).

Determination of Refractive Indices From the Mode Profiles of UV-Written Channel Waveguides in LiNbO3-Crystals for Optimization of Writing Conditions

Pranabendu Ganguly, Collin Lawrence Sones, Yongjun Ying, Hendrik Steigerwald, Karsten Buse,
Elisabeth Soergel, Robert William Eason, and Sakellaris Mailis

***Abstract*—We report on a method for the simultaneous determination of refractive index profiles and mode indices from the measured near-field intensity profiles of optical waveguides. This method has been applied to UV-written single-mode optical waveguides in $\mathrm{LiNbO_3}$ for the optimization of the writing conditions. The results for the waveguides written with light of the wavelengths 275, 300.3, 302, and 305 nm for different writing powers and scan speeds reveal that for optimum writing conditions a maximum possible refractive index change of $\sim$0.0026 can be achieved at a value of 632.8 nm transmitting wavelength. The computation process used in the presented technique may also become useful to extract absolute refractive index values of any slowly varying graded index waveguide.**

***Index Terms*—$\mathrm{LiNbO_3}$, mode index, near-field mode profile, refractive index profile, single-mode channel waveguides, UV-written waveguides.**

I. INTRODUCTION

LITHIUM NIOBATE ($\mathrm{LiNbO_3}$) is a versatile optical material commonly used in photonics because of its high electro-optic, acousto-optic, and nonlinear-optic coefficients [1]. Metal ion indiffusion, proton exchange, and ion-implantation are the techniques most widely used to fabricate waveguides in $\mathrm{LiNbO_3}$, which are a basic building block in optical integrated circuits (OICs). UV-writing of optical waveguides [2], [3] is a recent addition to this list of fabrication processes for this substrate, and offers a direct writing facility that obviates many fabrication steps of the former techniques. Direct writing of single- and multi-mode graded-index channel waveguides in congruent $\mathrm{LiNbO_3}$ has been demonstrated using c.w. laser light at a writing wavelength of 244 nm. The process has been modeled as a laser-induced thermal diffusion of lithium ions which locally increases the extraordinary refractive index in $\mathrm{LiNbO_3}$ [4]. Since its inception, the UV directly written waveguide procedure has held considerable promise because of its single-step process which is well suited for complex micro-optical devices such as MOEMS, where lithography cannot be applied for waveguide fabrication [5].

The mode index and refractive index profiles along transverse and depth directions are important characteristics for all channel waveguides. For most applications, single-mode waveguides are essential in order to achieve optimized device performance, and this is ultimately defined in turn by the generated refractive index profiles. The mode index, i.e., the effective refractive index of the waveguide mode, and hence the propagation constant, is an important parameter of single-mode channel waveguides and is an essential input for design consideration for several basic components of OICs, such as directional couplers and Y-junctions. Accurate determination of refractive index profiles and mode indices, as a function of fabrication parameters, is therefore fundamental for characterizing waveguide optical properties.

Several methods [6]–[16] have been developed for the measurement of refractive index profiles of a channel waveguide. A widely used technique is profile reconstruction by measuring the mode indices through a prism coupler in conjunction with an evaluation using the WKB approximation [6], [7]. For a precise determination, this method requires a relatively large number of modes. So the measurement is usually carried out at a wavelength much shorter than the desired operating wavelength. Another precise technique has been proposed using reflectivity measurement of an angularly polished substrate [8]. Even though this measurement can be carried out at the operating wavelength, this technique is inherently destructive due to the necessary angular polishing process. Presby and Marcuse [9] have determined the refractive index profiles of single- and multi-mode silver-ion exchanged glass waveguides by measuring the reflection and transmission coefficients perpendicular to the waveguide surface. However, because of some surface damage induced from the UV-writing process

---

Manuscript received November 05, 2008; revised February 11, 2009. First published April 24, 2009; current version published July 24, 2009. This work was supported in part by the Engineering and Physical Sciences Research Council (EPSRC) under Grant EP/C515668, in part by the European Union under the 3-D Demo grant, and in part by the Deutsche Forschungsgemeinschaft under Grant BU913/18. The work of P. Ganguly was supported by a international fellowship (IIF-2007/R2) from the Royal Society.

P. Ganguly is with the Optoelectronics Research Center, University of Southampton, Southampton, SO17 1BJ, U.K., on leave from the Advanced Technology Development Center, Indian Institute of Technology Kharagpur 721 302, India (e-mail: pran@ece.iitkgp.ernet.in).

C. L. Sones, Y. Ying, R. W. Eason, and S. Mailis are with the Optoelectronics Research Center, University of Southampton, Southampton SO17 1BJ, U.K. (e-mail: cls@orc.soton.ac.uk; yoy@orc.soton.ac.uk; rwe@orc.soton.ac.uk; sm@orc.soton.ac.uk).

H. Steigerwald, K. Buse, and E. Soergel are with the Institute of Physics, University of Bonn, 53115 Bonn, Germany (e-mail: steigerwald@physik.uni-bonn.de; kbuse@uni-bonn.de; soergel@uni-bonn.de).

Digital Object Identifier 10.1109/JLT.2009.2015963

in $LiNbO_3$, this technique cannot be applied in the present context.

Another direct technique to deduce the index distribution from optical measurements is the transmitted-beam near-field method, which is based on the measurement of the transmitted beam intensity near the guide facet, from which electric field intensity and index distribution can then be calculated [10]. This methods advantage is that it is numerically simple; however, it is very sensitive to spatial frequency noise. Moreover, the Laplacian operator, involved in the computation process, amplifies this noise [11]. To reduce the noise a tailored low-pass filter in the spatial frequency domain, such as a third-order Butterworth filter [12] or a Gaussian filter [13], must be applied. Using this technique, however, the mode index, in general, cannot be determined. As the relative index variations are small, the mode index required for calculation is approximated by the substrate refractive index value, thus inducing an underestimation of the refractive index variation.

A more refined algorithm for the estimation of refractive index profiles has been developed by Caccavale *et al.* [14], based on the knowledge of the fabrication process of the waveguide from which a hypothesis on the analytical form of the index profile has been made. The electric field profile of the fundamental mode is then calculated by a finite-difference scheme, and compared to the measured field. The error between the computed and measured field profiles is minimized by adjusting the refractive index profile parameters. High-frequency noise is averaged out by this method, and no low-pass filters are needed, however the method is very computation intensive in terms of both elapsed time and memory required. Nikolaev and Shevchenko [15] have developed a semi-analytical technique for reconstruction of refractive index profiles from the measured near-field patterns. Though this method is applicable for single-mode graded-index waveguides, it requires the mode propagation constants measured: 1) at two different wavelengths within the single-mode operating regime and 2) at different external media, which is problematical. Recently, Liu *et al.* [16] have reconstructed the extraordinary refractive index profiles of single-mode planar waveguides fabricated by O^{2+} ion implantation into $LiNbO_3$ using a beam propagation method and image processing for the purpose. Once again, however, the process requires m-line spectroscopic data for the analysis.

In the present work, the mode indices and refractive index profiles are determined simultaneously from the measured near-field intensity profiles of UV-written single-mode waveguides in $LiNbO_3$ under different writing conditions. The process yields accurate values of refractive indices from the near-field profiles which have generally been underestimated in the previous works. The theoretical background is discussed in Section II, and the experimental details of the waveguide fabrication and mode profile measurement are given in Section III. The results for waveguides produced under different writing conditions are discussed in Section IV, from which it is shown that an optimal writing condition exists for these waveguides, where the refractive index change and mode index are maximized.

II. THEORETICAL

The nondestructive method to estimate the refractive index distribution in a waveguide from its mode field intensity profile employs an inversion of the scalar wave equation. This technique requires the waveguide to be weakly guiding in which only the fundamental mode of propagation is excited. It requires no previous knowledge of the shape of the refractive index distribution, and does not require the waveguide to have any kind of cross-sectional symmetry. To evaluate the index profile from the mode field distribution, it is assumed that the refractive index change is very small compared to the refractive index of the substrate. Under these assumptions, we obtain the scalar wave equation for the fundamental mode [10]

$$\nabla^2 A(x,z) + \left[k^2 n^2(x,z) - \beta^2\right] A(x,z) = 0 \tag{1}$$

where $A(x,z) = [I(x,z)]^{1/2}$ and $I(x,z)$ is the normalized modal intensity, $k = (2\pi/\lambda)$ and λ is the transmitting wavelength, $n(x,z)$ is the refractive index of the waveguide, and β is the propagation constant of the fundamental mode, x and z correspond to lateral and depth dimensions of the waveguide, the light propagates along the y-direction. Equation (1) leads to the following expression for the refractive index distribution:

$$n^2(x,z) = \left(\frac{\beta^2}{k^2} - \frac{1}{k^2}\frac{\nabla^2 A}{A}\right). \tag{2}$$

Hence, the UV-induced refractive index change, $\Delta n(x,z)$, of a single-mode waveguide may be expressed as

$$\Delta n(x,z) = \left(\frac{\beta^2}{k^2} - \frac{1}{k^2}\frac{\nabla^2 A}{A}\right)^{\frac{1}{2}} - n_s \tag{3}$$

where n_s is the substrate refractive index at the transmitting wavelength. Thus, $\Delta n(x,z)$ can be evaluated numerically from (3) using the lateral and normal near-field profiles of the single-mode UV-written waveguides. Note that the substitution $A(x,z) = [I(x,z)]^{1/2}$ assumes that there is no phase variation across the measured wavefield. This approximation is quite valid since the mode field intensity is measured at the waveguide endface where the phase variation is negligible.

The square root of the first term within the parenthesis of (3) is called the effective refractive index of the mode or mode index. In principle, the mode index can be derived using (3) from the measurement of the intensity away from the channel waveguide, where $\Delta n(x,z)$ tends to zero [10]. In practice, however, due to high-spatial-frequency noise (which is amplified by the Laplacian operator) on the tails of the mode where the mode field is very small, it is impossible to evaluate the mode index accurately from (3). Since the electric field is very small outside the waveguide, the second term inside the square root in (3) tends to diverge and introduce errors in the measurement. As the difference between the mode index and substrate refractive index is a small quantity, the mode index may be approximated by the substrate index in (3). This incorporates an error in the absolute values of the induced refractive index change [12]. In this paper, we have adjusted the mode index value by using an algorithm, so that the minimum value of refractive index change is zero outside the waveguide boundary. By this process, one can determine the accurate refractive index change and mode index of the single-mode waveguide simultaneously. A similar approach has been adopted previously by Chakraborty *et al.* [17] to compute accurate mode profiles from one-dimensional effective refractive index distributions of $\mathrm{Ti:LiNbO_3}$ waveguides and directional couplers by a matrix method.

To reduce noise effects in (3) we have fitted the measured near-field intensity profiles of the UV-written waveguides by Gaussian (lateral profiles) and Hermite–Gaussian (depth profiles) distributions before processing. Application of a local least-squares method to minimize noise in measured intensity profiles is a common practice [11], [18] and these curve fits are fairly accurate for the intensity profiles of the UV-written waveguides in $\mathrm{LiNbO_3}$. The requirement of validity of the scalar-wave equation, namely that the index changes slowly, holds for all $n(x,z)$ in these waveguides except at the air-substrate interface where the refractive index changes abruptly ($\Delta n/n_\mathrm{s} \sim 0.55$). To avoid this problem, we computed the depth refractive index profile starting from slightly below the surface where the maximum mode intensity has been measured.

III. EXPERIMENTAL

Direct writing on $\mathrm{LiNbO_3}$ was achieved using a Coherent Innova Sabre 25/7 argon ion laser that produced continuous output at 275, 300.3, 302, and 305 nm wavelengths with a maximum power of 200 mW. The ~5-mm-diameter laser beam was focused by a UV lens (focal length: 40 mm) onto the crystal surface to a diameter of approximately 4 μm at the focal point. Waveguides were written by scanning the sample via a computer-controlled 2-D translation stage, along the y-axis on both $+z$ and $-z$ faces of the crystal at different laser beam powers (35–60 mW) and different scan speeds (0.1–1.0 mm/s). The UV energy fluence used in our writing process varied from 0.7–12.0 kJ/cm^2. The congruent $\mathrm{LiNbO_3}$ crystals (Crystal Technology Inc.) used in our experiment were pre-conditioned by performing five poling cycles (one cycle being a forward and subsequent reverse domain inversion process) before the writing process. Due to the high optical absorption of $\mathrm{LiNbO_3}$ at ultraviolet wavelengths, and hence high local temperatures induced, Li out- and/or side-diffusion takes place which induces an increase in the extraordinary index of refraction [2]. Some of the waveguides in our experiments, written with higher fluence, have observable surface damage because of the localized high temperature causing melting/cracking in the UV-exposed area of the crystal.

When measuring the mode profiles of these waveguides, it is most important that the waveguide end-face is polished optically flat and that no defects in the substrate are present on or near the ends of the waveguides. Any defects can induce diffraction of the mode field signal and introduce artefacts in subsequent data processing. The samples examined here were carefully edge-polished using a Logitech polishing machine (PM2A) and a chemo-mechanical colloidal silica polishing suspension (with a pH ~ 10.5, and particle size of 0.03 μm), until no defects were visible under inspection with an optical microscope.

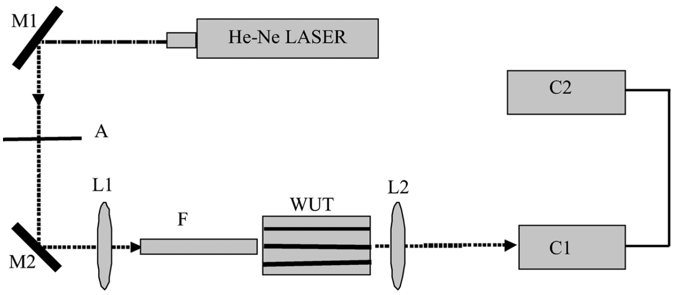

Fig. 1. Near-field intensity profile measurement setup (M1 & M2—Mirrors, A—Attenuator, L1—10× objective, L2—40× objective, F—Single mode fiber, WUT—Waveguide under test, C1—Camera, C2—Computer).

The mode field of the waveguides was measured using the standard near-field measurement setup shown in Fig. 1. The source used was a He–Ne laser (632.8 nm) at 1-mW power coupled via a 10× objective to a single-mode optical fiber, which was subsequently butt-coupled to one end of the UV-written waveguide. The length of the channels was ~14 mm. The substrate containing the waveguides was mounted on a high precision 4-axes translation stages in order to achieve the best possible coupling between the fiber and the waveguide. TM waveguide modes only could be excited in the UV written $\mathrm{LiNbO_3}$ waveguides suggesting an increment in the extraordinary refractive index only. The output of the waveguide was imaged onto a CCD camera by means of a 40× microscope objective (with a numerical aperture of 0.65). Image analysis was performed using a beam profiling software (Newport LBP, USB2). The resolution limit of the 40× objective is 0.8 μm, using Abbe's criterion for coherent light from an object [19]. Special care has been taken to image exactly the end-face and for perpendicular incidence of the optical beam on the camera, which otherwise would give rise to significant errors in measured mode profiles. Once the mode image of the waveguide was recorded, the normalized intensity profiles along horizontal (x-axis) and vertical directions (z-axis) were generated by the software. The magnification (~ ×300) of the mode image was measured by imaging a graticule, with a spacing period 10 μm, in place of the waveguide sample in the setup. All mode profile measurements in this work were performed within six months following the writing process of the waveguides.

IV. RESULTS AND DISCUSSION

A. *Refractive Index Profiles and Mode Index of the Waveguide*

To determine the refractive index profiles of the waveguide, (3) is solved numerically using [10], [12]

$$\frac{\nabla^2 A}{A} = \frac{A_{i-1,j} + A_{i+1,j} - 2A_{i,j}}{(\Delta x)^2 A_{i,j}} + \frac{A_{i,j-1} + A_{i,j+1} - 2A_{i,j}}{(\Delta z)^2 A_{i,j}} \tag{4}$$

where Δx and Δz are the horizontal and vertical spacing between the data points, i.e., the grid spacing resolution. Here i and j are the pixel numbers. A typical plot of the measured intensity profile at 632.8 nm wavelength along lateral (x-axis) direction is shown in Fig. 2. The raw data has been processed to generate the refractive index profile of the waveguide by assuming that the mode index is equal to the substrate index (which is equal to 2.202654 at 632.8-nm wavelength [20]). Obviously problems arise, because any calculation of a second derivative (4) is very sensitive to rapid intensity variations. Hence, a smooth profile

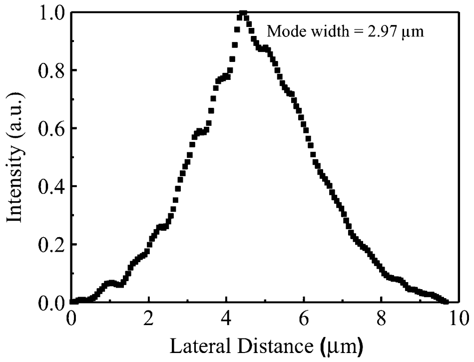

Fig. 2. Measured lateral intensity profile of a waveguide written with 305 nm at a writing power of 35 mW and a speed 0.1 mm/s.

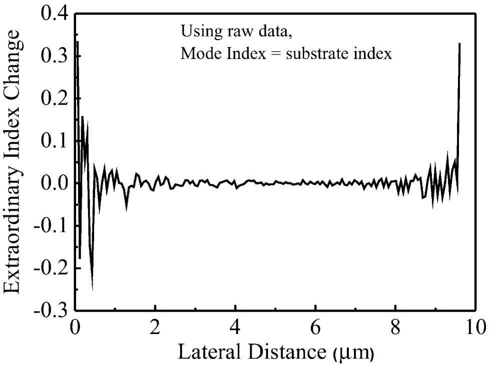

Fig. 3. Computed refractive index change from the raw data of the lateral mode profile of Fig. 2, assuming a mode index is equal to the substrate index.

is required for the calculations. Without any curve fitting, a determination of the refractive index seems to be impossible, as demonstrated in Fig. 3, which shows the index profile calculated from the intensity profile of Fig. 2 by referring to (3). In Fig. 3, the data for the change of the refractive index of the waveguide is submerged in the noise because of the random fluctuations of the modal intensity in the spatial domain. We therefore fitted the measured intensity profile with a Gaussian distribution and repeated the computation process thereby getting an index profile as shown in Fig. 4. It may be noticed from the figure that the refractive index changes become negative (-0.00123) at the two ends of the profile outside the waveguide boundary, where it should be nearly zero. This is the result of the assumption that the mode index is equal to the substrate index, which incorporates a large error in the absolute refractive index values of a weakly guiding waveguide where the refractive index change is a small quantity. We have therefore increased the mode index value in (3) to get the minimum refractive index change to be equal to zero ($\leq 10^{-6}$) outside the waveguide region. The reconstructed profile is shown in Fig. 5 with the mode index value 2.203894. By this process, we can simultaneously extract the values of refractive indices and mode index of the waveguide. The outline of the computation steps is as follows.

1) The measured near-field profile is fitted with a Gaussian distribution.
2) The result of the fit are used to compute the refractive index profile using (3) by taking the mode index equal to the substrate index.

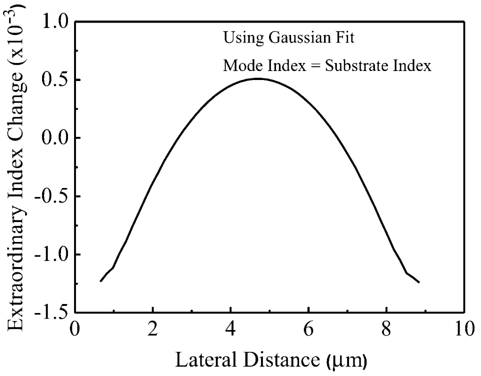

Fig. 4. Reconstructed refractive index profile of the waveguide using the fitted Gaussian distribution of the lateral mode profile of Fig. 2, taking mode index is equal to substrate index.

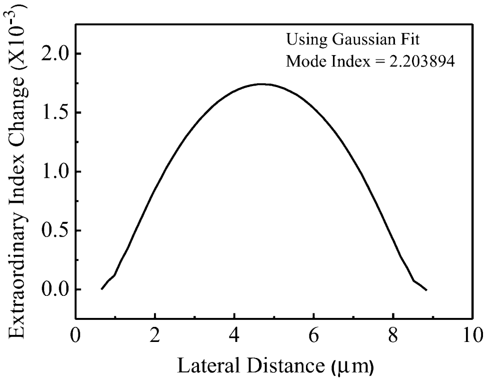

Fig. 5. Lateral refractive index profile of the waveguide with mode profile as in Fig. 2, for mode index $= 2.203894$.

3) Finally, the mode index value is increased to get the minimum refractive index change to be equal to zero outside the waveguide region.

It may be mentioned that the computed refractive index data diverges beyond the edges of the waveguide where the values of $\nabla^2 A$ tends to zero.

The same procedure is also followed for the reconstruction of depth (along the z-axis) refractive index profile (Fig. 6). In this case, the intensity profile is fitted with a Hermite–Gaussian function because of the asymmetry in the structure. Since at the air-LiNbO$_3$ interface the process incorporates an error because of the abrupt index change, the refractive index profile is computed starting from the peak intensity position of the measured mode intensity profile, which is 2.24 μm below the surface. The computed maximum refractive index changes and mode indices, for the same waveguide using lateral and depth intensity profiles, match within 2.3% and 0.0012%, respectively, which makes us confident about the computation process.

B. Refractive Index as a Function of Writing Power

Fig. 7 shows some of the computed results of maximum refractive index changes and mode indices extracted from the measured near-field intensity profiles of the UV-written single-mode waveguides for different writing powers at each of the writing wavelengths, 275, 302, and 305 nm. For all the data the writing speed was 1.0 mm/s. One may notice from these graphs that an optimum writing power exists for

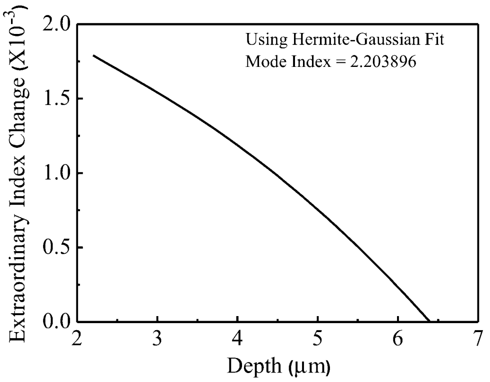

Fig. 6. Depth refractive index profile of the waveguide with writing conditions same as in Fig. 5.

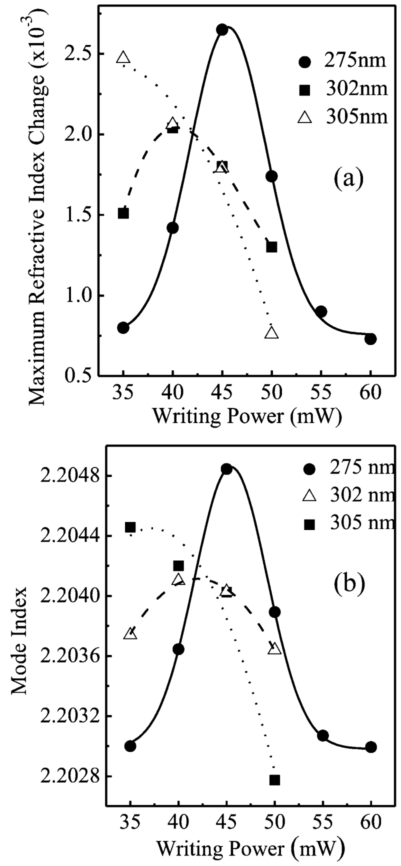

Fig. 7. (a) Computed maximum refractive index changes and (b) mode indices for waveguides with different writing powers and wavelengths.

each wavelength where the refractive index change and mode index are maximum. This is quite apparent for the two writing wavelengths of 275 and 302 nm, where the maxima occur at 45 and 41 mW, respectively. For 305 nm only part of the power dependence is observed in the investigated power range, where the indication of the maxima in refractive indices is estimated at ~35-mW writing power.

The main feature of the refractive index power dependence graphs (Fig. 7) is the existence of a useful writing power range, where an appreciable maximum refractive index change occurs. In the lower power limit of this range, the crystal is underexposed to the UV radiation, hence a smaller refractive index is observed. However, the fact that the refractive index change decreases in the higher power limit is counter-intuitive as the maximum refractive index change should continue to increase with increasing laser power and eventually saturate to a certain value. There must be therefore a mechanism to counter the refractive index change increase which is caused by the UV irradiation.

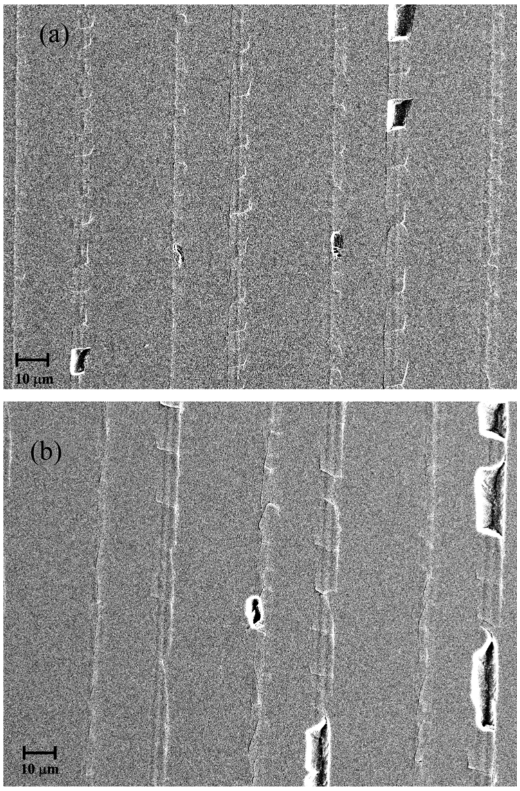

Fig. 8. SEM photo of surface damage of UV-written channel waveguides. (a) Written at writing wavelength 275 nm and power 55 mW. (b) Written at writing wavelength 305 nm and power 50 mW, (Magnification $= 600\times$).

A look at the surface topography of the UV-irradiated area provides a clue about the nature of this counter mechanism that causes a decrease of the measured refractive index change at the high power limit. Fig. 8 shows typical scanning electron microscopy (SEM) images of the UV irradiated crystal surface at the high power limit for two different wavelengths. These SEM images show extensive surface damage which is expected to induce a reduction of the maximum refractive index as measured in our method because this damage is more evident in the layers which are close to the surface where the refractive index should be maximum. As a result of the surface layer damage, the optical mode shifts further into the bulk (towards the undamaged volume), where however the refractive index change is smaller. The power dependence of the refractive index change which is shown in Fig. 7 is therefore the result of a tradeoff between underexposure (low power) and surface damage (high power).

UV laser-induced surface damage has been investigated elsewhere [21], which shows that it induces a permanent local stress on the micrometer-scale dimension, which may consequently decrease the local refractive index of $LiNbO_3$ to some extent [22]. Raman analysis of the exposed region also shows some loss of crystallinity of the material [23], indicating that while

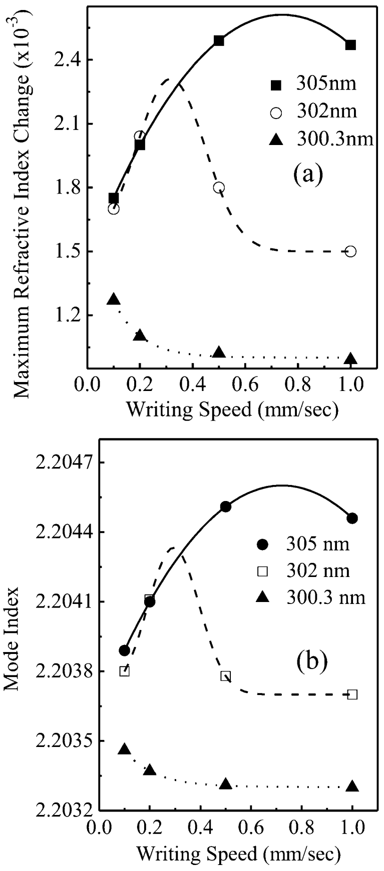

Fig. 9. (a) Computed maximum refractive index changes and (b) mode indices for waveguides with different writing speed and wavelength.

LiNbO$_3$ may suffer some change in chemical structure at the superficial surface layer, it remains largely unchanged in the bulk.

One additional issue concerns the use of longer wavelengths (300–305 nm) for waveguide writing. This wavelength range is close to the absorption edge of the crystal where the absorption length and hence the UV-heated volume, increases which consequently results in lower local temperatures as compared to shorter wavelengths, strongly absorbed, laser light. The reduction of the local temperature and the temperature gradient should influence the thermal diffusion of lithium ions which was held responsible for direct UV writing of waveguides at shorter wavelengths (244 nm) [4] resulting at lower maximum refractive index changes. It is observed however that the maximum refractive index value which is measured in waveguides written at both short and long UV wavelengths does not change significantly. As the absorption length at wavelengths around 300 nm is several μm it is likely that the direct photorefractive effect might be also contributing to the formation of optical channel waveguides at long wavelength writing. At shorter wavelengths (244 nm, 275 nm) however, temperature gradient-induced diffusion of lithium [4] should still remain the dominant mechanism.

C. *Refractive Indices for Different Writing Speeds*

Fig. 9 shows the variation of maximum refractive index changes and mode indices for different writing speeds at the writing wavelengths 300.3, 302, and 305 nm. The data points are fitted with Gaussian curves. In all cases the writing power was 35 mW. Once again an optimal writing speed exists for inducing a maximum refractive index change, which is approximately 0.75 and 0.3 mm/s for 305 and 302 nm wavelengths, respectively. At 300.3 nm, only a part of the distributions has been determined. Both the variations of maximum refractive index change and of mode index with writing speed follow the same trend.

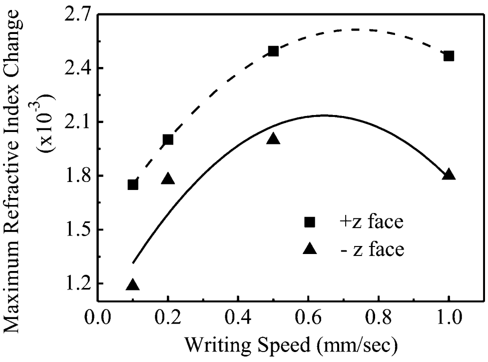

Fig. 10. Maximum refractive index change versus scan speed for $+z$ and $-z$ faces of LiNbO$_3$ (writing power $=$ 35 mW, and writing wavelength $=$ 305 nm).

From all the refractive index data, it seems that the maximum refractive index change for any writing condition is limited by the surface damage along the waveguide, and its maximum possible value is about 0.0026 at the guiding wavelength of 632.8 nm. This corresponds to a mode index value of ~2.2048. It is not possible to increase the UV-induced refractive index change indefinitely by increasing the laser fluence and/or decreasing the writing wavelength (due to the extremely rapid onset of absorption increase [24]).

We have also determined the refractive index of a waveguide written at 244 nm with power 45 mW and speed 0.83 mm/s. This waveguide was written almost two years ago. The computed maximum refractive index change and mode index for this waveguide are about 0.001297 and 2.203551, respectively.

D. *Effects of Crystal Orientation*

The optical properties of the UV-written waveguides in LiNbO$_3$ also depend on the crystal orientation. All data provided prior to this section are for $+z$ face of the crystal. Waveguides can also be produced by UV-writing on the $-z$ face of LiNbO$_3$, but in our experiments we found that for these waveguides the maximum index changes are lower than those for waveguides written on the $+z$ face. Fig. 10 shows a comparison of the maximum refractive index change induced at different scan speeds for the two z-faces of congruent LiNbO$_3$. The writing power was 35 mW, and the writing wavelength was 305 nm.

V. CONCLUSION

The simultaneous determination of refractive index change and mode index of UV-written waveguides in LiNbO$_3$ from the measured near-field intensity distribution is reported. Waveguides are written with UV-wavelengths of 275, 300.3, 302, and 305 nm for various powers and scan speeds. To avoid high-spatial-frequency noise we have fitted the lateral mode profiles with Gaussian distributions, and the depth profile with Hermite–Gaussian distributions before further processing. For accurate determination of absolute refractive index values, the mode index is adjusted to equate the minimal refractive index change outside the waveguide region to zero. Although a decrease of the refractive index from its substrate value at the waveguide edges has been predicted because of thermal inter-diffusion of Li-ions within the crystal [3], it is relatively small (∼2%), and can be neglected compared to the maximum refractive index change of the waveguide. The variation of maximum refractive index changes and mode indices of these waveguides with different writing conditions (laser power, speed, wavelength, and crystal face) have been studied. These indicate that for optimum writing conditions a maximum possible refractive index change of ∼0.0026 can be achieved at 632.8-nm probe wavelength. The process may also be useful to determine absolute refractive index values as well as mode indices of other graded-index waveguides such as Ti-indiffused and annealed proton exchanged lithium niobate.

REFERENCES

[1] R. S. Weis and T. K. Gaylord, "Lithium niobate: Summary of physical properties and crystal structure," *Appl. Phys. A*, vol. 37, pp. 191–203, 1985.

[2] S. Mailis, C. Riziotis, I. T. Wellington, P. G. R. Smith, C. B. E. Gawith, and R. W. Eason, "Direct ultraviolet writing of channel waveguides in congruent lithium niobate single crystals," *Opt. Lett*, vol. 28, pp. 1433–1435, 2003.

[3] K. Gallo, C. B. E. Gawith, I. T. Wellington, S. Mailis, R. W. Eason, P. G. R. Smith, and D. J. Richardson, "Ultraviolet writing of channel waveguides in proton-exchanged $LiNbO_3$," *J. Appl. Phys.*, vol. 101, p. 014110, 2007.

[4] A. C. Muir, G. J. Daniell, C. P. Please, I. T. Wellington, S. Mailis, and R. W. Eason, "Modelling the formation of optical waveguides produced in $LiNbO_3$ by laser induced thermal diffusion of lithium ions," *Appl. Phys. A*, vol. 83, pp. 389–396, 2006.

[5] C. L. Sones, S. Mailis, V. Apostolopoulos, I. E. Barry, C. B. E. Gawith, P. G. R. Smith, and R. W. Eason, "Fabrication of piezoelectric micro-cantilevers in domain engineered $LiNbO_3$ single crystals," *J. Micromech. Microeng.*, vol. 12, pp. 53–57, 2002.

[6] J. M. White and P. F. Heidrich, "Optical waveguide refractive index profiles determined from measurement of mode indices: A simple analysis," *Appl. Opt.*, vol. 15, pp. 151–155, 1976.

[7] J. Noda, M. Minakata, S. Saito, and N. Uchida, "Precise determination of refractive index and thickness in the Ti-diffused $LiNbO_3$ waveguide," *J. Opt. Soc. Amer.*, vol. 68, pp. 1690–1693, 1978.

[8] J. Heibei and E. Voges, "Index profiles of planar optical waveguides determined from the angular dependence of reflectivity," *IEEE J. Quantum Electron.*, vol. QE-14, pp. 501–506, 1978.

[9] H. M. Presby and D. Marcuse, "Direct index measurements of diffused channel waveguides," *IEEE J. Quantum Electron.*, vol. QE-16, no. 6, pp. 634–640, Jun. 1980.

[10] L. McCaughan and E. E. Bergman, "Index distribution of optical waveguides from their mode profile," *J. Lightw. Technol.*, vol. 1, no. 1, pp. 241–244, Mar. 1983.

[11] J. Helms, J. Schmidtchen, B. Schupper, and K. Petermann, "Error analysis for refractive-index profile determination from near-field measurement," *J. Lightw. Technol.*, vol. 8, no. 5, pp. 625–633, May 1990.

[12] I. Mansour and F. Caccavale, "An improved procedure to calculate the refractive index profile from the measured near-field intensity," *J. Lightw. Technol.*, vol. 14, no. 3, pp. 423–428, Mar. 1996.

[13] D. Brooks and S. Ruschin, "Improved near-field method for refractive index measurement of optical waveguides," *IEEE Photon. Technol. Lett.*, vol. 8, no. 2, pp. 254–256, Feb. 1996.

[14] F. Caccavale, F. Segato, I. Mansour, and M. Gianesin, "A finite difference method for the reconstruction of refractive index profiles from near-field measurements," *J. Lightw. Technol.*, vol. 16, no. 6, pp. 1348–1353, Jul. 1998.

[15] N. Nikolaev and V. V. Shevchenko, "Inverse method for the reconstruction of refractive index profile and power management in graded index optical waveguides," *Opt. Quantum Electron.*, vol. 39, pp. 891–902, 2007.

[16] X. Liu, F. Lu, F. Chen, Y. Tan, R. Zhang, H. Liu, L. Wang, and L. Wang, "Reconstruction of extraordinary refractive index profiles of optical planar waveguides with single or double modes fabricated by O^{2+} ion implantation into lithium niobate," *Opt. Commun.*, vol. 281, pp. 1529–1533, 2008.

[17] R. Chakraborty, P. Ganguly, J. C. Biswas, and S. K. Lahiri, "Modal profiles in Ti : $LiNbO_3$ two-waveguide and three-waveguide couplers by effective-index-based matrix method," *Opt. Commun.*, vol. 187, pp. 155–163, 2001.

[18] I. Fatadin, D. Ives, and M. Wicks, "Accurate magnified near-field measurement of optical waveguides using a calibrated CCD camera," *J. Lightw. Technol.*, vol. 12, no. 12, pp. 5067–5074, Dec. 2006.

[19] M. Born and E. Wolf, *Principles of Optics*, 6th ed. New York: Pergamon, 1980.

[20] D. S. Smith and H. D. Riccius, "Refractive indices of lithium niobate," *Opt. Commun.*, vol. 17, pp. 332–335, 1976.

[21] A. Rodenas, D. Jaque, C. Molpeceres, S. Lauzurica, J. L. Ocana, G. A. Torchia, and F. Agullo-Rueda, "Ultra-violet nanosecond laser-assisted micro-modifications in lithium niobate monitored by Nd^{3+} luminescence," *Appl. Phys. A*, vol. 87, pp. 87–90, 2007.

[22] D. C. Deshpande, A. P. Malshe, E. A. Stach, V. Radmilovic, D. Alexander, D. Doerr, and D. Hirt, "Investigation of femtosecond laser assisted nano and microscale modifications in lithium niobate," *J. Appl. Phys.*, vol. 97, 2005, 074316.

[23] J. Burghoff, C. Grebing, S. Nolte, and A. Tünnermann, "Waveguides in lithium niobate fabricated by focused ultrashort laser pulses," *Appl. Surf. Sci.*, vol. 253, pp. 7899–7902, 2007.

[24] D. Redfield and W. J. Burke, "Optical absorption edge of $LiNbO_3$," *J. Appl. Phys.*, vol. 45, pp. 4566–4571, 1974.

Pranabendu Ganguly was born in Kolkata, India, on October 25, 1968. He graduated in physics (hons.) from Scottish Church College, Calcutta University, West Bengal, India, in 1990 and received the M.Sc. (Tech.) degree in optics and optoelectronics from the Department of Applied Physics, Calcutta University, in 1993.

He has joined the same Department as a Research Fellow in November 1993 and worked on Fourier optics. In June 1994, he joined the Indian Institute of Technology, Kharagpur, as a Project Engineer and conducted research on integrated optics. His doctoral work deals with design, fabrication, and characterization of titanium indiffused lithium niobate waveguides and directional coupler devices. In 2001, he joined the Advanced Technology Development Center, Indian Institute of Technology, Kharagpur, as a Scientific Officer, where he is currently working as a Senior Scientific Officer. Apart from integrated optics, his research interest also includes fiber nonlinear optics, optical metrology, MEMS/MOEMS, and microelectronics.

Dr. Ganguly is a life member of the Optical Society of India and is a recipient of Royal Society Incoming Fellowship to the U.K. in 2008–2009.

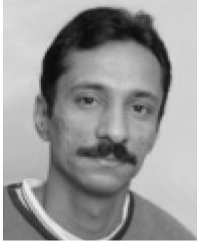

Collin Lawrence Sones was born in Valsad, India, on the May 1, 1968. He received the B.Sc. degree in physics from B. K. M Science College, South Gujarat University, Surat, India, in 1989, the M.Sc. degree from the Department of Physics, South Gujarat University, in 1991, and the Ph.D. degree from the Optoelectronics Research Center (ORC), University of Southampton, Southampton, U.K., in 2003.

He joined the Department of Physics, J. P. Arts and Science College, Bharuch, India, as a Lecturer in 1991. After the Ph.D. degree, he joined the ORC, University of Southampton, as a Research Fellow, where he is currently employed as a Senior Research Fellow. At the ORC, his research has been focused at developing effective techniques for micro domain engineering of nonlinear ferroelectric materials for the applications in fields as different as microelectromechanical systems and guided-wave integrated optical devices.

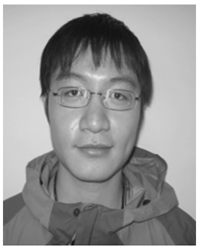

Yongjun Ying received the B.Sc. (hons.) degree in applied physics from City University of Hong Kong in 2007. He is currently pursuing the Ph.D. degree in the Optoelectronics Research Center, Southampton University, Southampton, U.K.

His research interests include lithium niobate domain engineering, waveguides, and microstructures.

Mr. Ying is a member of the OSA.

Hendrik Steigerwald was born in Germany in 1980. He studied physics at the University of Marburg, Marburg, Germany, and at the University of Bonn, Bonn Germany, where he obtained his final degree in 2007. He is currently working toward the Ph.D. degree in ferroelectric domains in photorefractive crystals in the group of K. Buse at the Physics Department, University of Bonn.

Karsten Buse received the Ph.D. (with honors) in physics from the University of Osnabrück, Osnabrück, Germany.

He was a Postdoctoral Member of the Scientific Staff of the University of Osnabrück and Guest Scientist in the group of Prof. Frejlich in the Laboratório de Óptica, University of Campinas, Brasil as well as in the group of Prof. Psaltis at the California Institute of Technology, Pasadena, CA. He is currently a Full Professor of physics at the University of Bonn, Bonn, Germany, (Heinrich Hertz Chair of the Deutsche Telekom AG) as well as the Director of the Institute of Physics at the University of Bonn. In 2000, he founded together with colleagues the company ONDAX (Los Angeles/Monrovia, CA) commercializing volume holographic optical filters. He is also a consultant of the Deutsche Telekom AG. He is Co-Editor of the journal *Applied Physics—Lasers and Optics* (Springer). He has published more than 200 refereed articles in scientific journals and contributed to more than 30 patents. His research is in the area of nonlinear optics and optical materials.

Prof. Buse has received the 1994 Ph.D. Award for Natural Sciences of the University of Osnabrück, the 1995 Rudolf Kaiser Award, the 1998 NASA Technical Briefs Award, and the 2001 Karl Heinz Beckurts Award.

Elisabeth Soergel received the Ph.D. degree in physics from the Ludwig-Maximilians University, Munich, Germany, in 1999 on the investigation of photorefractive crystals with scanning force microscopy.

Subsequently, she was as a Postdoctoral Researcher at the IBM Research Laboratories, Rüschlikon, Zurich, Switzerland, investigating the possibilities for storage devices based on scanning tunnelling microscopy. Since 2001, she has been with the University of Bonn, Bonn, Germany, working on the subject of visualization of ferroelectric domains with piezoresponse force microscopy.

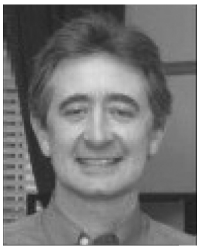

Robert William Eason is a Professor of Optoelectronics in the Optoelectronics Research Center (ORC), University of Southampton, Southampton, U.K. His research over the past 30 years had involved laser plasmas, photorefraction, pulsed-laser deposition, optical waveguide techniques, lithium niobate and microstructuring, holographic laser resonators, optical material growth, and applications of ultrashort pulse laser interactions. He is Deputy Head of School (Operations) for the ORC, and sits on the Graduate School Board and School Management Board. He has been an investigator on 20 U.K. Engineering and Physical Sciences Research Council research grants over the past 25 years, and publishes extensively in international journals, with a total of more than 350 journal and conference papers to date. He is also a keen advocate of the public understanding of science, and is a lifetime member of the Millennium Awards Fellowship sponsored by the Royal Society and the Millennium Commission.

Sakellaris Mailis received the Ph.D. degree from the University of Crete—Foundation for Research and Technology Hellas (FORTH), Crete, Greece, in 1996.

He is a Principal Research Fellow at the Optoelectronics Research Center(ORC), University of Southampton, Southampton, U.K. He was a Postdoctoral Research Fellow at FORTH until 1997 investigating photosensitivity of semiconducting oxides and laser micro-printing schemes for the fabrication of computer generated diffractive structures. Since January 1998, he has been with the ORC. His current research interests involve laser-assisted ferroelectric domain engineering and microstructuring of lithium niobate.

Appl Phys A
DOI 10.1007/s00339-010-5827-5

Applied Physics A
Materials Science & Processing

Laser-induced-forward-transfer: a rapid prototyping tool for fabrication of photonic devices

**C.L. Sones · K.S. Kaur · P. Ganguly · D.P. Banks ·
Y.J. Ying · R.W. Eason · S. Mailis**

Received: 4 November 2009 / Accepted: 10 May 2010

Abstract We propose a rapid prototyping method for the fabrication of optical waveguides based on the direct laser-printing method of ultrafast Laser-Induced Forward Transfer (LIFT) followed by further processing. The method was implemented for the fabrication of titanium in-diffused lithium niobate channel waveguides and X-couplers by LIFT-depositing titanium metal followed by diffusion. Propagation loss as low as 0.8 dB/cm was measured in preliminary experiments.

1 Introduction

A popular method for the fabrication of optical waveguide circuits in materials such as lithium niobate (LN) is by spatially selective deposition of titanium metal followed by thermal diffusion. This fabrication method is ideally compatible with current wafer-scale parallel techniques used by the microelectronics industry, such as photolithographic patterning and lift-off, which is of course excellent for mass production of devices.

However, these parallel techniques are somewhat inflexible in the device development stage where a fast production turnover of fundamentally different devices is required for conceptual testing. This creates a niche for simple prototyping production methods which are flexible enough to allow for rapid fabrication of good quality devices, particularly at the experimental one-off level.

LIFT is a rapid prototyping method which was first proposed by Bohandy et al. [1] and has since been utilized for the deposition of a variety of metals, semiconductors, superconductors, dielectrics, and biomaterials on a wide range of substrates [2–5]. The simple, non-stringent laboratory-environment based operational conditions for LIFT together with its single-step pattern-definition and material-transfer ability offer some significant experimental advantages inherently available by its usage. Additionally, this approach has some unique capabilities such as patterning of non-planar substrates [6], 3-d printing or stacking of dissimilar materials [7], and even the possibility of transfer of single-crystal materials with desired orientations. However, the pulsed nature and the quality of LIFT deposition are inhibiting factors for the direct deposition of superior quality waveguide layers.

In this paper, we propose the use of LIFT for the spatially selective deposition of materials onto optical substrates which can produce optical waveguides by further processing, e.g. thermal diffusion. Such a method will combine the flexibility of direct waveguide writing methods, which are suitable for rapid prototyping, with the large refractive index, longevity, and low propagation loss which is associated with conventional waveguide fabrication methods such as metal diffusion.

The use of a pulsed deposition method such as LIFT allows for further control over the optical waveguide structure by enabling the fabrication of higher refractive index segments the spatial distribution of which determines the average refractive index along the optical waveguide. By varying the spatial distribution of the segments (i.e. the separa-

---

C.L. Sones · K.S. Kaur · D.P. Banks · Y.J. Ying · R.W. Eason ·
S. Mailis (✉)
Optoelectronics Research Centre, University of Southampton,
Southampton, SO17 1BJ, UK
e-mail: sm@orc.soton.ac.uk
Fax: +44-23-80593141

P. Ganguly
Advanced Technology Development Centre, Indian Institute of
Technology, Kharagpur, 721302, India

tion between adjacent segments), it is possible to change the average refractive index along the optical waveguide. The impact of the segmentation on the waveguide propagation is demonstrated in some of the experimental results which are presented here.

Other advantages of this method include the ability to deposit more than one material or composite materials during a single deposition session and also the deposition of diffusion sources on non-planar (for example already microstructured) surfaces for the fabrication of rib waveguides which is challenging for conventional photolithographic methods.

Herein, we present our preliminary, proof-of-principle, results which demonstrate the feasibility of using a LIFT based material printing methodology in conjunction with high temperature post-processing for rapid prototyping of Ti-indiffused waveguides in LN [8, 9]. LN has a distinctive combination of inherent physical properties and is used in a diverse range of applications [10] and has consequently been the work-horse of the optoelectronics industry for switching applications and nonlinear frequency generation.

2 Experiments and results

The first step for the fabrication of channel optical waveguides in LN requires the spatially selective deposition of titanium metal onto LN substrates using ultrafast LIFT. The carrier-donor-substrate complex rests on a set of 2D translation stage and can be scanned with respect to the focussed or de-magnified incident beam. As illustrated in the schematic shown in Fig. 1, the transfer of the donor material (in this case Ti) onto the substrate, referred to as the receiver, is achieved on a pixel-by-pixel basis by scanning the donor-receiver assembly in front of a focussed pulsed laser source, resulting in a dot-matrix-like printing of individual donor-material pixels that are detached from the carrier and printed on the receiver. In the case for Ti printing here, melting of the donor occurs and a molten droplet is ejected onto the receiver. The dimension of the deposited droplet is similar to the dimensions of the incident laser spot. The melting and super-heating of the metal vapour trapped between the carrier and the donor film provides the required driving force to forward transfer the rest of the donor material, within the interaction volume, onto the receiver substrate. The laser system used to transfer the Ti-metal deposits was a fs laser operating at 800 nm, with a pulse duration of 130 fs and a repetition rate that could be tuned from single shot to 1 kHz. It is however, the high repetition rate of this laser source rather than the pulse width that made it suitable for the demonstration of this rapid prototyping method. The titanium donor film with a thickness of ∼150 nm had been previously deposited onto a transparent (borosilicate glass) carrier substrate via e-beam evaporation.

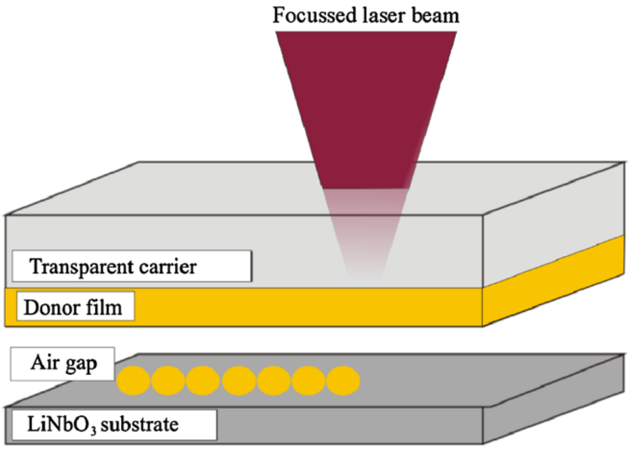

Fig. 1 Schematic of the LIFT deposition process. The carrier-donor-substrate complex rests on a set of 2D translation stage and can be scanned with respect to the focussed or de-magnified incident beam

Ti-metal line patterns were printed on the $-z$ faces of congruent undoped z-cut LN samples along the crystallographic y-directions. Several linear arrays of Ti metal pixels were deposited using different conditions for the intensity (or fluence) of the incident laser pulse and the separation between the centre of adjacent pixels which could be controlled by adjusting either the laser repetition rate or the scan speed. The separation of the centres of adjacent pixels varied from 5 μm (overlapping) to 20 μm (completely separated) while the laser fluence at the carrier/donor interface was in the range of 0.4–1.2 $\mathrm{J/cm^2}$.

The deposited metal pixels were approximately circular in shape and had a diameter of ∼10–15 μm. The holes which were created by missing metal on the carrier substrate (which correspond to the illuminating spot size) matched the size of the deposited metal dots as expected for deposits of this size. The distance between the donor-carrier composite and the receiver was maintained at less than 1 μm.

These variations of the writing parameters were aimed at identifying the optimum conditions for LIFT of Ti-metal onto the LN substrates under the reasonable assumption that there is a direct relationship between the metal deposition characteristics and the final optical waveguide mode profiles following the in-diffusion step. The metal line-patterns were successively in-diffused into the LN substrates by heating the LN substrates to a temperature of 1050°C in an O_2 environment for 10 hours.

A typical example of the deposited linear arrays of titanium pixels is shown in the optical microscope image of Fig. 2(a). The separation of the adjacent metal deposits in Fig. 2(a) has been varied from a slight overlap (top line) to complete separation (bottom line) by changing the scanning speed. The same area of the sample after the diffusion process is shown in the optical microscope image of

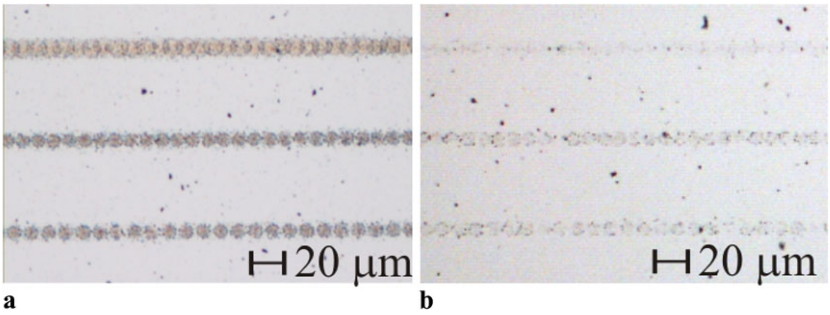

Fig. 2 (**a**) Optical microscope image of linear pixelated titanium LIFT-deposits at different separations. (**b**) The same surface of the sample after diffusion has taken place

Fig. 2(b). The outline of the deposited metal is still visible after diffusion due to the presence of TiO_2 residue on the surface of the sample. Note that the TiO_2 residue is not the same for all deposited lines. The top line showed significantly less residue possibly because the overlap between adjacent deposited metal pixels resulted in a partial re-ablation process for each subsequent laser pulse which removed metal from the sample surface thus reducing the available diffusion source.

The in-diffused LN substrates were subsequently edge-polished perpendicular to the titanium lines to enable characterization of the optical waveguides produced. For this purpose, laser radiation was coupled through one of the end-polished edges using a microscope objective into the waveguides and the near-field mode profile was monitored by imaging the opposite polished end of the waveguide onto a CCD camera.

The main feature of the optical waveguides which were fabricated by LIFT deposition is that the refractive index change along the length of the waveguide is not regular and continuous: there is a local refractive index increase within the volume where titanium metal has been diffused. Hence, the refractive index profile along the channel waveguide should reflect, to some extent, the titanium deposition pattern.

The separation of the adjacent pixels or segments should in principle define the average refractive index value along the waveguide. Hence, different separations should result in different waveguide confinement characteristics, and thereby different mode sizes. This was verified by the optical mode profile characterization results. The mode profiles for two distinct waveguides which correspond to different separation of the titanium segments are shown in Fig. 3. Both waveguides were single moded at the probe wavelength of 1.532 µm however, as shown in Fig. 3, the mode size of the waveguides varies significantly.

These waveguides were fabricated by scanning the sample at rates of 9 mm/sec and 19 mm/sec which corresponds to segment separation of 9 µm (and hence a slight overlap) and 19 µm (full separation), respectively (the laser repetition rate was 1 kHz in this experiment). Hence, the average refractive index change for the more closely spaced depositions, results in tighter confinement as observed in the mode profile shown in Fig. 3(a) while the less dense deposition results in a much larger waveguide mode profile shown in Fig. 3(b). In the case of waveguides with a partial overlap between successively deposited adjacent segments, any possible re-ablation of the deposited Ti-metal segments would reduce the total amount of the deposited metal in the overlapping area. However, our experimental results suggest that, for the range of overlaps used, it is the segment separation that predominantly determines the mode profile of the resulting waveguide, hence if any re-ablation does occur, it has negligible effect on the guiding conditions.

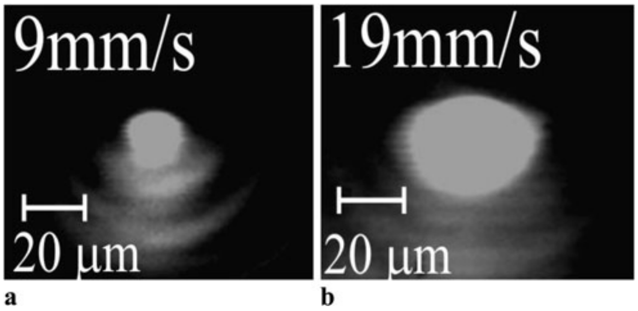

Fig. 3 Near-field waveguide mode profiles (at 1.532 µm) of LIFT/diffused segmented Ti:LN waveguides corresponding to different segment separation; (**a**) overlapped segments, (**b**) separated segments

It was mentioned in the previous paragraph that there should be some correlation between the refractive index profile along the channel waveguide and the titanium deposition pattern. In reality, the diffusion process will distribute titanium over an area which is (for Ti in LN) roughly 10% larger than the deposited pixel area and this process will smooth out any sharp features contained in the original deposited metal spot. As a result, the diffused profile will be much smoother than the deposited pattern which is beneficial to the waveguide performance because the elimination of sharp features is expected to keep the scattering losses of the waveguides at low level.

The optical loss of the waveguides was estimated by two different methods which were (i) cut-back and (ii) Fabry–Perot. Cut-back [11], which involves repetitive measurement of throughput for progressively shorter channel lengths, is clearly a destructive, time consuming method,

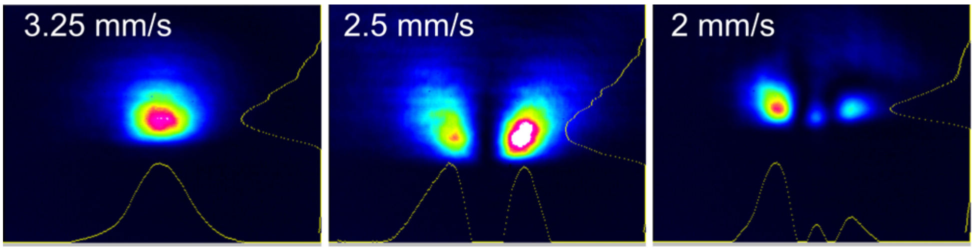

Fig. 4 Near-field mode profiles (at 633 nm) of three different waveguides fabricated with different segment separation by changing the deposition scanning speed as indicated in the figure

and is therefore of limited utility for measurement of waveguide loss. The second method relies on the formation of a low finesse Fabry–Perot cavity between opposite end faces of the waveguide. The contrast of the fringes of this optical cavity gives an estimate of the upper limit of the optical loss [12].

Both methods confirmed that large segment separations resulted in increased optical loss mainly due to poor confinement of the light inside the waveguide. The lowest propagation loss of ~0.8 dB/cm (for TM modes in the telecommunication wavelength range) was measured for waveguides written with a segment separation of 11 μm. For waveguides having larger segment separations of ≥13 μm, the measured loss was much higher (~7 dB/cm) due to optical leakage of the guided wave to the substrate. However, even for these preliminary attempts, with deposition quality being far from optimal, a loss measurement as low as ~0.8 dB/cm measured for some of the waveguides is very encouraging, further confirming the potential of this method for rapid prototyping of good quality optical waveguide devices. Typical loss values reported in literature for Ti-indiffused waveguides are of order ~0.1 dB/cm.

In order to evaluate the effective refractive index as a function of the fabrication conditions, it is necessary to fabricate single mode waveguides with different mode sizes. By monitoring the waveguide mode profile, it is possible to calculate the mode index of the waveguide [13]. We chose to fabricate the waveguides to be single moded at the wavelength of 633 nm in order to benefit from the measuring accuracy of our optical beam profiler (which has a silicon detector that is not sensitive to telecom wavelengths). The titanium donor layer used for the LIFT depositions was 150 nm thick, the laser repetition rate was 250 Hz and the laser fluence was in the range of 0.4 to 0.8 J/cm^2 while the segment separation varied between 8 μm and 16 μm.

Once again by varying the writing speed, it was possible to control the waveguide mode profile. Figure 4 shows three different mode profiles which correspond to different segment separation as a result of different scanning speeds during deposition. As can be seen in Fig. 4, the mode changed from single to higher order by just changing the scanning speed from 3.25 mm/sec to 2 mm/sec, which corresponds to segment separations of 13 μm and 8 μm, respectively (at 250 Hz laser repetition rate). This result reiterates the versatility of LIFT in the creation of waveguides with predesigned modal profiles.

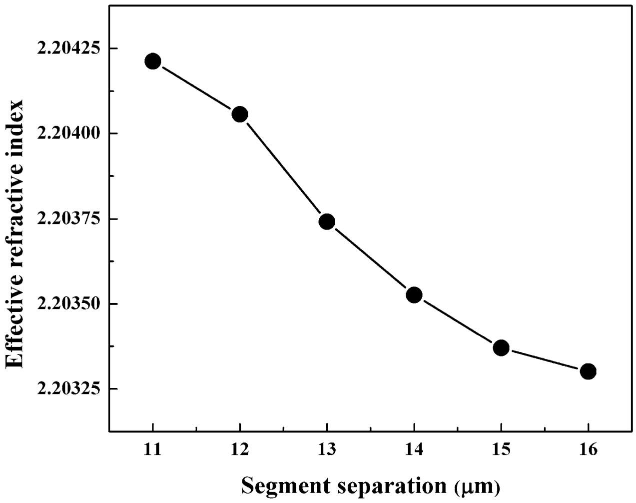

Fig. 5 Calculated effective refractive indices of single mode waveguides as a function of segment separation. These effective indices correspond to TM modes

The intensity profiles of the single mode waveguides (at 633 nm) which were fabricated using the conditions described in the previous section were used for the calculation of the effective mode profiles of the corresponding waveguides using the method which is described in [13]. A plot of the calculated effective mode indices (for TM modes) as a function of the segment separation is shown in Fig. 5. For segment separations longer than 16 μm, there was no confinement of light (cut-off) while for separation less than 11 μm the waveguides become multi-moded.

However, it seems that there is a good scope for manipulation of the effective mode index within the segment separation range that corresponds to single mode waveguides as shown in Fig. 5.

As expected the effective mode index decreases with increasing segment separation, as the average refractive index along the waveguide decreases, until cut-off is reached for a separation of 16 μm.

One of the advantages of using a method such as the one described here is the possibility of changing the waveguide propagation characteristics along the length of the waveguide by simply manipulating the segment separation along the length. However, with our current setup, it

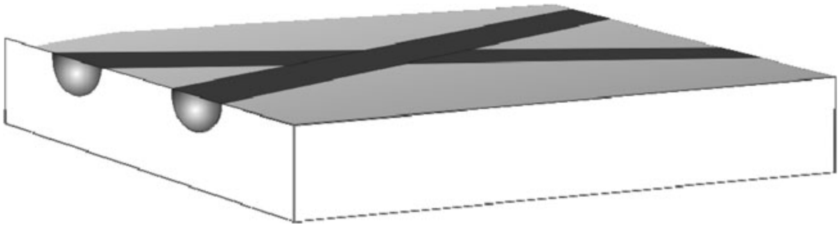

Fig. 6 Schematic of an X-coupler

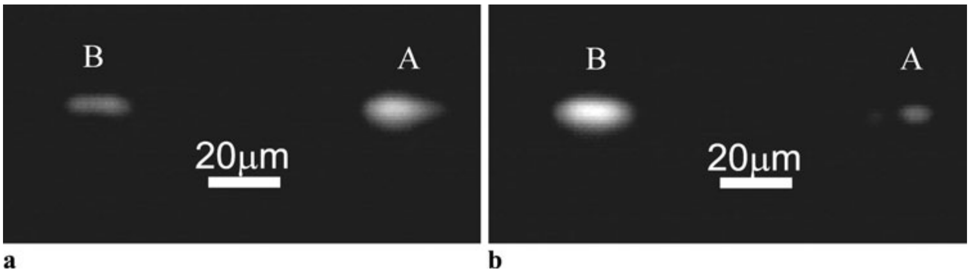

Fig. 7 Near-field intensity profiles of the X-coupler output

was not possible to demonstrate this capability during these initial experiments.

In order to demonstrate the device fabrication functionality of our rapid prototyping method, we chose to fabricate an X-coupler which consists of two straight waveguide channels crossing each other at a specific angle [14].

The waveguides that constitute the X-coupler, a schematic of which is shown in Fig. 6, were fabricated by LIFT depositing titanium metal with an incident laser fluence of 1 $\mathrm{J/cm^2}$ at a writing speed of 2.5 mm/s which, for a laser repetition rate of 250 Hz, corresponds to segment separation of 10 μm. The angle between the two crossing waveguides was kept at a small value (2°) to maximize their overlap.

The coupling ratio was measured at telecom wavelengths (1.55 μm) by coupling light into one of the channels and measuring the power output of each channel on the opposite edge. The coupling ratio (for TM modes) was measured to be ~0.2.

The output edge of the X-coupler was imaged onto an infrared camera and the images are shown in Fig. 7. Figures 7(a) and (b) show the device output when launching light into waveguide A (Fig. 7(a)) and waveguide B (Fig. 7(b)), respectively, as indicated in the mode images. Note that the mode profiles of A and B are not identical indicating an asymmetry in the fabrication of the constituent waveguides. This asymmetry was confirmed by investigation of the waveguides under an optical microscope and was attributed to a slight accidental misalignment of the LIFT apparatus during the deposition process.

3 Conclusions

We have proposed a method for the rapid prototyping of optical waveguide devices which is based on LIFT deposition followed by post processing and have demonstrated the utility of the method by fabricating good quality titanium in-diffused segmented channel waveguides and X-couplers in ferroelectric LN crystals. The preliminary results are encouraging and opens up a route for exploitation of this fabrication process not only as a rapid prototyping tool but also as a waveguide fabrication method to assist in situations where the waveguide propagation constant should change along the waveguide length, repair, or trim existing waveguides by co-doping, deposit overlayers for fine trimming of the waveguide mode, etc. Additionally, the inherent capability of the method to produce segmented waveguides can be used for the fabrication of long period gratings or even for quasi-phasematching of non-linear processes in waveguides by periodic variation of the propagation constant.

Other possibilities include the single-step multi-layer donor deposition process to produce, rare-earth (e.g. Er, Yb, and Nd) doped waveguide structures for optical amplifiers and lasers, and finally the selective deposition and subsequent waveguide fabrication on non-planar or microstructured surfaces which is normally challenging or impossible by conventional methods.

Acknowledgements We gratefully acknowledge the Royal Society for the International Fellowship of Dr. P. Ganguly (No. IIF-2007/R2), the Engineering and Physical Sciences Research Council (EPSRC) for the research funding under grant number EP/C515668, and the financial support of the European Union for funding under the STREP "3-D DEMO".

References

1. J. Bohandy, B.F. Kim, F.J. Adrian, J. Appl. Phys. **60**, 1538–1539 (1986)
2. D.P. Banks, C. Grivas, J.D. Mills, R.W. Eason, I. Zergioti, Appl. Phys. Lett. **89** (2006)
3. D.P. Banks, C. Grivas, I. Zergioti, R.W. Eason, Opt. Express **16**, 3249–3254 (2008)

4. A. Pique, D.B. Chrisey, R.C.Y. Auyeung, J. Fitz-Gerald, H.D. Wu, R.A. McGill, S. Lakeou, P.K. Wu, V. Nguyen, M. Duignan, Appl. Phys. A **69**, S279–S284 (1999)
5. W.A. Tolbert, I.Y.S. Lee, M.M. Doxtader, E.W. Ellis, D.D. Dlott, J. Imaging Sci. Technol. **37**, 411–422 (1993)
6. S. Mailis, I. Zergioti, G. Koundourakis, A. Ikiades, A. Patentalaki, P. Papakonstantinou, N.A. Vainos, C. Fotakis, Appl. Opt. **38**, 2301–2308 (1999)
7. R. Fardel, M. Nagel, F. Nuesch, T. Lippert, A. Wokaun, Appl. Phys. Lett. **91**, 3 (2007)
8. R.C. Alferness, L.L. Buhl, Opt. Lett. **5**, 473–475 (1980)
9. D. Hofmann, G. Schreiber, C. Haase, H. Herrmann, W. Grundkotter, R. Ricken, W. Sohler, Opt. Lett. **24**, 896–898 (1999)
10. R.S. Weis, T.K. Gaylord, Appl. Phys. A **37**, 191–203 (1985)
11. R.G. Hunsperger, *Integrated Optics: Theory and Technology* (Springer, New York, 1982)
12. R. Regener, W. Sohler, Appl. Phys. B **36**, 143–147 (1985)
13. P. Ganguly, C.L. Sones, Y.J. Ying, H. Steigerwald, K. Buse, E. Soergel, R.W. Eason, S. Mailis, J. Light Technol. **27**, 3490–3497 (2009)
14. H. Nakajima, T. Horimatsu, M. Seino, I. Sawaki, IEEE J. Quantum Electron. **18**, 771–776 (1982)

Origin of UV-induced poling inhibition in lithium niobate crystals

H. Steigerwald[1], M. Lilienblum[1], F. von Cube[1], Y. J. Ying[2],
R. W. Eason[2], S. Mailis[2], B. Sturman[3], E. Soergel[1], and K. Buse[1]
[1]*Institute of Physics, University of Bonn,*
Wegelerstraße 8, 53115 Bonn, Germany
[2]*Optoelectronics Research Centre, University of Southampton,*
Southampton, SO17 1BJ, United Kingdom and
[3]*Institute of Automation and Electrometry, 630090 Novosibirsk, Russia*

Abstract

Short-term exposure of the $+z$ face of $LiNbO_3$ crystals to focused UV laser light leads to persistent inhibition of ferroelectric domain reversal at the irradiated area, a phenomenon referred to as "poling inhibition." Different types of crystals (stoichiometric, congruent or Mg-doped ones) are exposed, creating the so-called "latent state" and domain growth during subsequent electric-field poling is visualized. The latent state is robust against thermal annealing up to 250 °C and uniform illumination. With the tip of a scanning force microscope the coercive field is mapped, showing not only the expected resistance against domain reversal in the UV-irradiated region, but also easier poling adjacent to the UV-irradiated section. These results and theoretical estimates point to the following mechanism of poling inhibition: the UV light-induced heating results in a local dip of the lithium concentration, via thermodiffusion. The required charge compensation is provided by UV-excited free electrons/holes. After cooling, the lithium ions become immobile, and the reduced lithium concentration causes a strong local increase of the coercive field in the exposed area, while the increased Li concentration next to this area reduces the coercive field.

PACS numbers: 77.80.Dj; 77.84.Ek; 68.37.Ps

I. INTRODUCTION

Ferroelectric lithium niobate ($LiNbO_3$) is a promising material for photonics because of the ease of fabrication, robustness, and excellent acousto-optic, non-linear, electro-optic, and photorefractive properties.[1,2] Plenty of advanced applications of this crystalline material can be realized employing specially engineered domain structures. The most prominent example is frequency conversion using quasi-phase matching in periodically poled crystals.[3] Sub-µm-sized domain structures have been used for switching and deflecting light,[4,5] and the record highest-density data storage realized on the basis of nm-sized domains.[6] Domain patterns in lithium niobate allow also the creation of photonic micro-components via domain-selective deep etching.[7] Based on this procedure, photonic crystals,[8] ridge-waveguides,[9] and whispering gallery mode resonators[10] have been fabricated.

Fabrication of the desired domain structures in lithium niobate is therefore a demanding issue. Domain reversal can indeed be achieved by application of an electric field that exceeds the coercive field E_c. However, the value of E_c is sensitive to the composition of the crystal.[11–14] In particular, it was found that the coercive field in nearly stoichiometric crystals (SLN) is roughly one order of magnitude smaller compared to that in the usual congruent lithium niobate (CLN), which is characterized by a Li deficiency of about 4 mol%. The Li content has therefore a strong impact on the value of E_c.

The lateral dimensions of ferroelectric domains intended for optical applications are in the range 0.1 to 40 µm. As for the domain depth, several tens of µm are necessary for bulk applications, whereas a few µm may be sufficient for waveguide implementations. In addition, most optical applications require large, up to mm^2-sized, domain patterns. The techniques known for domain patterning still have serious difficulties in fulfillment of these requirements. The most common technique is electric field poling (EFP) using structured electrodes.[15] The minimal domain size is limited here to several µm because of sideways spreading during the growth.[16,17] Auxiliary UV illumination[18–21] and the use of elevated temperatures[22,23] during the EFP procedure give incremental improvements in the domain quality but do not solve this fundamental problem.

A further issue when utilizing lithium niobate for, e.g., second harmonic generation applications is the so-called "optical damage". The use of congruent lithium niobate doped with magnesium (MgCLN) effectively removes this problem.[24] A serious drawback of Mg-

CLN is, however, its poling behavior: sideways domain spreading is even stronger in this material compared to that in CLN, thereby further hindering the fabrication of small-sized bulk domain patterns.

Recently, a new method for domain structuring in lithium niobate – poling inhibition – has been proposed.[25] To achieve poling inhibition (PI), the $+z$ face of a crystal is irradiated with a tightly focused, strongly absorbed UV laser beam. The irradiated locations maintain their polarization during subsequent EFP, indicating that the local coercive field has been significantly increased. Both the lateral width and the depth of the domains generated is on a µm scale.[26] The PI effect was found to be versatile: arbitrary shaped domain structures (dots, lines, circular features, etc.) can be reliably recorded on the $+z$ face.

It is evident that the crystal properties are strongly altered in the UV-irradiated areas, and this changed state of the crystal – referred to as *latent state* – is the cornerstone of the PI phenomenon. The latent state was found to be very stable under ambient conditions – no effect of the time interval between the primary UV irradiation and the subsequent EFP was observed. The aim of this contribution is to understand the mechanism of formation and the properties of this latent state.

The latent state can generally be attributed to structural changes – to local changes of the stoichiometry, of the concentrations of point defects, etc. But it could also be linked to internal space-charge fields caused by UV-induced charge separation. This is why special emphasis will be given to redistribution of species that become mobile under the experimental conditions (lithium ions at high temperatures and UV-excited electron/holes).

II. EXPERIMENTAL METHODS AND RESULTS

A. Samples and poling procedure

Our experiments were carried out with four different samples of lithium niobate: nominally undoped congruent – CLN (Crystal Technology, Inc.), 5 mol% Mg-doped congruent – MgCLN (Yamaju Ceramics Co. Ltd.), stoichiometric – SLN (Oxide Corp.), and 1.3 mol% Mg-doped nearly stoichiometric – MgSLN (Oxide Corp.). The crystals were optical-grade polished; their thickness was 500 µm. The coercive fields of the crystals were $E_c \approx 21\,\mathrm{kV/mm}$ (CLN), ≈ 6.5 kV/mm (MgCLN), ≈ 5 kV/mm (SLN), and ≈ 2.5 kV/mm (MgSLN).

For UV irradiation, we utilized an Ar^+-laser operating at 275 nm; the room temperature absorption coefficient α was more than 1 $\mu\mathrm{m}^{-1}$ for all materials investigated. We estimate this value from the extrapolation of published data using CLN[27,28] and of our own measurements using MgCLN. Note that at higher temperatures, the absorption coefficient increases strongly.[28] The laser beam was focused to a FWHM radius $r \approx 2.5\,\mu\mathrm{m}$, and laser power P ranged from 20 to 55 mW. This corresponds to a UV intensity $I \approx (1 - 2.75) \times 10^5$ W/cm^2. Surface melting was observed at the highest power used. The crystals were mounted on a computer-controlled 2D translation stage allowing writing of laser tracks of several millimeters in length. The typical scanning speed v was about 100 μm/s.

To perform EFP, we used a standard liquid-electrode setup as described in Ref. 21. The applied field was ramped up at 30 V/(mm s) until the domain inversion process started, which was determined by monitoring the poling current and observing the stress-induced birefringence originating from the domain boundaries.[29] We then kept the voltage constant at this level until completion of the poling process. Visualization of the domain patterns was realized by subsequent etching in hydrofluoric acid.

B. Influence of stoichiometry on poling inhibition

Firstly, we consider the influence of the stoichiometry on poling inhibition. Each sample was UV-irradiated at different powers (20 to 55 mW) and subsequently subjected to EFP, followed by examination of the domain patterns. For the congruent samples it was found that PI works well only at $P \approx 35\,\mathrm{mW}$. For the stoichiometric samples, PI was observed only for powers $P > 45\,\mathrm{mW}$, where already strong thermal damage on the crystal surface is induced. It is more difficult therefore to achieve the latent state in stoichiometric crystals compared to congruent ones.

C. Persistence of the latent state

Next, we consider stability of the latent state in the congruent crystals (CLN and MgCLN) under different treatments. Each sample underwent one of three treatments prior to EFP: annealing at temperature $T \approx 250\,^\circ\mathrm{C}$ for one hour, annealing at $T \approx 400\,^\circ\mathrm{C}$ for one hour, and uniform illumination with weakly absorbed UV light at 334 nm for 30 min (intensity

$I \approx 150\,\mathrm{mW/cm^2}$). The chosen annealing temperatures correspond to different charge-transport mechanisms: most likely only protons are relevant at $T \approx 250\,°\mathrm{C}$, whereas Li ions become mobile enough at $T \approx 400\,°\mathrm{C}$ to significantly contribute to the ionic conductivity. It is known also that the photo-conductivity becomes strong in MgCLN upon weakly absorbed UV irradiation with a wavelength of 334 nm, compared to the initial dark conductivity.[30]

TABLE I. Experimental results on the effect of intermediate treatments (annealing and illumination) on poling inhibition.

	1 h @ 250°C	1 h @ 400°C	30 min @ 334 nm
CLN	no effect	elimination	no effect
MgCLN	no effect	elimination	no effect

The influence of the intermediate treatments on PI can be summarized as follows, see also Table I: Annealing at 250 °C as well as the treatment with weakly absorbed UV light do not affect the latent state – poling inhibition occurs just as in non-treated samples. However, the higher-temperature annealing (400 °C) eliminates the latent state – poling inhibition does not occur. This behavior was found to be independent of both the type of crystal used (CLN or MgCLN) and the UV laser power utilized initially to create the latent state.

D. Mapping of the coercive field

Since PI is linked to a local alteration of the coercive field E_c, special efforts were made to examine the spatial distribution of E_c. Visualizing the EFP process allows us to determine the position where poling starts. Interestingly, we noticed that this always occurs right beside the laser-irradiated track. This observation makes us believe that the coercive field is lowered near to the PI area, while the PI area itself, of course, exhibits a larger value of E_c. In order to map even more precisely the spatial distribution of the coercive field, we performed local-poling experiments using a scanning force microscope (SFM).[31] We used a MgCLN crystal where the latent state was inscribed using different laser powers. The crystal had been thinned down by abrading and polishing to a thickness of only 26 µm. Note that the sample was not subjected to any of the intermediate treatments. We applied +100 V to the tip of a SFM while scanning a 5-µm-high stripe, consisting of 64 scanlines, perpendicularly

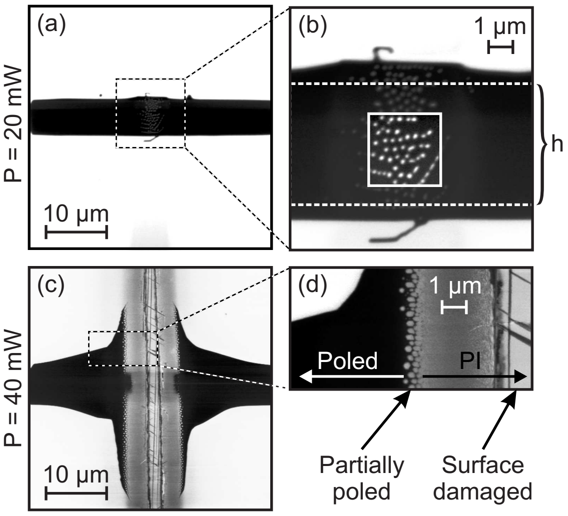

FIG. 1. Piezoresponse force microscope images obtained on MgCLN after locally poling a horizontal stripe of $h = 5$ µm height with the scanning force microscope tip. For the generation of the latent state, vertical laser tracks written with 20 mW (a) and 40 mW power (c) were used. The zoomed image (b) shows the generation of nano poling-inhibited domains within the UV laser-irradiated track. In (d) the formation of nano domains occurs only at the transition region between poled and poling-inhibited area. In the center of the UV-irradiated track the surface is strongly damaged.

to the laser-irradiated track. Because of the electric-field enhancement at the very sharp tip (radius of ≈ 50 nm), such low voltages are sufficient for poling. By subsequent piezoresponse force microscope (PFM) imaging, we were able to map the domain structures generated.

Figure 1 shows PFM images obtained after local poling with the SFM tip across UV-irradiated tracks, written with different laser powers (20 and 40 mW). In Fig. 1(a) the result for the lower power is seen, the laser-irradiated track passing vertically through the center of the image. Basically, two contrast levels can be distinguished: bright for the unpoled area and black for the poled area. Poling with the SFM tip was obviously successful within the full 5-µm-wide stripe, seen as the horizontal black bar. Upon closer inspection (Fig. 1b) it can be seen that the width of the poled area is slightly larger than $h = 5$ µm, thus sideways domain growth has occurred. As for the quality of the poling within the UV-irradiated area, it is found to be imperfect, showing an assembly of nanometer-size features of different contrast indicating local resistance of poling, in effect PI nano-domains. This can be best seen in the area within the white square, where the image contrast was enhanced by image processing software.

For the higher power, $P = 40\,\mathrm{mW}$, the situation is different (Fig. 1c). The image basically shows three contrast levels: bright and dark for the unpoled and the poled areas, respectively, and in addition a grey level along the UV-irradiated track. Figure 1c shows a clear broadening of the SFM-poled region in the vicinity of the UV-irradiated track. Although the SFM-scanned stripe maintained a height of 5 µm along the sample, the width of the actual poled area appeared to be a function of the proximity to the UV-irradiated track. In the meantime, no contrast change could be observed on the UV-irradiated track, which is an indication that no poling occurred there. This poling behavior indicates an increase of the coercive field along the UV-irradiated track. Interestingly, this is accompanied by a coercive field reduction in the adjacent region as indicated by the broadening of the SFM-poled stripe

The PFM signature of the PI area, i.e. the greyish area, needs further description. It can be subdivided in a central part of $\approx 2.5\,\mu\mathrm{m}$ width, showing indications of direct UV laser-induced surface damage, and adjacent 3-µm-wide regions, where the crystal structure was only marginally affected by the laser irradiation, and a transitory, partially poled region where nano domains emerged (Fig. 1d). The depth of the UV laser-inflicted surface damage is of the order of 100 nm.[26] Since the grey level of the PFM image within the UV-irradiated track is rather bright than black, we conclude that also this area has resisted poling; the reduced piezoelectric response results from the surface damage.

III. MODELING OF LITHIUM THERMODIFFUSION

Below, we intend to link the increase of the coercive field in the latent state to a UV-induced change of the lithium concentration. Since CLN crystals possess a large lithium deficiency, Li vacancies must be considered first as migrating species. These vacancies are charged and their concentration, N, can roughly be estimated as $\sim 10^{20}\,\mathrm{cm}^{-3}$ in the initial state.[32] What therefore are (i) the sign and (ii) the value of the concentration change δN in the latent state? These items are our main concern. With δN known, the change of the absolute Li concentration can obviously be evaluated as $\delta N_{\mathrm{Li}} = -\delta N$.

A claim for a perfect agreement between theoretical results and experimental observations would be unrealistic here because of the complexity of the problem and the uncertainty in the values of the main material parameters, especially in the high-temperature range. Our analysis and deductions are therefore a qualitative description of the PI phenomenon plus rough estimates.

Determination of the concentration changes generally splits into two problems. First of all, we need to know the temperature profile $T(\mathbf{r}, t)$ during UV exposure. This problem has been treated theoretically in Ref. 33. The main outcome is that the changes of T are well-localized (within roughly the beam radius r) and follow adiabatically the UV intensity distribution for the actual scanning velocity v. Hence, the characteristic time of the temperature changes is $t_0 = r/v$; it can be estimated as $t_0 \sim 3 \times 10^{-2}\,\mathrm{s}$ for our experimental conditions. As for the peak temperature T_*, it is close to the melting point, about 1450 K.

Next, we should deal with thermo-activated spatial migration of lithium vacancies. The necessary large changes of N are possible only under the condition of a strong charge compensation – otherwise huge electrostatic forces would quickly prevent the spatial changes of N. Free charge carriers (electrons and/or holes) UV-excited via band-to-band transitions best account for the charge compensation. We assert here that the UV-induced free-carrier conductivity exceeds the thermo-activated conductivity caused by Li ions, i.e. migration of lithium vacancies is the bottleneck for the spatial changes of N. The corresponding condition is therefore

$$\frac{\alpha I}{\hbar\omega}\,\mu\tau \gg \frac{eN}{k_B T_*}\,D_{\mathrm{Li}}(T_*)\;, \tag{1}$$

where e is the elementary charge, $D_{\mathrm{Li}} = D_0\,\exp(-E_a/k_B T)$ is the diffusion coefficient for Li vacancies, and $\mu\tau$ is the mobility-lifetime product for free carriers. Despite a rather large spread of the literature data on D_0 and E_a,[34,35] this restriction seems to be safely fulfilled for our experimental conditions.

Importantly, the Maxwell (space-charge field) relaxation time $t_M = \epsilon\epsilon_0\,\hbar\omega/(e\alpha I\,\mu\tau)$, where $\varepsilon\varepsilon_0$ is the permittivity, is expected to be much shorter than the heating time t_0. This means that the space-charge field E_{sc} driven by the pyro-electric effect is strongly compensated by the free carriers. The value of this field can be estimated as $|E_{\mathrm{sc}}| \lesssim (t_M/t_0)\,P_s/\epsilon\epsilon_0 \ll P_s/\epsilon\epsilon_0$, where P_s is the room-temperature value of the spontaneous polarization of lithium niobate.

Consider now the sign of the concentration changes. The whole situation is rather unusual for diffusion phenomena, because the changes are driven by ∇T instead of ∇N. This means that the usual Fick's law is not applicable, and we need to link the flux of lithium vacancies to the strong temperature gradients. This can be done within the standard hopping model, where the probability of a hopping event is proportional to the exponential factor

$\exp(-E_a/k_BT)$.

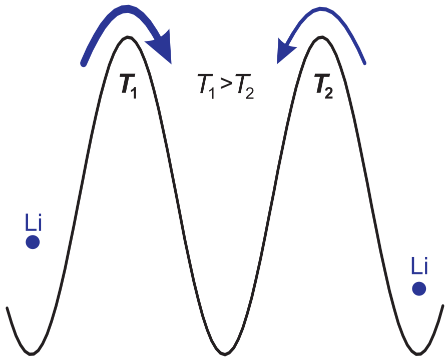

FIG. 2. Illustration of the hopping migration of Li ions, driven by a temperature gradient. Since the temperature T_1 at the left energy barrier is larger than the temperature T_2 at the right barrier, the thermally activated probability for the left ion to hop to the empty central position is larger than that for the right ion. Correspondingly, the vacancies/ions migrate on average to the left/right yielding the necessary direction of the Li flux.

It is not difficult to verify within this model, see also Fig. 2, that the flux of Li vacancies is aligned with the temperature gradient and, correspondingly, the flux of Li ions is opposite to ∇T. This leads to *depletion of lithium* in the illuminated area. The situation would be opposite for migrating interstitial ions.

Within the hopping model, the flux of Li ions, $J_{\rm Li}$, can be evaluated as $J_{\rm Li} = -N\nabla D_{\rm Li} \propto -\nabla T$. The change of the absolute Li concentration can now be estimated from the continuity equation $\partial \delta N_{\rm Li}/\partial t + \nabla J_{\rm Li} = 0$, which gives $|\delta N_{\rm Li}|/N \sim t_0\,(D_{\rm Li}/w^2)\,(E_a/k_BT_*)$. By setting $E_a = 1.4\,\mathrm{eV}$ (Ref 35), $D_0 = 0.1\,\mathrm{cm}^2/\mathrm{s}$ (Ref 35), $r = 2.5\,\mu\mathrm{m}$, we obtain $\delta N_{\rm Li}/N \sim 1$. The accuracy of this rough estimate is probably within one order of magnitude. Anyhow, it shows that the concentration changes during the UV exposure are high enough to provide a strong poling inhibition. By going into more detail, one can make sure that the UV-induced reduction of $N_{\rm Li}(r)$ at the beam center is accompanied by a noticeable increase at the beam periphery. This comes just from the fact that the lithium ions pushed out of the central region cannot go far away from it. Note that evaporation of lithium through the surface is neglected in our model as this potentially competitive process is characterized by a considerably larger activation energy.[35]

The pyroelectrically driven space-charge field $E_{\rm sc}(t)$, which is positive during the cooling stage and nonzero after this stage, additionally provides a shift of the depletion area to the crystal depth and non-equivalence of the $+z$ and $-z$ faces of the crystal. The value of the shift is controlled by the $\mu\tau$ product which cannot be reliably estimated at $T \approx T_*$.

IV. DISCUSSION

To begin with, we consider whether the latent state can be associated with the space-charge fields recorded during the UV irradiation, the mechanism of PI that was initially suggested.[25] Our experiments, however, allow us to exclude this hypothesis: During the annealing at 250 °C the hydrogen ions become mobile, and space-charge fields would be compensated within a few minutes via the ionic conductivity.[36] A similar fast compensation would occur during the illumination with weakly absorbed UV light which, as is known, causes a strong photo-conductivity in MgCLN.[30] Since poling inhibition is insensitive to these two intermediate treatments, it cannot be linked to space-charge fields.

We therefore turn to the explanation of the experimental data on PI by changes of the lithium concentration. According to the above estimates, these changes can be strong after the primary UV irradiation.

The absence of any effect of the above-mentioned two of three intermediate treatments on the latent state now looks understandable – these treatments do not make lithium ions mobile. However, heating to 400 °C is sufficient to activate diffusion of Li vacancies and to allow the Li ion concentration to become more evenly distributed during the one-hour annealing procedure.

The presence of a pronounced depletion of lithium in the latent state is furthermore sustained by the fact that the UV-irradiated tracks are found to act as channel waveguides.[37] From the studies of the mode profiles it is possible to evaluate the refractive index changes.[38] The latter can be directly linked to the Li depletion[39] which can be estimated as 4 mol%. This number is in reasonable agreement with the results of Section III.

How strong is the impact of the lithium content on the coercive field E_c? This can be assessed from Fig. 3 that is based on literature data.[11–14] One sees that the coercive field strongly increases with decreasing lithium concentration, and the rate of this increase can be evaluated as ≈ 10 kV/mm per 1 mol%. The UV-induced depletion of lithium can lead to a strong increase of E_c and, consequently, to poling inhibition.

The data on local poling, represented by Fig. 1, gives further insight into the physical

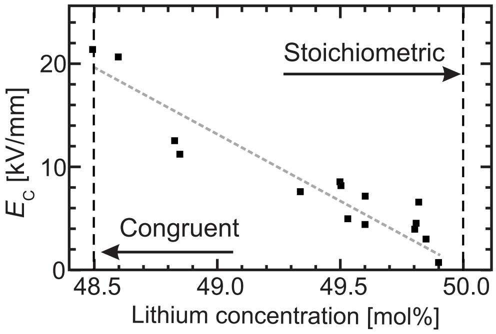

FIG. 3. Dependence of the coercive field E_c on the degree of stoichiometry of lithium niobate crystals (lithium concentration: $\mathrm{Li}/(\mathrm{Li}+\mathrm{Nb})$). The dots are taken from the literature[11–14], and the dashed line is a linear fit. Note that due to a different manufacturer of the SLN or different determination methods of E_c, values for SLN differ from our measured value of 5 kV/mm

mechanism responsible for PI. Two features are worthy of mentioning at the lower UV power range (20 mW): The first one is a broadening of the poled (black) area compared to the scanned one, see Fig. 1b. It is caused by sideways spreading of domains during the growth; this effect is well known in EFP, and it is even more pronounced when applying the electric field through a sharp tip since the field distribution is strongly non-uniform. The second feature is a slight deterioration of the poling quality within the UV-irradiated area, which manifests itself in numerous bright spots best seen in Fig. 1b. It can be attributed to statistically distributed PI nano-domains that emerge in regions where E_c is only slightly increased when compared to the untreated crystal.

In the case of irradiation with higher UV laser power (40 mW) the situation is very different, see Fig. 1c. The poled stripe is interrupted when crossing the laser track area and no poling occurs here. The transition from the poled to unpoled areas is not abrupt, it occurs via an intermediate state with a partial poling, see Fig. 1d. This state is similar to that shown in Fig. 1b, which indicates again a slight increase of E_c. The SFM-poled horizontal stripe experiences extensive broadening when approaching the vertical laser track. Obviously, sideways spreading of the domains is facilitated in this region. This can easily be attributed to the presence of an increase of the lithium concentration at the laser track periphery, mentioned in Section III: The coercive field is lowered in this area facilitating the sideways spread of the SFM-poled domain area beyond the nominally scanned region.

V. CONCLUSION

We have investigated, both experimentally and theoretically, the physical mechanism behind poling inhibition in undoped and Mg-doped lithium niobate crystals. The results obtained point to the following mechanism of the poling inhibition phenomenon: Strong local heating of the crystal surface by UV light leads, via thermodiffusion of Li vacancies, to a local reduction of the Li concentration and, correspondingly, to a strong local increase of the coercive field. The necessary charge compensation is provided by UV-excited charge carriers. The latent state with lowered Li concentration is responsible for the observed poling inhibition as it implies a local increase of the coercive field.

Acknowledgement: Financial support from the Deutsche Forschungsgemeinschaft, the EU (in the framework of the STREP033297 3D-DEMO) and the Deutsche Telekom AG is gratefully acknowledged.

---

[1] L. Arizmendi, Phys. Status Solidi A **201**, 253 (2004).

[2] R. S. Weis and T. K. Gaylord, Appl. Phys. A **37**, 191 (1985).

[3] M. M. Fejer, G. A. Magel, D. H. Jundt, and R. L. Byer, IEEE J. Quantum Elect. **28**, 2631 (1992).

[4] D. A. Scrymgeour, A. Sharan, V. Gopalan, K. T. Gahagan, J. Casson, R. Sander, J. M. Robinson, F. Muhammad, P. Chandamani, and F. Kiamilev, Appl. Phys. Lett. **81**, 3140 (2002).

[5] A. J. Boyland, S. Mailis, J. M. Hendricks, P. G. R. Smith, and R. W. Eason, Opt. Commun. **197** 193 (2001)

[6] Y. S. Cho, K. Fujimoto, Y. Hiranaga, Y. Wagatsuma, A. Onoe, K. Terabe, and K. Kitamura, Appl. Phys. Lett. **81**, 4401 (2002).

[7] I. E. Barry, G. W. Ross, P. G. R. Smith, R. W. Eason, and G. Cook, Mater. Lett. **37**, 246 (1998).

[8] N. G. R. Broderick, G. W. Ross, H. L. Offerhaus, D. J. Richardson, and D. C. Hanna, Phys. Rev. Lett. **84**, 4345 (2000).

[9] I. E. Barry, G. W. Ross, P. G. R. Smith, and R. W. Eason, Appl. Phys. Lett. **74**, 1487 (1999).

[10] Y. J. Ying, C. L. Sones, A. C. Peacock, F. Johann, E. Soergel, R. W. Eason, M. N. Zervas, and

S. Mailis, Opt. Express **18**, 11508 (2010).

[11] V. Gopalan, T. Mitchell, Y. Furukawa, and K. Kitamura, Appl. Phys. Lett. **72**, 1981 (1998).

[12] V. Bermudez, L. Huang, D. Hui, S. Field, and E. Dieguez, Appl. Phys. A **70**, 591 (2000).

[13] S. Ganesamoorthy, M. Nakamura, S. Takekawa, S. Kumaragurubaran, K. Terabe, and K. Kitamura, Mat. Sci. Eng. B **120**, 125 (2005).

[14] W. Yan, Y. Kong, L. Shi, L. Sun, H. Liu, X. Li, D. Zhao, J. Xu, S. Chen, L. Zhang, Z. Huang, S. Liu, and G. Zhang, J. Phys. D **39**, 21 (2006).

[15] M. Yamada, N. Nada, M. Saitoh, and K. Watanabe, Appl. Phys. Lett. **62**, 435 (1993).

[16] C. Baron, H. Cheng, and M. Gupta, Appl. Phys. Lett. **68**, 481 (1996).

[17] K. Nakamura, J. Kurz, K. Parameswaran, and M. M. Fejer, J. Appl. Phys. **91**, 4528 (2002).

[18] A. Fujimura, T. Sohmura, and T. Suhara, Electron. Lett. **9**, 719 (2003).

[19] M. C. Wengler, B. Fassbender, E. Soergel, and K. Buse, J. Appl. Phys. **96**, 2816 (2004).

[20] M. Fujimura and T. Suhara, Advances in Opto-Electronics **2008**, 421054 (2008).

[21] H. Steigerwald, F. Luedtke, and K. Buse, Appl. Phys. Lett. **94**, 032906 (2009).

[22] C. C. Battle, S. Kim, V. Gopalan, K. Barkocy, M. C. Gupta, Q. X. Jia, and T. E. Mitchell, Appl. Phys. Lett. **76**, 2436 (2000).

[23] H. Ishizuki, I. Shoji, T. Taira, Appl. Phys. Lett. **82**, 939 (2003).

[24] D. A. Bryan, R. Gerson, and H. E. Tomaschke, Appl. Phys. Lett. **44**, 847 (1984).

[25] C. L. Sones, A. C. Muir, Y. J. Ying, S. Mailis, R. W. Eason, T. Jungk, A. Hoffmann, and E. Soergel, Appl. Phys. Lett. **92**, 072905 (2008).

[26] F. Johann, Y. J. Ying, T. Jungk, A. Hoffmann, C. L. Sones, R. W. Eason, S. Mailis, and E. Soergel, Appl. Phys. Lett. **94**, 172904 (2009).

[27] B. M. Jin, I. W. Kim, W. B. White, and A. S. Bhalla, Mater. Lett. **30**, 385 (1997).

[28] D. Redfield and W. Burke, J. Appl. Phys. **45**, 4566 (1974).

[29] V. Gopalan, Q. Jia, and T. Mitchell, Appl. Phys. Lett. **75**, 2482 (1999).

[30] M. C. Wengler, U. Heinemeyer, E. Soergel, and K. Buse, J. Appl. Phys. **98**, 064104 (2005).

[31] B. J. Rodriguez, R. J. Nemanich, A. Kingon, A. Gruverman, S. V. Kalinin, K. Terabe, X. Y. Liu, and K. Kitamura, Appl. Phys. Lett. **86**, 012906 (2005).

[32] A. Briat, V. G. Grachev, G. I. Malovichko, O. F. Schirmer, and M. Whlecke, *Photorefractive Materials and Their Applications 2* (Springer, New York, 2007).

[33] A. C. Muir, G. J. Daniell, C. P. Please, I. T. Wellington, S. Mailis, and R. W. Eason, Appl.

Phys. A **83**, 389 (2006).

[34] A. Mehta, E. K. Chang, and D. M. Smyth, J. Mater. Res. **6**, 851 (1991).

[35] D. P. Birnie, J. Mater. Sci. **28**, 302 (1993).

[36] K. Buse, S. Breer, K. Peithmann, S. Kapphan, M. Gao, and E. Krätzig, Phys. Rev. B **56**, 1225 (1997).

[37] S. Mailis, C. Riziotis, I. T. Wellington, P. G. R. Smith, C. B. E. Gawith, and R. W. Eason, Opt. Lett. **28**, 1433 (2003).

[38] P. Ganguly, C. L. Sones, Y. J. Ying, H. Steigerwald, K. Buse, E. Soergel, R. W. Eason, and S. Mailis, J. Lightwave Technol. **27**, 3490 (2009).

[39] Y. Korkishko and V. Fedorov, IEEE J. Sel. Top. Quant. **2**, 187 (1996).